Metallic Materials with High Structural Efficiency

NATO Science Series

A Series presenting the results of scientific meetings supported under the NATO Science Programme.

The Series is published by IOS Press, Amsterdam, and Kluwer Academic Publishers in conjunction with the NATO Scientific Affairs Division

Sub-Series

I. Life and Behavioural Sciences	IOS Press
II. Mathematics, Physics and Chemistry	Kluwer Academic Publishers
III. Computer and Systems Science	IOS Press
IV. Earth and Environmental Sciences	Kluwer Academic Publishers
V. Science and Technology Policy	IOS Press

The NATO Science Series continues the series of books published formerly as the NATO ASI Series.

The NATO Science Programme offers support for collaboration in civil science between scientists of countries of the Euro-Atlantic Partnership Council. The types of scientific meeting generally supported are "Advanced Study Institutes" and "Advanced Research Workshops", although other types of meeting are supported from time to time. The NATO Science Series collects together the results of these meetings. The meetings are co-organized bij scientists from NATO countries and scientists from NATO's Partner countries – countries of the CIS and Central and Eastern Europe.

Advanced Study Institutes are high-level tutorial courses offering in-depth study of latest advances in a field.
Advanced Research Workshops are expert meetings aimed at critical assessment of a field, and identification of directions for future action.

As a consequence of the restructuring of the NATO Science Programme in 1999, the NATO Science Series has been re-organised and there are currently Five Sub-series as noted above. Please consult the following web sites for information on previous volumes published in the Series, as well as details of earlier Sub-series.

http://www.nato.int/science
http://www.wkap.nl
http://www.iospress.nl
http://www.wtv-books.de/nato-pco.htm

Series II: Mathematics, Physics and Chemistry – Vol. 146

Metallic Materials with High Structural Efficiency

edited by

Oleg N. Senkov

UES Inc., Dayton, OH, U.S.A.

Daniel B. Miracle

Air Force Research Laboratory,
Materials and Manufacturing Directorate,
Wright-Patterson Air Force Base, OH, U.S.A.

and

Sergey A. Firstov

Frantcevich Institute for Problems of Materials Science,
National Academy of Science of Ukraine, Kiev, Ukraine

Created in the United States of America

Visit Springer's eBookstore at: http://www.ebooks.kluweronline.com
and the Springer Global Website Online at: http://www.springeronline.com

Contents

PREFACE

In the fall of 1998, Prof. Sergey Firstov invited me to the Frantcevych Institute for Problems of Materials Science (IPMS) in Kyiv, Ukraine to discuss possible collaborations in the area of advanced metals research. During this visit, a strong mutual interest was evident in a broad range of structural metals technologies, and a quick friendship was established. Countless subsequent emails and a reciprocal visit to the U.S Air Force Research Laboratory by Prof. Firstov and a team of scientists from IPMS ensued to discuss and detail a broad collaboration in the area of structural metals. Two years after the initial visit, a major investment by the U.S. Air Force Office of Scientific Research (AFOSR) was established to pursue the technologies defined by these interactions.

The annual reviews of the AFOSR Ukrainian Metals Initiative were held in late May, a most beautiful time in Kyiv when the lilacs are in bright display and the air is scented with the smell of falling blossoms from the chestnut trees that line the major streets and many parks. The sunny days and mild evenings provide a welcome break from winter, and on weekend evenings festive crowds spill onto the Khreshchatyk, Kyiv's downtown boulevard, to listen to street musicians, watch jugglers and comedians, or simply to celebrate with friends. The annual reviews featured long days of intensive discussion of technical progress, followed in the evenings by the warm hospitality of the Ukrainian hosts. Discussions over dinner often centered on the future of structural metallic materials, and promising new ideas for significant technological advancements were explored and debated.

The idea for this Workshop was first suggested by Sergey Firstov during one of these dinnertime discussions on a mild Kyiv evening when Dr. Oleg Senkov and I visited IPMS in May 2002. The idea quickly blossomed into a working reality, and the eventual success of this NATO Advanced Research Workshop was the result of a coordinated and dedicated effort from a large team of contributors. As Co-Directors of the Workshop, Dr. Oleg Senkov and Prof. Sergey Firstov provided the broad scope and directions of the technical content, as well as selecting the venue and dates. Oleg Senkov accepted many of the day-to-day responsibilities, and his exceptional dedication and energy ensured the successful organization and completion of the seemingly endless details that accompany an undertaking of this magnitude. The International Program Committee included Drs. Sergey Firstov, George Frommeyer, Orest Ivasishin, Daniel Miracle, Andreas Mortensen, Oleg Senkov, and Robert Varin. These individuals contributed important details to the technical program and ensured that the Workshop participants included an international cadre of leaders. Accommodations,

poster sessions, conference banquets and the social programme were made possible through the efforts of the Local Program Committee, whose members included Drs. Oleksander Vasylyev, Leonid Kulak and Valentyna Avdeyeva. Operational details during the conduct of the Workshop were ably handled by the Workshop Secretariats, Oleksander Koval and Kelly Brown. A host of vital contributions, including computer support and poster set-up, was provided by a team from IPMS. Of course, the efforts of the Workshop participants in writing, reviewing and revising manuscripts for this book constituted a major effort and contribution. It is hoped that this Proceedings will become an excellent reference for graduate students, engineers and scientists working in this area.

The Workshop was held on 7-12 September 2003. The Hotel Jerelo, situated in the scenic wooded Puscha-Vodytcya resort area just north of Kyiv, was the site of the Workshop. Attendance was strong, drawing 50 scientists from 14 countries. Nearly one quarter of the scheduled time was devoted to discussion, which was robust and drew active participation from the full body of participants. A social programme, which included a welcome reception, a banquet with traditional Ukrainian musicians, an excursion to scenic and historic sites in Kyiv, and a farewell banquet at the close of the technical programme, provided opportunities for the participants to establish personal relationships and to discuss specific details of the research in a relaxed atmosphere. These interactions, along with the natural warmth of the Ukrainian hosts, provided the foundation for the successful achievement of the Workshop objectives. A follow-on NATO Workshop on this topic in two years was suggested to provide an on-going international forum for the interchange and discussion of research in this active scientific field.

Dr. Daniel B. Miracle
Senior Scientist and Group Leader
Air Force Research Laboratory, Materials and Manufacturing Directorate
Wright-Patterson Air Force Base, OH, USA

INTRODUCTION

This Proceedings contains the principle research papers presented at the first international scientific workshop devoted to the conception, development and application of metallic materials with high specific strength and high specific stiffness, or high structural efficiency. The Workshop topic, "Metallic Materials with High Structural Efficiency," encompasses the scientific foundation necessary to produce and control properties through control of composition, processing and microstructure, and also addresses the current state of development of such materials as well as the conception of new metallic materials with high structural efficiency. Although metallic materials with high structural efficiency are used in all segments of industry, requirements by the aerospace industry dominate, and this is reflected in the Workshop presentations.

The major themes in the technical programme of the Workshop included fracture toughness and plasticity; relationship between plasticity, strength and fracture toughness; mechanical behavior; mechanisms of strengthening and toughening; and relationships between microstructure and properties. Primary and secondary processing techniques required to produce metallic materials with high structural efficiency were explicitly discussed in a number of talks. Major metallic materials systems covered in the presentations included nanocrystalline and quasicrystalline materials, amorphous metals, ultra fine-grained materials, advanced aluminum, magnesium, titanium and refractory alloys, and metal matrix composites. Metallic materials spanning the full spectrum maturity were considered, including conventional metals, advanced metals, and revolutionary technologies based on nanocrystalline, quasicrystalline and amorphous metals. A strong emphasis on producing and controlling features at length scales of tens to hundreds of nanometers was evident in the talks. High structural efficiency was discussed for applications that spanned the range from cryogenic to ultra-high temperatures.

An overview introducing and defining the topic of high structural efficiency was provided (Miracle, USA), which described the needs for such materials, the opportunities enabled by application of these materials, technical objectives, and candidate technologies. A comprehensive description of specific technical approaches was presented, including an historical view and new opportunities (Firstov, Ukraine). The functions of component design and certification are typically isolated from the processing and development of new materials. The need to fully integrate component design and materials development functions was presented (Hartley, USA). Efforts now underway in the international community to establish new modeling and simulation methods to accelerate the

development of new materials, and computational tools to integrate materials development with component design were described and discussed.

A strong international effort on severe plastic deformation (SPD) to produce metallic materials with exceptionally high specific strength was represented in the presentations and discussions. An overview of SPD processes (Stuwe, Austria) described the general strain paths that lead to high strength and good ductility via dramatic refinement of the microstructure. Equal-channel angular extrusion (ECAE) as an effective method for grain refinement and powder consolidation was described in several presentations (Valiev, Russia; Hartwig, USA; Shagiev, Russia). Production of sub-micron grain sizes by forging in three orthogonal directions (Salishchev, Russia) was also described and discussed.

A theme of nanocrystalline, quasicrystalline and amorphous microstructures was evident in many of the talks in the Workshop. The key challenges in developing nanostructured metallic systems and the current status in the understanding of structure-property relationships in these materials were summarized and discussed (Subramanian, USA; Valiev, Russia; Radnoczi, Hungary). Use of nanostructured light-weight based compounds for hydrogen storage was overviewed (Varin, Canada).

Recent data were also presented for a broad range of metallic materials systems with high structural efficiency, including alloys based on Al (Mortensen, Switzerland; Milman, Ukraine; Senkov, USA; Cavaliere, Italy; Shagiev, Russia; Parilak, Slovak Republic), Mg (Sklenicka, Czech Republic; Varin, Canada), Ti (Frommeyer, Germany; Bulanova, Ukraine; Firstov, Ukraine; Gornaya, Ukraine; Vasylyev, Ukraine; Molyar, Ukraine), and refractory metals (Frommeyer, Germany; Mendiratta, USA; Menon, USA; Gimeno-Fabra, Germany). A significant emphasis was provided on titanium alloys modified with the addition of eutectic-forming elements B or Si. In addition to information in overviews on this new class of titanium alloys (Frommeyer, Germany; Bulanova, Ukraine), the unique microstructures, property, and fracture characteristics were developed (Vasylyev, Ukraine; Velikanova, Ukraine), and the properties of the refractory silicide compounds were given (Frommeyer, Germany). New developments in the infiltration of ceramic preforms to produce metal matrix composites (MMCs) with a high volume fraction of ceramic reinforcements, and hence high specific stiffness, while simultaneously achieving good ductility and toughness, were presented (Mortensen, Switzerland).

Additional topics relating to the theme of metallic materials with high structural efficiency included phase reactions and equilibria in relevant systems (Bulanova, Ukraine), fundamental mechanisms of dynamic recovery and recrystallization (Leffers, Denmark; Montheillet, France), joining by friction stir welding (Jata, USA), production of cellular metals (Sanders, USA) and

advanced materials characterization (Rustichelli, Italy). Primary metal processing methods such as electron beam melting (Zamkov, Ukraine) and the new process of magnetically controlled electroslag melting (Kompan, Ukraine) were also described and discussed.

Discussion amongst the participants spanned the full range of material presented. Particularly strong discussions covered the mechanisms of deformation in nanocrystalline metals, assessing the balance between grain boundary accommodation and dislocation glide. While high specific strength and stiffness were the theme of presentations, discussions expanded on the need for a broad range of properties such as ductility, fracture toughness, corrosion resistance and affordability in the same material. In the final discussion session of the Workshop, much of the time was spent evaluating the need for a strong balance between application-driven research and curiosity-driven research. Curiosity-driven research was felt to be essential to the vitality of the scientific endeavor, since it was felt that truly major innovations typically come from such efforts. The motivation for application-driven research was discussed to be the accelerated development of materials. Improved communication with the materials design community was acknowledged as essential for the timely insertion of new metals technologies, and specific methods for achieving this integration across disciplines was discussed. Although an extensive thermo-physical database will be required to support the intensive modeling necessary for rapid materials development, funding for such research was felt to be difficult to obtain in many countries.

The objectives of this Workshop, to present and discuss new results in the development and processing of metallic materials with high structural efficiency and to establish new interactions and networks between the participants, were successfully met. A number of new developments were presented and discussed at this Workshop, including recent information on titanium alloys modified with relatively small amounts of B and Si to provide dramatic improvements in strength and stiffness, and new Al alloys strengthened with quasicrystalline precipitates for good elevated temperature properties. In addition, a current extensive update on severe plastic deformation and on nanocrystalline metals for structural applications was provided.

Frantcevych Institute for Problems of Materials Science. Together, the financial contributions from these sponsors enabled a highly successful Workshop.

Oleg N. Senkov and Sergey A. Firstov
NATO ARW Co-Directors

PART 1

GENERAL OVERVIEWS

OPPORTUNITIES AND APPROACHES FOR DOUBLING THE STRUCTURAL EFFICIENCY OF METALLIC MATERIALS

Daniel B. Miracle
Materials & Manufacturing Directorate, Air Force Research Laboratory, Dayton, OH USA

Abstract: Significant reduction in system mass is required to achieve advanced aerospace objectives such as hypersonic flight, improved fuel efficiency and low cost access to space. The general needs for metallic materials with high structural efficiency will be outlined here, and current approaches for achieving significant improvements in specific strength and stiffness will be described.

Key words: structural efficiency; metal matrix composite; amorphous metals, superhigh strength Al, nanocrystalline metals, Ti-B alloys

1.   INTRODUCTION

Changing priorities in the aerospace industry have revitalized interest in structural metals with high specific strength and high specific stiffness. These are the two most pervasive material characteristics in aerospace systems, controlling system configuration and the size and spacing of nearly every structural component. Since system mass controls the ability to achieve advanced aerospace objectives such as hypersonic flight, global range and trans-atmospheric missions, structural weight is an enabling consideration. Thus, metallic materials with high structural efficiency can provide *enabling capabilities* through structural minimization. Although advanced methodologies in system design and assembly, such as unitized construction, can also contribute to structural minimization, these techniques typically rely upon

3

components with highly stressed multi-axial local loading, so that materials with high structural efficiency are required. Unitized construction has been achieved with graphite/epoxy systems, and the higher cost of graphite/epoxy materials and processing has been offset by the savings obtained via unitized construction. However, this approach has not been widely practiced with current metallic materials due to their lower specific properties. Metallic materials with high specific properties will therefore improve *affordability* by reducing the number of parts, and hence the significant cost associated with assembly, in aerospace systems. These materials are also enabling for the expanding emphasis on the utilization of *space*, and can provide *performance improvements* in existing aerospace systems by decreasing weight.

Over the past 20 years, research and development of aerospace metals has emphasized alloys for use at the highest operating temperatures. Research on metals with *higher structural efficiency*– to provide compelling improvements in specific strength and specific stiffness at more moderate temperatures– has declined dramatically during this period, even though the need for such materials has become acute. In many advanced systems, such as hypersonic and global transport vehicles, advanced liquid fuel rocket engines, and unmanned aerospace vehicles, dramatic reduction in structural mass is an enabling requirement. While organic matrix composites (OMCs) are often proposed extensively in the concept phase for such systems, designs for initial construction nearly always demand a higher fraction of metallic materials to satisfy additional requirements such as elevated temperature use, environmental stability, compatibility with aggressive fluids and gases or cost. Finally, metallic materials with high structural efficiency can provide dramatic performance improvements and a competitive advantage in commercial air and ground transportation, sports and recreation and medical applications. Metallic materials with higher structural efficiency are therefore a pervasive, foundational technology, with broad impact in the transportation and related industries.

OMCs, such as graphite/epoxy, provide the highest structural efficiency of current aerospace materials (Figure 1(a)). Aligned composites where the applied stress is parallel to the reinforcements (0°) provide the best response, but this same material subjected to a transverse load (90°) provides the poorest structural efficiency. Thus, both the best and the worst properties exist simultaneously in axially reinforced composites, and this is represented in Figure 1(a) by enclosing the 0° and 90° properties within a dotted envelope. Opportunities to best utilize these materials are limited to components where the stresses are primarily uniaxial, restricting the overall impact of this technology. Laminate technology has dramatically expanded the pervasiveness of OMCs by providing tailorable in-plane properties. In-plane isotropy is obtained by producing cross-ply quasi-isotropic (Q/I)
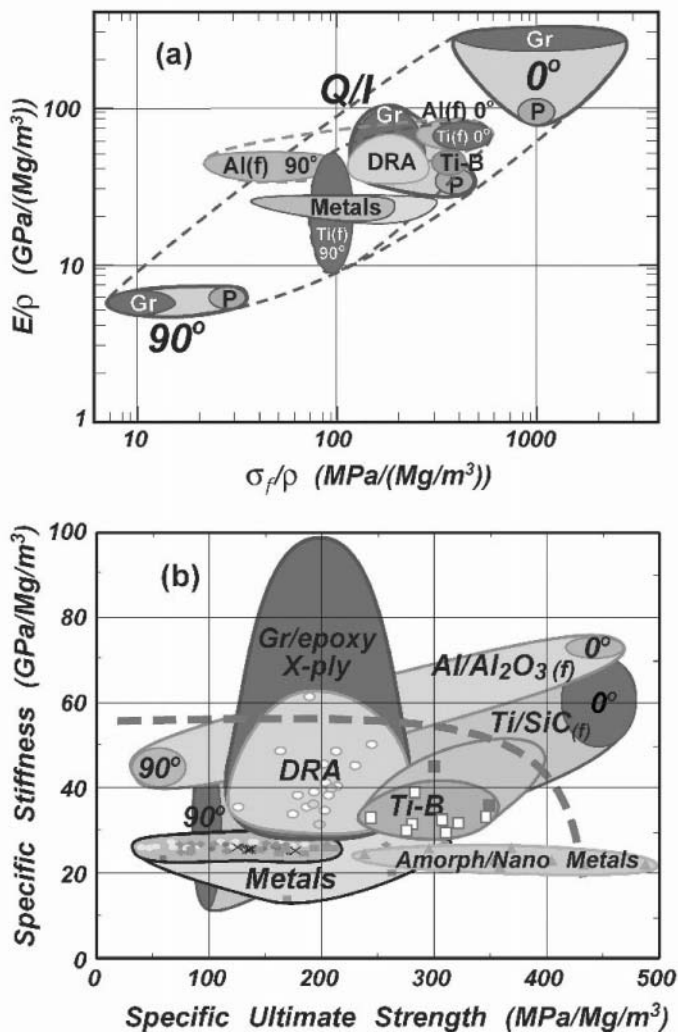
Figure 1. Specific ultimate tensile strength vs. specific stiffness of current and developmental aerospace structural materials. Data are displayed on a log-log plot in (a), where *P* signifies PAN-based reinforcements; *Gr* represents graphite fibers; *0°* and *90°* indicate data collected parallel to and transverse to the fiber direction in uniaxial composites, respectively; and *Q/I* represents quasi-isotropic laminates. The *(f)* represents fiber reinforcements in MMCs. The dashed line in (b) represents the combinations of specific strength and stiffness that are double those of conventional metal alloys.

laminates, where the specific strength and stiffness are higher than commonly used metallic materials (Figure 1). The high raw material and processing cost associated with graphite/epoxy have led to a high degree of

integration between component design, material specification and processing, and this has enabled unitized design and construction. Graphite/epoxy cross-plied laminates provide the state-of-the-art benchmark against which competing structural metallic technologies must be compared.

Although the transverse properties of continuously reinforced MMCs are significantly better than for aligned graphite/epoxy, the axial specific strengths and stiffnesses fall well below those of aligned graphite/epoxy. A similar situation is observed for structural materials with quasi-isotropic properties. Although a small number of specialty metals, such as β-Ti and ultra-high strength steels, possess specific strengths that are equivalent or superior to cross-plied graphite/epoxy, their specific stiffnesses are significantly poorer. Thus, metallic materials will not compete with OMCs when high structural efficiency alone is the only selection criterion. However, structural materials typically require secondary characteristics that enable the primary function to be achieved. These secondary requirements include full three-dimensional isotropy and compatibility with aggressive environments, such as cryogenic fuels and oxidizers, high-pressure hydraulic fluid, jet fuel and high temperature oxidizing and corrosive gases. Orbital systems require stability in high vacuum, and resistance to atomic oxygen and ultraviolet and ionizing radiation exposure. Fracture resistance, erosion resistance, resistance to ballistic impact and general damage tolerance are another important class of secondary characteristics. Other desired characteristics include ability to support high bearing loads, isotropic thermal and electrical properties, manufacturability into a range of shapes and good supportability. Finally, cost of manufacture is a dominant consideration. Metallic materials provide superior response relative to OMCs in nearly every one of these categories.

A comparison of the efficiency of most common structural materials is shown in Figure 1. The restricted envelope of conventional aerospace metals is enlarged by specialty alloys based on β-Ti or ultra high strength steels. Initial data for advanced amorphous and nanocrystalline metals are shown, along with a new class of alloys based on the titanium-boron system. While discontinuously reinforced Al (DRA) competes with some graphite/epoxy laminates, and some specialty metals possess superior specific strength, cross-plied graphite/epoxy nevertheless possesses a superior balance of structural efficiency relative to conventional metals. The development of isotropic metals technologies with double the structural efficiency of conventional metal alloys allow metals to compete more broadly with OMCs, and this objective is indicated in Figure 1(b) by the dashed line. Isotropic metals technologies with both double the specific strength and specific stiffness will provide a particularly compelling benefit over cross-plied graphite/epoxy composites.

Critical analysis of past and current research provides promising approaches for achieving high structural efficiency in metallic materials. Discontinuously reinforced metal matrix composites provide significant improvements in specific stiffness with a modest improvement in specific strength. The exploration of novel hybrid composites using both discontinuous and continuous reinforcements is also underway. A new class of superhigh strength Al alloys is now being developed for use at cryogenic temperatures, and related concepts may provide a credible approach for achieving good properties at temperatures of 200°C and above. Initial concepts and data in a new family of alloys based on the titanium-boron system have shown simultaneous significant increases in both specific strength and specific stiffness. Amorphous and nanocrystalline metals provide specific strengths more than double the values of current metallic materials. Microstructural quantification provides an important tool for extending the specific properties of discontinuously reinforced metals. A brief summary of the current status in each of these approaches is provided in the following sections.

2. CANDIDATE METALS TECHNOLOGIES

2.1 Metal Matrix Composites

Metal matrix composites (MMCs) are an established technology [1, 2]. In 1999, the world market was over 2500 metric tons valued at over $100M, with broad applications in the ground transportation (auto and rail), aerospace, thermal management, industrial and recreation markets [1]. Attractive characteristics include very good specific strength and stiffness; tailorable strength, stiffness, coefficient of thermal expansion (CTE) and thermal conductivity, and excellent wear resistance. Discontinuously reinforced MMCs also provide isotropic properties and moderate cost. A wide range of primary and secondary processes, finishing, joining and inspection techniques have been established, and allow use of existing infrastructure from the metals industry. While MMCs are now broadly applied and represent an important established class of metallic materials, a dramatic expansion of applications is expected from the significant additional improvements, which are still available in this relatively new class of materials.

Discontinuously-reinforced Al (DRA) provides specific strengths equivalent to the best cross-plied OMCs, and has specific stiffnesses that

compete with the lower range offered by OMCs (Figure 1). A wide range of applications are now established in the automotive [3], aeronautical [4], space [5], thermal management [6] and recreational [7] industries. More extensive utilization of DRA for structural applications is expected to follow improvements in the structural efficiency of these materials.

Higher specific stiffness is easily achieved in DRA by increasing the reinforcement volume fraction, *f*, to values as high as 55-70%. However, the fracture properties of DRA– ductility, toughness, and fatigue–are currently insufficient for structural use above a reinforcement volume fraction of about 20%. Phenomenological observations have implicated the particulate distribution in setting this limit. At present, there is a rather poor understanding of the influence of particulate distribution on the fracture properties of discontinuously reinforced metals. However, recent studies have shown a direct relationship between a homogeneous length scale [8] and the amount of ductility in DRA [9]. DRA with 25% by volume of SiC particulate reinforcement was processed with controlled levels of homogeneity. Room temperature tensile elongations ranged from ~4% in the most clustered condition to ~16% in the most homogeneous condition, demonstrating the potential for significant improvement in the fracture properties of DRA by controlling particulate distribution. Morphology of the reinforcement has also been demonstrated to have an important influence on ductility of DRA [10]. SiC particulate with a less angular morphology has been shown to increase the tensile ductility of DRA from 1-4%, depending on the strength of the DRA.

While promising results have been obtained in the laboratory, significant additional work is required to establish the full magnitude of the property improvements that may be achieved by controlling reinforcement distribution and morphology. It is a specific objective to identify the maximum volume fraction that can be produced while still retaining the required fracture properties for aerospace applications. This will require extension of the present research to include physically based modeling of deformation and fracture of DRA. This, in turn, will require an improved three-dimensional description of the relevant microstructural features that control deformation and fracture. This effort on microstructural quantification will be outlined in Section 2.6.

An approach to transition these findings into industrial practice is also necessary. Extension of the laboratory techniques employed to improve reinforcement distribution and morphology to the industrial scale is required, and certification of the improved materials and processes must be conducted.

2.2   Superhigh Strength Al Alloys

Discontinuously reinforced metals require a significant increase in specific strength to exceed the benchmark established by OMCs. The discontinuous reinforcements that provide isotropy typically offer only modest strengthening, so that matrix alloys with dramatic increases in specific strength are needed to achieve many aerospace goals. Initial development of these ultrahigh strength metals will provide benefits as monolithic metal alloys with high structural efficiency. The addition of discontinuous intermetallic or ceramic particles will provide additional specific strength, dramatic increase in specific stiffness, and the ability to tailor the CTE and thermal conductivity. These capabilities are important for growing requirements for metallic materials with high structural efficiency in enabling aerospace systems such as advanced liquid-fueled rocket engines and advanced gas turbine engines.

Recent efforts have produced significant progress in the development of superhigh strength Al alloys for use at cryogenic temperatures. [11]. The 7XXX series of age-hardenable Al alloys was used as a base, the Zn levels were increased to ~7%, and dispersoid-forming elements (Zr, Sc and others) were also added. The material was produced by direct chill continuous casting, and was subsequently tested in the cast, extruded and forged conditions. In all cases, properties were determined after a T6 temper. The first-tier mechanical properties are shown in Figure 2, and are summarized from [11].

At liquid nitrogen temperature, the yield and ultimate strengths of the new alloy in the cast condition are essentially equivalent to wrought 7075 Al. A tensile ductility of 10% is achieved in this condition. This remarkable result provides the possibility for an important improvement in the affordability of high strength Al alloys, as complex shapes may be cast rather than machined from a wrought perform. The strength of this new alloy increases dramatically after thermomechanical deformation, and ultimate strengths of 800 MPa and 920 MPa are achieved in the forged and extruded conditions, respectively. In each case, the tensile elongation is at least 10%. These strength improvements provide the possibility of replacing wrought Ti alloys as fuel turbopump components in advanced liquid rocket engines. In the near term, additional work is required to establish details relating to the engineering application of this new alloy. In the longer term, this alloy may be useful as a matrix alloy for a discontinuously reinforced MMC, where the reinforcement can increase the specific stiffness and can moderate the CTE. The research and results from this effort are described in more detail elsewhere in this volume [11].
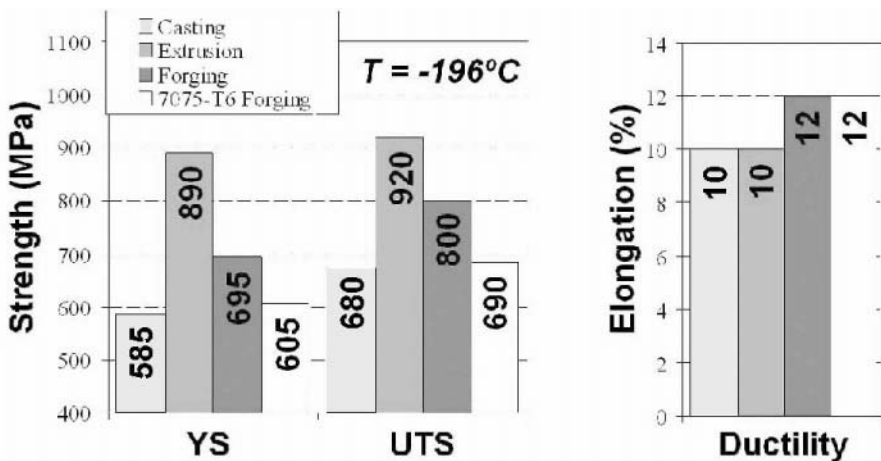
Figure 2. Mechanical properties of a new superhigh strength Al alloy tested in the T6 temper. See [11] in this volume for more details.

2.3   Titanium-Boron Alloys

Relatively small additions of boron to titanium alloys have a profound effect on the microstructure and properties of the resulting Ti-B alloys. The primary effects are the introduction of TiB, which provides strengthening, and stiffening, and grain refinement of the titanium alloy microstructure. Although B concentrations from <1 to ~14 wt % (2-40 atom%) have been studied, the primary emphasis for structural materials has been near the eutectic composition (~1.5-2 wt% B in conventional titanium alloys). These compositions provide a focus for cost-effective processing, and the modest volume fraction of TiB (10-12 volume percent) provides an attractive increase in strength and stiffness while retaining adequate ductility and good fracture toughness required for fracture critical structural applications.

Boron is essentially insoluble in titanium, so that the titanium alloy matrix is not embrittled. The TiB formed in the solid state has a needle-like morphology with an aspect ratio that ranges from 5:1 to 100:1 and a diameter that ranges from 1-5 μm, depending on processing conditions. For a modest quench rate from the liquid, typical values for aspect ratio and diameter are 10:1 and 1 μm (Figure 3(a)). Rapid cooling of a eutectic alloy, such as that produced in powder production, yields a fraction of the TiB whiskers (about 1/5 by volume) with a 10:1 aspect ratio and a diameter of 50-100 nm (Figure 3(b)). Slow cooling from the melt produces coarse primary TiB particles that are typically >100 μm in diameter (Figure 3(c)). These act as fracture initiation sites, and must be eliminated.
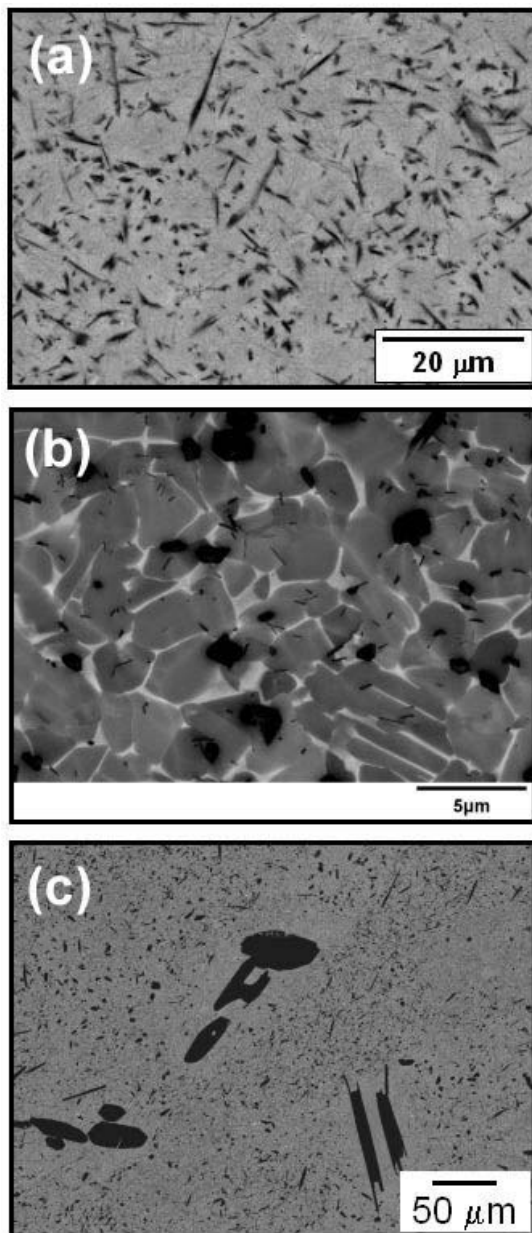
Figure 3. Microstructures ofTi-6Al-4V-1.6B (wt %) produced by (a) hot compaction of pre-alloyed powder, illustrating the typical micron-sized TiB needles with a random orientation; (b) hot extrusion, illustrating the submicron TiB whiskers and cross-sections of the TiB whiskers; and (c) hot compaction, illustrating primary TiB. The image in (b) is taken normal to the extrusion direction.

A range of processing approaches has been pursued for Ti-B alloys, including cast plus wrought, pre-alloyed powder production and compaction and elemental powder blending and compaction. Even though the eutectic reaction offers an affordable process route that also provides an effective means of microstructural refinement, little has been done to date in the area of casting to shape. As discussed above, each process route produces a different microstructure with respect to the size and morphology of the TiB needles. In general, the blended elemental approach produces a coarser microstructure due to the additional thermal exposure required to transform the boron source powder (boron powder or TiB_2 powder) to TiB, and the prealloyed approach produces finer TiB due to the relatively rapid cooling rate from the liquid state.

Initial mechanical properties for Ti-B alloys (Figure 1(b) and Figure 4) show specific stiffnesses that compete with many cross-plied graphite/epoxy systems, and specific strengths that significantly exceed this benchmark. The data represented by open squares in Figure 1(b) are for B-lean hypoeutectic alloys that are used commercially in limited applications. Significant additional improvements in specific strength and stiffness are anticipated for alloys with higher B contents as indicated in the expanded envelope for Ti-B in Figure 1(b), and the two filled squares represent the data shown in Figure 4. These data were collected by testing along the extrusion axis, and slightly lower properties are obtained in the transverse direction. The fracture toughness of these alloys ranges from 35–55 MPa√m, which is well above minimum values (~20 MPa√m) required for fracture-critical applications. The ductility is somewhat less than a desired level for fracture-critical applications of 5-7%, but elimination of primary borides, which typically initiate fracture in tensile loading, is expected to improve this property to acceptable levels.

A number of parallel future efforts are required in the Ti-B alloy system. The primary objective of future work is to eliminate primary TiB. Efforts to optimize processing to achieve the balance of first and second tier mechanical properties required for fracture-critical applications are also underway. Ti-B alloys may be considered as a matrix for continuously reinforced Ti MMCs, where the exceptional specific strength and stiffness of Ti-B alloys may help overcome current weaknesses in Ti-MMCs. In addition to the Ti-B alloys discussed here, exploration and development of similar *in-situ* eutectic composites are underway. Specifically, extensive efforts on the Ti-Si system are being pursed [12], and results similar to those reported here are now being obtained. These results are discussed in detail elsewhere in this volume.
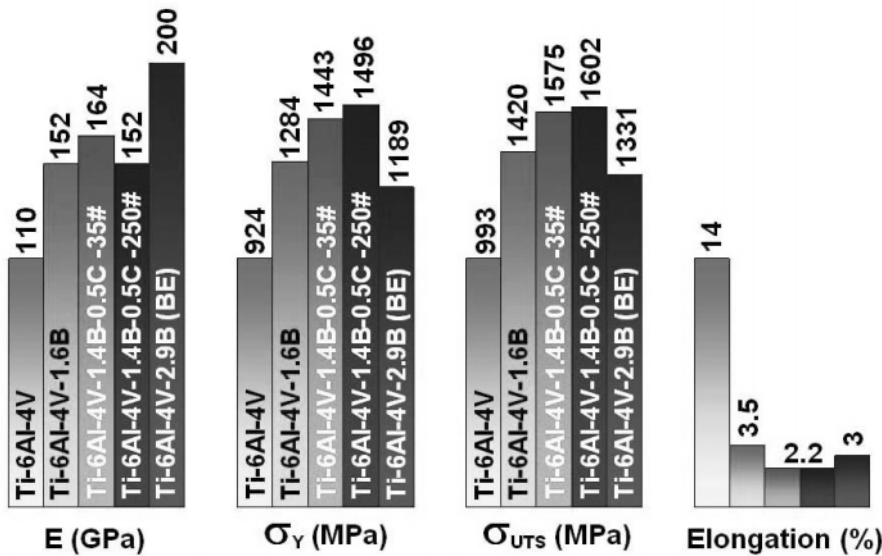
Figure 4. Tensile properties of wrought Ti-6Al-4V and extruded Ti-B alloys produced via prealloyed and blended elemental powder approaches. The loading axis is parallel to the extrusion direction. *BE* signifies material produced by the blended elemental approach. All compositions are in weight percent.

2.4 Nanocrystalline Metals

In a very real sense, the modern aerospace industry is built on a foundation of nanocrystalline metals. Age-hardenable aluminum alloys demonstrate manipulation and control of microstructural features at length scales of 1-10 nm, producing very high levels of strength. Ni-based superalloys demonstrate control of features from 10-1000 nm in alloys that retain a significant fraction of their room temperature strength at a maximum operating temperature that is 85% of the absolute melting temperature of the alloy. In steels, dimensions in pearlite colonies are controlled over length scales of 100-500 nm, producing a remarkable balance of exceptional strength and fracture resistance that no other structural material can match. However, significant further advances are possible, and efforts are underway in the structural metals community to explore and establish these gains.

It is well known that dramatic strengthening can be produced by reducing the relevant length scales for deformation in metallic alloys. Three length scales are shown in Figure 5. Reduction of the grain diameter (D) produces the well-known Hall-Petch relationship, while reducing the diameter (δ) of

strengthening precipitates or dispersoids at a given volume fraction increases the resistance to dislocation motion through bowing of dislocations around the barriers (Orowan strengthening). Below some critical diameter, particles are cut by moving dislocations, and the resistance for flow decreases with further decrease in δ. Finally, increasing the volume fraction of the strengthening precipitates at a fixed particle size decreases their mean separation (*d*), producing a third strengthening contribution. This general framework is valid for $D>\sim50$ nm and $\delta>\sim1$ nm. A great deal of effort is evident in the literature to produce nanocrystalline microstructures that approach these values. In carefully controlled experiments, remarkable strengths are sometimes reported. However, processing of high quality, fully dense nanocrystalline metals provides a significant technological challenge. Both 'bottom-up' (where nanocrystalline powders are produced and consolidated) and 'top-down' (where a bulk material is processed to produce nanocrystalline microstructural dimensions through work hardening or similar methods) approaches are being pursued. Since strengthening increases non-linearly with decreasing microstructural dimensions, significant strengthening is expected as these techniques are refined. However, this does not provide an intrinsic approach for increasing specific stiffness. Further, the influence of refining the microstructure on other properties required for aerospace structural applications, such as creep and fatigue, will need to be determined.
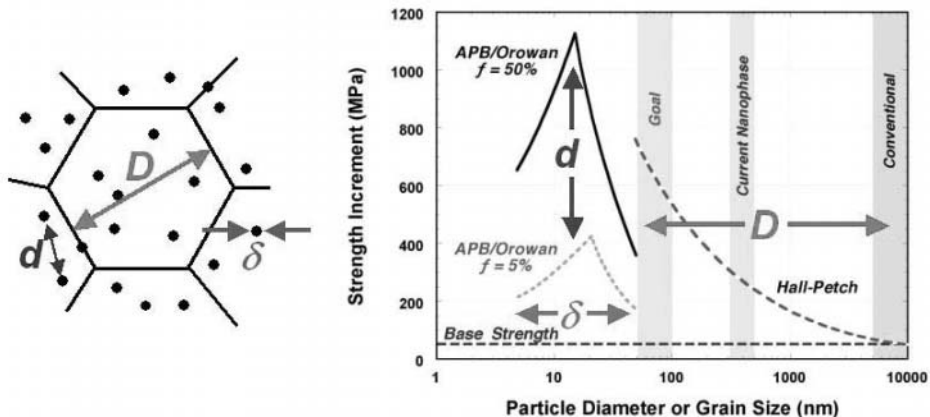
Figure 5. Influence of length scale on strengthening in nanoscale metals. The three length scales, *D*, *d* and δ influence different strengthening mechanisms and can provide additive strengthening contributionns.

2.5   **Amorphous Metals**

Amorphous metals are a relatively new class of materials, which possess exceptional specific strength (Figure 1(b)) along with other functional properties including exceptional 'soft' magnetic properties, exceptional corrosion resistance and unusual damping behavior. The loss of translational atomic symmetry provides profound changes in the basic physical and mechanical responses. The features that control and characterize the stability, the atomic structure, the mechanisms of deformation and strengthening and the kinetics of crystallization are still being established. The stability and mechanical properties of partially devitrified alloys also provide surprising responses that are not yet understood. Thus, the research on amorphous metals for structural applications is of a more fundamental and exploratory nature relative to other metals technologies presented here. Nevertheless, amorphous metals are now used in selected non-fracture critical structural applications such as golf club heads and micro-mirror hinges for digital projectors. Expanded applications are expected in the coming years as the fundamental behaviors of metallic glasses become better established.

Of primary importance is the stability of metallic glasses. Most glasses require very rapid quenching from the liquid to retain the amorphous structure in the solid state, so that material with at least one dimension of the solid product is of a length scale less than ~100μm. Consolidation of such material is difficult, since most amorphous metals crystallize below temperatures typically used for consolidation. On the other hand, a very small number of metallic glasses can be produced in the fully amorphous condition with cooling rates as slow as a few tenths of a degree Celsius per second. These bulk metallic glasses (BMGs) are favored for structural applications, and so the basic features that lead to this exceptional stability need to be established. Recent results have established a dominant role of the relative size and number of atoms (topology) [13-16]. A distinct system topology has been identified for BMGs, where the solvent atom is the largest atomic constituent, the next most concentrated constituent is the smallest solute, and constituents of intermediate size have the lowest concentrations. More recently, the principle of efficient atomic packing has been established, and this has led to the discovery that specific atomic radius ratios (relative to the solvent atom radius) are preferred in metallic glasses [17, 18]. Together, these recent findings provide specific guidance in the selection of new BMGs, and in the past year several new systems have been identified. Additional work is required to devise systems of practical significance, where the fundamental physical and chemical features of the solvent possess

the desired characteristics of low density and cost, stability in a range of aggressive environments and a high glass transition temperature. As discussed below, alloy base elements that also have high modulus (for high strength) and can co-exist with a chemically compatible ductile crystalline metal alloy (for ductility and damage tolerance) are also desirable.

Metallic glasses typically have a fracture stress that is about 2% of the elastic modulus, so that metallic glasses have roughly double the strength of crystalline alloys of the same alloy base element. Thus, strengths of up to 1500 MPa have been measured for Al alloys, and strengths up to ~4 GPa are obtained for Fe-based glasses. The specific strengths of amorphous metals are typically 400-500 MPa/Mg/m^3 (Figure 1(b)), so that compelling opportunities are offered by metallic glasses. The specific stiffness of metallic glasses are generally about 10% lower than a weighted average of the stiffnesses of the constituent elements, so that this property is not as attractive as for crystalline metals. However, a number of stable or metastable phases crystallize upon devitrification, including intermetallic compounds and quasicrystalline phases. These precipitates can offer an increase in the specific stiffness of partially devitrified metallic glasses.

The mechanism of deformation of metallic glasses is still a topic of debate, but it is certain that the loss of translational symmetry changes the physics of deformation and plasticity. This produces a unique plastic response in metallic glasses. Amorphous metals deform by intensely localized shear within a narrow band, typically on the order of a few tens of nanometers thick. Within the bands, strains over 100% can be achieved, but the number of these bands is very small, so that there is typically no macroscopic ductility measured in unconstrained loading, such as in a tensile test. On the other hand, constrained deformation leads to extensive slip multiplicity and plasticity, so that amorphous metals can be effectively rolled and formed below the glass transition temperature. The intrinsic resistance to fracture is generally good for amorphous metals, and K_{Ic} values are typically of the order of 20 MPa√m [19, 20]. For a blunt-notched crack, the fracture toughness increases to values of the order of ~50 MPa√m. Thus, the most serious limitation of metallic glasses for fracture-critical applications is the absence of general plasticity. *In-situ* composites of co-continuous BMG and ductile crystalline metal phases have been produced [21-23], and these provide enhanced plasticity and fracture properties. In addition to applying this approach to BMGs, it may also be applied to metallic glasses with marginal glass forming ability. Thus, a ductile crystalline metal can be combined with a marginal metallic glass, in a form such as powder or comminuted ribbon, and consolidated to produce a composite with the desired balance of strength and fracture properties. This provides an approach for further work.

Unique nanocrystalline microstructures can be produced by controlled crystallization of the fully amorphous product, including nanocrystalline precipitates homogeneously distributed in an amorphous alloy matrix. In some systems, both the strength and ductility increase in this partially crystalline state [24]. Other alloys produce nanocrystalline intermetallic or quasicrystalline precipitates, providing a credible path for increasing the specific stiffness. Thus, a significant effort is required to study the kinetics of crystallization, the devitrification pathways and the microstructures and properties that may be produced upon devitrification. The potential for exploration of novel compositions and microstructures in this class of materials is clearly promising.

2.6   Quantitative Description of Microstructures

Models based on simple scalar descriptions of microstructure, such as Hall-Petch strengthening (mean grain size), Orowan strengthening (mean interparticle spacing), and rule-of-mixtures strengthening (mean reinforcement volume fraction), adequately predict macroscopic strength or stiffness in a range of metallic materials. However, models for predicting fracture properties (such as ductility and toughness) of these same materials are inadequate, and often do not provide even a correct representation of trends. A fundamental distinction is that strength and stiffness are often controlled by the *mean values* of relevant microstructural features, and fracture properties are controlled by *extremes* in the distributions (that is, the 'tails' of distributions) in relevant microstructural features.

In discontinuously reinforced metals, a quantitative microstructural description is required as the basis from which physically based models of ductility, fracture toughness and damage tolerance may be developed. The characteristics of discontinuously reinforced metals that emphasize the importance of the second phase distribution result from the extreme differences in elastic and plastic response between the matrix and reinforcement. Dramatic differences in elastic constants, thermal expansion, strength and plasticity lead to residual stresses, stress concentrations, and elastic and plastic constraint. The spatial distribution of the particulates controls the local magnitude of these features, so that distribution becomes a controlling consideration. Further, interaction between local events related to particle distribution, such as clustering, and interaction with other microstructural features, such as oxide inclusions, provide a relevant system for interrogating and establishing multi-scale effects.

These same comments apply to the development and accelerated implementation of many conventional metal alloys, including alloys of Al,

Ti and Ni, and advanced metallic materials. Quantified three-dimensional (3D) descriptions of microstructural features, including the size, shape, distribution, orientation and volume fraction of grains, pores, and intrinsic and extrinsic flaws are required. Rigorous and quantifiable definitions of microstructural concepts such as homogeneity and clustering are also necessary. Thus, the quantitative description of microstructures is a pervasive scientific theme that is common amongst each of the metals technologies described above.

3.   CONCLUDING REMARKS

Significant promise exists for the development of metallic structural materials with specific strengths and specific stiffnesses (that is, structural efficiency) double the values of conventional metals technologies. These improvements will allow metals to compete with non-metallic structural materials such as cross-plied graphite/epoxy composites. These new materials can provide important performance and cost improvements for existing systems, and can also provide enabling capabilities for new aerospace systems. A broad range of technologies is being developed to achieve these goals, and promising early results have been obtained. Significant technical barriers exist, and credible approaches for overcoming these obstacles have been identified and are being pursued.

ACKNOWLEDGEMENTS

REFERENCES

[1]   M. N. Rittner, Metal matrix composites in the 21st century: Markets and opportunities, Report GB-108R, Business Communications Co., Inc., Norwalk, CT, 2000.

[2]   D. B. Miracle and S. L. Donaldson, "Composites," *ASM Handbook*, vol. 21. ASM, International, Material Park, OH: 2001.

[3]   W. H. Hunt and D. B. Miracle, Automotive applications of metal-matrix composites, in: D. B. Miracle and S. L. Donaldson, (Eds.), ASM Handbook, Vol. 21, Composites, ASM, International, Material Park, OH, 2001, pp. 1029-1032.

[4]   D. B. Miracle, Aeronautical applications of metal-matrix composites, in: D. B. Miracle and S. L. Donaldson, (Eds.), ASM Handbook, Vol. 21, Composites, ASM, International, Material Park, OH, 2001, pp. 1043-1049.

[5]   D. B. Miracle, Metal Matrix Composites for Space Systems: Current Uses and Future Opportunities, in: A. B. Pandey, K. L. Kendig, and T. W. Watson, (Eds.), Affordable Metal Matrix Composites for High Performance Applications, TMS, Warrendale, PA, 2001, pp. 1-21.

[6]   C. Zweben, Thermal management and electronic packaging applications, in: D. B. Miracle and S. L. Donaldson, (Eds.), ASM Handbook, Vol. 21, Composites, ASM, International, Material Park, OH, 2001, pp. 1078-1084.

[7]   T. W. Clyne and P. J. Withers, An Introduction to Metal Matrix Composites, University Press, Cambridge, 1993.

[8]   J. E. Spowart, B. Maruyama, and D. B. Miracle, Mat. Sci. Eng. A307 (2001) 51.

[9]   J. E. Spowart, Z.-Y. Ma, and R. S. Mishra, in: K. V. Jata, M. Mahoney, R. S. Mishra, S. L. Semiatin, and T. Leinert (Eds.), The effect of friction stir processing (FSP) on the spatial heterogeneity of discontinuously-reinforced aluminum (DRA) microstructures, TMS, Warrendale, PA, 2003, pp. 243-252.

[10]   J. E. Spowart and D. B. Miracle, Mat. Sci. Eng. A357 (2003) 111.

[11]   O. N. Senkov, S. V. Senkova, and R. B. Bhat, High Strength Aluminum Alloys for Cryogenic Applications, in: O. N. Senkov, S. O. Firstov, and D. B. Miracle, (Eds.), Metallic Materials with High Structural Efficiency, Kluwer Academic Publishers, Dordrecht, The Netherlands, 2004, p. This volume.

[12]   S. O. Firstov, L. D. Kulak, O. D. Vasyliev, and T. Y. Velikanova, "Science and Technology Center of Ukraine Partner Project Agreement P-060," Francevych Institute for Problems of Materials Science, Kyiv, Ukraine 2nd Annual Report, 2003.

[13]   O. N. Senkov and D. B. Miracle, Mat. Res. Bull. 36 (2001) 2183.

[14]   D. B. Miracle and O. N. Senkov, in: S. Hanada and N. Masahashi (Eds.), Proc. Fourth Pacific Rim Int. Conf. on Advanced Materials and Processing (PRICM4), vol. II, The Japan Institute of Metals, Tokyo, Japan, 2001, pp. 2893-2896.

[15]   O. N. Senkov and D. B. Miracle, J. Non-Cryst. Sol. 317 (2003) 34.

[16]   D. B. Miracle and O. N. Senkov, Mat. Sci. Eng. A347 (2003) 50.

[17]   D. B. Miracle, W. S. Sanders, and O. N. Senkov, Phil. Mag. A 83 (2003) 2409.

[18]   D. B. Miracle, O. N. Senkov, W. S. Sanders, and K. L. Kendig, Mat. Sci. Eng. (In press)

[19]   P. Lowhaphandu and J. J. Lewandowski, Scripta Mater. 38 (1998) 1811.
[20]   J. J. Lewandowski, Materials Transactions-JIM 42 (2001) 633.
[21]   C. C. Hays, C. P. Kim, and W. L. Johnson, Phys. Rev. Lett. 84 (2000) 2901.
[22]   F. Szuecs, C. P. Kim, and W. L. Johnson, Acta mater. 49 (2001) 1507.
[23]   G. He, W. Loser, J. Eckert, and L. Schultz, J. Mat. Res. 17 (2002) 3015.
[24]   A. Inoue, Prog. Mat. Sci. 43 (1998) 365.

THE CHALLENGE FOR MATERIALS DESIGN
Integrating Modeling and Computation

Craig S. Hartley
U.S. Air Force Office of Scientific Research, Arlington, VA USA

Abstract: The principal axiom of materials science and engineering asserts that material behavior, as measured by properties and performance, depends on structure and processing. It is now generally recognized that the application of this fundamental truth to the rational design of materials has emerged as one of the most challenging technical problems currently facing our industrial society. While the use of simulation and modeling in the computational part of the design process has reduced the product cycle from years to months by reducing the need for costly prototyping and serial experimentation, the development of new materials and processes remains an empirical endeavor guided by intuition with little quantitative scientific input. The reduction of product cycle time, increases in the agility of manufacturing processes and development of optimal materials for engineering applications depend on advances in our ability to generate reliable quantitative models of materials and processes that can be coupled with design codes. Although increases in computing power will aid this process, the most important developments will come in the development of a hierarchy of interoperable, physics-based models of material structure and properties that permit computation to reduce the lengthy experimentation currently required to produce reliable material data bases. This is the challenge to the next generation of mechanists and materials scientists and engineers.

INTRODUCTION

The increasing use of sophisticated software that permits the designer to test several design concepts *in silico* without construction of costly prototypes has dramatically reduced the time required to progress from an initial concept to a finished part ready for use. Design is typically initiated either by a "pull" in which the requirements of a specific application require the development of a new material or process or a "push" due to the development of new materials with unique properties that inspire the design of products having previously unavailable capabilities. In either case the nature of the interaction between material developer and designer is primarily serial [1].

The role of the materials developer in engineering design has historically been that of a provider of data, which designers use as input to the design process. The relatively recent recognition that materials development can be regarded as part of a system of design by employing verified computational models to develop new materials and processes and to populate Designer Knowledge Bases (DKB) has pointed the way to a revolutionary new paradigm for the engineering design process [2,3]. Basic and applied research programs sponsored by the U.S. Department of Defense have been initiated to develop the knowledge and procedures necessary for the implementation of this philosophy into the defense acquisition process.

The Accelerated Insertion of Materials (AIM) program sponsored by the Defense Advanced Research Projects Agency (DARPA) is an applied research program with the objective of reducing the insertion time for new materials into products by integrating materials models into design and optimization software currently in use for product design. Materials Engineering for Affordable New Systems (MEANS), a suite of research projects sponsored by the Air Force Office of Scientific Research (AFOSR), is intended to provide the basic knowledge required to implement and expand the AIM methodology.

The AFOSR MEANS program supports the implementation of computational materials science and engineering into engineering design. Ten projects comprise the entire effort: four in metallic materials, two in ceramic materials and four in polymer based composites. The four projects on Metallic Structural Materials complement approximately twenty-five research projects in the AFOSR core program. The following sections contain a brief description of MEANS projects involving structural metallic materials, followed by a discussion of five critical areas of research that must be addressed in order to realize the goals of the MEANS and AIM programs.

1. MEANS PROGRAMS IN METALLIC MATERIALS

1.1 Computational Design of Advanced Aeroturbine Materials

Dr. G. B. Olson at Northwestern University directs a multi-institutional, interdisciplinary program aimed at extending a revolutionary systems approach for computational materials design to the integrated design of high-performance alloys for defense applications in extreme environments. Design research centers on refractory-metal superalloys for higher temperature aircraft gas turbine blades, as a model example. Computational capabilities are being developed for the design of dynamic multilevel microstructures with predictable properties by integrating physics, chemistry, and materials science to provide bond topology-based atomistic chemistry of oxidation kinetic processes, total-energy quantum physics and chemistry of metal/ceramic adhesion and phase stability, and multicomponent thermodynamics and diffusion-based prediction of general precipitation strengthening behavior. An integral education component combines graduate research with innovative undergraduate design class projects.

1.2 A Physically Based Methodology for Predicting Material Variability in Fatigue Crack Initiation and Growth

Dr. Kwai Chan at Southwest Research Institute will develop a computation-based methodology for predicting fatigue crack initiation and growth response of structural alloys based on microstructural information and *ab initio* principles. Existing life prediction methodology requires computation of the shakedown or steady state stresses of the component during service, which are then used in life-prediction analyses using empirically derived S-N and Fatigue Crack Growth (FCG) equations. In the approach developed in this project the shakedown stresses will be used as the input to compute the shakedown substructure whose characteristic size is then used in a set of microstructure-based S-N, FCG, and FCG threshold equations for computing the low cycle fatigue (LCF) and high cycle fatigue (HCF) response. Computation of the shakedown substructure by fatigue is based on *ab initio* principles governing dislocation motion and cell structure formation.

The proposed methodology is not a life prediction tool, but a material tool that predicts the variability in S-N, FCG, and FCG threshold data that are used in life prediction methods. Upon completion, the computational tools to be developed can be used to efficiently develop a reliable LCF and HCF database, including confidence limits.

1.3   An Accelerated Methodology for the Evaluation of Critical Mechanical Properties of Polyphase Alloys

Since the current tendency is to include more and more simulation in the alloy development process, it is important to coordinate the simulation with experiment. Research conducted at Cornell University by Dr. Paul Dawson and Dr. Matthew Miller will develop an accelerated materials insertion methodology by conducting a coherent set of experiments and simulations, done within the framework of a practical and concrete material description, known as the Digital Material.

The Digital Material is a material description based on measurable quantities that provides the necessary link between simulation and experiment. Critical components of the Digital Material, a feature based material description with a statistical description of attributes, include 1) experimental methods that provide initial data for simulations and simulation methods to evolve the material attributes, 2) simulation tools that can be used to build virtual specimens, characterize them and compute material properties, 3) coordinated experiments to verify simulations and to supplement critical data and 4) accuracy assessment techniques for both simulation and experiment. Development of this program will itself require simulations and experiments of a fundamental nature. The output will be a model that will permit virtual experiments to be conducted on a two-phase material of previously selected and characterized microstructure.

1.4   Microstructure-Based Modeling for Life-Limited Components

Dr. Hamish Fraser at Ohio State University directs a project intended to develop modeling tools that will predict material properties for a set of components critical to the operation of aircraft gas turbine engines. The properties of interest are low cycle fatigue and fatigue crack growth. Expected outcomes of this research not only will effect an acceleration of the materials optimization and insertion process but also will play a major role in the reduction of costs associated with extension of component life.

The research objectives are: 1) development of microstructure-based databases for the alloys Ti-6-4 and Ti-6-2-4-2, 2) determination of the property-controlling microstructural features influencing low cycle fatigue and fatigue crack growth in Ti-6-4 and Ti-6-2-4-2, 3) development of a robust methodology for quantitatively determining microstructural features and their representation in modeling and simulation 4) development of quantitative simulation methodologies for the prediction of the development of microstructural features, which are key to influencing LCF and crack growth rate (da/dN), as a function of beat-treatment, development of a set of microstructure-based models for the prediction of low cycle fatigue and crack growth rate in Ti-6-4 and Ti-6-2-4-2 alloys and 5) provision of a set of tools based on the Finite Element Method (FEM) for the analysis of life-limiting features in turbine rotors.

To enable these computational tools to be physically relevant, they will be integrated with experimental efforts focused on the provision of accurate physical descriptions of new materials systems to increase the fidelity of predictive models, and critical validation of predictions. The integrated set of computational tools will significantly reduce extensive testing schedules and inspection procedures, and will contribute not only to development and optimization of new and existing materials within acceptable costs and time frames but also to component life extension programs.

2.   AREAS FOR RESEARCH AND DEVELOPMENT

2.1   Physics-based Model Development and Verification

> "I am never content until I have constructed a … model of the subject I am studying. If I succeed in making one, I understand; otherwise I do not." (Lord Kelvin)

There is no shortage of physics-based models of physical and mechanical properties of materials. However, many such models describe the response of materials under very restricted circumstances and consequently do not lend themselves to applications different from those for which they were developed. Neither is it common for models at one length and time scale to be interoperable, in the sense of accepting input or providing output in forms that are compatible with adjacent length and time scales. Such interoperability is essential if a hierarchy of models are to be developed linking atomistic models with the continuum models employed by engineers in designing structures. Engineers at the National Research Institute for

Metals (NRIM) in Japan have prepared an excellent summary of the current state of practice in this field [4].

One of the principal characteristics of the continuum description of materials is the frame-invariance of constitutive laws. That is, the form of the relationship relating the response of materials to changes in their thermo-mechanical environment must be independent of the coordinate system employed to describe the behavior [5,6]. This requires that material properties and descriptions of the structure of materials must be expressed in tensorially invariant form.

Theories of yielding and flow expressed in terms of invariants of the applied stress tensor are examples of appropriate constitutive laws. The design of complex engineering components must consider the response of the component to realistic states of stress, which are inevitably multiaxial. Consequently, models of yielding and flow that accommodate such conditions must be employed in constructing the design. Descriptions of the structure of material that appear in such theories must likewise be expressed in tensorially invariant form.

2.2   The Quantitative Description of Structure

> "I often say that when you can measure what you are speaking about, and express it in numbers, you know something about it; but when you cannot measure it, when you cannot express it in numbers, your knowledge is of a meagre and unsatisfactory kind." (Lord Kelvin)

The fundamental axiom of materials science and engineering holds that the properties and performance of materials are related to their structure, which is determined by chemistry and processing. Properties, in this context, refer to the behavior of atoms and groups of atoms over several orders of magnitude of length and time. Quantitative descriptions of structure at various length and time scales are essential in order to apply the fundamental axiom in the context of design.

In contrast to the nano-scale, where the periodic arrangement of atoms on crystal lattices is well established, and the macro-scale, where a continuous distribution of matter is assumed, adequate quantitative descriptions are notably lacking for structure at the micro- and mesoscales, where properties are described in terms of the behavior of dislocations, material in grains, particles of different phases and the boundaries among them. The traditional means of describing these microstructural attributes with descriptive terms that call to mind familiar shapes fails to provide an adequate quantitative basis for transferring this information to quantitative models.

Quantitative description at the mesoscale can be divided into three categories: topological [7], metric [8,9] and crystallographic [10]. The most familiar of these are metric and crystallographic measures. Common metric measures include scalar measures of internal boundary surface area per unit volume and volume fraction of distinct phases, both of which can be obtained by applying stereological techniques to measurements on a two-dimensional observation plane. Quantitative descriptions of the distribution of grains are generally expressed in terms of the Orientation Distribution Function (ODF) determined by diffraction techniques [11]. Topological measures are less frequently employed to characterize microstructures, but can often provide useful information about the evolution of microstructure with deformation and heat treatment [7].

While techniques presently employed for quantitative description of microstructure all provide some sort of numerical representation, none are completely adequate for insertion into continuum theories that describe material behavior at the next higher length and time scales. Some success has been achieved in this regard by employing the ODF with single crystal elastic constants to obtain the bulk elastic constants [12], or upper and lower bounds thereto [13], for a textured polycrystal.

An application of the bounding process employing distribution functions to describe microstructural features forms the basis for a developing discipline known as Microstructure Sensitive Design (MSD) [13]. While holding much promise as a tool for including quantitative descriptions of microstructure in more macroscopic design processes, as presently formulated MSD relies on the characterization of distribution functions in terms of their Fourier expansions using spherical harmonics as basis functions. This approach suffers from the disadvantages of often requiring several terms in the expansion to obtain an adequate representation of the function and expressing the expansion in terms of coefficients and basis functions that are not frame invariant, as required for a tensorial description of constitutive equations.

Employing a representation described by Kanatani [14] can eliminate the difficulties introduced by using spherical harmonics as basis functions for the Fourier expansion of distribution functions. This technique describes an anisotropic property in terms of a distribution function expressed as a Fourier expansion using as the basis functions moments of a unit vector along which the property is measured. This formulation has the advantage of yielding both basis functions and Fourier coefficients that are tensors. In later work Kanatani demonstrates how stereological measures can be employed to determine relevant Fourier coefficients for the description of anisotropic features in the microstructure of granular materials [15,16]. Kanatani also shows that an adequate representation of a mildly anisotropic property can be obtained with relatively few coefficients compared with spherical harmonics [14].

A similar description has been employed by Leckie and Onat [17] and Onat and Leckie [18] and Onat [19] to include damaged-induced microstructural anisotropy into constitutive equations. Despite its advantages over other forms of representation, this approach has not been applied widely to the description of anisotropic microstructures and its inclusion in constitutive laws for materials.

The importance of developing appropriate quantitative descriptions of microstructure that not only can be obtained by well-established stereological measurements but also can be expressed in a manner compatible with continuum descriptions of matter is fundamental to connecting the micro- and mesoscopic to the macroscopic descriptions of materials. Furthermore, such descriptions must be incorporated into macroscale models of material behavior in a manner that permits the calculation of macroscopic engineering properties in terms of the mesoscopic attributes of materials.

2.3   Experimental Techniques

" To measure is to know." (Lord Kelvin)

As experimental techniques for measuring displacement and strain become increasingly accurate at micro- and nano- length scales, experiments must be performed to verify the accuracy of predictions of models of material behavior at these scales. In particular, the use of diffraction techniques for measurements of lattice distortion [20] combined with surface measurement techniques such as micro-Moiré [21], speckle interferometry [22] and displacement mapping [23] promise to provide essential information on the local deformation behavior of metals and alloys in the vicinity of grain boundaries, voids and second phase particles. These techniques must be further developed and applied to the analysis of real materials to increase our knowledge of material behavior at these length scales.

As an example of such measurements, consider the determination of the Dislocation Density (Nye) Tensor [24], α, from measurements of lattice strain and curvature. Bilby, Gardner and Smith [25] show that this tensor is related to the local lattice curvature and lattice strain gradient by[1]

$$\alpha_{ij} = \kappa_{ji}^L - \delta_{ij}\kappa_{mm}^L + \varepsilon_{jk\ell}e_{i\ell,k}^L \tag{1}$$

---

[1] In equation 1, suffixes range from 1 to 3 and indicate the Cartesian coordinate axes along which the component is measured. Summation from 1 to 3 over repeated suffixes is implied, and a subscript comma indicates partial differentiation with respect to the indicated spatial coordinate. The Kroneker delta is δ_{ij}.

where $\boldsymbol{\kappa}^L$ and $\mathbf{e}^L$ are the lattice curvature and lattice strain tensors, respectively and the superscript L emphasizes that the quantity applies to the lattice. Present diffraction techniques, such as Electron Beam Backscatter Diffraction (EBSD), can accurately measure lattice rotations over very small volumes, permitting the calculation of lattice curvature [26], but only the most sophisticated techniques can measure lattice strains over comparable volumes [20].

Measurements at a comparable length scale of the deformation of a grid deposited on the surface of the body can provide additional information that will permit the measurement of $\boldsymbol{\alpha}$ within individual grains and particles. This information is essential for determining how deformation is transmitted across grain and interphase boundaries, so that models of plastic deformation that include the effects of internal boundaries can be appropriately constructed.

2.4 The Designer Knowledge Base

"I cannot doubt but that these things, which now seem to us so mysterious, will be no mysteries at all; that the scales will fall from our eyes; that we shall learn to look on things in a different way - when that which is now a difficulty will be the only commonsense and intelligible way of looking at the subject." (Lord Kelvin)

The body of information employed by designers to characterize material behavior is called the Designer Knowledge Base (DKB). The valuable collection of information obtained by years of experimentation and practice must be converted to quantitative knowledge using advanced techniques of information technology. Materials databases must be organized into forms that can be searched and interrogated to determine critical functional dependencies among structure and properties. The output of this effort must then be presented in a form that is accessible to engineering designers in order to incorporate into the DKB.

Techniques for the use of existing information and analyzing new data to identify causal relationships between structure, processing and properties is being developed using tools based on distributed data bases [27] and Bayesian neural networks [28]. These advanced mathematical techniques permit more effective searches for critical dependencies than traditional methods. In some cases virtual mathematical experiments can be conducted that vary only a single microstructural variable to determine material responses under conditions that are impossible to duplicate in real experiments [29].

Three important considerations in constructing a DKB are: 1) existing data must be carefully analyzed so that all useful information contained in the current knowledge store is effectively utilized, 2) new data must be characterized in sufficient detail that reliability estimates can be applied and 3) information must be organized and presented in a format that permits easy insertion into design codes. Materials designers must make these processes integral with the construction of models and the conduct of experiments that produce data for use in engineering design.

In employing models to calculate material behavior under a variety of thermo-mechanical conditions, it is frequently necessary to have access to fundamental thermo-physical data, such as diffusion coefficients, heats of formation and solution, and solidus and liquidus temperatures among others. As complex models are being developed and applied, it is frequently found that there is an absence of such information for use in these calculations. There does not exist a satisfactory database of verified experimental information covering the necessary range of material compositions and operating conditions required for use in a robust design.

Many fundamental properties are themselves amenable to computation if suitable models are available. However, experimental data is required in order to verify the models and establish reliability estimates. Research of this nature is not commonly performed on a sufficiently wide scale to improve the predictive ability of many important models of material behavior. Additional emphasis must be placed on acquiring this information to meet the requirements of the revolution in materials design

2.5   Integration of Materials Models with Engineering Design

"There cannot be a greater mistake than that of looking superciliously upon practical applications of science. The life and soul of science is its practical application." (Lord Kelvin)

The nature of the interaction of materials engineers with designers must be changed to permit materials and process design to proceed in parallel with component design. This requires a change in both cultures to create and implement a collaborative, interactive and parallel process of design [30]. The operational requirements of the product and its engineering and economic constraints must be coupled mathematically not only to the overall component design, as in present practice, but also to the design of materials and processes used in manufacture.

This cultural change means that materials engineers must think more quantitatively about the structure-processing-property relationships in

materials. A self-consistent model that describes the results of a specific set of experimental results but which cannot be generalized to other situations is not a satisfactory goal for materials modelers.

Engineering designers must regard materials as design elements whose properties can be manipulated and changed interactively with changes in total product design, rather than a "black box" of immutable properties. Finally, the concept of engineering design must be expanded into a systems approach that includes materials engineers as well as those that perform traditional design functions.

3.   CONCLUSION

"Large increases in cost with questionable increases in performance can be tolerated only in race horses and fancy women." (Lord Kelvin).

The projects funded under the MEANS initiative begin a process that will ultimately provide the scientific basis for design approaches that represent a paradigm shift in the way materials are included in the design process. Rather than providing a data base of experimental information described by empirical rules, materials scientists and engineers will have a physics-based mathematical foundation for predicting the effect of processing on structure and structure on properties required by designers to employ in product design.

This foundation will ultimately be cast into the form of design codes, compatible with product design and optimization codes that will permit parallel design of materials and processes resulting in optimal use of materials for specific applications. This development will result in increased reliability and economy for manufactured components.

REFERENCES

1. Materials in the New Millennium, National Research Council, National Academies Press, Washington, DC, 2001, p. 18.
2. Materials Research to meet 21st Century Defense Needs, National Research Council, National Academies Press, Washington, DC, 2003, p. 39.
3. G. B. Olson, Science, 277, 1997, 1237.
4. Computational Materials Design, edited by T. Saito, Springer-Verlag, Berlin, 1999.
5. A. C. Eringen, Nonlinear Mechanics of Continuous Media, McGraw-Hill, New York, NY, 1962.
6. C. Truesdell, W. Noll, The Non-linear Field Theories of Mechanics, Handbuch der Physik, III/3, Springer-Verlag, Berlin, 1965.

7.   R. T. DeHoff, Metallography, 8, 1975, 71.
8.   R. T. DeHoff , F. N. Rhines,, Quantitative Microscopy, McGraw-Hill, New York, 1968.
9.   E. E. Underwood, Quantitative Stereology, Addison Wesley Publishing Co., Reading, MA, 1970.
10. B. L. Adams, T. Olson, Progress in Materials Science,(Eds.M.F. Ashby, B. Cantor, J.W. Christian and T.B. Massalski), Vol. 43, Pergamon Press, Oxford, UK, 1998, p. 1.
11. H. J. Bunge, Texture Analysis in Materials Science, Butterworths, Boston, MA, 1982.
12. C. M. Sayers, J. Phys D., Appl. Phys., 15, 1982, 2157.
13. B. L. Adams, A. Henrie, B. Henrie, M. Lyon, S. R. Kalidindi, H. Garmestani,, J. Mech. Phys. Solids, 49, 2001, 1639.
14. K. Kanatani, Int. J. Engng. Sci., 22, 1984, 149.
15. K. Kanatani, Int. J. Engng. Sci., 22, 1984, 531.
16. K, Kanatani, Int. J. Engng. Sci., 23, 1985, 587.
17. F. A. Leckie, E. T. Onat, in: Proc. IUTAM Sym Physical Nonlinearities in Structures, Senlis, Springer-Verlag, Berlin, 1981, p. 140.
18. E. T. Onat, F. Leckie, J. Appl. Mech., 110, 1988, 55.
19. E.T. Onat, in Recent Advances in: Creep and Fracture of Engineering Materials and Structures, (Eds.B. Wilshire and D. R. J. Owen), Pineridge Press, Swansea, UK, 1982, p. 231.
20. G. Ice, B. C. Larson, Advanced Engineering Materials, 2, 2000, 243.
21. B. Han, Optical Engineering, 31, 1992, 1517.
22. F.-P. Chiang, Q. Wang, F. Lehman, in: Non-traditional Methods of Sensing Stress, Strain and Damage in Materials and Structures, ASTM STP 1318, (Eds. G. F. Lucas and D. A. Stubbs), American Society for Testing and Materials, Philadelphia, PA, 1997, p. 156.
23. N. Biery, T.M. Pollock, N.T. Nuhfer, M. De Graef, Microscopy and Microanalysis, 5 (sup 2), 1999, 334.
24. J. F. Nye, Acta Met., 1, 1953, 153.
25. B. A. Bilby, L. R. T. Gardner, E. Smith, Acta Met., 6, 1958, 29.
26. S. Sun, B. L. Adams, W. E. King,, Phil. Mag., 80, 2000, 9.
27. M. Fujita, J. Kinugawa, H. Tsuji, Y. Kaji, Y. Tachi, J. Saito, K. Shimura, R. Nakajima, d S. Iwata, Fusion Engineering and Design, 51-52,2000, 769.
28. H. Fujii. D. J. C. Mackay, H. K. D. H. Bhadeshia,, ISIJ International, 36, 1996, 1373.
29. H. Fujii, D. J. C. MacKay, H. K. D. H. Bhadeshia, H. Harada, K. Nogi, ISIJ International, 396, 1999, 966.
30. K. Lewis and F. Mistree , ASME Journal of Mechanical Design ,120, 1998,   643.

THE MAIN TENDENCIES IN ELABORATION OF MATERIALS WITH HIGH SPECIFIC STRENGTH
A Time-Honored Approach

Sergey Firstov
Institute for Problems of Materials Science, Kyiv, Ukraine

Abstract: The problems of elaboration materials with high specific strength and stiffness are discussed. Especially the hardening connected with creation of nanostructured materials is analyzed. Structure and properties of the new type *in situ* composites based on Ti-Si-X and Ti-B-X-systems are presented. The promising directions of further investigations are given

Key words: micro- and nanostructured materials, strength, stiffness, plasticity, Ti-based *in situ* composites.

1. INTRODUCTION

In elaboration of materials with high specific strength two basic directions are obvious:

1. Creation of high strength states (increase of yield stress and fracture stress), based on new achievements of materials science and on application of the innovative technologies of material producing and processing; increase of material stiffness (increase of its elastic moduli).
2. Diminishing of specific weight based on use of materials with low density, including porous materials. Both specific strength and rigidity increase at this.

Development of materials having high values of strength and producing structural states meeting these requirements remain in the center of

researchers attention. For example, for carbon-containing iron-based alloys the strength up to 6000 MPa is obtained [1-3] that consists of the essential part of theoretical strength. For deformed alloys of Mo-Re system an achievement of strength values up to 8500 MPa it was informed [4]. These results are obtained by application of the special thermo-mechanical treatment resulting in formation of superfine-grained states. Recently researches of the fine-grained states obtained as a result of use of various technologies based on the severe plastic deformations were essentially intensified. One of the reasons of such interest revival is the development of methods of volume hardening without essential change of billet cross-section (ECAP, rotation extrusion etc.).

Other interesting directions are hardening with intermetallics, quasi-crystals, borides, silicides, discrete fibres, creation of natural composites. Conscious regulation of structure and properties of such materials requires studying phase equlibria in multi-component systems, in particular on the basis of light metals like aluminum, magnesium, titanium. The important direction is also a creation of specially organized porous structures. To some extent these directions are presented in a number of papers of the present book.

Taking this circumstance into account some above topics will be analyzed lower in more details. Namely, these are limiting hardening created as a result of obtaining ultra-fine grains, some topics of deformation hardening; additionally, considered will be some aspects of development of new generation of titanium-based materials (systems Ti-B-X and Ti-Si-X, where X is Al, Zr, etc.).

2.   NANO-STRUCTURED MATERIALS

Creating superfine-grained structures is one of ways to obtain the high-strength conditions. Two main directions of both research and development of processing routes to obtain such structures may be distinguished. First of them is related to micro- and nano-crystalline materials result from severe plastic deformations. This direction experiences now the renewal of interest due to development of technological schemes, allowing the structures being characteristic for conditions of severe plastic deformations without essential change of cross-section of deformable billet to be obtained first of all. This is a method of angular pressing (or equal channel angular pressing), proposed by Segal [5], method of rotation extrusion [6]. The large deformation can be realized with torsion deformation under pressure [7] and also with various procedures of surface hardening.

The second direction includes various methods of vapor deposition, electrodeposition, crystallization from amorphous condition as well as technology of powder metallurgy using compacting of ultra-fine powders.

For fine-grained structures produced with both deformation and other technologies (e.g., magnetron sputtering) the characteristic size at which a change of dependence of strength characteristics on grain size is revealed may be found [7-11]. Reduction of grain size to ≈1 μm causes an essential increase of yield stress, being usually described by Hall-Petch equation.

Reducing grain size less 1 μm a change of parameter m in equation $\Delta\sigma = k\, d^{-m}$ from 0.5 to 1 occurs. Thomson [8] has assumed that the transition is associated with the fact that at grain size $d > d_{cr}$ hardening with parameter m=0.5 is more effective; on the contrary, hardening with m=1 is more pronounced at grain size $d < d_{cr}$. It seems that exact value of d_{cr} depends on material and deformation temperature. The reason of this transition, in our opinion, is due to the fact that at low temperatures when stress exceeds yield point the boundaries of structural elements contain high concentration of the disordered defects of dislocation type (lattice dislocations, products of dislocation interaction at transition of sliding through boundaries, half-ring dislocations generated by the sources being in boundaries etc.). At reduction of distance between such boundaries their stress fields are overlapped. The forces acting between two dislocations (dislocation charges) are known to be inversely proportional to distance between them. For this reason the transition to more intensive dependence of yield stress on the structural element size occurs.

The next dimensional effect is associated with transition in nano-structural state and is accompanied by absence of hardening or even by essential decrease of mechanical properties associated with sharp increase in a volume fraction of a "bad" material (grain boundaries, ternary joints) at the further reduction of grain size. Really, as it was discussed above such the transition is just inevitable at reduction of grain size up to 20 nm since at such grain sizes operation of a dislocation source requires stress around the shear theoretical strength. Real transition occurs at larger sizes ≤100 nm and at further reduction of grain size a consecutive decrease of strength is observed as it was discussed in [10-11]. However, for nano-structures having deformation origin reduction of strength or as at least termination of deformation hardening are revealed.

Gleiter [12] and other researchers [7, 10, 13] call attention to the fact that consecutive reduction of grain size results in increase of volume fraction of "a bad material" (actually it includes intrinsically grain boundaries and near-boundary volumes, ternary joints, points of contact of four grains), i.e. areas where atoms are located with displacement from their equilibrium positions being characteristic for an ideal crystal; besides, the coordination number differs

from the number of ideal lattice, bonding directions and inter-atomic distances are deformed, there are loosened areas. The detailed analysis made by Valiev and co-workers [7, 13] testifies that the ultrafine-grained materials produced with severe plastic deformations contain the deformed areas with elastic deformations of 1-3 %. The size of these areas reaches 3-5 nanometers. Heating such materials results in relaxation of internal stresses, dilatometry testifies a reduction of free volume at stages occurring before grain growth.

The marked features of influence of structural element size on mechanical properties are applicable for one-component materials (consisting of atoms of one kind). Really, it is not possible to prevent the effects of above mentioned increase in volume fraction of a "bad" material; and as consequence, it is not possible also to preclude the saturation or even decrease of strength properties. The level of hardening having been realized in the fine-grained materials consisting of atoms of one kind does not exceed, for example, 1300-1400 MPa for pure iron [14] even after significant deformations, and the hardening modulus is such that obtaining of strength comparable with theoretical strength is possible only at true deformations about 20 and greater [9]. At the same time for high-carbon steels there is the information about achievement of strength at a level of 4000-6000 MPa [1-3] as a result of complex thermomechanical treatment aimed at creation of ultrafine-grained structures where thin cementite precipitates are situated at grain boundaries. It was noted in [1] that this hardening is caused mainly by the size of deformation cells, while influence of the pearlite spacing and pearlite colony size is secondary contribution.

Thus, in materials consisting of atoms of two (and more) kinds in principle there is a possibility of additional influence of atoms of an impurity or alloying elements on properties. Related to this fact, in our opinion, is also a substantial increase of strength (yield stress) in deformed steels with ultrahigh carbon contents [1-3]. In such systems there is a possibility for grain boundary segregation of atoms of alloying elements to be formed. Due to the segregation both increase and decrease of cohesion energy of boundaries can take place. According to this feature surface-active elements can be divided on "useful" and "harmful". In particular, the impurities lowering grain boundary cohesion energy are considered as "harmful" elements; and the impurities raising the energy are regarded as being "useful" ones. Certainly, phosphorus and sulfur in iron (or in steels) as well as oxygen in molybdenum can be referred to as harmful elements. Carbon, on the contrary, is considered as useful impurity in molybdenum and iron. In more detail this question is considered in E.E. Glikman's work [15].

The important consequence of these ideas is, in our opinion, the opportunity of regulation of impurity composition of materials and, accordingly, of increase of grain boundary cohesion energy due to

segregation of useful elements. Such example was recently given in [16]. On research of structure of chromium, produced by magnetron sputtering on a cold substrate, an essential increase of hardness of the nano-crystalline metal in comparison with other metals being in the same condition has been found. In particular, hardness of nanocrystalline metals is several units of GPa. So, hardness of iron is 8 GPa, hardness of nickel reaches 5 GPa. In our case hardness of nanocrystalline chromium is 18 GPa [16]. There are data about higher hardness of about 30 GPa.
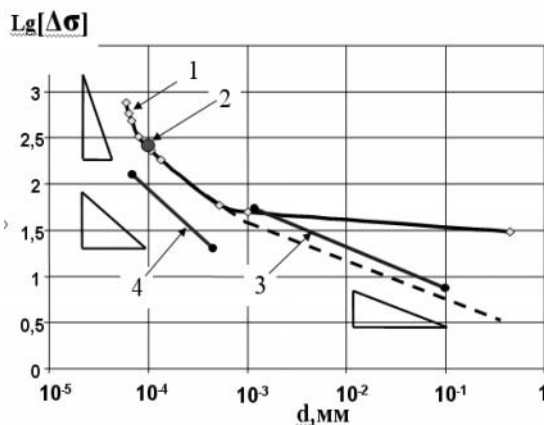
Figure 1. Lg Δσ (σ was estimated in MPa) as a function of grain size: 1-magnetron Cr coatings; 2- plasma Cr coatings; 3- Fe-C; 4-Fe-0.49Ti [16].

Fig. 1 illustrates the data on influence of reduction of grain size on yield stress of chromium films obtained by magnetron sputtering recalculated from hardness data. It was established that for grain size d>1 μm m=1/2, correlating with the Hall-Petch ratio. In a range of 0.1 <d <1 μm, m=1. Further decrease of grain size results in not stabilization of hardness (yield stress) or even to "negative" Hall-Petch ratio but to more intensive increase of hardness. Probably, the hardening is a result of oxygen atoms embedded in nanocrystals boundaries, i.e. "healing" of weak points on grain boundaries. For this reason we make the assumption of "useful" role of oxygen atoms in increase of grain boundary cohesion energy of nano-crystalline chromium. At the same time, hardness of molybdenum films produced in the similar conditions did not exceed 8 GPa.

It is necessary to note, that except of possible strengthening of intergranular strength due to segregation of an "useful" impurity enhancing a

level of interatomic force in grain boundaries of multicomponent systems, consisting of atom of several kinds, it is necessary to consider a distinction in atomic (ionic) radii of the basic and alloying elements. Taking into account that the volume of grain boundaries contains both the stretched area (loosening) and compressed one, one can expect that atoms of the big sizes will occupy willingly stretched areas, and small atoms will segregate in the compressed ones. Naturally, some healing of "weak" places of boundaries (loosening) will occur. The density of such boundaries should grow, being compared to density of intracrystalline volumes. The above reasons show, that engineering of intracrystalline interfaces along with usage of segregation effects (the concept of "useful" impurity) is the promising tool, allowing for substantial increase of strength of nano-crystals to be expected.

In conclusion we note that a lot of publications has recently appeared which inform about substantial increase of hardness of nano-composites of a variety of systems [17]. These systems are both metal-ceramics and ceramic compositions ones. It is of special interest the circumstance that hardness of such objects is at a level of the best superhard materials. According to S.Veprek's [17], an important point is a combination of nanocrystalline and amorphous phases in structure of such composites. The amorphous component is capable to be coordinated in the best way to a surface of nanocrystals providing good adhesion and resulting in essential increase of strength. Such structures are realized by him in system of TiN-Si$_3$N$_4$, and their hardness approaches to hardness of diamond! It is necessary to note that all three elements, which are included in the composition (titanium, nitrogen and silicon) form sufficiently strong bonds between them. But, certainly, the level of the bonds is essentially lower in comparison with this in diamond lattice. It is possible to assess the bonds, for example, by comparing elastic moduli of diamond, titanium and silicon nitrides, titanium silicide. Hence, high value of hardness of nanocomposites is caused by the small grain size in a combination with satisfactory strength of intergranular boundaries.

3.   NEW HIGH STRENGTH, HIGH TEMPERATURE AND HIGH MODULUS TITANIUM ALLOYS

Past year development of new titanium alloys was based on possibility of using phase transformations and on explorations to study alloying effect on these transformations. A wide range of α-, β- and (α+β)-alloys for various applications was created. The most widely known alloy is Ti-6Al-4V. The

big complex of investigations on influence of different heat treatment regimes on structure and properties of this alloy is in progress until now. The extended studies have been implemented also to obtain an improved complex of properties (rigidity, strength, plasticity, high temperature strength, oxidation resistance etc.). The main alloying elements used are Al, Sn, Mo, V, Zr, Fe, Mn, Cr. Among basic ways to increase strength the solid solution hardening and additional incorporation of reinforced phases (intermetallics, silicides, borides, carbides etc.) are considered [18]. Note that silicon content in real alloys does not usually exceed 0.4%, carbon and boron content are as a rule no more than 0.25% and 0.2%, respectively.

10μm
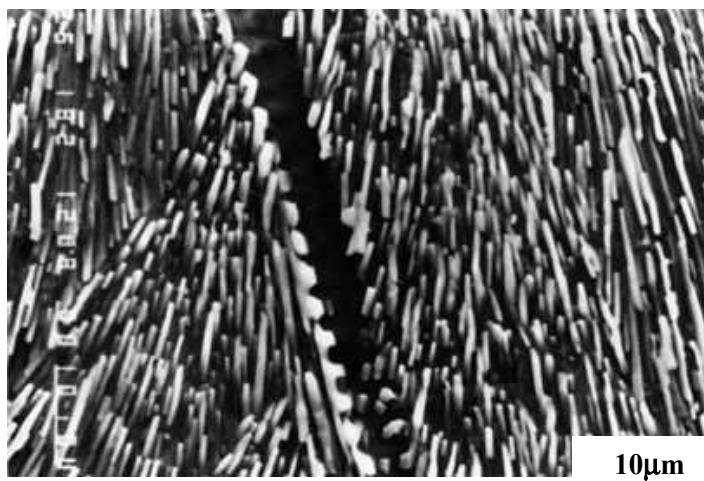
Figure 2. SEM image of as-cast Ti-8.5-wt.%Si alloy after deep etching.

Additional increase of properties of titanium-based materials is associated with composites. For example, reinforcement due to continuous fibres of silicon carbide (up to 40-wt.%) permits strength and rigidity of such materials to be essentially increased. However, the cost of such composites appears to be prohibitive (about several tens of thousands of USD per 1-kg [19]. Moreover, above temperatures of 600 ^{0}C an interaction of fibers and matrix is revealed.

For this reason, considered at present are possibilities of creating essentially more cheap materials, namely discontinuously reinforced Ti-matrix composites – so called DRTi. According to Miracle [20], the reinforcement with TiB fibres is the most effective one. For example, incorporation of reinforced phase up to 40 vol. % allows a combination of properties (especially stiffness) to be essentially increased.

In investigations [21-22] our attention was paid mainly to the development of natural composites with boride and silicide hardening, in which reinforced phase is formed through eutectic crystallization.

The volume fraction of reinforced phase in eutectics is 7.7 % and 31-wol.% for systems Ti-B and Ti-Si, respectively. The typical structures of eutectic alloys for Ti-Si system is shown in Fig. 2. According to binary diagrams of phase equlibria, an essential solubility of silicon in α- and β-phases is observed, which is dependent on temperature; there is an eutectoid transformation (in this respect diagram Ti-Si is similar to Fe-C diagram), but in system Ti-B essential solubility of boron in α- and β- phases does not occur. For this reason the structure of composites of Ti-B system is more stable at temperature variation.

The typical dependence of mechanical properties of Ti-Si binary alloys in as-cast and as-deformed states is shown in Fig. 3. It is seen that in as-cast state room temperature plasticity decreases with increase of silicon content, reducing practically to zero at silicon content of 2-3 wt. %; then it raises a little at eutectic formation. Unfortunately, our attempts to increase room temperature plasticity in as-cast condition more or less substantially via employing various kinds of heat treatment procedures were not successful. At the same time, using thermo-mechanical treatment (forging at temperature 1050 ^{o}C), it was possible to increase plasticity of deformed alloys essentially.
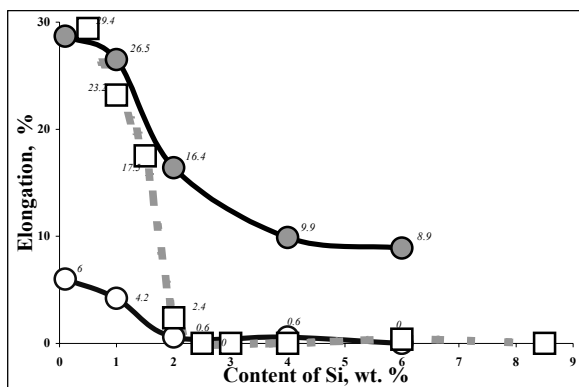

Figure 3. Plasticity of Ti-Si alloy vs. silicon content. Dotted curve is taken from [23]. Lower and upper curves represent as-cast and deformed alloys.

For improvement of a complex of physical and mechanical properties of alloys of the systems under study, researches of alloys of systems Ti-Si-X

and Ti-B-X have been carried out at their alloying with Al, Zr, V, Sn, Nb etc. Both ternary and quaternary systems were investigated.

The most attractive properties have alloys Ti-Si-Al-Zr, Ti-B-Al and Ti-B-Si-Al. Among these alloys the Ti-Si-Al-Zr system are represented as more attractive to obtain increased high temperature strength stability and heat resistance. Preliminary researches demonstrate high oxidation resistance of alloys of this system at high temperatures. Alloying with aluminum and zirconium results in both increase of strength of titanic matrix and alloying of silicide, resulting from formation of phase $(Ti,Zr)_5(Si,Al)_3$. Note that according to the diagram of phase equlibria Ti_3Si phase must be stable at temperatures below 1000 ^{o}C, however, special studies have shown that even at prolonged annealing (100 hours) phase Ti_5Si_3 retains its stability at suggested operation temperatures $\leq$800 ^{o}C.

Increase of zirconium content above 6 % results in formation of another eutectic composed not of $(Ti, Zr)_5(Si, Al)_3$, but of $(Ti, Zr)_2Si$ phase. This eutectic is much more disperse, and the volume fraction of the phase is a little bit higher, than in alloys without zirconium. Increase of aluminum content above 6 wt.% results in appearance of Ti_3Al α_2-phase structure, allowing expecting for additional increase of strength and thermal stability of such systems.

It was noted above, that the as-cast eutectic alloys of binary Ti-Si system have no appreciable plasticity at room temperature. Alloying with aluminum, zirconium and use of various modifiers has also not allowed appreciable RT plasticity to be obtained. Data on temperature dependence of mechanical properties of deformed alloys of system Ti-3Al 6Zr-(2-6) Si show that, in contrast to as-cast alloys, deformed state with about 2 % Si demonstrate high plasticity (~4%) reducing to 1.8 % in alloy with 6-wt.% Si. At the same time high-temperature strength of these alloys are practically the same, at 540-560 MPa level (600 ^{o}C). In such a way there is no reason to increase silicon content higher 2-wt.% in deformed state.

Besides, according to X-ray analysis, after thermomechanical processing the phase $(Ti,Zr)_5(Si,Al)_3$ transforms in phase $(Ti,Zr)_2(Si,Al)$, being stable at temperatures below 1000°C. Morphology of the phase has essentially changed. Isolated particles arise instead of a complex-shaped framework of as-cast state. Such structure is typical for the DRTi composites.

Researches of phase equlibria showed that two essentially various groups of alloys distinguished by silicon contents can be obtained. In alloys of the first group the silicon content does not exceed its limiting solubility in β phase. The alloys of the second group are hypoeutectic and eutectic ones, the content of silicon in them is within the limits of 3-8-wt. %. Alloys of the first group represent titanium "steels", and the second group alloys could be named as titanium "cast irons". Taking into account the analogy of Fe-C and

Ti-Si phase diagrams, such terminology seems to be justified. The fact, that silicon is a substitutional impurity in titanium and carbon is the interstitial impurity in iron affects only kinetics of corresponding transformations. In the rest, the analogy is represented as being deep enough due to the facts that both groups of alloys suppose similarity of heat treatment regimes, have eutectoid transformation, can be mar-quenched etc.

Table 1. Mechanical properties of deformed selected alloys. α and β marks mean that deformation was finished in α or β regions.

Alloy	RT strength, MPa	RT elongation, %	Elasticity modulus, GPa	600°C strength, MPa
Ti-6.3Al-5Zr-1.8Si	α 1220	α 5.4	134	α 338
Ti-9.0Al-2.2Zr-1.6Si	β 1180 α 1234	β 1.6 α 6.1	140	β 923 α 608
Ti-5.5Al-1.9B	β 1184	β 6.24	152	β 1140
Ti-6.6Al-3.5Zr-1.3Si-1.1B	β 1530	β 1.4	158	β 1469
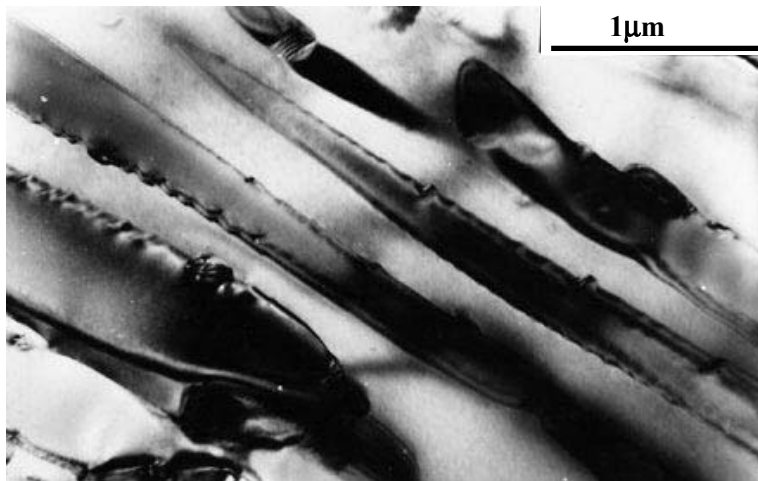
Figure 4. TEM image of as-cast Ti-B-Si alloys. Fine silicoborides are clearly visible.

Thus, in the future all great experience of processing iron-based alloys could be employed to produce the alloys on the basis of titanium. The preliminary data show that a level of properties, which could be realized with titanium "steels" appears to be attractive enough. Some properties of the deformed alloys of system Ti-Si-Al-Zr are listed in the Table 1. It is obvious also some distinction in properties of titanium steels depending on deformation temperature. Namely, alloys deformed in α phase field, have higher plasticity; conversely, alloys deformed in β phase field, possess higher heat resistance.

System Ti-B-X represents a basis for development of alloys with a high stiffness, especially at additional alloying with aluminum [24]. Titanium boride has high Young modulus and simultaneously it is practically insoluble in titanium matrix. Aluminum is one of few elements, which being dissolved in titanium increases Young modulus of matrix.

The further progress can be related to the development of alloys of Ti-B-Si-X system. Preliminary study of these alloys has shown an availability of some additional early unknown phase. In addition to typical lamellar borides visible in structure of the alloys is extremely disperse phase having boron and silicon in its composition. Electron microscopy image of this phase is shown in Figure 4. Structural identification of this silicoboride is not completed yet, however it is already possible to note appreciable increase of stiffness of the alloys at simultaneous presence of boron and silicon (Table 1).

It is necessary to note that both borides and silicides in the investigated systems exhibit a good cohesion with titanium matrix. In particular, it is practically never revealed on fracture surfaces of these alloys any lamination of particles of the strengthening phase from matrix.

4. CONCLUSIONS

The following directions of R&D in the field of elaboration of materials with high specific strength can be highlighted:

1. Grain boundary engineering of nanostructured materials including thermo-chemical treatment based on concept of "useful" additives.

2. Clarifying of mechanisms of plasticity in nanostructures. Achievement of a good combination of different mechanical properties (σ, δ, ψ, K_{1c}, fatigue properties, heat resistance etc.)

3. Ti-Si-X systems alloys are attractive for creation of heat resistant materials.

4. Ti-B-X systems alloys are promising for achievement of high specific stiffness.

5. Ti-B-Si-X alloys, where X is Al, Zr etc, is a promising system to achieve a good combination of high specific stiffness, specific strength and heat resistance.

ACKNOWLEDGEMENTS

REFERENCES

1. D.Lesuer, C.K.Syn, O.D.Sherby. In Investigations and Applications of Severe Plastic deformation. NATO Science Series. Series 3, High Technology, V.80, Kluwer Academic Publishers, Netherlands, 2000, pp. 357-366
2. Sherby O.D. et al. In: THERMEC'2003, Part 1, Trans Tech Publications, Switzerland, 2003, pp 11-18
3. S.Takaki. In: THERMEC'2003, Part 1, Trans Tech Publications, Switzerland, 2003, pp 215-222
4. V.E.Panin, V.A.Likhachov, Yu.V.Grinyaev. Structural levels of deformation of solid bodies. Nauka, Novosibirsk,1985, 230p., in Russian
5. Segal V.M. Materials Sci. Eng. A.- 1995.-**197** - p.157-164
6. Beygelzimmer Y.,.Varyukhin V, Orlov D. - In: Proceedings of the Second Int. Symp., Los Alamos Nat. Lab. Edition, 2002- p.234-238
7. Valiev R.Z., Alexandrov I.V., Nanostructurnyje materialy poluchennyje intensivnoj plasticheskoy deformacijey, Moscow, Logos, 2000. -272p., in Russian
8. Thompson A.W. Met.Trans. - 1977.- .**8A**, №6,- pp.833-842
9. Grajvoronsky N.V., Sarzhan G.F., Firstov S.A. Met. Phys.Adv.Tech., 1998, v.17,pp.105-118
10. Andrijevsky R.A. Glezer A.M. Physica Metallov i Metallovedeniye. Part 1, 1998, V.88, N1, pp.50-733; Part 2. 2000, V.89, N1, pp.91-112, In Russian
11. Pozdnyakov V.A., Glezer A.M. Pisma v JTF, 1995, 1995, V.21, N1, pp.31-36, in Russian
12. Gleiter H. Progress in Materials Science. - 1989.- **33**.- p.223-315
13. Valiev R.Z., Korznikov A.V., Mulyukov R.R. Materials Science and Eng. A.- 1993.- **168** - pp.141-148
14. Langford G. and Cohen M. Transactions of the ASM.- 1969. **62,** №3 - p. 623-638
15. Glickman E., Bruver R., Metallophisica, 1972, V.43. pp.42-51, In Russian
16. Firstov S.A. et al. Problems of Materials Science, 2003, N1 (33), pp.201-204
17. Veprek S., Reiprich S. Thin Solid Films. – 1995. - **268**, p.64-71
18. Moiseev V.N., Syisoyeva N.V., In: Titanium'99, Proceedings of the Ninth World Conference on Titanium, CRISM "Prometey", 2000, v.1., pp.48-52
19. Froes F.H. et al. J. Mat. Sci. 1992 v.27, pp. 5113-5140
20. S. Gorsse and D. Miracle. Acta Mater., 2003, to be published.
21. Firstov S. In Advanced Multilayered and Fibre-Reinforced Composites, 1998, Kluwer Publ., pp.175-186
22. Mazur V. I. et al, US Patent Titanium matrix composite, N5366570, Nov. 22, 1994
23. Saha R.L., Nandy T.K., Misra R.D.K. et al. J.Mater.Sci, **26**(1991), pp.2637-44
24. Miracle D., Firstov S., Kulak L et al. In: THERMEC'2003, Part 5, Trans Tech Publications, Switzerland, 2003, pp.4591.

PART 2

AMORPHOUS, NANOCRYSTALLINE AND
QUASICRYSTALLINE MATERIALS

NANOSTRUCTURED MATERIALS PRODUCED BY SEVERE PLASTIC DEFORMATION

Hein Peter Stüwe

Erich Schmid Institute of Materials Science, Austrian Academy of Sciences and Institute of Metal Physics, University Leoben, Jahnstrasse 12, A-8700 Leoben, Austria

Abstract: Severe plastic deformation of metals leads to an extremely fine microstructure. This is produced by "fragmentation" of the original crystal structure. The mechanisms for this fragmentation are discussed. Various methods for severe plastic deformation are classified according to the strain paths involved:

– Continuous strain without change of strain path,
– Accumulated strain without change of strain path,
– Accumulated strain with reversal of strain path,
– Accumulated strain with variable strain path

For comparison of different experiments the concepts of "equivalent strain" and "strain efficiency" are discussed.

Key words: Severe plastic deformation, strain path, fragmentation, geometric recovery, strain efficiency, equivalent strain

1. INTRODUCTION

Severe plastic deformation (SPD) of metals is defined as "intense plastic straining under high imposed pressure" [1]. It is receiving increasing attention because it produces extremely fine-grained structures (with grain sizes <100nm) and, consequently, unusual mechanical properties (very high strength combined with good ductility or, on the other hand, superplasticity).

The first part of this paper will deal with the problem of "fragmentation", i.e., with the mechanisms leading to the fine-grained structure. The second part will deal with the efficiency of different SPD-techniques to produce such structures.

2.   FRAGMENTATION

2.1   Creation of Interfaces

Consider a typical high pressure torsion (HPT) experiment on copper with an original equiaxed grain size D_o of 80μm. After a shear strain of $\gamma=20$ it shows "structural elements", which are again about equiaxed and have a size D_s of about 250nm (see, e.g. [2]). These volume elements have a fairly uniform orientation, which differs from their neighbours by large and almost random misorientations [2]. This is why they are often called "grains". In contrast to conventional grains they are not separated by well defined grain boundaries but rather by disordered layers that can best be described as dislocation arrangements [9]. This is confirmed by an experimental observation, which, in the author's opinion, has not received enough attention. It is the fact that the structural elements of SPD materials are always roughly equiaxed. Even where they are described as "elongated" their apex ratio is rarely larger than two. Their shape, therefore, does not reflect the large strains the material has seen in experiments without change of strain path. This means that the interfaces between them are not fixed in the material but will dynamically rearrange themselves during continuing strain.

This is different for true grain boundaries. They are fixed in the material (at least at temperatures below The temperature for recrystallization). This leads to an increase in grain boundary area with increasing strain as shown in fig.1. This increase is alimented by the incorporation of dislocations into the boundary [4]. One sees that shear is quite inefficient to increase the boundary area. Even a shear strain of $\gamma \approx 20$ (corresponding to about $\varphi \approx 10$, see section 3 of this paper) will increase the grain boundary density by a factor of 7 only, whereas the true density of interfaces in our example increases by $D_o/D_s = 320$. The original grain boundaries of the virgin material, although important for the first stages of work hardening can be neglected at high strains.

2.2   Model for Creation of New Interfaces

Several models for the creation of interfaces by dislocation reactions have been surveyed in [5]. The basic idea is shown in fig.2. In the interior of one crystal dislocations of opposite sign move in opposite directions. They
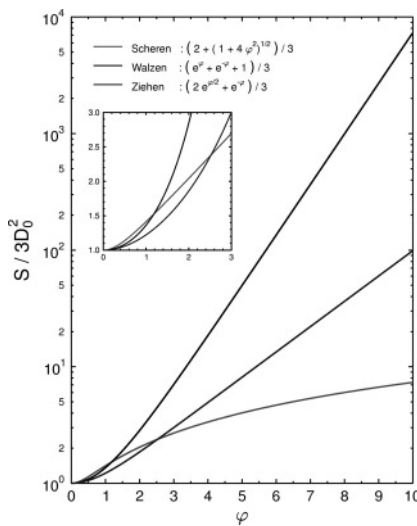
Figure 1. Relative increase of boundary area as a function of strain for a cubic grain deformed by different techniques. ($\varphi = \gamma/2$ was used as equivalent strain in shear)
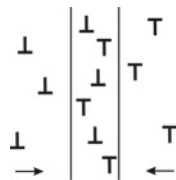
Figure 2. Formation of a planar arrangement of dislocations within one crystal, schematic

can trap each other and form a dislocation wall. As long as the two fluxes are equal, this wall will not lead to a misorientation between the two parts of the crystal even if several kinds of dislocations on several slip systems are involved. Since in a polycrystal the local stress field varies (with a wavelength of about the grain size) one would expect that even a homogeneous strain would be accommodated by different combinations of slip systems in different parts of one crystal. That this is really so, can be seen metallographically even at small strains. Fig. 3 shows an example. The fluxes from both sides in Fig. 2 will then not be equal and the dislocation wall will then lead to a growing misorientation according to Frank's formula [6]. (For a closer discussion see [7].)

We conclude that the SPD structure is built up from the many dislocations produced during high strain. Their production rate can easily be estimated as

$$\frac{d\rho}{d\varphi} \approx \frac{2M}{\Lambda b} \tag{1}$$

where M is the Taylor factor, Λ the mean free path of a dislocation and φ the logarithmic strain.
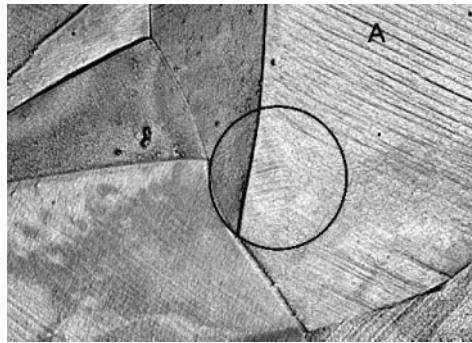
Figure 3. Copper deformed by 6% (courtesy O. Kolednik). The circle marks slip lines different from the main set in grain A.

3.   EQUIVALENT STRAIN AND STRAIN EFFICIENCY

A number of SPD techniques have been developed (for a survey see [8]). They can be classified by their strain paths:

(a) Continuous strain without change of strain path.
(b) Accumulated strain without change of strain path.
(c) Accumulated strain with reversal of strain path.
(d) Accumulated strain with variable strain path

If we want to discuss the efficiency of various techniques to produce SPD structures, we should compare samples that have experienced equivalent strains.

3.1   Equivalent Strain Under Uniaxial Stress and in Simple Shear

The conventional definition of equivalent strain is based on the proposition that samples should be compared on which the same amount of plastic work has been spent. For comparison of two specimens deformed in compression and torsion this would read

$$\frac{W_{pl}}{V} = \int \sigma \frac{dl}{l} \equiv \int \sigma \, d\varphi = \int \tau \, d\gamma \tag{2}$$

where γ is the tangent of the shear angle. This equation is fulfilled when

$$\sigma = a\,\tau \quad and \quad d\varphi = \frac{d\gamma}{a} \tag{3}$$

The value of **a** can be determined from a yield criterion. The criterion of Tresca yields **a** = 2 (This has been used in fig.1). The criterion of v. Mises yields a = √3. A more refined analysis of the Taylor type yields

$$\sigma = M\,\tau_{res} \quad and \quad d\varphi = \frac{d\Gamma}{M} \tag{3a}$$

where M is the Taylor factor, τ_{res} the average resolved shear stress, and Γ the accumulated shear on a set of active slip systems [9]. Such a treatment can take into account the development of deformation textures. The first two criteria cannot do this because they are conceived for an isotropic material.

The value of **a** can, of course, also be determined point by point from a comparison of the two stress-strain curves according to eq.(2). **a** will then in general be a (weak) function of strain, but never deviate much from the values 2 or √3 as has been shown (explicitly or implicitly) by numerous experiments during the last century.

For a discussion of SPD without change of strain path a rough estimate of equivalent strains using, e.g., **a** =2 may be reasonable. Caution is necessary when strain is accumulated with changing strain path. This is so because there is no reason to believe that the total plastic work put into a material is a sufficient measure to determine its microstructure (for a more detailed discussion, see [10]).

3.2 Accumulated Strain with Reversal of Strain Path

Fig.4 shows deformation by cyclic extrusion and compression (CEC). A cylindrical specimen of diameter d_o is pushed through a die of diameter d_m into a recipient of diameter d_o. During one pass it suffers an extension by $\Delta\varphi = \ln(d_o/d_m)^2$ and a compression by $\Delta\varphi = \ln(d_m/d_o)^2$. In terms of plastic work spent, the accumulated strain after n passes is then

$$\varphi = \sum_{1}^{2n} |\Delta\varphi| \quad . \tag{4}$$
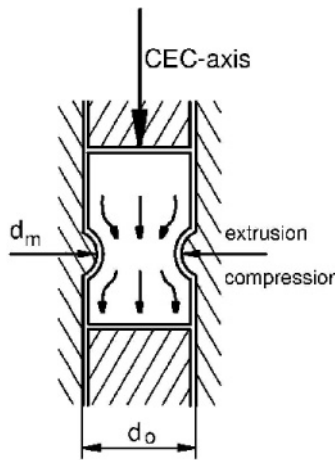
Figure 4. Cyclic extrusion and compression (CEC), schematic

This value has been used as abscissa for the stress/strain curve in fig.5. Fig.6 shows a corresponding curve obtained without change of strain path. It shows the well-known stages III, IV and V. Fig.5 has been similarly divided into stages B, C and D. Careful investigations of microstructure [3,11] have shown that stages B, C and D correspond to II, IV and V. Comparison of the onset strains shows that the strain defined by eq.(4) is much less efficient to produce the corresponding structures. It should therefore be corrected by an efficiency factor η so that

$$\varphi_{eff} = \eta \sum_{1}^{2n} |\Delta\varphi| \tag{5}$$

where $0.1 < \eta < 0.2$.
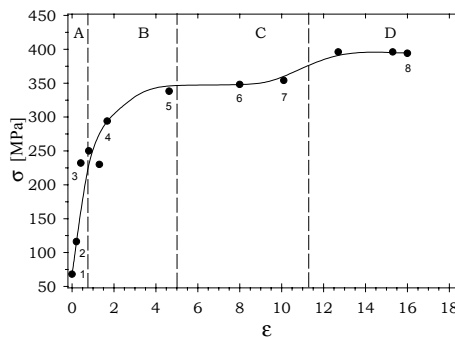
Figure 5. Stress-strain curve for AlMg5 deformed by CEC [11]
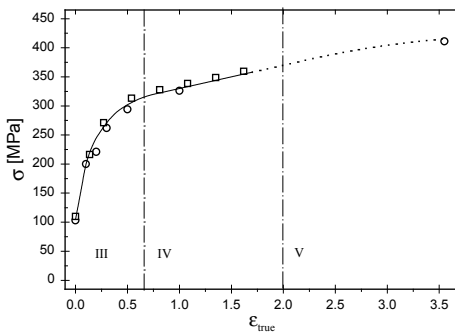
Figure 6. Stress-strain curve for AlMg5 deformed without change of strain path [11]

3.3 Dislocation Density and Accumulated Strain

In order to understand the efficiency of strains to form SPD structures one must look at the development of the dislocation density because these dislocations are the elements for building the many interfaces characteristic for these structures (as has been shown in section 2). It is not sufficient just to integrate eq.(1), one has to subtract terms for the annihilation of dislocations during deformation. For a continuous strain path such processes (like annihilation of screw dislocations by cross slip) have been studied extensively under the name of "dynamic recovery". Upon reversal of strain path, dynamic recovery is supplemented by "geometric recovery" [10]. It takes into account that the probability for moving dislocations to meet dislocations of opposite sign is strongly enhanced when the strain path is reversed. It is this second process that so strongly diminishes the efficiency η in eq.(5). For very high strains the recovery processes can balance the production of new dislocations so that a steady state is reached where fragmentation stops.

The importance of geometric recovery is quite plausible when the strain path is reversed. It is not so obvious when the strain path changes in more complicated ways. Experiments on the cold swaging of copper [10,12,13] indicate that geometric recovery is also important for an irregular sequence of strain paths. This problem should therefore be looked at more closely for ECA-pressing.

4. CONCLUSIONS

SPD produces microstructures with very small structural elements separated by interfaces built up of many dislocations produced by straining. The process of fragmentation is discussed.

For a comparison of the efficiency of different SPD techniques to produce such structures the traditional concept of "equivalent strain" based on equal mechanical work is problematic, especially when strain is accumulated in steps with varying strain path where "geometric recovery" must be taken into account.

REFERENCES

1. R.Z. Valiev, in: Investigations and Applications of SPD, Eds. T.C. Lowe, R.Z. Valiev, (Kluwer Academic Publishers, Norwell, 2000).
2. T. Hebesberger, R. Pippan, H.P. Stüwe, in: Proc. Ultrafine Grained Materials II, Eds. Y.T. Zhu, T.G. Langdon, R.S. Mishra, S.L. Semiatin, M.J. Saran, T.C. Lowe, (TMS, Warrendale, PA, 2002) 133-140.
3. M. Richert, H.P. Stüwe, J. Richert, R. Pippan, Ch. Motz, Mater. Sci. Engr. A301 (2001) 237-243.
4. J. Gil-Sevillano, P. van Houtte, E. Aernoudt, Progr. Mat. Sci. 25 (1980) 69.
5. W. Pantleon, in: Local Lattice Rotations and Disclinations in Microstructures of Distorted Crystalline Materials, Eds. P. Klimanek, A.E. Romanov, M. Seefeld, (SEITEC Publications Ltd.)
6. James M. Howe, Interfaces in Materials, (J. Wiley & Sons 1997) 332.
7. H.P. Stüwe, R. Pippan, T. Hebesberger, A. Vorhauer, Sci. Techn. J. Problems of Materials Science 1/33, (2003) 55-60.
8. T. Hebesberger, A. Vorhauer, R. Wadsack, H.P. Stüwe, R. Pippan, Berg- und Hüttenmännische Monatsh. 147, 11, (2002) 358-364.
9. I. Kopacz, L.S. Toth, M. Zehetbauer, H.P. Stüwe, Modeling Simul. Mater. Sci. Eng. 7, (1999) 875-891.
10. H.P. Stüwe, Advanced Eng Mats. 5 (2003) 291-295.
11. M. Richert, H.P. Stüwe, M.J. Zehetbauer, J. Richert, R. Pippan, Ch. Motz, E. Schafler, Mat. Sci. Eng A355, (2003) 180-185.
12. A. Grabianowski, A. Danda, B. Ortner, H.P. Stüwe, Mech. Res. Comm., 7 (1980) 125.
13. J. Schrank, B. Ortner, H.P. Stüwe, A. Grabianowski, Mater. Sci. Techn., 1 (1985) 544.

DEVELOPMENT OF NANOSTRUCTURED AND NANOPARTICLE DISPERSION-REINFORCED METALLIC SYSTEMS
- *Progress and Challenges*

P. R. Subramanian[1], Reed R. Corderman[1], Sundar Amancherla[2], Ramkumar Oruganti[2], Thomas M. Angeliu[1], Shyh-Chin Huang[1], Suchismita Sanyal[2], Dheepa Srinivasan[2], K. Anand[2], Michael Larsen[1], Judson S. Marte[1], Dennis M. Gray[1]

[1]*GE Global Research Center, Niskayuna, New York, USA;* [2]*GE Global Research - JFWTC, Bangalore, India*

Abstract: Investigations on nanostructured metallic systems have shown that exceptional property enhancements are potentially achievable through structural refinement to the nano-scale. While dramatic property improvements have been reported on these materials in the past, significant technical challenges exist in processing, as well as in retention of microstructural stability and useful properties at elevated temperatures. This presentation will summarize the key challenges in developing nanostructured metallic systems, and highlight our progress and selected successes in the understanding of structure-property relationships in bulk nanostructures as well as nanostructured multilayered systems. Work in nanoparticle dispersion-strengthened metallic systems will also be highlighted in this presentation.

Key words: nanostructured metallic systems/microstructural stability/structure-property relationships/metallic nanostructures/nanostructured multilayers

1.   BACKGROUND

The field of nanotechnology is in a state of revolution, with scientific literature growing exponentially in the past few years. In the conventional definition, nanotechnology refers to building of structures from atomic to near-molecular building blocks, with recent emphasis primarily in devices and novel structures such as carbon nanotubes. However, nanocrystalline metallic systems and nanostructured coatings are also emerging materials with interesting physical

and mechanical properties [1,2]. A brief discussion of some of the underlying concepts in nanostructured materials will serve to highlight the potential benefits as well as technical challenges in the development of these materials. While nanoparticle dispersion-reinforced metallic systems do not truly come under the class of nanostructured materials, work in the area will also be highlighted.

1.1   Structure-Property

In conventional materials, strengthening from microstructural refinement (Hall-Petch effect) arises from dislocation pileup at grain boundary, and the stress to nucleate dislocations in the adjacent grains. As the grain size decreases, the number of dislocations in the pile-up goes down dramatically, and instead of pile-up, the dislocations cross grain boundaries one at a time. At these sizes, the large fraction of grain boundaries contributes to a competing mechanism of grain boundary sliding, which weakens the material (Fig. 1). Thus, in nanocrystalline single-phase materials, there is a competition between grain boundary sliding at nanoscale dimensions vs. strengthening via dislocation-dominated processes [3]. The critical size for this transition varies from metal to metal, but generally lies below 25 nm. In layered structures, a similar Hall-Petch type deformation mechanism holds, wherein dislocation pile-up at the layer interface at large layer thickness gives rise to strengthening. However, as the layer thickness approaches nanoscale dimensions, plastic flow occurs by single dislocations moving by bowing within layers, leaving misfit dislocations at the interface.
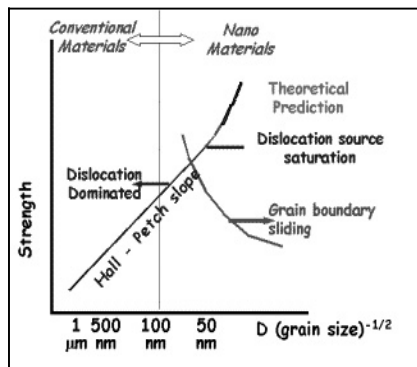

Figure 1. Effect of microstructural scale on strength in single-phase materials and multilayers.

Reinforcement by a fine, homogeneous dispersion of second-phase nanoscale particles is an effective way to achieve strengthening and stability. Oxide dispersion strengthened (ODS) superalloys (Ni-base alloys such as

MA754, MA956, and Fe-based alloy such as PM2000) and dispersion strengthened copper are well-known examples in this class. The ODS alloys are reinforced by <50 nm size yttria nanoparticles with an average spacing of 100 to 250 nm in a metallic Ni or Fe matrix. The low-to-intermediate temperature strengthening in these alloys is based on the particle interactions with dislocations, resulting in the pinning of dislocations by the array of non-shearable particles via the Orowan mechanism. Typically, a dispersoid radius of <100 nm would be required for strengthening by the Orowan mechanism [4]. At high temperatures, creep strengthening by dispersoids occurs by an attractive interaction between dislocations & the incoherent particle-matrix interface, leading to dislocation pinning at the departure end of the particles [5-7]. Nanostructures with a high volume of second-phase nanoscale dispersoids can also provide enhanced wear resistance by increasing the overall hardness & fracture toughness of the material [8].

Another role of hard particles or dispersoids is in limiting grain boundary migration by a mechanism called Zener pinning, which reduces the driving force for grain growth. Thus, a fine dispersion of nanosize dispersoids can provide some measure of microstructural stability, although at extremely fine sizes, thermal activation mechanism becomes important, and the particles may no longer be effective at pinning grain boundaries. It has been shown in dispersion-reinforced Cu that stability of grain sizes down to below 40 nm can be explained in terms of Zener pinning of grain boundaries [9]. Movchan [10] has shown that maximum ductility is seen in dispersion-reinforced systems when the grain size is approximately equal to the mean free path between the particles. Stability of nanostructured polycrystalline alloys has been addressed by another concept called segregation stabilized grain structure [11-12], wherein segregation of solutes at grain boundaries causes an overall reduction in the specific grain boundary energy.

1.2   Processing-Structure

Typically, nanostructured metallic materials have been produced using a range of techniques, including gas-condensation, vapor deposition, rapid solidification, electrodeposition, and mechanical alloying [13-18]. A variation of the conventional high-energy ball milling approach, termed cryomilling or cryogenic ball-milling, has been successful in producing thermally stable nanostructures [19-23]. While the mechanical milling process provides significant grain refinement, the nanosized dispersoids incorporated during the cryomilling process serve to enhance thermal stability by functioning as grain-growth inhibitors via Zener pinning of grain boundaries. In some cases, impurity or solute segregation at the grain

boundaries may provide supplementary mechanisms for grain growth retardation [20]. Recently, nanocrystalline Cu with exceptional strength and ductility have been produced by sub-ambient temperature deformation at liquid nitrogen temperature, followed by secondary recrystallization [24].

Processing by severe plastic deformation (SPD) is rapidly emerging as a viable route for making bulk nanostructured, ultra-fine grained (UFG), or submicrometer-grained (SMG) metals [25-28]. SPD techniques such as equal channel angular extrusion (ECAE), or high-pressure torsion (HPT) lead to a fully-dense microstructure with ultra-fine grains separated by non-equilibrium, defected grain boundaries containing a high density of extrinsic grain boundary dislocations. The severe deformation process initiates shear bands within a material, with subgrain formation within these shear bands [29]. The severe deformation process thus leads to grains with a high density of dislocations and non-equilibrium grain boundaries.

2.   OUR APPROACH

The focus of our efforts centered on exploring nanoscale dispersion reinforced metallic materials and multilayered structures as model systems, primarily to obtain a fundamental understanding of the underlying mechanisms governing strength and thermal stability in these systems. Parallel efforts were initiated in exploring practical methods to produce such structures. Physical vapor deposition (PVD) was selected as the primary method for fabricating controlled structures for structure-property understanding. Bulk fabrication techniques, such as casting, powder metallurgy (PM) & deformation processing were examined in an effort to produce scalable structures. In this section, results on selected nanostructured and dispersoid-reinforced systems are presented in order to highlight successes in specific areas, while bringing out the overall challenges in developing this class of materials.

2.1   Nanoparticle Dispersion-Reinforced Systems

Efforts were initiated to produce nano-oxide reinforced alloys by mechanical mixing of alloy powders (-325 mesh) and Y_2O_3 (average size 35-50 nm), using a novel mechano-chemical bonding process [30]. This process causes the Y_2O_3 particles to be physically embedded on the alloy powder particle surface, thus allowing for controlled distribution of the dispersoids. The mechanofused powders were canned and hot-extruded at 1100°C. In parallel, electron beam-PVD was also employed to produce the nano-oxide reinforced alloys, using metal and oxide targets. The

microstructural scale of the deposits was tailored by controlling deposition parameters as well as substrate temperatures. Figure 2 compares the PM and PVD microstructures of a typical metallic alloy with 4 vol. % Y_2O_3. The dispersoids range in size from 40 to ~300 nm in the PM structures and from 75 to 200 nm in the PVD structures. The grain sizes in the PVD structures were in the range 200-500 nm, while the PM structures typically had grain sizes <5 µm. Figure 3 shows a plot of the hardness as a function of the grain size for both the PVD and PM structures, along with a datum for the same metal reinforced with micron-size dispersoids - no definite Hall-Petch type correlation can be made from the sparse data; however, there is a definite increase in the hardness in the nano-dispersoid reinforced structures.
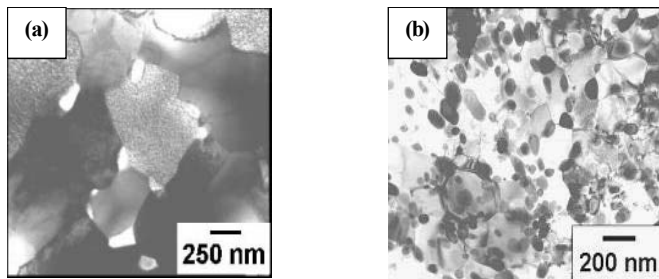
Figure 2. TEM micrographs of (a) PM structure – white particles are Y_2O_3 nanodispersoids; (b) PVD structure, showing a high volume of Y_2O_3 particles in a metallic matrix.
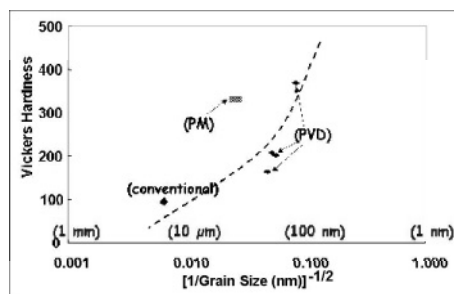
Figure 3. Hardness vs. layer spacing for PVD and PM dispersion-reinforced alloys.

2.2   Cast Nano-Dispersion Reinforced Structures

The objective of the cast dispersion reinforcement approach was to develop an affordable, thermally stable, high-volume, oxide dispersion-strengthened alloy. The development of cast nano-oxide dispersion

reinforced alloys is in its infancy because of the limited availability of non-agglomerated nanoparticles. A fundamental problem in the casting of dispersion-reinforced alloys is the rejection of the particles during solidification. Solidification gradients can be typically controlled by spray dispersion or high intensity ultrasonics. Spray dispersion involves spraying oxides into molten metal as it is poured and has been demonstrated with ferrous and Ni-base alloys [32]. High intensity ultrasound creates acoustic streaming and cavitation in solutions and has been used to disperse nanoparticles in more conventional liquids [33].

Feasibility experiments were conducted on materials with a range of melting points, using vacuum arc remelting (VAR), vacuum induction melting (VIM), and stir-casting. Initial experiments focused on the wetting and thermal stability of nano-oxides (alumina, yttria and zirconia) as a function of temperature and processing parameters. VAR and casting of commercial ODS alloys under high-intensity ultrasound was not successful - it was speculated that the process was too aggressive and decomposed the oxides during melting. A relatively high melting-point alloy was vacuum induction melted, but due to the high temperatures, it was difficult to adequately agitate the melt to promote wetting and dispersion of nano-oxides. Several stir-casting experiments were attempted with various processing and chemistry conditions. Initial results showed that 0.4 wt.% of nano-yttria was adequately dispersed on the length scale of composites with the addition of 0.2 wt.% active elements (Fig. 4).
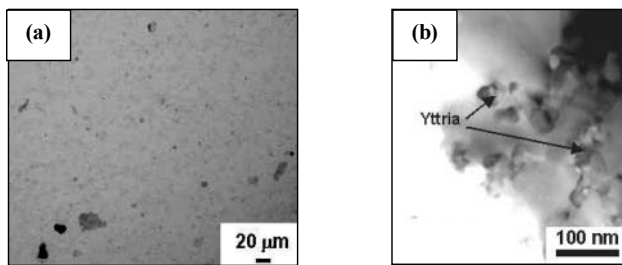
Figure 4. Nano-yttria dispersed in metal using stir-casting: (a) agglomerated nano-yttria, an active element-rich phase + microporosity; (b) TEM showing agglomerated nano-yttria + detached nano-oxides.

2.3   **Cryomilled Nano-Al**

The current study was aimed at understanding the thermal stability of an Al-7.5 wt.% Mg alloy processed by cryomilling. Following milling in liquid nitrogen for 8h, the Al-Mg powder was consolidated by canning and forging at 454°C, and then heat-treated. Typical microstructures of the as-forged and

heat-treated (350°C/24h) alloys are shown in Fig. 5. The grain structure is observed to be stable even after heat treatment at high homologous temperatures. In certain regions, large (0.75 to 1 μm) grains constituting around 10% of the total area were observed, with the grains lying in bands. Grain size data for the areas containing only small grains in material heat-treated at 450°C for 4h and 24h are shown in Fig. 6 - the mean grain size does not change substantially, ranging from 177 nm for the as-forged material to 286 nm after annealing at 450°C/24h. As shown in Fig. 7, the room-temperature hardness is also found to be nearly constant after over 16h of exposure at 450°C. Hardness reductions are seen at 520°C and 535°C, which are close to the melting temperature of this alloy.

The remarkable feature of the alloy studied here is the stability of the microstructure as a function of temperature. Such stability has been observed earlier [34,35] and has been attributed mainly to two reasons. One is the possible presence of grain boundary solutes that have been incorporated and stabilized during the mechanical milling process. Another possibility is the presence of nano-scale nitride/oxynitride particles that have formed as a result of milling in liquid nitrogen. Possible evidence of this mechanism is shown in Fig. 8, which shows a micrograph of a specimen heat-treated at 350°C for 24h. It is seen that a 40 nm particle is pinning a grain boundary - bowing on either side of the particle suggests a Zener-type pinning mechanism. Further work is being carried out to identify even finer scale particles that have been reported earlier but not confirmed.
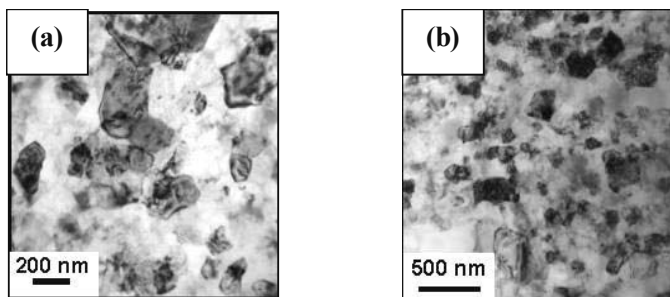
Figure 5. SEM microstructure of cryomilled Al-Mg: (a) as-forged ; (b) after heat-treatment at 350°C for 24h. Grain structure remains largely unchanged after the heat-treatment.
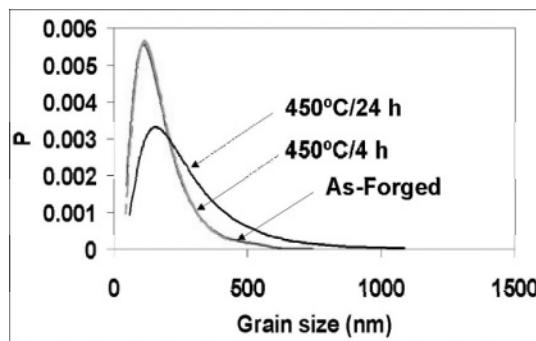
Figure 6. Grain size distribution in cryomilled Al-Mg after heat treatment at 450ºC.
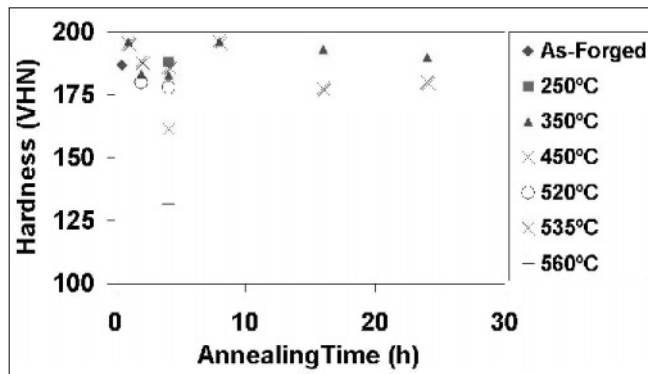
Figure 7. Room-temperature hardness of cryomilled Al-Mg as function of annealing time and temperature.
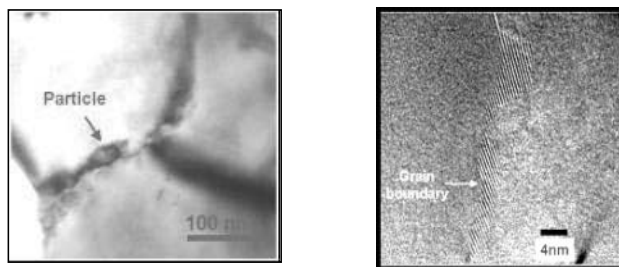
Figure 8. TEM of 350°C/24h heat-treated Al-Mg alloy, showing nanoparticles at grain boundary.

2.4   **Multilayered Cu-Mo structures**

Cu-Mo nanolayered structures with individual layer thickness ranging from 5 nm to 200 nm were produced by magnetron sputtering on various substrates. The multilayers with various combinations of Cu/Mo layer spacing had layer thickness ratios ranging from 0.1 to 10.   Efforts were concentrated on understanding the stability and strength of these systems. Figure 9 shows TEM micrographs of the 100 nm Cu/50 nm Mo as well as the 5 nm Cu/5 nm Mo layered structures.   The layers have typical bamboo structures with the grain boundaries in the individual layers normal to the layer interfaces. Figure 10 shows the room-temperature hardness of the various Cu/Mo multilayers. Comparing the properties of the as-deposited multilayer with that of as-deposited Cu and Mo, a substantial increase is observed in the hardness of the multilayers. After annealing the 100 nm Cu/50 nm Mo multilayer at 800°C/1h, there is a drop in hardness from 4.8 to 1.7 GPa, although the data still conform to the rule-of-mixtures hardening. As shown in Figure 11, the 800°C-annealed sample no longer retains the layer morphology – a fully spheroidized structure was observed, which explains the decrease in hardness.
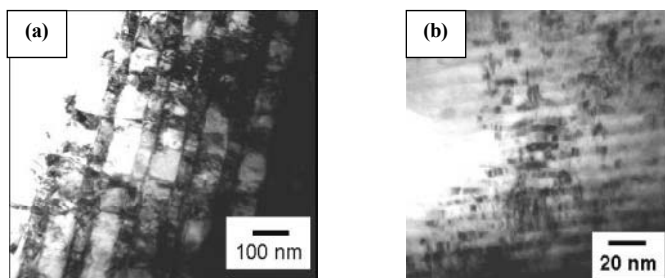
Figure 9. TEM of as-deposited multilayers: (a) 100 nm Cu/50 nm Mo; (b) 5 nm Cu/5 nm Mo.
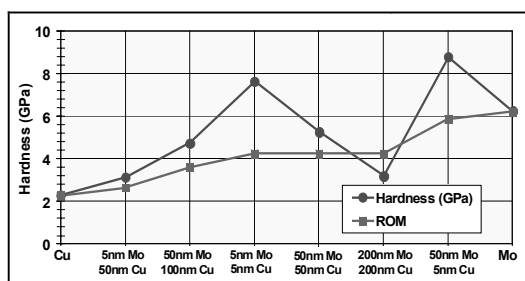
Figure 10. Room-temperature hardness of the as-deposited Cu-Mo multilayers.
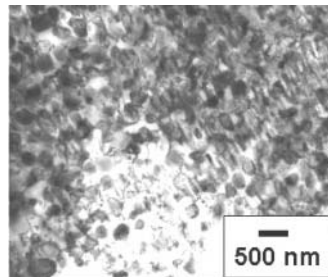
Figure 11. Spheroidization of the 100 nm Cu/50 nm Mo structure after an 800°C/1h anneal.

The stability of the Cu/Mo multilayered structures was analyzed in terms of the kinetics of thermal grooving of grain boundaries normal to the layer interface, as given by the following equation [36]:

$$d = (0.78)(Tan\beta)[(\Omega^{4/3}D_{int})\frac{\gamma_{int}}{kT}]^{1/4}t^{1/4} \tag{1}$$

where d = groove depth, β=groove angle, Ω is the atomic volume and given by $0.5(\Omega_{Cu} + \Omega_{Mo})$, D_{int} is the grain boundary diffusivity of Cu and is approximated as the self-diffusion coefficients of Cu [37], γ_{int} is the interface energy of Cu-Mo and calculated using Miedema's method [38-40], t is the time, and T is the temperature. Using Eq. [1], the time for grooving in a 50 nm Cu/50 nm Mo multilayer was estimated as ~12 h, 0.16 h, and 0.006 h at 300, 500, and 800°C, respectively. Refinements to this model are in progress to obtain a predictive understanding of kinetics of multilayer stability.

2.5   **Thermal Stability of Nanostructures**

Bulk metallic nanostructures comprising of either nanostructured grains and/or nano-scale second phase particles do tend to coarsen at elevated temperatures. Thus, there is a need for a detailed understanding of the thermal instability mechanisms such as grain growth and second-phase growth. Following the recent advances in computational materials science and particularly in the area of microstructural evolution, the phase-field modeling approach [42] has been selected for modeling the thermal stability mechanisms for the nanostructured materials. Efforts are underway to understand grain growth kinetics and how this changes with different changes in the microstructure, such as impurities that induce solute drag [43] or ceramic particulate dispersoids that pin the grain boundary.

3.   FUTURE DIRECTIONS

We have shown that strength and stability can be obtained under selected conditions in nanostructured and dispersion reinforced systems. However, for structural applications, a balance of properties is critical - fracture and fatigue behavior of these systems are not well-established. Processing scale-up is another big challenge in these systems; most of the properties have been demonstrated on laboratory-scale materials. Process scale-up is required to produce useful quantities of materials for sub-scale component demonstration as well as design property evaluation. The retention of useful microstructures, microstructural homogeneity as well as critical material properties has to be demonstrated in scaled-up materials. While our focus has been on structural applications, there may be other non-structural or functional applications for these systems. Future investigations will be focused on such opportunities.

ACKNOWLEDGMENTS

REFERENCES

1. C. Suryanarayana, in: Physical Chemistry of Powder Metals (Ed. W. M. Small), TMS, Warrendale, PA, 1989, 279.
2. H. Gleiter, Acta Mater. 48, 2000, 1.
3. H. Hahn, P. Mondal, and K.A. Padmanabhan, Nanostructured Materials, 9, 1997, 603.
4. J. Rosler and M. Baker, Acta Mater. 48, 2000, 3553.
5. D. Srolovitz, M.J. Lutton, R.A. Petkovic-Lutton, D.M. Barnett, and W.D. Nix, Acta Metall., 32, 1984, 1079.
6. J. Rosler and E. Arzt, Acta Metall. Mater., 38, 1990, 671.
7. J. Rosler and M. Baker, Acta Mater. 48, 2000, 3553.
8. A.S. Argon and S. Veprek, in: Proc. 22nd Riso Intern. Symp. on Materials Science, Science of Metastable and Nanocrystalline Alloys – Structure, Properties and Modeling (Eds. A. R. Dinesen et al.), Riso National Laboratory, Roskilde, Denmark, 2001, p. 183.
9. D.G. Morris and M.A. Morris, Acta Metall. Mater., 39(8), 1991, 1763.

10. B.A. Movchan, Mater. Sci. Engg., A138, 1991, 109.
11. J. Weissmuller, Nanostructured Metals, 3, 1993, 261.
12. R. Cahn, Materials Today, November/December 2001, 13.
13. H. Hahn, Nanostructured Materials, 9, 1997, 3.
14. A.L. Greer, Mater. Sci. Engg., A133, 1991, 16.
15. R.R. Oberle, M.R. Scanlon, R.C. Cammarata, and P.C. Searson, App. Phys. Lett., 66(1), 1995, 19.
16. H. J. Fecht, Nanostructured Materials, 1, 1992, 125.
17. J. Ecken, J.C. Holzer, , C.E. Krill, III and W.L. Johnson, J. Mater. Res., 7(7), 1992, 1751.
18. D.G. Morris and M.A. Morris, Acta Metall. Mater., 30(8), 1991, 1760.
19. R.J. Perez, H.G. Jiang, C.P. Dogan, and E.J. Lavernia, Metall. Mater. Trans. A, 29A, 1998, 2469.
20. V.L. Tellkamp, A. Melmed, and E.J. Lavernia, Metall. Mater. Trans. A, 32A, 2001, 2335.
21. J. Lee, F. Zhou, K.H. Chung, N.J. Kim, and E.J. Lavernia, Metall. Mater. Trans. A, 32A, 2001, 3109.
22. R. Rodriguez, R.W. Hayes, P.B. Berbon, and E.J. Lavernia, Acta Mater., 51, 2003, 911.
23. M.J. Luton, C.S. Jayanth, M.M. Disco, S. Matras, and J. Vallone, in: Multicomponent Ultrafine Microstructures (Eds. L. E. McCandlish et al.), Mat. Res. Soc. Symp. Proc., Vol. 132, 1989. p. 79.
24. Y. Wang, M. Chen, F. Zhou, and E. Ma, Nature, 419, 2002, 912-915.
25. R.Z. Valiev, Nanostructured Materials, 6, 1995, 73.
26. J. Wang, Y. Iwahashi, Z. Horia, M. Furukawa, M. Nemoto, R. Z. Valiev, and T. G. Langdon, Acta Mater. 44(7), 1996, 2973.
27. R.Z. Valiev, I. V. Alexandrov, and R. K. Islamgaliev, in: Nanostructured Materials (Eds., G. M. Chow and N. I. Noskova), Kluwer Academic Publishers, Netherlands, 1998, p. 121.
28. K. Neishi, Z. Horia, and T. G. Langdon, Mater. Sci, Engg. A, A325, 2002, 54.
29. H.-J. Fecht, Nanostructured Materials, 6, 1995, 33.
30. C.C. Huang, Hosokawa Nano Particle Technology Center, Minneapolis, MN; private communication (2003).
31. A.Kelly and R.B. Nicholson, Strengthening Methods in Crystals, John Wiley and Sons, New York, 1971, 553.
32. M. Hasegawa and M. Osawa, Metall. Trans. A., 16A, 1985, 1043.
33. O.V. Abramov, High-Intensity Ultrasonics, Gordon and Breach Science Publishers, 1998, 567.
34. T.R. Malow and C.C. Koch, Acta Mater., 45(5), 1997, 2177.
35. R.J. Perez, B. Huang and E.J. Lavernia, Nanostructured Materials, 7(5), 1996, 565.
36. W.W. Mullins and P.G. Shewmon, Acta Metall., 7, 1959, 163.
37. T. Surholt and C.H.R. Herzig, Acta Mater., 45(9), 1997, 3817.
38. A.R. Miedema, Z. Metallkde., 69, 1978, 287.
39. A.R. Miedema and Frits J.A. den Broeder, Z. Metallkde., 70, 1979, 14.
40. A.R. Miedema, Z. Metallkde., 69, 1978, 456.
41. E. Arzt, et al, Mater. Sci. & Engg., A234-236, 1997, 22.
42. L-Q. Chen and Yunzhi Wang, JOM, Dec. 1996, 13.
43. J.W. Cahn, Acta Metall., 10, 1962, 789.

NANOSTRUCTURED AND NANOCOMPOSITE LIGHT METAL-BASED COMPOUNDS FOR HYDROGEN STORAGE

Robert A. Varin[1], Liren Guo[1], Songlin Li[1]*), Chun Chiu[1], Andrzej Calka[2]

[1]*Department of Mechanical Engineering, University of Waterloo, Waterloo, Ontario, Canada N2L 3G1*

*) On leave of absence from Powder Metallurgy Research Academy, Central South University, Changsha 410083, P.R. China

[2]Faculty of Engineering, University of Wollongong, Wollongong, NSW 2522, Australia

Abstract: The present paper is an overview of our recent results on the nanostructural processing and synthesis of complex hydrides in the Mg-M-H (M= Co, Mn, B and Fe) systems by using Controlled Reactive Mechanical Alloying (CRMA) and Milling (CMM) in the magneto-mill Uni-Ball-Mill 5. Under *shearing* mode of milling the principal nanocrystalline hydride being created in the 2Mg-Co, 3Mg-Mn and Mg-2B mixtures is β-MgH$_2$ whose nanograin size can be immensely reduced to the range of ~10-5 nm. For the Mg-2B mixture X-ray diffraction seems to provide some evidence for the presence of a small amount of nanostructured Mg(BH$_4$)$_2$. In the 2Mg-Fe mixture *amorphization* of elemental Mg and formation of *amorphous* MgH$_{0.6-1.1}$ hydride is observed.

Key words: hydrogen storage/nanostructured light metal-based hydrides/controlled reactive mechanical alloying/magnesium hydride/amorphous hydrides

1.   INTRODUCTION

Hydrogen is emerging rapidly as a major component of clean, sustainable energy systems. However, onboard hydrogen storage for proton exchange membrane (PEM) fuel cells for vehicular applications remains an undisputed problem. The most common storage systems such as high pressure gas cylinders and cryogenic tanks for liquid hydrogen suffer from inherent safety problems

and relatively low *volumetric* densities (~40 kg m^{-3} for gas under 80 MPa and ~71 kg m^{-3} for liquid hydrogen) [1,2]. The highest volumetric densities of hydrogen are found in solid metal hydrides (80-150 kg m^{-3}) [2] and simultaneously, high *gravimetric* densities can be achieved by utilizing light-metal compounds based on Li, Mg, B and Al. For vehicular applications the storage capacity requirement varies from slightly in excess of 3wt% (Japanese World Energy Network) to more than 6wt% (US Department of Energy) [3]. From this standpoint, the most interesting compounds for further development as hydrogen storage materials which are based on light elements, specifically suitable for mobile applications, are listed in Table 1. Theoretical hydrogen capacity, density and decomposition temperature are shown. The compounds are listed in the order of decreasing theoretical hydrogen capacity. The hydrides listed in Table 1 are usually referred to as "complex metal hydrides" whose general characteristic is a mixed ionic-covalent bonding between metal and hydrogen complex [6]. For example, Mg-transition-metal (TM) complex hydrides have TMH$_x$ anion complex such as $(FeH_6)^{4-}$ or $(CoH_5)^{4-}$ in Mg_2FeH_6 and Mg_2CoH_5, respectively. A number of them have excellent theoretical hydrogen storage capacity much exceeding the storage capacities required by various agencies for vehicular application. However, their fatal drawbacks are high decomposition (desorption) temperature which is much higher than ~100-150°C tolerable by PEM fuel cell [3] and relatively slow kinetics. Therefore, it is important to learn how to make complex hydrides more reversible, especially in the low temperature desorption mode.

Table 1. Properties of selected hydrides based on light-metal hydrogen systems [1,4,5].

Metal-hydrogen system	Hydride	Theoretical hydrogen capacity (wt%)	Density (g/cm^3)	Decomposition temperature (°C)
Li-B-H	LiBH$_4$	18.4	0.67	380
Mg-B-H	Mg(BH$_4$)$_2$ or MgB$_2$H$_8$	15.3	0.99	300-800(?)
Na-B-H	NaBH$_4$	10.6	1.07	400
Mg-Fe-H	Mg$_2$FeH$_6$	5.4	2.72	320
Mg-Mn-H	Mg$_3$MnH$_7$	5.2	2.30	280
Mg-Co-H	Mg$_2$CoH$_5$	4.5	2.70	350(?)

It has been reported in the past decade that a substantial enhancement of hydrogen sorption/desorption properties of various hydrides could be achieved by creating *nanostructured*/*nanocomposite* materials using mechanical alloying (MA) and/or milling (MM) [7,8]. In this context nanostructured/nanocomposite means that each phase present in the individual powder particle of the alloy is in the form of grains with nanometer size. In other words, one powder particle can be considered as a

polycrystal but with enormously refined grains. Usually, suitable nanostructured/nanocomposite hydrides can be fabricated by ball milling from elemental powders (MA) or polycrystalline bulk alloys (MM) under an inert atmosphere and subsequent hydrogenation in a separate step. However, for cost reduction and ease of hydride formation a very attractive process in which nanostructured hydrides can be produced in a single step is milling directly under hydrogen. The process is referred to as reactive mechanical alloying (RMA) if two or more elemental powders/compounds are milled and reactive mechanical milling (RMM) if one element/alloy/compound is milled [7]. In conventional ball mills (planetary or shakers) the trajectories of grinding balls are rather chaotic. That creates a continuous and erratic change of various modes of milling from *shearing* to *impact* during the same milling cycle. However, in a unique magneto-mill Uni-Ball-Mill 5 (A.O.C. Scientific Engineering Pty, Australia) the trajectories of the balls are controlled by strong magnetic field provided by the NdFeB external magnets [9-11]. The milling modes can be then easily adjusted from shearing to impact by changing the angular position of the external magnets. MA/RMA and MM/RMM under controlled conditions in the Uni-Ball-Mill 5 can be now referred to as *controlled* mechanical alloying/reactive mechanical alloying (CMA/CRMA) or milling (CMM/CRMM).

The present paper is an overview of our recent efforts on the nanostructural synthesis and/or processing of complex metal (M) hydrides in the Mg-M-H (M=Fe, Co, Mn, B) systems by using controlled reactive mechanical alloying (CRMA) and milling (CMM) in the magneto-mill Uni-Ball-Mill 5. The results presented here are limited to only those obtained under *shearing* mode. The synthesis of hydrides during reactive mechanical alloying was carried out under hydrogen at pressures of about 400-500 MPa. Ball-to-powder weight ratio (BPWR) was 10:1 for the 2Mg-Co and 3Mg-Mn mixtures and ~40:1 for the other mixtures. A very important technological parameter in magneto-milling is a distance between the milling vial and NdFeB magnet which is referred to as "working distance" (WD). It governs the force of the magnetic attraction exerted onto the steel balls. It was adjusted from 10 to 3 mm depending on the specific alloy. SEM combined with EDS and X-ray diffraction (XRD) were used for microstructural investigations. More experimental details can be found in recent publications [12,13].

2.   NANOSTRUCTURED HYDRIDES

A dramatic effect of the working distance (WD) and to some extent the powder-to-ball weight ratio (BPWR) during mechanical alloying on the morphology of synthesized powders is shown in Fig.1. Powders 2Mg-Co
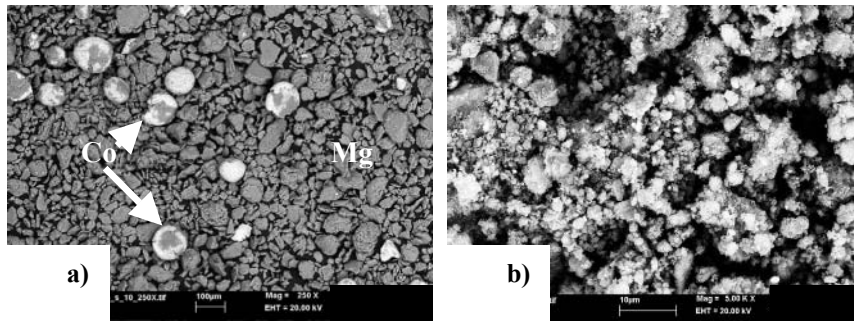
Figure 1. Backscattered electron (BSE) images of the morphology of powders processed under shearing mode by reactive mechanical alloying under hydrogen. a) 2Mg-Co mixture milled for 30h using WD=10 mm and BPWR=10:1 and b) Mg-2B (crystalline *(c)* boron) mixture milled for 5h using WD=5 mm and BPWR=44:1. RPM=60 applied during milling.

shown in Fig.1a which were mechanically alloyed under hydrogen for 30h using WD=10 mm and BPWR=10:1 do not exhibit any refinement and intimate mixing of the elemental Mg and Co powders. On the other hand, the Mg-2B (crystalline *(c)* boron) mixture which was reactively alloyed for only 5h using WD=5 mm and BPWR=44:1 shows substantial reduction of the powder particle size and very intimate mixing of both elements (Fig.1b). In general, we have found in due course of these studies that more effective factor during CRMA under shearing mode, leading to relatively fast hydrogenation, is the reduction of the working distance rather than increase of BPWR. Although, it seems that even with relatively small working distance the minimum BPWR should be kept at no less than around 30:1 to 40:1 for effective hydriding/alloying under shearing mode.

In the 2Mg-Co, 3Mg-Mn and Mg-2B mixtures after appropriate duration of CRMA the principal hydride which was synthesized was tetragonal magnesium dihydride, β-MgH$_2$ (JCPDS Powder Diffraction File No.12-0697). In order to increase the magnetic attraction force exerted onto the balls and the intensity of milling the 2Mg-Co and 3Mg-Mn mixtures after reactive milling for 100h using WD=10mm were additionally milled for 20h (100+20h) and 50h (100+50h) using WD=3mm. Fig.2 shows an example of XRD patterns for the 2Mg-Co illustrating the evolution of microstructure of powders occurring with increasing milling time. Two important features of the XRD patterns can be seen. First, there is steady increase in the intensity of the β-MgH$_2$ peaks which attain some saturation level and then become extensively broadened indicating nanograin formation and/or lattice strain.
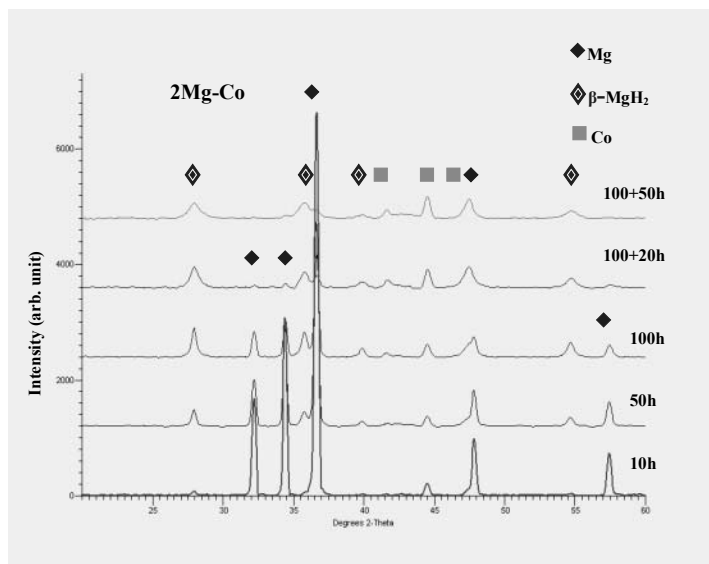
Figure 2. The effect of milling time on the XRD pattern of 2Mg-Co mixture. Up to 100h powders were milled using WD=10mm and afterwards for additional 100+20h and 100+50h they were milled using WD=3mm. BPWR=10:1; RPM=60 applied during milling.

Second, there is a gradual reduction of the intensities of Mg peaks in the pattern. The simultaneous change of peak intensities of the strongest Mg and β-MgH$_2$ peaks as a function of milling time for the mixture 2Mg-Co is shown quantitatively in Fig.3. From the microstructural evolution standpoint these changes clearly indicate that Mg is being gradually consumed during reactive milling in the reaction to form β-MgH$_2$, i.e. Mg+H$_2$$\Rightarrow$$\beta$-MgH$_2$ [14-18]. After milling for 100+50h the intensity of the strongest Mg peak (101) is almost negligible (Fig.3a) indicating that, in practical terms, the entire Mg phase has already been consumed to form β-MgH$_2$. In turn, the intensity of the strongest peak (110) β-MgH$_2$ remains somehow saturated after milling for 120-150h (Fig.3b). There is no further formation of β-MgH$_2$ during milling for over 100h due to the lack of elemental Mg. It must be pointed out that we did not found any evidence of the formation of metastable orthorhombic γ-MgH$_2$ whose formation was observed during reactive ball milling of β-MgH$_2$ [3] and reactive mechanical alloying of Mg-Ge mixture [17]. The behavior of intensities in Fig.3 has been a common observation
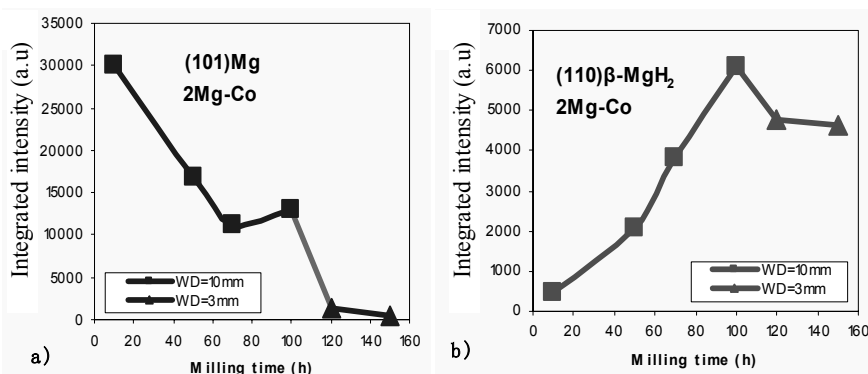
Figure 3. Integrated intensities of the strongest peak a) (101)Mg and b) (110) β-MgH$_2$ vs. milling time for the mixture 2Mg-Co. Integrated intensities calculated using software TRACES^{TM} v.6.5.1. Milling up to 100h was carried out using WD=10mm and for further 100+20h and 100+50h WD was reduced to 3mm. BPWR=10:1; RPM=60 applied during milling.

in all three 2Mg-Co, 3Mg-Mn and Mg-2B mixtures during CRMA. It means that in all three systems Mg is consumed to form the β-MgH$_2$. In the mixtures 2Mg-Co and 3Mg-Mn, the Mg phase was almost entirely consumed for the formation of the β-MgH$_2$ hydride (Fig.3). However, in the mixture Mg-2B some Mg still remained in the structure even after completion of the β-MgH$_2$ reaction forming a nanocomposite Mg/MgH$_2$.

As mentioned earlier, the mixtures 2Mg-Co and 3Mg-Mn after CRMA for 100h were additionally milled for 100+20h and 100+50h under hydrogen using WD reduced from 10mm to 3mm in order to increase the magnetic attraction force exerted onto the balls and the intensity of milling. Despite such measures no peaks from the Mg$_2$CoH$_5$ or Mg$_3$MnH$_7$ hydrides (Table 1) ever appeared on XRD patterns (Fig.2). Huot et al [19] also failed in synthesizing Mg$_2$CoH$_5$ directly by reactive milling under hydrogen. However, subsequent sintering of Mg-Co powders pre-milled either under argon or hydrogen yielded a modest quantity of Mg$_2$CoH$_5$ in the microstructure [19]. The enthalpy of formation of β-MgH$_2$ is quoted as 72-75 kJ/mol H$_2$ [5] and that of Mg$_2$CoH$_5$ has been reported by various authors as 60 kJ/mol H$_2$ (absorption) [20], 86 kJ/mol H$_2$ (desorption) [20], and 76 kJ/mol H$_2$ [5]. It appears that the difference in the enthalpy of formation of β-MgH$_2$ and Mg$_2$CoH$_5$ is not large enough to be solely responsible for the ease of β-MgH$_2$ formation and difficulty of Mg$_2$CoH$_5$ formation during RMA/CRMA, especially if the milling time is substantially extended as in the present work. However, one difficulty with the Mg$_2$CoH$_5$ hydride is that the intermetallic compound Mg$_2$Co does not exist in equilibrium binary system Mg-Co which can make its hydrided form difficult to synthesize.
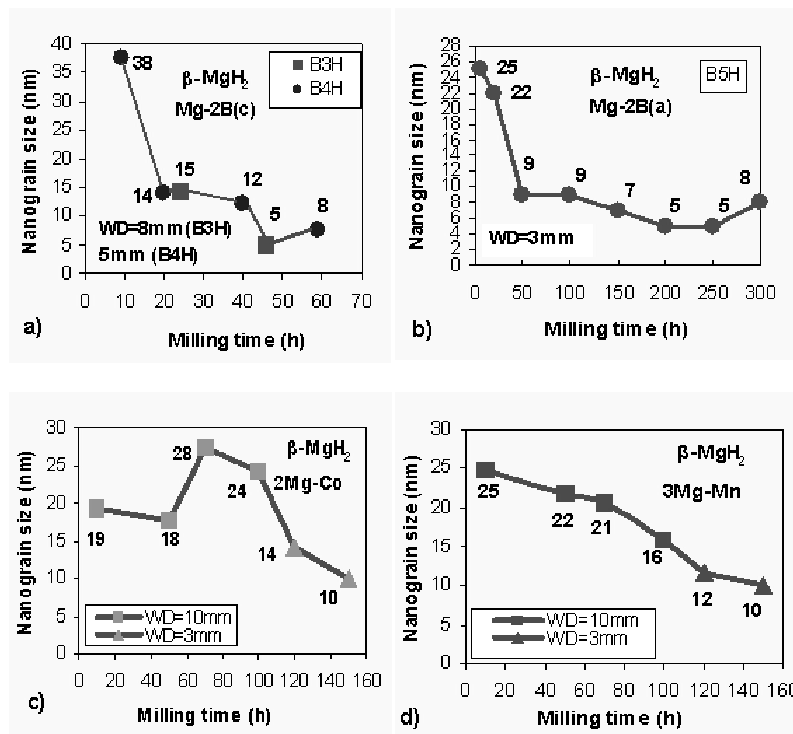
Figure 4. Nanograin size of the β-MgH₂ hydride as a function of milling time. a) Mixture Mg-2B crystalline *(c)*; BPWR=44:1, b) Mg-2B amorphous *(a)*; BPWR=40:1 c) 2Mg-Co; BPWR=10:1 and d) 3Mg-Mn; BPWR=10:1. RPM=60 applied for all mixtures during milling.

There is no data on the thermodynamic properties of the Mg₃MnH₇ hydride [21] and it is difficult to assess its propensity for the synthesis during CRMA. Originally, the hydride was synthesized from the mixture of MgH₂ and elemental Mn by high temperature sintering under 20 kbar of hydrogen [21]. The present work is the first attempt to synthesize this hydride by CRMA.

Despite that no synthesis of the desired Mg₂CoH₅ and Mg₃MnH₇ hydrides has been achieved, the CRMA under shearing mode turned out to be a very effective method for the synthesis of the nanostructured β-MgH₂ hydride and nanostructurization of other phases co-existing in the microstructure of the milled powders (nanocomposites). Fig.4 and 5 show the variation of nanograin size of the β-MgH₂ and Mg phases as a function of milling time for the mixtures Mg-2B, 2Mg-Co and 3Mg-Mn studied in this work.
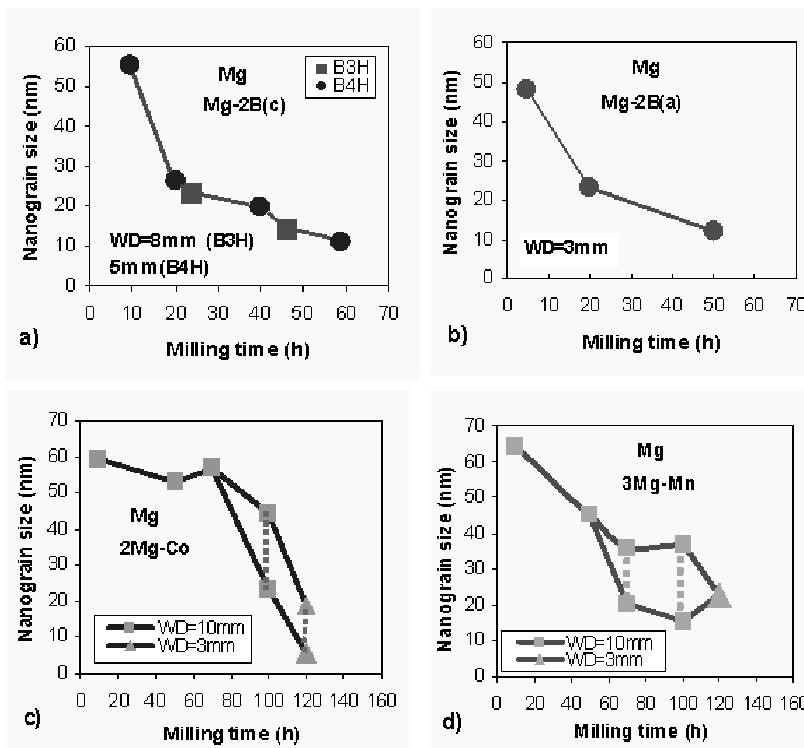
Figure 5. Nanograin size of the Mg phase as a function of milling time. a) Mixture Mg-2B crystalline *(c)*; BPWR=44:1, b) Mg-2B amorphous *(a)*; BPWR=40:1, c) 2Mg-Co; BPWR=10:1 and d) 3Mg-Mn, BPWR=10:1. RPM=60 for all mixtures during milling.

In the Mg-2B system both crystalline *(c)* and amorphous *(a)* boron (B) powders were used for the processing by CRMA (Fig.4, 5). In the XRD pattern of the mixture of Mg and crystalline (c) boron shown in Fig.6 besides peaks from β-MgH$_2$ and Mg some peaks labeled by "**x**" are also observed.

These peaks are very close to the 2θ positions corresponding to the principal peaks from the Mg(BH$_4$)$_2$ hydride (JCPDS Powder Diffraction File No.26-1212) (the "**x**" position shows the exact position of the relevant peak from Mg(BH$_4$)$_2$ in PDF). Thus, there is some evidence that the Mg(BH$_4$)$_2$ hydride could have been synthesized in the Mg-B(c) mixture. It must be pointed out that some of these peaks, although much weaker, also appeared in the XRD patterns of the mixture Mg-2B amorphous *(a)* after reactive milling up to 300h. Regarding thermal behavior, the peak intensities from the assumed Mg(BH$_4$)$_2$ hydride were slightly reduced in the XRD patterns of Mg-B(c) powders which were milled for 59h and subsequently annealed in argon at 400°C for 1h. This kind of thermal behavior might indicate that

some desorption of hydrogen from the $Mg(BH_4)_2$ hydride occurred upon annealing. However, the intensities of the same peaks remained unchanged in powders that were subjected to DSC testing up to 550°C which would rather suggest thermal stability of the hydride. More studies are needed.
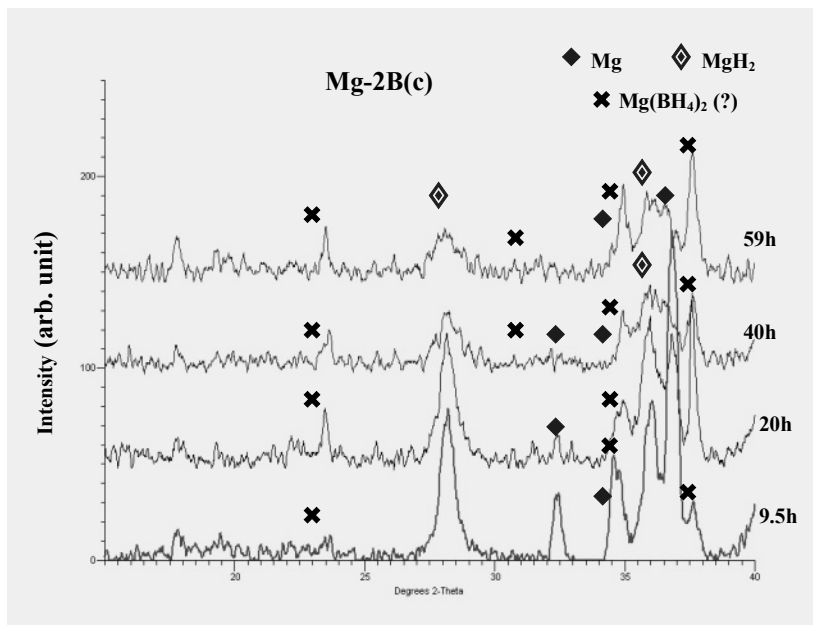

Figure 6. Isometric overlay of XRD patterns from the Mg-2B crystalline *(c)* mixture reactively milled for various time durations.

3. AMORPHOUS HYDRIDES

No peaks from the Mg_2FeH_6 hydride (JCPDS Powder Diffraction File No. 38-0843) have been observed in XRD patterns of the mixture 2Mg-Fe even after the longest reactive milling time of 59h under hydrogen. The principal hydride formed is β-MgH_2. However, the behavior of the XRD intensities of Mg and β-MgH_2 peaks in the mixture 2Mg-Fe as a function of milling time is completely different than that for the mixtures Mg-2B, 2Mg-Co and 3Mg-Mn as presented in the preceding section. Fig. 7 shows the changes in the intensities of the strongest peaks (101) Mg as well as (110) and (101) β-MgH_2 hydride in the mixture 2Mg-Fe as a function of milling time. The intensity of Mg peak decreases with increasing milling time and eventually reaches almost zero after 20h (Fig. 7a). The intensity of the β-MgH_2 hydride peaks reaches maximum after 10h and then starts decreasing

drastically with further increase of milling time reaching almost zero after 59h of milling. Qualitative EDS analysis showed the presence of strong peaks from Mg in the EDS spectrum from the powder particles after milling. Based on the fact that Mg is still detectable by EDS but not by XRD we postulate here that within the first 10h of alloying, the Mg phase is consumed to form some amount of β-MgH$_2$ whose XRD peaks show a maximum intensity after 10h of milling (Fig. 7b). However, with increasing milling time both Mg and MgH$_2$ start the *amorphization* process with the concomitant reduction of their XRD intensities (Fig. 7a,b).
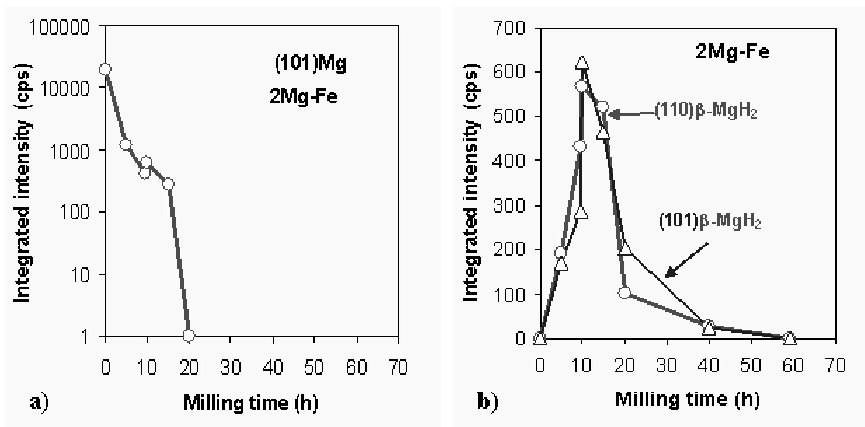

Figure 7. Variation of the intensity of the strongest peaks (101) Mg as well as (110) and (101) β-MgH$_2$ with increasing milling time of the mixture 2Mg-Fe (intensities computed by the software TRACES™ v.6.5.1).

Figure 8 shows an example of thermogravimetric (TG) and DSC curves after 59h of milling. The total TGA weight loss is ~6% at ~340˚C (Fig.8a), i.e. less than the theoretical hydrogen capacity of β-MgH$_2$ (7.66 wt%). The weight loss measured between the tangent points in Fig.8a in the temperature range ~270˚C to ~340˚C, corresponding to the fastest desorption rate, is only ~2.5 wt%. This value is remarkably close to the hydrogen content in an amorphous "MgNi" phase as reported by Orimo et al [22]. DSC curves in Fig.8b of four powder samples milled for 59h show large endothermic peaks within the temperature range 321-329˚C which corresponds very well to the temperature range of ~270˚C-340˚C where the fast desorption occurs during TGA run (Fig.8a). Most likely, these endothermic peaks correspond to the dehydriding reaction from the *amorphous hydrides*. Assuming that the weight loss measured between the tangent points represents desorption of hydrogen from the amorphous hydride then its stoichiometric formula can be estimated as being close to MgH$_{0.6-1.1}$ based on several results obtained from

TGA runs which were in the range of 2.21-4.16wt% (unpublished results). The hydrogen-to-metal ratio in this formula is nearly 1 which strongly implies that $MgH_{0.6-1.1}$ amorphous hydrides have a *metallic* character in excellent agreement with Orimo et al [22]. This is the first time that the formation of this type of amorphous hydrides has been observed in the mixture 2Mg-Fe after reactive mechanical alloying under hydrogen. Sai Raman et al [23] only reported some amorphization of the Mg_2FeH_6 hydride after long reactive milling duration of the 2Mg-Fe mixture under hydrogen.
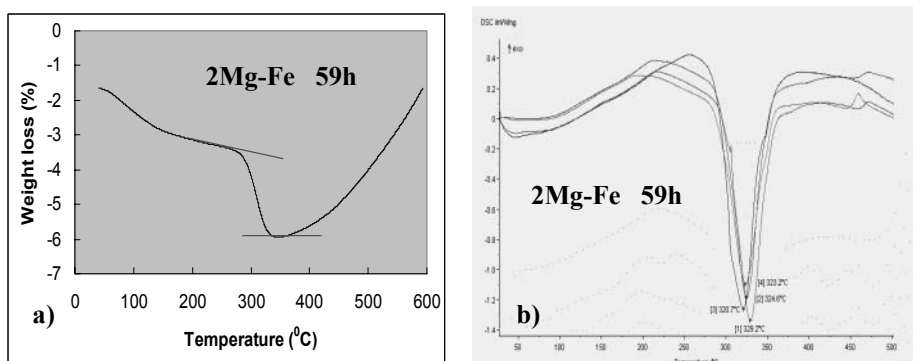

Figure 8. Thermal behavior of 2Mg-Fe powders ball milled for 59h. a) Thermogravimetric analysis (TGA) curve and b) four overlaid DSC curves.

ACKNOWLEDGEMENTS

REFERENCES

1. A. Züttel, P. Wenger, S. Rentsch, P. Sudan, Ph. Mauron, Ch. Emmenegger, J. Power Sourc. 118, 2003, 1-7
2. L. Schlapbach, A. Züttel, Nature 414, 2001, 353-358.
3. R. Schulz, J. Huot, G. Liang, S. Boily, A. Van Neste, Mater. Sci. Forum, 312-314, 1999, 615-622.
4. V.N. Konoplev, V.M. Bakulina, Izv. Akademii Nauk SSSR (Seriya Khimiczeskaya), 1, 1971, 136-138 (Engl. Transl.).
5. A. Reiser, B. Bogdanović, K. Schlichte, Int. J. Hyd. Energy 25, 2000, 425-430.
6. B. Bogdanović, G. Sandrock, MRS Bulletin 27, 2002, 712-716.
7. R.A. Varin, T. Czujko, Mater. Manuf. Processes 17, 2002, 129-156.
8. A. Zaluska, L. Zaluski, J.O. Ström-Olsen, Appl. Phys. A 72, 2001, 157-165.
9. A. Calka, A.P. Radlinski, Mater. Sci. Eng. A 134, 1991, 1350-1353.

10. Patents: WO9104810, US5383615, CA2066740, EP0494899, AU643949.
11. A. Calka, R.A. Varin, in: Proc. Int. Symp. Processing and Fabrication of Advanced Materials IX (PFAM-IX) (Eds. T.S. Srivatsan, R.A. Varin and M. Khor), ASM International, Materials Park, OH, 2001, p.263-287.
12. R.A. Varin, T. Czujko, J. Mizera, J. Alloys&Comp. 350, 2003, 332-339.
13. R.A. Varin, T. Czujko, J. Mizera, J. Alloys&Comp. 354, 2003, 281-295.
14. P. Tessier, E. Akiba, J. Alloys&Comp. 293-295, 1999, 400-402.
15. F.C. Gennari, F.J. Castro, G. Urretavizcaya, J. Alloys&Comp. 321, 2001, 46-53.
16. J.-L. Bobet, E. Akiba, B. Darriet, Int. J. Hydrogen Energy 26, 2001, 493-501.
17. F.C. Gennari, F.J. Castro, G. Urretavizcaya, G. Meyer, J. Alloys&Comp. 334, 2002, 277-284 .
18. F.C. Gennari, F.J. Castro, J.J. Andrade Gamboa, J. Alloys&Comp. 339, 2002, 261-267.
19. J. Huot, H. Hayakawa, E. Akiba, J. Alloys&Comp. 248, 1997, 164-167.
20. P. Zolliker, K. Yvon, P. Fischer, J. Schefer, Inorg. Chem. 24, 1985, 4177-4180.
21. M. Bortz, B. Bertheville, K. Yvon, E.A. Movlaev, V.N. Verbetsky, F. Fauth, J. Alloys&Comp. 279, 1998, L8-L10.
22. S. Orimo, K. Ikeda, H. Fuji, Y. Fujikawa, Y. Kitano, K. Yamamoto, Acta mater. 45, 1997, 2271-2278.
23. S. S. Sai Raman, D.J. Davidson, J.-L. Bobet, O.N. Srivastava, J. Alloys&Comp. 333, 2002, 282-290.

STRENGTH AND DUCTILITY OF NANOSTRUCTURED SPD METALS

Ruslan Z. Valiev

Institute of Physics of Advanced Materials, Ufa State Aviation Technical University, 12 K. Marx st., 450000 Ufa, Russia, e-mail: RZValiev@mail.rb.ru

Abstract: In contrast to many ultrafine-grained materials demonstrating very high hardness but poor ductility, nanostructured metals produced by severe plastic deformation (SPD) can exhibit exceptionally high strength and ductility. Apparently, the origin of this phenomenon is closely related to microsructural features of SPD-processed materials which in their turn are determined by processing conditions. This paper considers several examples of an advanced combination of high strength and ductility focussing on critical SPD processing and microstructural processing parameters resulting in appearance of unique mechanical properties in these materials.

Key words: severe plastic deformation, bulk nanostructured materials, strength and ductility

1.   INTRODUCTION

It has been established that many ultrafine-grained materials with nanocrystalline or submicrocrystalline structures typically possess very high hardness but exhibit low ductility during tensile tests [1-3]. This produces serious problems in developing new advanced structural and functional materials based on nanostructuring. In this connection, recent findings of extraordinarily high strength and ductility in a number of ultrafine-grained metals produced by severe plastic deformation (SPD) [4-6] have a special interest. SPD-produced nanostructured materials obtained through microstructure refinement in bulk billets are fully dense, and their large geometric dimensions make it possible to perform careful mechanical tests [7]. At the same time, SPD-processed materials have a very complex microstructure and can differ not only in ultrafine grain (UFG) size, but also

in atomic structure of grain boundaries, crystallographic texture, morphology and nature of the second phases [7,8]. All of the above should be taken into consideration when investigating mechanical properties of SPD nanomaterials.

The present work continues our investigations of high strength and ductility in SPD-produced metals and focuses on analysis of critical SPD processing and microstructural parameters resulting in appearance of unique properties. Several UFG materials exhibiting extraordinary mechanical behaviour are studied and discussed in the present research: pure Cu [4], CP Ti [4,9] and the Cu+0.5%Al_2O_3 composite [10].

2.   MATERIALS AND SPD PROCESSING TECHNIQUES

Pure copper (99.9), commercially pure (CP) titanium (0.12%O;0.18%Fe;0.07%C;0.04%N;0.01%H; balance Ti) named VT1-0 (Russia) and the Cu+0.5wt%Al_2O_3 composite (Glip Cop ® A1-25) were used for this study. These specimens were processed by severe plastic deformation using equal channel angular pressing (ECAP) or high pressure torsion (HPT). Let us consider briefly the principles, the main parameters and new trends in developing these SPD processing techniques.

High pressure torsion (HPT) (Fig. 1a) and equal-channel angular (ECA) pressing (Fig. 1b) refer to the techniques which were used in pioneer works devoted to UFG structures formation in metals and alloys [11,12] by severe plastic deformation. These methods have been further developed lately.


a   b
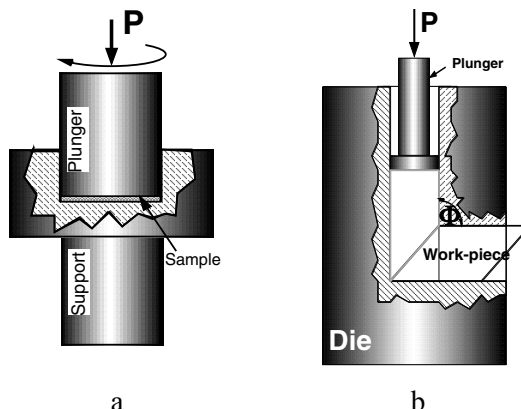
Figure 1. Principles of severe plastic deformation techniques:
a – high pressure torsion, b – ECA pressing.

2.1 High Pressure Torsion

Previous investigations have demonstrated that use of HPT provides an ability to produce homogeneous nanostructures with a grain size of about 100 nm and less [7,11,13]. These earlier studies have allowed to consider this method as an SPD technique for bulk nanostructured materials processing.

Samples processed under high pressure torsion are disk-shaped (Fig. 1a). In this process the sample is being put between anvils and compressed under the applied pressure (P) of several GPa. The lower anvil turns and friction forces result in shear straining of the sample. As a result, the deforming sample does not break notwithstanding high strains of deformation [7].

Samples processed by HPT are typically simple disk-shaped with a diameter from 10 to 20 mm and thickness of 0.2÷0.5 mm. Essential structure refinement is observed after half- or one complete (360°) turn deformation [14,15]. However, to create a homogeneous nanostructure, deformation by several turns is necessary (Fig. 2). The important role of applied pressure in the formation of a more homogeneous nanostructured state during HPT is also shown in the recent work on Ni [16].

HPT has been successfully applied for microstructure refinement in metals, alloys and not long ago in composites and in semiconductors [17,18], as well as consolidation of nanopowders [7]. Among new developments in HPT processing we would like to emphasize also the observation of SPD-induced nanocrystallization in initially amorphous alloys producing nanocrystalline materials with a grain size of 10-15 nm [19].

2.2 ECA Pressing

In the early 1990's we developed and performed first works demonsrating the ability to produce microstructures with submicro- and nanometer grain sizes using ECA pressing [11,12]. In these early experiments original ingots with square or round cross section were cut from rods with length from 70 to 100 mm. The diameter of their cross section or their diagonal did not exceed 20 mm.

During ECA pressing implementation the ingot is being pressed in a special die through two channels with equal cross section [20], intercrossing usually at an angle of 90° (Fig. 1b). In the case of hard-to-deform materials the deformation is realized at elevated temperatures or with increased channel intersection angles, if it is necessary. Each pass imparts a supplementary strain, approximately 1, for the most often applied channel intersection angle of 90°.

<center>*a*   *b*</center>
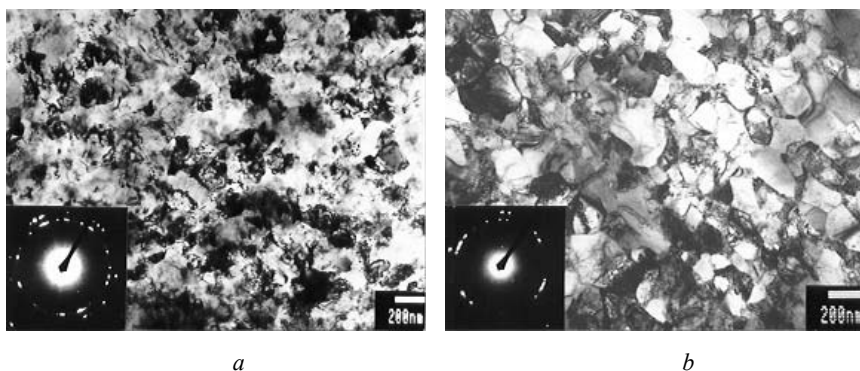
Figure 2. TEM images of UFG Cu nanostructures formed at room temperature by HPT (P = 6 GPa, 5 turns) (a) and by ECA pressing (12 passes, route B_C) (b)

A strong microstructure refinement by ECA pressing technique can quite easily be achieved both in pure metals and in alloys, using straining with one or a few passes. However, producing homogeneous UFG structures with predominantly high-angle grain boundaries by ECA pressing is a special problem. In order to solve it, much more passes should be made (as a rule, 8 and more), see Fig. 2b. Formation of an ultrafine-grained structure can be evidenced by SAED patterns showing numerous diffraction spots situated along rings, thus indicating appearance of high misorientations in the structure. Such modern diffraction methods as orientation imaging microscopy or back electron scattering diffraction also show presence of mostly high-angle boundaries after multipass ECAP [21].

It is well known that the selected ECA pressing route is also a very important parameter of the processing. The influence of ECA pressing routes on microstructure evolution for Al-Mg alloys [22] and pure Ti [23] has been investigated in detail. It was shown that the most homogeneous microstructure in alloys can be observed very often following route B_C. During this process the billet is turned between consecutive passes in one direction around its axis by an angle of 90°.

The experimental and theoretical modelling of a billet forming during ECA pressing, e g. involving the stress-deformed state, contact stresses, friction conditions [24,25], made it possible to fabricate ECAP dies for processing bulk billets with uniform ultrafine grains of various metals, including hard-to-deform Ti and its alloys. Here a maximum size of CP Ti billets equal to 60 mm in diameter and 200 mm in length (Fig. 3) was reached.
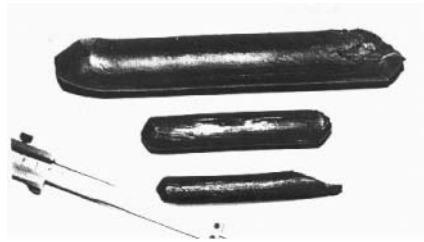
Figure 3. Bulk Ti billets of different sizes produced by ECA pressing.

3. ADVANCING OF MECHANICAL PROPERTIES IN SPD-PRODUCED NANOMATERIALS

In the investigation [4], pure Cu (99.996%) was processed using ECAP with 90° clockwise rotations along the billet axis between consecutive passes (route B_C), while pure Ti (99.98%) was processed using HPT. All processes were performed at room temperature.

Strength and ductility were measured by uniaxial tensile tests performed using samples with gauge dimensions of 5 ×2 ×1 mm. The resulting engineering stress–strain curves are shown in Fig. 4. The results for Cu tested at room temperature in its initial and three processed states are shown in Fig. 4a. The initial coarse-grained Cu, with a grain size of about 30 μm, has low yield stress but exhibits significant strain hardening and a large elongation to failure. Cold rolling of the copper to a thickness reduction of 60% significantly increased strength (curve 2 in Fig. 4a), but dramatically decreased elongation to failure. This tendency is also true for Cu subjected to two passes of ECA pressing (curve 3 in Fig. 4a). However, further pressing of the copper to 16 ECAP passes simultaneously increased both strength and ductility (curve 4 in Fig. 4a). Furthermore, the increase in ductility is much more significant than the increase in strength. Such results have never been observed before and challenge our current understanding of mechanical properties of metals processed by plastic deformation.

Similar results were also observed in Ti samples subjected to HPT which were tested in tension at 250 °C. The coarse-grained Ti with a grain size of 20 μm exhibits low strength and a large elongation to failure (curve 1 in Fig. 4b). After being processed by HPT for 1 revolution, the Ti material had very high strength but significantly decreased ductility. Further HPT processing to 5 revolutions dramatically increased the ductility and slightly increased the strength (curve 3 in Fig. 4b).
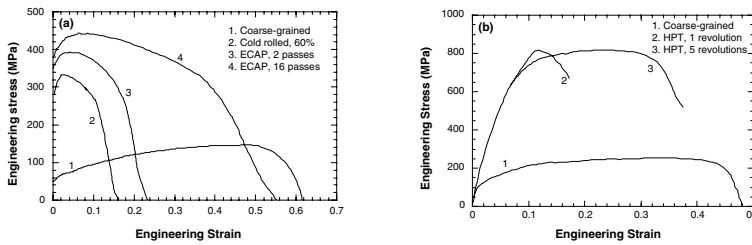
Figure 4. Tensile engineering stress-strain curves of (a) Cu tested at 22 °C and (b) Ti tested at 250 °C. Both were tested at a strain rate of 10^{-3} s^{-1}. The processing conditions for each curve are listed in the figure.

Fig. 4 shows that small SPD strains (2 ECAP passes or 1 HPT revolution) significantly increase strength at the expense of ductility, while very large SPD strains (16 ECAP passes or 5 HPT revolutions) dramatically increase ductility and at the same time further increase strength. This is contrary to the classical mechanical behavior of metals that are deformed plastically. Greater plastic deformation by conventional techniques such as rolling, drawing or extrusion introduces greater strain hardening, which in turn increases the strength, but decreases the ductility of the metal.

The strain-rate sensitivity of stress was also measured using the standard jump-test method [4]. The samples with high ductility were found to have higher strain rate sensitivity. For instance, the value *m* was equal to 0.14 for ECAP-produced Cu (16 passes) in contrast to *m* = 0.06 for ECAP Cu (2 passes). Higher strain rate sensitivity renders the materials more resistant to necking [26,27].

Another exhibition of exceptionally high strength and ductility was also revealed in HPT-produced Ti, when we studied the influence of annealing on its tensile mechanical properties at room temperatures [9]. In this case enhanced strength and ductility was observed in CP Ti after HPT and short annealing at temperatures below 300 °C. Let us consider the features of mechanical behavior of this CP Ti with a linkage to its microstructure.

Tensile tests at room temperature have shown that HPT-processed titanium demonstrates yield stress higher that 800 MPa, ultimate strength of 980 MPa and elongation to fracture of 12% (Fig. 5). A strain-rate jump test of this material has revealed an increased strain rate sensitivity value of 0.12-0.15, which is visibly higher than that for conventional coarse-grained Ti where this parameter is less than 0.05.

The short annealing at 300 °C results in a 30% increase in strength combined with enhanced ductility (Fig. 5, curve 2) as compared to the as-produced state (Fig. 5, curve 1) or with higher temperatures annealing. The

material showed the peak in strength and ductility after annealing at this temperature range. Fig. 6 shows typical TEM images of HPT-processed structure in CP Ti at different magnifications. It is evident that a homogeneous ultrafine-grained structure with a mean grain size of about 120 nm is formed (Fig. 6a and b). It is typical for this structure that the grain boundaries are not well-defined and there is no banded contrast at the boundaries which is characteristic of well-formed grain boundaries as observed by TEM. The HREM images of grain boundaries in the processed material are usually wavy, curved, or corrugated (Fig. 6c) indicating their highly non-equilibrium character [7,11]. Moreover, we observed a variation in the misorientation angle along the same boundary by about 5 °, probably as a result of the presence of disclinations. A high level of defects was also observed in grain interiors. In many regions of the grain interior the lattice fringes are poorly defined (the area marked by square in Fig. 6c) suggesting local distortions of the crystal lattice.
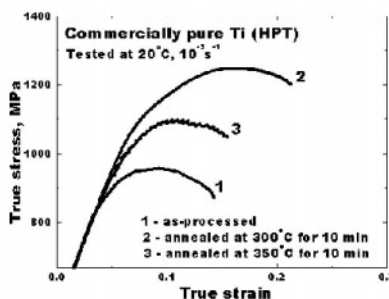

Figure 5. True stress-strain curves of CP Ti after HPT and annealing.

Since grain growth in the HPT-processed Ti starts at temperature 350 ºC and higher [4], the investigation was focused on microstructure evolution after heating below this temperature.

A short annealing for 10 min at temperatures up to 300 ºC resulted in important changes compared to the as-produced state. Here there is a significant decrease in the lattice distortions without visible grain growth during annealing. This is confirmed by SAED pattern where the level of asterism or streaking of diffraction spots is decreased. Investigations at higher resolution showed also that HPT induced into the material a high dislocation density with distribution of dislocations both in grain interiors and grain boundaries. There were no visible changes in the structure after annealing at 200 ºC for 10 min. But annealing at 250-300 ºC revealed a rearrangement of defects resulting in their movement from grain interiors to the near grain boundary region [9]. However, as with any ordering

phenomenon, this process lowers the internal stresses in the structure as a system that was corroborated by analysis of XRD patterns which exhibited peak sharpening after this heat treatment (Fig. 7). A schematic illustration of the defect rearrangement is presented in Fig.8. The figure stresses that although during low-temperature annealing the total density of dislocations is decreased, the local density of dislocations at grain boundaries can grow thus increasing their non-equilibrium.
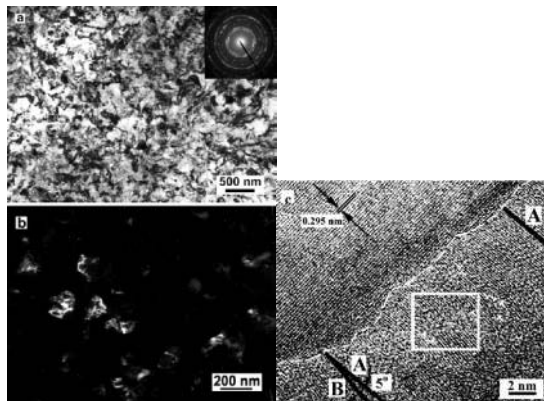

Figure 6. Typical TEM bright field (with SAED as an insert) (a) and dark field (b) micrographs and HREM image (c) of as-processed CP Ti.
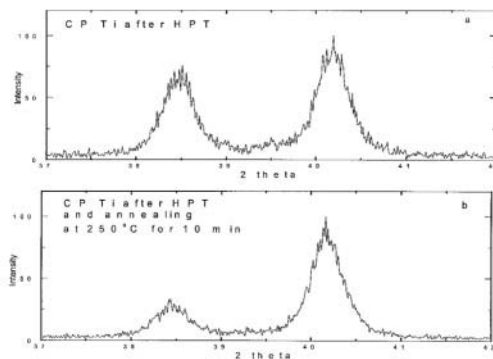

Figure 7. X-ray data for CP Ti after HPT (a) and additional annealing at 250 ºC for 10 min (b).

SEM observations showed that fracture surface of the HPT-processed Ti tested at room temperature has the dimpled surface typical for many nanomaterials, but after annealing the dimples looked lager and their orientation in the direction of shear fracture was observed [9].
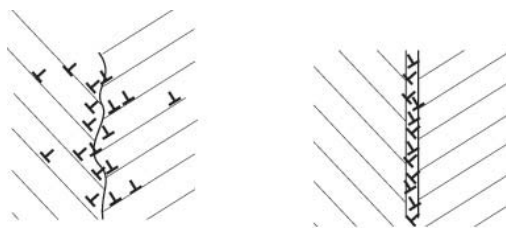
Figure 8. Schemes illustrating the dislocation structure of grain boundaries in CP Ti as-processed by HPT (a) and after low temperature annealing (b).

The SEM analysis of the formation of the surface relief of the samples' gages after testing has also revealed a specific 'step' relief with no slip lines. It was quite similar to a surface relief originating from grain rotation and grain boundary sliding, e.g. as during superplastic deformation [28]. This indicates that these processes take place in this material even at room temperature. Similar observations were made during studies of another material under investigation, i.e., the Cu+0.5% Al2O3 nanocomposite [10]. After HPT processing this Cu+0.5%Al_2O_3 alloy had a mean grain size of 80 nm and during tensile tests at room temperature also demonstrated very high strength and significant ductility. The performed tests revealed a very high ultimate strength (up to 600 MPa) accompanied by elongation to failure δ=17%, the strain rate being $\dot{\varepsilon}$ =10^{-3}s^{-1}. As it can be seen from stress-strain curves for two strain rates (10^{-4}s^{-1} and 10^{-3}s^{-1}), the behaviour of this nanocomposite was characterized by lack of distinct hardening, but also noticeable strain rate sensitivity of flow stress. The strain rate sensitivity was equal to 0.12.

4. DISCUSSION

The results presented in this work provide new evidences that ultrafine-grained SPD metals can demonstrate an extraordinary combination of very high strength and ductility during tensile mechanical tests at room temperature.

In our recent works [4,5] we made an assumption that such unique mechanical behavior in metals processed by SPD suggests a fundamental change in deformation mechanisms after the metals have been processed by SPD to very large strains.

For coarse-grained metals, dislocation movement and twinning are well known primary deformation mechanisms. Ultrafine, equiaxed grains with high-angle grain boundaries impede the motion of dislocations and

consequently enhance strength. At the same time, these grains may also facilitate other deformation mechanisms such as grain boundary sliding and enhanced grain rotation, which enhances ductility. We experimentally observed significant grain boundary sliding in ultrafine-grained copper deformed at room temperature [29]. The enhanced strain rate sensitivity observed in this work also indicates an active role of grain-boundary sliding [26,27]. Morever, the above mentioned observations of formation of a specific deformation relief on the surface of UFG Ti samples after tension, as well as appearance of a 'dimple' fracture surface, verify this hypothesis as well.

However, the question is why grain boundary sliding (GBS) in SPD-produced materials can take place at relatively low temperatures? GBS is a diffusion-controlled process and usually occurs at elevated temperatures. The following explanation associated with features of grain boundary structure in nanostructured SPD materials can be offered here:

As early as in mid-1990's a conjecture was made [7,30] that depending on the conditions of severe straining the produced UFG materials may have highly non-equilibrium grain boundaries, i.e. boundaries with high angle misorientations, but containing a high density of extrinsic dislocations and as a result possessing excess energy and long-range stress fields. Subsequent TEM/HREM observations gave direct evidence of formation of such non-equilibrium grain boundaries in SPD-processed metals [7,31,32]. Recent investigations also testify that in SPD-produced metals the diffusion coefficient grows considerably (by two or three orders), and this may be associated with non-equilibrium of grain boundaries [33]. In this connection, it can be suggested that grain boundary sliding should be facilitated in UFG metals with non-equilibrium boundaries, and such sliding can be developed considerably during straining even at room temperature. It is interesting that enhancement of GBS along non-equilibrium grain boundaries was already noted earlier in model experiments performed on bicrystals [34].

Another interesting feature revealed during mechanical testing of SPD-produced metals is absence of essential strain hardening at true stress-strain curves (see, e.g., Fig.4). It is well known from the mechanics of tensile straining that exhibition of stable flow and consequently high ductility is closely connected with strain hardening. However, the experimental data obtained here suggests that the high ductility found in UFG metals is not associated with considerable strain hardening. Recently a similar behaviour was observed during tension of nanostructured Cu [35], and the authors concluded that stability criteria should be re-examined when analyzing the deformation behaviour of UFG materials. However, the present work provides evidence that deformation of the materials under investigation is characterized by enhanced strain rate sensitivity of flow stress m. It is well

known that it is high sensitivity to strain rate of flow stress that provides for superplasticity in materials. It is evident that during straining of UFG materials the increased value of *m* also contributes to increasing elongation to failure. In its turn, an increase in the parameter *m* may result from development of grain boundary sliding. This fact is also well known from experiments on superplasticity.

Thus, this work demonstrates the possibility of tailoring microstructures by SPD techniques to produce ultrafine nanostructured metals and alloys that have a combination of high strength and high ductility. Investigating the extraordinary strength and ductility of nanostructured materials is of fundamental as well as practical importance. At the fundamental level, the insight into deformation mechanisms improves our understanding of mechanical behaviour. On the practical side, there is the prospect of using nanostructured metals and alloys for many applications, among them micromechanical systems and biomedical implants [36]. In fact, processing nanomaterials to achieve both strength and ductility can enhance the material's resistance to fatigue and fracture toughness [37], which are also important requirements for developing new advanced materials.

ACKNOWLEDGEMENTS

REFERENCES

1. J.R. Weertman, Mater. Sci. Eng. A 166, 1993, 161.
2. T.D. Shen and C.C. Koch, Acta Mater. 44, 1996, 753.
3. C.C. Koch, D.G. Morris, K. Lu, A. Inoue, MRS Bull. 24, 1999, 54.
4. R.Z. Valiev, I.V. Alexandrov, Y.T. Zhu, T.C. Lowe, J. Mater. Res. 17, 2002, 5.
5. R.Z. Valiev, Nature 419, 2002, 887.
6. Y. Wang, M. Chen, F. Zhou, E. Ma, Nature 419, 2002, 912.
7. R.Z. Valiev, R.K. Islamgaliev, I.V. Alexandrov, Prog. Mater. Sci. 45, 2000, 103.
8. T. Ungar, I. Alexandrov, M. Zehetbauer, JOM 52 (4), 2000, 34.
9. R.Z. Valiev, A.V. Sergueeva, A.K. Mukherjee, Scripta Mater. 49, 2003, 669.
10. N.M. Amirkhanov, R.K. Islamgaliev, R.Z. Valiev, Phys. Met. Metallogr. 92 (5), 2001, 518.
11. R.Z. Valiev, A.V. Korznikov, R.R. Mulyukov, Mater. Sci. Eng. A186, 1993, 141.
12. R.Z. Valiev, N.A. Krasilnikov, N.K. Tsenev, Mater. Sci. Eng. A137, 1991, 35.
13. Investigations and Applications of Severe Plastic Deformation (Eds. T.C. Lowe and R.Z. Valiev), NATO Science Series: 3. High technology, Vol. 80, Kluwer, Dordrecht, Netherlands, 2000.

14. R.Z. Valiev, Yu.V. Ivanisenko, E.F. Rauch, B. Baudelet, Acta Mater. 44 (12), 1996, 4705.
15. A.A. Tarakanova, I.V. Alexandrov, in: Abstracts of NATO ASI "Multiscale Phenomena in Plasticity: from Experiments to Phenomenology, Modelling & Materials Engineering" (Ouranopolis, Greece, September 8-19, 1999).
16. A.P. Zhilyaev, S. Lee, G.V. Nurislamova, R.Z. Valiev, T.G. Langdon, Scripta Mater. 44, 2001, 2753.
17. I.V. Alexandrov, Y.T. Zhu, T.C. Lowe, R.K. Islamgaliev, R.Z. Valiev, Metall. Trans. A29, 1998, 2253.
18. R.K. Islamgaliev, R. Kuzel, S.N. Mikov, A.V. Igo, J. Burianek, F. Chmelik, R.Z. Valiev, Mat. Sci. Eng. A266, 1999, 205.
19. R.Z. Valiev, Adv. Eng. Mat. 5 (5), 2003, 296.
20. V.M. Segal, V.I. Reznikov, A.E. Drobyshevskiy, V.I. Kopylov, Metalli 1, 1981, 99, in Russian.
21. A.P. Zhilyaev, B.-P. Kim, G.V. Nurislamova, M.D. Baró, J.A Szpunar, T.G. Langdon, Scripta Mater. 46, 2002, 575.
22. T.G. Langdon, M. Furukawa, M. Nemoto and Z. Horita, JOM 52 (4), 2000, 30.
23. V.V. Stolyarov, Y.T. Zhu, I.V. Alexandrov, T.C. Lowe, R.Z. Valiev, Mat. Sci. Eng. A299 (1-2), 2001, 59.
24. I.V. Alexandrov and R.Z. Valiev, Scripta Mater. 44, 2001, 1605.
25. V.S. Zhernakov, I.N. Budilov, G.I. Raab, I.V. Alexandrov and R.Z. Valiev, Scripta Mater. 44, 2001, 1765.
26. T.G. Nie, J. Wadsworth, and O.D. Sherby, Superplasticity in Metals and Ceramics, Cambridge University Press, United Kingdom, 1997.
27. O.A. Kaibyshev, Superplasticity in Commercial Alloys and Ceramics, Springer-Verlag, Germany, 1993.
28. M.G. Zelin, N.A. Krasilnikov, R.Z. Valiev, M.W. Grabski, H.S. Yang, A.K. Mukherjee, Acta Metall. Mater. 42, 1994, 119.
29. R. Z. Valiev, E. V. Kozlov, Yu. F. Ivanov, J. Lian, A. A. Nazarov, and B. Baudelet, Acta Metall. Mater. 42, 1994, 2467.
30. R.Z. Valiev, Nanostr. Mater. 6, 1995, 73.
31. Z. Horita, D.J. Smith, M. Nemoto, R.Z. Valiev, T.G. Langdon, J. Mater. Res. 13, 1998, 446.
32. Y.T. Zhu, J.Y. Huang, J. Gubicza, T. Ungar, Y.M. Wang, E. Ma, R.Z. Valiev, J. Mater. Res. 18, 2002, 1908.
33. Yu.R. Kolobov, G.P. Grabovetskaya, M.B. Ivanov, A.P. Zhilyaev, R.Z. Valiev, Scripta Mater. 44, 2001, 873.
34. R.Z. Valiev, V.Yu. Gertsman, O.A. Kaibyshev, Phys. Stat. Sol. (a) 97, 1986, 11.
35. Y. Champion, C. Langlois, S. Guérin-Mailly, P. Langlois, J.-L. Bonnentien, M. J. Hÿtch, Science 300, 2003, 310.
36. R.Z. Valiev, V.V. Stolyarov, H.J. Rack, T.C. Lowe, Proceedings of the Materials and Processes for Medical Devices Conference (8-10 September 2003, Anaheim, USA), to be published.
37. H.W. Höppel and R.Z. Valiev, Z. Metallkunde 93, 2002, 641.

CONSOLIDATION OF CU AND AMORPHOUS ZR-BASED POWDERS BY SEVERE PLASTIC DEFORMATION

K.T. Hartwig, I. Karaman, M. Haouaoui, and S.N. Mathaudhu
Texas A&M University, College Station 77843, USA

Abstract: Consolidation of amorphous Zr-based and Cu nanoparticles is achieved by multipass equal channel angular extrusion (ECAE). Experimental results for four different materials are reported: wrought Cu, microcrystalline Cu, nanocrystalline Cu and Zr-based amorphous metal alloy. Results show that route 2B provides better consolidation characteristics than other routes. The consolidated microcrystalline Cu showed mechanical properties comparable to deformed wrought material while the nanocrystalline Cu demonstrated high tensile strengths, but only limited ductility. The Zr-based amorphous metal consolidate retains amorphous character after consolidation to near full density with one extrusion pass. The resulting mechanical properties are comparable to those of a similar cast Zr-based amorphous alloy. These results show that ECAE possesses interesting benefits and significant challenges for the effective consolidation of particulate into materials with high structural efficiency, and may be a viable method for fabrication of bulk nanostructured materials.

Key words: equal channel angular extrusion, powder, metallic glass, consolidation.

1.   INTRODUCTION

Advances in the production of amorphous and nanostructured powders over the past decade have given materials scientists new opportunities for the creation of high strength bulk materials. Bulk material with extraordinary properties should result if such powders can be consolidated without significant changes to the microstructure, and strong interparticle bonding is achieved. There are several methods available to consolidate

91

metallic powders. The most common include hot isostatic pressing (HIP) and conventional extrusion. For consolidation of advanced powders that possess highly metastable microstructures such as amorphous metal, these methods have limitations. Long cycle times at elevated temperatures are needed for HIPing which can cause coarsening. Significant area reductions (reduction ratios of more than 10) are used to consolidate powders by conventional extrusion. Significant area reductions give small cross-section product dimensions that may be unsuitable for certain structural applications.

Equal channel angular extrusion (ECAE) [1] is a processing method that has some beneficial characteristics for powder consolidation: little change in the cross-sectional shape of the work-piece, uniform plastic strain across the work-piece cross-section, high levels of plastic strain are attainable, alternative product micro-structures can be produced and relatively low extrusion (punch) loads are needed to produce large cross-section products. It is expected that the combined actions of hydrostatic pressure and simple shear during ECAE deformation will lead to consolidation at lower temperatures than are needed for HIP consolidation. This may be crucial for effective consolidation of powdered materials with highly metastable microstructures such as nano and/or amorphous powders when one wants to retain starting material microstructure. Table 1 presents a description of the ECAE routes used for the work reported here. Note that route C gives the highest billet yield and that route A results in the largest amount of increased particle surface area after processing through four passes.

Table 1 Description of ECAE routes along with route yields and effects on microstructure.

Route Name	Minimum Number of Passes[1]	Sequence of Billet Rotations Between Passes After Pass One	Four Pass Material Yield[2]	Percentage Increase in Particle Surface Area After One, Two, and Four Passes[3]
A	1	(no rotations)	0.58	41, 103, and 235
B (B$_A$)	2	+90°, -90°, +90°, etc.	0.67	41, 67, and 158
C	2	180°, etc.	0.83	41, 0, and 0
C' (B$_c$)	4	+90°, etc.	0.68	41, 67, and 0
E	4	180°, +90°, 180°, etc.	0.78	41, 0, and 0

[1]   Minimum number of consecutive passes to achieve one full cycle of processing by the corresponding route.
[2]   This is the theoretical volume fraction of fully processed four pass material for a billet aspect (width/length) ratio of six.
[3]   These are theoretical calculations based on a cubic particle.

Previous work on powder consolidation by ECAE has been reported by several research groups [2-5]. Past work has shown the method to have promise by finding that near-full consolidation occurs after the first pass and that mechanical properties improve quickly and can reach near peak values after only two passes.

The work reported here is meant to show that ECAE has viability for producing high strength bulk material from rapidly solidified powder precursor materials with a metastable microstructure. The examples given include Cu nano-powder produced by electro-explosion and Vitreloy 106a powder manufactured by high pressure gas atomization. More detailed descriptions of the experiments, results, and evaluations are given elsewhere [4-7].

2.   MATERIALS AND METHODS

Results on four materials are presented in this report: wrought copper, two different copper powders and a zirconium-based amorphous metal alloy powder. The wrought copper began as half-hard 25.4 mm square extruded CDA-101 bar stock manufactured by Furikawa. It was preconditioned by room temperature ECAE through two passes (2C) and annealed at 800°C for one hour to give an average grain size of 75 μm. One Cu powder, which we call "micro-crystalline" powder, was gas atomized at the Materials Processing Center (MPC), Ames DOE Laboratory and screened to -325 mesh. It is 99.99 pure and has a particle size of less than 20 μm. The "nano-crystalline" Cu powder was prepared by electro-explosion of 99.99 pure wire, and has an average particle size of about 130 nm.   The Zr-based amorphous metal powder was prepared by gas atomization at the MPC and screened to the size range of 38-150 μm. It is fully amorphous, has a composition of $Zr_{58.5}Nb_{2.8}Cu_{15.6}$, $Ni_{12.8}Al_{10.3}$ and is called Vitreloy 106a. Two batches of the Zr powder were made: Batch 1 contains 1280 ppmw oxygen and Batch 2 has 780 ppmw oxygen. The morphology of the Cu- and Zr-based powders are shown in Figure 1.

The micro-crystalline Cu powder was vacuum encapsulated in $25 \times 25 \times 150$ mm (with a 19 mm dia. × 100 mm long cavity) CDA-101 Cu cans after baking in vacuum at 150°C for eight hours. The nano-crystalline Cu powder was vacuum out-gassed for eight hours at room temperature and vacuum encapsulated in $19 \times 19 \times 100$ mm (12 mm dia. by 50 mm length cavity) pure Ni cans. The Zr-based powder was vacuum out-gassed at 150°C for eight hours and vacuum encapsulated in either CDA-101 Cu (Batch 1) or pure Ni (Batch 2). All powders were placed into the cans in an uncompacted condition.

ECAE processing was done according to the specifications given in Table 2. Refer to Table 1 for clarification of ECAE route descriptions. In all cases, ECAE processing was done at slow speed in order to minimize the heat of deformation and associated temperature rise. Time-temperature data were recorded for the Zr-based materials by type K thermocouples embedded in the front and back regions of the extrusion cans.
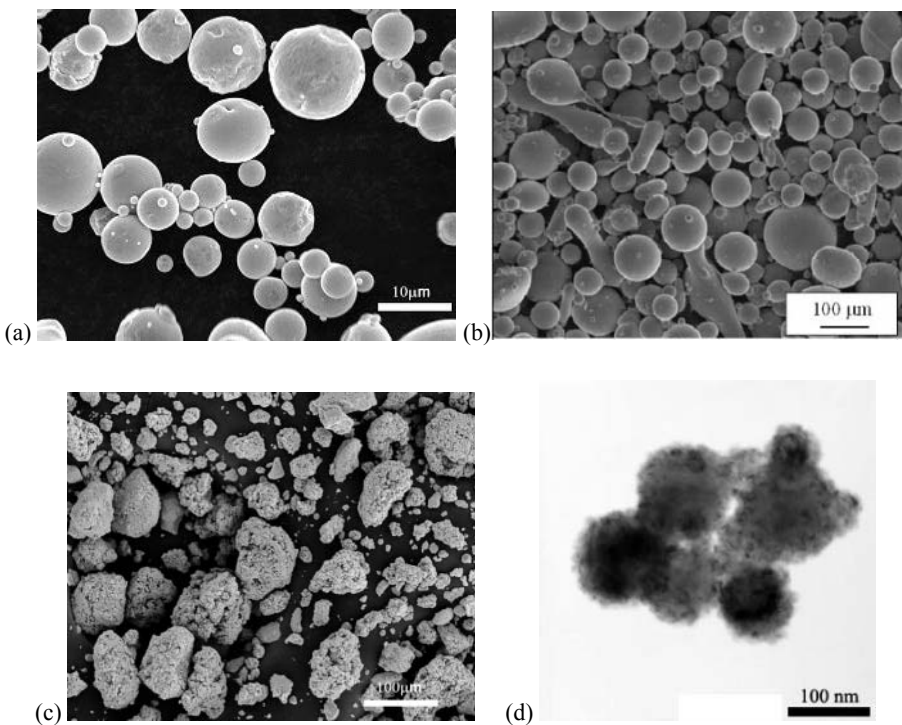
Figure 1. Microscopy images of the Cu and Zr-based powders:SEM images of the a) micro-crystalline Cu, b) Vitreloy 106a, and c) agglomerated Cu nanopowder. d) a bright field TEM image of the Cu nanopowder.

Table 2. ECAE Processing Conditions for Cu- and Zr-Based Powders

Material	Temperature (°C)	Punch Speed (mm/s)	Processing Routes Examined
Wrought Cu	23	5	1A, 2C, 4C
Micro-Cryst. Cu Powder	23	2.5	1A, 2A, 2B, 2C, 4C
Nano Cu Powder	23	2.5	2B, 2C, 2C × 2C
Vitreloy 106a Powder	400-440	0.5, 6.0	1A, 2B

Dog-bone shaped flat tensile specimens with dimensions of $8 \times 3 \times 1.5$ mm in the gage length and compression specimens with dimensions of $4 \times 4 \times 8$ mm were machined by electrical discharge machine (EDM). All tensile specimens were cut so that the gage length lined-up with the extrusion direction. The compression specimens were cut with their long axis perpendicular to the billet side plane for the micro-crystalline Cu and normal to the extrusion direction for the nano-powder Cu. Tension and compression testing was done with an MTS hydraulic test frame at a strain rate of $5 \times 10^{-4} s^{-1}$; strain was measured with a small (3 mm gage length) extensometer. X-ray

analysis and and SEM/TEM microscopy were used to characterize the average grain sizes and particle sizes of the starting and consolidated materials.

Optical microscopy was used to observe the microstructure in the consolidated Zr-based powder. Samples were polished and then etched at room temperature in 10% HF and 90% water. Vickers micro-hardness measurements were performed using a 500 g load for 13 seconds on polished and unetched specimens. Differential scanning calorimeter measurements were taken on starting powder and consolidated specimens to evaluate changes in the level of amorphous character. Compression samples (3 mm diameter by 6 mm long) of consolidated Vitreloy 106a were EDM cut along the extrusion direction. Compression tests were done at room temperature at a strain rate of 10^{-4} s^{-1}. Strain was measured by the miniature extensometer described above. Fracture surfaces were examined using a JEOL JSM-6400 SEM.

3.   RESULTS AND DISCUSSION

Figure 2 shows the room temperature true stress-strain tensile response of the wrought Cu for the annealed (starting/or initial conditions), 1A, 2C, and 4C conditions. Increases in both yield strength and ultimate tensile strength are seen with increases in plastic strain (number of ECAE passes). In addition, increases in ductility are seen in going from the single to four pass material. The maximum values of YS, UTS, and %El for each case are given in Table 3. The average grain size or grain size range of the different materials is also presented in Table 3.
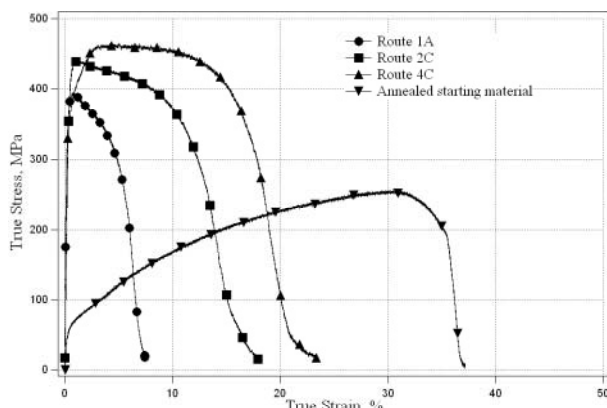

Figure 2. Tensile true stress- true strain curves for ECAE processed CDA-101 wrought copper.

The increase in stress with plastic strain for the annealed sample follows expected behavior as the material elongates and work hardens. The peak stress of 260 MPa is reached at a true elongation strain of about 31 percent. The failure strain is 37 percent. For ECAE processed material, the maximum YS and UTS values increase with processing strain because of higher levels of cold work in the higher pass material. The 1A and 2C materials show significant rates of softening after the UTS is reached because of a necking instability that decreases in strength as the level of work hardening increases. The microstructure of the 1A material contains elongated sub-grains (300-500 nm wide by / 1000 nm long) with low mis-orientation angle boundaries and a low density of internal dislocations. The 2C material has smaller elongated sub-grains with higher levels of internal dislocations and more mis-oriented boundaries. The 4C material has a microstructure similar to the 1A material except that the substructure is finer and the boundary walls are sharper and more mis-oriented.

Table 3. Summary of Grain Size and Mechanical Property Results for Copper

Material	Processing Schedule	Grain Size	Mechanical Properties [1]				
			Tension			Compression	
			(MPa)		(%)	(MPa)	
			YS	UTS	EL	YS	UTS
Wrought	Annealed	75mm	51	260	37	--	--
Cu	1A	300-500 nm x 1mm	290	390	7	--	--
	2C	200-500 nm	310	440	18	--	--
	4C	200-500 nm	350	460	23	--	--
Micro-Cu	2A	200-300 nm	410	420	1.9	440	495
	2B	50-300 nm	430	470	19	430	510
	2C	200-300 nm	--	410	0.5	440	500
	4C	250 nm	420	440	9.4	420	490
Nano-Cu	2B	70-100 nm	690	720	1.2	400	690
	2C	50-80 nm, few ~200 nm	--	--	--	560	760
	4E	40-80 nm, few ~250 nm	520	530	0.9	470	620
(1) Values rounded to two significant figures							

Figure 3 shows the true stress strain curves for the consolidated micro-crystalline powder. Both tensile and compression results show that sample 2B gives the best UTS and ductility. In tension, the 2B sample shows nearly ideal elasto-plastic response without necking until about 17 percent elongation. The

elongation at failure was 19 percent. The 4C sample also shows elasto-plastic response in tension but failed at about 10 percent elongation. The compression behavior for all two pass (and higher) specimens also shows nearly ideal elasto-plastic response. The elasto-plastic behavior is attributed to the microstructure which contains a wide range of grain and sub-structure sizes with many of the larger grains having low dislocation density interiors. A small amount of porosity was observed in all samples. The microstructure of the 2B specimen, in particular, is composed of fairly equiaxed sub-grains in the size range of 50 to 300 nm with many of the larger sub-grains free of dislocations. The 4C specimen has a large fraction of elongated sub-grains in the size range of 200-300 nm × 500 nm, and high dislocation densities in many of the sub-grains. The sub-grain boundary walls in the 4C specimen appears to have on average higher values of mis-orientation than do those in the 2B specimen.


(a)

(b)
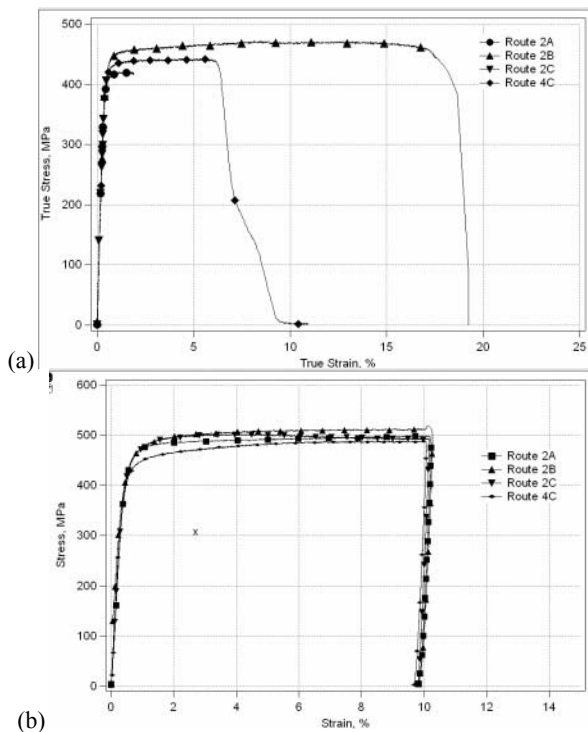
Figure 3. a) Tensile and b) compressive true stress- true strain curves for consolidated micro-crystalline copper powder.

The tensile and compression true stress strain curves for the nano particle Cu consolidates are shown in Figure 4. The 2B material gives a tensile UTS of over 700 MPa, but failed at only 1.2 percent strain. The response in

compression is more dramatic with the 2B and 2C specimens reaching the highest level ultimate compressive strength reported to date: 690 and 760 MPa, respectively. Ideal elasto-plastic behavior is not present in the nano Cu samples. The microstructure of the 2B and 2C samples is composed of a matrix of fine grains (50-100 nm) containing a noticeable number of relatively large low dislocation density sub-grains (200-500 nm). This microstructure would likely accommodate a larger amount of tensile and compressive ductility if it were not for what appears to be a small number of micro cracks dispersed throughout the matrix. Micro cracks appear on the fracture surface and are believed to originate from poorly bonded nanoparticle agglomerates.


(a)

(b)
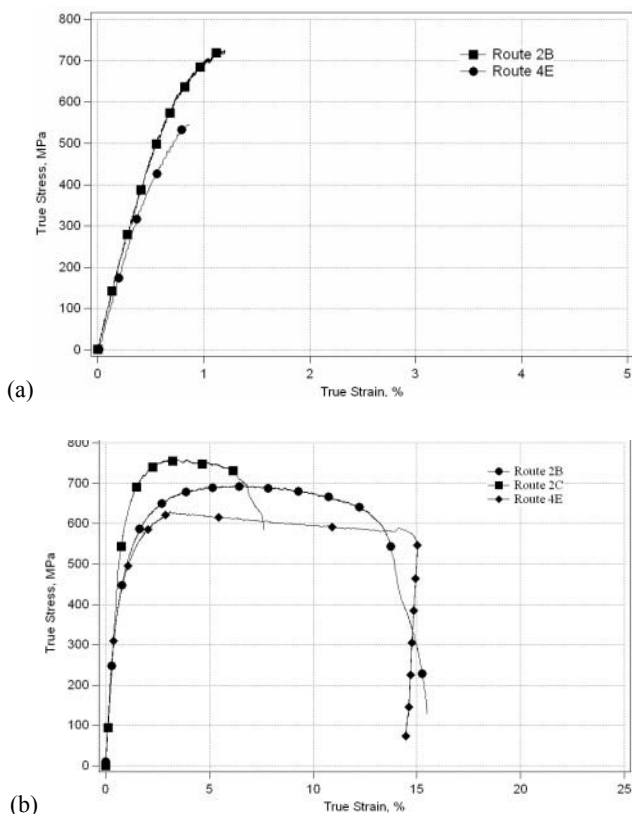
Figure 4. a) Tensile and b) compressive true stress- true strain curves for consolidated nanocrystalline copper powder.

Some results of ECAE consolidation of Vitreloy 106a powder are presented in Table 4. Notice that the micro-hardness values are nearly the same and are estimated to be only slightly higher than the value for the initial powder. DSC scans for the consolidated materials also indicate that the consolidates are largely

amorphous, i.e. there is little change in the Tg and Tx values from the original powder values (403ºC and 480ºC, respectively). A decrease in Tx following ECAE, may be an indication of a small amount of nano-crystallization. Optical metallography of samples Ni023 and Ni029 (see Fig. 5) show nicely deformed particles with little porosity in the consolidate. The particle aspect ratio is close to ideal (l/w = 5) for the 1A sample; and both consolidates show sharp triple junctions at the prior particle boundaries. Neither consolidate shows signs of large scale shear banding which is an indication of uniform homogeneous deformation during ECAE. The consolidated samples show substantial mechanical strength and ductility because they do not crack during micro-hardness testing but show shear banding around the indents. However, Rockwell C testing leads to cracking emanating from the indent along interparticle boundaries. In addition, fine interparticle cracks are sometimes observed along the material flow direction and parallel to the ends of the consolidate-can end boundary. On the other hand, compression testing of ECAE consolidated Vitreloy 106a powder containing 1280 ppmw oxygen gave a compressive strength of only 10-15% lower than the corresponding cast material. In addition, the stress-strain curves exhibit signs of ductility (serrated yielding) before failure and the fracture surface shows substantial regions of adiabatic shear banding and material flow as evidenced by vein patterns. The 780 ppmw oxygen powder consolidate probably has better mechanical properties than the 1280 ppmw material because of better flow characteristics and less oxygen in the particle surface region.

Table 4. ECAE Conditions and Micro-Hardness Results of Consolidated Amorphous Zr-Based Powder

Billet ID	Ni023	Ni029a	Ni029b
ECAE Route	1A	1A	2B
Extrusion Temp (ºC)	430	410	420
Time Above Tg (s)	382	231	(230)
Micro-Hardness (HVN$_{500}$)	490	--	493

4. FINDINGS AND CONCLUSIONS

1. ECAE route 2B appears to be better than 1A, 2C, and 4C for powder consolidation.
2. Consolidated micro-crystalline Cu powder has mechanical properties comparable to severely plastically deformed wrought Cu.
3. Nano-sized Cu powder can be consolidated to give a high tensile strength but substantial ductility, in the consolidate, is difficult to achieve.

4. Amorphous metal powder that possess a substantial Tx-Tg region (ΔT), say 50ºC, can be consolidated in the super-cooled region to near-full density bulk amorphous metal with one ECAE pass.

(a)   (b)
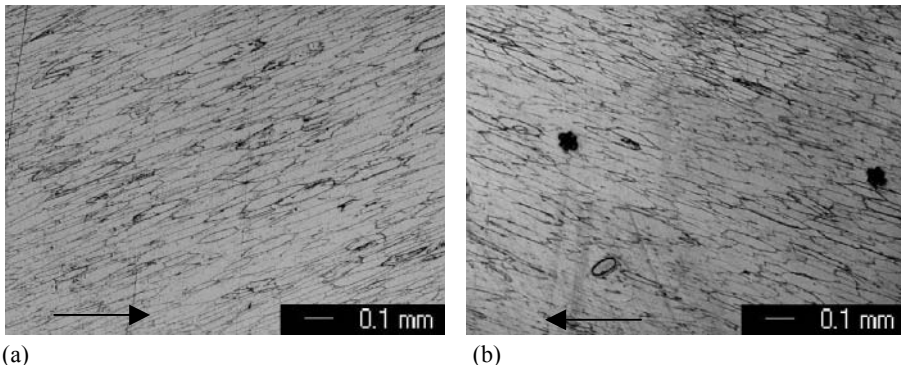
Figure 5. Optical micrographs of the flow plane on specimens extruded through a) 1A at 430°C and b) 2B at 420°C. Arrow indicates extrusion direction.

ACKNOWLEDGEMENTS

REFERENCES

1. V.M. Segal, *Mater. Sci. Eng., A.*, **A197** (1995) 157.
2. K. Matsuki, T. Aida, T. Takeuchi, J. Kusui and K. Yokoe: *Acta Mater.*, 48 (2000) 2625.
3. K.T. Hartwig, H. Zapata, A. Parasiris and S.N. Mathaudhu, in *Powder Materials: Current Research and Practices*, edited by F.D.S Marquis, N.N. Thadhani and E.V. Barrera, (TMS, Warrendale, PA 2001), pp. 211-221.
4. K.T. Hartwig, G. Chase and J. Belan: *Applied Superconductivity, IEEE Trans.*, 13 (2003) 3548.
5. Karaman, J. Robertson, J-T. Im, S.N. Mathaudhu, Z.P. Luo and K.T. Hartwig, *Metall. Mater. Trans., A.,* (2003) accepted for publication.
6. M. Haouaoui, I. Karaman, M.T. Maier, and K.T. Hartwig, *Metall. Mater. Trans. A.*, (2003) submitted.
7. S.N. Mathaudhu, J.-T. Im, R.E. Barber, I.E. Anderson, I. Karaman, and K.T. Hartwig, in *Supercooled Liquids, Glass Transition, and Bulk Metallic Glasses*, edited by A.L. Greer, T. Egami, A. Inoue, S. Ranganathan, MRS Proceedings, Vol. 754 (2003) pp. 191-198.

STRUCTURE AND PROPERTIES OF CARBON BASED NANOCOMPOSITE FILMS

G. Radnóczi, Gy. J. Kovács, G. Sáfrán, K. Sedlácková #, O. Geszti, T. Ujvári*, I. Bertóti*

Research Institute for Technical Physics and Materials Science, H 1525 Budapest, P.O. Box 49, Hungary
*Research Laboratory of Materials and Environmental Chemistry, Chemical Research Center, H-1525 Budapest, P.O. Box 17, Hungary
#Institute of Electrical Engineering, Slovak Academy of Sciences, Dubravska Cesta 9, 84101 Bratislava, Slovakia

Abstract: DC co-sputtered Carbon–Nickel and Carbon-Nitride–Nickel thin films were investigated by transmission electron microscopy, XPS and nanoindentation to clarify the influence of Nitrogen and Ni additions on the structure formation and mechanical properties of the films. The films were deposited by magnetron sputtering in argon or nitrogen plasma at temperatures from 25 to 800^oC onto NaCl and Si+SiO_2 substrates. The microstructures of the films can be described as nanocomposites, built from Ni or Ni_3C nanocrystals in a carbon/CN_x matrix. The mechanical properties of the films were found to be dependent on the substrate temperature during deposition along with the changes of the structure. The highest nanohardness of 14 GPa was measured for the film grown at 200^oC, while low values (2 GPa) were obtained for high temperature deposition. The change of the hardness is thought to be primarily the consequence of morphological and phase changes of the films in the temperature range 200-800^oC.

Key words: Carbon-nickel, CN_x-nickel, nanocomposites, mechanical properties, structure

1.   INTRODUCTION

Magnetron sputtered amorphous CN_x films constitute a relatively new class of industrially applied thin films [1-5]. They have been used since the

1990's as protective coatings of hard disks and recorder heads e.g. [1]. Presently, the research is focused on metal containing amorphous and fullerene-like carbon and CN_x films. The fullerene-like films themselves have similar mechanical properties to amorphous CN_x. They are modestly hard (max. 18-20 GPa) compared to nowadays' super hard coatings, and have a fairly high elastic modulus (130-200 GPa) [6-9]. The most interesting property of the fullerene-like films is their extreme elasticity (nearly 90% elastic recovery), fracture-toughness and good wear resistance [10-11] with a friction coefficient similar to non-hydrogenated diamond-like carbon [8].

In the case of metal containing films prepared by different techniques, electrical [12, 13], magnetic [14], mechanical [15] and hydrophobic [16] properties are tested together with the peculiarities of the structural properties.

In this paper, the structure, morphology and the mechanical properties of d.c. magnetron sputtered nanocomposites of carbon or CN_x and nickel are investigated. The addition of a metallic component to the amorphous or fullerene-like material aimed to create new structural and physical properties in this kind of materials.

2.   EXPERIMENTAL

C-Ni and CN_x-Ni films of 10-30 nm and 200-300 nm thickness were deposited by d.c. magnetron sputtering onto SiO_2 covered Si and also onto NaCl substrates (NaCl was used up to 200^oC only). The background pressure of the magnetron chamber was of $1x10^{-6}$ mbar. Nitrogen (for CN_x-Ni) and argon (for C-Ni) of 5N purity were used as sputtering gases. The pressure was of $2.5x10^{-2}$ mbar during sputtering. As sputtering source we used a high purity standard carbon target partly covered by a 3 mm wide diagonal strip of technical grade nickel. The area-ratio of Ni to C was 1:15. The film thickness and growth rate were monitored by a quartz-oscillator. The substrates were placed on a holder, the temperature of which could be set between 20 and 800^oC, measured by Ni-CrNi thermocouple.

Transmission electron microscopy (TEM), X-ray microanalysis (EDS) and high resolution transmission electron microscopy (HREM) investigations were carried out by a Philips CM20 200 kV analytical microscope and by a JEOL 3010 300 kV microscope, respectively. For TEM investigations, the layers were removed from their substrate, by dissolving the latter by water in the case of NaCl and by hydrofluoric acid (10% HF in water) in the case of SiO_2. Low angle Ar^+ ion milling at 10 kV followed by a low energy cleaning step at 200eV ion energy (Technoorg-Linda) was used for cross sectional sample preparation.

Dynamic nanohardness, elastic modulus, friction coefficient and dynamic scratch-depth were measured by a NanoTest 600 nano-mechanical tester (Micro Materials Ltd., UK) [17]. A Berkovich type indenter-head was applied for hardness measurements in depth control mode with 50 nm maximum penetration, while a 'Sharp Rockwell' head was used for scratch-tests with 1 micron/sec velocity and 1 mN load.

XPS (ESCA) studies were performed by a Kratos XSAM 800 spectrometer using Mg $K\alpha_{1,2}$ excitation, with fixed analyzer transmission of 80 or 40 eV pass energy, 0.5 or 0.1 eV step size for survey and high-resolution spectra, respectively. The accuracy of binding energy determination was ±0.2 eV or better. Data acquisition, processing and quantification were done with the Kratos Vision 2 and XPS MultiQuant programs.

3. RESULTS AND DISCUSSION

3.1 Structure and Morphology

The general characteristics of the films is that their major part (80-90 vol %) is crystalline. Cross-sectional TEM images of CNx-Ni films, deposited below 400°C show a columnar structure (Fig.1 and 2). The elongated crystalline grains are oriented practically normally to the substrate surface. The observable slight inclination to the surface normal is due to the slightly oblique deposition of the films. The grains have their width between 15-25 nm, while their length is roughly 3-4 times larger. The light strips between the crystalline particles represent the CN_x phase. The shape and grain boundary structure of the columns change as the deposition temperature is changed. The structure of C-Ni films is rather similar to the CN_x-Ni ones. The most uniform columnar structure was observed at 200°C in both C and CN_x based films.

According to electron diffraction analysis, the crystals in the samples grown below 400°C are of hexagonal symmetry being either Ni (JCPDS 45-1027, stabile up to 380°C) or Ni_3C (JCPDS 04-0853). The similarity of their lattice does not allow revealing the difference between these two phases by electron diffraction (ED). This question will be answered below by the help of XPS investigations. No crystallographic texture was observed in the films.

High resolution cross sectional TEM and ED investigation of these films revealed that the inter-grain matrix material shows graphite-like ordering displaying 3-5 graphene layers of 0.35 nm spacing in samples, grown at 200-300°C range (fig. 2) [18]. Below this temperature the matrix can be

considered amorphous. Above 400°C the ordering into graphene sheets increases together with the thickness of the matrix material between the crystalline grains. From the diffraction patterns the ordering of the graphene sheets parallel to the surface normal can be established (Fig. 3). Ordering starts at lower growth temperature for C than for CN_x.
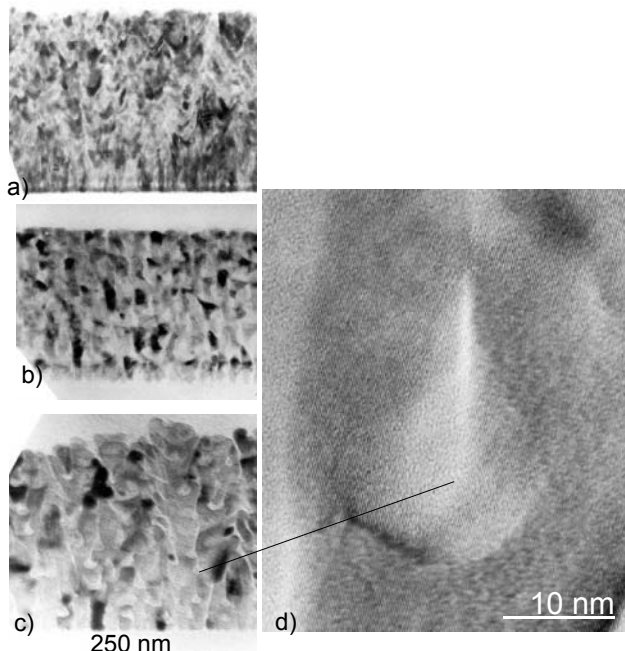

Figure 1. Cross section TEM images of CN_x-Ni films deposited at 120°C (a), 200°C (b) and 300°C (c). A high resolution TEM image of a detail in (c) is shown in (d).

In Fig.3 and Fig.4. the cross section of a C-Ni film deposited at 800°C and a cross section of a CN_x-Ni film is shown, respectively. One can observe the significant difference in shape and size of the crystalline grains compared to Fig.1 and 2. The columnar morphology changed to globular with sizes ranging between 10 and 100 nm, separated by the carbon matrix (fig.3). The crystalline phase in this case is identified as an fcc Ni characteristic for all samples grown above 400°C. However, the presence of fcc Ni_xC [19] cannot be excluded, either. Preliminary X-ray diffraction data also support the occurrence of the carbide phase. High resolution view of the same film shows the lattice image of the crystals and also the 0.35 nm spacing between the layers of the highly ordered graphitic matrix, reaching a thickness of 20-50 layers in many places (fig.3).
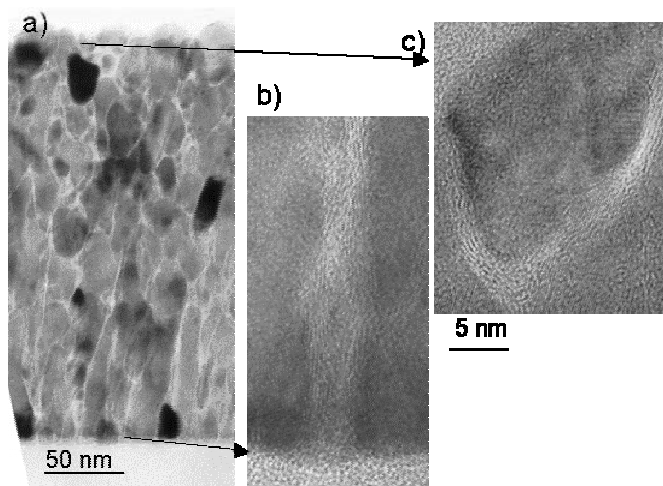
Figure 2. The columnar structure as seen in TEM cross section of a C-Ni nanocomposite film (left). The HREM images (centre and right) show the graphene structure of the carbon matrix between the Ni_3C grains near the bottom and the top of the film, respectively.
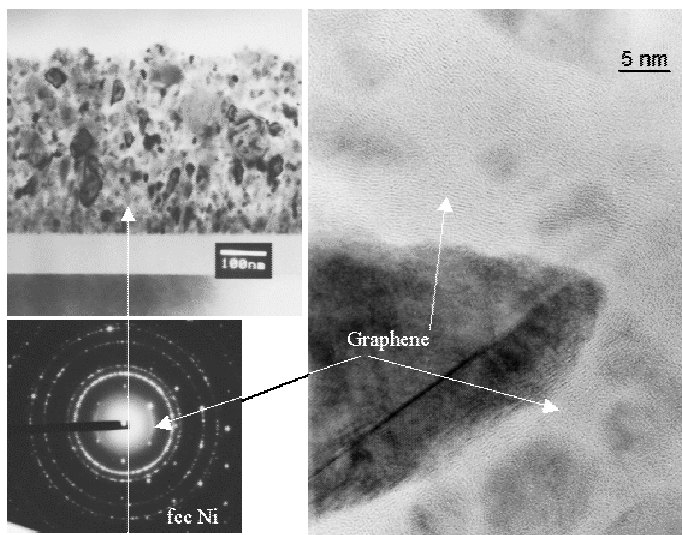

Figure 3. C-Ni nanocomposite deposited at 800°C, showing globular structure (a). The intergrain matrix layer is thick, compared to fig. 2 (b). The diffraction pattern shows mainly FCC Ni phase and graphene sheets of C, oriented parallel to the surface normal.
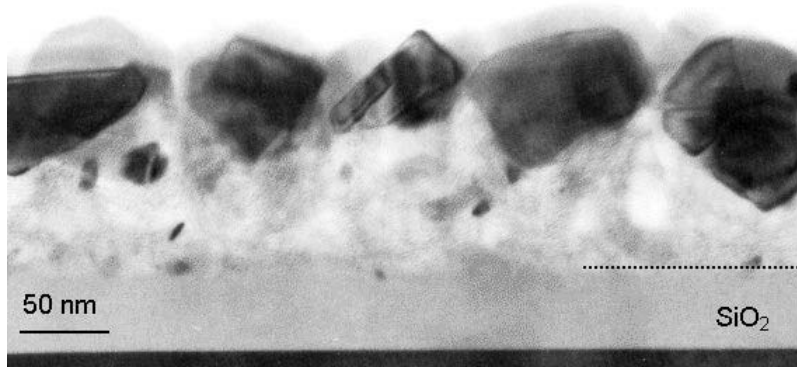
Figure 4. Cross section of a CN_x-Ni film deposited at 600^oC. The dotted line marks the surface of the SiO_2 substrate. The large black grains are fcc Ni.

3.2   XPS Analysis

An essential feature of these films is that they are prone to oxidation. The surface oxygen content, with a few exceptions, varies between 10 and 20 at%. This surface oxide contamination could be removed completely (to a trace level of 1-2 at % of O) by applying a short (10 min) 1keV Ar^+ ion etch. As calculated by the TRIM 95 program [21] the penetration of Ar^+ ions into Ni and Ni-C (Ni/C=1:1) alloy is ranging from 1.2 to 2 nm only. On this basis we consider that Ar^+ bombardment would not alter significantly neither the 'bulk' composition of the layers, nor the chemical states of the constituent elements.

The overall composition of the layers can be characterized by the C/Ni atomic ratio, which was found to be about unity for all of the Ar ion etched samples, except the ones grown at 600 °C, having this ratio of 2.4 and 1.8 for C-Ni and CN_x-Ni films, respectively. In comparison with fig. 4, this can be interpreted, that the 10 min etching was sufficient to remove the majority of the Ni particles situated on the film surface.

It is important to point out that two low energy components were found on the C1s lines in the as prepared samples, as depicted in Fig 5. The position of these lines is at 282.8-283.5 eV and at 280.8-281.3 eV when the major C1s component is set at 284.6 eV. This fact is a clear indication of carbide formation in these films. It is obvious from Fig 5., that after removing the oxidized layer from the surface the lower binding energy C1s carbide component (NiC_x) increases while the change of the high energy one (Ni_3C) is only slightly detectable. The carbide C1s component at 283.5 eV can be assigned to Ni_3C based on some early and recent results, citing 283.4

eV and 283.9 eV for this compound [15, 22]. In layers grown at or above 400°C a minor part of the carbon is also present in carbide state, i.e. is bonded to Ni.
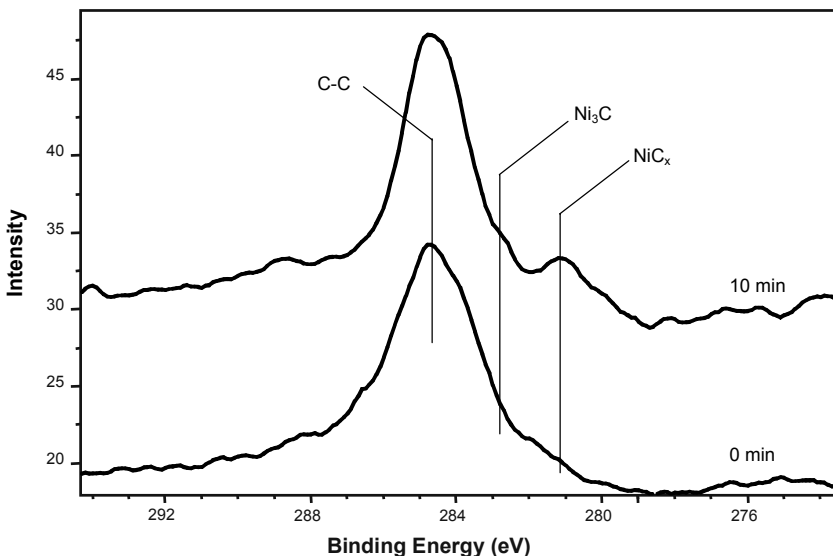

Figure 5. XP spectra of the C1s region of a C-Ni sample deposited at 280°C before and after Ar^+ ion etching.

Combining the results of the TEM+ED and XPS analysis we may conclude that at the low deposition temperatures, i.e. below 400°C the films consist mainly of Ni_3C type crystalline phase. Films grown at or above 400°C have a cubic (fcc) Ni or NiC_x structure constituting the crystalline part of the structure [19, 23]. The access carbon, which is not incorporated into the Ni_xC carbide, constitutes the multi-layered graphitic 'walls' separating the Ni-Ni_xC crystalline grains.

Concerning the measurements on nitrogen, the maximum value of approx. 8 at% of N in low temperature samples (corresponding to an approximate x≅0.2, if CN_x is considered to be the nitrogen containing phase) decreases to 2 at % in films deposited above 400°C. However, nitrogen is bonded to Ni as judged by the position of the N1s component being at 397.6 eV. As has been repeatedly measured, the N1s component for C-N bonds in CN_x layers was found at or above 398.2 eV [24, 25]. Consequently, the N must be incorporated either into the crystalline phase, identified as Ni_3C phase and/or as Ni_3N (JCPDS 10-0280) having a lattice, practically identical to Ni_3C, or Ni must be part of the amorphous or ordered CN_x matrix. The

formation of Ni_3N was also observed in [26] by sputtering Ni in nitrogen atmosphere above 220^oC substrate temperature.

3.3   Mechanical properties

The nanohardness of the films can be considered relatively high (10-14 GPa) below 200^oC, tending to the value of metallic Ni (2 GPa) above 600^oC. The elastic modulus, giving a maximum value at 200^oC of 130 GPa, shows the same behavior as the nanohardness.
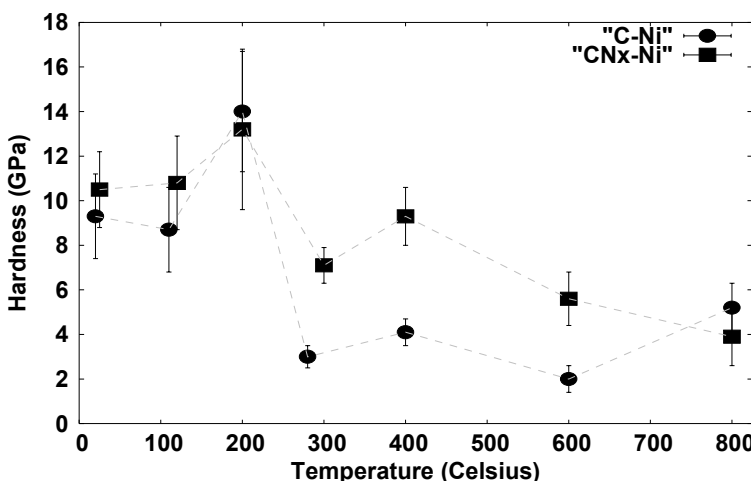

Figure 6. Nanohardness of C-Ni and CN_x-Ni films as the function of deposition temperature.

The hardness and modulus values must be determined by the carbide nature of the crystalline phase, the atomic structure of the matrix, and the growth morphology of the film. The films deposited at 25-200^oC can be described as columnar structures of Ni_3C grains embedded into an amorphous C or CN_x matrix, starting to be ordered into graphene sheets at 200^oC. Elastic recoveries of 50-55% were measured in the nano-indentation tests for these samples. This high elastic recovery and the relatively high ($\sim$0.1) H/E ratio indicate [27] that the deformation of these films arises mainly from the deformation of the matrix. The common dislocation activity may be strongly reduced in the crystals of this grain size, and sliding of the hard crystalline particles in the amorphous or ordered (at 200^oC for C+Ni) matrix may be present. The ordering in the matrix phase into closed cells of graphene sheets [18] can hinder this sliding, since it would need tearing the very strong bonds inside the graphene layer. The result is a peak hardness as well as increased elastic modulus at 200^oC. The increase of hardness at 200°

C is also thought to be the consequence of the columnar morphology and increased density (less porous nature) of the film due to the increased atomic mobility of carbon during deposition [1].

At temperatures above 400°C, the films are quite soft, 2-4 GPa, and have only about 30% elastic recovery. This decreased elastic recovery and decreased H/E ratio (~ 0.05) suggest [27] that the measured hardness and modulus mainly come from the large crystalline particles (fig. 3 and 4), especially at the highest temperatures. Simultaneously with the structural changes of the matrix above 200°C, the crystalline phase becomes cubic and coarse grained. Globular grains with 10-100 nm in diameter can be observed, the larger grains being most probably fcc Ni.
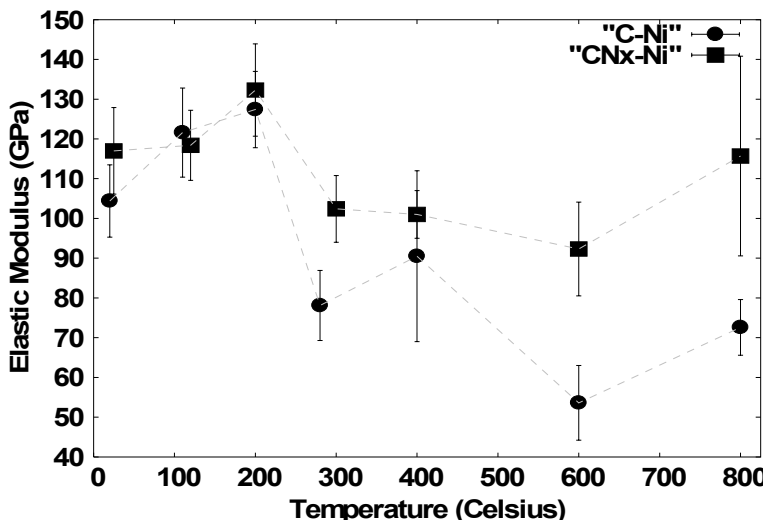

Figure 7. Elastic modulus of C-Ni and CN$_x$-Ni films as the function of deposition temperature.

Nanohardness and elastic modulus measurements on grains of the size of 100 nm can already give results, corresponding to their macroscopic phase, i.e. metallic Ni. At 800°C, a slight increase of the elastic modulus was found. It also suggests, that the role of the coarse fcc Ni grains (with E = 207 GPa for compact Ni) becomes significant in the mechanical properties of these films. The increasing width of the matrix phase and the globular grain growth morphology, favoring both the deformation in the matrix itself and the sliding of the grains, can also contribute to the decrease of the measured mechanical parameters (fig. 6 and 7).

It is worth mentioning, that the N-containing layers deposited at intermediate temperatures are substantially harder than the C-Ni ones. This

behavior must be in connection with the difference in the structure of the ordered graphitic planes of the matrix in N-containing films, discussed above. As in the films, deposited at and above $200^{o}C$, the matrix is gradually becoming fullerene-like; there are at least 2-5 layer thick curved graphitic shells around the Ni_3C particles. The presence of N results in more pronounced cross-linking between the layers, making the matrix stronger and harder in three dimensions, so the CN_x-Ni films, with x=0.2, must have higher hardness than the C-Ni ones, as observed (fig.6). As the nitrogen content decreases with increasing temperature, and above $700^{o}C$ it becomes practically zero, the difference in hardness and elastic modulus, if due to difference in nitrogen cross-links of carbon and CN_x matrix samples at lower temperatures, vanishes. This is in rather good agreement with the measurements (Fig. 6 and 7).
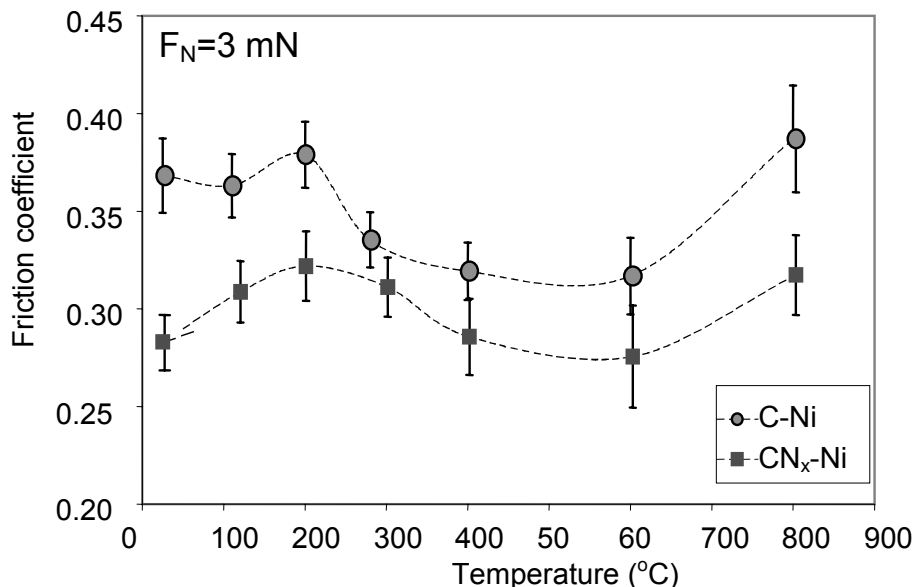

Figure 8. Friction coefficient of C-Ni and CN_x-Ni films as the function of deposition temperature.

The friction coefficient (fig. 8), being fairly low for the whole temperature range, shows also a significant dependence on the deposition temperature. The most important feature worth mentioning is that it is always lower for the nitrogen containing layers than that for C-Ni ones. The lowest values were measured for samples, deposited at 400-$600^{o}C$ range, for

which a decreasing amount of cubic carbide and relatively high amount of graphite-like carbon phase were detected. The substantial increase in the friction coefficient at 800°C may be the result of the increased surface roughness.

4. CONCLUSIONS

Novel C-Ni and CN_x-Ni nanocomposite films have been deposited on SiO_2 covered Si substrates at temperatures ranging between 20-800 °C.

The major part (80-90 vol %) of the films is crystalline. On the basis of XPS and ED data, for films deposited below 400°C the hexagonal crystalline phase was assigned to Ni_3C, in the nitrogen containing films the formation of Ni_3N is also possible, while above 400°C the crystalline phase is fcc structured Ni, and NiC_x. .

The crystalline grains form a columnar morphology below 300°C which gradually changes to a globular one as the growth temperature increases. From 600°C a separation of Ni into a layer of large grains of fcc metallic phase was observed

The matrix of the films deposited between 20-200°C can be described as a 1-2 nm thick amorphous carbon/CNx, separating the crystalline columns of elongated Ni_3C grains. From 200°C, the C/CN_x matrix gradually becomes graphitic-like and shells of at least 2-5 layers appear around the crystalline grains. At higher temperatures the C/CN_x matrix becomes thicker and more ordered.

Nanomechanical properties show a distinct dependence on the deposition temperature. Films deposited at 20-200°C possess the highest hardness up to 14 GPa. The lowest friction coefficient was measured for films deposited at 400-600°C. Generally, the CN_x-Ni films have higher hardness and elastic modulus but lower coefficient of friction than their C-Ni counterpart films probably due to nitrogen cross-links between graphitic layers.

ACKNOWLEDGEMENTS

REFERENCES

1. L. Hultman, J. Neidhardt, N. Hellgren, H. Sjöström, J.-E. Sundgren, MRS Bulletin March, 2003, 194.
2. X. Wang, P. J. Martin, Appl. Phys. Lett. 68, 1996, 1177.
3. K. Suenaga, M.P. Johansson, N. Hellgren, E. Broitman, L.R. Wallenberg, C. Colliex, J.-E. Sundgren, L. Hultman, Chem. Phys. Lett. 300, 1999, 695.
4. S. Kumar, T.L. Tansley, J. Appl. Phys. 76, 1994, 4390.
5. D. Li, S. Lopez, Y.M. Chung, M.S. Wong, W.D. Sproul, J. Vac. Sci. Technol. A13, 1995, 1063.
6. Th. Malkow, I. Arce-Garcia, A. Kolitsch, D. Schneider, S. J. Bull, T.F. Page, Diamond Rel. Mater. 10, Issue 12, 2001, 2199.
7. Mingwu Bai, Koji Kato, Noritsugu Umehara, Yoshihiko Miyake, Thin Solid Films 377-378, 2000, 138.
8. E. Broitman, N. Hellgren, O. Wannstrand, M.P. Johansson, T. Berlind, H. Sjöström, J.-E. Sundgren, M. Larsson, L. Hultman, Wear 248, Issues 1-2, 2001, 55.
9. Yuki Togashi, Yuko Hirohata, Tomoaki Hino, Vacuum 66, Issues 3-4, 2002, 391.
10. A. Khursudov, K. Kato, S. Daisuke, J. Vac. Sci. Technol. A14, 1996, 235.
11. M.Y. Chen, X. Lin, V.P. Dravid, Y.W. Chung, N.S. Wong, W.D. Sproul, Surf. Coat. Techol. 54-55, 1992,360.
12. B. F. Dorfman, Thin Solid Films 330, 1998, 76.
13. Q.F. Huang, S.F. Yoon, Rusli, Q. Zhang, J. Ahn, E.J. Teo, T. Osipowicz, F. Watt, Diamond and Related Materials 11, 2002, 1031.
14. Xiang-Chen Sun, J.A. Toledo, Current Applied Physics 2, 2002, 113.
15. N. Laidani, L. Calliari, G. Speranza, V. Micheli, E. Galvanetto, Surf. Coat. Technol. 100-101, 2003, 116.
16. J.S. Chen, S.P. Lau, Z. Sun, G.Y. Chen, Y.J. Li, B.K. Tay, J.W. Chai, Thin Solid Films 398-399, 2001, 110.
17. Y. Kusano, I.M. Hutchings, Surf. Coat. Technol. 169-170, 2003, 739.
18. Gy. J. Kovács, G. Sáfrán, O. Geszti, T. Ujváry*, I. Bertóti*, G. Radnóczi, Surface and Coatings Technology, in press.
19. L. Kepinski, Carbon 30, Nr7, 1992, 949-955.
20. D. Bíró, A. Kovács, F. Misják, T. Szüts, P.B. Barna, Surface and Coatings Technology, in press.
21. J.P. Biersack, J.F. Ziegler, Transport of Ions in Matter, TRIM, Version 95.9, IBM Research: Yorktown Heights, NY 10598, USA, 1995.
22. S. Sinharoy, L.L. Levenson, Thin Solid Films 53, 1978, 31.
23. J. Pugh , C. Lees, D. Bland, Nature 191, 1961, 865.
24. T .Ujvári, A. Kolitsch, A. Tóth, M. Mohai, I. Bertóti, Diamond Relat. Mater. 11, 2002, 1148.
25. T. Ujvári, B. Szikora, M. Mohai, A. Tóth, G. Keresztury, I. Bertóti, Diamond Relat. Mater. 11, 2002, 1199.
26. M. Kawamura, Y. Abe, K. Sasaki: Vacuum 59, 2000, 721.
27. J. Neidhardt, Zs. Czigány, I.F. Brunnel, L. Hultman, J. Appl. Phys. 93, 2003, 3002.

NANOCRYSTALLIZATION IN IRON ALLOYS INDUCED BY FRICTION TREATMENT AND NITROGEN DIFFUSION

A. Yurkova[a], F. Belots`ky[a], A. Byakova[a,b], Yu. Podrezov[b], M. Danylenko[b]
[a]National Technical Universsity of Ukraine "Kiev Polytechnic Institute", Kiev, Ukraine
[b]Frantcevych Institute for Problems of Materials Science, Kiev, Ukraine

Abstract: It was found that both surface friction treatment in inert gas (FT) and friction nitriding in ammonia atmosphere (FN) are capable to form gradient nanostructured surface layers on Fe-alloys. Specific features of the nanostructured surface layers were investigated using XRD–analysis, optical and transmission electron microscopy (TEM).

Key words: nanostructured materials, iron–alloys, friction treatment, nitriding

1.   INTRODUCTION

The combination of the processes of the severe plastic deformation of the surface with their physical-chemical treatment can provide the unique opportunity of the controlled formation of nano-sized grain structure for the strength and corrosion stability increasing. By applying both surface plastic deformation and nitriding process simultaneously nanostructured material could be determined. This kind of surface treatment related to refinement of grain could be helpful for considerable modification of material service properties.

The use of severe high rate friction treatment can give grain structure of different scale, i.e. nano-, submicro-, and micro-sized grain structures. These structures of different grain scale take place one after another in the direction to center of sample when deformed surface layer has been formed.

113

Objective of this work is to investigate the specific features of modified layer structure formed on the surface of Fe alloys by friction treatment being occurred in nitrogen medium.

2.   EXPERIMENTAL

The samples from Armco Fe and Fe–Ti (0.7; 1.2; 1.6wt.%Ti) alloys were treated by friction for obtaining the surface layer of nanocrystalline structure. Before treatment the samples were annealed in vacuum at the temperature as high as 1373K to obtain homogeneous coarse grain structure and also to refuse the effect of previous mechanical treatment. Duration of annealing process was about to 360 min. The average grain size of annealed samples was 100–150 µm.

According to procedure published previously the cylindrical samples were heated by friction during sample rotation [1]. Hard alloy blocks being pressed to sample surface were used for friction process. Friction treatment was held either in Ar-gas (FT) or in ammonia medium (FN). The temperature of sample ranged from 773 to 853K was controlled by chromel–alumel thermocouple. Duration of treatment was about to 60 min. After FT and FN processes the sample surface was smooth similar to that of original polished one.

X–Ray diffraction analysis of the surface layer was performed by X-ray diffractometer (20kV) with Fe K_α radiation. By using repeated electrochemical etching the treated surface layers were removed layer-by-layer. Thus, the grain structure in the direction from the treated surface to sample center was investigated using stepwise XRD analysis. The average grain size was determined by Scherrer method using the broadening of bcc Fe Bragg diffraction peaks compared to annealed sample [2].

The structure of modified surface layer was investigated using powerful optical microscope Neophot–21 (resolution up to 0.4 µm). Furthermore, TEM images and selected area electron diffraction (SAED) patterns were obtained to study structural evolution caused by simultaneous friction treatment and nitriding.

2.1   RESULTS

Table 1 shows structural parameters and Vickers hardness of modified layers formed by simultaneous friction treatment and nitriding.

Table 1. Surface layers parameters after friction treatment.

Sample material	Treat- ment type	Layer depth, mm	HV, GPa	Phase composition	α – phase lattice para- meter, nm	Nitrogen content in α – phase, wt.%
Armco Fe	FT	0.1	4.5	α	0.28667	–
	FN	0.45	6.5	$\alpha_N + \gamma'$	0.2871	0.32
Fe+0.7wt.%Ti	FN	0.33	9	$\alpha_N + \gamma'$	0.2874	0.58
Fe+1.1wt.%Ti	FN	0.22	11	$\alpha_N + \gamma'$	0.2890	0.65
Fe+1.2wt.%Ti	FT	0.06	7	α	0.28725	–
	FN	0.15	12	$\alpha_N + \gamma'$	0.2893	0.7
Fe+1.6wt.%Ti	FT	0.13	13.7	$\alpha_N + \gamma'$	0.2920	0.85

Grain morphology (size and shape) of modified surface layers is different compared to central part of sample, as shown in Fig. 1. Both FT process and FN one cause to refinement of surface layer grain structure. Additionally, increasing the grain boundaries extension occurs. The depth of modified layer determined by FN-process is larger than that formed by FT-process (Tab. 1, Fig 1). Gradient of grain size across cross-section of modified layer occurs due to friction. Gradient of deformation results in grain structure gradient. Fine-grained structure is observed only on short distance to the surface. Fig 1a, b shows that optical microscopy was not helpful to recognize grain size located very close to surface.
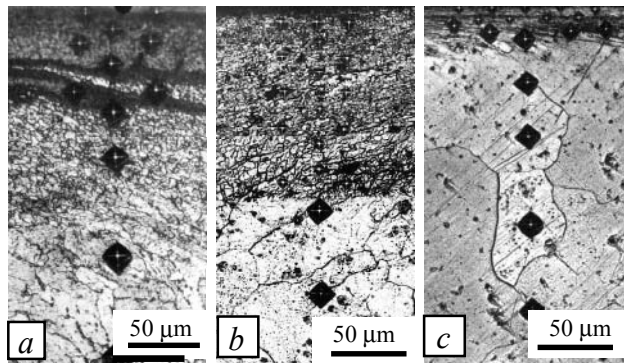

Figure 1. Optical micrographs of structure observed in cross-section of treated sample: a – Armco Fe treated by FN process at 773K during 60 min; b – Fe+1.2wt.%Ti, treated by FN process at 823K during 60 min; c – Fe+1.2wt.%Ti, treated by FT process at 823K during 60 min.

According to the results obtained in the present study (see Tab.1) nitrogen content in α_N – phase is higher that formed by usual nitriding without friction. For modified layer formed on Armco Fe nitrogen content in α_N – phase is higher by 3 times than that indicated by state diagram for system Fe-N [3]. It was assumed that the essential increase of nitrogen

content in $\alpha_N -$ phase could be caused both by the increase of dislocation density and by the increase of grain boundaries occurred due to grain refinement. To verify this assumption dislocation density was determined by XRD method analysis when physical broadening the diffraction peaks is used [4]. Dislocation density was calculated using the equation:

$$\rho = \frac{3\beta^2 ctg^2\theta}{K'b^2 l} \tag{1}$$

where $\rho -$ dislocation density; $\beta -$ XRD diffraction peak broadening; $K' -$ coefficient that depends on both reciprocal lattice vector orientation and dislocation type; $b -$ Burgers vector length; $l \approx 5$ is the constant taken for condition of random dislocation distribution; $\theta -$ Bragg angle.

The annealed sample that was not treated by friction has been used as a standard one. Dislocation density caused by friction process was investigated using the sample treated in Ar-gas medium at 823K during 60 min. For the sample treated by friction calculated dislocation density was determined in the range from 10^{10} to 10^{11} cm^{-2} whereas that for the annealed sample was obtained in the range 10^6 to 10^8 cm^{-2}. Thus, plastic deformation occurred due to friction causes the increase of total dislocation density.

Broadening the diffraction peaks of $\alpha_N -$ phase formed in modified layer indicates that substructure that was consisted of small individual blocks could be formed additionally inside the grains being refined by friction. Blocks size of bcc-Fe being formed at the very surface layer of the sample treated by FT process was about to 16 nm. Compared to the above block size of $\alpha_N -$ phase formed by FN process is found about to 8 nm while it was not more then 10-15 nm at the distance to 0.1 mm from the surface. Indications were obtained that block size increases mostly up to submicro-scaled one when the distance from the surface increases.

Bright-field TEM images of surface for the samples treated either by FT process or by FN one are shown in Fig. 2. Blurred rings related to bcc-Fe treated by FT process can be caused by high degree of grain refinement. Since nanostructured layer determined by FT process was too small, separate spots placed on blurred diffraction rings is observed, as shown in Fig.2a. These spots occur because of submicro-scaled bcc-Fe that is placed beneath nanostructured surface layer. When the samples were treated by FN process, blurred rings, which could be associated both with grain refinement of α_N - phase and with coherent nitrogen precipitations, are recorded only (see Fig. 2b, c).
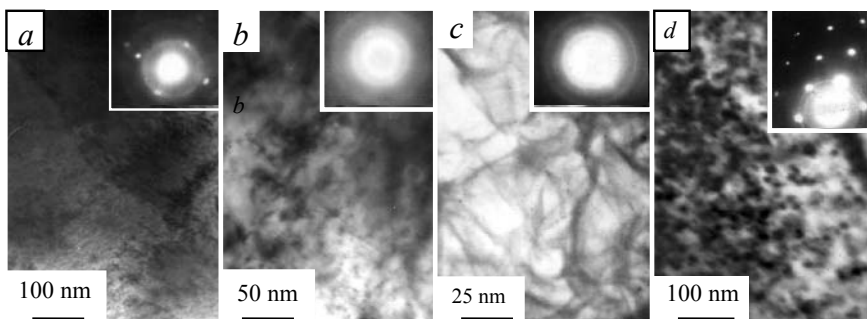
Figure 2. Bright-field TEM images showing (a, b, c) microstructures of surface layer and (*d*) that determined at the distance of 0.1mm from the surface: *a, b*– Armco Fe treated by FT and FN processes at 773K during 60 min respectively; *c,d* - Fe+0.7wt.%Ti treated by FN process at 823K during 60 min. Inserts present SAED pattern.

It is seen in Fig.2 that both FT process and FN one result in formation of nanostructure consisted of polyhedral cells/blocks of different sizes.

Two different groups of cells/blocks could be pointed out and classified considering to their sizes, which were determined directly using TEM images and by means of calculations using electron diffraction patterns [2]. The first group unites the cells/blocks of largest sizes, which are ranged from 150-200 nm and from 50 to 70 nm for FT and FN processes respectively. The second group includes the cells/blocks, which have the smallest sizes. They are located inside the cells/blocks of the first group. FN process causes the formation cells/blocks of second group for which their sizes were ranged from 5 to 10 nm. The each cell/block is rounded either by dislocation walls or dislocation tangles, forming sub-boundaries.

Fig. 2 d shows that instead of blurred rings belonged to α_N-phase, which were determined in the modified layer formed in the samples treated by FN process, individual blurred spots are detected in SAED pattern when the distance to surface was about to 0.1 mm. Additionally, blurred rings belonged to fcc γ`-phase appears in SAED pattern. Several aspects could be mentioned considering the results obtained by TEM analysis. The first is that the nanostructured $\alpha_N -$ phase transforms in submicro-scaled one as distance to the surface increases. Additionally, coherence disruption happens and, if so, inclusions of γ`-phase are formed.

It should be note the important role of nitrogen diffusion for determining the nanostructured material. Nitrogen atoms being consolidated at the sub-boundaries could block the processes of recovery and stress relaxation, resulting in pronounces refinement of grain structure.

3.   CONCLUSIONS

It was found that both surface friction treatment in inert gas (FT) and friction nitriding in ammonia atmosphere (FN) are capable to form gradient nanostructured surface layers on Fe-alloys. By using XRD-analysis and TEM technique polyhedral cells/blocks of different sizes are recognized in grains of α–phase. Two different groups of cells/blocks were pointed out and classified considering to their sizes. The first group united the cells/blocks of largest sizes whereas the second group included the cells/blocks, which are located inside the cells/blocks of the first group and have the smallest sizes ranged for FN process from 5 to 10 nm. Generally, FN process resulted in the cells/blocks of smaller sizes than that caused by FT process. The sizes of the first group of cells/blocks were ranged from 150–200 nm and from 50 to 70 nm for FT and FN processes respectively. It was assumed that nitrogen atoms being consolidated at the sub-boundaries could block the processes of recovery and stress relaxation, resulting in pronounces refinement of grain structure.

REFERENCES

1. Bilots`ky A.V., Yurkova A.I.Strengthening of Valve Steel by Friction Nitriding, Technologiya i Organizatziya Proizvodstva, 1988, No. 2, 40–41.
2. C.S.Barrett, T.B.Massalski, Structure of Metals. Crystallography Methods, Principles and Data, Pergamon Press, Oxford – New York, 1980.
3. V.G.Paranjipe, M.Cohen, M.B.Bever, and C.F.Floe. J.Metals. 1950, **182**, No. 2, 261–267.
4. A.N.Ivanov, Yu.O.Megenniy, A.E.Ostrov, and E.I.Fomichova. Zavodskaya Laboratoriya, 1987, No. 2, 43.

INFLUENCE OF SCANDIUM ON AMORPHIZATION OF ALUMINUM ALLOYS

A. Slipenyuk, D. Lotsko, Yu. Milman, V. Kuprin, M. Yefimov, M. Danylenko

I.M. Frantsevych Institute for Problems of Material Science of National Academy of Sciences of Ukraine

Abstract: Structure of $Al_{100-x}Sc_x$, $Al_{91}Ce_{9-x}Sc_x$, and $Al_{85}Ni_{10}Ce_{5-x}Sc_x$ alloys manufactured in the form of melt-spun ribbons was investigated in order to establish the influence of scandium on the tendency to amorphization of aluminum alloys alloyed with rare-earth metals. Ribbons structure was compared with their hardness. Thermal stability of ribbon structure was studied.

Keywords: Amorphization, aluminum alloys, scandium, rare-earth metals

1.   INTRODUCTION

It was previously shown that rapidly solidified Al-RE and Al-TM-RE alloys (RE is rare earth metal or yttrium, TM is transition metal) have amorphous structure in relatively wide range of compositions and alloying elements [1]. Similarly to rare earth metals and Y, Sc belongs to the IIIB group of the Periodic Table of Elements, but we have found no data on the influence of Sc on the formation of amorphous structure in Al alloys in the literature. On the other hand, Sc is known for a many-sided improving action on many crystalline Al alloys [2]. The aim of this work was to investigate the effect of Sc on the structure and mechanical properties (hardness) of rapidly solidified binary Al-Sc alloys as well as of Al-Ce-Sc and Al-Ni-Ce-Sc amorphous alloys.

2.   EXPERIMENTAL

Ribbons of $Al_{100-x}Sc_x$, $Al_{91}Ce_{9-x}Sc_x$ and $Al_{85}Ni_{10}Ce_{5-x}Sc_x$ alloys were manufactured by the single-roller melt-spinning technique using a copper wheel with the peripheral velocity of about 40 m/s (cooling rate of 10^5-10^6 K/s). The temperature of the melt before pouring was 180-240 °C higher than the liquidus temperature. X-ray and TEM techniques were used for structural investigations, ribbon microhardness HV was measured at a load of 2 N. The thermal stability of amorphous structure was studied by differential scanning calorimetry (DSC) technique.

3.   RESULTS OF INVESTIGATION

In $Al_{100-x}Sc_x$ alloys with x≤15 no amorphization was revealed (Fig. 1).
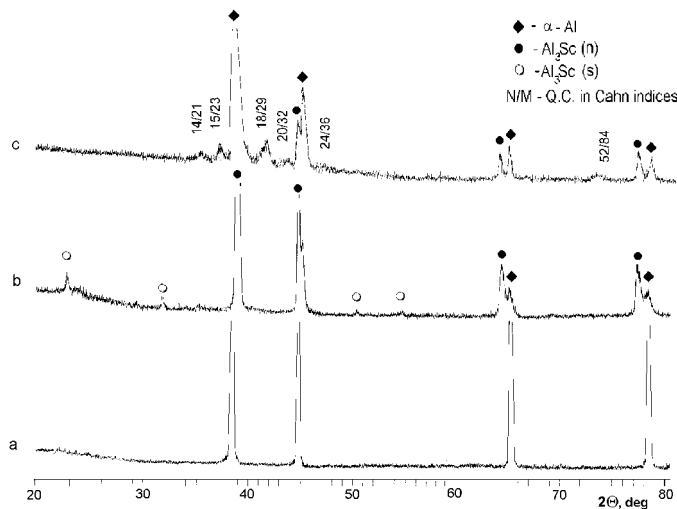
Figure 1. Fragments of X-ray diffraction patterns of rapidly solidified $Al_{100-x}Sc_x$ alloys, CuKα radiation: x = 1 (a), x = 11 (b), x = 15 (c)

In the X-ray diffraction pattern (XRDP) of $Al_{99}Sc_1$ ribbon (Fig. 1a) peaks of only α-Al solid solution were detected. Signs of appearing Al_3Sc intermetallic were seen in the XRDP for x=3 in the form of an asymmetry in the left part of α-Al peaks. At x=7 superstructural Al_3Sc peaks (100) and (110) appeared, and at x≥10 the intensity of Al_3Sc peaks became larger than one of α-Al (Fig. 1b). In the ribbon $Al_{85}Sc_{15}$ we first discovered peaks of an icosahedral quasicrystalline phase. In Fig. 1c Cahn indices [3] for these

peaks are given. Quasicrystalline particles were of about 100 nm in size (Fig. 2a), TEM investigation confirmed their icosahedral symmetry (Fig. 2b).
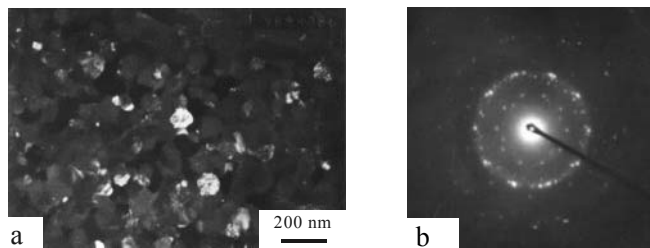

Figure 2. TEM dark field image (a) and electron diffraction pattern (b) of particles in $Al_{85}Sc_{15}$ ribbon

The Al-Sc quasicrystalline phase was unstable, and after 300 days holding at room temperature ribbon phase composition transformed to α-Al+Al_3Sc. Ribbon hardness increased with growing the content of the intermetallic Al_3Sc phase to x=9 and practically stabilized at the level of about 2.3 GPa (Fig. 3). The appearance of the quasicrystal component did not increase this level.
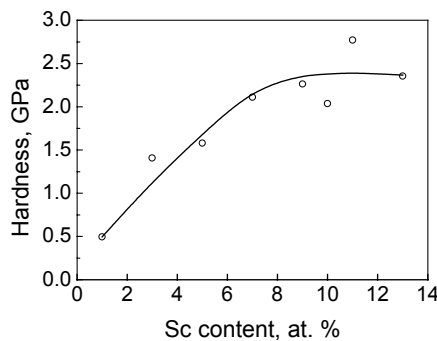
Figure 3. Effect of Sc content on the hardness of binary Al-Sc alloys

Substituting Ce for Sc in $Al_{91}Ce_{9-x}Sc_x$ ribbons decreased the alloy glass forming ability and stipulated a transformation of amorphous structure into crystalline one (Fig. 4). Substituting 1 at. % Ce (x=1) did not change the amorphous character of ribbon structure (Fig. 4a), but increased its thermal stability (Fig. 5). This fact may be connected with a known deceleration of diffusion processes in Al alloys under the influence of Sc [2]. However, in the XRDP of the ribbon $Al_{91}Ce_6Sc_3$ (x=3) together with a halo characteristic for amorphous structure a small peak in the place of the strongest α-Al peak (111) is seen (Fig. 4b). It corresponds to the formation in the amorphous matrix of

very small (of 5-10 nm in size) α-Al precipitates (Fig. 6a) just as in the class of
the most fast Al alloys distinguished by Inoue [1]. Such structure caused a
strong increase of ribbon hardness from 2 to 3.5 GPa (Fig. 7).
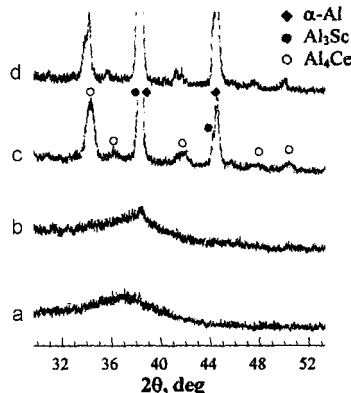
*Figure 4.* Fragments of XDRPs of Al-Ce-Sc ribbons: x=1 (a), x =3 (b), x=5 (c), x =7 (d)
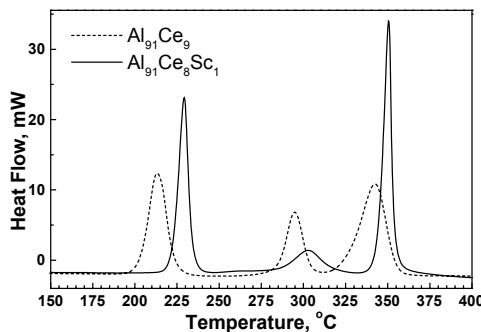
Figure 5. Influence of Sc on the DSC curve of amorphous Al-Ce-(Sc) ribbons

In the ribbon with x=5 the amorphous structural component was absent,
X-ray study registered the existence of α-Al together with Al_4Ce and Al_3Sc
crystalline intermetallics (Fig. 4c). However. ribbon hardness remained at
almost the same level (Fig.7). Evidently, it can be explained by the
formation of a very fine-scale structure of a eutectic type with a relatively
small amount of α-Al grains (Fig. 6b). Small plates of both intermetallics of
20-60 nm in thickness were found in the eutectic by dark-field TEM
investigation. A further increase of x caused a drop of hardness (Fig. 7), and
in the ribbon $Al_{91}Ce_2Sc_7$ no areas with eutectic structure were found (Fig.

6c,d). The structure was formed by α-Al grains of about 500 nm in size. The amount of Al_4Ce intermetallic is in this ribbon rather small, and its particles of about 50 nm in size are situated presumably in grain boundaries (Fig. 6c). The amount of Al_3Sc is much larger, and together with grain boundary particles it forms coarser precipitates of about 200-300 nm (Fig. 6d).


a

b

c

d
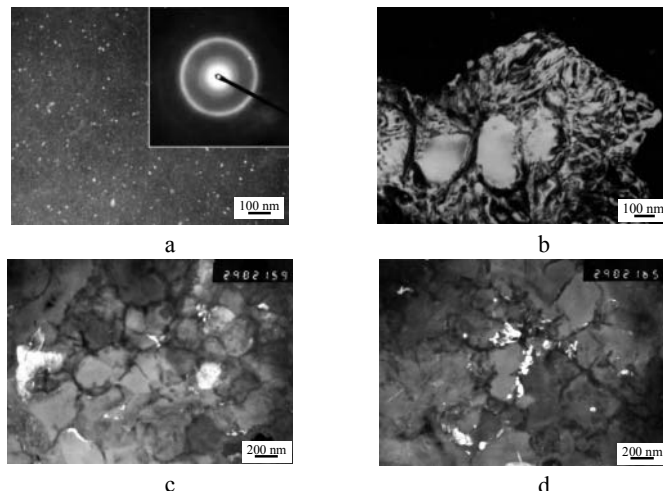
Figure 6. Structure of Al-Ce-Sc ribbons, TEM: x=3 (a), x=5 (b), x=7(c, d); dark field images with using: a part of ring (a), Al_3Sc reflection (c), Al_4Ce reflection (d); bright field image (b)
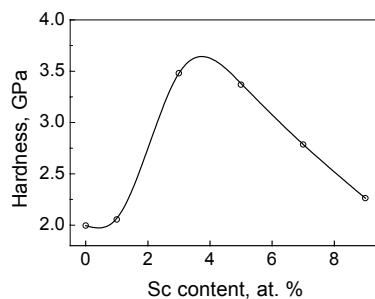

Figure 7. Effect of Sc content on the hardness of $Al_{91}Ce_{9-x}Sc_x$ ribbons

In accordance to the common rule of an increased glass ability in multicomponent alloys [4], the amorphous structure in Al-Ni-Ce-Sc ribbons appeared to be more stable than in Al-Ce-Sc ribbons: an XRDP with a small α-Al peak of the type of Fig. 4c was registered only for the ribbon $Al_{85}Ni_{10}Sc_5$ of 50 μm in thickness, and for the same ribbon of 35 μm in thickness no such peak was observed. The influence of Sc on the thermal stability in this group of alloys had a non-monotonous character: introducing

1 at. % Sc instead of Ce (x=1) lowered ribbon crystallization temperature, and in the ribbon with x=2 it increased again. In addition, introducing Sc to this alloy changed the crystallization character from one-stage to two-stage mode.

Evidently, at least in part, the lower glass forming ability of the alloys containing Sc instead of Ce can be connected with smaller atomic radius of Sc (0.143 nm for Al, 0.164 nm for Sc and 0.183 nm for Ce) because a certain difference in atomic radii of alloy components is one of the necessary conditions for alloy amorphization [4].

4.   CONCLUSIONS

Sc considerably lowers the glass forming ability of Al alloys compared to rare earth metals (Ce). No amorphous phase was formed in rapidly solidified binary Al-Sc alloys. An unstable quasicrystalline icosahedral phase was first found in the alloy $Al_{85}Sc_{15}$. Substitution of Ce for Sc in $Al_{91}Ce_{9-x}Sc_x$ alloys caused a transfer to a mixed amorphous-nanocrystalline and then to nanocrystalline structure. In $Al_{85}Ni_{10}Ce_{5-x}Sc_x$ alloys a mixed amorphous-nanocrystalline structure appeared in the alloy with x=5 at a lowered solidification rate (increased ribbon thickness).

The appearance of mixed amorphous-nanocrystalline and nanocrystalline structures strongly increased the ribbon hardness.

ACKNOWLEDGEMENT

REFERENCES

1. Inoue, Amorphous, nanoquasicrystalline and nanocrystalline alloys in Al-based systems // Progress in Mater. Science 43 (1998), P. 365-520.
2. Yu.V. Milman, D.V. Lotsko, and O.I Sirko, 'Sc effect' of improving mechanical properties in aluminum alloys // Mater. Sci. Forum 331-337 (2000), P. 1107-1112.
3. J.W. Cahn, D. Shechtman, D. Gratias, Indexing of icosahedral quasiperiodic crystals // J. Mater. Res. 1 (1986), No. 1, P. 13-26.
4. A. Inoue, Stabilization of metallic supercooled liquid and bulk amorphous alloys // Acta mater. 48 (2000), P. 279-306.

STRUCTURE PECULIARITIES OF $Al_{63}Cu_{25}Fe_{12}$ INGOTS WITH A QUASICRYSTALLINE COMPONENT

M. Yefimov, D. Lotsko, Yu. Milman, A. Sameljuk, O. Opanasenko,
M. Krapivka
I.M.Frantsevych Institute for Problems of Material Science of the NAS of Ukraine (IPMS)

Abstract: For manufacturing ingots two techniques were used: the technique of drawing the melt into a thin quartz tube; the technique of melting in a copper water-cooled crystallizer. The structural condition of $Al_{63}Cu_{25}Fe_{12}$ ingots produced with various cooling rates was characterized by the presence of phases i (quasicrystalline), β (bcc of AlFe type), and λ (monoclinic of $Al_{13}Fe_4$ type). The size of phase components lowered with increasing the cooling rate. A single-phase ψ-condition was obtained by annealing at 750 °C.

Keywords: quasicrystal, ingot, annealing, crushing, phase components

1. INTRODUCTION

As for most quasicrystals, the reaction of solidifying Al-Cu-Fe alloys in the concentration range of the existence of a quasicrystalline ψ-phase is peritectic. In this process at the beginning of the crystallization crystalline phases λ and β of different compositions are precipitated from the melt, and for obtaining the ψ-phase a significant diffusion of elements in solid phases is necessary [1]. Both λ and β phases are ternary phases of variable composition: the β-phase on the base of AlFe has a cubic body-centered lattice, the lattice of the λ-phase based on $Al_{13}Fe_4$ is monoclinic. Due to strongly slowed diffusion in quasicrystals in process of manufacturing ingots at middle crystallization rates it has no time to proceed, and as a rule in ingots from alloys in the concentration range corresponding to the ψ-phase together with this phase crystals of the β-phase,

the λ-phase and even the tetragonal θ-phase based on Al_2Cu are formed [2]. The leveling of the phase composition yields to annealing with difficulty. Therefore, in spite of the equilibrium character of the Al-Cu-Fe ψ-phase, for its manufacture it is expedient to use large crystallization rates. It provides smaller dimensions of phase constituents and smaller concentration gradients as well.

2.   EXPERIMENTAL

For manufacturing ingots, two techniques were used: the technique **1** of drawing the melt into thin quartz tube; the technique **2** of melting in a copper water-cooled crystallizer with repeated remelting. The melt was produced directly from the initial metals, the charge composition corresponded to $Al_{63}Cu_{25}Fe_{12}$ (40.3 Al + 40.1 Cu + 16.9 Fe in wt. %). Using the method 1, the melt was prepared in the arc furnace with non-consumed tungsten electrode in argon medium on the water-cooled copper bottom. The obtained ingots were of 6-13 mm in diameter and of 50-120 mm in length. The cooling rate while solidification was of about 150-300 °C/s depending on the tube diameter. Using the method 2, ingots were melted in an argon-arc furnace MIFI-9-3 with non-consumable tungsten electrode in pure argon atmosphere in a copper water-cooled crystallizer. Ingots in the form of cylinders or disks were produced. Low crystallization rates (5-50 °C/s) were obtained by means of gradual lowering the current strength in the arc while melting, and high crystallization rates (100-800 °C/s) were achieved by using copper crystallizers with flooded space in the form of a cylinder on a stand.

Crushing ingots was carried out in a steel mortar in air. After each 3-5 min of crushing the powder was sieved through a sieve of 100 μm, and the coarser rest was crushed further. Ingot microstructure was studied by SEM technique in microscopes JSM-840 and Superprobe-733, the last microscope having an attachment for X-ray microanalysis. X-ray investigations were carried out in the X-ray unit DART-UM1 in CuKα emanation.

3.   RESULTS

The ingot of $Al_{63}Cu_{25}Fe_{12}$ alloy of 6 mm in diameter manufactured by the technique **1** was non-uniform along its length. Thus, approximately in one third of the ingot from the beginning X-ray investigation revealed the existence of ψ-, β- and λ-phases, whereas in the remaining part of the ingot the amount of λ-phase was very insignificant (Fig.1A).

In back-scattered electron image (BEI, SEM investigation) these phases, as in work [2], have the following contrast: ψ-phase ($Al_{63}Cu_{25}Fe_{12}$) looks gray, β-

phase ($Al_{55}Cu_{40}Fe_5$) looks light, λ-phase ($Al_{72}Cu_5Fe_{23}$) looks dark-gray, and particles of β- and λ-phases are embedded into the ψ-phase matrix (Fig. 2).
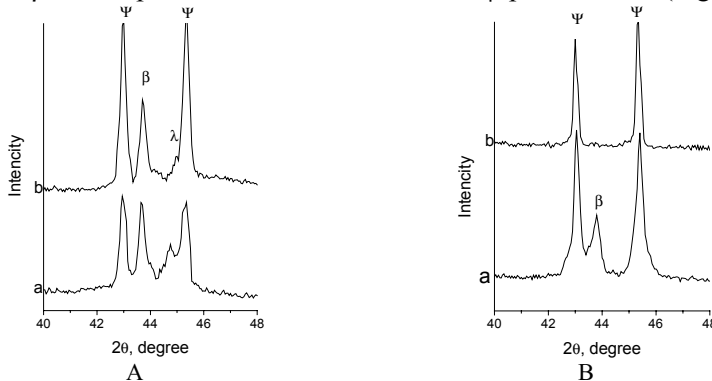

Figure 1. Fragments of X-ray patterns of various parts of $Al_{63}Cu_{25}Fe_{12}$ ingot of 6 mm in diameter produced by the technique **1** (longitudinal section): initial part of the ingot (A), the rest of the ingot (B); without annealing (a), after annealing in vacuum at 750 °C during 5 h (b)
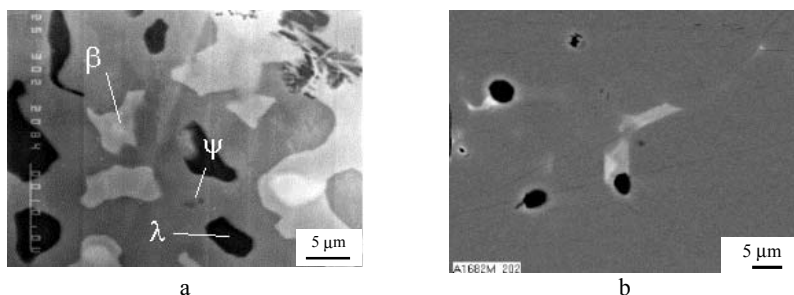

Figure 2. SEM photos (BEI) of the longitudinal section of $Al_{63}Cu_{25}Fe_{12}$ ingot of 6 in diameter (middle part) manufactured by the technique **1**: a – initial condition, b – annealing at 750 °C for 5 h (black spots in (b) are pores).

The ingot was annealed in vacuum at temperatures of 700 and 750 °C. A single-phase i-condition (by X-ray data) was obtained in the middle and end parts of the ingot by annealing at 750 °C for 5 h (Fig.1B). However, SEM investigation revealed an insignificant amount of β-phase in the annealed sample (Fig. 2b). A prolongation of annealing the initial part of ingot at 750 °C to 25 h did not led to obtaining the single-phase i-state.

The structure of ingots manufactured by drawing into a quartz tube of 13 mm in diameter was more uniform. The phase composition of this ingot was the same as of previous one (Fig. 3), and the size of β and λ phase components was larger (Fig. 4), evidently, due to a lower crystallization rate. Annealing this ingot at 750 °C led to gradual lowering the intensity of X-ray peaks from β- and λ-phases, but a prolongation the annealing time to 100 h did not convert it to the single-phase state (Fig. 4).
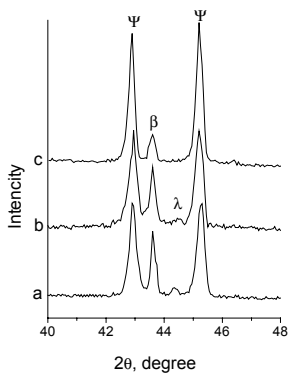
Figure 3. Fragments of X-ray patterns of the ingot of 13 mm in diameter manufactured by the technique **1**: initial condition (a); after vacuum annealing at 750 °C for 5 h (b); after vacuum annealing at 750 °C for 100 h (c)
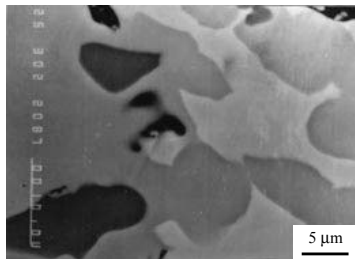

Figure 4. SEM photo (BEI) of the longitudinal section of the ingot of 13 mm in diameter manufactured by the technique **1**

The structural condition of $Al_{63}Cu_{25}Fe_{12}$ ingots produced by the technique **2** with various cooling rates was characterized by the presence of the same three phases (Fig. 5). SEM investigation (Fig. 6) has confirmed the existence in ingots of these phases as well as pores. In all manufactured ingots the existence of the θ-phase that was revealed in $Al_{64}Cu_{24}Fe_{12}$ ingots of 50 mm in diameter produced by induction melting in the work [2] was not established either by X-ray or by SEM analyses. Evidently, this fact is connected with higher cooling rate in our ingots. Compared to ingots drawn into quartz tubes, particles of phases were more elongated. The size of phase components lowered with increasing the cooling rate (Fig. 6).

Annealing to the single-phase ψ-state at 750 °C was successful only for ingots manufactured with a cooling rate of 300 °C/s. It took 10 h. The maximum annealing time of all ingots was of 25 h, and in the rest of ingots it gave no single-phase state (Fig. 5B). The sizes of phase components in ingots manufactured by the techniques 1 и 2 that can be annealed to the single-phase ψ-state were approximately equal. Average hardness (HV, P = 2 N) of as-cast ingots was about 7.8 GPa. Annealing lowered it to about 7.65 GPa. The batch of ingots produced by the technique **2** with a cooling rate of 300 °C/s was crushed into powder. The ratio of peak intensities of ψ-phase after crushing somewhat changed (Fig 7). These changes are explained by the elimination in powder of texture and inhomogeneities possible in the ingot. The amount of the ψ-phase in this powder was of 55 wt. %. It is interesting that annealing duration necessary for attaining the single-phase state in the powder obtained by ingot crushing decreased from 10 to 2 hours.

(A)   (B)
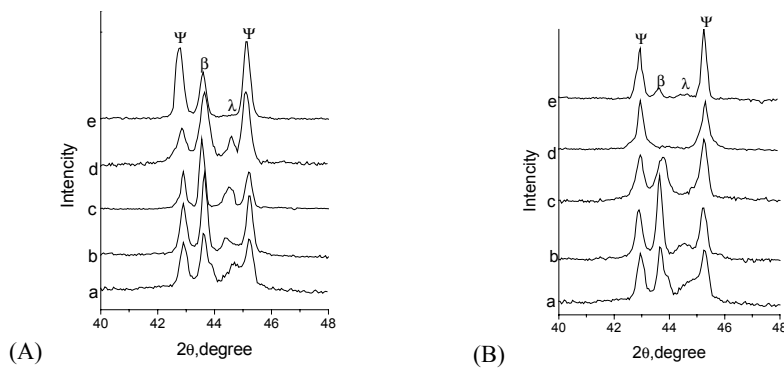
Figure 5. Fragments of X-ray patterns of longitudinal section of Al$_{63}$Cu$_{25}$Fe$_{12}$ ingots manufactured by the technique **2** with various cooling rates: a - 10 ^{0}C/s, b - 20 ^{0}C/s, c - 50 ^{0}C/s, d* – 300 ^{0}C/s, e – 800 ^{0}C/s; A – initial state, B – after annealing at 750 °C during 25 h; * - X-ray pattern after annealing for 10 h is given
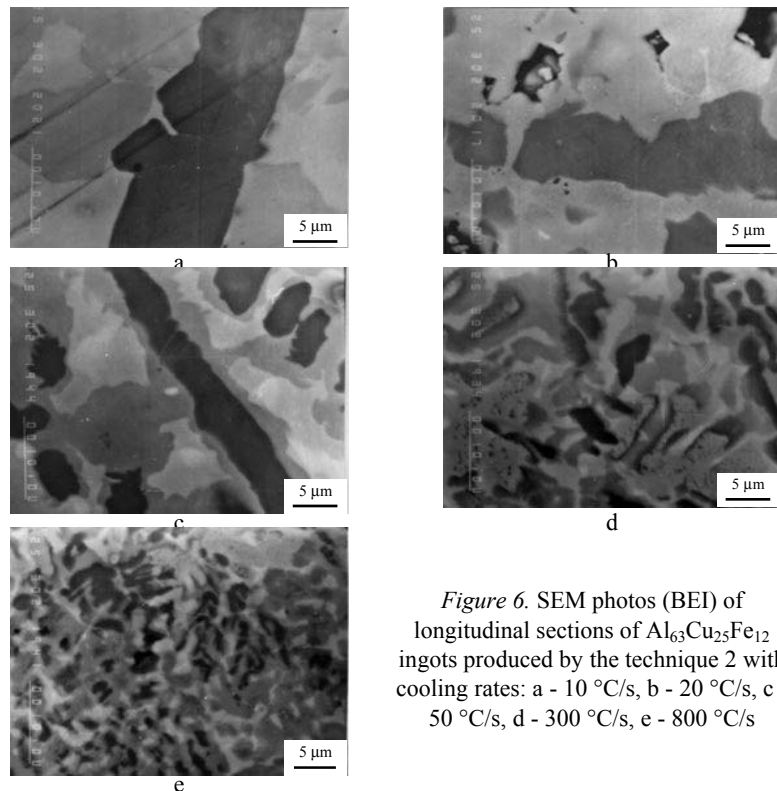

Figure 6. SEM photos (BEI) of longitudinal sections of Al$_{63}$Cu$_{25}$Fe$_{12}$ ingots produced by the technique 2 with cooling rates: a - 10 °C/s, b - 20 °C/s, c - 50 °C/s, d - 300 °C/s, e - 800 °C/s
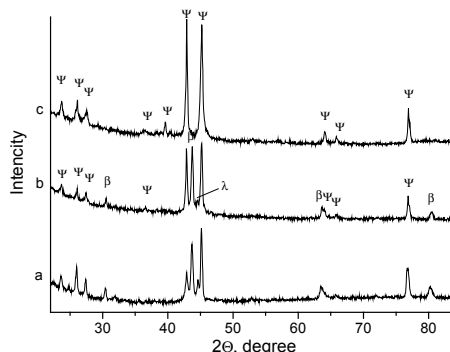
*Figure 7*. X-ray patterns of $Al_{63}Cu_{25}Fe_{12}$ ingot produced by the technique **2** with a cooling rate of 300 ^{0}C/s: a - initial state; b - powder produced by crushing ingots; c - powder produced by crushing ingots after 2 h annealing at 750 °C.

4. CONCLUSIONS

$Al_{63}Cu_{25}Fe_{12}$ ingots produced by rapid solidification consist of three phases: icosahedral quasicrystalline phase ψ (matrix), and crystalline β- and λ-phases (embedded particles), the size of which depending on the solidification rate. Only ingots with the size of β- and λ-phase particles of approximately 3–5 μm could be annealed to a single-phase ψ-state. Annealing to the ψ-state of the powder of crushed ingot proceeded at 750 °C for about 2 h, whereas this state in the ingot was obtained only after 10 h annealing.

ACKNOWLEDGEMENTS

REFERENCES

1. G. Michot, Production of icosahedral Al-Cu-Fe powders by centrifugal atomization method, in: C. Janot, R. Mosseri (Eds.), Proc. of the 5th Internat. Conf. on Quasicrystals, (Singapore: World Scientific,1996) p. 794-797.
2. D.J. Sordelet, M.J. Kramer, O. J. Unal, Thermal Spray Techn., **4** (3) (1995) 235-244.
3. Cahn J.W., Shechtman D., Gratias D. J. Mater. Res., **1** (1986) 13-26.

CONSOLIDATION OF AL-CU-FE POWDERS WITH QUASICRYSTALLINE COMPONENT BY USING HIGH QUASIHYDROSTATIC PRESSURES

O. Bykov, I. Timofeeva, D. Lotsko, Yu. Milman, S. Ulshin
Frantsevych Institute for Problems of Material Science of the NAS of Ukraine (IPMS), Kyiv, Ukraine

Abstract: The technique of powder consolidation under a high quasi-hydrostatic pressure was used for consolidating quasicrystalline AlCuFe powders manufactured by water-atomization technique. The optimum conditions for the consolidation were selected through the analysis of the dependence of sample porosity on pressure and temperature in various stages of the consolidation process. The consolidation process took 2-3 min. X-ray investigation of sintered samples was performed, their hardness was measured. A softening of samples with the growth of pressure was revealed, which was interpreted as the influence of phason defects created by deformation while consolidation.

Key words: quasicrystalline powders, consolidation, high quasihydrostatic pressure

1.   INTRODUCTION

Quasicrystalline powders behave while consolidation in many features like ceramic materials and are consolidated with difficulties. Usually it is performed by HIP technique, but this process takes rather much time and requires complicated equipment. In our former works [1] it was shown that the consolidation of ceramic powders is significantly easier when using high quasihydrostatic pressure that activates particle contact interaction, and high-temperature sintering requires 2-3 min.

The technique of high-pressure consolidation was used to the water-atomized powder $Al_{63}Cu_{25}Fe_{12}$, size fraction of (-63) µm. Phase composition

of powder: QC-phase ψ + bcc crystalline intermetallic β, the volume content of ψ-phase being of 60 %. The process includes three operations:

- preliminary molding of powder at ambient temperature in a mold piston cylinder at a pressure to 1 GPa;
- compression to pressures of 7 GPa in high-pressure cells;
- sintering under the same pressures at a high temperature.

High pressures to 4.5 GPa and from 4.5 to 7 GPa were realized in "envil with hole" cells of lentil and toroid types, respectively.

2. ANALYSIS OF CONSOLIDATION PROCESS

2.1 Preliminary Pressing

The phenomenological equation for the porosity Θ of a plastic billet formed in the press die "piston-cylinder" is [2]:

$$\sigma_z = \frac{2(1-\Theta)}{3}\sqrt{\frac{1-\Theta}{\Theta}} \cdot \sigma_s \tag{1}$$

where σ_z is the stress on the punch, σ_s is the yield stress of the porous material.
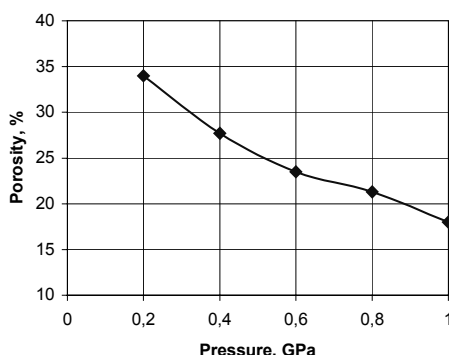
Figure 1. Porosity of preliminary formed billet from water-atomized $Al_{63}Cu_{25}Fe_{12}$ powder versus forming pressure

From the utmost points in the curve in Fig. 1 we obtained an average evaluative value of the yield stress of the porous billet from quasicrystalline powder σ_s=0.6 GPa in the process of preliminary pressing. Just this stress is optimum for forming billets. The shape of the curve is an evidence of the powder with quasicrystalline component to conduct while preliminary

pressing as high-modulus ceramics [3]. The deviation from the average value of σ_s values for the utmost points of the curve in Fig. 1 is rather large and on average equals to 0.26 GPa. It is caused by the difference of quasicrystal physical-mechanical properties from the properties of plastic metals.

2.2 Compression in High-Pressure Cells at Ambient Temperature

For compressing a porous sample under a pressure P in the solid medium cell of high pressure the following equation is proposed [2]:

$$P = \frac{2(1-\Theta)^2}{3\sqrt{\Theta}} \cdot \sigma_s \cdot \tag{1a}$$

The evaluation of σ_s from Fig. 2 and Eq. (1a) gives the average value of the yield stress of the porous material of σ_s=1.5 GPa.
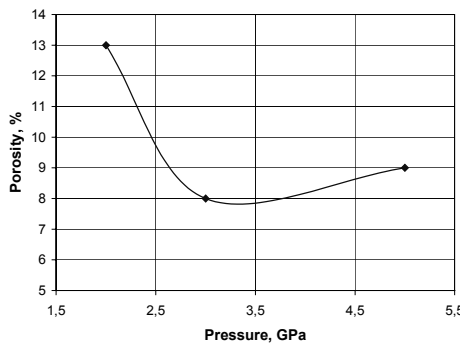

Figure 2. Pressure dependence of the porosity of the compressed billet

The deviations from the average value for the utmost points of the curve do not exceed 0.1 GPa (6 %). This result is an evidence of the fact that a porous body from the quasicrystalline powder deforms under a high quasihydrostatic pressure as porous bodies from plastic material. Thus, it is shown that the effective pressure P for the consolidation of a powder billet of $Al_{63}Cu_{25}Fe_{12}$ in the high-pressure apparatus is

$$P \geq 5\sigma_s, \tag{2}$$

where σ_s is the yield stress of the porous body obtained by preliminary pressing by the scheme "press die – punch".

It is seen from Fig. 2 that the increase of pressure to 3.0-3.5 GPa led to consecutive consolidation of samples. A growth of porosity in samples obtained at pressures higher than 3.0 GPa occurs due to elastic aftereffect.

2.3   Sintering in Compressed Condition

The influence of temperature on the process of consolidating quasicrystalline powders $Al_{63}Cu_2Fe_{12}$ at the effective pressure of P = 3 GPa with holding of 2 min was investigated (Tab. 1). Noteworthy that the increase of temperature in sintering process causes a certain growth of compressing pressure (by about 0.5 GPa) because of thermal expansion of the sintered material. The optimum sintering temperature of 700 °C was determined from the conditions of existing the ψ-phase in Al-Cu-Fe system and its ability to a significant plastic deformation [4-6].

Table 1. Influence of sintering temperature on the density of $Al_{63}Cu_{25}Fe_{12}$ samples (P=3GPa)

Sample #	Sintering temperature, °C	Relative density, %
1	200	88
2	400	90
3	600	93
4	700	98
5	800	98

Thus, there are found the technological conditions for consolidating powders with quasicrystalline component that allow to sinter dense quasicrystalline samples with the porosity θ ≤ 2 %. Compacted samples in the form of cylinders of 6 mm in diameter and of about 5 mm in height were manufactured.

3.   PLASTIC DEFORMATION IN COMPACTS

A large X-ray line broadening in both β- and ψ-phases in compacted samples (Fig. 3) is an evidence of a strong plastic deformation in compact samples sintered under high quasihydrostatic pressure.

4.   HARDNESS OF SINTERED COMPACTS

Hardness was measured by Vickers indenter in PMT-3 microhardness tester at a load of 2 N. The observed sinking of compact hardness with the growth of pressure, i.e. with growing deformation (Fig. 4), is an evidence of strain softening characteristic for quasicrystalline materials [5, 6]. Plastic

deformation in process of sintering occurs as a consequence of closing pores as well as due to shear components of the pressing stress.


As-atomized powder   Compact sintered at T= 700 °C, P=5 GPa
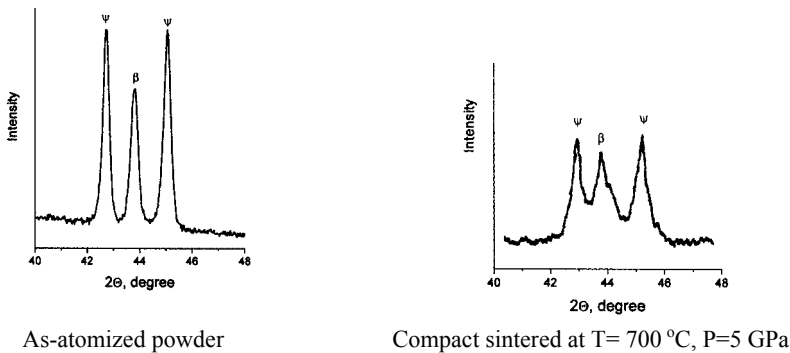
Figure 3. Fragments of X-ray patterns, CuKα radiation
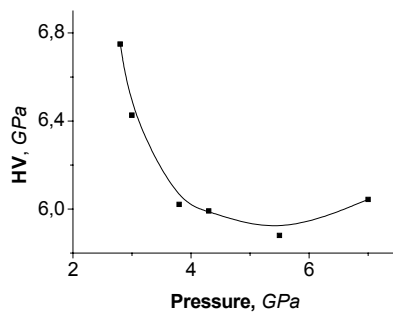
Figure 4. Hardness of sintered compacts: T = 700 °C, P = 5 GPa, τ = 2 min

Thus, it is shown that the behavior of the two-phase ψ+β material while high-temperature sintering under high quasihydrostatic pressure is determined by the quasicrystalline ψ-phase.

5.   CONCLUSIONS

1) There was developed the procedure for manufacturing low-porosity compacts from water-atomized $Al_{63}Cu_{25}Fe_{12}$ powders that includes processes of manufacturing the billet pressed at ambient temperature, inserting the billet into the high-pressure cell, imposing a high pressure (to 7 GPa), heating the cell with the billet to the working temperature and holding it at this temperature under the pressure. There are selected

the optimum pressure of cold pressing (0.6 GPa), the optimum sintering temperature under a pressure (700 °C), and the optimum pressure of 3-4 GPa that permits to obtain compacts with the porosity lower than 2 %.

2) It is shown that the process of pressing quasicrystalline $Al_{63}Cu_{25}Fe_{12}$ powder at room temperature with using high quasihydrostatic pressure can be described by the model of visco-plastic behavior. This powder in process of room temperature pressing by the scheme "pressing die – punch" at a pressure to 1 GPa behaved as low-plasticity ceramic powders, and in the cell of high quasihydrostatic pressure at pressures to 5 GPa it revealed the features of a plastic porous body.

3) X-ray investigation discovered a large plastic deformation in $Al_{63}Cu_{25}Fe_{12}$ sintered compacts. Measuring hardness has shown that this deformation proceeded with strain softening characteristic for quasicrystalline materials. Thus, the behavior of the two-phase $\psi+\beta$ material under investigation while high-temperature sintering under high quasihydrostatic pressure is determined by the quasicrystalline ψ-phase.

ACKNOWLEDGEMENTS

REFERENCES

1. Milman Yu.V., Gridneva I.V., Chugunova S.I., Timofeeva I.I., Bykov A.I., Science of Sintering, 28/3 (1996) 145-150.
2. Radomyselski I.D., Bagliuk G.A., Powder Metallurgy, No. 2, (1985) 7-13.
3. Timofeeva I.I., Smolin M.D. Effect of high pressures on the structure and properties of refractory compounds, in: Physics and Technique of High Pressures. (Kyiv: Naukova. Dumka, 1981).
4. Quiquandon M., Calvayrac Y., Quivy A. et al. in: J.M. Dubois, P.A. Tiel, A.P. Tsai, K. Urban (Eds.), Quasicrystals, MRS Symposium Proc., Vol. 553, (MRS, Warrendale, PA 1999) p. 95-106.
5. Milman Yu.V., Lotsko D.V., Bilous A.M. in: M.-I- Baraton and I. Uvarova (Eds.), Functional Gradient Materials and Surface Layers Prepared by Fine Particles Technology, (Kluwer Academic Publ., Netherlands, 2001) p. 289-296.
6. Kang S.S., Dubois J.M. Phil. Mag. A. 66 (1992) 151-163.

PART 3

ADVANCED ALUMINUM AND MAGNESIUM

ALLOYS

HIGH-STRENGTH ALUMINUM ALLOYS

Yuly V. Milman

Frantsevych Institute for Problems of Materials Science, Ukrainian Academy of Sciences, 3 Krzhizhanovsky Str, 03680 Kiev-142, Ukraine

Abstract: The perspective directions of increasing mechanical properties of wrought and cast aluminum alloys are discussed. It is shown that additional alloying of high-strength $Al - Zn - Mg - Cu$ alloys by Sc is very effective. The Al wrought alloys for elevated temperatures application with strength more than 300 MPa at 300 ^{o}C and satisfactory plasticity may be obtained using dispersion strengthening by quasicrystalline particles $50 \div 600$ nm in diameter. The high-strength cast alloys with good castability and increased mechanical properties were elaborated on the base of eutectic composition $Al - 13$ vol. % Mg_2Si with additional alloying by transition and rare-earth metals. The development of this direction is the elaboration of cast eutectic alloys in the system $Al - Ti - Cr$, containing $L1_2$ phase. These alloys have higher melting point (1275 ^{o}C), high Young's modulus (up to 190 GPa), essential ductility in compression tests and high hardness and strength up to 800 ^{o}C.

Key words: high-strength aluminum alloys, dispersion hardening, quasicrystals, eutectic alloys, mechanical properties

1.   INTRODUCTION

The pure aluminum is the very soft metal with hardness 210 MPa and yield stress $10 \div 15$ MPa. But the modern methods of alloying made possible to increase hardness of Al alloys to 2200 MPa, yield stress to 700 MPa and ultimate tensile stress to 800 MPa. High strength characteristics of these alloys are combined with plasticity to fracture $5 \div 15$ % that is enough for the practical use. This dramatic increase of strength has been possible due to very high plasticity of pure Al (which has FCC structure) and due to fundamental and experimental investigations in the theory of alloying and physics of strength and plasticity.

In the present paper we consider some perspective directions of investigation, in which the further increasing of mechanical properties of aluminum alloys is possible.

2.   "SC EFFECT" OF IMPROVING MECHANICAL PROPERTIES IN ALUMINUM ALLOYS

After very numerous theoretical and experimental works devoted to creation of high-strength $Al - Zn - Mg$ alloys (7075 and 7050 by USA standartds and B95 by Russian clasification) there was   opinion that the further considerable increasing mechanical properties of aluminum alloys is impossible. But as it has been shown lately [1 − 7 et al.], the additions of scandium to aluminum cause a very strong hardening, so that the specific increase of the yield stress of the alloy $\Delta\sigma_s / \Delta C \approx 1000$ MPa / at. % that is essentially higher in comparison with the influence of other alloying elements. This influence of Sc is conditioned by the presence of the intermetallic Al_3Sc in the $Al - Sc$ phase diagram, this intermetallic having the same FCC crystalline lattice as Al, and parameters of their lattices differ only by 1.3 %. The solubility of Sc in Al at the melting point of Al is approximately 0.3 at. % and sharply decreases while cooling. This conditions the possibility for the creation of a supersaturated solid solution by quenching and the precipitation of very disperse particles of Al_3Sc type, which are coherently bound to matrix, during ageing (Fig. 1). The size of disperse Al_3Sc particles after ageing at the temperature close to 300 ^{o}C is usually about several nanometers (from 3 to 10 ÷ 15), which just causes a very strong hardening. The size of these particles grows very slowly with an increase in the temperature to 400 ^{o}C.
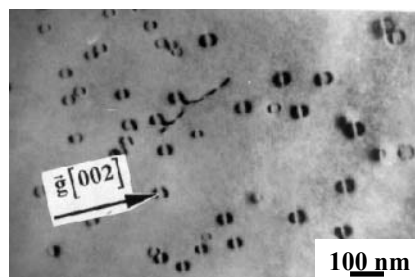
Figure 1. $Al_3(Sc_{1-x}Zr_x)$ particles in as-cast $Al - 6.8Zn - 1.3Mg - 0.12Zr - 0.05Sc$ (wt. %) alloy subjected to the homogenisation at 470 ^{o}C during 3 h, light-field image, foil plane (110), the forming reflection $\vec{g} = [002]$ [7]

Scandium atoms in aluminum solid solution have the maximum value of binding energy with the vacancy [8] (see Tab.1) that can provide for additional strengthening for aluminum alloys containing Sc.

Table 1. Binding energy between the vacancy and soluted atoms of different elements in α-Al

Element	Sc	Mg	Si	Cu	Zn
U, eV	0.35	0.29	0.26	0.20	0.18

Positive influence of scandium has a complex character. Thus, the additions of Sc not only increase the yield stress and the ultimate tensile strength, but improve also the workability of alloy and its production ductility, decrease the grain size in as-cast condition, eliminate the dendrite structure and lead to the formation of a fine-grained equiaxial structure, sharply increase the recrystallization temperature (Tab.2), improve metal weldability and raise its corrosion resistance.

Table 2. The temperature of recrystallization beginning T_r in Al alloys containing Sc [7]

Alloy composition, wt. %	T_r, ^oC
Al	$100 \div 200$
Al – 0.26Sc	540
Al – 0.2Sc – 0.18Zr	610
Al – 7Zn – 2Mg – 0.14Zr – 0.2Sc	No recrystallization to the melting point
Al – 6Mg – 0.14Zr – 0.2Sc	— ″ —

The increase of the weldability in Al-Sc alloys is stipulated by two factors: lowering the grain size in the welded joint (as well as in as-cast metal) and decreasing the zone of thermal influence in connection with increased recrystallization temperature. As a result the tendency to the formation of hot cracks during welding is lowered, and mechanical properties of the welded joint at ambient temperature are increased. Modern Al alloys are multi-component ones, and therefore alloying by Sc shall be co-ordinated with the hardening effect of other elements, and the conditions for the thermomechanical treatment shall be significantly correlated.

2.1   Classification of alloying elements with respect to "scandium effect"

Taking into account physical-chemical interaction of alloying elements with Al as well as with Sc, the following classification of alloying elements which includes 5 groups was proposed [7]:

1) elements which increase or don't decrease significantly the solidus temperature of aluminum T_s and don't form with Sc strong intermetallics distributed in aluminum solid solution (Ti, Zr, Hf, V, Nb, Ta, Mn, Cr, Mo, W, Re, i.e. mainly transition metals);

2) elements which lower T_s, but have high solubility in Al at the temperature of ageing by Sc (about 300 ^oC). They are in the first line Zn, Mg, Li;

3) elements which lower T_s and have low solubility at the temperature of ageing by Sc (Cu and Si);

4) elements which form strong compounds with Sc and exclude Sc from hardening process (Fe, Co, Ni, and Cu and Si at high concentrations as well);

5) elements which partially substitute Sc in Al_3Sc and lower the consumption of Sc with the preservation of hardening effect (Zr, Y and rare-earth elements).

Some elements (Zr, Cu, Si et al.) may have the properties of several groups.

2.2   Superplasticity

Al-Sc alloys in consequence of high recrystallization temperature are the best materials for creation of the superplastic state. Al – Mg – Sc alloys are used as the superplastic materials the most frequently [9–13]. These alloys are natural superplastic materials, since they are superplastic after standard thermomechanical treatment, for example after cold rolling and following annealing. Elongation to fracture in Al – Mg – Sc alloys maybe up to 1000 % and parameter m that characterizes the sensibility of yield stress to the deformation rate maybe $m = 0.6 \div 0.7$.

3.   HIGH-STRENGTH Al-Zn-Mg-Cu ALLOYS, ADDITIONALY ALLOYED BY Sc

The alloys of Al – Zn – Mg – Cu system have the higher strength characteristics among wrought Al alloys. These alloys are the basic structural materials for aerospace engineering. Their strengthening is due to a very fine precipitation of η'-phase, which is enriched with Zn and Mg. The strength of these alloys increases when the concentration of Zn increases. However, an increase in the concentration of Zn above 7 % leads to a dramatic decrease in fracture-related properties as well as deterioration of weldability and corrosion resistance. It was recently found that mechanical properties of these alloys containing up to $6 \div 7$ % Zn can be improved considerably by addition of small amounts of Sc and Zr [7, 14-16].

Combined alloying with Sc and Zr in the amount as low as 0.2 % of every element refines microstructure of casting and welding [15], improves workability and deformability of castings [7, 16, 17], leads to formation of a very uniform and fine cellular dislocation structure in wrought products, and impedes recrystallization during heat treatment due to the obstacle action of the coherent particles. The last two factors facilitate an increase in strength and ductility of these wrought alloys in T6 or T7 conditions.

Composition of some alloys investigated in [16] and their mechanical properties (yield stress *YS*, ultimate tensile stress *UTS* and elongation to fracture δ) are given in the Tab.3. It is seen from Fig.2 that additions of Sc have eliminated the dendrite structure and leads to the formation of a fine-grained equiaxial structure.

Table 3. Composition and mechanical properties of high-strength Al − Zn − Mg − Cu alloys after extrusion and thermotreatment T6 [16]

#	Chemical composition, wt. %	*UTS*, MPa	*YS*, MPa	δ, %
1	Al−11.0Zn−3.3Mg−1.2Cu	554	-	0
2	Al−9.0Zn−3.1Mg−1.2Cu−0.2Zr	786	727	5.0
3	Al−10.8Zn−3.5Mg−1.2Cu−0.15Zr−0.39Sc	790	748	10.0
4	Al−10.0Zn−2.8Mg−1.1Cu−0.14Zr−0.25Cr	785	729	8.4
5	Al−10.0Zn−3.1Mg−1.1Cu−0.16Zr−0.28Cr−0.45Sc	775	742	10.7
6	Al−10.3Zn−2.7Mg−1.3Cu−0.15Zr−0.4Mn−0.49Sc	793	738	8.7
7	Al−12.0Zn−3.3Mg−1.2Cu−0.13Zr−0.4Mn−0.49Sc	820	790	5.8

a   b

c   d
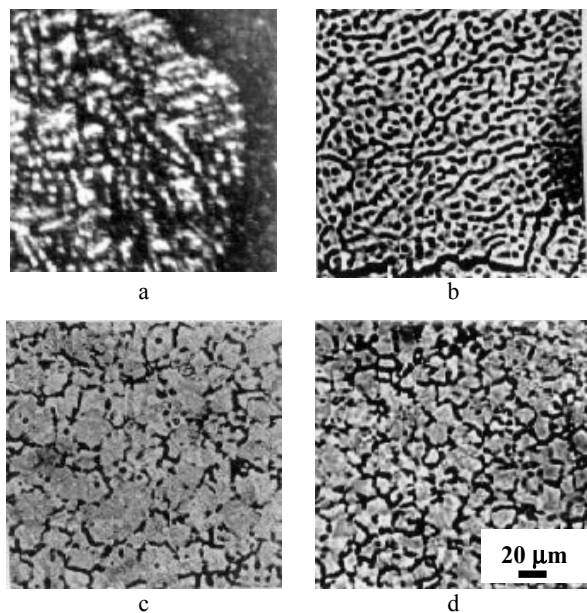
Figure 2. Microstructure of as cast alloys of Al − Zn − Mg − Cu system:
a − alloy 1; b − alloy 4; c − alloy 5 and d − alloy 7 by Tab.3

For example, in the Al−12.0Zn−3.3Mg−1.2Cu−0.13Zr−0.4Mn−0.49Sc alloy high mechanical properties were obtained, i.e. *YS* = 790 MPa and *UTS* = 820 MPa. This high strength was achieved due to additional combined alloying with transition metals, such as Sc, Zr, Cr and Mn, which retard

recrystallization during heat treatment and retain cellular dislocation structure of deformed material, with a dislocation cell size of $1 \div 2$ μm.
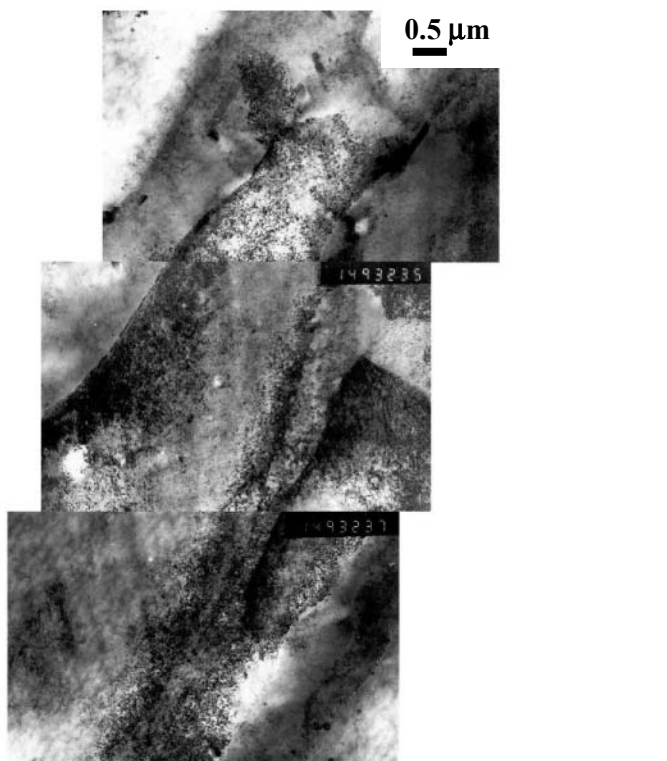

Figure 3. The band of localized deformation in the working part of specimen after the tension test of alloy Al − Zn − Mg − Cu system in T6 condition (TEM, the photograph was obtained by G. Sarzhan)

This non-recrystallized structure is more ductile, because brittle fracture along grain boundaries is not developed. An addition of Sc in combination with Zr, Mn and Cr increases the size of η′-particles, leading to an increase in ductility. A decrease in strength accompanying this growth is compensated and even exceeded by contribution to hardening of small $Al_3(Sc_{1-x}Zr_x)$ coherent particles. The beneficial effect of alloying with Sc in combination with Zr is the possibility of increasing the concentration of Zn without loss in ductility. It is known that fracture of high-strength Al–Zn–Mg alloys is connected with localization of deformation (Fig. 3). The deformation localization is very essential for alloys with small particles of the second phase (smaller than $3 \div 5$ nm), when the mechanism of cutting particles by dislocations is operated, because deformation localizes in planes where particles were cut. An increase in the size of the η′-particles in alloys containing Sc decreases the deformation localization and leads to the growth of plasticity. It was shown [18] that an

addition of Sc increases the resistance of Al and its high-strength alloys against general and pitting corrosion in the seawater. Al−Zn−Mg−Cu alloys containing Sc can be used even at cryogenic temperatures where these alloys have good combination of strength and ductility [19].

The high-strength Al−Zn−Mg−Cu alloys may be produced not only by casting, but by PM technology as well. The special equipment for water atomization of Al alloys by high-pressure water (up to 200 kbar) has been elaborated. Cooling rate during producing powders by this technology may be up to 10^6 K/c. The PM technology makes possible to increase plasticity of high-strength Al−Zn−Mg−Cu alloys without Sc additions [20−22].

4. RAPIDLY SOLIDIFIED ALUMINUM ALLOYS, CONTAINING QUASICRYSTALLINE PARTICLES, FOR ELEVATED TEMPERATURES

Rapid solidification processes are successfully used for Al alloys to form a dispersion particles of intermetallic phases, which resist coarsening and strengthen the alloys at elevated temperatures. It has recently been shown that metastable intermetallic phases with a quasicrystalline structure, mainly of the icosahedral type, can also be produced by rapid solidification [23]. As distinct from a crystalline state, translational long-range order is absent in quasicrystals, but there is rotational symmetry with 5-, 8-, 10- or 12-fold axes, which is forbidden in crystalline materials. The absence of translational symmetry in all three orthogonal directions is characteristic of the icosahedral structure [24].

The special atomic structure of quasicrystals is responsible for a number of unique physical and chemical properties; in particular, a very high hardness (up to 10 GPa) with some microplasticity for indentation at room temperature. The majority of studied quasicrystals are Al-base intermetallic phases.

The best Al wrought alloys for elevated temperatures application were obtained using dispersion strengthening by quasicrystalline particles $50 \div 100$ nm in diameter with volume fraction of $30 \div 50$ % in Al matrix (Fig.4) [25]. We have used in our experiments a quasicrystalline phase $Al_{84.2}Fe_7Cr_{6.3}Ti_{2.5}$. For the alloy of Al−Fe−Cr−Ti system obtained by rapid solidification technique with the following compacting of powders the strength at 300 ^{o}C was more than 300 MPa and plasticity at room temperature was $5 \div 10$ %, that corresponds to the air-force goal level. The structure and mechanical properties of these alloys are stable up to 400 ^{o}C.
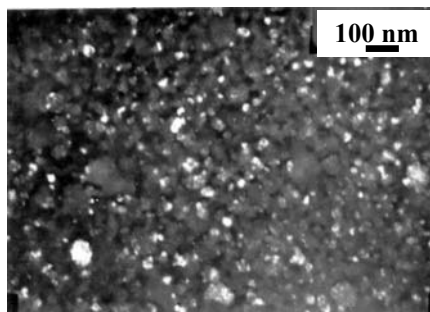
Figure 4. Quasicrystalline particles in $Al_{93}Fe_3Cr_2Ti_2$ melt-spun ribbon, dark field image

5.   HIGH-STRENGTH CAST EUTECTIC ALUMINUM ALLOYS

Progress of the automotive, aviation and shipbuilding industries requires the development of advanced cast aluminum alloys, having a high level of mechanical properties. Traditionally cast aluminum alloys are eutectic ones, whose structure and phase composition is formed immediately during crystallization. Phase constituents of these alloys, possessing high thermal stability, are close to the thermodynamic equilibrium. Besides, the presence of the eutectic results in improved castability. However, the resource to improve properties of existing alloys, including high-temperature strength, which is directly bound with their melting temperature, at present, is practically exhausted. Complex alloying of these alloys, as a rule, gives rise to decreasing eutectic constituent volume fraction, to widening temperature melting range and consequently to a loss of castability.

The high-strength cast alloys with good castability and increased mechanical properties were elaborated on the base of eutectic composition Al − 13 vol. % Mg_2Si with additional alloying by transition and rare-earth metals [26, 27].

There was proposed [26, 27] a new approach to design cast aluminum alloys, based on using of ternary and more complicated phase diagrams, containing eutectic quasi-binary sections of aluminum and intermetallic phases and detailed investigation of topology of corresponding fusion diagrams. Creation of different systems of particles, coherent to matrix and non-interacting with eutectic colonies, allows to improve the level of mechanical properties and to widen the temperature range of usage of the alloys. The complex alloying by transition and rare earth metals should not change phase composition and structure of basic alloys.

The proposed approach is realized in designing new cast α-Al−Mg_2Si alloys of Al − Mg − Si ternary system. By means of additional alloying of these alloys all mechanisms of hardening (composite, solid solution and

precipitation) are realized. Such an approach provides a substantial increase of operational characteristics of materials both at room and elevated temperatures (300 ÷ 350 °C) and a development of new cast Al alloys with a unique complex of physical and mechanical properties (see Tab. 4).

Table 4. Tensile properties and temperature parameters of alloyed eutectic α-Al + Mg_2Si alloys

Alloy	Mechanical properties				Temperature range of crystallization °C
	Testing temperature °C	*UTS,* MPa	*YS,* MPa	$\delta,$ %	
For high-temperature application	260*	180 ÷ 203	146÷164	5 ÷ 10	595 ÷ 599
	315*	102 ÷ 130	91÷115	13÷15	
For operating up to 150 °C	20	310 ÷ 501	300÷460	< 1	575 ÷ 590

  * holding time at the testing temperature was 100 h

6.　CAST EUTECTIC ALUMINUM ALLOYS CONTAINING L1$_2$ PHASE

　The development of direction given above is the elaboration of cast eutectic alloys in the system Al − Ti − Cr, containing L1$_2$ phase. These alloys have higher melting point (1275 ^{o}C), essential ductility in compression tests and high hardness and strength up to 800 ^{o}C [28, 29].

At present, intense studies of the structure and properties of alloys based on titanium trialuminide with the L1$_2$ lattice are underway. High melting temperatures, a high elastic modulus, low density, and excellent durability in oxidizing environments allow such intermetallic compounds to be promising for the development of new light-weight high-modulus refractory materials. Though the L1$_2$ structure promises higher plasticity as compared with that of Al$_3$Ti (the structural type DO$_{22}$), it is still insufficient for many applications.

Among many alloys based on Al$_3$Ti with the Ll$_2$ structure, particular attention is attracted by alloys doped with Cr. They reveal the best resistance to oxidation, minimum hardness, and some plasticity in compression tests [28, 30, 31].

In the ternary Al − Ti − Cr system a large compositional region has been established experimentally, in which the eutectic transformation of a melt into two solid phases is realized: L $\Leftrightarrow$ L1$_2$ + β. This transformation is univariant and occurs in a narrow temperature interval [29]. The alloys formed by two cubic phases L1$_2$ and β possess a more attractive combination of strength and deformation before fracture (see Fig.5) than alloys, in which the decomposition of the β-phase produces the less symmetric intermetallic compounds AlCr$_2$ or TiAlCr.

The formation of a periodic microstructure due to eutectic crystallization allows significant enhancement of the strength and deformation before fracture as compared to single-phase material. In this case, high values of the modulus of elasticity are obtained, micro-plastic deformation in bending tests appears, and the eutectic character of alloys ensures their high casting properties.


a

b

c
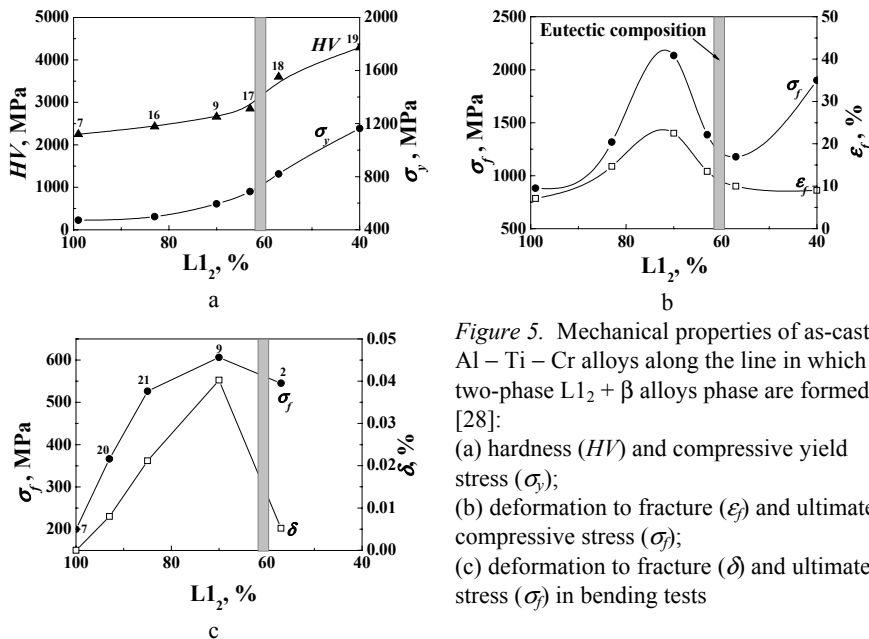
Figure 5. Mechanical properties of as-cast Al − Ti − Cr alloys along the line in which two-phase $L1_2 + \beta$ alloys phase are formed [28]:
(a) hardness (HV) and compressive yield stress (σ_y);
(b) deformation to fracture (ε_f) and ultimate compressive stress (σ_f);
(c) deformation to fracture (δ) and ultimate stress (σ_f) in bending tests

ACKNOWLEDGEMENTS

REFERENCES

1. Willey, L.A. (1971) US Patent 3619181.
2. Yelagin, Y.I., Zakharov, V.V. and Rostova, T.D. (1992) Aluminum alloys alloyed with scandium, *Metal Science and Thermotreatment of Metals* No.1, 24-28.

3. Drits, M.Ye., Toropova, L.S. and Bykov, Yu.G. (1985) Effect of dispersity of precipitates of ScAl$_3$ phase on the recrystallization of Al-Sc alloys *Izv.VUZ'ov: Colour Metals* No.4, 80-84.

4. Parker, B.A., Zhou, Z.F. and Nolle, P. (1995) The effect of small additions of scandium on the properties of aluminum alloys, *J.Mater.Sci.* **30**, 452-458.

5. Milman, Yu.V., Yemelyanov, K.V., Ivashchenko, R.K., Sirko, A.I., Zakharova, N.P. and Ishchenko, A.Ya. (1998) Influence of Sc additions on the structure and mechanical properties of aluminum alloys and their welded joints, *Electron Microscopy and Strength of Metals, Kiev: IPMS of NASU* **9**, 83-92.

6. Pan, S.V., Milman, Yu.V., Slipeniuk, A.N. and Kuprin, V.V. (1998) Effect of rapid solidification on structure and strength characteristics of aluminum alloyed with Sc, *DAN Ukrayiny* No.10, 117-121.

7. Milman, Yu.V., Lotsko, D.V. and Sirko, O.I. (2000) "Sc effect" of Improving Mechanical Properties in Aluminum Alloys, *Mater. Science Forum* **331-337**, 1107-1112.

8. Miura Y., Joh C.H., Katsube T. (2000) Determination of vacancy-Sc interaction energy by electrical resistivity measurements, *Mater.Science Forum* **331-337**, 1031-1036.

9. Akamatsu H., Fujinami T., Horita Z., Langdon T.G. (2001) Influence of rolling on the superplastic behavior of an Al-Mg-Sc alloy after ecap, *Scripta Mater.* **44**, 759-764.

10. Filatov, Yu.L. (1996) Wrought alloys on the base Al-Mg-Sc system, *Metal Science and Thermotreatment of Metals* No.6, 33-36.

11. Komura Sh., Berbon P.B., Furukawa M., Horita Z., Nemoto M., Langdon T.G. (1998) High strain rate superplasticity in Al-Mg alloy containing scandium, *Scripta Materialla* **38**, No.12, 1851-1856.

12. Nieh, T.G., Hsiung, L.M., Wadsworth, J. and Kaibyshev, R. (1998) High strain rate superplasticity in a continuously recrystallized Al-6%Mg-0.3%Sc alloy, *Acta mater.* **46**, No.8, 2789-2800.

13. Lee, S., Utsunomiya, A., Akamatsu, H., Neishi, K., Furukawa, M., Horita, Z., Langdon, T.G. (2002) Influence of scandium and zirconium on grain stability and superplastic ductilities in ultrafine-grained Al-Mg alloys, *Acta mater.* **50**, 553-564.

14. Senatorova, O.G., Uksusnikov, A.N., Legoshina, S.F., Fridlyander, I.N. and Zhegina, I.P. (2000) Influence of different minor additions on structure and properties of high-strength Al-Zn-Mg-Cu alloy sheets, *Mater. Science Forum* **331-337**, 1249-1254.

15. Davydov, V.G., Yelagin, V.I., Zakharov, V.V. and Rostova, T.D. (1996) About alloying of aluminum alloys by additions of scandium and zirconium, *Metal Science and Thermotreatment of Metals* **8**, 25-30.

16. Milman, Yu.V., Sirko, A.I., Lotsko, D.V., Senkov, O.N. and Miracle, D.B. (2002) Microstructure and mechanical properties of cast and wrought Al-Zn-Mg-Cu alloys modified with Zr and Sc, *Mater. Science Forum* **396-402**, 723-728.

17. Eskin, G.I. (2000) Non-dendritic crystallization of light alloys, *Technology of Light Alloys* **2**, 17-25.

18. Vyzovikina, N., Milman, Yu. and Sirko, A. (2002) New high-strength corrosion resistance aluminum alloys, *Problems of Corrosion and Corrosion Protection of Materials, Physico-Chemical Mechanics of Materials*, spec.issue No.3, 554-558.

19. Senkov, O.N., Miracle, D.B., Milman, Y.V., Scott, J.M., Lotsko, D.V. and Sirko, A.I. (2002) Low temperature mechanical properties of scandium-modified Al-Zn-Mg-Cu alloys, *Mater.Science Forum* **396-402**, 1127-1132.

20. Neikov, O.D. (2000) Water Atomized Powder Technologies for Advanced Aluminum Alloy Production. *Proc. of 2000 Powder Metallurgy World Congress, Kyoto, Japan,* part 1, 464-466.

21. Neikov, O.D., Milman, Yu.V., Miracle, D.B., Lotsko, D.V., Sirko, A.I. and Yefimov, N.A. (2001) Effect of Sc alloing additions on atructure and mechanical properties of PM and cast high-strength Al alloys of same composition, *Proc. of EURO PM2001, Nice, France* **2**, 219-224.

22. Neikov, O.D., Lotsko, D.V., Sirko, A.I., Sameljuk, A.V., Thompson, G.E., Zakharova, N.P. and Yefimov, N.A. (2002) Properties of rapidly solidified powder alloys of the Al-Zn-Mg system, *Mater.Science Forum* **396-402**, 1223-1228.

23. Inoue, A. (1998) Amorphous, nanoquasicrystalline and nanocrystalline alloys in Al-based systems, *Progress in Mater.Sci.* **43**, 365-520.

24. Milman, Yu.V., Lotsko, D.V., Bilous, A.M. and Dub S.M. (2001) Quasicrystalline materials. Structure and mechanical properties, *Functional Gradient Materials and Surface Layers Prepared by Fine Particles Technology, Kluwer Acad.Publ.* 289-296.

25. Milman, Yu.V., Lotsko, D.V., Neikov, O.D., Sirko, A.I., Yefimov, N.A., Bilous A.N., Miracle, D.B. and Senkov, O.N. (2002) Processing, structure and mechanical behavior of rapidly solidified aluminum alloys containing quasicrystalline particles, *Mater.Science Forum* **396-402**, 723-728.

26. Barabash, O.M., Legkaya, T.N., Sylzhenko, O.V. and Korzhova, N.P. (1999) Thermodynamic analysis of fusion diagram for Al-Mg-Si, *Metallofiz. Noveishie Tekhnol.* **21**, No.5, 24-28.

27. Barabash, O.M., Milman, Yu.V., Voskoboinik, I.V., Korzhova, N.P. and Legkaya, T.N. (2001) Structure and Physical-Mechanical Properties of Gradient Eutectic Materials Al-Mg$_2$Si (GE), *Functional Materials* **8,** No.1, 159-161.

28. Milman, Yu.V., Miracle, D.B., Chugunova, S.I., Voskoboinik, I.V., Korzhova, N.P., Legkaya, T.N. and Podrezov Yu.N. (2001) Mechanical behavior of Al$_3$Ti intermetallic and L1$_2$ phases on its basis, *Intermetallics* **9,** 839-945.

29. Barabash, O.M., Milman, Yu.V., Miracle, D.V., Karpets, M.V., Korzhova, N.P., Legkaya, T.N., Mordovets, N.M., Podrezov, Yu.N. and Voskoboinik, I.V. (2003) Formation of periodic microstructure involving the L1$_2$ phase in eutectic Al-Ti-Cr alloys, *Intermetallics* **11**, 953-962.

30. Lee, J.K., Park, J.Y., Oh, M.H., Wee, D.M. (2000) Microstructure control in two-phase Al-21Ti-23Cr alloy, *Intermetallics*, **8**, 407-416.

31. Zhang, S., Nic, J.P. and Mikkola, D.E. (1990) New cubic phases formed by alloying Al$_3$Ti with Mn and Cr, *Scripta Metall. Mater.* **24**, 57-62.

HIGH STRENGTH ALUMINUM ALLOYS FOR CRYOGENIC APPLICATIONS

O.N. Senkov, R.B. Bhat, and S.V. Senkova
UES, Inc., 4401 Dayton-Xenia Rd. Dayton, OH 45432, USA

Abstract: A super-high strength cast and wrought aluminum alloy with specific strengths exceeding that of a Ti-5Al-2.5Sn alloy and tensile ductility of about 10% or higher, both at room and cryogenic temperatures, has been developed by modifying the composition and heat treatment of a 7XXX series alloy. This aluminum alloy is a potential candidate to replace the more expensive titanium alloy, which is currently used in some cryogenic rocket engine applications. Microstructure and tensile properties of the aluminum alloy after casting, extrusion and forging and after different heat treatment are presented and the effect of processing parameters on the properties is discussed.

Key words: Al-Zn-Mg-Cu alloys, effect of scandium alloying, tensile properties, microstructure, cryogenic temperatures.

1.   INTRODUCTION

Revolutionary rocket propulsion systems require advanced metallic materials to reduce launch costs and enable extended space missions. Improved materials with higher strength-to-weight ratios, resistance to fuel environments at high pressures, and good ductility are required for further improvements in engine performance. The reduction in weight can most efficiently be realized by the use of low-density alloys such as aluminum and titanium [1,2]. If only high specific strength and ductility were important, titanium alloys would probably be ideal materials for many applications in a wide temperature range [3,4]. In particular, a Ti-5Al-2.5Sn extra low interstitial (ELI) alloy is currently used for rocket engine liquid hydrogen

turbopump impellers. This material has, however, a high cost associated with the cost of raw titanium and difficulties in processing, machining and maintenance. Titanium impellers require complex, high-maintenance, polymeric seals because of concerns about metal-to-metal contact and titanium hydriding. Even small absorption of 200 ppm hydrogen by alpha titanium may lead to cracking and catastrophic failure [5,6]. Alpha+beta or beta titanium alloys, although they are less sensitive to the hydrogen addition at ambient temperatures, cannot be used in the hydrogen atmosphere at cryogenic temperatures because hydrogen increases significantly the brittle-to-ductile transition temperature of the beta phase and reduces strength. Aluminum alloys are of particular interest to replace titanium alloys, especially in ambient and cryogenic applications, because their density is about 38% lower than the density of titanium alloys and they have low susceptibility to hydrogen embrittlement. In addition, these materials are less expensive in production and processing than titanium alloys. However, the specific strength of currently available aluminum alloys at cryogenic temperatures is less than that of the titanium alloy.

Table 1 and Table 2 show tensile properties of the Ti-5Al-2.5Sn ELI alloy and several commercial aluminum alloys, respectively, at room and cryogenic temperatures. Table 1 also provides calculated strengths required for an aluminum alloy to achieve specific strengths similar to the titanium alloy. Although several 7XXX series aluminum alloys show room temperature specific strengths similar to that of the Ti-5Al-2.5Sn ELI alloy, none of the currently available commercial aluminum alloys can compete with the titanium alloy at cryogenic temperatures. To be considered for use in the hydrogen turbopump impellers, an aluminum alloy must have UTS exceeding 620 MPa at room temperature (298K), 800 MPa at 77K, and 900 MPa at 20K, and the tensile ductility of 7% or higher in this temperature range [9].

Table 1. Yield strength (YS), ultimate tensile strength (UTS) and corresponding specific strengths of the Ti-5Al-2.5Sn ELI alloy at room [3] and cryogenic [4] temperatures and calculated strengths for an aluminum alloy ,which provide similar specific strengths.

Temperature (K)	Ti-5Al-2.5Sn ELI (density is 4.6 g/cc)				Al alloy (2.8 g/cc)	
	YS (MPa)	UTS (MPa)	Specific YS (kN m/kg)	Specific UTS (kN m/kg)	YS (MPa)	UTS (MPa)
298	780	890	170	195	476	546
77	1100	1260	240	274	672	767
20	1270	1420	276	309	773	865

Several approaches have been used to achieve these required properties in aluminum alloys. One of these is a nanophase aluminum program being carried out since 1992 [10-12]. In this program, grain refinement to a nanometer-size range is being tried to achieve the required high strength.

This rather expensive powder metallurgy approach uses mechanical milling in liquid nitrogen followed by powder compaction by hot isostatic pressing, extrusion and forging. YS = 518 MPa, UTS = 659 MPa and elongation of 5% were reported for an Al-7.5%Mg binary alloy at 77K. Although these properties are outstanding for the binary alloy, they are far below the goal properties. Other alloy compositions are in the process of development to improve both strength and ductility.

Table 2. Yield strength, ultimate tensile strengths, and elongation of several commercial aluminum alloys at room and cryogenic temperatures [7,8] .

Material	2024-T3	5083-H321	6061-T6	7075-T6	A356.0-T6
Room Temperature (298K) Properties					
YS, MPa	345	230	275	570	205
UTS MPa	485	315	310	620	285
EL (%)	17	16	17	10	10
Cryogenic Temperature (77K) Properties					
YS, MPa	425	270	325	635	250
UTS MPa	585	440	415	705	370
EL (%)	18	27	22	8	10

Very high tensile strengths of about 800 MPa at 298K and 1000 MPa at 77K have recently been reported for several highly alloyed cast-and-wrought Al-Zn-Mg-Cu alloys after T6 treatment [13,14]. These alloys however had almost zero ductility at the cryogenic temperature. Both high strength and low ductility were due to a high concentration of Zn, from 9 to 12%. The ductility was slightly improved by additional alloying with Sc and Zr, but it was still below 1%. These two elements are known to be dispersoid-strengtheners, grain refiners, and recrystallization inhibitors for Al alloys. Sc also improves ductility and stress-corrosion resistance.

In the present work, properties of two developmental Al-Zn-Mg-Cu wrought alloys that have about 7% Zn are reported. The alloy compositions were based on the composition of a 7XXX commercial alloy; however, the alloys were additionally alloyed with Zr, Sc, and some other dispersoid-forming elements. The required combination of high strength and high ductility was achieved by proper selection of the alloy composition and modification of the processing parameters.

2. EXPERIMENTAL PROCEDURES

Two alloys, the chemical compositions of which are shown in Table 3, were produced by continuous direct chill (DC) casting in Wagstaff, Inc., Spokane, WA. The cast billets had 76 mm diameter and 4 m length. Blanks of 150 mm long were cut from the billets and homogenized at 733K for up

to 48 hours. Extrusion of the blanks was conducted at 673K with the extrusion ratio of 16:1. Upset forging of blanks pre-heated to 723K was conducted using open cold dies. Processed material was then solution treated, water quenched, and aged to a peak-aged condition (T6 temper). Tensile tests of flat specimens with the gauge length of 20 mm and the gauge cross-section of 5 x 2.5 mm were cut from the blanks after different processing steps and tensile tested at 298K and 77K and a constant ram speed of 0.02 mm/s (initial strain rate is 10^{-4} s^{-1}) using a servo-hydraulic MTS machine. An optical microscope Neophot 23, scanning electron microscope LEICA 360FE, and transmission electron microscope Phillips CM200 were used for microstructural analysis.

Table 3. Composition of alloys used in this work.

Alloy #	Zn	Mg	Cu	Zr	Sc	Others	Al
SSA000	7.14	2.30	1.61	0.17	0	0.8	Bal.
SSA018	7.17	2.20	1.58	0.18	0.18	0.8	Bal.

3.   RESULTS AND DISCUSSION

3.1   Microstructure and Properties of Cast Alloys

In as-cast condition, the alloy SSA000 (without Sc) has a non-homogeneous, columnar structure, with grains of several millimeters in size growing from the surface of the billet to the center. The alloy SSA018, containing 0.18% Sc, has a fine and homogeneous microstructure throughout the cross-section, with a grain size of about 100 µm (Figure 1). Dendrites are present in both alloys; however, in the alloy without Sc, they are coarse and produce a columnar structure (Figure 2). With addition of Sc, the dendritic structure tends to become finer and more homogeneous.

Tables 4 and 5 present the room temperature and cryogenic temperature tensile properties, respectively, of the alloy SSA000 in as-cast condition, as-cast plus heat-treated (T6) condition and in the condition that includes homogenization and heat treatment (H+T6) after casting, while Tables 6 and 7 present the same for the alloy SSA018. Longitudinal direction is parallel to the cast billet axis, and transverse direction is the radial direction in the transverse cross-section of the billet. At both temperatures, the alloy SSA000 shows very anisotropic properties in all three conditions. Although longitudinal properties are outstanding, transverse ductility is very low, and fracture of this alloy at 77K occurs before macroscopic yielding. Homogenization does not improve transverse properties of this alloy. In as-cast condition, the SSA000 alloy showed tensile strength of 378 MPa and

15% elongation in the longitudinal direction, but only 318 MPa and almost zero elongation in the transverse direction. The alloy SSA018, which contains 0.18% Sc, has transverse properties that are closer to the longitudinal property values (see Tables 6 and 7). The homogenization treatment improves tensile ductility of this alloy significantly, both in longitudinal and transverse directions. The reason for the anisotropic properties in the SSA000 is the columnar grain structure and the refined, equiaxed grain structure of the Sc modified alloy SSA018 leads to near isotropic properties in this alloy. The finer dendrite size in this alloy helps in efficient homogenization of the cast structure and consequent property improvements.
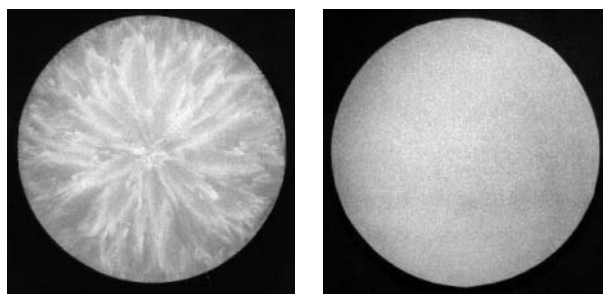
Figure 1: Photographs of etched transverse cross-sections of DC cast billets of alloys SSA000 (left) and SA018 (right).
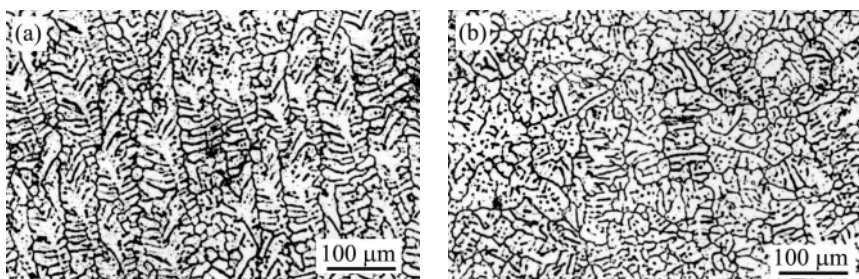
Figure2: Optical micrographs of longitudinal cross-sections of DC cast billets of alloys (a) SSA000 and (b) SSA018.

Table 4. Room temperature tensile properties of the SSA000 alloy after casting and heat treatment.

Alloy	Longitudinal			Transverse		
Condition	As-cast	Cast+T6	Cast+H+T6	As-cast	Cast+T6	Cast+H+T6
YS (MPa)	257	447	439	318	511	304
UTS (MPa)	378	511	520	318	529	304
EL (%)	15	7	15	0.3	0.8	0.25

Table 5. Cryogenic temperature (77K) tensile properties of the SSA000 alloy after casting and heat treatment.

Alloy	Longitudinal			Transverse		
Condition	As-cast	Cast+T6	Cast+H+T6	As-cast	Cast+T6	Cast+H+T6
YS (MPa)	357	551	528	369	378	384
UTS (MPa)	439	621	607	377	378	384
EL (%)	8.6	12	19	0.2	0.2	0.15

Table 6. Room temperature (298K) tensile properties of the SSA018 alloy after casting and heat treatment.

Alloy	Longitudinal			Transverse		
Condition	As-cast	Cast+T6	Cast+H+T6	As-cast	Cast+T6	Cast+H+T6
YS (MPa)	292	483	457	284	478	452
UTS (MPa)	402	570	552	378.5	563	559
EL (%)	5	7	14	3	5	11

Table 7. Cryogenic temperature (77K) tensile properties of the SSA018 alloy after casting and heat treatment.

Alloy	Longitudinal			Transverse		
Condition	As-cast	Cast+T6	Cast+H+T6	As-cast	Cast+T6	Cast+H+T6
YS (MPa)	395	602	584	368	599	570
UTS (MPa)	462	674	674	414.5	679	668
EL (%)	2	5	10	1.3	4	7

3.2   Microstructure and Properties of Extruded Alloys

After extrusion and heat treatment, the dendrite structure disappeared and a non-recrystallized grain structure with grains elongated in the extrusion direction is developed for both alloys. The grains were much smaller in the alloy SSA018 than in the alloy SSA000 due to a finer microstructure in as-cast condition. TEM analysis showed a sub-grain structure (Figure 3), with the sub-grain size of about 10-20 µm in the alloy SSA000 and 1-5 µm in the alloy SSA018. A very high number density ($\sim 10^{22}$-10^{23} m^{-3}) of elliptical particles of η' phase, from 2 to 10 nm in size, was detected in the heat-treated specimens (Figure 3). In addition, coherent Al$_3$(Sc,Zr) dispersoids are present in the heat-treated alloy SSA018 (Figure 4); their size varies from 5 to 30 nm.
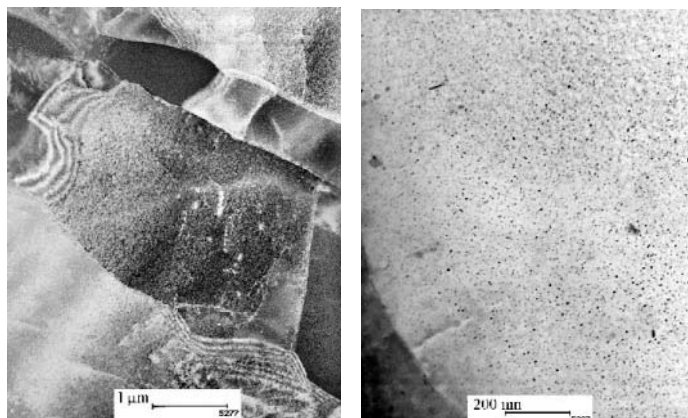
Figure 3: TEM micrographs showing subgrain structure (left) and high density of precipitates (right) in the extruded and T6 tempered SSA018 alloy.
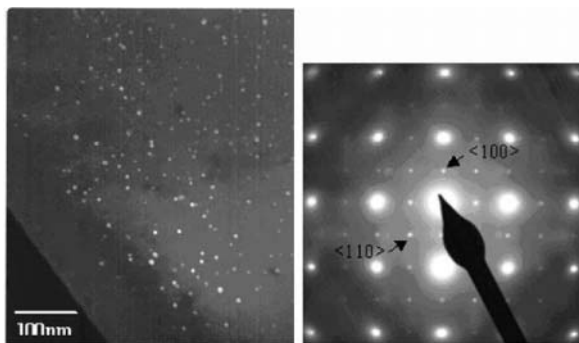

Figure 4: TEM dark field image of SSA018 alloy after solution annealing and water quenching shows $Al_3(Sc,Zr)$ particles (left) and corresponding selected area diffraction pattern (right) shows that the particles have an $L1_2$ crystal structure and are coherent with matrix.

Room and cryogenic temperature tensile properties of the extruded alloys in T6 temper are given in Figures 5 and 6, respectively. For comparison, properties of a commercial 7075-T6 alloy are also given in these figures. Both developmental alloys show very high yield and ultimate tensile strengths, much exceeding the strengths of 7075-T6; the difference is even larger at the cryogenic temperature. Ductility of the developmental alloys is about 12% or higher at room temperature and about 8% or higher at the cryogenic temperature. The addition of Sc has resulted in both high strength and ductility in the SSA018 alloy. UTS and elongation as high as 740 MPa and 15% at 296K and 920 MPa and 10% at 77K were achieved in extrusions of the Sc-containing alloy SSA018. The increase in strength is evidently due

to the presence of nanometer-sized dispersoid particles and fine-grained fiber-like structure in the Sc-containing alloy.
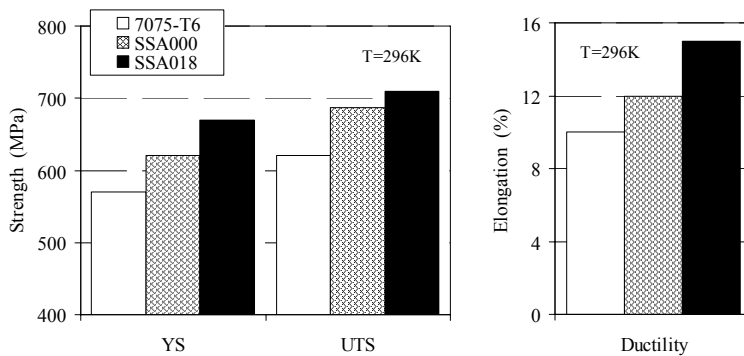

Figure 5: Room temperature tensile properties of extruded rods of developmental alloys SSA000 and SSA018 and a commercial alloy 7075 in T6 temper.
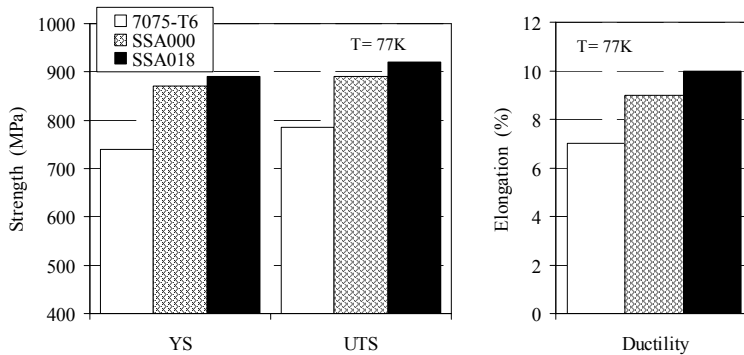

Figure 6: Cryogenic temperature tensile properties of extruded rods of developmental alloys SSA000 and SSA018 and a commercial alloy 7075 in T6 temper.

3.3 Microstructure and Properties of Forgings

Figure 7a shows a forging pancake produced by upset forging from a 150 mm long and 76 mm in diameter cast billet homogenized at 733K and pre-heated for forging at 723K. The thickness of the pancake is 30 mm, which corresponds to the compression strain of 80%. Figures 7b and 7c illustrate microstructures of the pancake in the short transverse cross-section (this cross-section is parallel to both the radial direction and main forging axis), in

the middle part and near the surface that was in contact with the forging die, respectively.

A very non-homogeneous microstructure along the forging direction can be seen. In the middle part of the forging, fiber-like grains elongated in the radial direction are seen (Figure 7b). In the near-surface part, the grain elongation is much less extensive, which indicates that this region of forging experienced much smaller deformation. A reason for the non-homogeneous microstructure in the forging is flow localization due to a temperature gradient across the thickness. This temperature gradient is the result of chilling of the contact surfaces of the billet by cold forging dies. Pre-heating of the forging dies is required to improve microstructural homogeneity of the forging. Room and cryogenic temperature tensile properties of a forging pancake made of the developmental alloy SSA018 are given in Figures 8 and 9, respectively, in comparison with properties of 7075-T6 forging.
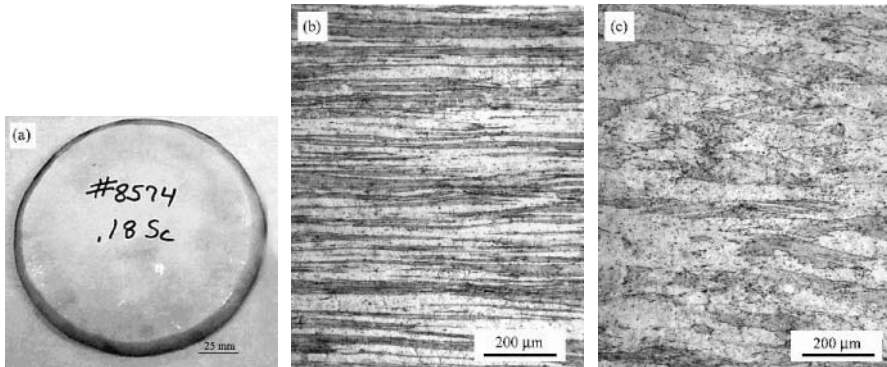

Figure 7: (a) Forging pancake of 165 mm diameter and 30 mm height and (b,c) microstructure of the pancake (b) in the middle part and (c) near the surface contacting with the forging die.
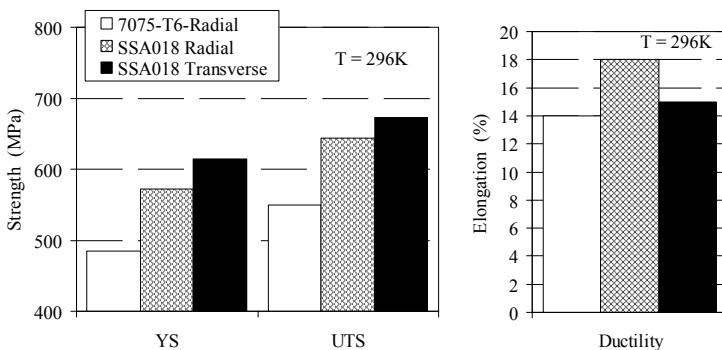

Figure 8: Room temperature tensile properties of forgings of the developmental alloy SSA018 in the radial and transverse directions and of a commercial alloy 7075-T6 in radial direction.

Forging from the developmental alloy shows YS and UTS about 15-17% higher than 7075-T6 forging, both at room and cryogenic temperatures. The strengths in the transverse direction are slightly higher than in the radial direction. Ductility of the SSA018 forging is about 14-18% at 296K and 10-12% at 77K. Although the tensile strength of forging is less than that of extrusion, it is high enough to meet the design goal for the cryogenic turbo-pump impeller. Indeed, UTS above 620 MPa at 296K and 800 MPa at 77K was achieved, indicating that the SSA018 forging has specific strength exceeding the specific strength of the Ti-5Al-2.5Sn ELI alloy. The Sc modification not only refines the grain size in the as-cast condition, but also effectively prevents recrystallization of the deformation processed material during high temperature solution treatment which is a part of the heat treatment in 7XXX alloys to get the T6 temper.
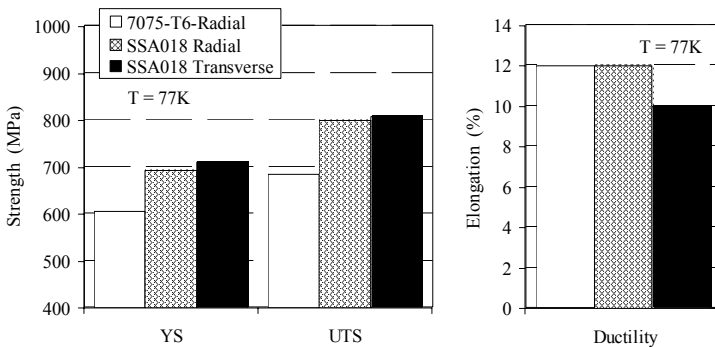

Figure 9: Cryogenic temperature tensile properties of forgings of the developmental alloy SSA018 in the radial and transverse directions and of a commercial alloy 7075-T6 in the radial direction.

The difference in strength of the alloy in extruded and forged conditions is evidently due to the finer microstructure of the extruded material, because of heavier hot work. Indeed, the true strain for the extrusion with an extrusion ratio of 16:1 is 2.77, while for the forging with an upset of 80% the true strain is only 1.6. In addition, the temperature of deformation (723K for forging and 673K for extrusion) determines the extent of recovery and dynamic recrystallization, if any, during the hot working process. The relatively lower temperature adopted for the extrusion also seems to have contributed to the improved properties.

4. CONCLUSIONS

1. A 7xxx series alloy modified with Sc has been developed with potential to replace the titanium alloy used for a cryogenic fuel pump component application.

2. The as-cast material with Sc modification has a fine equiaxed grain structure as compared to a columnar grain structure in the alloy without Sc modification. After hot working, the alloy has fine elongated, fiber-like non-recrystallized grain structure and a well-developed fine subgrain structure. A high density of nano-meter size η' precipitates and $Al_3(Sc,Zr)$ dispersoids is typical for the heat treated alloy.

3. The tensile properties have been evaluated and reported in as-cast, extruded and forged conditions with optimized heat treatments, at both room and cryogenic temperatures. Both strength and ductility values of the developmental alloy exceed the properties of the existing Al alloys. The specific strength of the developmental alloy is higher than the specific strength of the Ti-5Al-2.5Sn ELI alloy, both at room and cryogenic temperatures.

ACKNOWLEDGEMENTS

REFERENCES

1. C.M. Ward-Close, F.H. Froes, and S.S. Cho, Synthesis/Processing of Lightweight Metallic Materials II (The Minerals Metals and Materials Society, Warrendale, PA, 1997), pp. 1-15.
2. D. K. Huzel and D.H. Huang, Modern Engineering for Design of Liquid-Propellant Rocket Engines, Vol. 147 (AIAA, Washington, DC, 1992).
3. R. Boyer, G. Welsch, and E.W. Collings, Materials Properties Handbook: Titanium Alloys (ASM,Materials Park, OH, 1994).
4. F.R. Schwartzberg, S.H. Osgood, R.D. Keys, and T.F. Kiefer, Cryogenic Materials Data Handbook, PB 171809, Supplement 3 (AFRL, WPAFB, OH, 1966).
5. A.W. Thompson and N.R. Moody (Eds.) Hydrogen Effects in Materials (The Minerals Metals and Materials Society, Warrendale, PA, 1996)
6. O.N. Senkov and F.H. Froes, Internat. J. Hydrogen Energy, 24 (1999), 565-576.

7. J.E. Hatch (Ed.), Aluminum: Properties and Physical Metallurgy, ASM, Metals Park, OH, 1984.

8. J.G. Kaufman (Ed.), Properties of Aluminum Alloys: Tensile Creep and Fatigue Data at High and Low Temperatures, ASM Internat., Materials Park, OH, 1999.

9. O.N. Senkov, Advanced Aluminum Materials for Rocket Turbopump Rotors, SBIR Phase I Final Report, AFRL-PR-ED-TR-2002-0014, AFRL/AFMC, Edwards Air Force Base, CA, 2002.

10. P.E.Perez and T.V.Daam, Large Scale Powder Processing: Nanophase Aluminum Alloys, ASM Round Table, California State University, Northridge, CA, May 3, 2000.

11. G.Canzona and D.Matejczyk, Mechanical Properties of Large Scale Nanophase Aluminum Extrusions and Forgings, ASM Round Table, California State University, Northridge, CA, May 3, 2000.

12. C.C.Bampton, Rocketdyne Propulsion and Power, Private Communication, October 2001.

13. O.N. Senkov, D.B. Miracle, Y.V. Milman, J.M. Scott, D.V. Lotsko, A. Sirko, Mater. Sci. Forum, 396-402 (2002) 1127.

14. Y.V. Milman, A.I. Sirko, D.V. Lotsko, D.B. Miracle, O.N. Senkov, *Mater. Sci. Forum,* 396-402 (2002)*, 1217*.

15. L.S. Kramer, W.T. Tack and M.T. Fernandes, Adv. Mater. Processes, No. 10 (1997), 23-24.

16. L.S. Toporova, D.G. Eskin, M.L. Kharakterova, T.V. Dobatkina, Advanced Aluminum Alloys Containing Scandium (Gordon & Beach Science Publishers, The Netherlands, 1998).

17. Y.W. Riddle and T.H. Sanders, Jr., Mater. Sci. Forum, 331-337 (2000), 939-944.

18. Y.V. Milman, D.V. Lotsko, and O.I. Sirko, Mater. Sci. Forum, 331-337 (2000), 1107-1112.

EFFECT OF FE AND SI ON THE STRUCTURE AND MECHANICAL PROPERTIES OF COMPLEX AL-ZN-MG-CU ALLOYS PRODUCED BY P/M AND CASTING TECHNIQUES

Yu. Milman[1], D. Lotsko[1], A. Sirko[1], O. Neikov[1], N. Zakharova[1],
V. Goncharuk[1], A. Koval[1], V. Voropaiev[1], A. Sharovski[1],
O. Senkov[2], D. Miracle[2]
[1]*I.M. Frantsevych Institute for Problems of Materials Science of the NAS of Ukraine (IPMS), Kyiv, Ukraine*
[2]*Air Force Research Laboratory, Materials and Manufacturing Directorate, Wright-Patterson AFB, OH, USA*

Abstract: In order to establish the possibility of using recycled aluminum, which usually has an increased content of Fe and Si, the structure and mechanical properties of high-strength Al-Zn-Mg-Cu alloys additionally alloyed with only Fe and Si as well as additionally alloyed with Mn, Zr, Sc, Fe and Si were studied. Rods were manufactured from ingots cast into water-cooled copper molds as well as by a P/M technique using powders atomized from the melt by high-pressure water. The microstructure and distribution of elements in the starting condition and in the T6 treated extruded rods were studied by OM and SEM techniques and compared with rod tensile properties. An addition of Fe up to 1 wt.% led to a 5-7% increase in strength. This increase was accompanied by a decrease in ductility in the cast and cast-and-wrought alloys. In alloys prepared by P/M the technique, the addition of Fe led to about 20% increase in strength, as compared to the baseline alloy, without any detrimental effect on elongation. An addition of ≥ 0.5 wt.% Si to the P/M alloys decreased strength and slightly increased ductility. Thus, reasonable properties were obtained in high strength Al-Zn-Mg-Cu alloys containing significant amounts of Fe and Si.

Key words: high-strength aluminum alloys, heat treatment, mechanical properties, structure, casting, water atomization.

1.   INTRODUCTION

Rational alloying with transition metals (TM) and rare-earth metals (REM) gives a progressive way to the enhancement of the balance of mechanical properties of high-strength Al-Zn-Mg-Cu alloys [1-5]. In order to enable the possibility of using recycled aluminum that usually has an increased content of Fe and Si [4], the structure and mechanical properties of high-strength Al-Zn-Mg-Cu alloys additionally alloyed with only Fe and Si as well as additionally alloyed with Mn, Zr, Sc, Fe and Si were studied. Prior to the present investigation, there were no data on the influence of these admixtures on the properties of high-strength alloys additionally alloyed with Sc. Tensile mechanical properties were determined for extruded rods after the T6 treatment (quenching and artificial aging). Rods were manufactured from ingots cast into water-cooled copper molds as well as by a P/M technique using powders atomized by high-pressure water. The structure and distribution of alloying elements were studied for alloys in the starting condition, after extrusion and T6 treatment by OM, SEM and TEM techniques. The SEM apparatus had a device for X-ray microspectral analysis. We studied the character of fracture of the baseline alloy with admixture of only Fe and that of the alloy additionally alloyed with Sc, Zr, and Fe.

2.   1. COMPLEX Al-Zn-Mg-Cu ALLOYS PRODUCED BY CASTING TECHNIQUES

Al-Zn-Mg-Cu alloys with additions of Fe, as well as with combinations of Fe, Mn, Zr and Sc, were produced by induction melting using ceramic crucibles and supplementary methods of melt purification, which included ceramic filters and blowing the melt with argon. Rods of 6 mm in diameter were manufactured by extrusion at 400 C with extrusion ratio λ=84. The T6 treatment consisted in water quenching from 465 °C and aging at 120 °C for 24 h. The alloy compositions and the properties of rods in the T6 condition are given in Table 1.

The structure of Al-Zn-Mg-Cu-xFe ingots was of a dendritic character (Fig. 1a). Zr and Sc additions led to the formation in ingots of a grain structure with a grain size of 15 - 25 µm (Fig. 1b).

We have studied the distribution of alloying elements in the above-mentioned alloys with Fe in the as-cast state and in rods in T6 condition. Primary particles of $Al_3(Sc_{1-x}Zr_x)$ intermetallic were observed inside of grains, and a presumable precipitation of Zn, Mg, and Cu in grain boundaries was revealed. In grain boundaries of ingots alloyed with Fe the

eutectic (Al+ FeAl$_3$) was found. In rods manufactured from ingots after T6 treatment SEM investigation detected the existence of rather coarse intermetallics containing Fe (Fig. 2a,b) that has led to some lowering of the plasticity together with increasing the strength. In Al-Zn-Mg-Cu-Mn alloys additionally alloyed with Zr, Sc, and Fe we did not find the eutectic microconstituent (Al + FeAl$_3$).

Table 1 Mechanical properties of rods from cast alloys in T6 condition

| ##	Chemical composition, wt. %	YS, MPa	UTS, MPa	EL, %
Al - 9Zn - 3Mg - 2.3Cu - xFe				
1	Al - 9.6Zn - 2.6Mg - 2.6Cu	530	619	20.4
2	Al - 9.4Zn - 3.1Mg - 2.34Cu - 0.11Fe	546	625	16.2
3	Al - 9.3Zn - 3Mg - 2.32Cu - 0.14Fe	544	626	15.1
4	Al - 9.7Zn - 3.3Mg - 2.5Cu - 0.33Fe	572	636	16.2
5	Al - 9.66Zn - 3.5Mg - 2.5Cu - 0.62Fe	572	645	14.3
6	Al - 9.25Zn - 3Mg - 2.26Cu - 0.78Fe	550	637	13.3
7	Al - 9.8Zn - 4Mg - 2.6Cu - 1.0Fe	547	641	13.0
Al - 9Zn - 3Mg - 2.3Cu - 0.3Mn - 0.15Zr - 0.3Sc - xFe				
9	Al - 9.2Zn - 2.4Mg - 2.17Cu - 0.26Mn - 0.19Zr - 0.41Sc	696	789	12.3
10	Al - 9.25Zn - 3Mg - 2.35Cu - 0.36Mn - 0.17Zr - 0.35Sc - 0.33Fe	741	802	9.3
11	Al - 9.4Zn - 3.15.Mg - 2.6Cu - 0.3Mn - 0.12Zr - 0.37Sc - 0.64Fe	741	791	7.3
12	Al - 9.45Zn - 3.2Mg - 2.6Cu - 0.15Mn - 0.14Zr - 0.42Sc - 1.0Fe	746	796	6.2

a   b
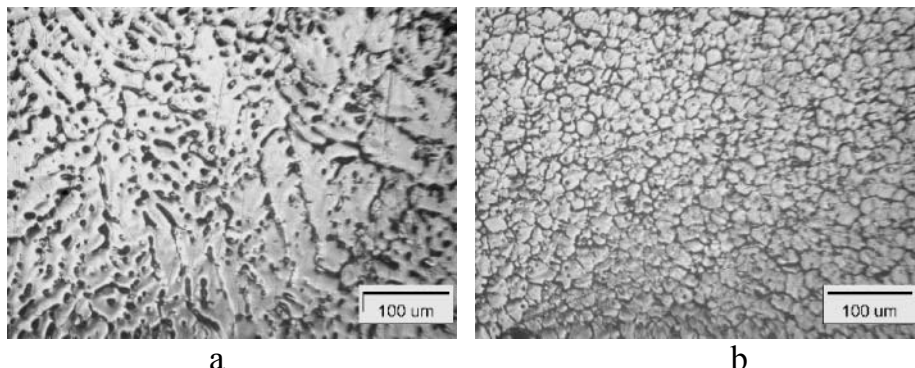
Figure 1. Structure of ingots from alloy #4 (a) and alloy #10 (b), OM photos

| BEI | Cu-Kα emanation | Mg-Kα emanation |

| Zn-Kα emanation | X-ray Fe-Kα emanation |

a

| BEI | Zn-Kα emanation | Mg-Kα emanation |

| Cu-Kα emanation | Fe-Kα emanation | Sc-Kα emanation |

b
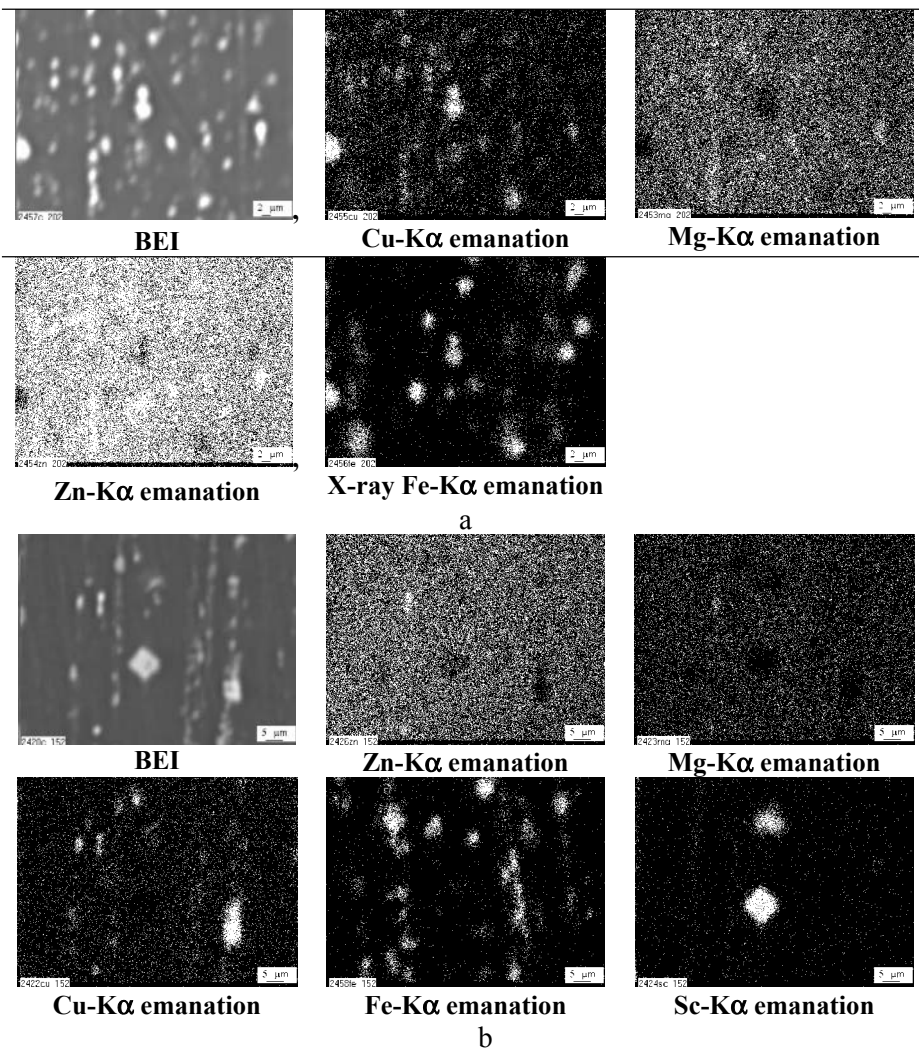
*Figure 2.* Distribution of elements in cross sections of rods ∅ 6 mm in T6 condition from cast alloy #7 (a); and #12 (b), SEM investigation.

In Al-Zn-Mg-Cu alloys that contain up to 1 % Fe as well as Mn, Zr, Sc, the fracture of rods in T6 state was ductile with EL = 6-9 % (see Table 1) due to the beneficial influence of alloying with Zr and Sc on the microstructure.

In Al-Zn-Mg-Cu alloys alloyed only with Fe, fracture had a mixed character: it was ductile and semibrittle, transcrystalline with the formation of pores around the spherical second phase particles. The plasticity of these alloys was EL = 13-20 % depending on the content of Fe. As was shown by X-ray microanalysis, the phase that is situated in dimples and has spherical form contains Zn, Mg, Cu, and Fe.

3.   2. Al-Zn-Mg-Cu ALLOYS FROM RAPIDLY SOLIDIFIED POWDERS

Rapidly solidified powders of Al-Zn-Mg-Cu alloys were produced by high-pressure water atomization of the melt (method WA-N) [4]. This process provides cooling rates up to 10^6 K/s. Compaction was performed by the preliminary compaction at room temperature of powder into briquettes, followed by insertion into a capsule. The capsules were hermetically sealed, then the briquettes were subjected to hot degassing and compaction. The composition, powder size fraction used from the WA-N process, and properties of rods of 6 mm in diameter ($\lambda = 17.7$) in T6 condition are given in Table 2.

Table 2. Mechanical properties of P/M rods Al-Zn-Mg-Cu

##	Chemical composition, wt. %	Fraction, μm	YS, MPa	UTS, MPa	EL, %
1	Al-9.3Zn-2.9Mg-1.9Cu	0-63	641	691	7.0
2	Al-9.4Zn-2.8Mg-1.6Cu-0.4Fe	0-63	642	699	9.2
3	Al-9.4Zn-2.9Mg-1.44Cu-0.6Fe	0-63	649	703	7.6
4	Al-10Zn-2.9Mg-1.38Cu-0.93Fe	0-63	687	748	9.2
5	Al-9.4Zn-4Mg-1.3Cu - 0.3Si	0-63	643	698	8.9
6	Al-10Zn-3.2Mg-1.35Cu - 0.55Si	0-63	562	616	9.6
7	Al-8.9Zn-3.0Mg-1.3Cu - 0.8Si	0-63	402	508	13.9
8	Al-9.4Zn-3.3Mg-1.3Cu –0.9Si	0-63	531	602	9.9
9	Al-8.6Zn-3.5Mg-1.3Cu - 1.0Fe	0-63	671	718	8.9

| BEI | Fe-Kα emanation | Cu-Kα emanation |
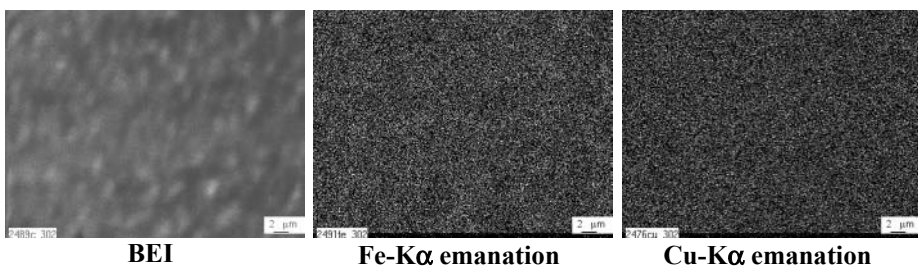
Figure 3. Distribution of Fe and Cu in the extruded rod from P/M alloy #9, SEM investigation

As distinct from cast alloys, in powders of Al-Zn-Mg-Cu alloys with Fe and Si additions a uniform distribution of all elements in the powder body was observed (Fig. 3). However, precipitates of Mg_2Si type were registered in T6 treated rods of alloys with Si additions. TEM investigation of T6 treated rods of both P/M and cast alloys revealed a large amount of

reinforcing η'-particles as well as of secondary coherent $Al_3(Sc_{1-x}Zr_x)$ particles of several nanometers in size.

CONCLUSION

The casting and powder metallurgy techniques described here permit may permit the use of recycled aluminum with a significant content of Fe and Si for producing high-strength aluminum alloys. Powder metallurgy rod of the baseline Al-Zn-Mg-Cu alloy without additional alloying had the level of strength characteristics about 20 % higher than the rod from cast alloy due to grain refinement introduced by the technique of manufacture.

ACKNOWLEDGEMENT

REFERENCES

1. Milman, Yu.V., Lotsko, D.V., and Sirko, O.I. (2000). "Sc effect" of improving mechanical properties in aluminum alloys, *Mater.Sci.Forum* **331-337**, 1107-1112.
2. Milman, Yu.V., Lotsko, D.V., Sirko, O.I., Senkov O.N., and Miracle D.B (2002). Microstructure and Mechanical Properties of Cast and Wrought Al-Zn-Mg-Cu Alloys Modified with Zr and Sc, *Mater.Sci.Forum* **396-402,** 1217-1222.
3. Lotsko, D.V., Milman, Yu.V., Yefimov, N.A., Rachek, A.P. and Trofimova L.N. (1999) Structure and mechanical properties of Al-Zn-Mg alloy doped by scandium and zirconium, *Metallofiz. Noveishie Tekhnol.* **21**, No.6, 9-16.
4. Mondolfo L.F. (1976) *Aluminum Alloys: Structure and Properties*. Butter Worths Publ., London-Boston, 639 p.
5. Neikov, O.D. (2000) Water atomization powder technologies for advanced aluminum alloys production, *Proc. of 2000 Powder Metallurgy World Congress*, Kyoto, 464-466.

STUDY OF A ZIRCONIUM MODIFIED 2014 ALUMINUM ALLOY: ANALYSIS OF THE BEST WARM FORMING CONDITIONS

Pasquale Cavaliere

Dept. of Ingegneria dell'Innovazione, Engineering Faculty, University of Lecce, I-73100-Lecce, Italy

Abstract: The warm forming plasticity conditions of a Zr modified 2014 aluminum alloy has been widely studied in the present work. The microstructure of the material was analysed by TEM in the as-received and as-deformed conditions. Torsion tests were performed in the temperature and strain rate ranges of 250-300 °C and 10^{-3}-1 s^{-1} respectively. The effect of Zr stabilization on material ductility was established in the present study.

Key words: Zr-modified Al-Alloy, Torsion tests, TEM.

1.   INTRODUCTION

In the recent years new aluminum based alloys have been developed for applications in new generation aerospace vehicles in which the low weight, high rigidity and potentially good mechanical properties of these alloys are of crucial importance. When transition elements such as zirconium, forming trialuminades are alloyed in aluminum, they have low solubilities and low diffusion coefficients in the aluminum matrix. If particles precipitate as trialuminades intermetallics, they maintain a small lattice mismatch with the matrix reducing the interfacial energy between the matrix and precipitates. As a result, the precipitates present a large coarsening resistance in the matrix and in addition a large thermal stability because of their high melting points compared with that of aluminum matrix as showed by the analysis of binary diagram Al-Zr [1-5].

A major reason why Zr (rather than Cr, Mn, V or Ti) has become the preferred choice as the recrystallization inhibiting element relates to its relatively low effect on quench sensitivity in commercial aluminum alloys [6].

Following these considerations the Al_3Zr intermetallic compounds are used as dispersoids or precipitates in the $Al-Al_3Zr$ composite system, rather than the monolithic ones [7, 8]. Many previous works have been concentrated on the microstructural stability, mechanical properties and thermomechanical processing of these kind of systems. Some authors have studied the hot formability of the same alloy by demonstrating the microstructural stability of Zr-stabilized aluminum alloy from 300 and 500 °C [7].

In the present study the warm forming of the same alloy has been analysed by considering the ductility of the material and the microstructural evolution in consequence of warm forming deformation.

2.   EXPERIMENTAL PROCEDURE

The alloy used in the present work had the following chemical composition (wt.%): Cu=4.32, Mg=0.49, Zr=0.12, Si=0.68, Fe=0.23, Mn=0.77, Ti=0.03, Al=bal.; the material was supplied in form of extruded rods of 80 mm diameter.

Torsion tests were carried out at the temperatures of 200, 225, 250, 275, 300 °C and strain rate range 10^{-3}-1 s^{-1}. The samples were heated using an induction furnace; the temperature stabilization time was 6 min. The gauge section of samples was a solid cylinder with a length (L) of 7 mm, and a radius (R) of 4 mm; the fillet radius between the gauge section and the shoulders was 0.5 mm. The torque (Γ) and the twist angle (θ) were converted to surface shear stress (τ) and strain (γ) by the relationships:

$$\tau = \frac{\Gamma}{2\pi\pi^3}(3 + n'+m') \qquad \gamma = \frac{R\theta}{L} \qquad\qquad (1)$$

where n' $(= dlog\Gamma log\Gamma/\theta|_{\dot{\theta},T})$ is the work hardening rate and m' $(= dlog\Gamma log\Gamma/\theta|_{\theta,T})$ is the revolution rate sensitivity coefficient of torque. Equivalent stresses (σ) and strains (ε) were derived from surface shear stresses and strains by means of the Von Mises yield criterion:

$$\sigma=\tau\sqrt{3}, \qquad \varepsilon=\gamma/\sqrt{3} \qquad\qquad (2)$$

Because of the temperature increase (ΔT) due to the deformation heating, the flow curves for $\varepsilon \geq 10^{-1}$ s^{-1} did not correspond to isothermal conditions.

Therefore, a temperature correction was applied to flow stress under such conditions. For each value of equivalent strain, the temperature increase was calculated using the following relationship:

$$\Delta T = \frac{\beta \int_0^\varepsilon \sigma d\varepsilon}{\rho c} \tag{3}$$

where β the deformation heat factor, ρ is the material density, and c is the heat capacity. The temperature increase was used to offset flow-softening effects due to the deformation heating by correcting flow stress employing the equation:

$$\sigma_c = \sigma + \Delta\sigma = \sigma + \Delta T \frac{d\sigma}{dT} \tag{4}$$

where σ_c is the flow stress corrected for the deformation heating. Specimens for transmission electron microscopy (TEM) were ground to a thickness of about 100 μm, then discs were prepared by means of double-jetting with a solution of 1/3 HNO_3 in methanol at –35°C, 20 V and a current of 40-50mA/mm².

3.   RESULTS AND DISCUSSION

The optical microstructure of the material in the as-received condition is shown in Figure 1. The observations revealed very small equiaxed grains obtained thanks to the presence of trialuminades formed during the solidification of the material.

The active strengthening mechanism at room temperature of the studied material was identified as solid solution strengthening, grain boundary strengthening, and Al_3Zr precipitate strengthening.

Strengthening due to the sub-micron grain size was the largest contribution to alloy strength, followed by precipitate strengthening and solid solution strengthening. The addition of a transition element and in particular the Zr one provides, on one hand the increasing of strength level at room temperature, and on the other hand the microstructural stability at higher temperatures by forming very fine stable dispersoids [1]. These dispersoids represent very efficient nuclei for precipitation of coarse, equilibrium precipitates the precipitates structures revealed in the present alloy are shown in Figure 2.

The effectiveness of Zr to inhibit the recrystallization in a wide range of aluminum alloys is due to the presence of spherical and coherent Al_3Zr (β') precipitates in a metastable cubic ($L1_2$) form [1]. The TEM inspection of the

as-received Zr- modified material revealed the presence of a very fine subgrain structure as expected following the previous observations (Figure 3); the presence of very fine precipitates within the grains was observed.
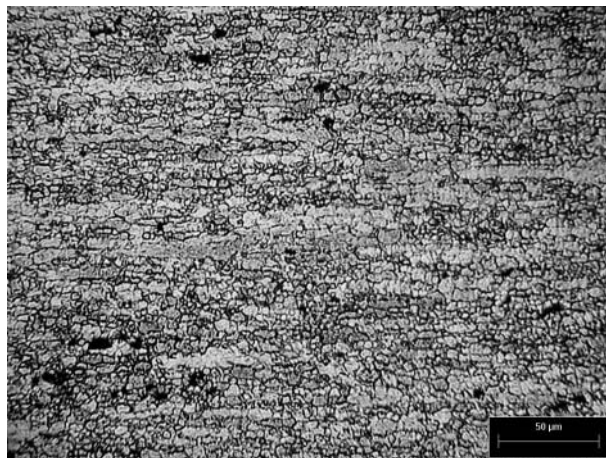

*Figure 4.* Optical micrography of Zr modified 2014 aluminum alloy.
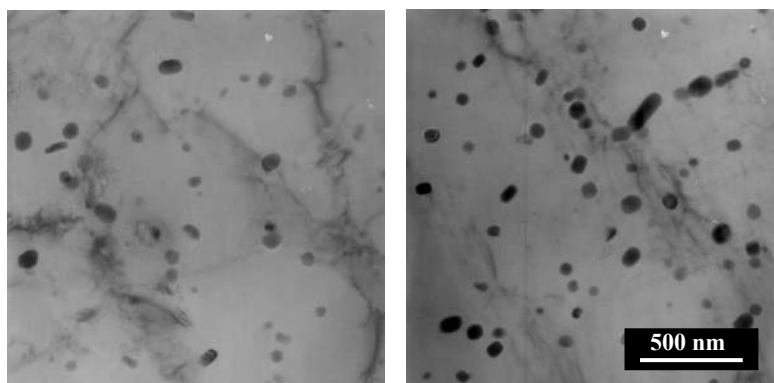
Figure 2. Al₃Zr precipitates individuated in the Zr modified 2014 aluminum alloy.

The modified 2014Zr is designed to improve the mechanical properties of the base 2014 Al-Cu-Mg alloy. Zr additions form the L12–ordered Al$_3$Zr phase which lead to the formation of coherent strengthening particles that result thermodynamically stable in a wide range of temperatures thanks to the effect of reducing the coarsening kinetics. It causes more uniform distribution of dislocations and it pins grain boundaries; this metastable trialuminade is very stable against coarsening and against redissolution. Metastable Al$_3$Zr forms from the melt as primary phase during rapid solidification, the particles act as nuclei for solidification of Al, and Zr can thus operate as grain refiner of Al [1, 9-10].
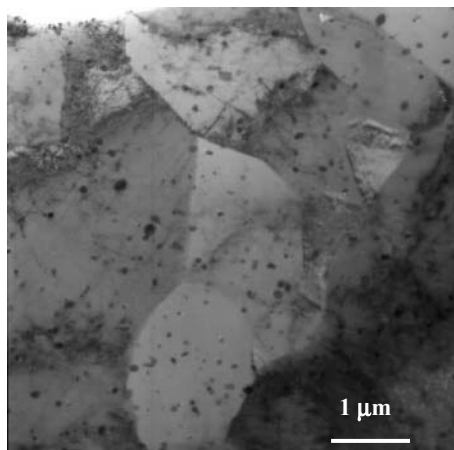
Figure 3. TEM microstructure of the as-received Zr modified 2014 aluminum alloy showing a very fine grain structure, the Al_3Zr precipitates are clearly evident.

The crystallographic nature of precipitates was showed a very small misfit with the matrix of aluminum (a=4.08 Å, misfit close to 1%).

Al_3Zr is also tetragonal; however, there is a good matching between the $a(Al=4.08; Al_3Zr=4.01)$ lattice parameters of aluminum and Al_3Zr and between $4a_0$ of Al and c of Al_3Zr.

This low misfit accompanied with very low solid solubility of Zr in Al favors the stability of the precipitates. The reason of stability was showed by the study of peritectoid reaction (998±12 °C) (βZr)+Zr2Al ↔ Zr3Al [1]. These small precipitates act to inhibit recrystallization and pin grain boundaries through a Zener drag process.

With a Zr concentration of more than 0.1 %, according to the Al-Zr phase diagram primary Al_3Zr precipitate from the melt during solidification refine heavily the grain size of the alloy. On the one hand Al_3Zr represents very intense obstacles to the dislocations movement. Consequently, these precipitates result very effective in grain pinning and subgrain boundaries during all thermal and mechanical processing of aluminum alloys [1, 7, 10].

For the Al-Cu-Zr alloy, 0.02 μm precipitates were identified inside the grains, and precipitates with a maximum size of 0.2-0.3 μm were occasionally observed, they were all in epitaxial orientation with the matrix ({100} $_{Al3Zr}$ ∥ {100} Al), regardless of the grain orientations the dispersoids are oriented in relation with each grain or subgrain [1]. Given their small size and low misfit, this means that they are probably totally coherent with the matrix, and therefore that the driving force for heterogeneous precipitation is mainly the reduction of the misfit elastic energy, because of the low energy of the coherent interface.
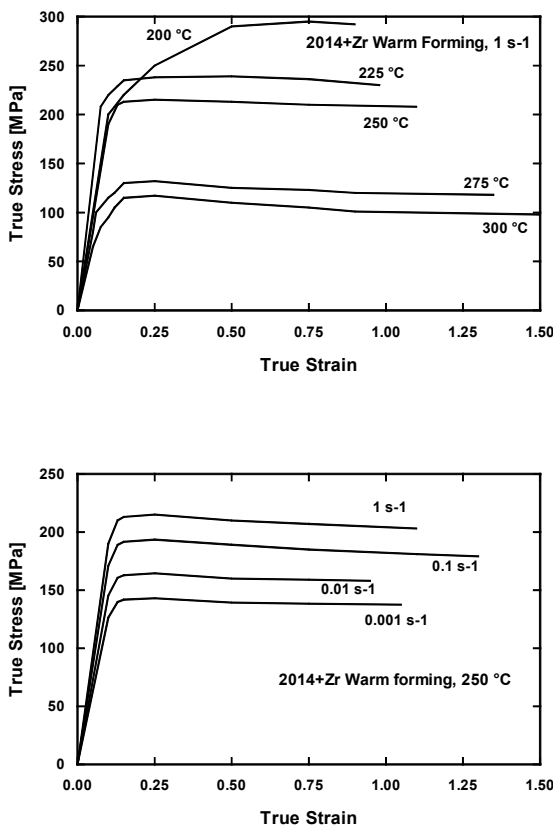
Figure 4. True stress vs. True strain curves for torsion tests at different temperatures and different strain rates.

Another important effect of Zr addition is the effect associated with vacancies, in particular it reduces the concentration of the free vacancies. In Figure 4 the warm forming torsion curves are plotted; the flow curves of the material after 200 °C show a classical behavior with a net increase in stress with strain up to the maximum followed by a limited flow softening. The flow stress of the material increases with increasing strain rate and decreasing temperature.

A big difference behavior, as expected, was evaluated from hot torsion conditions, the ductility of the material was evaluated as a plot of strain to fracture vs. Strain rate (Figure 5). A big difference was evaluated between 200 and 225 °C for all the strain rates investigated. Two different behavior were evidenced from 200 and 225 °C and 250°C. In this temperature condition good ductility values were recorded, in particular for 10^{-2} s^{-1} strain rate. At 250 °C, in fact the strain to fracture increase with increasing strain rate up to 10^{-2} s^{-1} and then decreases with increasing strain rate.
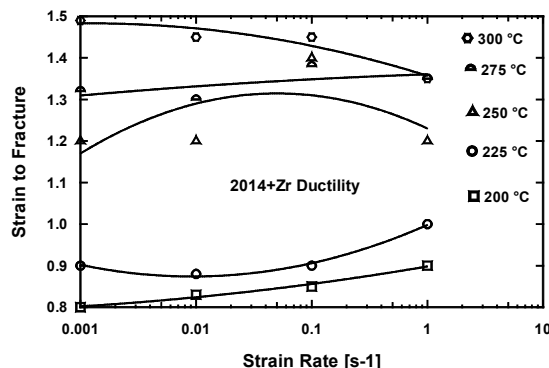
Figure 5. Ductility of the material calculated as Strain to fracture vs. Strain rate for all the temperatures investigated.
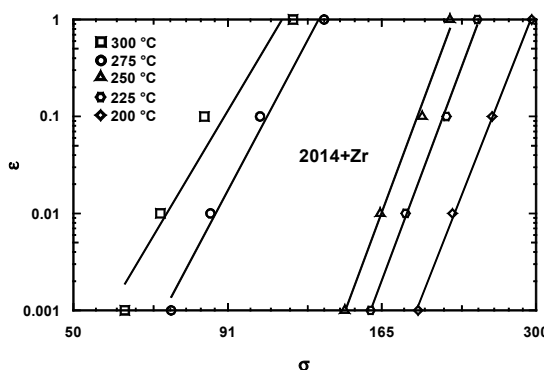

Figure 6. Calculation of constitutive parameters: log (strain rate) vs. log (flow stress).

In Figure 6 the peak stress vs. Strain rate is plotted, the picture show two different behavior in the curves as shown by ductility measurements, the strain rate sensitivity of the material ($m = (\partial \log \sigma / \partial \log \dot{\varepsilon})$) shows two well defined different behaviors in the warm forming conditions. The alloy shows two different deformation regimes: in the first case, corresponding to the temperature range 200-225 °C, n assumes the value of 4.7, while at the higher temperatures investigated n assumes a value of 2.5. The peak stress was plotted vs. 1000/T and reported in Figure 7.

The warm forming behavior of Zr-stabilized 2014 aluminum alloy was subsequently modelled by correlating flow stress to strain rate and temperature according to the well known constitutive equation:

$$Z = \dot{\varepsilon}\exp(Q/RT) = A[\sinh(\alpha\sigma)]^n \tag{5}$$

where Z is the Zener –Hollomon parameter representing the temperature modified strain rate, Q is the activation energy for deformation, R is the universal gas constant, T is the absolute temperature, $\dot{\varepsilon}$ is the strain rate, A, n and α are material parameters.
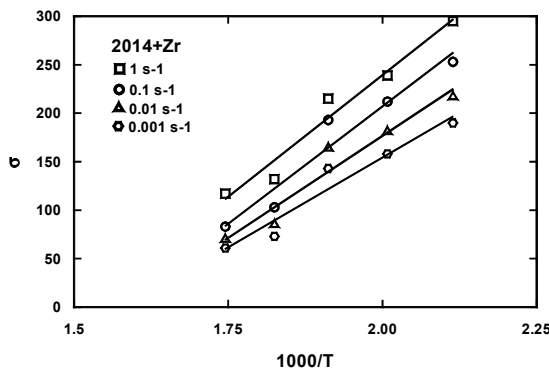

Figure 7. Calculation of constitutive parameters: log (flow stress) vs. log (1000/T).

The activation energy was calculated by the relationship:

$$Q = -R\frac{\partial \ln \dot{\varepsilon}}{\partial(1/T)}\bigg|_{\sigma} = 2.3R\frac{\partial \log \dot{\varepsilon}}{\partial \log sinh(\alpha\sigma)}\bigg|_{\varepsilon,T}\frac{\partial \log sinh(\alpha\sigma)}{\partial(1000/T)}\bigg|_{\varepsilon,\dot{\varepsilon}} = 2.3Rns \tag{6}$$

The slopes of $\log(\dot{\varepsilon}) - \log[\sinh(\alpha\sigma)]$ at constant T and $\log[\sinh(\alpha\sigma)] - 1000/T$ at constant strain rates were calculated, leading to a value of the activation energy of 195 kJ/mol by using the results from 250 to 300 °C. The value of the stress multiplier α was calculated by means of an optimization procedure and $\alpha = 0.014$ (MPa)$^{-1}$ gave the best correlation coefficient for the linear relationships $\log(\dot{\varepsilon}) - \log[\sinh(\alpha\sigma)]$ and $\log[\sinh(\alpha\sigma)] - 1000/T$; the value of the activation energy resulted very close to the one presented in literature [7]. The microstructure of the material torsioned at 250 °C, 10^{-1} s^{-1} is reported in Figure 8; the torsioned elongated grains are easily recognized, many subgrains few micron in dimension were individuated inside the grains.

Very fine precipitates are clearly identified inside the grain and subgrain structures, and the grain boundary pinning effect can be seen very clearly. The effect of precipitates particles on dislocation movement is also shown in Figure 9; the interaction between precipitates and dislocations is widely clearized. The TEM micrograph of samples deformed at 225 °C 10^{-1} s^{-1} is shown in Figure 10.
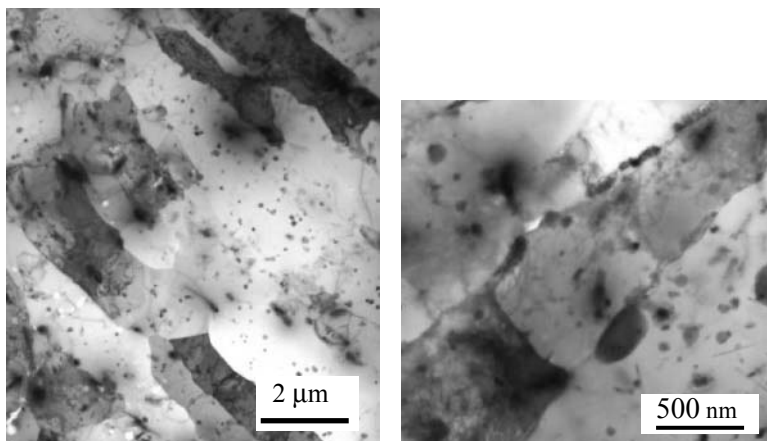
Figure 8. TEM micrograph of Zr modified 2014 aluminum alloy torsion strained at 250 °C, 10^{-1} s^{-1} showing the grain boundary pinning effect of Al_3Zr precipitates.
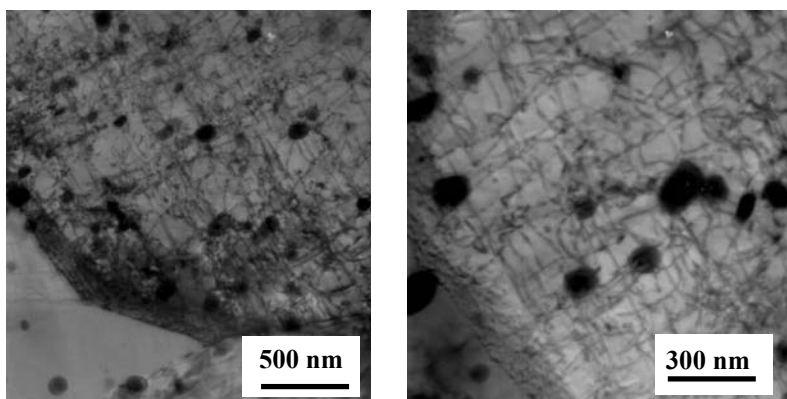

Figure 9. TEM micrograph of Zr modified 2014 aluminum alloy torsion strained at 250 °C, 10^{-1} s^{-1} showing the grain boundary pinning effect of Al_3Zr precipitates.

4. CONCLUSIONS

The warm forming behavior of 2014 aluminum alloy stabilized with small Zr additions was studied by employing torsion tests in the temperature and strain rate ranges of 200-300 °C and 10^{-3}-1 s^{-1} respectively. The alloy ductility was measured as strain to fracture in all the temperature and strain rate investigated by showing a different behavior between 250-300 °C and the lower temperatures. The activation energy of the material was calculated

in warm forming conditions and the Zr effect on microstructural modifications was observed by means of electron microscopy (TEM).
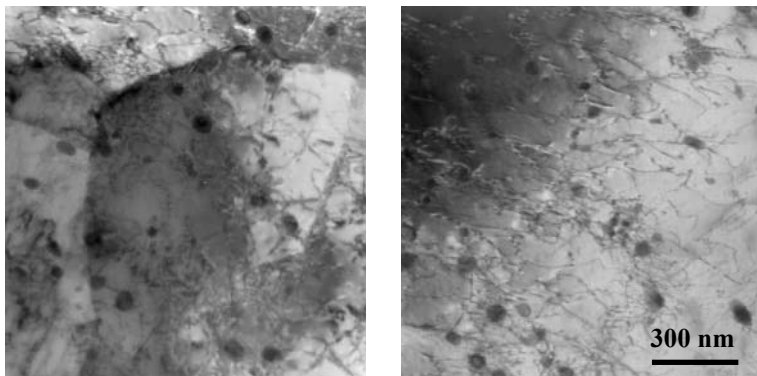

Figure 10. TEM micrograph of Zr modified 2014 aluminum alloy torsion strained at 225 °C, 10^{-1} s^{-1} showing the interaction between precipitates and dislocations.

REFERENCES

1. J. Murray, A. Peruzzi, J.P. Abriata, Journal of Phase Equilibria **13/3** (1992) 277-291.
2. Z. Yin, Q. Pan, Y. Zhang, F. Jiang, Mater. Sci. Eng. **A280** (2002) 151-155.
3. C. B. Fuller, A. R. Krause, D. C. Dunand, D. N. Seidman, Mater. Sci. Eng. **A338** (2002) 8-16.
4. K.L. Kendig., D.B. Miracle, Acta Materialia, **50** (2002) 4165-4175.
5. A. Deschamps, Y. Brechet, Mater. Sci. Eng. **A251** (1998) 200-207.
6. J.S. Vetrano, S.M. Bruemmer, L.M. Pawlowski, J.M. Robertson, Mater. Sci. Eng. **A238** (1997) 101-107.
7. S. Spigarelli, M. Cabibbo, E. Evangelista, J. Bidulska, J. Mater. Sci. **38** (2003) 81-88.
8. K. Satya Prasad, A.A. Gokhale, A.K. Mukhopadhyay, D. Banerjee, D.B. Goel, Acta Materialia, **47** (1999) 2581-2592.
9. S.I. Park, S. Han, S.K. Choi, H.M. Lee, Scripta Mater. **34** (1996) 1697-1704.
10. S. Z. Han, S.I. Park, J.S. Huh, Z.H. Lee, H.M. Lee, Mater. Sci. Eng. **A230** (1997) 100-106.

STUDY OF FATIGUE RESISTANCE PROPERTIES OF A ZIRCONIUM MODIFIED 2014 ALUMINUM ALLOY

Pasquale Cavaliere

Dept. of Ingegneria dell'Innovazione, Engineering Faculty, University of Lecce, I-73100-Lecce, Italy

Abstract: This work presents and discusses many results on fatigue properties and fracture behavior of Zr-stabilized 2014 aluminum alloy. The fatigue crack growth and propagation of the material has been studied by employing a fatigue tests machine working at 250 Hz. The alloy response was analysed in the as received condition and was compared with the unstabilized alloy, the mechanisms governing fatigue life, cyclic deformation and fracture characteristics are analysed in function of magnitude of applied stress, intrinsic microstructural evolution and material deformation behavior. The material microstructure in the as-received condition was characterized by using transmission electron microscopy technique; the fatigue life of the material has been studied in different stress regimes, the crack growth and propagation was analysed by using electron microscopy technique (FEGSEM).

Key words: 2014+Zr, Fatigue life, FEGSEM.

1. INTRODUCTION

In the recent years new aluminum based alloys have been developed for applications in new generation aerospace vehicles in which the low weight, high rigidity and potentially good mechanical properties of these alloys are of crucial importance. The cyclic fatigue process comprises many macro and microscopic phenomena such as cyclic plastic deformation of the material and damage initiation due to the formation of microscopic cracks which grow and coalesh forming one or more macroscopic cracks that propagating in the material lead to

catastrophic failure. The analysis of fatigue crack growth is a very difficult task to fulfill due to the complexity of the fatigue damage processes involved. Microstructure play an important role in the fatigue crack growth resistance of aluminum alloys controlling the deformation mode and the subsequent crack initiation and propagation behavior [1-3].

Interest of scientists in fatigue resistance of materials is due to the usefulness of many informations regarding the cracks initiation and propagation in order to develop the optimum microstructures for load-critical and fatigue sensitive applications of aluminum alloys [4, 5]. When transition elements such as zirconium, forming trialuminades are alloyed in aluminum, they have low solubilities and low diffusion coefficients in the aluminum matrix. If particles precipitate as trialuminades intermetallics, they maintain a small lattice mismatch with the matrix reducing the interfacial energy between the matrix and precipitates. As a result, the precipitates present a large coarsening resistance in the matrix and in addition a large thermal stability because of their high melting points compared with that of aluminum matrix as showed by the analysis of binary diagram Al-Zr [6-10].

A major reason why Zr (rather than Cr, Mn, V or Ti) has become the preferred choice as the recrystallization inhibiting element relates to its relatively low effect on quench sensitivity in commercial aluminum alloys [11]. Following these considerations the Al3Zr intermetallic compounds are used as dispersoids or precipitates in the Al-Al3Zr composite system, rather than the monolithic ones [12, 13]. Many previous works have been concentrated on the microstructural stability, mechanical properties and thermomechanical processing of these kind of systems, the percent study is concentrated on the study of fatigue response of Zr-stabilized 2014 aluminum alloy.

2.   EXPERIMENTAL PROCEDURE

The alloy used in the present work had the following chemical composition (wt.%): Cu=4.32, Mg=0.49, Zr=0.12, Si=0.68, Fe=0.23, Mn=0.77, Ti=0.03, Al=bal.; the material was supplied in form of extruded rods of 80 mm diameter ALCAN (USA).

Endurance fatigue tests were performed on a resonant electro-mechanical testing machine under constant loading control up to 250 Hz sine wave loading TESTRONIC[TM] 50± 25 KN, produced by RUMUL (SUI) . The cyclic fatigue tests were conducted in the axial total stress-amplitude control mode under fully-reversed, push-pull, tension-compression loading such that the magnitude of negative stress amplitude equals the magnitude of positive one ($R=\sigma_{min}/\sigma_{max} =-1$). The cylindrical test specimens were machined from the as-received roads with the axis parallel to the extrusion direction, at the

gage section they measured 25 mm in length and a minimum diameter of 6 mm according to the actual standard codes (ASTM E466-72T). All mechanical tests were performed up to failure in the as-received condition. The Zr stabilized aluminum alloy fatigue curve was compared with the unstabilized one deformed in the same way of the previous one.

TEM observations were performed in the as-received and deformed samples in order to reveal the effects of microstructure on the fatigue response of the studied alloy. Fracture surfaces of the deformed fatigue test specimens were comprehensively examined in a scanning electron microscope (JEOL JSM6500F) equipped with field emission gun to determine the macroscopic fracture mode and characterize the fine-scale topography and microscopic mechanisms governing fatigue fracture.

3.   RESULTS AND DISCUSSION

The active strengthening mechanism at room temperature of the studied material was identified as solid solution strengthening, grain boundary strengthening, and Al_3Zr precipitate strengthening. Strengthening due to the sub-micron grain size was the largest contribution to alloy strength, followed by precipitate strengthening and solid solution strengthening. The addition of a transition element and in particular the Zr one provides, on one hand the increasing of strength level at room temperature, and on the other hand the microstructural stability at higher temperatures by forming very fine stable dispersoids [6]. These dispersoids represent very efficient nuclei for precipitation of coarse, equilibrium precipitates.

The curve representing the stress amplitude-fatigue life response of the material in the Zr stabilized and non-stabilized conditions is reported in Figure 1, the curve shows a classical behavior for the aluminum alloys, revealing a trend of increasing fatigue life with decreasing cyclic stress amplitude in both the studied materials; the difference in the number of cycles to failure, at the same stress amplitude, resulted more marked at higher stresses than at lower ones. Some materials, such as aluminum alloys, display fatigue limits at very high number of cycles (normally $>10^6$), many other materials do not exhibit this response, instead displaying a continuously decreasing stress-life response, even at a greater number of cycles. Following these observations it is more correct to describe the fatigue strength of these kind of alloys at a given number of cycles; the endurance limit of AA2014+Zr aluminum alloy was not so clearly recognized at 10^6 cycles as normal in many aluminum alloys, a fatigue life of 10^7 cycles at 110 MPa was recorded in the as received condition while a fatigue life of 10^7 cycles at 100 MPa was recorded for the unstabilized alloy [14, 15]. The

addition of a very small quantity of Zr produce an increase of fatigue resistance of the material in all the stress conditions investigated.
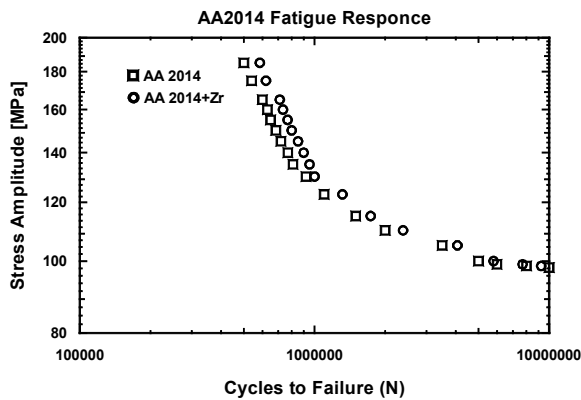

Figure 1. Endurance fatigue curve (S-N) for the AA2014 aluminum alloy in the in the Zr-modified and non modified conditions.

The optical microscopy observations (Figure 2) showed very small equiaxed grains produced obtained thanks to the presence of trialuminades in the structure of the material. The effectiveness of Zr to inhibit the recrystallization in a wide range of aluminum alloys is due to the presence of spherical and coherent Al3Zr (β') precipitates in a metastable cubic (L12) form [6, 15]. The TEM inspection of the as-received Zr- modified material revealed the presence of a very fine subgrain structure as expected following the previous observations (Figure 3); the presence of very fine precipitates within the grains was observed.
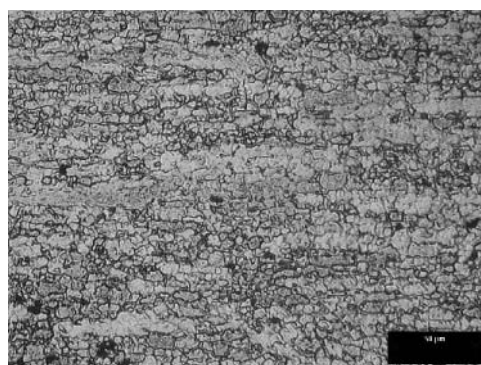
Figure 2. Al_3Zr precipitates individuated in the Zr modified 2014 aluminum alloy.

Zr additions form the $L1_2$–ordered Al_3Zr phase which lead to the formation of coherent strengthening particles that result thermodynamically

stable in a wide range of temperatures thanks to the effect of reducing the coarsening kinetics. It causes more uniform distribution of dislocations and it pins grain boundaries; this metastable trialuminade is very stable against coarsening and against redissolution. Metastable Al_3Zr forms from the melt as primary phase during rapid solidification, the particles act as nuclei for solidification of Al, and Zr can thus operate as grain refiner of Al [6, 16-17].
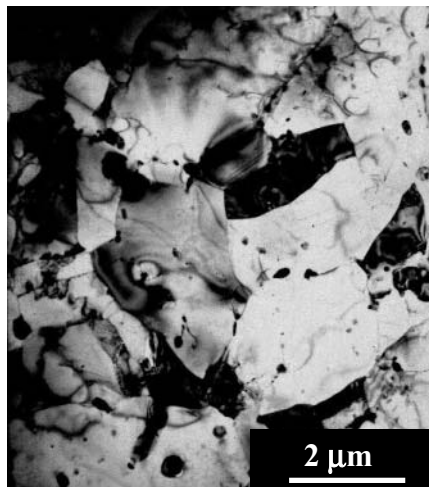

Figure 3. TEM microstructure of the as-received Zr modified 2014 aluminum alloy revealing the very fine subgrain structure and precipitates dispersed within the grains.

The crystallographic nature of precipitates was showed a very small misfit with the matrix of aluminum (a= 0.408 nm, misfit close to 1%). Al3Zr is also tetragonal; however, there is a good matching between the a(Al=0.408 nm; Al3Zr=0.401 nm) lattice parameters of aluminum and Al3Zr and between $4a_0$ of Al and c of Al3Zr. This low misfit accompanied with very low solid solubility of Zr in Al favors the stability of the precipitates. The reason of stability was showed by the study of peritectoid reaction (998±12 °C) (βZr)+Zr2Al $\leftrightarrow$ Zr3Al [6]. These small precipitates act to inhibit recrystallization and pin grain boundaries through a Zener drag process.

With a Zr concentration of more than 0.1 %, according to the Al-Zr phase diagram primary Al_3Zr precipitate from the melt during solidification refine heavily the grain size of the alloy. On the one hand Al_3Zr represents very intense obstacles to the dislocations movement. Consequently, these precipitates result very effective in grain pinning and subgrain boundaries during all thermal and mechanical processing of aluminum alloys [6, 12, 16].

For the Al-Cu-Zr alloy, 0.02 μm precipitates were identified inside the grains, and precipitates with a maximum size of 0.2-0.3 μm were occasionally observed, they were all in epitaxial orientation with the matrix ($\{100\}$ Al$_3$Zr $\|$ $\{100\}$ Al), regardless of the grain orientations the dispersoids are oriented in relation with each grain or subgrain [6]. Given their small size and low misfit, this means that they are probably totally coherent with the matrix, and therefore that the driving force for heterogeneous precipitation is mainly the reduction of the misfit elastic energy, because of the low energy of the coherent interface.

Another important effect of Zr addition is the effect associated with vacancies, in particular it reduces the concentration of the free vacancies. The Zr modified ally result more resistant to cyclic deformation than the unmodified one the precipitation of trialuminades and the consequent more stable structure results in the increase of fatigue life of the material.

Fatigue failure is governed, in metallic materials, by nucleation of microcracks which propagate slowly during cyclic deformation until one of them reaches critical dimensions producing catastrophic failure. Large precipitates are responsible for fatigue crack initiation in commercial aluminum alloys, strain localization occurs in such materials upon cyclic deformation, this result in increasing in dislocation density, large slip offsets on the surface or stress concentration at the grain boundaries, and early fatigue crack initiation by either grain boundaries or inclusion fracture.

The microstructure of the as-received material showed very small equiaxed grains. At higher allowable magnification of the optical microscope coarse- and intermediate-size second phase particles were observed inside the grains and at grain boundaries.
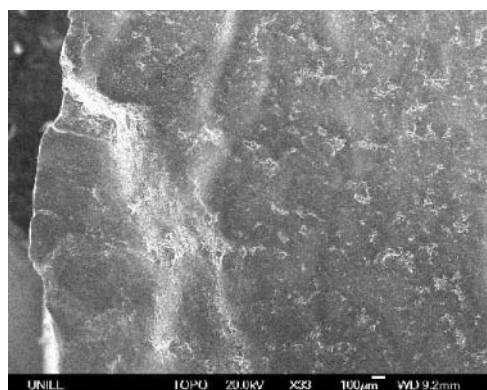

Figure 4. FEGSEM micrographs of the fracture surfaces of Zr-stabilized 2014 aluminum alloy tested at 125 MPa failed after $3.5*10^5$ Cycles.

Fracture surfaces of the cyclically deformed fatigue specimens were observed at low magnification in order to identify the zones of fatigue initiation and final failure, at higher magnifications in order to identify the regions of microscopic crack formation and growth and microscopic plastic mechanisms.

Typical fracture surface obtained by fatigue tests is shown in Figure 4.All the fracture surfaces show distinct regions of stable crack growth and overload, the distance between the two regions is more marked by increasing the cyclic stress (Figure 5). The variation of the distance between stable crack growth and overload is clearly showed in Figure 6.
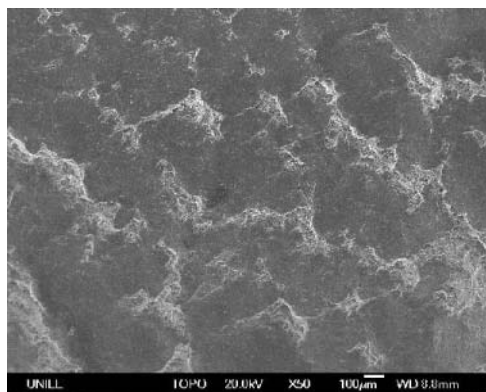
Figure 5. Regions of stable crack growth and overload observed in the Zr-stabilized 2014 aluminum alloy tested at 125 MPa fractured after $3.5*10^5$ cycles.

In this kind of materials the microcracks formed initially in direction parallel to the principal stress axis, grow and coalesh forming one or more macroscopic cracks that propagate in the same direction leading to the material failure. During cracks growing, the plastic zone at the crack tip begin to increase and many grains are so involved in the plastic deformation; the crack is able to propagate along different slip planes by simultaneous or alternating shear on two slip systems. This double slip mechanism produces a crack path normal to the load direction producing many fatigue striations. All the FEGSEM observations revealed the presence of the classical fine striations in the regions of stable crack growth, all the evenly spaced striations give the behavior and the direction of crack propagation in the microstructure and localized microplasticity (Figure 7). These fine spaced striations are proper of the initiation of stable crack growth through the alloy during deformation. All the crack initiation and growth is normally attributed to the incremental accumulation of microplastic damage of the material, under cyclic loading, at a localized level.
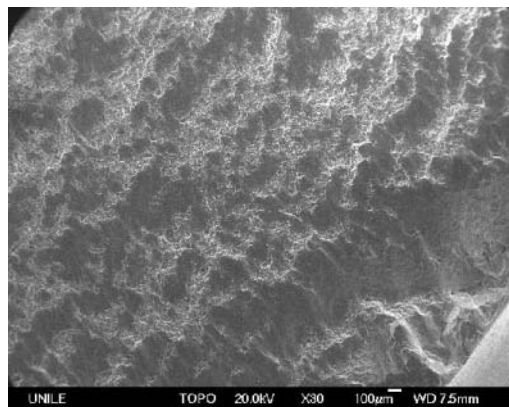
Figure 6. Regions of stable crack growth and overload observed in the Zr-stabilized 2014 aluminum alloy tested at 115 MPa
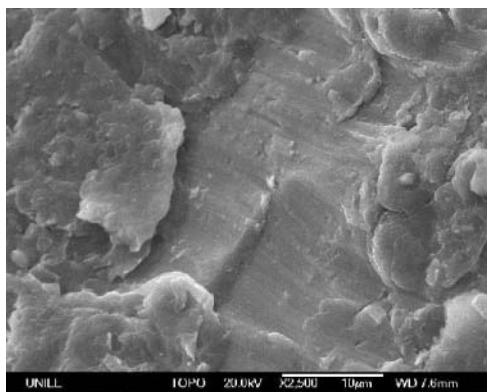

Figure 7. Fine and shallow fatigue striations observed in the region of early crack growth in the specimen tested at 110 MPa.

The accumulation of damage at every cycle in the micro sites and the initiation of slip band activity in the grains oriented along the slip direction lead to the nucleation of many microscopic cracks; isolated areas of small voids were recognized in the regions of stable flow and crack growth (Figure 8), this slow and stable flow regions are also characterized by clam shell formation adjacent to the shown small voids (Figure 8).

The nucleation of voids produce a decrease of the macroscopic response of the material, by continuing deformation, they growth and coalesh as a result of strain localization causing small increments, at every cycle, of crack tip extension.
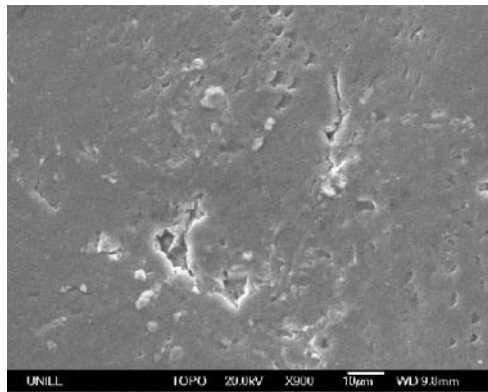
*Figure 8.* Microscopic cracks observed in the sample tested at 120 MPa.
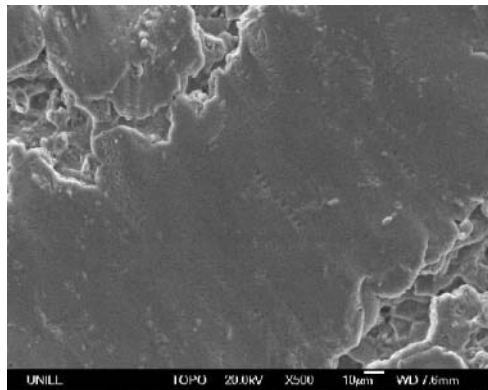
Figure 9. Clam shell formation in the Zr-stabilized 2014 aluminum alloy, specimen tested at 110 MPa.

4. CONCLUSIONS

The response of a Zr stabilized 2014 aluminum alloy to cyclic loading was studied in the present work. The cycles to failure at different stress amplitude levels were compared with those obtained for the unstabilized alloy. The TEM observation of the modified material showed a very fine subgrain structure characterized by the presence of very fine Al_3Zr within the grains, the particles play the role of stabilize the structure, inhibit the recrystallization and increase the strength of the alloy in all the tested conditions. Fracture observations were performed by using a scanning

electron microscope equipped with field emission gun in order to describe the behavior of the material during cyclic loading.

REFERENCES

1. S. Suresh, "Fatigue of Materials", 2nd London, UK: Cambridge University Press, 1998.
2. T.S. Srivatsan, D. Kolar, P. Magnusen, Materials and Design, **23** (2002) 129-139.
3. T.S. Srivatsan, S. Anand, S. Sriram, V.K. Vasudevan, Mater. Sci. Eng., **A281** (2000) 292-304.
4. S.E. Stanzl-Tschegg, H. Mayer, Internat. J. Fatigue, **23** (2001) S231-S237.
5. T.S. Srivatsan, Materials and Design, **23** (2002) 141-151.
6. J. Murray, A. Peruzzi, J.P. Abriata, J. Phase Equilibria, **13** (1992) 277-291.
7. Z. Yin, Q. Pan, Y. Zhang, F. Jiang, Mater. Sc. Eng., **A280** (2002) 151-155.
8. C. B. Fuller, A. R. Krause, D. C. Dunand, D. N. Seidman, Mater. Sci. Eng., **A338** (2002) 8-16.
9. K.L Kendig., D.B. Miracle, Acta Materialia, **50** (2002) 4165-4175.
10. A. Deschamps, Y. Brechet, Mater. Sci. Eng. **A251**, (1998) pp. 200-207
11. J.S. Vetrano, S.M. Bruemmer, L.M. Pawlowski, J.M. Robertson, Mater. Sci. Eng., **A238** (1997) 101-107.
12. S. Spigarelli, M. Cabibbo, E. Evangelista, J. Bidulska, J. Mater. Sci., **38** (2003) 81-88.
13. K. Satya Prasad, A.A. Gokhale, A.K. Mukhopadhyay, D. Banerjee, D.B. Goel, Acta Mater., **47** (1999) 2581-2592.
14. C. Bathias, D. Droullac, P. Le Francois, J. Fatigue, **23** (2001) S143-S151.
15. Xu-Dong Li, L. Edwards, Engineering Fracture Mechanics, **54** No.1, (1996) 35-48.
16. S.I. Park, S. Han, S.K. Choi, H.M. Lee, Scripta Mater., **34** (1996) 1697-1704.
17. S. Z. Han, S.I. Park, J.S. Huh, Z.H. Lee, H.M. Lee, Mater. Sci. Eng., **A230** (1997) 100-106.

HIGH STRAIN RATE SUPERPLASTIC BEHAVIOR OF Al-Li-Mg-Cu-Sc ALLOY SUBJECTED TO SEVERE PLASTIC DEFORMATION

M.R. Shagiev[1,2], Y. Motohashi[1], F.F. Musin[2],
R.O. Kaibyshev[2], O.Sh. Sitdikov[2,3]

[1] *Research Center for Superplasticity, Faculty of Engineering, Ibaraki University, 4-12-1 Nakanarusawa, Hitachi, 316-8511, Japan;*
[2] *Institute for Metals Superplasticity Problems, Russian Academy of Sciences, 39 Khalturin Str., Ufa, 450001, Russia;*
[3] *Department of Mechanical Engineering and Intelligent Systems, The University of Electro-Communications, Chofu, 182-8585, Japan*

Abstract: Superplastic properties of an advanced Al-Li-Mg-Cu-Sc alloy with fine-grained microstructure produced by two different processing ways (equal-channel angular extrusion and hot rolling) were studied in the temperature range of 350-525°C and at strain rates of 1.4×10^{-3}-1.4×10^{-1} s^{-1}. In both conditions the total elongations of about 400% were obtained at 450°C and a strain rate of 1.4×10^{-2} s^{-1} indicating a high strain rate superplasticity. The higher homogeneity of microstructure in the condition after equal-channel angular extrusion resulted in higher elongations and lower cavitation during superplastic deformation as compared to the hot rolled condition.

Key words: aluminum alloy, equal-channel angular extrusion, hot rolling, superplasticity, microstructure, cavitation.

1.   INTRODUCTION

A novel commercial Al-Li-Mg-Cu-Sc alloy, designated in Russia as 1443 aluminum alloy and denoted as 1443 Al herein, is considered as a promising material for aerospace applications due to the optimal combination of strength and crack propagation resistance [1,2]. Achievement of

superplasticity in the 1443 Al will allow developing a superior high-strength aluminum alloy which can be superplastically formed into complex shape parts. For that the simple and effective processing way for grain refinement should be developed. It was recently shown [3-5] that equal-channel angular extrusion (ECAE) is capable of producing a significant grain refinement resulting in high superplastic (SP) properties. On the other hand, aluminum-lithium alloys with unrecrystallized microstructure subjected to extensive warm working also can exhibit superplasticity [6,7].

Thus, the aim of the present work was to study a feasibility of achieving SP properties in the 1443 Al by subjecting this material to ECAE and extensive hot rolling.

2.   EXPERIMENTAL PROCEDURE

The 1443 Al with a chemical composition of Al-1.9Li-1.0Mg-1.7Cu-0.03Sc-0.08Zr (in weight %) was manufactured by direct chill casting followed by solution treatment at 530°C for 20 hours. The ECAE of the cylinders $\varnothing 20 \times 100$ mm^2 was performed using an isothermal die with a circular internal cross-section at temperature of 325°C to a total true strain e≈16 by route B_C [8]. Hot rolling of $60 \times 40 \times 20$ mm^3 preforms was carried out in a duo rolling mill with 300 mm-diameter rolls using a speed of 100 mm/s and 10-20% nominal reduction per pass to a total reduction in thickness of 90% (e≈2.3). Prior to rolling the preforms were soaked at 300°C for 15 minutes. Time of interpass reheatings was 5 minutes.

Flat samples with a gauge size of $6 \times 3 \times 2$ mm^3 were tensile tested using a Shimadzu AG-G machine in the temperature interval 350-525°C and at strain rates ranging from 1.4×10^{-3} to 1.4×10^{-1} s^{-1}. The strain rate sensitivity coefficient, m, was determined from the slope of the log σ vs. log $\dot{\varepsilon}$ curves.

Orientation imaging microscopy (OIM) maps were obtained from electron backscattering diffraction pattern (EBSP) using JEOL JXA8100 electron probe micro-analyzer with OIM software provided by TexSEM Lab., Inc.

3.   RESULTS AND DISCUSSION

Figure 1 shows typical microstructures of the 1443 Al before and after hot working. One can see that both ECAE at 325°C and hot rolling at 300°C resulted in formation of partially recrystallized structure. Fine recrystallized grains with sizes of 1-5 μm alternated with unrecrystallized areas containing recovered subgrains. EBSP analysis revealed that after ECAE the volume recrystallized fraction was 70-75% and about 60% of grain boundaries had

high-angle misorientation, Figure 1b. In the hot rolled condition the volume recrystallized fraction was a little smaller – 65-70% and almost 50% of boundaries had low-angle origin, Figure 1c.
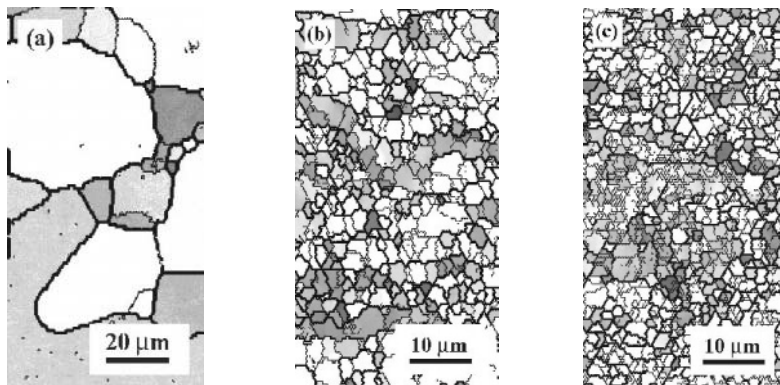

Figure 1. Typical OIM maps of the 1443 Al before and after hot working: (a) initial condition, (b) condition after ECAE and (c) hot rolled condition. Thin lines correspond to boundaries of misorientation 2-15° and bold lines - more than 15°. Extrusion and rolling directions are horizontal.

The temperature dependence of the total elongation at a strain rate of 1.4×10^{-2} s^{-1} is shown in Figure 2a. In the ECAE condition a well-defined elongation maximum of 420% was observed at 450°C indicating a high strain rate superplasticity in the 1443 Al. In the hot rolled condition, the samples cut along the rolling direction (RD) also exhibited the maximum elongation of 415% at 450°C, while the samples cut along the transverse direction (TD) – only 385% at a higher temperature of 500°C. At 450°C, the elongation in the ECAE condition tended to increase with decreasing the strain rate and reached the maximum of 650% at 1.4×10^{-3} s^{-1}. While for the RD of the sheet it remained unchanged – 415%.

Figure 2b presents the plots of the flow stress taken at ε=50% as a function of initial strain rate at 450°C in a double logarithmic scale. The strain rate sensitivity coefficient m>0.3 was observed in all the strain rate range examined both for the ECAE and hot rolled (RD) conditions. The flow stress was lower and the strain rate sensitivity was higher in the ECAE condition as compared to the hot rolled one.

EBSP analysis of the grip sections of deformed samples revealed that, in general, the non-uniformity of structure evolved during hot working remained under static annealing, Figures 3a and 4a. Initial recrystallized grains were essentially stable under annealing up to 500°C. At the same time, in the hot rolled condition the bands of unrecrystallized areas and coarse grains with sizes ranging from 10 to 50 μm were observed along the former RD of the sheet.
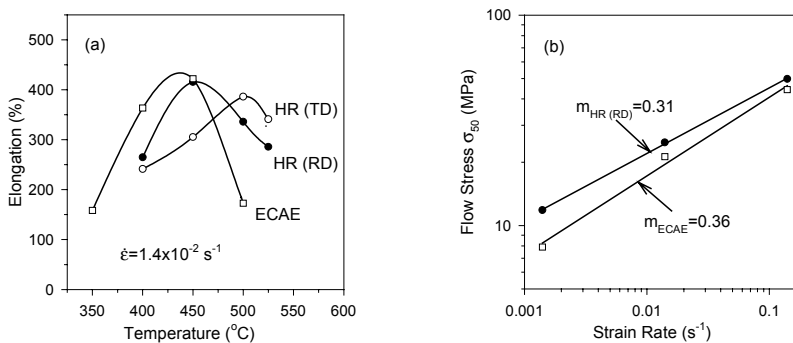
Figure 2. (a) Temperature dependence of the total elongation and (b) strain rate dependence of the flow stress σ_{50} at 450°C for the 1443 Al both in the ECAE and the hot rolled conditions. HR (RD) and HR (TD) are the rolling and the transverse directions of the sheet, respectively.
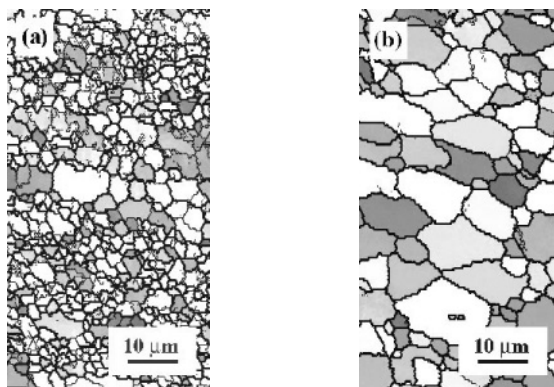

Figure 3. OIM maps of (a) grip and (b) gauge sections of the ECAE 1443 Al specimen after SP deformation (T=450°C; $\dot{\varepsilon}$=1.4×10^{-2} s^{-1}; δ=420%). Thin lines correspond to boundaries of misorientation 2-15° and bold lines >15°. Both extrusion and tensile directions are horizontal.

SP deformation led to decrease in the volume fraction of unrecrystallized areas and an increase in the fraction of high-angle grain boundaries, Figures 3b and 4b. After deformation under the optimum superplastic conditions, the volume fraction of unrecrystallized areas decreased from 25-35% to as low as 0.5% in the ECAE condition and to 5% in the hot rolled (RD) one. The fraction of high-angle boundaries increased from 60 to ~90% in the condition after ECAE, Figure 3b, and from 50 to ~70% in the hot rolled condition, Figure 4b.

The plot of the volume fraction of cavities near the fracture zone vs. testing temperature in the 1443 Al at a strain rate of 1.4×10^{-2} s^{-1} is shown in Figure 5. In the ECAE condition the volume fraction of cavities never

exceeded 3.5% while in the hot rolled condition it approached 9.5%, even the elongations in the former were higher. An extensive cavitation in the hot rolled condition seems to be caused by the less homogeneous microstructure in the sheet as compared to ECAE processed material.
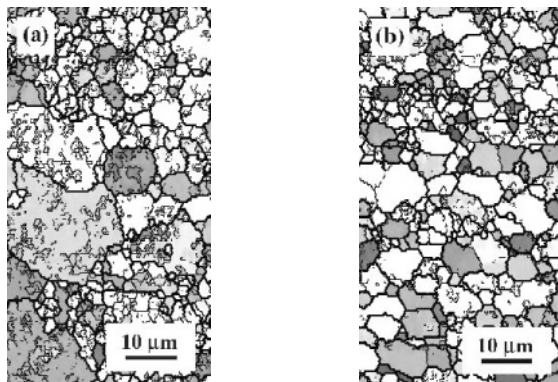

Figure 4. (a) OIM maps of (a) grip and (b) gauge sections of the hot rolled (RD) specimen after SP deformation (T=450°C; $\dot{\varepsilon}$=1.4×10^{-2} s^{-1}; δ=415%). Thin lines correspond to boundaries of misorientation 2-15° and bold lines >15°. Both rolling and tensile directions are horizontal.
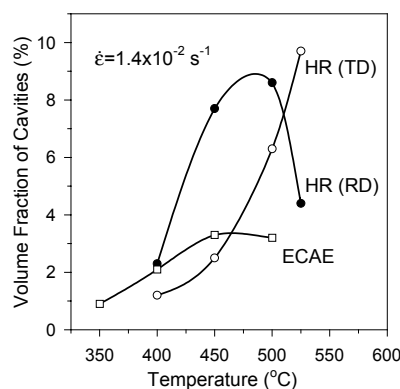

Figure 5. The volume fraction of cavities vs. testing temperature in SP deformed 1443 Al specimens both in the ECAE and the hot rolled conditions. HR (RD) and HR (TD) are the rolling and the transverse directions of the sheet, respectively.

Thus, the results of the present study demonstrated that both ECAE and hot rolling are effective processing routes for production of partially recrystallized fine-grained microstructure in the 1443 Al. The 1443 Al with such microstructure is capable of SP deformation as the other alloy

belonging to the similar system [9]. Dispersion particles prevent static recrystallization of the warm worked 1443 Al, and the low-angle boundaries become progressively high-angle due to continuous dynamic recrystallization during the early stages of the deformation [10] and thus able to contribute to grain boundary sliding.

4.   CONCLUSIONS

1. Both ECAE at 325°C and hot rolling at 300°C resulted in formation in the 1443 Al of partially recrystallized (about 70%) microcrystalline structure with the mean size of recrystallized grains of 3 μm.
2. SP properties of the 1443 Al were studied in the temperature range of 350-525°C and at strain rates of 1.4×10^{-3}-1.4×10^{-1} s^{-1}. In both conditions the total elongations of about 400% were obtained at 450°C and a strain rate of 1.4×10^{-2} s^{-1} indicating a high strain rate superplasticity.
3. The higher homogeneity of microstructure in the condition after ECAE resulted in higher elongations and lower cavitation during SP deformation as compared to the hot rolled 1443 Al.

ACKNOWLEDGEMENTS

REFERENCES

1. A.R. Shekhirev, E.V. Shiryaev, A.I. Tsarev, Technology of Light Alloys, 4, 2000, 9.
2. R.K. Bird, D.L. Dicus, I.N. Fridlyander, V.S. Sandler, Met. Sci. Heat. Treat., 43, 2001, 298.
3. Y. Iwahashi, Z. Horita, M. Nemoto, T.G. Langdon, Acta Mater., 45, 1997, 4733.
4. M. Furukawa, A. Utsunomiya, K. Matsubara, Z. Horita, T.G. Langdon, Acta Mater., 49, 2001, 3829.
5. F. Musin, R. Kaibyshev, Y. Motohashi, T. Sakuma and G. Itoh, Mater. Trans., 43, 2002, 2370.
6. M.V. Markushev, C.C. Bampton, M.Yu. Murashkin, D.A. Hardwick, Mater. Sci. Eng., A234-236, 1997, 927.
7. G.J. Mahon, R.A. Ricks, Scripta Metall. Mater., 25, 1991, 383.
8. M. Furukawa, Y. Iwahashi, Z. Horita, M. Nemoto, T.G. Langdon, Mater. Sci. Eng., A257, 1998, 328.
9. Q. Liu, X. Huang, M. Yao, J. Yang, Acta Metal. Mater., 40, 1992, 1753.
10. R. Kaibyshev, A. Goloborodko, F. Musin, I. Nikulin, T. Sakai, Mater. Trans., 43, 2002, 2408.

MICROSTRUCTURE AND MECHANICAL PROPERTIES OF AL-AL₄C₃ MATERIALS

Michal Besterci, Ľudovít Parilák
Institute of Materials Research, Slovak Academy of Sciences, Košice, Slovak Republic

Abstract: Dispersion strengthened aluminum compacts have been prepared by powder metallurgy. The base microstructure is aluminum matrix strengthened with dispersed ceramic particles. The strengthening is direct by dislocation movement retardation, and indirect by deformation induced microstructure modification in the next technological steps. The method of mechanical alloying process is described. Carbon transformation to carbide Al4C3 is characterised for different heat treatment schedules and nine commercial carbon powders tested. The micromechanism of carbon incorporation into the metallic powder, and the compacting of it are described. The influence of dispersed carbides on mechanical properties is evaluated together with the influence of deformation on microstructure and properties. Ductility anomalies up to a type of superplasticity were observed at certain tensile testing strain rates.

Key words: Dispersion strengthened materials, aluminum, microstructure, mechanical properties

1. INTRODUCTION

A mode of mechanical alloying is reaction milling, developed for dispersion strengthened aluminum production [1]. To produce aluminum dispersoid the aluminum powder is intensively dry milled with carbon powder. The transformed dispersed phase Al_4C_3 is than produced by a chemical reaction, which starts during milling, and it is completed at the next heat treatment process. The resulting powder mixture is then pressed,

compacted and isostatic pressing and hot extrusion prepare the final compacts.

The aim of this paper is to study the influence of the various graphite types when mixed with Al powder, and heat treatment procedure on the microstructure and properties of dispersion strengthened aluminum type Al-Al_4C_3. The influence of carbides characteristics on mechanical properties is evaluated together with the influence of applied deformation mode on the microstructure development and mechanical properties.

2.   EXPERIMENTAL MATERIAL AND METHODS

The experimental material - dispersion strengthened aluminum with Al_4C_3 particles, was prepared by intense milling of aluminum powder with different types of carbon, as shown in Tab.1. The prime aluminum powder grain size was 100 μm with the carbon content of 0.6 - 3 wt. %. The final carbide content was in the range of 2.5 - 12 vol.%. The obtained mixture was compacted at 600 MPa and thermally treated at 450, 500, 550, and 600°C whereas treatment times of 1, 3, 10, and 30 hours were employed. The final compacting by hot extrusion at a temperature of 550°C and a reduction rate of 94% on the cross section was applied [5]. The experimental material has been both prepared, and tested by gas chromatography for carbides Al_4C_3 content, at the Institute for Chemical Technology of Anorganic Materials, TU Vienna.

Table 1. Types of different carbon types used

Notation	Type	Commercial Carbon	Notation	Type	Commercial Carbon
A	a_1	LTD	F	a_2	Farbruss FW 2
B	a_1	Spezialschwarz 5	G	a_2	Flammruss 101
C	a_1	Spezialschwarz 500	H	c	Thermax
D	a_1	Printex 30	I	b	Grafit KS 2.5
E	a_2	Printex 400			

2.1   Carbonization kinetics

For the employed nine types of commercial carbon system $Al - 8Al_4C_3$ labelled A to I correlation were sought between physical and chemical properties and milling parameters, or carbide transformation rate, and properties of the produced compacts. The different carbon types showed different distributions of carbon in the aluminum powder. Their susceptibility to milling was measured by the ability to prepare

homogeneous distribution without being formed clusters. According to the obtained results the carbon forms were divided into 4 types:

a_1) porous types of furnace black, made by uncomplete burning of carbohydrates at low temperatures, with very good properties. They are fine, with high contact surface, and easy destruction of clusters.

a_2) porous types of furnace black, made by uncomplete burning of carbohydrates at higher temperatures. They are fine, but they form more stable clusters, resistant to desintegration.

b) electrographite, with layered structure, with good susceptibility to milling, though coarse grained and with smaller contact surface; comparable to furnace black (a_1, and a_2)

c) cracked carbon, forms strong clusters, and the carbon to carbide transformation rate is low.

The milling kinetics of the system is described in more detail in reference [6]. From the results, the homogeneity of carbide distribution and contact surface area influence the Al+C transformation kinetics to Al_4C_3. The dependence of the transformation rate on temperature and hold time for the 4 carbon types is shown in Fig.1. The good susceptibility to transformation for porous furnace black (a_1 and a_2) and that of electrographite (b) is evident.

The dependence of tensile strength and elongation on carbon content (wt.%) for Flammrus LTD is presented in Fig.2.
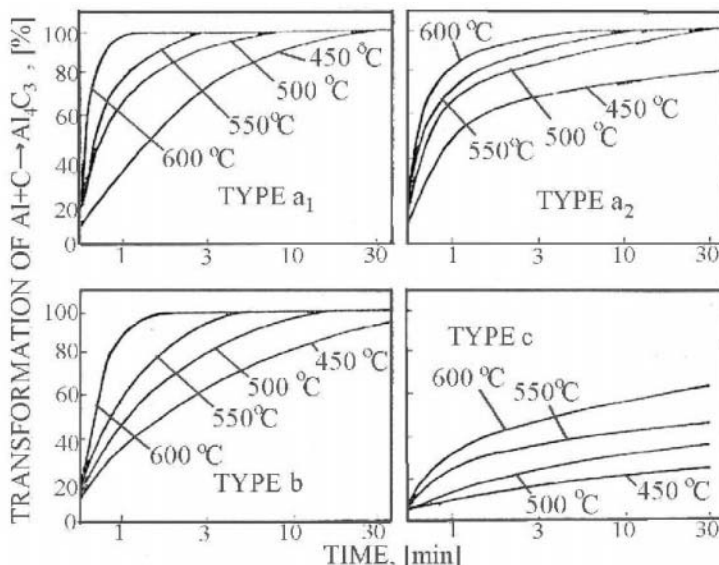

Figure1. Dependence of carbon to the carbide transformation rate on heat treatment temperature and hold time for four carbon types.
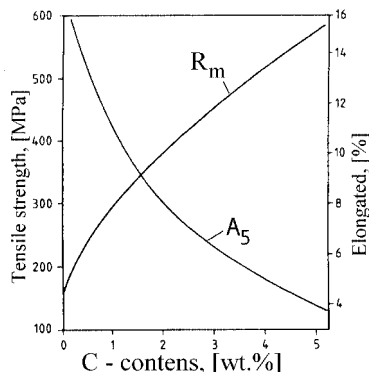
Figure 2. The dependence of tensile strength and elongation on carbon content (wt.%) for Flammrus LTD

2.2   **Microstructure and mechanical properties**

Light microscopy microstructure analysis of the produced compacts proved a high homogeneity of dispersed particle distribution in the direction perpendicular to the direction of hot extrusion. In the longitudinal direction of the bar as a result of hot extrusion the Al_4C_3 carbide particles were arranged into bands.

Electron microscopy analysis was conducted using carbon replicas and thin foils. The carbon replicas were not of help for quantitative evaluation. Transmission electron microscopy of thin foils offered better results. For all the tested carbon combinations from the A to I labels, thin foils were produced for the heat treatment 450°C/30 h. The Al_4C_3 particle size and the subgrain size were measured using the thin foils. The dispersed phase Al_4C_3 particle size was measured on 200 to 300 thin foil structures, and it was constant and as small as 30 nm. The particle size was influenced neither by the carbon type nor by the heat treatment technology applied.

The mean distance between the particles depended strongly on the carbon type, as it depends on the efficiency of transformation. Subgrain size measured in the range of 100 grains in thin foils depended on the carbon type, as well. It ranged from 0.3 to 0.7 μm. The stability of properties, resulting from graphite type I (KS 2.5), led to the highest production and utilization of this type of dispersion strengthening. The results on mechanical behavior of the compacted system, listed in the next parts of this paper are for this material selected.

In our previous works [8, 9, 10], we have evaluated the distance between the particles by point object simulation methods. The example of four

interparticle distance categories is shown in Fig.3. This includes the mean interparticle distance λ_μ, the mean minimum distance λ_ρ, the mean visibility λ_v, and the mean free spherical contact distance λ_ϑ. The characteristics and properties of these parameters have been analyzed in [9].

During the last years, a new approach to the description of point systems has been developed intensively, which is referred to as polygonal methods [1]. The dual representation formed in the above way describes completely the given point system. Properties of Voronoi tessellation and their various generalizations are being very intensively studied now, the state of this study is given in the monograph [11]. Intermediate stages of evaluation for this foil (a), outlines of particles (b), and of reference points (c) are documented in Fig.4.
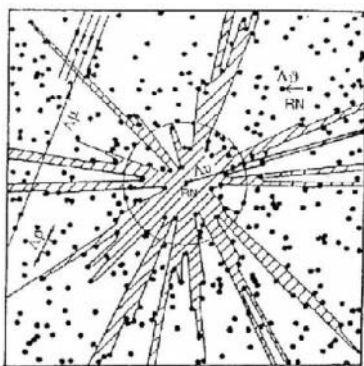

*Figure 3*. Interparticle distance categories
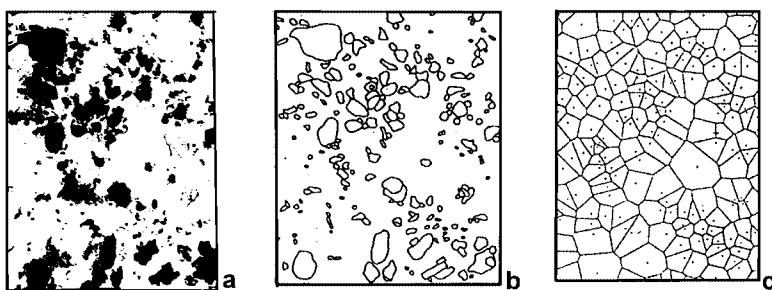
Figure 4. Intermediate stages of evaluation for this foil (a), outlines of particles (b) and reference points (c)

Mechanical properties and microstructure of dispersoid are influenced by the technology applied. With the near-constant dispersed particle grain size, the influence on strength and plasticity corresponds to the subgrain size and the

mean dispersed interparticle distance. The effect of a low temperature of the heat treatment on carbide reaction, revealed more differences in structural parameters, tensile strength and elongation. From the point of a strength increase, the carbon types A, C and I showed the best results. Increasing the transformed carbon content, and increasing the volume content of the dispersed phase in the aluminum matrix, the tensile strength increased and plastic properties decreased as interparticle distance λ decreases.
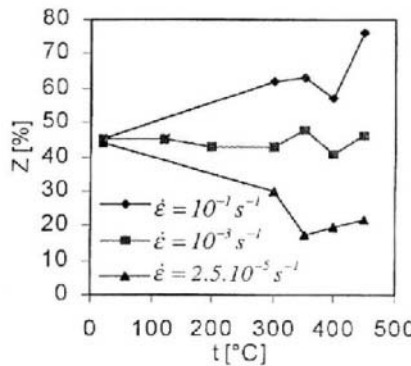

Figure 5. Reduction of area Z as a function of strain rate and temperature.

The Al-Al$_4$C$_3$ system with 4 vol. % of Al$_4$C$_3$ was tested under different tensile conditions, where three different strain rates and different testing temperatures up to 450°C were used [12]. The deformation mechanism and fracture mechanism were analyzed corresponding to different testing conditions. For the higher strain rates of $10^{-1}s^{-1}$ at 450°C, a significant growth of plastic properties was observed. The high uniform elongation A$_5$ of the specimen gauge length, and corresponding reduction values of the reduction in area Z were manifested in Fig.5. The ductility anomalies are showing an onset of a type of superplasticity. On the other hand, when testing temperature was of 450°C and low strain rates $10^{-5}s^{-1}$, the microstructure was polygonized. Sliding along grain boundaries, accommodated by dislocation creep, would be the prevailing mechanism of deformation and plastic properties are extremely low. According to [13] it was proved that for materials Al - 12Al$_4$C$_3$, the main mechanism responsible for superplastic behavior is the grains rotation process and not sliding. As an evidence of this process, one mayuse the result on grain size and measurement shape control at longitudinal and transverse direction carried out in this foils. The mechanisms of grain re-arrangement in superplasticity deformation process by sliding (a) and by rotation (b) are documented on Fig.6. The fracture mechanism was dominantly intergranular.
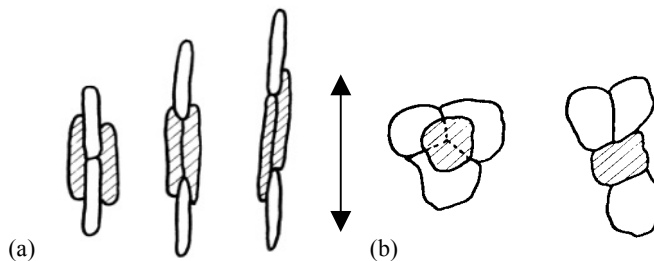
Figure 6. The mechanisms of grain re-arrangement in superplasticity deformation process by sliding (a) and by rotation (b)

Figure 7 shows the dependence of optimum superplastic strain rate on the inverse grain size for a large variety of superplastic aluminum alloys produced by different routes [14]. These dependencies suggest that the strain rates up to 10^{-1} s^{-1}, limited by the testing equipment, were out of the optimum conditions to get superplastic behavior.
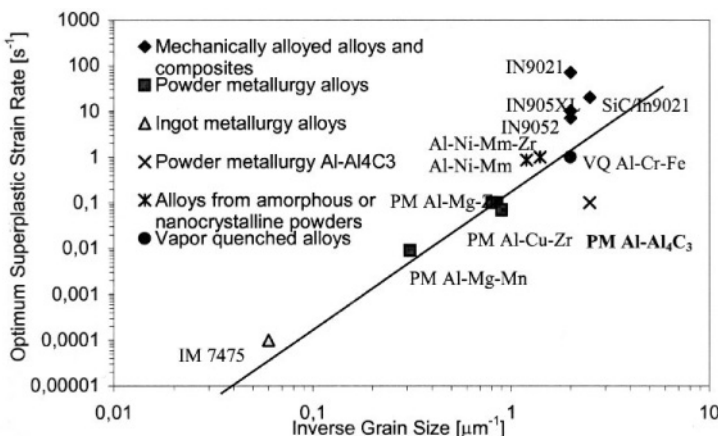

Figure 7. Dependence of optimum superplastic strain rate on the grain size for superplastic Al alloys produced by different routes.

3.   CONCLUSIONS

The obtained results on the mechanical alloying process and heat treatment of Al - C system, and on deformation behavior of dispersion strengthened Al – Al$_4$C$_3$ system prepared under different conditions, can be summarized as follows:

- It was shown that the transformation efficiency of carbon to Al_4C_3 by heat treatment of aluminum with the porous furnace black a) and electrographite b) is higher, than that of the hard cracked graphite c).
- The volume fraction of carbide phase Al_4C_3 and the efficiency of transformation are in good agreement with resulting microstructure and achieved mechanical properties.
- Microstructure and mechanical properties showed that the best strengthening is obtained with carbon types LTD (A) and KS 2,5 (I) with a high transformation rate, high Al_4C_3 carbide content, and low subgrain size. On the other side, the strengthening resulted from the cracked Thermax (H) graphite is the lowest due to the low transformation rate $Al + C \rightarrow Al_4C_3$
- The temperature dependencies of ductility, and reduction of area in temperature range of 350–450°C and strain rate of 10^{-1} s^{-1}, indicated a considerable increase of these properties. In a case when the volume fraction of Al_4C_3 changes from lower to higher, the grain rotation mechanism dominates instead of the grain boundary sliding.

ACKNOWLEDGEMENT

REFERENCES

1. Besterci, M.: Dispersion strengthened Al prepared by mechanical alloying. Cambrige: Int.Science Publ, 1999. ISBN 189832655
2. Weissgäerber, T., Kieback, B.: Materials Science Forum, 8, (2000), p. 275.
3. Korb, G., Jangg, G., Kutner, F.: Draht,. 30, (1975), p. 318.
4. Jangg, G., Kutner, F., Korb, G.: Aluminum, 51,(1975), p. 641 Publ, 1999, ISBN 189832655.
5. Besterci, M., Šlesár, M., Jangg, G., et al.: Kovové materiály, 27, (1989), no. 1, p. 77.
6. Jangg, G., Šlesár, M., Besterci, M., Zbiral, J.: Zeischrift f. Werkstofftechnik, 20, (1989), p. 226.
7. Jangg, G., Vasgyura, J., Schröder, K., Šlesár, M., Besterci, M. In: Inter. Conf. Powder Metallurgy and Exh. Düsseldorf, 1986, p. 989.
8. Saxl, I., Besterci, M., Pelikán, K.: Pokroky práškové metalurgie, 3, (1986).
9. Saxl, I., Pelikán, K., Rataj, J., Besterci, M.: Quantification and Modelling of Heterogenous Systems. Cambridge Int. Publication, 1995. ISBN 1898326045
10. Besterci, M., Kohútek, I., Saxl, I., Sülleiová, K.: Journal of Materials Science, 34, (1999), p. 1055.
11. Okabe, A., Boots, B., Sugihara, K.: Spatial Tessellation. Chichester : J. Wiley, 1992
12. Besterci, M., Zrník, J., Šlesár, M.: Kovové materiály, 35, (1997), p. 344.
13. Besterci, M., Velgosová, O., Ivan, J., Kováč, L.: Kovové materiály, 39, (2001), no. 5, p. 309.
14. Mishra, R.S., Mukherjee, A.K.: Mater. Sci. Eng., A234-236, (1997), pp. 1023.

CREEP BEHAVIOR AND STRENGTH OF MAGNESIUM-BASED COMPOSITES

V. Sklenicka, M. Pahutova, K. Kucharova and M. Svoboda
Institute of Physics of Materials, Academy of Sciences of the Czech Republic, CZ-616 62 Brno, Czech Republic

Abstract: Due to increasing interest in light-weight materials, magnesium and its alloys have come under growing focus, particularly in respect to the high volume commercial automotive sector. An often real or perceived constraint has been creep resistance. A considerable improvement in the creep properties of the currently available commercial magnesium alloys can be potentially achieved by the incorporation of high stiffness ceramic reinforcement (fibres and/or particles) into the matrices of monolithic alloys – metal matrix composites, MMC.

This paper provides a report on comprehensive experiments which were conducted on the two representative magnesium alloys (AZ 91 and QE 22) and their discontinuous composites in order to evaluate the creep properties and to clarify the direct and indirect strengthening effects of reinforcement in creep. A comparison between creep characteristics of squeeze-cast AZ 91 and QE 22 magnesium alloys reinforced with 20vol.%Al$_2$O$_3$ short-fibres and unreinforced matrices shows that the creep resistance of the reinforced materials is considerably improved compared to the monolithic alloys. Better creep resistance arises from a load transfer effect in which part of the external load is carried by the reinforcement. Indirect composite strengthening may be caused by microstructural effects leading to a threshold stress that increases the creep resistance. By contrast, the investigation of the creep behavior of a particulate QE 22-15 vol.% SiC composite prepared by powder metallurgy has revealed no increase in the creep strength of the composites compared to the matrix QE 22 alloy. These results indicate a paramount importance of the choice of the composite matrix alloy and the reinforcement used.

1.   INTRODUCTION

The primary benefit of magnesium in structural applications is its low density which is two-thirds that of aluminum. However, the use of magnesium alloys in the automotive sector continues to be restricted for more arduous applications where improved designs have increased component temperatures. Creep is considered a most important factor at working temperatures at or more than 423 K.

The creep resistance of the currently available commercial magnesium alloys is rather limited at temperatures above ~ 400 K. Therefore improved high temperature performance has been an important task of magnesium alloy development for the last three decades [1]. The alloy design culminated in alloys such as WE 43 and WE 54 which show the creep strength at 523 K significantly better than the earlier alloys could achieve at 423 K [2]. However, this level of performance has been achieved by the use of relatively expensive alloying elements such as silver, yttrium and combinations of other rare earth mixtures, including heavy rare earth (e.g. Gd). Thus, there is still considerable interest in novel alloy design.

There is a potential for achieving a considerable improvement in the creep properties of magnesium alloys through the inclusion of non-metallic reinforcements to form metal matrix composites (MMCs). Although the creep properties of complex magnesium alloys have been extensively investigated and discussed, comparatively little research has been carried out on the creep behavior of Mg-based fiber or particle-reinforced composites. Therefore, the present work was initiated in order to provide a systematic assessment of the creep properties of selected discontinuous composites having magnesium alloys as the matrix materials and different systems of reinforcement.

Thus, the aim of the present paper is not to review the bulk of the results published to date relating to the creep response of various magnesium-based composites. Instead of such an approach this paper provides a comprehensive report on the extensive experimental results obtained by authors in an investigation of the high temperature creep behavior of the two magnesium alloys, AZ 91 and QE 22, and their discontinuous composites. The objective of the present research is a further attempt to clarify the direct and indirect strengthening effects of short-fiber and particulate reinforcements in creep of magnesium-matrix composites.

2. STRENGTHENING IN A DISCONTINUOUSLY REINFORCED MAGNESIUM COMPOSITE

It is well known that, in general, the incorporation of high stiffness ceramic fibers or particles into magnesium results in a composite with enhanced stiffness and high temperature strength over the unreinforced alloy [3]. Strengthening in the composite in creep can be partitioned into direct and indirect strengthening [4] – Fig. 1. Direct strengthening is achieved by classical shear lag mechanisms, i.e., where load transfer takes place from the matrix to the stiffer reinforcement. Indirect strengthening arises from changes to the matrix microstructure in the composite by the addition of the reinforcement. In general, the resultant creep properties of discontinuously reinforced magnesium alloys are strongly influenced by the processing routes, heat treatment conditions, reinforcement type and volume fraction and the structure and composition of the matrix/reinforcement interfaces. However, there are insufficient data to assess the influence of these factors, and creep models are not well developed to make any predictions. Therefore, the present work provides an assessment of the creep properties of two representative magnesium monolithic alloys and their various discontinuous composites with the objective to present information on the significance of creep strengthening in selected discontinuously reinforced magnesium alloys.
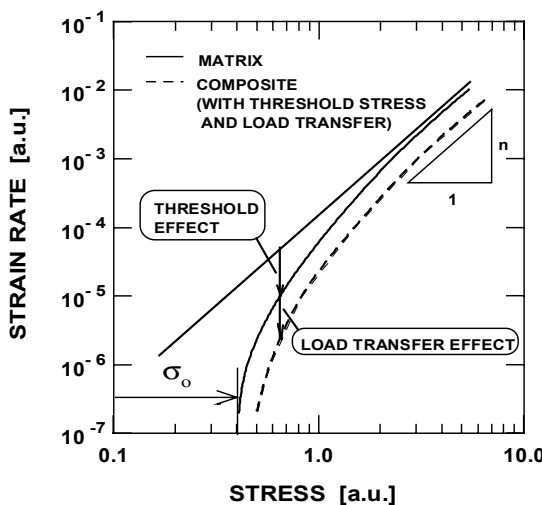

Figure 1. Schematic representation of the power-law creep ($\dot{\varepsilon} \sim \sigma^n$) in conjunction with the effects of the threshold stress σ_0 and load transfer.

3. EXPERIMENTAL MATERIALS AND PROCEDURES

Short-fiber reinforced and unreinforced blocks of the most common alloy AZ 91(Mg-9wt.%Al-1wt.%Zn-0.3wt.%Mn) and the high strength silver-containing alloy QE 22 (Mg-2.5wt.%Ag-2.0wt.%Nd-rich rare earths-0.6wt.%Zr) were produced by squeeze casting. The fibre preform consisted of planar randomly distributed δ-alumina short fibres (Saffil fibres from ICI, 97%Al$_2$O$_3$, 3%SiO$_2$, ~ 3 μm in diameter with varying lengths up to an estimated maximum of ~ 150 μm). The final fibre fraction after squeeze casting in both composites was about 20 vol. %. For comparison purposes, some experiments were also conducted using commercial purity Mg.

Powder metallurgy was used to fabricate SiC particle-reinforced and unreinforced QE 22 alloy. The QE 22 + 15vol.%SiC composite was prepared from gas-atomized metal alloy powders of various sizes (ASTM sieve sizes 230 and 600 corresponding to mean particle diameters of 30 and 10 μm, respectively) and various shapes of the SiC particles (bulky particles – BL, rounded particles – HD).

Flat tensile creep specimens were machined from the blocks so that the longitudinal specimen axes were either parallel to the plane containing the majority of the long axes of the fibres for the squeeze-cast composites or parallel to the extrusion direction for powder metallurgy materials. Constant stress tensile creep tests were carried out at temperatures from 423 to 523 K. The applied stresses ranged from 10 to 200 MPa. Creep tests were performed in purified argon in tensile creep testing machines with the nominal stress maintained constant to within 0.1% up to a true strain of about 0.35. Almost all of the specimens were run to final fracture.

Following creep testing, samples were prepared for examination by transmission electron microscopy (TEM). Fractographic details were investigated using either light microscopy or scanning electron microscopy.

4. RESULTS AND DISCUSSION

4.1 Monolithic and short-fibre reinforced squeeze cast AZ 91 and QE 22 alloys

The creep data for the AZ 91 and QE 22 alloys and the AZ 91 + Saffil and QE 22 + Saffil composites at a testing temperature of 473 K are shown in Fig. 2a, where the minimum creep rate $\dot{\varepsilon}_m$ is plotted against the applied stress σ on a logarithmic scale. Inspection of the creep data in Fig. 2a leads to two observations. First, the AZ 91 + Saffil composite exhibits improved creep

resistance by comparison with the AZ 91 monolithic alloy over the entire stress range used at this temperature. Second, the creep resistance of the QE 22 + Saffil composite is also considerably better than that of the matrix QE 22 alloy at low stresses. All magnesium alloys and their composites exhibit better creep resistance than commercially pure magnesium.
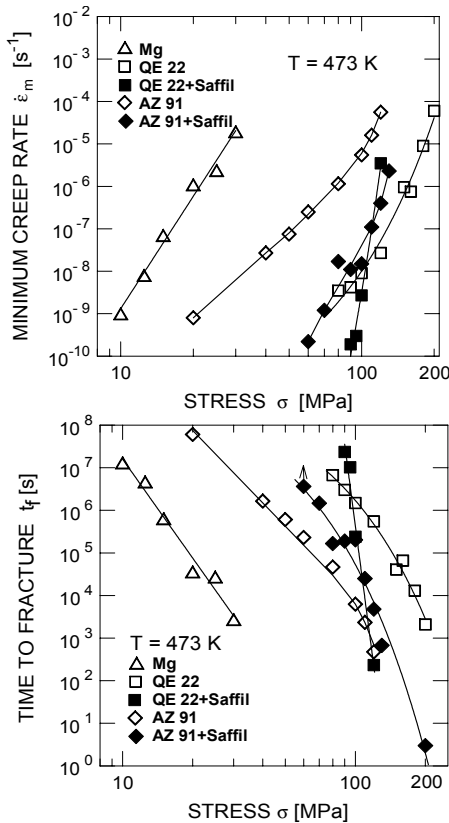

Figure 2. Minimum creep rate (a) and time to fracture (b) versus stress for the monolithic alloys and their short fiber composites.

Fig. 2b shows the variation of the time to fracture with the stress for the same specimens tested in Fig. 2a. The results for AZ 91 alloy and its composite demonstrate the creep life-times of the composite may be up to one order of magnitude longer than those for the monolithic alloy although this difference decreases with increasing applied stress so that ultimately there is very little difference at stresses > 100 MPa. By contrast, the creep life of the QE 22 + Saffil composite is markedly shorter than that of the unreinforced alloy at stresses > 100 MPa. The presence of a reinforcement leads to a substantial decrease in the overall ductility of matrix alloy. Thus,

the values of the strain to fracture ε_f in both composites were only ~ 1-2 %, the strains to fracture in the monolithic alloys were markedly higher; typically up to $\sim 10 - 15\%$ in the AZ 91 alloy and up to ~ 30 % in the QE 22 alloy [5]. Despite a general similarity of the creep behavior of both composites, the presence of the same type and amount of the reinforcement in the unreinforced AZ 91 and QE 22 alloys results in a significantly different increase in the creep resistance of the composite by comparison to the matrix alloy (Fig. 3). Thus it will be only appropriate here to describe differences that can be inferred from a comparison between creep characteristics of both composites and the unreinforced alloys.
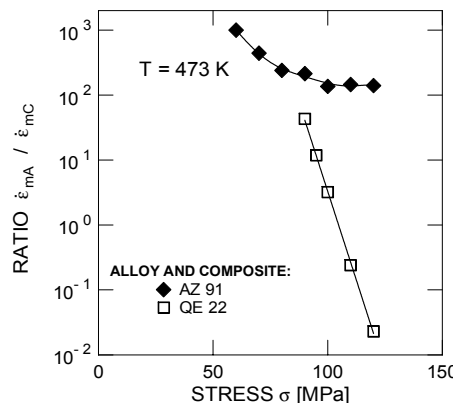

Figure 3. Effect of short-fibre composite strengthening demonstrated by the ratios of minimum creep rate (alloy) to minimum creep rate (composite).
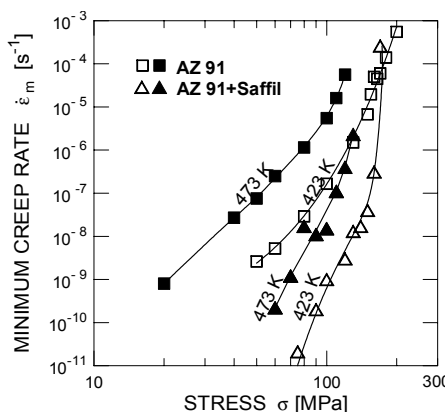

Figure 4. Minimum creep rate versus stress for the AZ 91 alloy and the composite.

The stress dependences of the minimum creep rates for the AZ 91 + Saffil composite and its unreinforced alloy at 423 and 473 K are shown in Fig. 4. The trend in these plots is different because the unreinforced alloy exhibits a decreasing value in the stress exponent, $n = (\partial \ln \dot{\varepsilon} / \partial \ln \sigma)_T$, at the lower stresses whereas the composite exhibits a higher value of n with decreasing stress. The increase in n at the lower stresses in the composite is a fundamental property of many metal matrix composites and it is generally associated with the presence of a threshold stress σ_0 marking a lower limiting stress below which no measurable strain rate can be achieved [6]. The data for the unreinforced alloy suggest a transition to a value of n close to ~ 3 at the lower stress. This value suggests that viscous glide is the rate-controlling mechanism in the matrix alloy and the increase of n at the higher stresses is then due to the breakaway of the dislocations from their solute atmospheres. Since the creep data in Fig. 4 suggest the presence of a threshold stress in the composite, σ_o, it is possible to extend the analysis by determining the magnitudes of the threshold stresses at 423 and 473 K. For estimation of σ_o it is necessary to plot, on linear axes, the datum points for the strain rates raised to a power of 1/n against the values of the applied stress and then to extrapolate to zero strain rate [6]. Taking a value of n = 3 for viscous glide, Fig. 5 shows this plot for the composite for the two testing temperatures and the extrapolations give threshold stresses of ~ 74 and ~ 59 MPa for 423 and 473 K, respectively, which indicates a temperature dependence of the threshold stress.
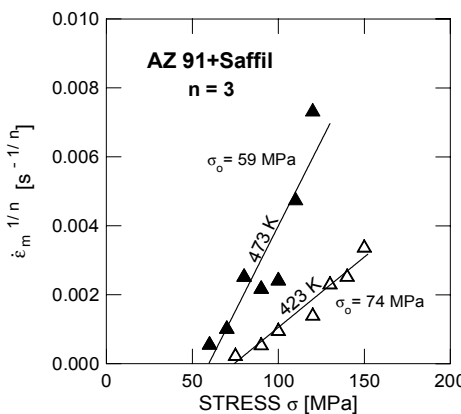

Figure 5. Procedure for determining the threshold stress in the composite at 423 and 473 K using a stress exponent of n = 3.

The presence of short fiber reinforcement leads to a reduced creep rate in the AZ 91 + Saffil composite by two to three orders of magnitude (Fig. 4). Such a difference can arise when significant load transfer partitions the

external load between the matrix and the reinforcement [4, 7]. In the presence of load transfer, the creep data may be successfully reconciled by putting the ratios of the minimum creep rates of the composite and the rates of the matrix alloy at the same loading conditions equal to a factor given by $(1-\alpha)^n$, where α is a load transfer coefficient having values lying within the range from 0 (no load transfer) to 1 (full-load transfer). The values of α inferred from the data in Fig. 4 using $n = 3$ are within the range 0.8 to 0.9. The predicted values are in reasonable agreement with the theoretical predictions according an analytical treatment by Nardone and Prewo [8]. Further, greater creep resistance exhibited by the AZ 91 + Saffil composite may arise from a substructural strengthening effect due to the increased dislocation density which is present in the composite because of the thermal mismatch between the matrix and fibers.
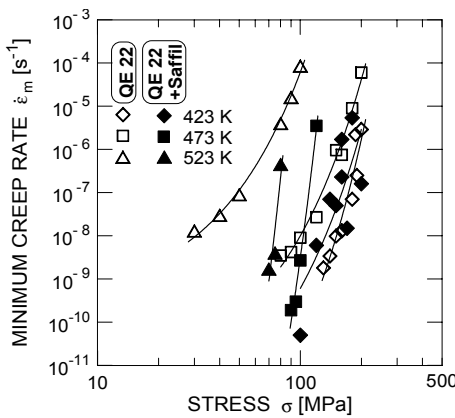

Figure 6. Minimum creep rate versus stress for the QE 22 alloy and the composite

The stress dependences of the minimum creep rates for the QE 22 + Saffil composite and its monolithic alloy are shown in Fig. 6. The experimental data show that the creep behavior of the composite is similar to that of the alloy in regard to the high stress exponents which suggests that the creep behavior of both materials may be controlled by precipitation strengthening due to the interaction of fine precipitates with mobile dislocations. While the values of the apparent stress exponent for the alloy slightly decrease with decreasing applied stress, no curvatures on the plots of the creep rate versus stress for the QE 22 + Saffil composite were found. However, the experimental data from this work describe the creep behavior of the composite only over three orders of magnitude of creep rate or less. Thus it is difficult to establish whether the stress exponent is genuinely constant, or increases with decreasing the applied stress indicating the potentiality of the threshold stress. Thus, it is nearly impossible for the

technical reasons to perform additional tests at very low stresses. Further, no values of a load transfer coefficient α for the composite have been obtained due to insufficient creep data and thus no valuable information regarding the value of the true stress exponent n. It can be concluded that the QE 22 + Saffil composite exhibits superior creep resistance compared to its monolithic alloy at a temperature of 523 K. This difference decreases with increasing stress and there is a tendency for the reinforcement to have no significant effect on the creep strength at a temperature of 423 K.
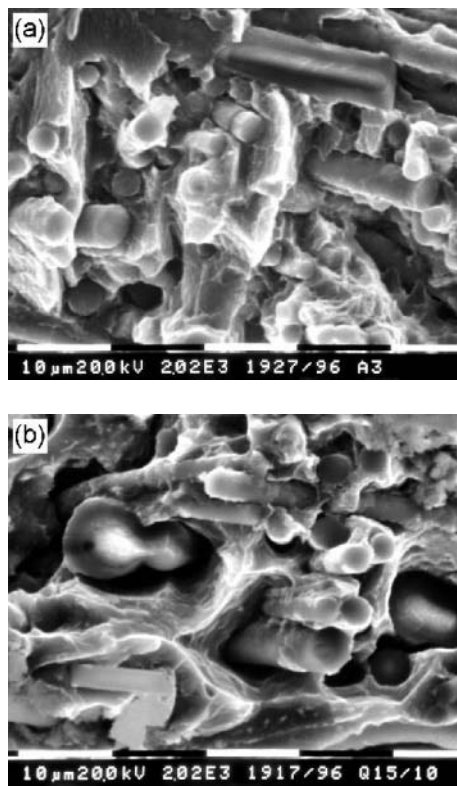

Figure 7. The creep fracture surfaces after testing at 473 K: (a) the AZ 91 composite (stress 70 MPa), (b) the QE 22 composite (stress 120 MPa), SEM.

Creep behavior of the composite can be substantially influenced by the matrix/fiber interfaces [9, 10]. Weak matrix/reinforcement bonding may lead to inferior creep properties of the composite. Thorough fractographic investigations of the AZ 91 + Saffil composite did not reveal either substantial creep fiber cracking and breaking or any debonding at the interface between the fibers and the matrix due to creep (Fig. 7a). By contrast, an intensive debonding was revealed at the creep fracture surfaces

of the QE 22 + Saffil composite (Fig. 7b). The extent of debonding was markedly increasing with decreasing temperature. Thus, in the limit of zero interface strength, where no stress can be transmitted to the fibers, the composite may be weaker than the matrix alone (see Fig. 6, temperature 423 K). Further, detailed microstructure investigations [5] revealed enhanced precipitation of secondary phases at the interfaces in the QE 22 + Saffil composite which can detrimentally affect the creep behavior of the composite by progressive interfacial debonding and matrix depletion producing precipitate inhomogeneity and deficiency in the matrix precipitate structure leading to the composite weakening. As a consequence of these features the Saffil reinforcement in the QE 22 alloy gives more modest improvements in the creep properties than it does in the AZ 91 alloy.

4.2   Particle-reinforced QE 22 – SiC composite fabricated by powder metallurgy

Particulate reinforced MMCs may give more modest improvements in the creep properties than their fiber-reinforced counterparts, nevertheless, they can be formed into useful shapes using conventional metal working processes such as powder metallurgy methods and extrusion and also they exhibit more isotropic properties. Moll et al. [11] reported recently, in an investigation conducted to evaluate the creep behavior of 15 vol.% silicon carbide particulate reinforced PM magnesium AZ 91 and QE 22 alloys, that the reinforcing effect of SiC particles on the creep resistance is not uniform and depends strongly on the matrix alloy. While the creep resistance of the AZ 91 alloy is increased through particle reinforcement, the creep resistance of the reinforced QE 22 alloy is decreased. This unexpected result provided a strong motivation for the following more detailed study of the QE 22-15 vol.% SiC composite in this work.

The creep data of the QE 22 monolithic alloy and the QE 22 composites are shown in Fig. 8. Inspection of the creep data leads to two observations. First, the unreinforced QE 22 alloy exhibits better creep resistance than the composites both in the as-cast state (Fig. 8a) and after a T6 heat treatment (Fig. 8b). Second, the T6 heat treatment tends to have a detrimental effect on the creep resistance of both monolithic alloy and its composite.

Detailed microstructural investigation [12] revealed enhanced precipitation of Nd-rich phases at the SiC/matrix interfaces in the QE 22 – SiC composite after T6 heat treatment and during creep (Fig. 9). Such precipitation can detrimentally affect the creep behavior in a similar way as to fiber-reinforced composites. Further, Moll et al. [11] have proposed that poor creep resistance of the QE 22-SiC composite may be explained by taking into account interfacial sliding as an additional creep mechanism

acting in the composite. As a consequence of interfacial sliding, many cavities can occur at interfaces giving rise to macroscopic cracks and the debonding of matrix/SiC interface.
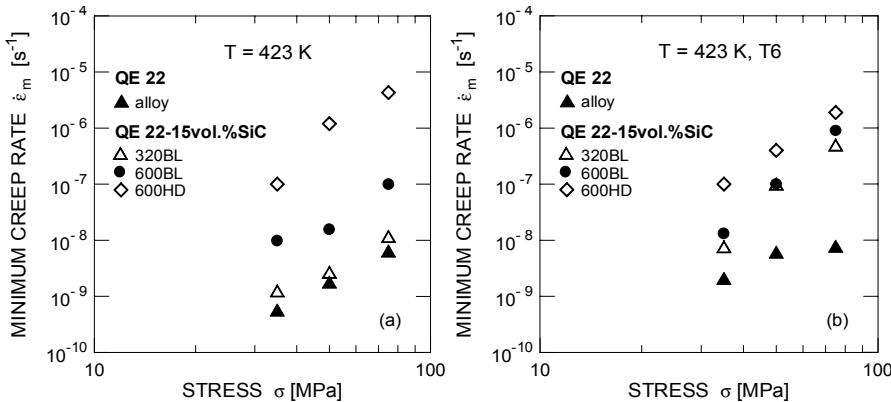

Figure 8. Stress dependences of minimum creep rates for the QE 22 alloy and the QE 22 – SiC composites at 423 K in: (a) as received state, and (b) after T6 heat treatment.
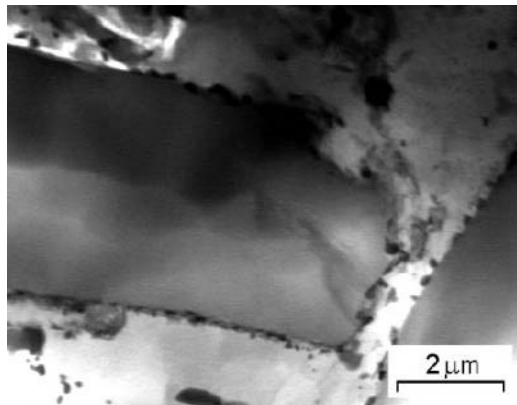

Figure 9. TEM micrograph showing enhanced precipitation of Nd-rich phases at the SiC/matrix interfaces in the QE 22 – SiC after T6 heat treatment and creep at 423 K.

5.   CONCLUSIONS

The creep resistance of discontinuous magnesium composites can be significantly improved by comparison with the unreinforced matrix alloys in two separate ways. Direct strengthening of the composites arises mainly from effective load transfer provided that no debonding of the

particle/matrix or fiber/matrix interfaces occurs. Indirect strengthening can arise from changes to the matrix microstructure in the composite by the addition of the reinforcement. An example of a positive indirect strengthening is the presence of a threshold stress in the composite. Further, indirect composite strengthening may be caused by additional temperature – dependent precipitation processes which lead to an attractive interaction between dislocations and inherent second – phase particles. By contrast, matrix depletion due to preferential precipitation at the reinforcement/matrix interface can produce precipitate inhomogeneity and deficiency in matrix precipitate structure leading to the composite weakening which indicates a dominant importance of choice of the matrix alloy and the reinforcement in the composite design.

ACKNOWLEDGEMENTS

REFERENCES

1. B.L. Mordike, Mater. Sci. Eng. A324, 2002,103.
2. J.F. King, Magnesium industry 1, 2000, 22.
3. S.T. Mileiko, Metal and Ceramic Based Composites, Elsevier, Amsterdam, 1997, p. 1.
4. K.T. Park, F.A. Mohamed, Metall. Mater. Trans. 26A, 1995, 3119.
5. V. Sklenička, M. Pahutová, K. Kuchařová, M. Svoboda, T.G. Langdon, Metall. Mater. Trans. 33A, 2002, 883.
6. Y. Li, T.G. Langdon, Scripta Materialia 36, 1997, 1457.
7. A. Kelly, K.N. Street, Proc. R. Soc. London 328, 1972, 283.
8. V.C. Nardone, K.M. Prewo, Scripta Metallurgica 20, 1986, 43.
9. B.L. Mordike, P. Lukáč, Surface and Interface Analysis 31, 2001, 682.
10. Z.F. Yue, Z.Z, Lu, Mater. Sci. Eng. A352, 2003, 266.
11. F. Moll, K.U. Kainer, B.L. Mordike, in: Magnesium Alloys and their Applications, (Eds. B.L. Mordike and K.U. Kainer), Werkstoffinformationsgesellschaft, Frankfurt, Germany, 1998, p. 647.
12. M. Svoboda, M. Pahutová, F. Moll, J. Březina, V. Sklenička, in: Magnesium Alloys and their Composites, (Ed. K.U. Kainer), WILEY-VCH, Weinheim, Germany, 2000, p. 234.

PART 4

ADVANCED TITANIUM ALLOYS AND
COMPOSITES

MULTICOMPONENT TI-SI-BASED SYSTEMS

Marina Bulanova[1], Sergey Firstov[1], Leonid Kulak[1], Daniel Miracle[2], Lyudmila Tretyachenko[1] and Tamara Velikanova[1]

[1] *I.N. Frantsevich Institute for Problems of Materials Science, Krzhyzhanovsky Street 3, 03142 Kiev, Ukraine*
[2] *Air Force Research Laboratory, Materials and Manufacturing Directorate, 2230 Tenth Street, Wright-Patterson AFB, OH 45433 USA*

Abstract: The present paper provides a rewiev of our results on the phase equilibria and phase reactions in theTi-corners of the Ti-Si-{Al,Sn,Zr}, Ti-Si-Al-{Ge,Sn,Zr} systems. The relation between the character of the phase diagrams, the crystal structure of the phases, mechanical properties of the individual phases and materials are discussed. It is shown that a basic understanding of phase equilibria can provide useful guidance for the selection and development of alloys for high temperature structural applications.

Key words: phase diagrams, phase transformations, structure, properties

1.   INTRODUCTION

The Ti-Si binary phase diagram (Fig. 1) represents a prospective basic system for development of high temperature alloys with a combination of strengthening mechanisms. Mechanical properties of these materials depend on the topology of the appropriate phase diagrams in the concentration intervals of interest. Systematic information is absent on many relevant multicomponent phase diagrams based on the Ti-Si binary system. Thus, the goal of this paper is to present new results on phase relationships in the ternary and quaternary Ti-Si-{Al, Sn, Zr} and Ti-Si-Al-{Ge, Sn, Zr} systems, as well as to discuss some examples of the relation between the details of the phase diagrams with the properties of individual phases and materials.
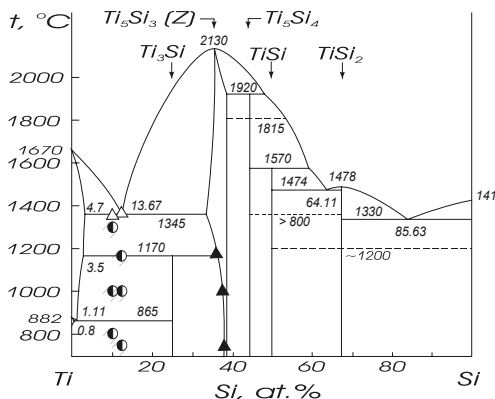
Figure 1. The Ti-Si binary phase diagram [1-4]

2.   ON THE FORMATION OF THE TI₃SI PHASE

The question concerning possibility of the formation of the <Ti₃Si> phase is one of the key questions in the study of Ti-Si-based composite materials. Examination by X-ray diffraction, metallography and electron microprobe of the binary 90Ti-10Si (all compositions are provided in atomic percent), ternary 90Ti-5Si-5Sn, 85Ti-5Zr-10Si and quaternary 85Ti-5Si-5Sn-5Al, 75Ti-10Zr-10Si-5Al samples annealed according to the schedules 1300°C/30h + 1000°C/30h and 1300°C/30h + 1000°C/30h + 800°C/100h has revealed both <Ti₃Si> (3/1) and <Ti₅Si₃> (Z) silicides in all the samples. However, the 3/1 phase was more evident in the binary sample. This might result both from lower temperatures of its formation in the multicomponent systems as compared to the binary, and from decreasing of the rate of diffusion when adding the third, fourth and more elements to the binary Ti-Si alloys. Annealing as-cast samples of the same alloy compositions listed above at 800°C/100h resulted in the presence of the 3/1 phase in only the binary sample. Thus, despite the fact that the 3/1 phase should be shown in equilibrium phase diagrams, for practical usage its presence, as well as phase transformations that involve the 3/1 phase, can be ignored in ternary and higher order systems based on Ti-Si.

3.   THE SYSTEMS TI—SI—*P*-ELEMENTS

The Ti-corners of the Ti–Si–*p*-element melting diagrams (liquidus + solidus) are available only for the Ti–Si–Al [3], Ti–Si–Ga [5] and Ti–Si–Sn [6] systems. The Ti-Si-Ge system can be predicted with good reliability (Fig. 2).
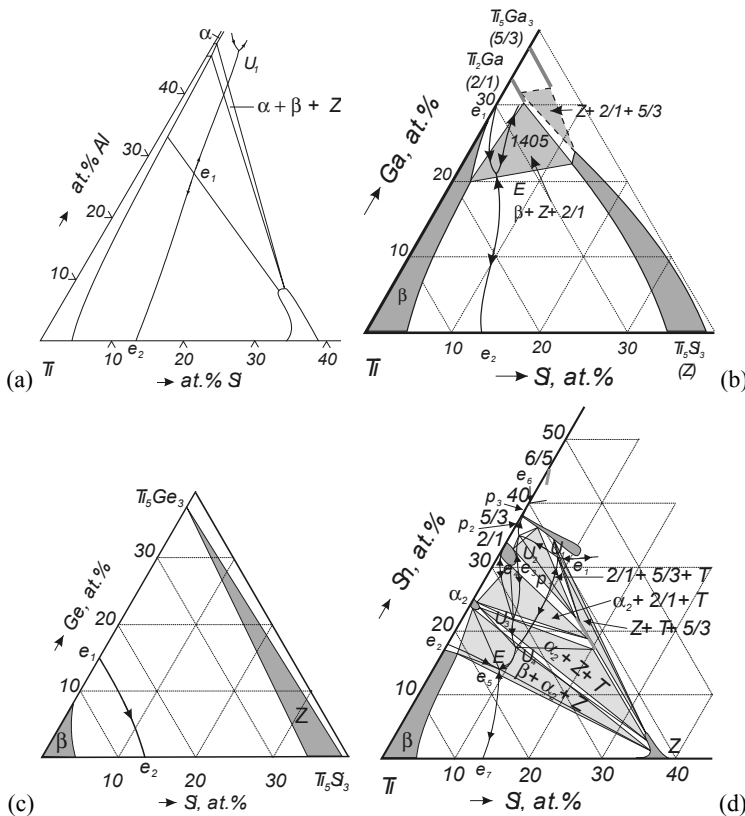
Figure 2. The Ti–Si–*p*-element melting diagrams: a – Ti-Si-Al [3]; b – Ti-Si-Ga [5];
c – Ti-Si-Sn [6]; d – Ti-Si-Ge, our prediction.

Among these systems, Ti-Si-Al is the most practically important. Much information available in the literature on phase equilibria in the Ti-corner of this system is discussed in [3]. The isopleth at 10Si (Fig. 3a) shows a number of solid-state transformations, particularly with participation of the 3/1 phase, in the Ti-corner. As discussed above, for practical purposes, the 3/1 phase can be ignored, and then the section (Fig.3b) becomes similar to the binary Ti-Al system. This last system shows rather wide, both by concentration and by temperature, two-phase fields (α+Z, α_2+Z) where no solid-state transformations occur, and which are, thus, appropriate for the development of high-temperature materials. Partial substitution of Si for Ge or Sn does not significantly change the topology of the appropriate melting diagrams in limited concentration intervals (Fig.4, compare with Fig.2a). The differences involve the width of the homogeneity ranges of coexisting phases. When a fourth element is added, the widths of the homogeneity regions of <Ti> increase, while the solubility of Si in the quaternary solid solutions becomes lower than in the ternary <Ti,Si,Al> system. This results

from the fact that when Al is added to the ternary <Ti,Si,Ge> and <Ti,Si,Sn> solid solutions, its atoms first substitute for Si, and then for Ge or Sn atoms. In the case of the Ti-Si-Ge-Al system, the temperatures of phase transformations do not differ from those in the ternary Ti-Si-Al system.
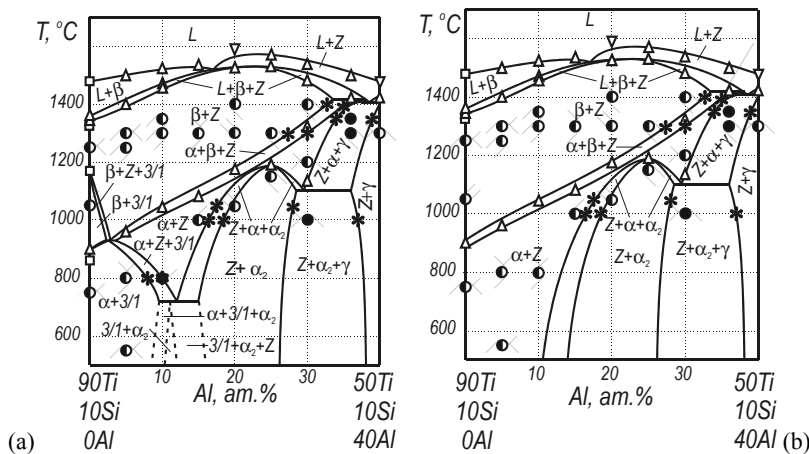

Figure 3. The isopleth at 10 at.% Si of the Ti-corner of the Ti-Si-Al system: a – equilibrium variant according to [3] and assessment of this work; b – the variant for the practical usage; ◑ – two-phase sample, ● – three-phase sample, Δ – DTA results, ∗ – data from other sections.

It should be noted that for presentation of the quaternary systems the sum of two elements (5Si+5Ge, 9Si+1Sn, 7Si+3Sn, 5Si+5Sn) is taken as a hypothetic element, so the system degenerates to a ternary system, as discussed in [7-9]. Increasing the aluminium content results in strengthening of the alloys, as is seen from the concentration dependences of microhardness. The microhardness is measured in two-phase samples, and thus corresponds to the boundaries of the homogeneity ranges of the phases according to the tie-lines. The curves for the ternary Ti-Si-Al and quaternary Ti-Si-Ge-Al alloys coincide. Tin additions increase the microhardness, while the curve for 5Sn lower the microhardess. For these alloys microhardness antibatically correlates with the Sn/Si ratio at the boundary of the homogeneity range (Fig. 5).
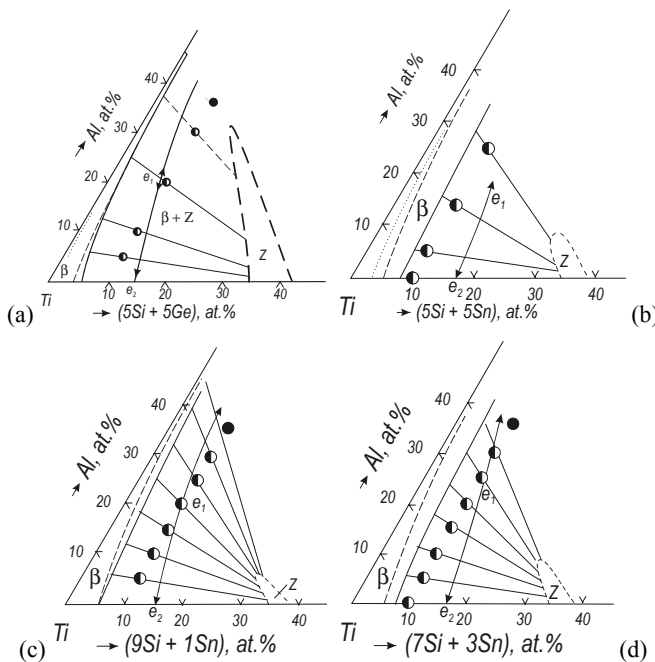
Figure 4. The Ti-corners of the Ti-Si-Al-{Si,Sn} melting diagrams: a – Ti-(5Si+5Ge)-Al [7], b – Ti-(5Si+5Sn)-Al [8], c – Ti-(9Si+1Sn)-Al [8,9], d – Ti-(7Si+3Sn)-Al [8]; ◑ – two-phase sample, ● – three-phase sample, ┈┈┈ – Si solubility in the quaternary <Ti>-solid solutions, – – – – - Si solubility in the ternary <Ti,Si,Al> solid solution.
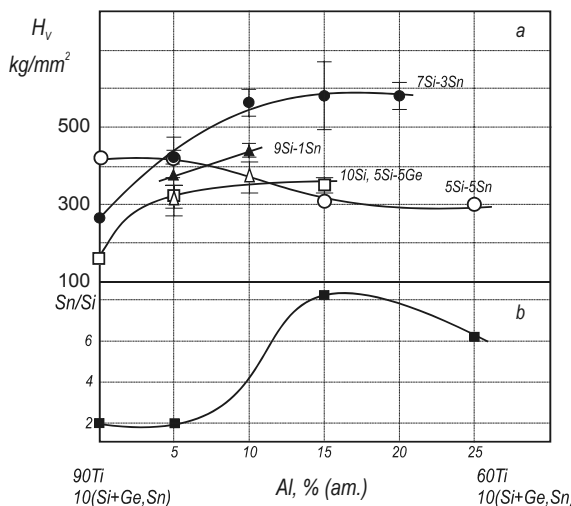

Figure 5. Microhardness of Ti-based solid solution (a) and Sn/Si ratio at the boundary of the homogeneity range of <Ti> at 5Si+5Sn (b) versus Al content in the alloys [7,8,10].

The bend of the Ti-rich boundary of the homogeneity range of the Z-phase at ~2 at.% Al (see Fig.2a) is of both theoretical and practical interest. This results from the sequence of the mutual substitution of components (Al↔Ti at <2 at.% Al and Al↔Si at >2 at.% Al) along the boundary, and corresponds to the crystal structure of the compound as discussed in [3]. This is reflected in both the lattice parameters and microhardness of the phase along the boundary. Both dependencies show a local minimum at ~2 at.% Al, corresponding to the above bend, and a maximum, corresponding to the maximum solubility of Al in the phase. Similar maxima were observed also for alloys with Sn [8], while for alloys with Ge [7] neither minima nor maxima were revealed. The first results from the absence of the bend of the boundary of the homogeneity range, and the second is due to the fact that for the alloys studied (see Fig.4a) the maximum Al solubility in the Z-phase is not reached. Thus, the lattice parameters and microhardness of <Ti> and Z of the ternary and quaternary phases correlate with Al content both in the alloys and at the boundaries of the homogeneity ranges of the phases.

Similar behavior was observed for the microhardness of eutectic mixtures (Fig. 6). The curve for the β+Z eutectic of the Ti-Si-Al system correlates with the lattice spacing and microhardness curves of the Z-phase and shows both local minimum and maximum. The concentration dependence of eutectic microhardness of the alloys with Ge is similar to that with Si, however does not reveal the bend at low Al concentrations. The dependencies for the alloys with 9Si-1Sn and 7Si-3Sn (Fig. 6b) also have maxima. For all the above alloys the maxima correlate with the solidus temperatures (Fig. 6c). For the alloys with 5Si-5Sn the curve has a different shape, which correlates with the curve for Ti-solid solution.

The appearance of the above bend results in a significant decrease of the volume fraction of Z-silicide in the eutectic, and thus provides an additional possibility to vary the balance of properties. Isopleths of the above systems (Fig.7) show that when ignoring the 3/1 phase there are rather wide concentration and temperature intervals free from solid-state transformations, which are suitable for the materials design. However, additions of Sn decrease the temperature of the α↔β transformation of Ti, and therefore also limit the higher limit of working temperatures. So, the tin content in industrial alloys should be defined by considerations of workability.
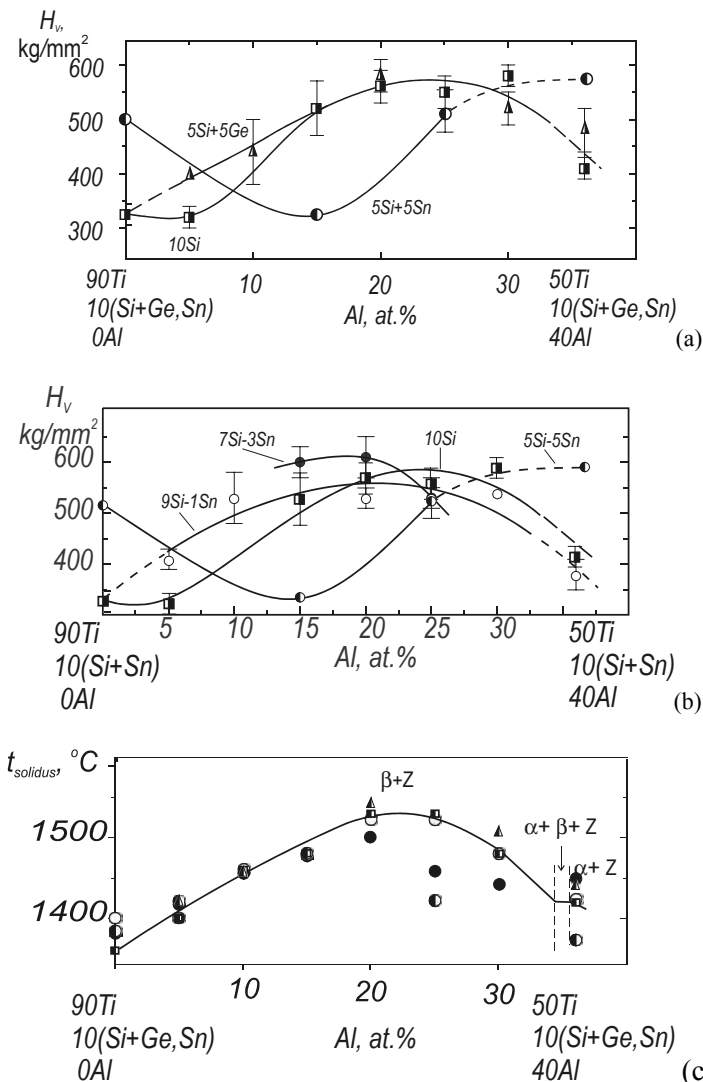
Figure 6. Correlation of the eutectic microhardness (a,b) with the solidus β+Z
temperatures (c) [3,7,8].

4.   THE SYSTEMS TI–ZR–SI AND TI–ZR–SI–AL

Information on the phase relationships in the Ti-Zr-Si systems is contained in [11,12]. Authors [11] report a continuous solid solution of Ti$_3$Si and Zr$_3$Si. In [12] two isothermal sections, at 1200 and 1050°C, are proposed, but a continuous solid solution of Ti$_3$Si and Zr$_3$Si is not shown. The ternary compound (Ti,Zr)$_2$Si (S2) was found. In the Ti-corner of the system the three-

phase field β+Z+S2 is shown. The information given concerning the phase composition of as-cast alloys does not allow an unambiguous conclusion of the character of the crystallization of the alloys. Besides, the section at 1050°C does not contain the phase field with participation of the Ti$_3$Si phase.
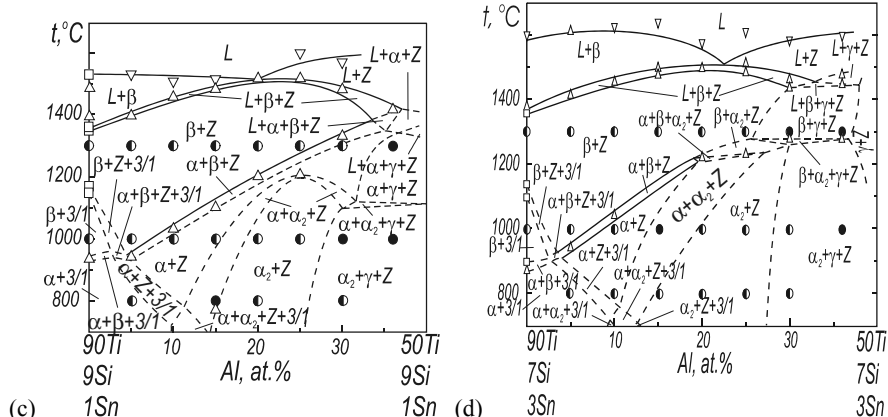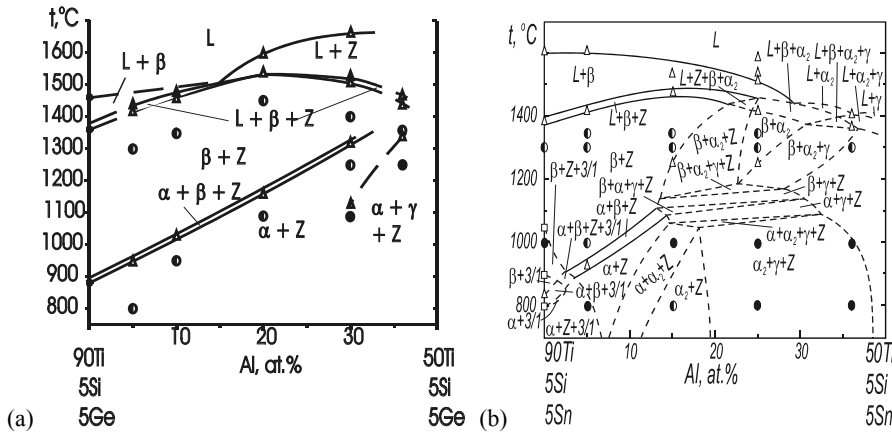
Figure 7. The isopleths of the Ti-corner of the Ti-Si-Al-{Ge,Sn} systems: a – at 5Si+5Ge [7], b – at 5Si+5Sn, c – at 9Si+1Sn, d – at 7Si+3Sn; ◐ – two-phase sample, ● – three-phase sample, Δ – DTA results.

The results of our investigation of the Ti-corner of the Ti-Zr-Si system (Fig.8) show that the above three-phase fields form by invariant eutectic equilibrium. The coordinates of the invariant point *E* were determined to be 1330°C and ~78Ti-11Zr-11Si (Fig.8a). In the solid state the three-phase field α+β+S2 was found with the temperature decreasing when the Zr concentration increases.
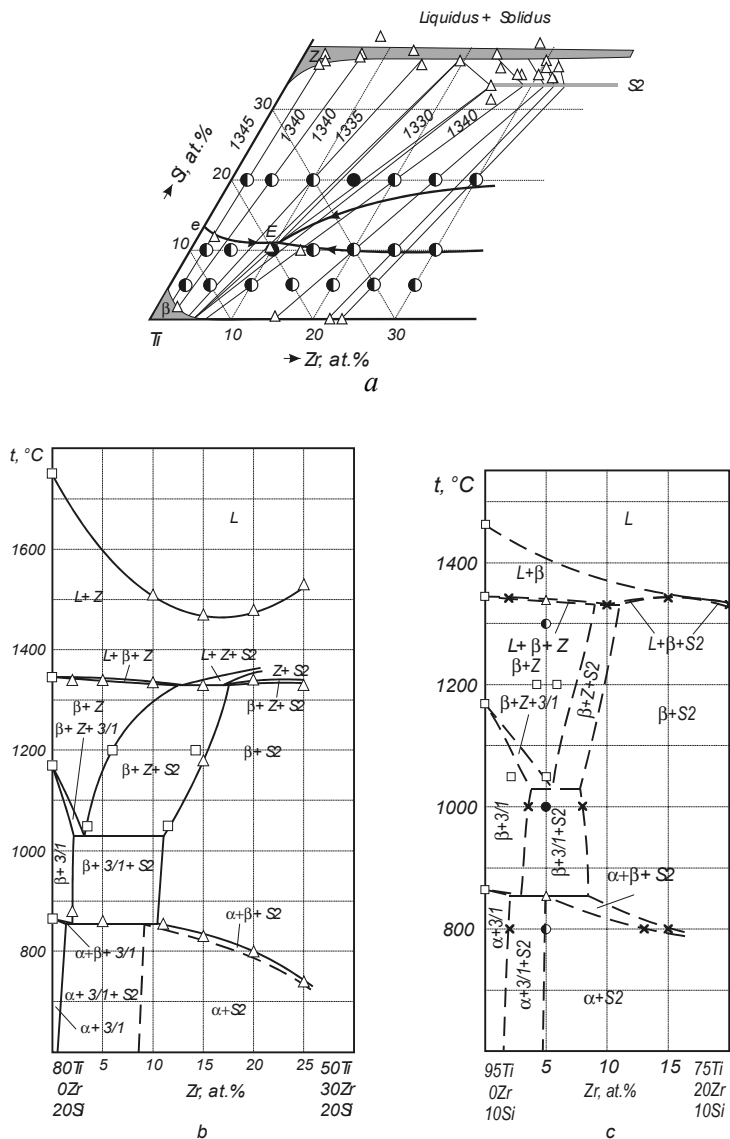
Figure 8. Phase equilibria in the Ti-corner of the Ti-Zr-Si system according to our unpublished results: a – the fragment of the melting diagram, b – the isopleth at 20 at.% Si, c – the isopleth at 10 at.% Si; ◑- two-phase sample, ● – three-phase sample, △ – microprobe (Fig.8a) or DTA (Fig.8b,c) results, □ – the data from the literature, ∗ - the data taken from the other sections.

Thus, at Si concentrations outside its solubility in the <Ti,Zr> solid solution, increasing of the Zr concentration should decrease the high-temperature properties of the alloys. So, the conclusion [13] concerning the negative joint influence of Si and Zr on the high-temperature strength of Ti-Al alloys results

from the bounding ternary Ti-Zr-Si phase diagram. However, the long-term hot hardness measurements for the alloys Ti-Zr-10Si (Fig. 9) have shown that below 550°C it is significantly higher for the alloy with 15Zr, than for the alloys with 2 and 10Zr. This might result from highly refined nature of the microstructure of the first alloy as compared with the two other (Fig.10). This, in turn, might result from the eutectic reaction and the influence of Zr, which promotes refinement of the mcirostructure. At 600°C, the hardness of the alloy Ti-2Zr-10Si is the highest, that results from the higher strengthening influence of the Z-phase as compared to S2. The testing temperature of 700°C is close to that for the α↔β transformation, and the values for all the samples are low.
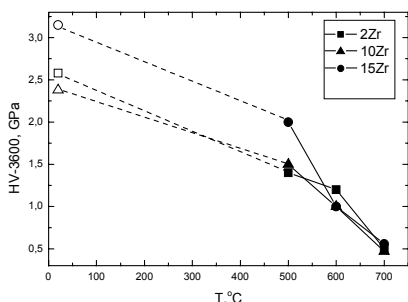

Figure 9. Long-term hot hardness of the Ti-Zr-10Si alloys.

| a | b | c |
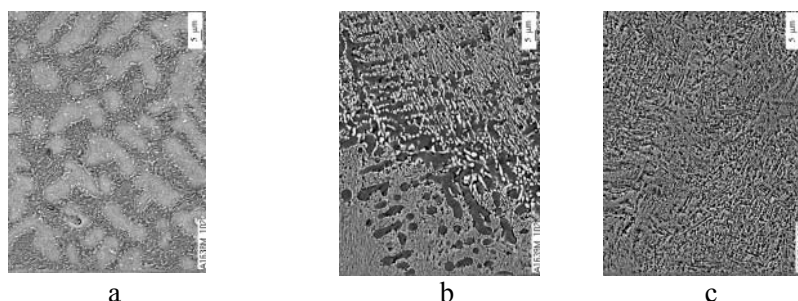
Figure 10. The microstructures of as-cast Ti-Zr-10Si alloys: a – 2Zr, ×1000; β + eutectic (β+Z); b – 10 Zr, ×1000; β + eutectic (β+Z+S2); c – 15 Zr, ×1000; eutectic (β+S2).

Information on the phase relationships in the Ti-Zr-Si-Al system is very limited and is mostly contained in the papers [14,15]. According to our results, at stable 5Al or 5Zr, the system behaves similar to the ternary Ti-Zr-Si or Ti-Si-Al, respectively (Fig.11). The isopleth at 5Si + 5Al (Fig.12) is similar to those of the ternary Ti-Zr-Si system, while the temperatures of the α+β+S2 three-phase field in the quaternary system are about 100°C higher than in the ternary. Aluminum additions to ternary Ti-Zr-Si alloys result in significant strengthening of both the Ti-matrix and the β+S2 eutectic when Zr concentration increases (Fig.13). In the case of the eutectic alloy this is in contrast with ternary Al-free alloys. This explains some of the increase in the long-term hot hardness versus Zr

concentration (Fig.14). Thus, joint analysis of the character of the phase equilibria, properties of individual phases and multicomponent materials should make more effective the process of materials elaboration.

(a)

(b)
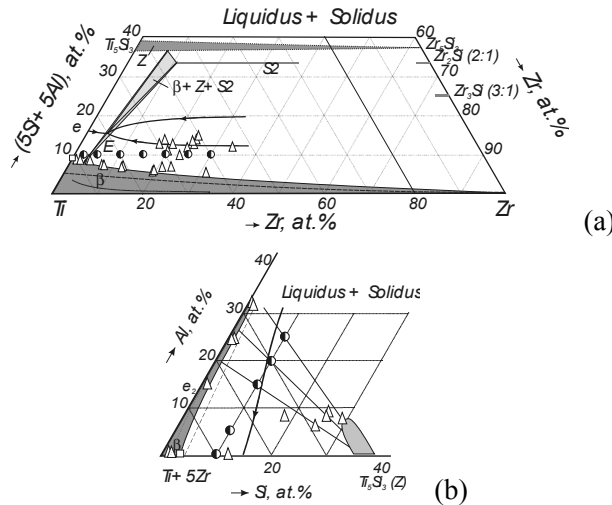
Figure 11. The melting diagram of the Ti-Zr-Si-Al system in a way of Ti-(5Si+5Al)-Zr (a) and (Ti+5Zr)-Si-Al (b) hypothetic systems; ◑- two-phase sample; △ – microprobe results; □ – data from the literature; – – – – - the boundary of the homogeneity region in the appropriate ternary; ⋯⋯⋯ - Si solubility in the quaternary Ti-matrix.
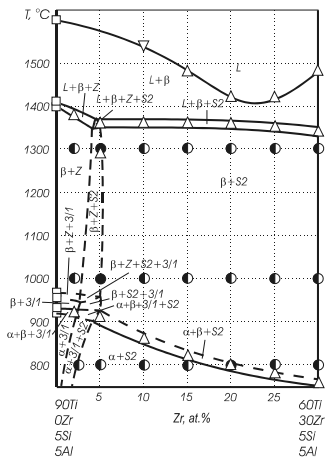
Figure 12. The isopleth at 5at.% Si + 5 at.% Al of the Ti-corner of the Ti-Zr-Si-Al system: ◑- two-phase sample, ● – three-phase sample, △ – DTA results, □ – the data from the literature.
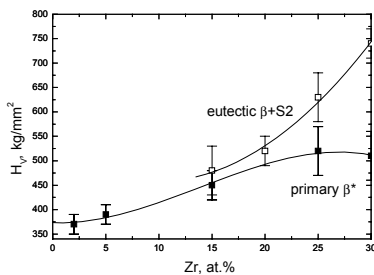
Figure 13. Microhardness of the primary Ti-matrix and eutectic (β+S2) versus Zr content.
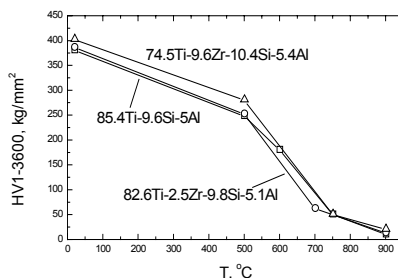
Figure 14. The long-term hot hardness of the Ti-Zr-Si-Al alloys.

ACKNOWLEDGEMENTS

REFERENCES

1. V.N.Svechnikov, Yu.A.Kocherzhinsky, L.M.Yupko et.al. Dokl. AN SSSR **193** (2) (1970) 393-396. (In Russian).
2. H.J.Seifert, H.L.Lukas and G.Petzow. Z.Metallkd. **87** (11) (1996) 2-13.
3. M.Bulanova, L.Tretyachenko and M.Golovkova. Z.Metallkd. **88** (3) (1997) 256-265.
4. V.V.Zavodyanny, V.Ya.Markiv and N.M.Belyavina. Dop. NAN Ukrainy 10 (1997) 117-121. (In Ukrainian).
5. L.A.Tretyachenko, N.V.Antonova, P.S.Martsenyuk and T.Ya.Velikanova. J. Phase Equilibria **20** (6) (1999) 581-592.
6. M.Bulanova, L.Tretyachenko, K.Meleshevich et.al. JALCOM **350** (2003) 164-173.
7. M.Bulanova, L.Tretyachenko, M.Golovkova, A.Soroka. Z. Metallkd. **89** (11) (1998) 783-789.
8. M.Bulanova, O.Ban'kovsky, A.Soroka et.al. Z.Metallkd. **91** (1) (2000) 64-70.
9. M.Bulanova, A.Soroka, P.Zheltov et.al. J.Mater.Sci. **35** (2000) 1-6.
10. M.Bulanova, A.Soroka, L.Tretyachenko, D.Stakhov. Z. Metallkd. **89** (1998) 442-444.
11. I.I.Kornilov, U.A.Asanov and V.M.Dembrovsky. In: Structure, properties and utilization of intermetallics, Moscow, Nauka, 1974, 107-110. (In Russian).
12. N.H.Salpadoru and H.M.Flower. Metall. Mater. Trans. **26A** (1995) 243-257.
13. A.A.Popov and N.A.Drozdova. Fiz.Metallov Metalloved. **84** (4) (1997) 123-132.
14. F.W.Crossman and A.S.Yue. Metall. Trans. **2** (1971) 1545-1555.
15. Z. Zhang and H.M.Flower. Mater. Sci. Techn. **7** (1991) 812-817.

EFFECT OF ZR ON STRUCTURE AND MECHANICAL BEHAVIOUR OF TI-AL-SI ALLOYS

I. Gornaya[1], O. Bankovsky[1], N. Bega[1], L. Kulak[1], D. Miracle[2], S. Firstov[1]
[1]Frantsevych Institute for Problems of Materials Science of NAS of Ukraine, Kyiv, Ukraine

[2]Air Force Wright Laboratory, Dayton, USA

Abstract: Multicomponent alloys based on the Ti-Si system are attractive structural materials with high oxidation resistance and high temperature strength. Zr is one of the elements that may further improve these properties, but there is little systematic information about the combined influence of Si and Zr in wide concentration ranges on the structure and mechanical behaviour of titanium and titanium-aluminium alloys. The features of structure, phase composition, and mechanical properties of as-cast Ti-3Al-XSi alloys (where X=2,4,6-wt.%) vs. Zr content (0-18-wt.%) have been studied in the present work. It is shown that Zr additions promote essential refinement of alloy microstructure and the formation of ternary $(Ti,Zr)_2Si$ silicides. It was found that hypoeutectic Ti-3Al-(4, 6)Si alloys with high Zr content have very refined microstructures based on an α-Ti $+(Ti,Zr)_2Si$ eutectic. Such alloys demonstrate high strength at room temperature and up to 400ºC. Hypoeutectic alloys with 5-wt.% Zr reinforced by eutectic Ti_5Si_3 silicides are characterised by higher strength in the temperature range from 400 to 600 ºC.

Key words: Ti-Si-in situ composites; Zr effect, microstructural effect, mechanical properties

1. INTRODUCTION

Zirconium is known as an alloying element that improves the high temperature properties of Ti-Si alloys via increasing the matrix hardenability as well as through microstructural modification [1-4]. The formation of two

different eutectics are possible in alloys of Ti-Si-Zr and Ti-Si-Al-Zr systems [2,4]. The first one is well studied for Ti-Si alloys, and is based on the binary compound Ti_5Si_3 (S1). The second eutectic based on the ternary compound $(Ti,Zr)_2Si$ (S2) is observed in Ti-Si-Zr and Ti-Si-Al-Zr alloys with high Zr content [2]. This latter eutectic is at present not widely studied. Further, systematic studies regarding the mutual influence of Si and Zr in wide concentration ranges on the microstructure and mechanical behaviour of titanium and titanium-aluminium alloys are not available in literature.

The microstructure, phase composition and mechanical properties of Ti-3- wt.% Al alloys alloyed with 2- 6- wt.% Si and 0-18-wt.% Zr were studied in the present work. A comparison of mechanical behavior of alloys based on (α-Ti+Ti_5Si_3) and (α-Ti+$(Ti,Zr)_2Si$) eutectics were also studied.

2.   EXPERIMENTAL PROCEDURE

Ingots ~15 mm in diameter and ~80 mm in length (80-100 g weight) were arc-melted in a vacuum of 10^{-1} Pa. Iodine titanium, zirconium, technically pure aluminum and silicon were used as initial materials.

Light microscopy with Jenaphot 2000, X-ray diffraction analysis with a DRON-3X-ray diffractometer, measurement of Vickers hardness, and long-term hardness were used. The long-term hardness (1 hour at 1 kg load) was carried out at temperatures of 500 ºC and 700 ºC. Uniaxial tensile tests were done in a temperature range from RT to 800 ºC in air at a strain rate of $7\cdot10^{-3}$ s^{-1}.

3.   RESULTS AND DISCUSSION

The compositions of as-cast Ti-3Al-XSi-XZr alloys studied, and the phases present according to X-ray diffraction are given in Table 1. Microstructures of selected alloys are shown in Fig. 1.

As-cast Ti-3Al-2Si alloy has a typical polycrystalline microstructure of a solid solution of β-transformed Ti (α-Ti) with single particles of the secondary silicides (Fig.1a). Additions of Zr promote the precipitation of the silicide (Fig.1b) and arising the first portion of eutectic (Fig.1c). Ti-3Al-2Si-5Zr and Ti-3Al-2Si-15Zr are two-phase alloys consisting of α-Ti and Ti_5Si_3 and α-Ti and $(Ti,Zr)_2Si$ phases, respectively (Table 1).

Table 1. Phases present in as-cast Ti-3Al-XSi-XZr alloys

| Alloy	Phase composition	Alloy	Phase composition
Ti-3Al-2Si	α-Ti	Ti-3Al-4Si-12Zr	α-Ti+ Ti$_5$Si$_3$+(Ti,Zr)$_2$Si
Ti-3Al-2Si-5Zr	α-Ti+Ti$_5$Si$_3$	Ti-3Al-4Si-15Zr	α-Ti+(Ti,Zr)$_2$Si
Ti-3Al-2Si-8Zr	α-Ti+Ti$_5$Si$_3$+(Ti,Zr)$_2$Si	Ti-3Al-6Si	α-Ti+Ti$_5$Si$_3$
Ti-3Al-2Si-15Zr	α-Ti+(Ti,Zr)$_2$Si	Ti-3Al-6Si-5Zr	α-Ti+Ti$_5$Si$_3$
Ti-3Al-4Si	α-Ti+Ti$_5$Si$_3$	Ti-3Al-6Si-12Zr	α-Ti+Ti$_5$Si$_3$+(Ti,Zr)$_2$Si
Ti-3Al-4Si-5Zr	α-Ti+Ti$_5$Si$_3$	Ti-3Al-6Si-18Zr	α-Ti+(Ti,Zr)$_2$Si
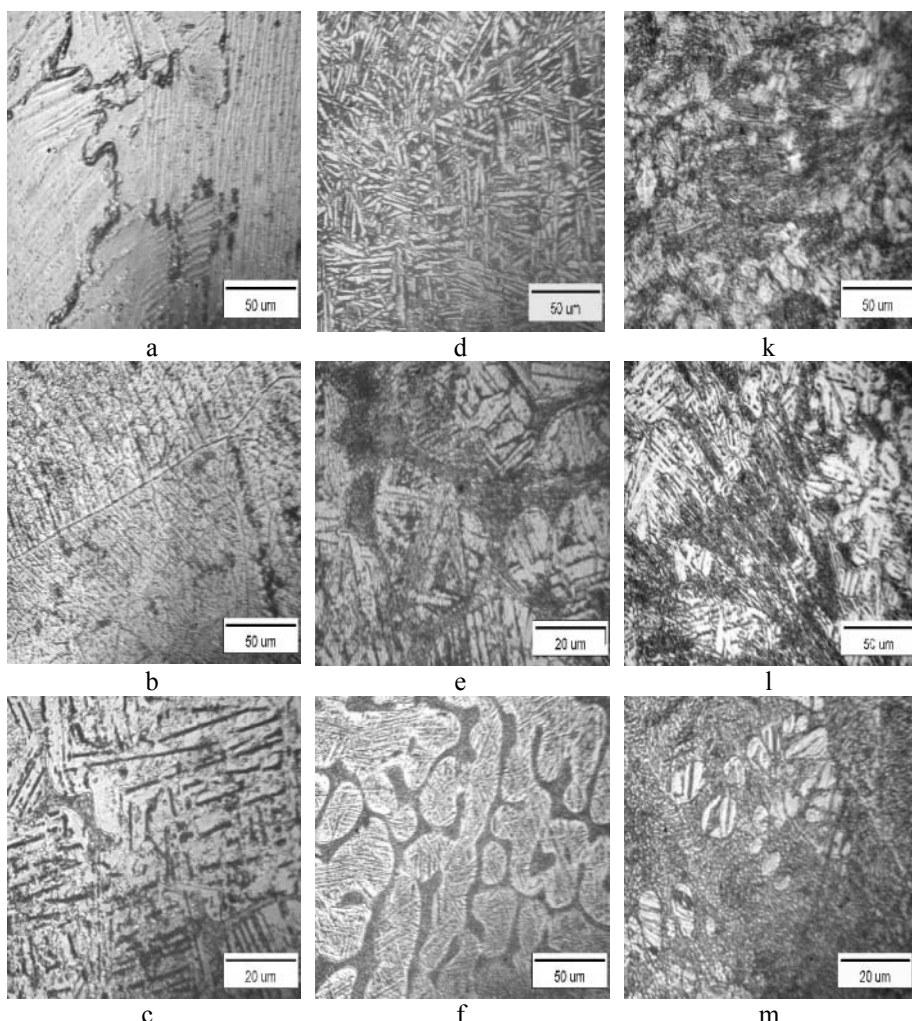
Figure 1. Microstructure of as-cast Ti-3Al-XS-XZr alloys: a - Ti-3A-2Si, b - Ti-3Al-2Si-5Zr, c - Ti-3Al-2Si-15Zr, d – Ti-3Al-4Si , e - Ti-3Al-4Si-5Zr, f - Ti-3Al-4Si-15Zr , k – Ti-3Al-6Si, l - Ti-3Al-6Si-5Zr, m - Ti-3Al-6Si-18Zr alloys. Optical micrographs.

Hypoeutectic Ti-3Al-4Si and Ti-3Al-6Si alloys have a dendrite-like microstructure with eutectic colonies between dendrites, which is typical for alloys of the Ti-Si-system (Fig. 1e,k). The introduction of Zr to these alloys results in both refinement of the alloy microstructure and the eutectic silicides, and a changing of phase composition (Table 1). Another type of eutectic based on the ternary $(Ti,Zr)_2Si$ silicides is formed in hypoeutectic alloys containing a high content of Zr (Fig. 1m).

The dependence of Vickers hardness of alloys under investigation vs. Zr content is demonstrated in Fig. 2. It is seen that Vickers hardness of as-cast Ti-3Al-2Si alloy decreases with Zr additions. For hypoeutectic Ti-3Al-4Si and Ti-3Al-6Si alloys a non-monotonous dependence is observed.

It is known that zirconium additions decrease the silicon solubility in the titanium-based solid solution and promote silicide precipitation and eutectic formation [2]. Therefore, superposition of a number of strengthening mechanisms such as solid solution hardening, composite reinforcement and dispersion strengthening defines the complicated character of the dependence of Vickers hardness vs. Zr content for the alloys studied. One can see a decrease of Vickers hardness of as-cast Ti-3Al-2Si alloy in the solid solution state and a non-monotonous dependence of Vickers hardness for hypoeutectic alloys with increasing Zr content (Fig. 2). The Vickers hardness of the near eutectic Ti-3Al-6Si-18Zr alloy based on a refined α-Ti+$(Ti,Zr)_2Si$ eutectic is the highest (Fig. 2, Fig. 1m). Three-phase Ti-3Al-4Si12Zr and Ti-3Al-6Si-12Zr alloys have the lowest values of Vickers hardness.
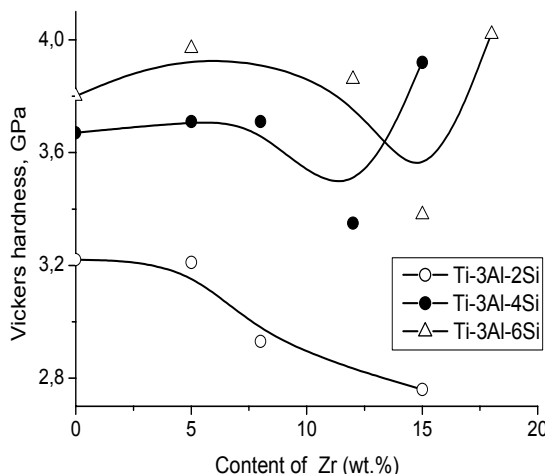
Figure 2. The effect of Zr on Vickers hardness of as-cast Ti-3Al-XSi alloys

The temperature dependencies of strength and plasticity of as-cast Ti-3Al-XSi (where X=2,4,6- wt.%) alloys vs. Zr content are shown in Fig. 3. Zr additions increase the high temperature strength and decrease the RT plasticity of the alloys. The temperature dependence of plasticity of Ti-3Al-XSi alloys with Zr exhibits a typical brittle-to-ductile behaviour.

The ultimate tensile stress (UTS) of hypoeutectic Ti-3Al-6Si-18Zr based on α-Ti+(Ti,Zr)$_2$Si eutectic is the highest one measured in the temperature range from RT to 400 °C. A dramatic increase in plasticity of this alloy is observed at 750 °C. Hypoeutectic Ti-3Al-6Si-5Zr based on the α-Ti+Ti$_5$Si$_3$ eutectic demonstrates high strength and intermediate plasticity in the temperature range of 400-600 °C. The long-term hardness of this alloy is the best at 500 and 700 °C in comparison with all other alloys studied (Table 2).

a   b   c
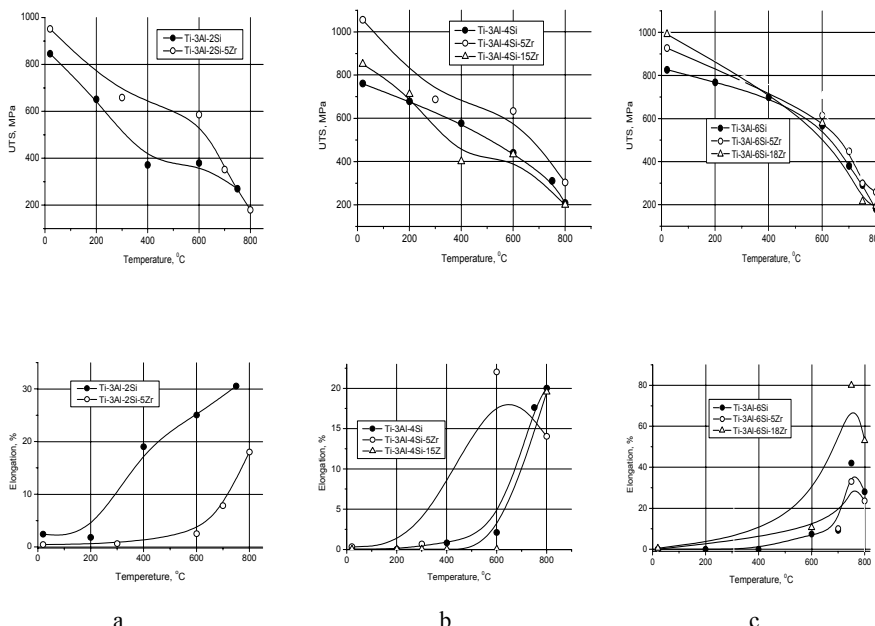
Figure 3. Mechanical properties of as-cast Ti-3Al-XSi alloys with different content of Zr: a - Ti-3Al-2Si , b – Ti-3Al-4Si, c – Ti-3Al-6Si alloys

Table 2. Long-term hardness of selected as-cast Ti-3Al-XSi-XZr alloys, GPa

Alloy	Temperature, °C	
	500	700
Ti-3Al-2Si	1.5	0.6
Ti-3Al-4Si	2.2	0.8
Ti-3Al-6Si	2.5	0.5
Ti-3Al-4Si-5Zr	2.0	0.8
Ti-3Al-6Si-5Zr	2.7	1.1
Ti-3Al-6Si-18Zr	2.8	0.5

4.   SUMMARY

It is shown that alloying with Zr Ti-3Al-XSi (where X=2, 4, 6- wt.%) alloys provides important refinement of the alloy microstructure and formation of ternary $(Ti,Zr)_2Si$ silicides. Alloys with high Zr content have a refined microstructure based on the $(\alpha\text{-}Ti +(Ti,Zr)_2Si)$ eutectic. Such alloys demonstrate high strength at RT and up to 400 ^{0}C. Hypoeutectic alloys with 5-wt.% Zr reinforced by Ti_5Si_3 silicides are characterized by higher strength in a temperature range from 500 ºC to 600 ºC.

ACKNOWLEDGEMENTS

REFERENCES

1. Bankovsky O., Gornaya I., Kulak L., Firstov S. (2003) Structure and properties of eutectic alloys of Ti-Al-Si-Zr system. In: Proc. of the VI Int. Conf. on Eutectics, 23-26 October 2003, Zaporozh`e,Ukraine, pp. 226-229. (In Russian)
2. Salpadoru N.H., Flower H.M. (1995) Phase equilibria and transformations in a Ti-Zr-Si system. Metall. Mater. Trans**., 26A**, 243-257.
3. Popov A.A., Drozdova N.A. (1997) Principles of alloying of two-phase high-temperature alloys based on Ti.–Fizika Metallov Metallov., **84**, 123-131. (In Russian)
4. Bulanova M., Tretyachenko L., Mileshevich K. et al. (2002) Joint influence of zirconium and silicon on the structure and properties of Ti and Ti-Al alloys. In: Coll. Abstracts of the VIII Int. Conf. on Crystal Chemistry of Intermetallic Compounds, Lviv, Ukraine, p. 40.

HIGH-TEMPERATURE FATIGUE CRACK GROWTH RESISTANCE OF THERMO-MECHANICALLY AND HEAT TREATED CAST Ti-Si-Al-Zr COMPOSITES

B. Vasyliv[1], A. Ivasyshyn[1], O. Ostash[1], S. Firstov[2], V. Mazur[3], M. Kuzmenko[2], S. Kapustnikova[3]

(1) Karpenko Physico-Mechanical Institute of NAS of Ukraine, Lviv
(2) Frantcevych Institute for Problems of Materials Science of NAS of Ukraine, Kyiv
(3) National Metallurgical Academy of Ukraine, Dnipropetrovsk

Abstract: Fatigue crack growth resistance of Ti-4Si-4Al-5Zr composites have been investigated at room and elevated (500°C, 700°C and 800°C) temperatures. Various modifications were manufactured with electron-arc smelting, the thermo-mechanical deformation (of 41 % and 90 %) and heat treatment (quenching). It was found that the high-temperature effect on the crack growth in the materials tested is negligible in threshold (ΔK_{th}) and critical (ΔK_{fc}) regions of the $da/dN - \Delta K$ diagram and the maximum acceleration of the crack growth occurs in the middle ΔK region. The satisfactory fatigue crack growth resistance at temperatures of $500\,^{\circ}\text{C}$ and $700\,^{\circ}\text{C}$ has been observed in thermodeformed modifications but thermo-mechanical treatment causes the increase in fatigue crack growth resistance at high ΔK level and its decrease at low ΔK level. Microstructure and failure micromechanisms have been analysed in accordance with crack growth resistance of the composites.

Key words: Ti-based composites, fatigue crack growth, high temperature

1.   INTRODUCTION

An operating temperature of conventional titanium alloys is limited by $300 - 500$ °C. The known Ti-based composites possess high strength under

tensile and bend loading, fracture toughness under static loading in the temperature range from 20 °C up to 600 – 650 °C [1, 2], but there is the need to increase the operating temperature range of their utilization up to 700 – 800 °C. Owing to their high strength-to-weight ratio, these composites offer the potential for promising improvements in component design for engines (aircraft, rocket and internal combustion) as well as for other power equipment (gas turbines, compressors etc.). However, there is the significant difference (up to 5 times) between long-term static and cyclic crack growth resistance threshold parameters of composites [3]. Moreover, there are few results on corrosion fatigue behaviour of microstructural heterogeneous composites reinforced by particles. Like conventional titanium alloys the titanium-matrix composites are sensitive to the influence of hydrogenous service environment if fatigue cracks appear in the stressed composite parts. Therefore it is important to elaborate structural materials with improved fatigue crack growth resistance in wide temperature range (up to 700 – 800 °C), which are insensitive to the influence of corrosion and hydrogenous environments.

The objective of the first stage of this work is to evaluate reliability of Ti-Si-Al-Zr composites using the fatigue crack growth resistance (FCGR) data (fatigue crack growth rates, da/dN, versus stress intensity factor range, ΔK, dependences) obtained in the temperature range of industrial composite parts operation.

2.   MATERIALS AND TEST PROCEDURE

Modifications of Ti-4Si-4Al-5Zr composite manufactured with electron-arc smelting (variants M0 and T0) and using the thermo-mechanical deformation of 41 % and 90 % (variants M4 and T1, respectively) and also heat treatment (quenching) after casting (variants M01 and M022) have been examined (see Table 1 and Fig. 1).

Table 1. Chemical composition and treatment of composites.

Modification	Alloying elements, %				Thermo-mechanical deformation	Heat treatment
	Si	Al	Zr	Fe		
M0	4.0	4.87	5.33	1.28	–	–
M4	4.0	4.87	5.33	1.28	1050°C, 41%	–
T0	3.8	3.1	4.7	–	–	annealing 650°C, 2h
T1	4.0	3.5	5.5	–	1050°C, 90%	annealing 600°C, 2h
M01	4.0	4.87	5.33	1.28	–	quenching 860°C, water
M022	4.0	4.87	5.33	1.28	–	quenching 1000°C, oil

The single edge specimens were loaded under three-point bending at cyclic frequency of 10 Hz, stress ratio of 0.1. The FCGR tests were carried out in the laboratory air at the temperature of 20 ˚C and 700 ˚C. Several control tests of the composites were performed at the temperature of 800 ˚C. Optical and scanning electronic microscopy was used for analysis of microstructure and fracture micromechanisms of the materials.
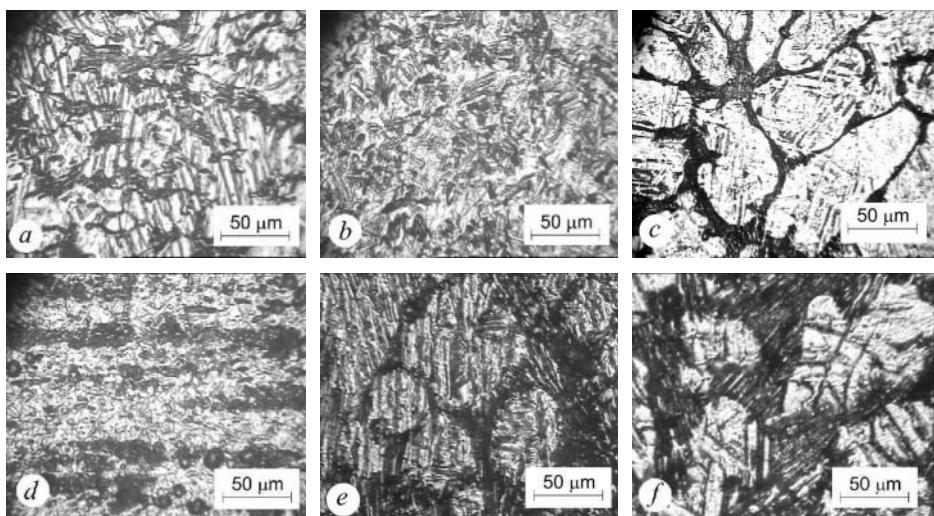
Figure 1. Microstructures of (a) M0, (b) M4, (c) T0, (d) T1, (e) M01 and (f) M022 modifications.

3. RESULTS AND DISCUSSION

In general the influence of high temperature on the crack growth peculiarity in tested materials depends on ΔK range (Fig. 2). It is negligible in threshold (ΔK_{th}) and critical (ΔK_{fc}) regions of the $da/dN - \Delta K$ diagram and the maximum acceleration of the crack growth occurs in the middle ΔK region. The cast modifications after quenching in the oil and in the water are the most sensitive to the negative influence of high temperature. The satisfactory fatigue crack growth resistance at high temperatures of 500 ºC and 700 ºC is demonstrated by cast and thermodeformed modifications.

It is shown that in base M0 and T0 modifications α-Ti grains plate structure dominates (Fig. 1 *a,c*). Owing to annealing at 650 ºC T0 modification has less percentage of secondary phase and bigger α-Ti grains in comparison with M0 modification. The main fracture mechanism in Region I of $da/dN - \Delta K$ diagram is α-titanium quasicleavage which is supported by localized microcracking of ceramic phase. As a result the threshold ΔK level (4 MPa·√m) of T0 modification at room temperature is

lower than of M0 modification (5 MPa·√m) because the crack growth through α-grains requires less energy than through the secondary phase. Besides, in the fine structure the crack growth decelerates due to frequent changing of a sliding plane. Such prevalence of the fine-grained modification is lost gradually with the increase of process zone size when SiO_2 phase microcracking occurs [4]. Rough fracture surface of T0 modification distinguished with coarse grains and higher critical ΔK_{fc} level (17 MPa·√m) demonstrate that this fracture micromechanism becomes dominant during Region II to III transition.
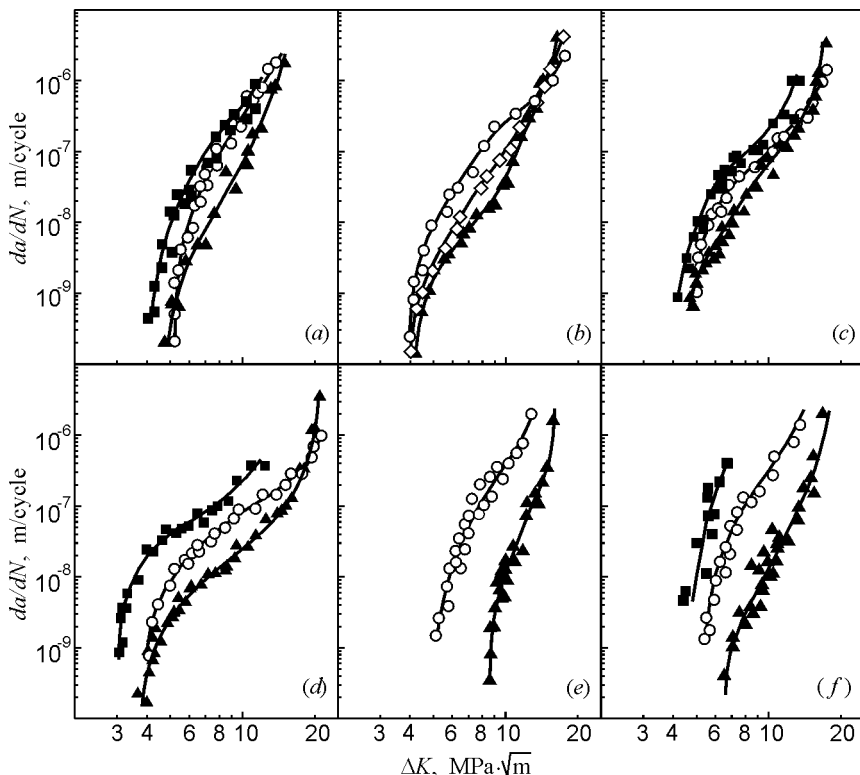
Figure 2. Fatigue crack growth rates, *da/dN*, versus stress intensity factor range, ΔK, for (*a*) M0, (*b*) M4, (*c*) T0, (*d*) T1, (*e*) M01 and (*f*) M022 modifications at temperatures 20°C (▲), 500°C (◇), 700°C (○) and 800°C (■).

At room temperature thermo-mechanically treated M4 and T1 modifications showed the higher crack growth resistance in Region II and especially in Region III (ΔK_{fc} = 21 MPa·√m for T1 modification) (Fig. 3 *a*). Crack growth rates in Region III for T1 modification is much lower than for cast materials because there are no large eutectic regions and globular particles of eutectic is evenly distributed in the matrix (Fig. 1 *c,d*).   The

mixed-type fracture along the Ti-grains and through little silicide particles is seen in Region III in contrast to cast modifications. Thermodeformed modifications trade off the cast ones in Region I what is connected also with the decrease of the crack closure in fine-grained material.
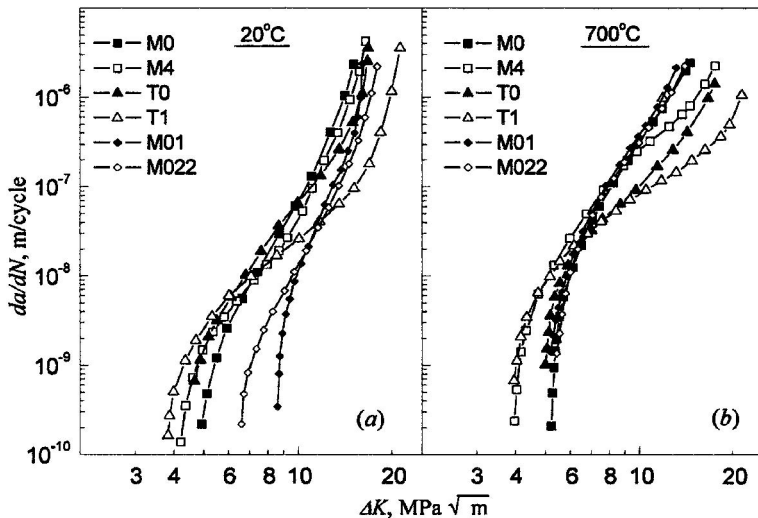
Figure 3. Comparison of FCGR of Ti-4Si-4Al-5Zr composites.

Heat treated (as-quenched) M01 and M022 modifications showed higher level of crack growth resistance in threshold region (ΔK_{th} is 6.6 and 8.5 MPa·√m for M022 and M01, respectively) in comparison with M0 (Fig. 3). It can be explained by the increase of Ti-grain size and some changes of ceramic phase structure (Fig. 1 *e, f*). In high-amplitude region FCGR of these modifications ($\Delta K_{fc} = 18 - 19$ MPa·√m) is almost the same as for M0 and T0 modifications but less than for T1 (Fig. 3).

The results obtained at 700 °C show that the common trends of FCGR advancing by thermo-mechanical treatment did not change (Fig. 3 *b*). In general material does not lose FCGR taking into account the threshold ΔK_{th} and critical ΔK_{fc} values. The fatigue crack growth mechanism due to void coalescence dominates here [5, 6]. The oxide film formed under long-term cyclic loading on the crack surface near its tip causes the crack closure effect and this effect counteracts the threshold ΔK_{th} decrease, because without the crack closure the fatigue crack growth rate would accelerate due to easy sliding near the crack tip. In the near threshold region *da/dN − ΔK* curves are more headlong because the effect of the crack closure quickly decreases with the increase of ΔK. Owing to SiO_2–phase softening [4] high-temperature plastic fracture mechanisms dominate at high ΔK values. These mechanisms

ensure the cyclic fracture toughness ΔK_{fc} on the level determined at room temperature.

The increase of threshold ΔK_{th} values established at room temperature for heat treated M01 and M022 modifications in comparison with M0 and T0 modifications disappears at the temperature of 700 $^{\mathrm{o}}$C (Fig. 3 *b*).

Particular investigations of composites at the temperature of 800 $^{\mathrm{o}}$C confirmed the domination of the mentioned above fracture micromechanisms. At this temperature only cast modifications without thermo-mechanical and heat treatment still have satisfactory fatigue crack growth resistance.

4.   CONCLUSIONS

Ti-4Si-4Al-5Zr composites after quenching in the water and in the oil demonstrate at room temperature high threshold ΔK_{th} (up to 9 MPa·√m).

The maximum acceleration of fatigue crack growth at elevated temperatures (500°C, 700°C and 800°C) occurs in the middle ΔK region of $da/dN - \Delta K$ curves.

Thermo-mechanical deformation (up to 90%) of cast Ti-4Si-4Al-5Zr composites causes the increase in their fatigue crack growth resistance at high ΔK level ($\Delta K_{fc} = 21 - 22$ MPa·√m) but decreases it at low ΔK level ($\Delta K_{th} = 3.5 - 4.0$ MPa·√m).

REFERENCES

1. V.I. Mazur, Y.N. Taran, S.V. Kapustnikova, S.A. Firstov et al., US Patent, 5366570, 1994.
2. F.W. Crossman, A.S. Yue, Metall. Trans. **2**(6), 1971, 1545.
3. O. P. Ostash., A. D. Ivasyshyn, B. D.Vasyliv et al., Materials Science, **38** (1), 2002, 55.
4. G. Frommeyer, R. Rosenkranz, C. Ludecke, Metallkunde, **81**(5), 1990, 307.
5. S.A. Firstov, N.N. Kuzmenko, Y.N. Podrezov et al., in: Proc. XXXVII Int. Sem.”Topical Problems of Strength”, Kyiv, 3-5 July 2001, p. 253 (in Russian).
6. O.I. Ban'kovsky, O.D. Vasylyev, L.D. Kulak et al., in: Proc. XXXVII Int. Sem.”Topical Problems of Strength”, Kyiv, 3-5 July 2001, p. 356 (in Ukrainian).

STRUCTURE AND FRACTURE FEATURES OF TI-SI- AND TI-B-BASED IN SITU COMPOSITES

Oleksandr D. Vasylyev and Mykola D. Bega
Frantcevych Institute for Problems of Materials Science
3, Krzhyzhanivskoho Str., Kyiv-142, 03680, Ukraine

Abstract: The data on structure and mechanical behavior of Ti-Si-composites with different silicon content, both binary and alloyed with 3-wt.% Al and 5-wt.% Zr, as well as of some Ti-B-composites are given. At general embrittling influence, 2-3-wt.% of silicon is critical for as-cast titanium that results in near zero plasticity and intergranular fracture at room temperature. Hot deformation suppresses this silicon effect increasing room temperature ductility from zero to ~16 % in binary alloy and to 4% in Ti-3Al-5Zr one at 2-wt.% Si. Strength of deformed alloys increases with silicon from ~800 to 1000-1050 MPa reaching its saturation at around 4.0-wt.% Si. Reinforcing titanium with borides and jointly with borides and silicides shows clearly that Young modulus near 160 GPa at 1500 MPa strength and 2-4 % room temperature ductility may be ensured.

Key words: Titanium in-situ composites, discontinuous reinforcement, silicide reinforcement, boride reinforcement, mixed silicide-boride reinforcement, ductile reinforcement, microstructure, α'-phase, β-phase, mechanical properties, fracture mechanisms.

1. INTRODUCTION

Research and development in the aerospace industry have revitalized interest in structural metals with high specific properties. Specific strength and stiffness are two mechanical characteristics, which are the most important for nearly each structural component of aerospace systems.

Titanium-based composites discontinuously reinforced with silicides, borides and their mixtures are an attractive candidate to be a material with

high structural efficiency for a wide range of applications owing to their high specific strength and stiffness, high working temperature and good fracture-related properties. But their practical use is still limited by low ductility at low temperatures.

Titanium composites offer significant increases in specific stiffness relative to the matrix alloy. However, only limited data is available in the literature for this new class of materials. The Ti-Si-system is considered as more developed ensuring tensile strength 1150 MPa, ~4 % elongation and ~135 GPa Young modulus at room temperature [1]. Data available on the Ti-B-system shows the same level of strength at near zero plasticity with sintered Ti-6Al-4V/TiB composite containing ~40 vol. % of reinforcing TiB phase. It is important that its Young modulus is near 210 GPA [2]. Concerning the properties of as-cast Ti-B-composites literature notes, e.g., "because of …low fiber volume fraction the directionally solidified Ti-TiB eutectic showed no significant fiber reinforcement of the composite structure". The calculated volume of TiB in the titanium rich matrix was 7.7 % at eutectic 1.7 wt. % boron content [3].

The purpose of the work given was to study the features of structure and mechanical behavior of Ti *in-situ* composites reinforced with silicide, boride and their joint phases arising in Ti-Si and Ti-B-systems being in as-cast and deformed states.

2.   MATERIALS AND METHODS

All the alloys studied were smelted on a base of commercial titanium alloy of technical purity BT1-0 (Fe<0.25; Si<0.1; C<0.07; N<0.04; O<0.2; others<0.3. Compositions are provided in wt. %) with plasma-arc method in argon atmosphere. The BT1-0 alloy itself is determined as pseudo α-alloy, which has coefficient of β-phase stabilization $k_\beta = 0.05$ [4, 5]. Temperatures of smelts were between 1620-1660 $^\circ$C. Liquid metal was decanted into graphite mold inside of melting chamber. Obtained cylindrical ingots of 60 mm diameter and 150-400 mm length were cooled to 600 $^\circ$C inside of chamber and after that to room temperature in air outside of equipment.

Alloys were forged in such a way [6]. Their blanks were turned to cylinders of 58 mm diameter, sealed in steel pipe and heated at first from room temperature to 900 $^\circ$C in electric air furnace together with it during 1 hour. After that blanks were carried manually from the electric furnace into gas one where they were heated up to 1100 $^\circ$C. Blanks heated at this temperature for 1 hour were forged manually to 90% power of deformation.

Cylindrical specimens with fillets were used for mechanical tests at uniaxial tension. Their working length and diameter were 15 mm and 3±0.01

mm respectively. Surface of their working part was polished with diamond abrasive. Samples were annealed at 800 $^\circ$C for 1 hour in vacuum 10^{-3} Pa.

Tensile strength and elongation at the loading rate of $1.2 \cdot 10^{-3}$ s^{-1} were measured in air with universal testing machine U2 manufactured by the former NIIKIMP, the Russian Federation.

Fracture mechanisms and microstructure as well as distribution of chemical elements along it were studied with scanning electron microscopy (SEM) and X-ray microanalysis (XRMA) using Superprobe-733, JEOL, Japan, after deep electrolytic etching with an etchant based on acetic acid. X-ray diffraction phase analysis was done with DRON diffractometer, Burevestnik, the Russian Federation.

3.   RESULTS AND DISCUSSION

3.1   Binary Ti-Si-System

The data on elongation (δ) and tensile strength (UTS) of binary Ti-Si system tested at room temperature (RT) together with literature data [7] are summarized in Fig. 1. As it is seen an increase of silicon content to 2.0-wt.% decreases plasticity of as-cast BT1-0 alloy from around 6 % practically to zero whereas its strength increases from around 762 MPa to 892 MPa. Further increase of silicon content result in some negligible increase of plasticity and strong increase of strength up to 982 MPa where it reaches its maximum at 4.0-wt.% Si. At 5.7-wt.% Si Ti-alloy has around zero plasticity and decreased to 851 MPa strength.

Hot plastic deformation with forging changes the behavior of all alloys of the Ti-Si-system favorably. As it is seen the elongation of forged alloys decreases with silicon increase not so drastically as in as-cast state namely from 31-32% in original BT1-0 alloy only to 8-9% in Ti-5.7wt.% Si alloy practically monotonously. There is no more well-known drop of plasticity to zero at around 2-wt.% Si [1, 7]. At 2.0-wt.% Si deformed Ti-Si-alloy has 16-17% plasticity. Strength of deformed Ti-Si-alloys increases monotonously too from ~800 MPa of the original BT1-0 alloy to ~1050 MPa at 5.7-wt.% Si with no maximum at 4.0-wt.% Si.

Study of structure and fracture micromechanisms give us the clear answer on the question on the reasons of such the behavior of titanium in dependence on silicon in it. There is no place to demonstrate all the sequential changes of structure observed in Ti with different silicon content increase however at least the only must be outlined here: An increase of silicon content result in visible decrease of grain size as well as an arise of

film-like titanium-silicides eutectic along them at 2.1-wt.%. The further increase of silicon makes the polygonal structure is visible at ~3.0-wt.%.
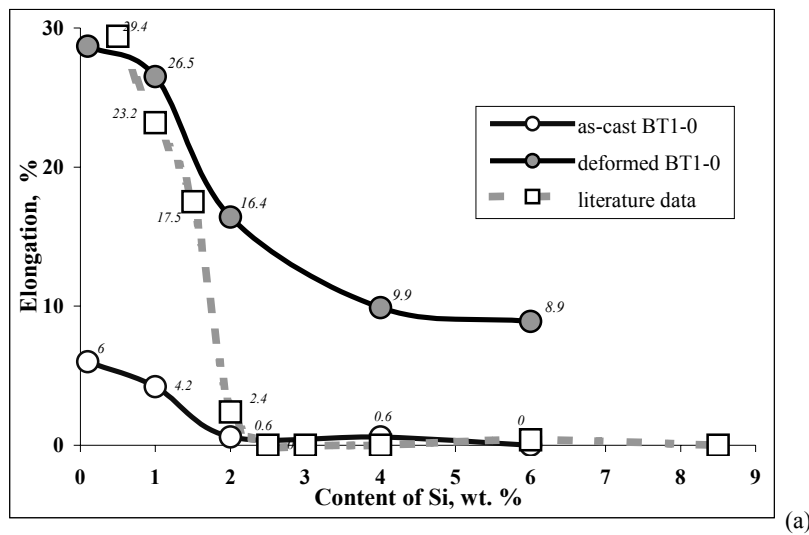

(a)
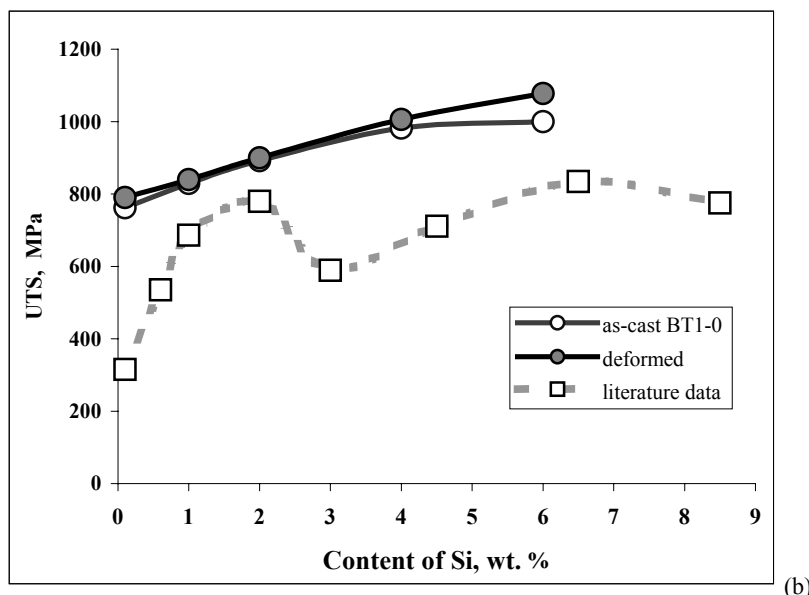
(b)

Figure 1. (a) Room temperature elongation, and (b) tensile strength, UTS of binary Ti-Si-alloys vs. silicon content. Literature data is [6].

At ~4- and higher wt.% Si the transition from polycrystalline structure to dendritic-eutectic one must be recognized. The Ti-silicide eutectic is disposed between α'-dendrites. In general, the structure of Ti-Si-composite with silicon content ~2-wt.% and higher is heterogeneous. It consists of polygonal grains (dendrites) and Ti-silicide eutectic along them. Body of grains (dendrites) consists of at least three phases - α-lamellas, β-phase along them and silicides of solid solution decomposition of probably two kinds, namely precipitating at upper and lower transus temperature (Fig. 2). Fractographical study strengthens the impression arising from structural one. It was found the samples with ~2-3.5-wt.% Si, which have near zero plasticity, fail with clear intergranular fracture mode (Fig. 3). Their strength is the lowest. The higher portion of intergranular failure mode in the fracture the lower strength the sample has, though the strength of titanium alloyed with silicon is higher of pure titanium in general (Fig.1b). Samples with lower than 2-wt.% Si fail with ductile mode (void coalescence). Samples with 4- and higher wt.% silicon fail with mixed modes – cleavage along dendrites and void coalescence along interdendritic eutectics. Dendritic structure in fracture is recognized well.

Hot plastic deformation does change radically the appearance of fractures of these alloys and hence their fracture micromechanisms. All the deformed Ti-Si-alloys fail with ductile "cup and cone" way evidencing their high ductility.
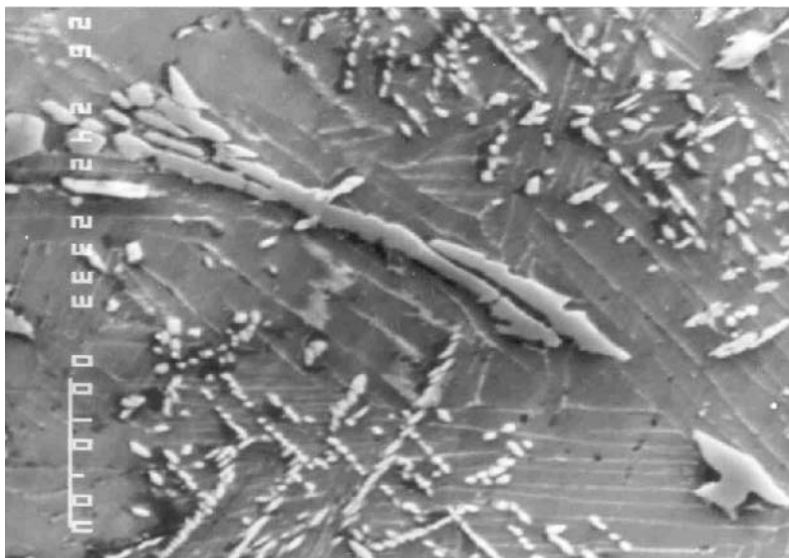

Figure 2. SEM view of structure of deeply etched sample of as-cast Ti-5.7Si-alloy.
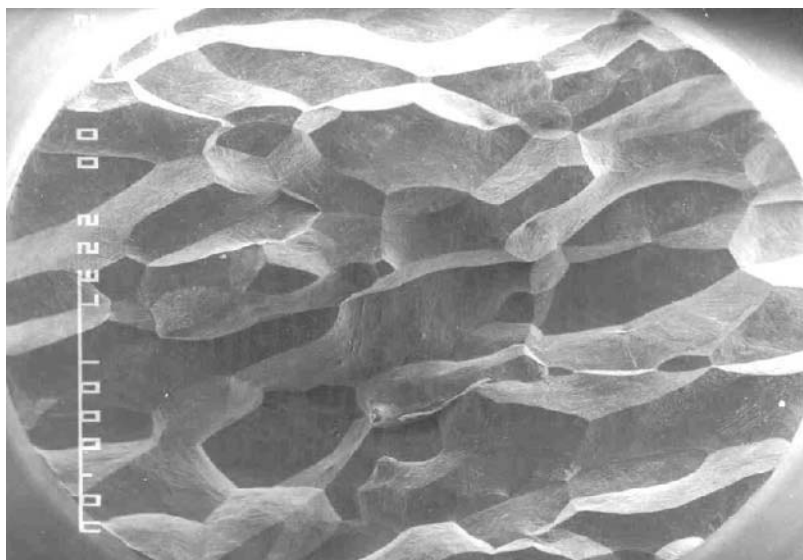
Figure 3. SEM view of fracture of as-cast Ti-3.0 Si-alloy.

3.2   Complex Ti-3Al-5Zr-Si System

The above study shows clearly that alloying titanium of technical purity (alloy BT1-0) with silicon may ensure tensile strength around 1050 MPa at around 9 % of elongation (Fig. 1). It means that a margin to enhance these properties with alloying by other elements like aluminum and zirconium traditionally introduced to improve high temperature properties of titanium.

Three alloys Ti-3Al-5Zr with 2, 4 and 6-wt.% [1] Si were studied. It was found that properties of these alloys may be enhanced seriously with hot plastic deformation [1]. Alloy with ~2-wt.% Si being deformed may ensure room temperature ductility (elongation) near 4% (Fig. 4) at around 1150 MPa tensile strength. However the reasons of this phenomenon were not clear and had required the further study. It was established with XRMA that the refinement of complex alloyed Ti-Si-*in situ* composite with hot plastic deformation, especially containing 2-wt.% Si, results from not only dispersion of eutectic silicides Ti_5Si_3, however mostly refinement of α-solid solution for silicon, formation of Ti_2Si eutectoid of solid solution decomposition, increasing of volume of β-phase along α'-lamellas. In its turn it results in suppression of intergranular fracture for transgranular ductile void coalescence and increasing room temperature ductility (Fig. 4). Figure 5 shows structure of deformed composite demonstrating pronounced

---

[1] Amounts of alloying elements are approximate and may differ by several tenths.

β-phase in view of rather thick interlayers (soft ductile gaskets) between α′-lamellas and pieces of silicide bars of hexagonal cross-sections.
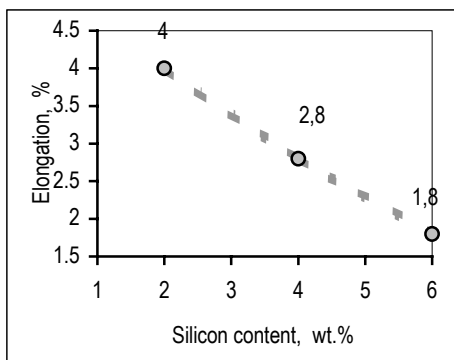

Figure 4. Room temperature plasticity (elongation at uniaxial tension) of 90 % forged Ti-3Al-5Zr vs. silicon content.
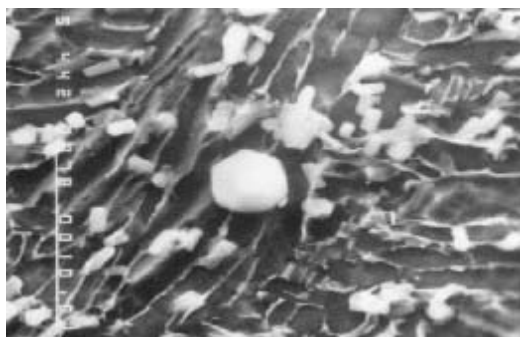
Figure 5. SEM view of structure of deformed Ti-3Al-5Zr-2Si-alloy.

Precise x-ray phase analysis has confirmed the presence of all the phases observed with electron microscopy. Moreover it is evidence of arise of the second silicide phase close to Ti_2Si (S_2) except of Ti_5Si_3 (S_1) after plastic deformation as well as after additional annealing (Fig. 6). It is become obvious why β-phase, which is well-visible with both light and electron, SEM and TEM, microscopies, is not observed with conventional x-rays analysis of the Ti-Si-alloys. The answer is very simple. Comparing Fig. 6 and Fig. 7 it is seen that the reflex referencing to β-phase is overlapped by one of the S_2 reflexes that does it invisible.

As to the chemical composition of phases, one sample of it is shown in Table 1. In spite of all the problematicity of chemical microanalysis of such a kind it is seen that except silicides silicon and zirconium prefer β-phase.

Iron likes β-phase too. These data show directly that silicon, zirconium and iron are β-stabilizers. Please note too that content of silicon in eutectic is 0.5-0.6-wt.% that is exact as Ti-Si-phase diagram predict [8].

Comprehensive structural study of Ti-3Al-5Zr-Si-alloys, as-cast and deformed, confirmed the features found with the binary Ti-Si-system described above. The transition from polygonal to dendritic structure takes place between 2- and 4-wt.% Si. Alloy with 2-wt.% Si fails with intergranular (but ductile) mode whereas alloys with 4- and 6-wt.% fail with mixed mode where dendritic structure may be recognized. In any case, eutectic areas, in contrast to dendrite or polygonal bodies, which are of α-phase failing with cleavage microcracking, fail with ductile mode – with voids coalescence (Fig. 8). Hot plastic deformation transforms the alloys studied into ductile or semi-ductile materials, which fail only with ductile void coalescence mode [1].

Table 1: Compositions of structural constituents in as-cast +2Si alloy.

Name of structural unite		Chemical element, wt. %			
		Al	Si	Zr	Fe
Matrix of α'-lamellas		3.2 ÷ 3.3	0.6 ÷ 1.3	2.1 ÷ 3.4	0.03 ÷ 0.04
β-Interlayers		2.4 ÷ 2.8	1.1 ÷ 3.6	2.9 ÷ 7.8	0.1 ÷ 0.5
Secondary silicides, S_2, $(Ti,Zr)_x(Si,Al)_y$	wt.%	2.3 ÷ 2.7	1.7 ÷ 4.3	4.2 ÷ 8.9	0.04 ÷ 0.1
	at.%	*4.1 ÷ 4.8*	*2.9 ÷ 7.4*	*2.2 ÷ 4.7*	*0.04 ÷ 0.08*
Eutectic silicides, S_1, $(Ti,Zr)_5(Si,Al)_3$	wt.%	0.7 ÷ 1.8	7.0 ÷ 23.9	6.6 ÷ 28.0	0.1 ÷ 0.4
	at.%	*1.2 ÷ 3.2*	*11.8 ÷ 35.7*	*3.1 ÷ 15.1*	*0.08 ÷ 0.16*
Matrix between eutectic silicides		2.8 ÷ 3.1	0.5 ÷ 0.6	1.2 ÷ 1.9	0.01 ÷ 0.04
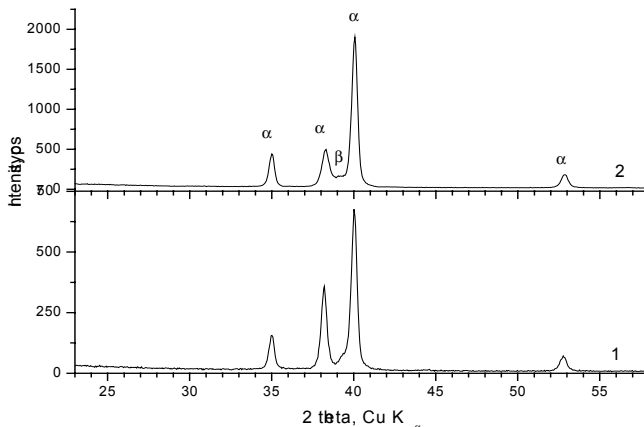
Figure 6. X-ray spectrum of BT1-0 alloy. 1 – as-cast, 2 – forged.
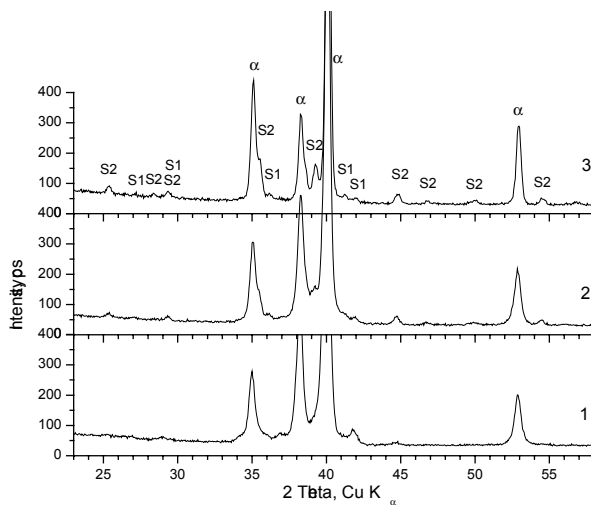
Figure 7. X-ray spectrum of Ti-3Al-5Zr-2Si based on BT1-0.
1 – as-cast, 2 – forged, 3 – forged+annealed at 800°C, 1 hour.
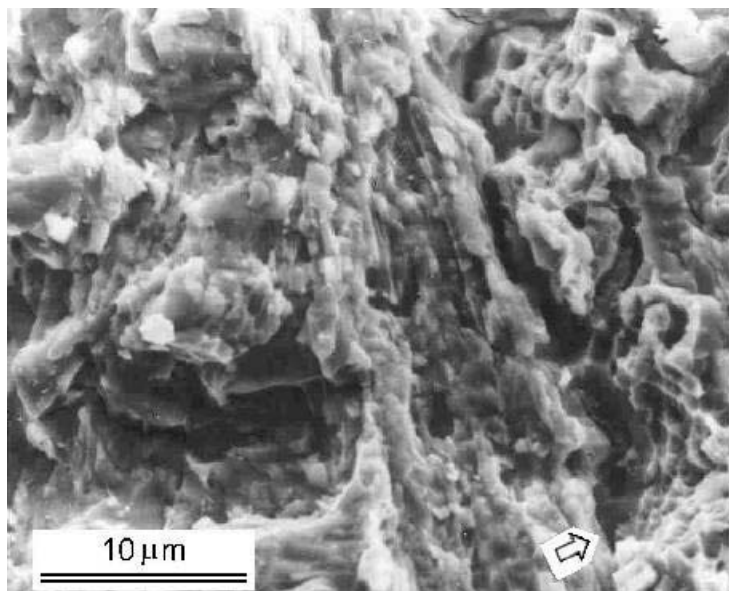
Figure 8. SEM view of fracture of Ti-3Al-5Zr-4Si alloy at 400 °C. Picture shows cleavage microcracking of α′-lamellas, ductile with formation of "knife" fracture of interlamellar β-phase and ductile void coalescence of eutectic between dendrites (shown by arrow).

3.3   Binary Ti-B and Complex Ti-6.6Al-3.5Zr-1.3Si-1.1B Alloys

Table 2 summarizes the best data obtained with binary and complex alloys strengthened with borides, and borides and silicides [9].

Table 2. Mechanical properties of forged discontinuously reinforced Ti-B- and Ti-B-Si-alloys studied.

Property of alloys	Ti-1.6B	Ti-6.6Al-3.5Zr-1.3Si-1.1B
Yield strength, $\sigma_{0.2}$, MPa	944	1469
Strength, UTS, MPa	977	1530
Elongation, δ, %	6.4	1.4
Young modulus, E, GPa	136	158
Fracture mechanism	void coalescence	

It is seen that titanium alloyed with boron and silicon is promising owing to high strength and Young modulus, and has high ductile potential because fails with ductile fracture mode. As to the structural and fractographical features of the alloys studied they are as follows:

Ti-1.6 wt.% B.   In as-cast state, as-dendritic structure is well visible. Structure of matrix is martensite. Borides have rod- and strip-like morphology with hexagonal cross-section. Size of rods is around between 0.1 μm and 3 μm in cross-section and a few hundreds of μm length. Borides have rod- and strip-like morphology of hexahedral cross-section. Size of rods is around 1 μm (or even less) in cross-section and a few hundreds of μm length. These rods form strips or plates of a few hundreds of μm width, which may split like a wood showing weak adhesion between rods. Fracture of alloy at RT is ductile one with portion of cleavage, close to near 50-50%, where matrix between borides fails with void coalescence in general opening rod-like structure of reinforcing phase and its high adhesion with matrix. Cleaved areas look like splitted wood. Fracture of alloy at 500 and 600 ºC is ductile one demonstrating the high adhesion between borides and matrix as well as longitudinal cracking of borides. In as-forged state, martensite structure of matrix is not visible. Crashed borides forms chains of particles of rod and strip (hexagonal in cross-section) morphology. Thickness of strips is less 1 μm. Fracture of alloy at room temperature and 600 ºC is ductile one.

Ti-6.6Al-3.5Zr-1.3Si-1.1B.   In as-cast state, as-dendritic structure is practically invisible. Lamellar α'-structure of matrix is recognized well. Close to uniformly distributed borides have rod-like morphology and fogged like brushwood. Thickness of rods is between 0.1-1.5 μm. Their length is up to 0.2 mm. Fine (0.1-0.3 μm) silicides are uniformly distributed along matrix. Fracture feature is intensive cleavage microcracking of RT and

600 ºC samples. Long borides (even more than 150 µm of length) do not break to peaces under shear stresses but only split along their long axes. Silicides are not distinguished in fracture surfaces at all. Delamination of borides from matrix is not observed that evidences the high adhesion between borides and matrix. In as-forged state, structure of matrix is close to polygonal. Crashed borides form chains of particles of rod and strip morphology. It is strange but it is seen that boride strips are often splitted for three ones. Preliminary qualitative x-ray microanalysis shows that borides are compounds containing, except boron and titanium, all the additives added specially like Al, Si, Zr, and present in the basic BT1-0 alloy like Fe, O and possibly C. Matrix, to our surprise, is pure in comparison with original BT1-0 alloy. Matrix, unexpectedly; consists of Ti, Al, Si, and Zr only. Thickness of silicides likes to as-cast one. Fracture of this forged alloy at room temperature and 600 ºC is ductile one and uniform. It is clear that some unhealed cleavage cracks of matrix as well as broken particles, silicides and borides, may be found yet in both samples.

4.   CONCLUSIONS

1.   Alloying titanium with silicon is influencing on final structure of as-cast alloy. Interval of silicon content 2-3-wt.% is critical. At the critical amount of silicon the Ti-Si-alloy solidifies with formation of polygonal structure with decreasing grain size at increase of silicon content. At higher silicon content structure of the Ti-Si-alloys is dendritic-eutectic one with the titanium-silicide eutectic between dendrites.
2.   Alloying with silicon is embrittling titanium decreasing its room temperature ductility. As-cast titanium may has zero ductility at critical silicon content. The most probable reason of such drastic decreasing of ductility is formation of the first portion of eutectic along polygonal grains at critical 2-3-wt.% value of silicon.
3.   Ultimate tensile strength of deformed alloys of technical purity increases with silicon increase from ~800 to 1000-1050 MPa reaching its saturation at around 4.0-wt.% Si.
4.   Fracture mechanism of the Ti-Si-alloy at the critical content of silicon is intergranular one resulting in both zero plasticity and decrease of yield strength and ultimate tensile strength.
5.   Hot plastic deformation suppresses the negative effect of critical (2-3-wt.%) content of silicon that results in increasing room temperature ductility from zero to ~16 % and keeping it on level not less 9 % at higher silicon content. The reason of this phenomenon is plastifying of solid solution that results in a change of fracture micromechanism from mixed cleavage + void coalescence fracture mode in as-cast state for only void coalescence in

deformed state. Yield stress and tensile strength are enhanced with plastic deformation too.

6.   Additional alloying Ti-Si-alloys with 3-wt.% Al and 5-wt.% Zr does not change the principal influence of silicon on titanium however suppresses strongly its ductility (from ~16% to ~4% at 2-wt.% Si) and enhances slightly tensile strength (for ~100 MPa).

7.   Reinforcing titanium with borides and jointly with borides and silicides especially shows clearly that Young modulus at level of 160 GPa at around 1500 MPa strength and 2-6 % room temperature plasticity may be ensured. It is important that all the alloys studied being in deformed state fail with ductile mode that, in its turn, points out that mechanical properties of alloys may be enhanced with optimization of structure. It is important too that volume of reinforcing phase is unexpectedly high, roughly in 2-3 times, in comparison with predicted by the equilibrium phase diagram.

ACKNOWLEDGEMENTS

REFERENCES

1. S. Firstov, L. Kulak, D. Miracle et al. 8-th Annual International Conf. on Composites Engineering ICCE/8, Aug. 5-11, 2001, Tenerife, Canary Islands, Spain. Ed. D. Hui, p. 245-246.
2. S. Gorsse, D. Miracle: Acta Materialia (2003), to be published. F.W. Crossman, A.S. Yue: Met. Trans. Vol. 2 (1971), p.1545.
3. F.W. Crossman, A.S. Yue. Met. Trans., 6(2) (1971), 1545-1555.
4. V. Gridnev, O. Ivasishin, C. Oshkaderov. Physical fundamentals of high-speed thermal treatment of titanium alloys. Naukova Dumka, Kyiv, 1986, 253 p., in Russian.
5. S. Glazunov, V. Moiseev. Structural titanium alloys. Metallurgiya, Moscow, 1974, 338 p., in Russian.
6. M. Kuzmenko. Metallic Materials with High Structural Efficiency, NATO Science Series, This Volume.
7. R.L. Saha, T.K. Nandy, R.D.K. Misra et al. J. of Materials Science, 26 (1991), p. 2637-44.
8. C. Farias Azevedo, H. Flower. Mater.Sci.& Technology, 16 (2000), p. 372-81.
9. D. Miracle, S. Firstov, L. Kulak et al. Mater. Sci. Forum, 426-432 (2003), p. 4591-96.

EFFECT OF THERMOMECHANICAL TREATMENT ON STRUCTURE AND PROPERTIES OF TI-B-X ALLOYS

Mykola Kuzmenko
Frantsevych Institute for Problems of Materials Science, Kiev, Ukraine

Abstract: The work is devoted to the study of influence of plastic deformation on structure of in-situ Ti-TiB discontinuously reinforced composites, namely Ti-1.6-wt.% B; Ti-5.5Al-1.9B, and Ti-6.6Al-3.5Zr-1.2Si-1.1B, and their fracture mechanisms and mechanical properties. Composites were produced with casting technology. The mechanical properties were measured at tension and bending at room temperature and 500-700 ºC. Young's modulus of deformed composites was 136 GPa in Ti-1.6B alloy; Ti-5.5Al-1.9B alloy gives 152 GPa. Joint reinforcement of titanium with borides and silicides in the Ti-6.6Al-3.5Zr-1.2Si-1.1B alloy enhances Young's modulus to 158 GPa at 1530 MPa strength. All the composites demonstrate ductile fracture behavior at room temperature ensuring high potential of plasticity.

Key words: Titanium discontinuous composites, microstructure, mechanical properties, plastic deformation.

1.   INTRODUCTION

The titanium-based composites with discontinuous reinforcement are attractive materials for a wide range of applications because of their high specific strength and stiffness and good fracture-related properties. Mechanical behavior of these materials depends strongly on both composition and microstructure of matrix and type, size and volume fraction of reinforcing phase. Hot plastic deformation is a powerful tool enhancing mechanical properties of titanium alloys.

The present work gives the data on structure, mechanical properties and fracture mechanisms of in-situ Ti-TiB discontinuously reinforced

composites, namely Ti-1.6-wt.% B; Ti-5.5Al-1.9B, and Ti-6.6Al-3.5Zr-1.2Si-1.1B, produced with casting technology. The objectives of the work were also to: i) optimize melting regimes of Ti-TiB alloys; ii) explore the features of their forging plastic deformation; iii) estimate mechanical properties under bending and tension.

2.   EXPERIMENTAL

The ingots of alloys under study were made on the commercial titanium alloy BT1-0 base using arc and electron beam melting. The BT1-0 alloy contains admixtures as follows: Si < 0.1; Fe < 0.25; C < 0.07; N < 0.04; O < 0.2; others <0.3 wt.% according to the FSU standard. Chemical compositions of the studied alloys are given in Table 1.

Table 1. Chemical composition of the alloys

Alloys	Chemical composition, wt.%						
	Al	Si	Zr	Fe	C	O	B
Ti-1.6 B	-	-	-	0.1	0.25	0.019	1.6
Ti-5.5Al-1.9B	5.5	-	-	0.1	0.24	0.023	1.9
Ti-6.6Al-3.5Zr-1.2Si-1.1B	6.6	1.3	3.5	0.1	0.2	0.02	1.1

Temperature of the smelt was between 1620-1660 $^{\circ}$C. Liquid metal was decanted into graphite mold inside of melting chamber. Obtained cylindrical ingots of 60 mm diameter and 150 mm length were cooled to 600 ºC inside of chamber and after that to room temperature in air outside of equipment. Blanks of alloys were deformed with forging for 90% strain. Before deformation 60-mm diameter blanks were turned to cylinders of 58 mm diameter (Fig. 1a) and heated at first from room temperature to 900 ºC in electric air furnace together with it slowly, 0.4 º/s. After that blanks were brought manually from the electric furnace into gas one where they were heated quicker, 0.15 º/s, up to 1100 ºC. Heated at this temperature for 1 hour blanks were forged manually to necessary power of deformation controlling their side surface against cracks. Schematic of thermomechanical treatment is presented in Fig. 2. A plate with dimensions of 220 mm x 100 mm x 15 mm was produced after deformation (Fig. 1b).

For uniaxial tension cylindrical specimens without fillets were used. Their working length and diameter were 15 mm and 3±0.01 mm respectively. Surface of their working part was polished with diamond abrasives. Yield strength, uniaxial strength and elongation at the loading rate of 1.2 10^{-3} s^{-1} in the temperature range of 20–800 ºC were measured at

tension in air with universal testing machine U2 manufactured by NIIKIMP, the Russian Federation. Young modulus was measured at bending loading.

Structure of alloys as well as their fracture micromechanisms was studied with scanning electron microscopy (SEM) and X-ray microanalysis with Superprobe-733 (JEOL). To reveal the inner structure of samples, deep electrolytic etching with etchant based on acetic acid was used.

a   **b**
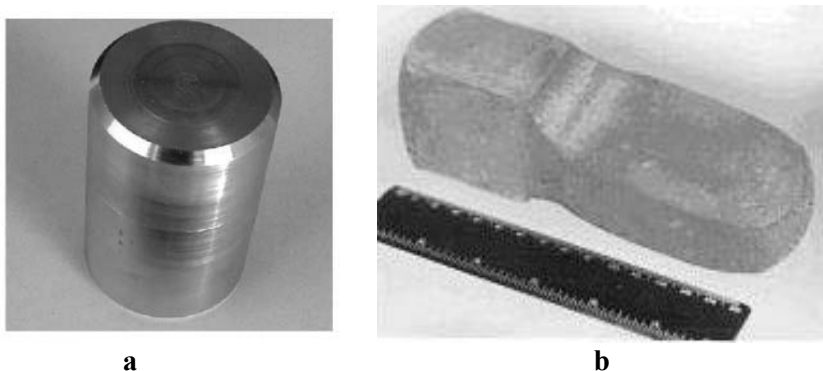
Figure 1 The specimens before plastic deformation (a) and after forging (b).
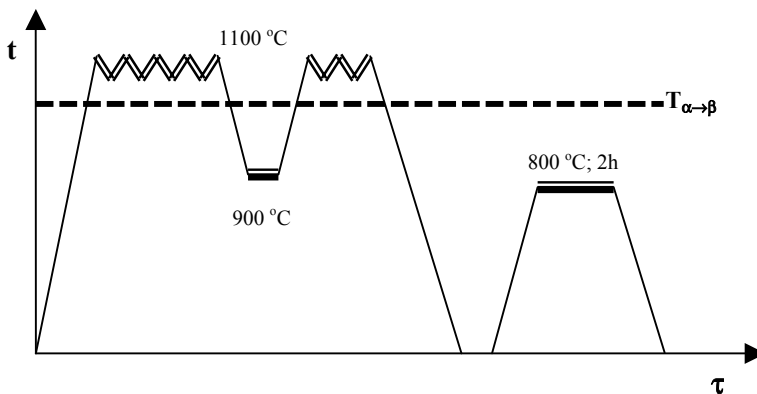
Figure 2 Schematic of thermomechanical treatment of alloy.

3.   EXPERIMENTAL DATA AND DISCUSSION

Ti-1.6 wt.% B alloy. *In as-cast state,* as-dendritic structure is well visible. Structure of matrix is martensite (Fig. 3a). Borides have rod- and strip-like morphology with hexagonal cross-section. Size of rods is around between 0.1 mm and 3 mm in cross-section and a few hundreds of mm length. These rods form strips or plates of a few hundreds of mm width,

which may split like a wood showing weak adhesion between rods. Volume of borides is higher than phase diagram predicts. Fracture of alloy at room temperature is ductile one with portion of cleavage, close to 50-50% that is larger than in Ti-0.9 B alloy, where matrix between borides fails with void coalescence in general opening rod-like structure of reinforcing phase and its high adhesion with matrix. Cleaved areas look like splitted wood. Fracture of alloy at 500 and 600 ºC is ductile one demonstrating the high adhesion between borides and matrix as well as longitudinal cracking of borides. *In as-forged state,* martensite structure of matrix is not visible (Fig. 3b). Crashed borides forms chains of particles of rod and strip (hexagonal cross-section) morphology (Fig. 3c). Thickness of strips is less 1 µm. Volume of boron containing phase is practically the same like in as-cast state. Fracture mechanism of alloy at room temperature and 600 ºC is ductile one.
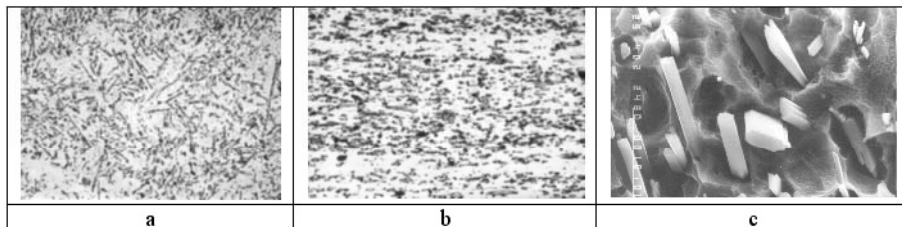

Figure 3. Structure of Ti-1.6 wt.% B alloy: as-cast (metallography, x400, a), as-forged (metallography, x400, b; SEM, x4000, c).

Ti-5.5Al-1.9B alloy. *In as-cast state,* as-dendritic structure is well visible. Structure of matrix is martensite. Borides of eutectic are located between dendrites. Borides have rod- and strip-like, and plate-like morphologies. Plates are splitting well. *In as-forged state,* martensite structure of matrix is not visible. Crashed borides form chains of particles of rod and strip morphologies. Thickness of strips is less 1 pm.

Ti-6.6Al-3.5Zr-1.3Si-1.1B alloy. *In as-cast state*, as-dendritic structure is practically invisible (Fig. 4a). Lamellar structure of matrix is recognized well (Fig. 4b). Close to uniformly distributed borides have rod-like morphology and fogged like brushwood (Fig. 4c). Thickness of rods is between 0.1 – 1.5 µm. Their length is up to 0.2 mm. Fine (0.1-0.3 mm) silicides are uniformly distributed along matrix. Volume of reinforcing phases is higher than phase diagram could predict.
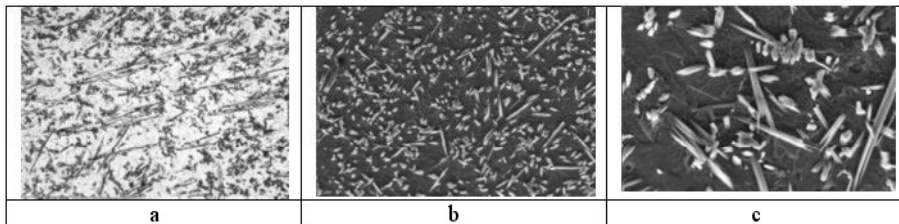
Figure 4. Structure of as-cast Ti-6.6Al-3.5Zr-1.3Si-1.1B alloy: metallography, x400 (a); SEM, x400 (b); SEM, x1000 (c).

In as-forged state, structure of matrix is close to polygonal (Fig. 5a). Crashed borides form chains of particles of rod and strip morphology. It is seen that boride strips are often splitted for three ones (Fig. 5b). Preliminary qualitative X-ray microanalysis shows that borides are compounds containing, except boron and titanium, all the additives added specially like Al, Si, Zr, and present in the basic BT1-0 alloy like Fe, O and possibly C. Matrix is pure in comparison with original BT1-0 alloy. It consists of Ti, Al, Si, and Zr only.
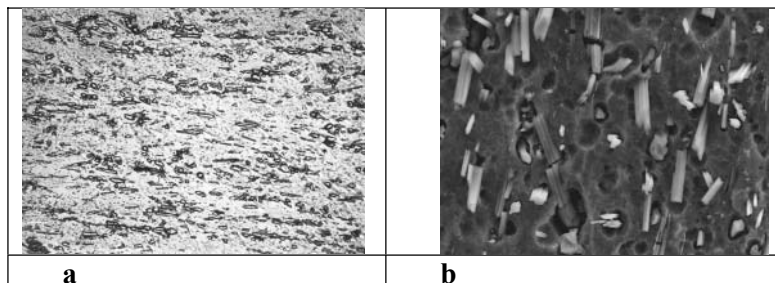
Figure 5 Structure of as-forged Ti-6.6Al-3.5Zr-1.3Si-1.1B alloy: metallography, x400 (a); SEM, x1600 (b).

Table 2 summarizes the best data obtained in three groups of alloys namely binary, ternary and complex alloys with combined strengthening with borides and silicides. The binary alloys is practically quasi-binary ones because contain enough content of iron, which transforms these formally alpha-alloys into practical pseudo-alpha ones containing small but important amount of beta-phase.

Table 2 Mechanical properties of titanium alloys

Property of alloys	Ti-1.6B	Ti-5.5Al-1.9B	Ti-6.6Al-3.5Zr-1.3Si-1.1B
Yield strength, $\sigma_{0.2}$, [MPa]	944	1140	1469
Strength, UTS, [MPa]	977	1184	1530
Elongation, d, [%]	6.4	6.24	1.4
Young modulus, E, [GPa]	136	152	158
Fracture mechanism	*Void oalescence*	*Void coalescence*	*Void coalescence*

One can see from Table 2 that alloying of titanium with boron in amounts till 1.6 % increases its elastic modulus from 110-112 GPa до 135-143 GPa. Additional alloying of Ti-B alloy with Al and Si enhances, while Zr addition does not affect the elastic modulus. Plastic deformation of boron-containing titanium alloys results in inconsiderable diminishment of the Young modulus. Note that plastic deformation followed by annealing promotes some Young modulus increasing too. Plasticity of boron-containing titanium alloys increases after deformation (in binary alloys up to 6-11%, in complex-alloyed alloys to 2-7.2 %).

4.   CONCLUSIONS

Feasibility study of reinforcing titanium with borides and jointly with borides and silicides especially shows clearly that using casting technologies with arc and electron beam melting Young modulus at level of 158 GPa at around 1500 MPa strength and 2-6 % room temperature plasticity may be ensured. It is important that all the alloys studied being in deformed state fail with ductile mode evidencing that mechanical properties of alloys may be enhanced via optimization of structure. It is important too that volume of reinforcing phase is unexpectedly high (in 2 and more times) in comparison with predicted by the brium phase diagram that nee in ditional

ACKNOWLEDGEMENTS

REFERENCES

1. D. Miracle, S. Firstov, Yu. Milman: Proc. Int. Conf. "Science for Materials in the Frontier of Centuries: Advantages and Challenges" (2002), IPMS Publ., Kyiv, p. 634
2. S. Firstov, L. Kulak, and D. Miracle et al: Proc. 8-th Internat. Conf. Composites Engineering ICCE/8, Ed. D. Hui, (2002) p. 245
3. S. Gorsse, D. Miracle: Acta Materialia (2003) to be published
4. F.W. Crossman, A.S. Yue: Met. Trans. Vol. 2 (1971), p.1545
5. S. Firstov, D. Miracle, and O. Vasylyev et al: Acta Materialia to be publishedstudy.

TITANIUM–BORIDE COMPOSITES
Influence of Alloying on the Constitution and Properties of Titanium-Boride Eutectic Alloys

Tamara Velikanova[1]*, Anatoliy Bodar[1], Ludmyla Artyukh[1], Olga Bilous[1], Sergei Firstov[1], Daniel Miracle[2]

[1]Frantsevich Institute for Problems of Materials Sciences, Kyiv, 03680, Ukraine

[2]*Materials and Manufacturing Directorate, Air Force Research Laboratory, Wright-Patterson AFB, OH 45433-7817, USA*

*Corresponding author: velikanova@ipmls.kiev.ua (T. Velikanova)

Abstract: Alloy properties and phase constitutions for ternary Ti-Al-B and Ti-B-*X*, quaternary Ti–10 at.% Al–*X* (where *X* = Si, Ge, Sn, Zr, V, or Nb) and some multi-component alloys were investigated on alloys prepared by arc melting. As-cast and annealed samples were studied by metallography, electron probe microanalysis, XRD, DTA, Vickers hardness at temperatures up to 800°C, and compression and bend tests. Phase equilibria in the Ti-rich portions of the systems were studied in the two-phase (Ti) + (TiB) and conjugate three-phase fields. Based on the experimental data obtained, contributions of alloying additions to the mechanical properties are estimated and discussed for eutectic alloys.

Key words: titanium, boride, aluminium, eutectic, Si, Ge, Sn, V, Nb, phase equilibrium, reinforcement, hardness, strength, alloy

1. INTRODUCTION

Titanium boride TiB is a promising reinforcing phase for titanium alloys due to its properties. Saito et al. [1] obtained titanium-boride composites with good strength properties even at the 10 vol.% content of reinforcing boride phase TiB, which is close to the boride content in the (Ti) + TiB eutectic, although Grossman & Yue [2], who investigated the (Ti)+TiB binary eutectic for the first time, noted that the (Ti)+TiB eutectic contains too little volume fraction of reinforcing phase, 7.7 vol.%. However, other

literature data and the present work provide evidence that there are a number of advantages of the eutectic titanium-boride alloys. Along with the superior properties of the boride reinforcing phase, it is the established that the boron saturation of titanium matrix does not deteriorate the titanium matrix properties. So, further improvement of the titanium matrix and ensuring suitable morphology of boride reinforcement can be considered as an accessible way to develop the eutectic boride-titanium alloy.

Before the present work, insufficient data were available in the literature for phase equilibria of systems based on Ti-B. There is a large body of data in literature on the properties of titanium-boride materials, but there is no systematic information regarding the specific role(s) of candidate alloying elements. Thus, the present effort was undertaken to explore the role of alloying additions through the study of phase equilibria and alloy properties, as well as their interrelation, from the binary Ti-B system to the Ti-rich portions of ternaries Ti-Al-B and Ti-B-X, further to quaternaries Ti–10 at.% Al–B–X (where X = Si, Ge, Sn, Zr, V, or Nb) and to some multi-component alloys.

2.   EXPERIMENTAL DETAILS

The following starting materials were used: iodide titanium and zirconium; aluminum (99.99 %), bar niobium"NBSh-00" (0.05 % Ta, 0.02 % Fe, less 0.03 % N, less 0.03 % C, less 0.03 % O, 0.009 % Ti, and 0.009 % Si); tin (99.9995 %); monocrystalline semiconductor germanium; boron melted in an arc furnace for purification, initial powder boron contained 5.27 % O, 0.055 % H, about 0.1 % Cu, less 0.01 % Fe, and less 0.01 % Si (all in mass %). The alloys studied here contained not more than 0.13 mass % O.

The master alloys and ingots for the investigation were obtained by melting in an arc furnace with a water-cooled copper hearth. An argon back pressure of 50-80 kPa was used, and the chamber environment was purified by preliminary melting of a titanium getter for 5 min. A tungsten non-consumable electrode was used. Initial mixtures weighing typically 15 g were sintered under a weak arc and then remelted 6 times, each time being turned over. The cooling rate of the samples was about 100°C/s. Since the mass losses on melting for all the alloys were not more 0.2 %, their actual compositions were adopted as the nominal ones. In the case of higher loss of alloy mass and for master alloys, compositions were checked by chemical analysis.

As-cast alloys were studied by metallography, XRD, electron probe microanalysis (EMPA), microhardness and hot hardness. Temperatures of the alpha-to beta transformation and melting points were determined by DTA using Al_2O_3 and Ta crucibles and W/W-20Re thermocouples under high purity helium with heating and cooling rates of 0.5°C/s. Interaction of

molten alloys and both crucible materials was observed and so only heating curves were taken into consideration. Measurements of melting points by DTA for the Ti-Al system and some others were not essentially different from literature data but for the Ti-B the difference was considerable (1500°C against 1540 ± 10°C in [90Mas]). Using the Pirani-Alterthum technique we checked the temperature and obtained 1491 ± 6°C, where ± 6 is the combination of the standard deviation in the measurements with the calibration error. Our Pirani-Alterthum furnace and pyrometer are similar to [3]. More experimental details are available elsewhere [4].

Vickers hardness (HV) from RT to 800°C (hot hardness) was measured in a vacuum of 10^{-3} Pa at a 9.8 N load for 1 min. There is a valid reason to use the 1 min hardness for estimation of yield strength as $\sigma_{bend} = HV/3$ [5-7]. As shown our compression tests at a strain rate of $\sim 6 \cdot 10^{-4}$ s^{-1} (Table 1), this estimation for the alloys under studying is quite efficient, and is valid within just a few percent.Bending tests were performed using three points technique on as-cast samples of 25 mm gauge length and 1 x 4 mm^2 gauge section at ambient temperature.

3. RESULTS AND DISCUSSIONS

Data obtained on the extensions of two-phase (Ti) + (TiB) fields are summarized in Table 2. For the as-cast alloys the two-phase regions are more restricted. So, the metal matrix of Ti-Al-B alloys contains the α_2-phase at composition the $Ti_{85}Al_{15}$.

As an instance, the partial Ti-Si-B phase diagram is presented in Fig. 1. Silicon is not practically dissolved in TiB, and is fully concentrated in the metal matrix and in a ternary boro-silicide when it forms. This ternary boro-silicide phase of unknown structure (designated here as the T-phase) was found to be present as a very fine dispersoid around 200 nm in diameter in the three-phase eutectic (Ti) + T + TiB (Fig. 2). The ternary eutectic alloy hardness *vs* temperature plot shows a great potential for strengthening up to ~600°C in comparison with the binary (Ti) + TiB (Fig. 3).

Table 1. Yield stress via compression testing and by estimation as HV/3 for Ti-V-9B (at.%).

Alloy	Yield Stress (GPa)	
	From compression testing	Estimated as HV/3
$Ti_{86}V_5B_9$	0.865	0.89
$Ti_{81}V_{10}B_9$	1.399	1.32
$Ti_{76}V_{15}B_9$	1.455	1.40
$Ti_{71}V_{20}B_9$	0.925	0.89

Table 2. Extensions of two-phase (Ti) + (TiB) fields in the Ti-B-*X* ternary systems at solidus temperatures

System	Content of Alloying Element (at.%) in Phases of Tie-Line Restricting the (Ti) + (TiB) Two-Phase Field		Solidus Tempe-rature (°C)
	Metal Matrix	Monoboride	
Ti-Al-B	37	N.D.[*]	1540
Ti-Si-B	3.0	N.D.[*]	1325
Ti-Ge-B	7	N.D.[*]	1322
Ti-Sn-B	13	~0.1	1575
Ti-V-B	40	25	1460
Ti-Nb-B	~57	~30	~1800

[*]Not detected (below threshold of sensitivity).
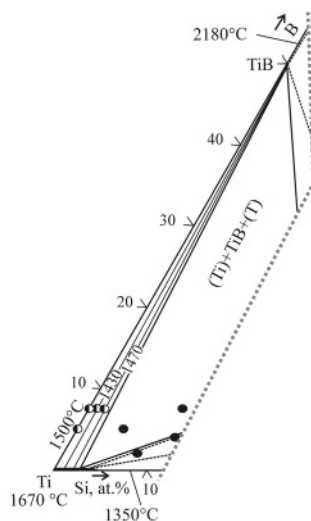
Figure 1. The Ti-Si-B solidus projection in the Ti-rich corner.
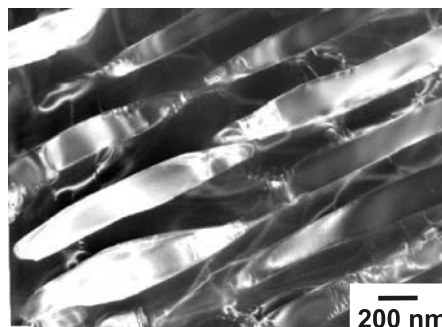

Figure 2. TEM image of eutectic (Ti) + T + TiB.
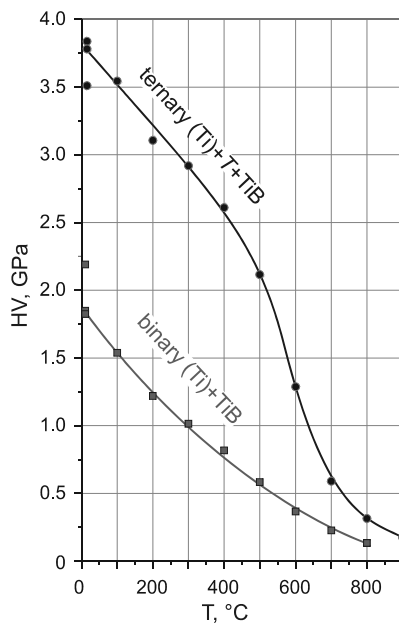
Figure 3. Temperature dependences of hardness (HV) for the ternary (Ti) + T +TiB and binary (Ti) +TiB eutectic alloys.

The ternary and quaternary partial phase diagrams, constructed in the Ti-rich regions, allows the following conclusions to be drawn:

i) The alloying additions under studying do not affect the specific titanium-boride two-phase (Ti) + (TiB) eutectic structure in wide content ranges.

ii) Alloying initiates a small change in the eutectic compositions. *p*-elements (Al, Si, Ge, and Sn) reduce the boron content in the eutectic by ~1-2 at.% and *d*-metals (Zr, V, and Nb) raise the content by ~1-2 at.% B. Thus, a slightly increased boride content in the eutectic is characteristic of the alloys β(Ti,V) + (TiB) or β(Ti,Nb) + (TiB)).

Figures 4 and 5 summarize effect of *p*-elements (Al, Si, Ge, Sn) and *d*-elements (Zr, V, Nb) on Vickers hardness of the ternary Ti-B-*X* and quaternary Ti–10 at.% Al–B–*X* eutectic alloys at selected temperatures. As can be seen, alloying with *p*-elements causes significant strengthening of both ternary and quaternary eutectic alloys in the entire temperature interval under investigation. The maximal strengthening was determined for alloys containing both Si and Ge. In contrast to *p*-elements, alloying with β-stabilizing elements V and Nb substantially increases hardness up to ~400°C, but degrades this property above 500°C. A ternary alloy containing 45 at.% V, of which the hardness at 700°C is quite high (~1 GPa) is an exception to this observation.
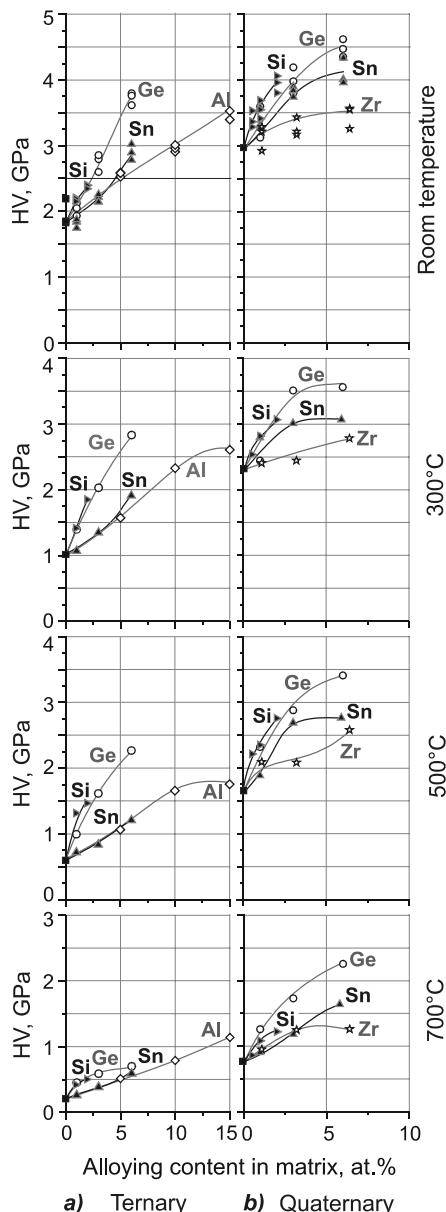
Figure 4. Hardness isotherms vs. contents of alloying elements in metal matrices (X) for alloys Ti-7.5B-X (a) and Ti-8.5Al-7.5B-X (at.%) (b), where X = Al, Si, Ge, Sn, and Zr.
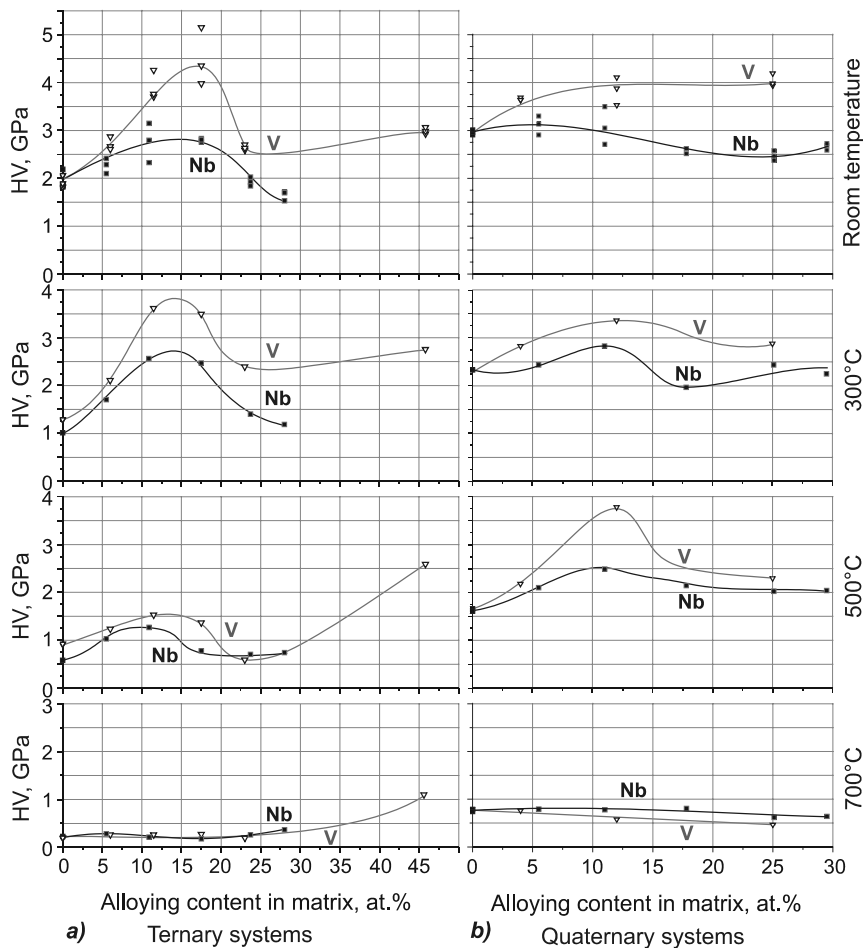
Figure 5. Hardness isotherms vs. contents of alloying elements in metal matrices (X) for alloys Ti-7.5B-X (a) and Ti-8.5Al-7.5B-X (at.%) (b), where X = V and Nb.

Taking into account that the volume content, size, distribution and properties of the reinforcing boride phase practically do not change with the alloying studied here, the strengthening of the ternary and quaternary eutectic alloys should be attributed practically in full to solid- solution strengthening of the titanium alloy matrix.

The contributions of the alloy constituents to the alloy hardness are demonstrated in Fig. 6, where the quaternary $Ti_{81.4}Al_{8.5}Sn_{2.6}B_{7.5}$ alloy is compared with appropriate ternaries. One can see that alloying with Sn and especially with Al leads to significant increase of hardness (and therefore strength properties). Besides, the boride reinforcement has a strong effect on the hardness up to 600°C (compared to the boron-free matrix alloy composition). This upper temperature limitation (incipient temperature of

sharp softening) could be treated as the temperature of transition from nondiffusion to diffusion-type mechanism of alloy deformation [8-10]. Thus, this approach reveals the significant role of the matrix, in particular, the hardness of the matrix $Ti_{90}Sn_3Al_{10}$ is almost equal to that for the alloy $Ti_{89.9}Sn_{2.6}B_{7.5}$ up to 400°C, and at higher temperatures the metal alloy is even harder than the alloy containing the titanium-boride.
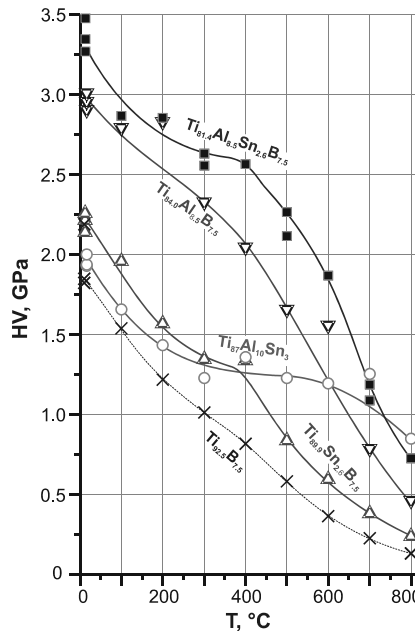
*Figure 6.* Contributions of alloying additives to Vickers hardness of $Ti_{81.4}Sn_{2.6}Al_{8.5}B_{7.5}$ alloy compared with the appropriate ternaries and $Ti_{92.5}B_{7.5}$.

The elastic modulus (Young's modulus) estimated from three point bending tests (Table 3) reaches ~150 GPa. This level is close to the data obtained by Fan *et al.* [11] for an as-cast alloy based on a Ti-6Al-4V matrix reinforced with 10 vol.% boride and to composites containing 20 vol.% boride phase which were produced by blending Ti, Al, V, *etc.* and TiB_2 powders [12,13]. Our alloys containing 7.5 at.% B include ~10 vol.% boride, as calculated basing on XRD lattice parameters and the boron solubility in titanium matrix as ~0.1 at.% and the lower boron content in the TiB monoboride of ~49.5 at.%. A comparison between the elastic modulus for the titanium-boride alloys and titanium alloys of the matrix compositions shows that the estimated contribution of the boride reinforcement is ~30 GPa. This value is somewhat higher than ~20-25 GPa obtained for the titanium-boride composites produced via powder metallurgy [12-14].

The bend tests also show that the yield stress of the quaternary Ti-10Al-*X*-(5 or 7.5)B (at.%) alloys is quite high, and that the hypo-eutectic alloys have a lower yield stress but their plasticity is much larger.

Table 3. Elasticity modulus estimated from tree points bend tests.

Alloy compositions	Elasticity Modulus (GPa)
$Ti_{87}Al_{10}Ge_3$	126
$Ti_{83.3}Al_{9.0}Ge_{2.7}B_{5.0}$	157
$Ti_{81.4}Al_{8.5}Ge_{2.6}B_{7.5}$	148
$Ti_{78.9}Al_{8.5}Ge_{5.1}B_{7.5}$	151
$Ti_{87}Al_{10}Sn_3$	108
$Ti_{83.3}Al_{9.0}Sn_{2.7}B_{5.0}$	145
$Ti_{81.4}Al_{8.5}Sn_{2.6}B_{7.5}$	146
$Ti_{78.9}Al_{8.5}Sn_{5.1}B_{7.5}$	140
$Ti_{81.2}Al_{8.5}Zr_{2.8}B_{7.5}$	134

4.   CONCLUSIONS

1.   Each of alloying additions contributes to increased hot hardness of ternary and quaternary alloys. Zr and *p*-elements have this effect at all the temperatures studyied, and V and Nb act up to 400°C for ternary alloys or to ~600°C for quaternary alloys.
2.   The boride reinforcement contributes significantly to hot hardness (0.5-1 GPa) up to the temperature of sharp softening.
3.   The incipient temperature of sharp softening is defined by a titanium matrix composition in full and can be increased by rational alloying from ~500°C for the binary Ti-B alloy to ~650°C.
4.   Bending tests showed that as-cast alloys with boride reinforcement have noticeable RT plasticity ε, high yield stress $\sigma_{0.2}$ and high Young's modulus E: $\varepsilon = 0.6$ % (the $Ti_{79.3}Al_{9.0}Sn_{2.7}B_{9.0}$ alloy), $\sigma_{0.2} = 1600$ MPa and $E \approx 150$ GPa (the Ti-Al-Ge-B alloys) which is ~30 GPa higher than the unreinforced alloy of matrix composition at the expense of boride reinforcement.

ACKNOWLEDGEMENT

REFERENCES

1. T.Saito, T.Furuta, T.Yamaguchi, in: Titanium '95 Science and Technology (Eds. P.A.Blenkinsop, W.J.Evans, H.M. Flower), The Inst. of Materials, London, 1996, Vol. 3, p. 2859.
2. F.W.Grossman, A.S.Yue, Metall. Trans. 2, 1971, 1545.
3. E.Rudy, J.Progulski, Planseeber. Pulvermet. 15, 1967, 13.
4. T.Ya.Velikanova, A.A.Bondar, A.V.Grytsiv, J. Phase Equi. 20 (2), 1999, 125.
5. V.A.Borisenko, Probl. Prochnosti 8, 1975, 58 (in Russian).
6. V.I.Trefilov, Yu.V.Milman, S.A.Firstov, "Physical Foundation of Strength of Refractory Metals", Naukova Dumka, Kiev, 1975 (in Russian).
7. V.A.Borisenko, "Hardness and Strength of Refractory Materials of High Temperature", Naukova Dumka Kiev, 1984 (in Russian).
8. J.Rösler, J.J.Valencia, C.G.Levi, A.G.Evanc, R.Mehrabian, in: Mat. Res. Soc. Symp. Proc., Materials Research Society, 1990, Vol. 194, p. 241.
9. S.L.Kampe, J.Christodoulou, C.R.Feng, L.Christodoulou, D.J.Michel, Acta Mater. 46 (8), 1998, 2881.
10. O.M.Ivasishin, V.I.Bondarchuk, I.V.Moiseeva, P.M.Okrainets', V.K.Pishchak, Met. Phys. Adv. Tech. 19, 2001, 397.
11. Z.Fan, A.P.Miodownik, L.Chandrasekaran, M.Ward-Close, J. Mat. Sci. 29, 1994, 1127.
12. T.Saito, T.Furuta, T.Yamaguchi, in: Titanium '95 Science and Technology (Eds. P.A.Blenkinsop, W.J.Evans, H.M. Flower), The Inst. of Materials, London, 1996, Vol. 3, p. 2859.
13. S.Gorsse, D.B.Miracle, Acta Mater. 51 (9), 2003, 2427.
14. S.Gorsse, Y.Le Petitcorps, S.Matar, F.Rebillat, Mater. Sci. Eng. A340, 2003, 80.

NEW HIGH-STRENGTH WELDABLE TITANIUM ALLOY T110

V.N. Zamkov, S.L. Antonyuk, A.G. Molyar
E.O.Paton Electric Welding Institute, ASTC Antonov

Abstract: T110 experimental high-strength weldable titanium alloy was developed. Distribution of alloying elements and impurities in length and section of 400 mm diameter ingots from alloys of Ti-Al-Mo-V-Nb-Fe-Zr system, produced by the method of electron-beam melting with an intermediate crucible (EBMC) was investigated. Optimal operating modes of melting, deformation, heat treatment, welding of T110 alloy based on this alloying system were determined in order to obtain required chemical composition, macro- and microstructure, a level of mechanical characteristics. The mechanical and fatigue characteristics for parent metal and welded joints were determined. It was found that by mechanical characteristics the alloy does not comply and by a level of plasticity exceeds VT22 commercial alloy. The cyclic life of T110 titanium alloy for parent material exceeds this characteristic of VT22 alloy. The cyclic life of T110 alloy welded joints does not depend on welding method. The alloy developed is good technological material: it is easily deformed, quenched by air after annealing, good welded by all kinds of welding. In this case the welded joint have a strength level of 0,95 and KCV of 0,8 of a parent metal properties, minimum.

Key words: titanium, alloys, properties, strength, fatigue, welding, heat treatment.

1.   INTRODUCTION

Welded structures of high-strength titanium alloys (UTS ≥ 1100 MPa) find an increasingly wide application in aircraft engineering. For example, elements of landing gear, frames, runways, cross pieces, wing slides and other elements of Antonov aircraft, such as AN-124, AN-225, AN-70, AN-140 and AN-148, are made from alloy VT22 (Ti-5Al-5Mo-5V-1Fe-1Cr)

269

extensively used in aircraft engineering.In this case welding is one of the leading processes, allowing manufacture of large-size complex-configuration components and assemblies with a high material utilisation factor.Efficiency of using welded structure of high-strength titanium alloys depends upon the extent to which the performance of welded joints, and the level of their fatigue strength under low-cycle loads in particular, matches this property of the parent metal.Tensile strength of semi-finished products of alloy VT22 is approximately 1100…1200 MPa. So far there is no way of achieving this level of strength in welded joints.Alloy VT22 in welding is very sensitive to overheating in β-region, and in the as-welded condition the weld and HAZ metals are characterised by a very low ductility.Arc welding of alloy VT22 is performed using filler wire SPT-2 (Ti-4Al-3V-1.5Zr), while in electron beam welding the use is made of inserts of low titanium alloys. This allows ductility and impact toughness of the weld metal to be increased to those of the parent metal, although strength of the weld in this case decreases down to 850 MPa.To raise ductility of metal in the HAZ a welded joint is subjected to heat treatment under the following conditions: heating to 830°C, holding for 2 h, cooling with furnace to 750°C, holding for 2 h, air cooling, reheating in the furnace to 600°C, holding for 3 h, air cooling.This multistage annealing provides a substantial improvement in ductile properties of a welded joint, but its strength remains at a level of 850-900 MPa. In addition, this leads to a simultaneous decrease in strength of the parent metal.Traditional method for improvement of performance of welded joints in hard-to-weld alloys, i.e. thickening of the welding zone, is usually employed for VT-22 welded structures. This method involves a dramatic decrease in the material utilisation factor, makes a structure mush heavier and much less cost-effective.The E.O.Paton Electric Welding Institute in collaboration with ASTC Antonov performed comprehensive studies aimed at development of a more workable weldable alloy with a level of performance not lower than that of alloy VT22.The above efforts resulted in the development of a new experimental alloy conditionally called T110 (Ti-Al-Mo-V-Nb-Fe-Zr). This alloy meets the following requirements: UTS $\geq$ 1100 MPa, $\delta \geq 10$ %, $\psi \geq 35$ %, KCV ≥ 25 J/cm^2.In this case the level of strength of the welded joints is not less than 0.95, and that of impact toughness – not less than 0.8 of the corresponding characteristics of the parent metal.

2.   RESULTS

In addition to laboratory ingots, also industrial round ingot 400 (dia.) x 1000 mm and flat ingots, i.e. slabs, 400x200x1000 mm in size were used for

the studies. Ingots of alloy T110 were melted at the RPC "TITAN" of the E.O.Paton Electric Welding Institute by the electron beam cold-hearth (EBCH) method using the technology developed earlier for production of ingots of multi-component high titanium alloys, including VT22.Results of chemical and gas analyses of the ingots are indicative of a uniform distribution of alloying elements in the bulk of metal (Tables 1 and 2). The difference between maximum and minimum concentrations of aluminium in alloy T110 was not in excess of 0.25 wt. %, which is much lower than scatter of the aluminium content, e.g. in Ti-6Al-4V ingots, permitted by Russian and ASTM standards.

Table 1. Distribution of alloying elements and impurities along the length of ingots (400 mm dia.) of titanium alloy T110 produced by the EBCH method

Sampling location	Content of elements, wt. %							
	Al	Mo	V	Nb	Fe	Zr	O	N
Top	5.47	1.03	1.33	5.04	1.60	0.36	0.09	0.02
Centre	5.29	1.10	1.48	5.32	1.62	0.35	-	-
Bottom	5.35	1.16	1.37	4.93	1.58	0.32	-	-
Tentative specifications	5.0-6.0	1.0-1.5	1.2-2.0	4.5-5.5	1.5-2.0	0.3-0.5	≤ 0.15	≤ 0.04

Table 2. Distribution of alloying elements and impurities across the section of ingots (400 mm dia.) of titanium alloy T110 produced by the EBCH method

Sampling location		Content of elements, wt. %					
		Al	Mo	V	Nb	Fe	Zr
Top	A*	5.48	1.02	1.18	5.32	1.63	0.40
	C	5.52	1.01	1.41	4.91	1.61	0.35
	P	5.57	1.06	1.40	5.02	1.60	0.33
Centre	A*	5.45	1.02	1.50	5.45	1.58	0.37
	C	5.30	1.12	1.49	5.26	1.60	0.31
	P	5.28	1.14	1.45	5.27	1.61	0.37
Bottom	A*	5.54	1.01	1.42	4.98	1.59	0.32
	C	5.43	1.12	1.39	4.78	1.69	0.34
	P	5.29	1.31	1.33	4.84	1.47	0.30

*A – near the ingot axis; C – at 0.5 R of the ingot; P – in the peripheral zone (about 10 mm from the ingot surface)

Macrostructure of ingots as cast is shown on fig. 1. The macrostructure of ingots consisted of equiaxed polyhedral β-grains or grains slightly extended in a direction of heat removal. The cast metal was defect-free.
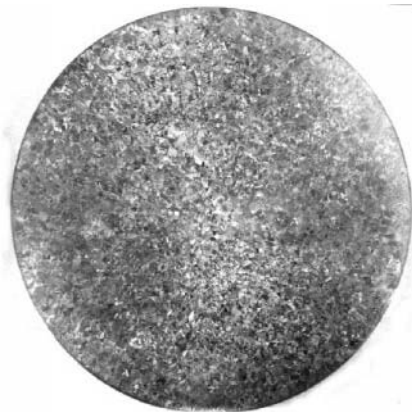
Figure 1. Macrostructure of ingots as cast.

Temperature of polymorphic $(\alpha + \beta) \rightarrow \beta$ transformation of the cast metal was determined to select temperature conditions for deformation of ingots and parameters of subsequent heat treatment. This temperature was 905°C for both ingots.

The round ingot was subjected to preliminary forging into a rod 120 mm in diameter. This rod with a diameter of 120 mm was again forged into a square bar with a side of 50 mm and then subjected to heat treatment. Deformation into the intermediate (next to last) and final sizes was performed at a temperature lower than that of the $\beta \rightarrow (\alpha + \beta)$ transition by not less than 50°C.

Macrostructure of the bar metal after forging corresponded to index 4-5 of the 10-index macrostructure scale. Microstructure of the forged metal corresponds to type 3-4 of the 8-type microstructure scale (fig. 2).

Three operating modes of heat treatment for the forged bars were tried out:

1. Annealing at 750°C, t - 1 h, air cooling.

2. Heating to 870°C, t - 0.5 h, cooling with furnace to 800°C, t - 0.5 h, cooling with furnace to 750°C, t - 1 h, air cooling; heating up to 380°C, t - 8 h, air cooling; heating up to 570°C, t - 2 h, air cooling.

3. Vacuum annealing at 850°C, t - 1 h, cooling with furnace to 250°C, air cooling.

After heat treatment according to operating modes 2 and 3, the intragranular structure is characterised by a globular morphology of α-precipitates (fig. 2). Moreover, the stepwise treatment process provides comprehensive globularisation of the α-phase. The structure comprises also the laminated precipitates, in addition to the globular ones.

In the case of vacuum treatment (operating mode 3) the number of the globular precipitates is much lower, while the laminated precipitates form the "basket-work" type structure.

Mechanical properties of forged bars of alloy T110 after appropriate heat treatments are adduced in Table 3.


a)   b)   c)
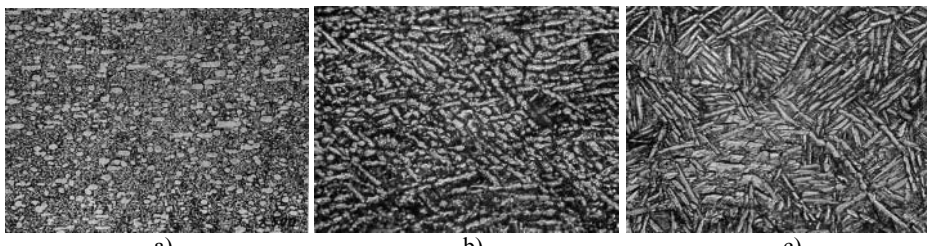
Figure 2. Microstructures, x 500; operating modes of heat treatment: a – 1, b – 2, c – 3.

Table 3. Mechanical properties of forged bars of alloy T110

Heat treatment operating mode	Mechanical properties			
	UTS, MPa	δ, %	ψ, %	KCV, J/cm^2
1	1100 – 11501130	10,5 – 13,512,2	38,0 – 49,842,6	25,3 – 28,226,1
2	1180 - 12401217	11,0 – 16,913,7	41,6 – 53,748,3	27 – 3529
3	1130 – 11951165	13,1 – 20,816,3	48,0 – 58,252,4	30,6 – 35,634,4

Fatigue characteristics of the alloy were evaluated by testing standard eye specimens 100x40x5.6 mm in size with a stress raiser $\alpha_\sigma = 2{,}8$. The tests were carried out at two levels of loading: (1) $\sigma_{max} = 600$ MPa, $P_{max} = 65.92$ kN; and (2) $\sigma_{max} = 400$ MPa, $P_{max} = 43.95$ kN. The load application frequency was $f = 2\text{-}3$ Hz, $R = 0$.

Typical destructions of standard eye specimens after fatigue tests are shown on fig. 3. During the process of cyclic tests of the eye specimens the fatigue cracks initiated on the surface of holes of 20 mm in diameter (stress raisers) and propagated outward to the external part of the specimens.

Results of low-cycle fatigue tests of eye specimens of alloy T110 are adduced in Table 4.

a)   b)
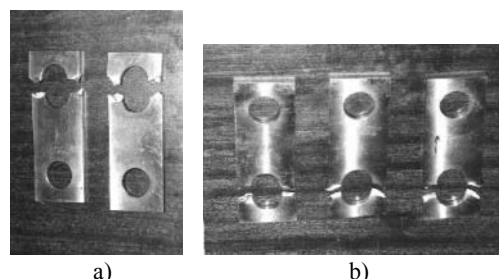
Figure 3. Typical destructions of standard eye specimens after fatigue tests: a – load-ing of 600 MPa; b – loading of 400 MPa.

Table 4. Results of low-cycle fatigue tests of eye specimens of alloy T110

Specimen No.	Load, σ_{max}, P_{max}	Number of cycles	Mean number of cycles	Scatter coefficient h
1	600 MPa, 61 kN	8260	8235	1.006
2		8240		
3		8210		
4	400 Mpa, 44 kN	24250	24540	1.33
5		27710		
6		25410		
7		20790		

Fractography of fracture surfaces showed that fracture of the specimens was of a clearly defined fatigue character (fig. 4). Microgrooves corresponding to the programmed loading cycles were seen on the surface of the fatigue cracks, while a tough pit-like surface relief was formed in the zone of static complete fracture.


a)   b)
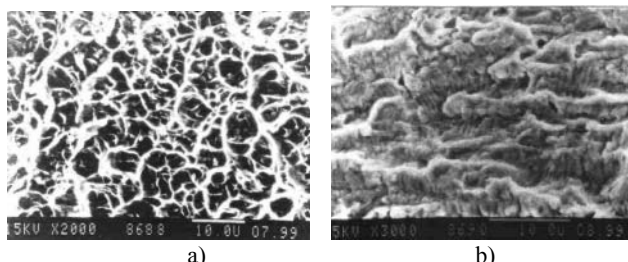
Figure 4. Microstructure of fracture surface:
a – micro furrows in the zone of propagation of fatigue cracks;
b – tough pit micro relief in the zone of static complete fracture.

The character of fracture was identical at both levels of loading. The only difference was that at a higher load the fatigue cracks initiated from many centers. The results obtained were compared with data of low-cycle fatigue tests conducted earlier on similar eye specimens of alloy VT22 (Table 5).

Table 5. Results of low-cycle fatigue tests of eye specimens of alloy VT22.

Load, σ_{max}, MPa	Q-ty of specimens, pcs.	Mean number of cycles	Scatter coefficient, η
700	3	2993	1,33
500	5	12904	1,71
400	4	19600	1,76

10 mm thick plates of alloy T110 were used as the parent metal for the studies welding joints. The plates were produced by rolling of slabs first in β- and then (α + β)-temperature region. The rolled plates were subjected to grit blasting and etching. Butt joints were made by automatic TIG welding in argon atmosphere in a single pass without groove preparation and without filler wire, as well as in three passes with groove preparation. Welding of the root bead was done over the layer of ANT-23A flux without a filler wire. The second and third passes to fill the groove and provide a full-size weld were made using filler wire of SP15 grade. Some of the plates were electron beam welded (Table 6). After welding the samples were subjected to heat treatment. In compliance with the results of preliminary studies, the joints made by the TIG method in argon had optimal mechanical properties after annealing at 750°C for 1 h and subsequent air cooling (operating mode 1 of heat treatment). Multi-stage annealing (operating mode 2 of heat treatment) was used for heat treatment of EBW joints.

Table 6. Parameters of welding of samples of alloy T110

Welding method	Pass No.	Welding current, A	Arc voltage, V	Welding speed, m/h	Wire* feed speed, m/h
EBW (1)	1	0,080	60 kV	24	-
TIG without filler wire (2)	1	450	12	15	-
TIG using filler wire SP15 - (3)	1**	100	11	18	-
	2	180	10	9	9
	3	200	10	12	9

*diameter of filler wire – 2.5 mm; ** TIG-(F), flux grade ANT-23A

Static and fatigue strength of welded joints, as well as impact toughness of the weld and HAZ metals were evaluated. Mechanical properties of welded joints of alloy T110 are adduced in Table 7.

Table 7. Mechanical properties of welded joints of alloy T110

Welding method	Heat treatment	UTS, MPa	KCV, J/cm^2		Fracture location
			Weld	HAZ	
1	Operating mode 2	1150	27	22	HAZ
2	Operating mode 1	1070*	43	23	WELD
3		1030	35	38	WELD

*Mean values of properties over the results of testing 5 specimens.

As seen from the data obtained, strength of the arc-welded joints is close to that of the parent metal, and strength of the joints made by EBW is actually identical to that of the parent metal. The values of impact toughness of the weld and parent metals are also close to each other. Some decrease in KCV takes place in the HAZ of the joints made in one pass.

Lower values of strength of the joints made by using a filler wire, compared with single-pass welding, is associated with decrease in the degree of alloying of the weld metal. However, multi-pass welding has a favourable effect on impact toughness of the HAZ metal, and properties of the weld metal allow wire SP15 to be recommended also for welding alloy T110.

Flat specimens ($\alpha_\sigma = 2.8$) 300x70x10 mm in size with a gauge length 7.5 mm thick were used for fatigue tests. The basic number of cycles was 500000, after which testing was stopped (Table 8). The specimens were tested in two groups, 7 specimens in each group. A group included two specimens for each of the arc welding methods and three specimens for EBW. The results of fatigue tests of welded joints of T110 alloy are adduced in Table 9.

Table 8. Conditions of low-cycle fatigue tests of welded specimens

Specimen group No.	Basic loading	
	σ_{max}, MPa	P_{max}, kN
1	500	110
2	300	66

Table 9. Fatigue properties of welded joints in T110 alloy

Welding method	σ_{max}= 500 MPa; P_{max}= 110 kN			σ_{max}= 300 MPa; P_{max}= 66 kN		
	Specimen No.	Number of cycles	Fracture location	Specimen No.	Number of cycles	Fracture location
EBW	1-1	75470	Radius transition	1-3	534550	No fracture
	1-2	75620	Radius transition	1-4	536050	No fracture
TIG without filler wire	2-1	460960	In test machine grip	2-4	441320	Machine switched off
	2-2	461060	Nick in specimen	2-5	521040	No fracture
	2-3	68300	Radius transition	2-6	511570	No fracture
TIG using filler wire SP15	3-1	49990	Weld metal defect	3-3	475270	Weld metal defect
	3-2	93090	Radius transition	3-4	513790	No fracture

Almost no specimens tested under a load of 300 MPa fractured after the basic number of cycles equal to 500000. Two specimens were the exception. One of them withstood 441320 cycles and fractured as a result of emergency switching off of the testing machine. Fracture of the second specimen after 475270 cycles was caused by the presence of the technology defect in the weld metal. In both cases the premature fracture of the specimens was associated neither with the welding method nor with the peculiarities of phase composition and microstructure of the welded joints. Quality of manufacture of the specimens had a decisive effect on the results of testing under a load of 500 MPa. For example, four specimens of the joints made by different welding methods fractured in the parent metal at a distance from the weld in a radius transition region after 68300 to 93090 cycles. Two specimens made by arc welding without a filler wire fractured after 460960 and 461060 cycles, respectively, in a region of the testing machine grip and due to a nick on the specimen surface. And only one specimen fractured in the weld after 49990 cycles, which was caused by the presence of a technology defect.

These results do not give true values of the number of cycles to fracture and, therefore, true values of fatigue life of welded joints. However, they allow draw a conclusion that performance of welded joints in alloy T110 under cyclic load σ_{max} = 500 MPa does not depend upon the welding method, provided that welds contain no technology defects.

On the other hand, it can also be concluded that the defect-free weld of alloy T110 is a less effective stress raiser than the radius transition in a specimen tested.

3.   CONCLUSIONS

Conditions for forging of the experimental titanium alloy T110 to ensure metal structure meeting the requirements for structure parameters of this type of semi-finished products were selected.

Vacuum annealing leads to a higher ductility and impact toughness of alloy T110. Its multistage heat treatment provides the best combination of strength and ductility values. Annealing at $750°C$ is the simplest type of heat treatment and provides the required level of mechanical properties.

Strength of the T110 alloy welded joints made by the arc method is 0.93-0.97 of that of the parent metal, and for the EB welded joints this property amounts to one. All welded joints in alloy T110 have the level of impact toughness in excess of that of welded joints in alloy VT22.

Wire of the SP15 grade is recommended for use as a filler metal for multi-pass arc welding of alloy T110.

Under cyclic loading conditions the mean number of cycles of the typical eye specimens of alloy T110 can withstand is higher than that for similar specimens of alloy VT22.

Under a load of 300 MPa the specimens withstood the basic number of cycles and were taken from the tests without fracture. Ambiguous results of fatigue tests of welded joints under a load of 500 MPa are caused by an insufficient quality of manufacture of specimens.

The number of cycles the defect-free welded joints in alloy T110 can withstand does not depend upon the welding method.

The experimental titanium alloy T110 produced by EBCH melting, subjected to plastic deformation and heat treatment, has characteristics of strength at a level of commercial alloy VT22, and is superior to this alloy in ductility and fatigue strength. The alloy is well-weldable with any fusion welding method.

ACKNOWLEDGEMENTS

FEATURES OF APPLICATION OF HIGH-STRENGTH MATERIALS FOR UNITS OF THE LANDING GEAR OF AIRCRAFTS "AN"

A.G. Molyar, V.A. Trofimov
ASTC Antonov, Kiev, Ukraine

Abstract: For manufacturing the critical landing gear parts of aircrafts "AN" 30CrMnSiNi2Mo high-strength steel, UTS = 1900 MPa, is used. The maximal operation stresses in the landing gear units are 854 MPa. At operation for 15 years, in spite of insignificant stresses, cases of failures by means of a corrosion mechanism (intergranular brittle fracture) and by means of corrosion-fatigue mechanism had taken place. The researches have shown that the failure of parts was provided by technology factors – the presence of a decarburized layer etc. Based on the analysis of operating conditions of the parts, their fractures the followed conclusion was drawn: the steel applied behaves on a limit of its capabilities, does not have a margin of plasticity, is sensitive to presence of surface defects, has low corrosion resistance and is not the best material for the loaded units with long term of operation. In last aircrafts "AN" for the loaded landing gear units a high-strength titanium alloy VT22 and maraging steel VKS-170 are used which have the much greater resistance for corrosion cracking.

Key words: landing gear, steel, corrosion mechanism, titanium alloy.

1.   MATERIALS ASSESSMENT

Feature of many airplanes "AN" is the opportunity of their exploitation at ground airfields that imposes especial requirements to stiffness and strength of a structure of the landing gear. For super-heavy airplanes a serious problem is the requirement of the maximal maneuverability at movement of moving along the airfield. This requirement is resolved by applying the multi-bearing landing

gear, which gives over the big concentrated dynamic loadings from wheels onto units of an airframe of the airplane, provided that the overall dimensions of load-bearing structures and weight of parts are highly limited. Due to these circumstances all parts of the landing gear are calculated and produced from high-strength steels. A traditional material for manufacturing the main units of the landing gear is high-strength structural steel 30CrMnSiNi2Mo which along with significant strength UTS = 1700-1900 MPa, high value of specific strength (UTS/ρ = 20.6) has the increased fatigue strength.

Taking into account a long term of the exploitation for the landing gear unit parts the maximal (extreme) operational stresses in the parts made of the specified steel are UTS$_{operat.}$ = 854 MPa.

Nevertheless at exploitation of airplanes during ~ 15 years, in spite of insignificant stresses, cases of failures of the parts by means of a corrosion mechanism (intergranular brittle fracture) and by means of a combined corrosion-fatigue mechanism had taken place.

At operation of aircrafts during ~ 15 years, in spite of insignificant stresses, cases of parts by means of a corrosion mechanism (intergranular) - fatigue initiation and primary original growth of a crack with the subsequent intergranular growth of this crack and tough fracture. It is typical, that initiation of a crack and its growth by a mechanism of stress corrosion occurs in zones of the maximal influence of the corrosion environment (stagnant zones) which do not necessarily coincide with maximal operation working stresses. For example, the origin of a corrosion crack initiation on a cross-piece of the landing gear support carriage frame of AN-12 airplane was formed on an internal surface of the cylinder (fig. 1) where there was a congestion of a condensate although operational stresses of the part subjected to bending are much above on an external surface. Failure of the specified part occurred according to the intergranular corrosion mechanism (fig. 2) with developing into viscous pitted rupture. Attributes of fatigue on a fracture surface are not revealed that indicates to prevailing influence of the corrosion factor on failure of the part.
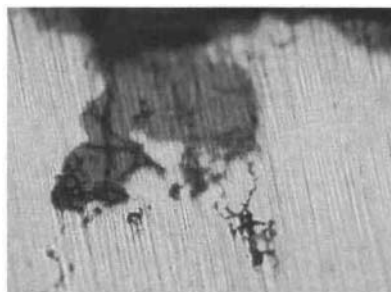

Figure 1. The origin of a corrosion crack initiation on a cross-piece of the landing gear support carriage frame of AN-12 airplane, x 500.
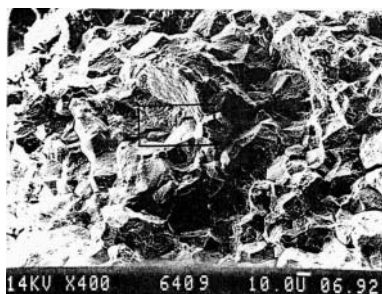
Figure 2. Microfractographic particularities the intergranular corrosion mechanism, x 400.

At exploitation the cases of failure of the parts according to the combined corrosion-fatigue mechanism [1] also were revealed. The feature of such failures is that the mechanism is changed from corrosion to fatigue or on the contrary depending on operational factors, as well as presence of technological violations during manufacturing the parts. In particular if on a surface of the parts in the failure zone a decarburized layer is present (fig. 3) that as a rule the initiation of the failure occurs according to the corrosion intergranular mechanism. This is caused by weakening boundaries of former austenite grains (fig. 4. The further crack growth occurs as a rule according to the fatigue mechanism (fig. 5. If on a surface the decarburized layer is not present the nucleation of a crack and its initial growth occurs according to the fatigue mechanism. The further growth after achievement of critical length occurs according to the corrosion mechanism under action of constant stand stresses and corrosion-active environment. The rupture of the part in all cases is pitted and viscous.
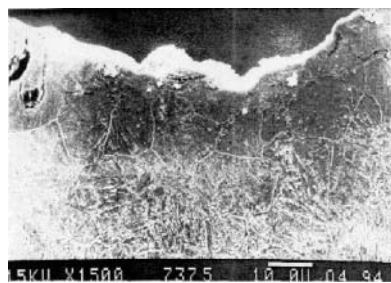

Figure 3. Decarburized layer, x 1500.
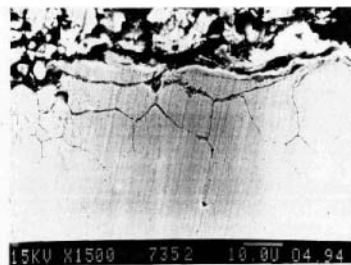
Figure 4. A net of intergranular cracks on the unetched microsection metallographic specimen near the external surface of the traverse, x 1500.
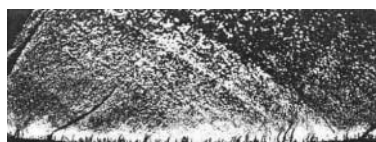
Figure 5. Fracture and crack initiation places on the traverse external surface, x 10.

The specified factors indicate that high-strength structural steel of 30CrMnSiNi2Mo grade as heat treated works at a limit of its capabilities, without a reserve of plasticity is sensitive to presence of surface defects, has low corrosion resistance and is not the best material for the loaded units with long term of operation.

Since the premature failure is mainly caused by a surface condition and action of the corrosion environment than natural interest to use other materials having the increased corrosion resistance and fracture toughness for the loaded units of the landing gear arises.

In this direction at ASTC "Antonov" the researches concerning maraging steels such as VKS-170 and high-strength titanium alloys were carried out.

VKS-170 maraging steel at equal strength with 30CrMnSiNi2Mo steel has much more fracture toughness ($K_{1C\ 30CrMnSiNi2Mo}$ = 11.6-13.3 MPa√m; $K_{1C\ VKS-170}$ = 70-73.3 MPa√m) and a threshold stress at corrosion cracking ($\sigma_{CR\ 30CrMnSiNi2Mo}$ = 700 MPa; $\sigma_{CR\ VKS-170}$ = 1450 MPa), that promotes its as rather perspective for the loaded units of the landing gear where along with high strength as well as large elastic modulus is required. For new AN-148 airplane some parts of the landing gear were manufactured of VKS-170 steel.

The most interesting material for manufacturing the landing gear units are high-strength titanium alloys, in particular of VT22 alloy having very high specific strength (UTS/ρ = 26) and excellent corrosion resistance. Besides VT22 alloy is welded by all kinds of welding, heat strengthened by

air cooling, has a good combination of strength and plasticity. The chemical composition and mechanical properties of VT22 alloy are adduced in tab. 1.

Table 1. Composition and properties of VT22 titanium alloy

Alloy	Chemical composition, % by weight					Mechanical properties			
	Al	Mo	V	Fe	Cr	UTS, MPa	δ, %	ψ, %	KCU, MJ/m²
VT22	4.4-5.9	4.0-5.5	4.0-5.5	0.5-1.5	0.5-2.0	1100-1250	8	25	0.3

The accomplished researches of VT22 alloy and also significant experience of the exploitation of the parts made of this alloy indicate that providing the decision of two primary problems the alloy is suitable for manufacturing the landing gear of the airplane as complete unit from this alloy.

The first problem consists in maintenance of stable characteristics of strength. The exploitation and actual size test experience has shown direct dependence of characteristics of strength on a structure condition of the alloy especially for massive semifinished work-pieces from which the parts of the landing gear are machined. Traditionally die forgings of VT22 alloy intended for the gear are manufactured by using hammers and have a microstructure with β-the transformed grain and rough edging of α-phase along boundaries of a former β-grain (fig. 6). Such structure in particular formed at slow cooling from a temperature of deformation is sensitive to surface defects and as a result can lead to decreasing fatigue characteristics. To avoid forming such shown structure the semifinished work-pieces are necessary to manufacture with using hydro-presses and in α+β-area. In this case the structure adduced on fig. 6 is obtained. The latter has advantages before β-transformed structure as by a complex of strength/plastic properties and by fatigue characteristics. That is caused by absence of weakening the boundaries of grains.

The second problem concerns increasing tribotechnical characteristics of titanium alloys for maintenance of serviceability of units working at a presence of friction.
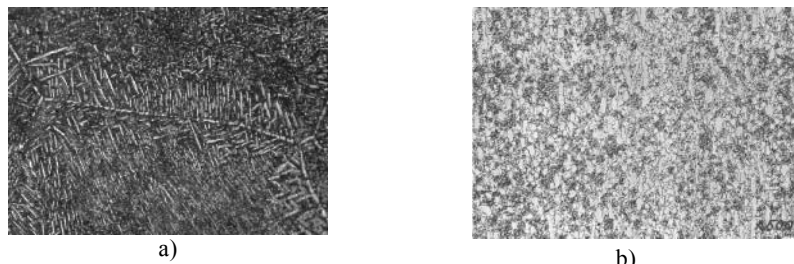

a)   b)

Figure 6. β-transformed grain and rough edging of α-phase along boundaries of a former β-grain (a), bimodal structure (b),   x 500.

This problem can be solved by applying wear resistance coatings with using

gas-thermal techniques since electrochemical coatings on titanium alloys either are not technological or have low performance characteristics. Diffusion coatings in connection with chemical activity of titanium highly embrittle the parts.

For maintenance of serviceability of the units of the landing gear which work at a presence of friction, at ASTC "Antonov" some technologies of applying plasma and ion-plasma coatings on titanium alloys are developed. It has allowed to design the fully titanium landing gear of AN-148 airplane which today is in a condition of manufacturing.

Thus, we consider, that the most perspective material for the landing gear of airplanes with a long-term resource is high-strength welded titanium alloys.

2.   CONCLUSIONS

The most perspective materials for the landing gear of airplanes with a long-term resource are high-strength welded titanium alloys.

ACKNOWLEDGEMENTS

REFERENCE

1. *V. A. Trofimov and A.G. Molyar* Certain causes of fracture of the AN aeroplane landing gear parts made from the high-strength steels. Physicochemical Mechanics of Materials, No. 3 (2002), 107-109.

PART 5

ADVANCED REFRACTORY ALLOYS

STRUCTURES AND PROPERTIES OF THE REFRACTORY SILICIDES TI$_5$SI$_3$ AND TISI$_2$ AND TI-SI-(AL) EUTECTIC ALLOYS

G. Frommeyer and R. Rosenkranz
Max-Planck-Institute for Iron Research, Duesseldorf, Germany

Abstract:

The refractory titanium silicides Ti$_5$Si$_3$ and TiSi$_2$ with complex hexagonal D8$_8$ and orthorhombic C54 lattice structures exhibit superior physical and mechanical properties, such as high lattice energies and melting temperatures; high hardness, elastic stiffness and flow stresses; low densities and excellent creep and oxidation resistance. The complex lattice structures and a large contribution of covalent bonding to the total binding energies of these compounds cause a lack in ductility due to sessile superdislocations. In order to improve the ductility and fracture toughness of silicide containing titanium-based alloys, binary and ternary Ti-Si-(Al) systems have been considered. Alpha titanium forms with the Ti$_5$Si$_3$ compound an eutectic system possessing large volume fractions of about 30 vol.% Ti$_5$Si$_3$ in the hexagonal α-Ti(Si) solid solution matrix.

For the development of high temperature oxidation resistant Ti-Si-(Al) based alloys two different processing routes were used: Directional solidification in order to achieve an effective fiber reinforcement of α-Ti matrices due to high strength and elastically stiff discontinuous Ti$_5$Si$_3$ fibers which are parallel aligned in the microstructure. The other one is to produce eutectic or hypoeutectic alloys with ultra-fine microstructures consisting of α-Ti(Al) solid solutions with a fine dispersion of Ti$_5$Si$_3$ particles of several microns in size. These materials show improved ductility and fracture toughness. This paper presents basic physical and mechanical properties of the high melting point silicides Ti$_5$Si$_3$ and TiSi$_2$ as well as of hypoeutectic Ti-Si-(Al) alloys possessing superior high temperature properties.

Key words: lattice structure, bonding energy, elasticity, strength, creep resistance, fracture toughness

1.   INTRODUCTION

High melting point intermetallics based on titanium silicides are very attractive for application temperatures up to 1300 °C and above. The titanium silicides Ti_5Si_3 and $TiSi_2$ exhibit low density, high elastic stiffness, high creep strength, and excellent oxidation resistance. In addition titanium silicides possess appropriate electrical and thermal conductivity, and good compatibility to silicon and titanium substrates. Therefore, these silicides are also suitable for electronic interconnections, diffusion barriers and graded bioactive glass coatings [1,2].

However, the monolithic compounds possess a lack of room temperature ductility and toughness because of their complex lattice structures and sessile superdislocations with large Burgers' vectors. The brittle-ductile transition temperatures of these silicides are quite high of the order of 800 to 1050 °C, respectively.

In order to take advantage of the superior properties of these refractory silicides in combination with a ductile titanium matrix particle and fiber reinforced composites based on α-Ti-Si-(Al) have been developed. Two different processing routes have been performed:

- Directional solidification to produce fiber reinforced composites with high strength and elastically stiff discontinuous Ti_5Si_3 fibers aligned with the solidification direction.

- The preparation of fine-grained hypoeutectic or eutectic microstructures consisting of an α-Ti matrix with a fine dispersion of Ti_5Si_3 particles of few microns in size.

The present paper describes the complex lattice structures, the physical and mechanical properties of the refractory silicides Ti_5Si_3, $TiSi_2$ as well as α-Ti/Ti_5Si_3 composite materials of higher strength as function of the temperature. The results will be discussed with respect to microstructural features.

2.   CONSTITUTION, LATTICE STRUCTURES AND BINDING ENERGIES

Comprehensive studies on the binary titanium-silicon phase diagram have been carried out by [3,4]. Gase-phase reaction metallurgy of the titanium-silicon system was employed by [5]. The equilibrium phase diagram Ti-Si, reported by MASSALSKI [6], is presented in fig. 1. It consists among others of the two prominent compounds Ti_5Si_3 and $TiSi_2$ with congruent melting temperatures of 2130 °C and 1500 °C.

The homogeneity range of Ti_5Si_3 is between 36.5 and 39.5 at% Si and the line compound $TiSi_2$ is of the composition 66.6 at% Si. The incongruently melting silicides Ti_5Si_4 and $TiSi$ in between are formed by peritectic reactions at

intermediate temperatures of 1920 °C and 1570 °C. The titanium rich side exhibits an eutectic at 1330 °C and 13.5 at% Si with the constituent phases of β-Ti and Ti_5Si_3. At lower temperature of about 1170 °C the Ti_3Si compound will be formed peritectoidally from β-Ti and Ti_5Si_3. However, the reaction kinetics is very sluggish, so that the formation of Ti_3Si can be suppressed in the cooling stage of the eutectic reaction L→β-Ti+ Ti_5Si_3. This is an important aspect for the production of directionally solidified eutectic α-Ti- Ti_5Si_3 samples by electron beam zone melting. On the silicon rich side of the phase diagram the $TiSi_2$ compound and pure silicon are forming an eutectic at about 85 at% Si. The eutectic temperature was determined to 1330 °C.
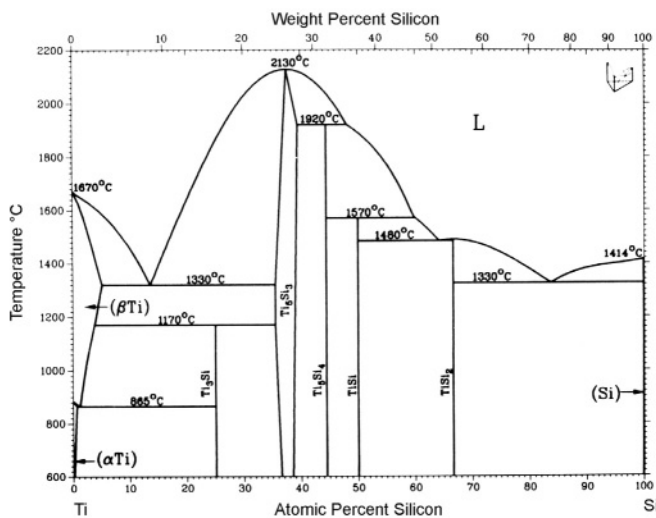
Figure 1. Equilibrium phase diagram of the binary Ti-Si system.

The refractory compound Ti_5Si_3 exhibits the complex hexagonal $D8_8$ structure (Strukturberichte designation) representing the space group $P6_3/mcm$ (Pearson symbol hP 16) with the lattice parameters: a =5.143Å and c =7.444 Å [7]. The compound contains two formula units per unit cell and belongs to the Mn_5Si_3 prototype of structure [8], as shown in fig. 2a. The $D8_8$ structure is built up by two different atomic species, which are occupying three different crystallographic positions. The Ti(I) atoms form columns of octahedrons connected along the c-axis, whereas Ti (II) atoms are arranged in chains parallel to each other. The Si atoms are surrounding by octahedral Ti(II) atoms. The octahedral interstices along the c-axis might be partially or completely filled by interstitials [9].

$TiSi_2$ is a stoichiometric line compound of ordered orthorhombic C 54 type of structure, space group F ddd (Pearson symbol oF24). The unit cell of

$TiSi_2$ is illustrated in fig. 2b. The orthorhombic structure consists of 24 atoms referring to 8 formula units. Hexagonal close-packed atomic silicon layers are forming perpendicular to the c-axis planar ring structures possessing centered Ti atoms. The lattice parameters are: a=8.267 Å, b=4.800 Å, and c=8.5505 Å [10].
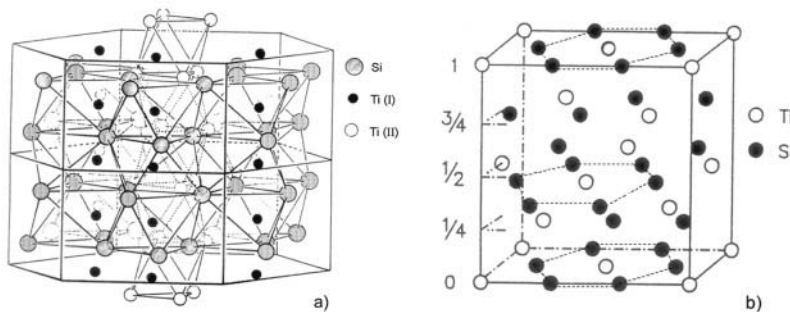

Figure2. Crystal structures of the intermetallic Ti_5Si_3 (a) and $TiSi_2$ (b) compounds.

The densities of the stoichiometric compositions were determined to 4.32 g/cm^3 for Ti_5Si_3 and 4.07 g/cm^3 for $TiSi_2$. Both compounds possess lower densities than titanium base alloys. A good correlation between binding energies, melting temperatures and microhardness of the investigated silicides is shown in table I.

Table I: Relation between binding energy, melting temperature and Vickers' hardness.

	binding energy (kJ/mole)	melting temperature (K)	Vickers' hardness (load : 1kp) (HV1)
Ti_5Si_3	- 1095 ± 40	2403	970 ± 20
$TiSi_2$	- 687,5 ± 25	1773	870 ± 15

The maximum binding energy or lattice cohesion causes the highest melting temperature -exactly the highest sublimation temperature. The hardness is also a direct measure for the cohesive force of the lattice.

Structures and properties of the refractory silicides Ti_5Si_3 and $TiSi_2$ and Ti-Si-(Al) eutectic alloys

3.   EXPERIMENTAL PROCEDURES

3.1   Material Preparation

The monolithic intermetallic Ti_5Si_3 and $TiSi_2$ compounds were prepared by solid state reaction from pure titanium and silicon powders. The conglomerates obtained were ground in argon atmosphere to powders of final grain sizes ranging from 10 to 50 microns. The fine grained alloy powders were precompacted by uniaxially pressing at room temperature in mild steel cans using molybdenum foils as inlets. After degassing at 400 °C the cans were sealed under vacuum and densified by HIP process at T=1250 °C in argon atmosphere under p=2000 bar pressure for 10 hrs. The microstructure of the processed material possessed grain sizes of about 20 to 50 microns.

The fine-grained hypereutectic TiSiAl alloys were melted in an argon arc furnace and cast to ingots. The unidirectionally solidified Ti-Ti_5Si_3 eutectic alloy was produced by electron beam zone melting technique using a zone velocity of 60 mm/h and a temperature gradient of about 50 K/mm. As starting material, precompacted rods of 25 mm in diameter and 300 mm in length have been prepared by a mixture of Ti_5Si_3 powder and α-Ti powder (99.9% purity). Test specimens of the monolithic Ti_5Si_3 compound material and the eutectic α-Ti-Ti_5Si_3(Al) alloy were cut by spark erosion and machined using diamond tools.

3.2   Material Testing

The microstructures of the consolidated and deformed samples were characterized by X-ray diffraction, optical and electron microscopy (SEM and TEM). The samples for mechanical testing have been prepared by spark erosion. The linear thermal expansion was determined by using a thermomechanical system (TMA). The temperature-dependent elastic moduli have been measured by the resonance frequency and the pulse-echo method. The bulk moduli were determined by synchrotron radiation diffraction using a high-pressure diamond-die cell at HASYLAB. The compression and creep tests were performed with computer-controlled tensile testing and creep machines.

4.   RESULTS

4.1   Microstructures of the silicide compounds

The microstructures of the hot isostatically pressed and of the creep deformed silicides were studied by light and transmission electron microscopy (TEM). Fig. 3a represents an optical micrograph of the grain structure of the intermetallic Ti_5Si_3 compound after compaction. The randomly distributed Ti_5Si_3 grains are of 10 to 40 µm in size. Some grains are showing twins. The $TiSi_2$ material reveals a more uniform polygonal grain morphology with an average grain size of about 30-35 µm, as shown in fig. 3b (polarized light). Both titanium silicides exhibit similar grain structures. After the HIP process no porosity of the silicides appeared and the edges of the grains possess a more rounded shape.
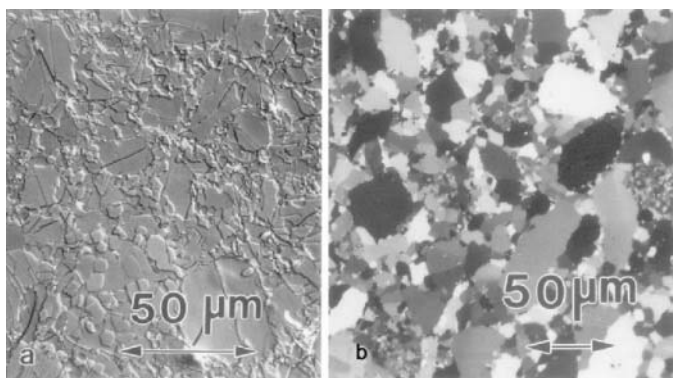
Figure 3. Optical micrographs of as compacted Ti_5Si_3 (a) and $TiSi_2$ (b) compounds.

TEM investigations of undeformed Ti_5Si_3 samples reveal two distinct microstructural features, as illustrated in fig. 4a. Some areas are free of dislocations whereas other regions exhibit dislocation networks and subgrain boundaries. It should be mentioned that planar defects, such as stacking faults and incoherent deformation twins occurred by accumulated plastic strain in the grains. The microstructure of the intermetallic $TiSi_2$ compound is shown in fig. 4b revealing parallel-aligned dislocation segments forming a dislocation pile up.

The TEM images of figs. 5a and 5b are showing the dislocation structures of creep deformed Ti_5Si_3 and $TiSi_2$ samples. Ti_5Si_3 reveals after high temperature deformation at 1000°C under compressive creep stresses low dislocation densities and few stacking faults. In contrast the $TiSi_2$ samples possess higher dislocation densities in the deformed state, as presented in fig. 5b. During creep subgrains have been developed in Ti_5Si_3 and $TiSi_2$ with average subgrain sizes

of about 0.5 to 3 µm. Although stable hexagonal dislocation networks were observed in TiSi$_2$ samples as illustrated in fig. 5b. It should be noted that the subgrain density in the silicides does not vary with the applied stress levels in the creep tests.
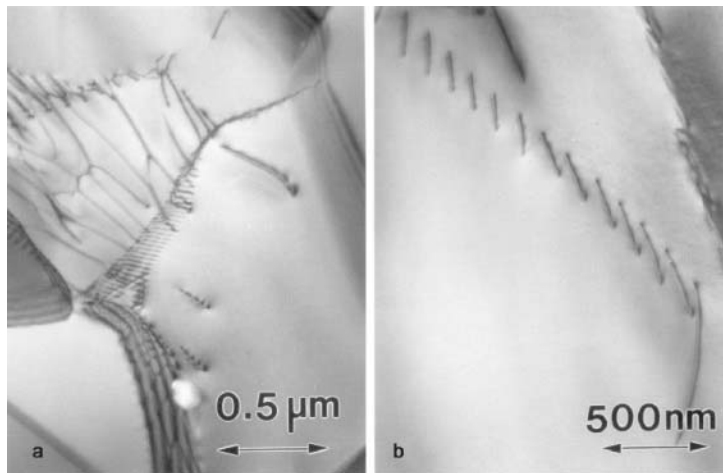

Figure4. TEM bright field images illustrating the dislocation structures in the as compacted samples of Ti$_5$Si$_3$ (a) and TiSi$_2$ (b).
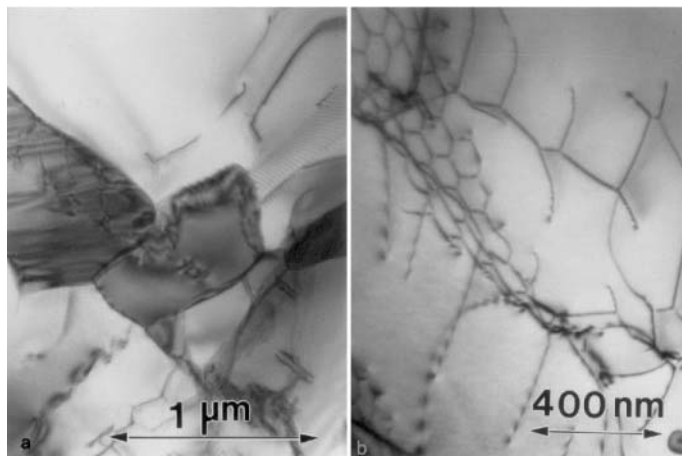

Figure 5. TEM bright field images of creep deformed Ti$_5$Si$_3$ (a) and TiSi$_2$ (b) samples tested at 1000 °C, strain rate $\dot{\varepsilon} = 10^{-7} \text{s}^{-1}$.

4.2   Thermal expansion coefficients

The temperature dependence of the linear thermal expansion coefficients $\alpha(T)$ of the investigated titanium silicides are illustrated in fig. 6. The complex hexagonal Ti_5Si_3 compound exhibits α (T) values lower than those of the disilicide $TiSi_2$ with the closer packed C54 structure. Another reason is that the anharmonicity of the   lattice vibrations -phonons- and the asymmetry of the lattice potential curves of the Ti-Si and Si-Si bonds of the C54 structure are more pronounced compared to that of the $D8_8$ lattice.

The expansion coefficients of the $TiSi_2$ compound determined in the temperature range from 25 to 200 °C is of about $9.9x10^{-6}K^{-1}$. The complex Ti_5Si_3 compound exhibits lower linear thermal expansion coefficients of about $\alpha = 7.1x10^{-6}K^{-1}$ in the same temperature range. At 1000 °C the thermal expansion coefficient of the intermetallic $TiSi_2$ compound increases to $11.7x10^{-6}K^{-1}$ and for the Ti_5Si_3 compound to $9.1x10^{-6}K^{-1}$. From the second Grüneisen law the Grüneisen's constant 'γ' were derived to about $\gamma=1.44$. This is comparable with the γ-value of the high melting point transition metal molybdenum of about $\gamma=1.55$, respectively.
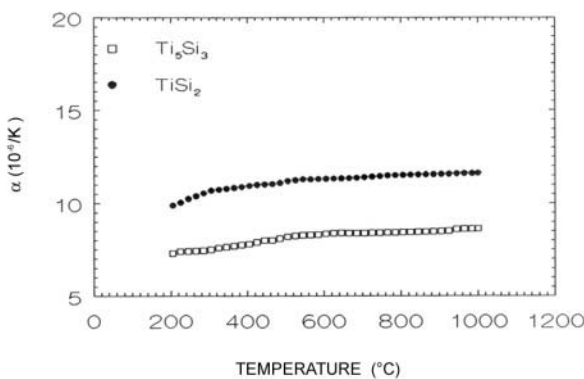
Figure 6. Temperature dependence of the thermal expansion coefficients of the monolithic Ti_5Si_3 and $TiSi_2$ compounds.

Generally, the thermal expansion is based on the interrelationships between thermal lattice vibrations and the shape of the potential curves of the atomic species, e.g. curvature of the potential trough, position of its minimum, and the asymmetry of the potential curves. The refractory Ti_5Si_3 compound exhibits a strong covalent bonding characterized by its high cohesion energy of -1094 kcal/mole. Other important facts are the low degree of anharmonicity of the phonons, the asymmetry of the potential curves, and the tight binding between the titanium and silicon atoms.

4.3   Elastic moduli

The resonance frequency technique has been used for determining the adiabatic Young's moduli in dependence on test temperatures up to 1000 °C. The shear moduli were measured by the pulse-echo ultrasonic technique. The bulk moduli were determined by synchrotron radiation diffraction. The temperature-dependent Young's and shear moduli are plotted in fig. 7.
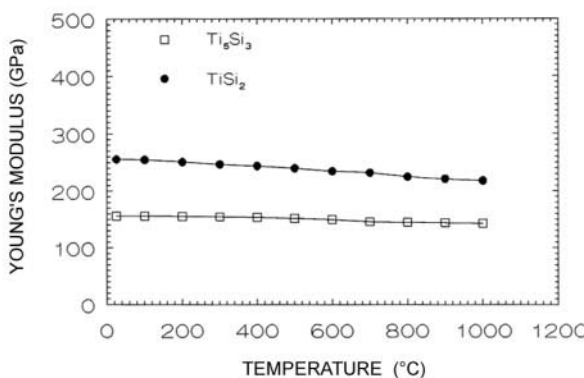

Figure 7. Young's moduli of the monolithic Ti₅Si₃ and TiSi₂ compounds as function of temperature.

Ti$_5$Si$_3$ exhibits at room temperature a Young's modulus of 156 GPa and with increasing temperature a small decrease occurred . The elastic modulus at 1000 °C was determined to be 140.5 GPa. The Young's modulus of the intermetallic TiSi$_2$ compound exhibits much higher values of about 256 GPa at room temperature and 205 GPa at 1000 °C, respectively [11]. An interesting result is that the shear modulus of TiSi$_2$ is about 103 GPa. This value is significantly higher than the shear modulus of 60.8 GPa of the Ti$_5$Si$_3$ compound. An explanation for the higher elastic stiffness of TiSi$_2$ is its closer packed lattice structure and the shorter interatomic Si-Si bond length in comparison with the not so densely packed hexagonal D8$_8$ structure of Ti$_5$Si$_3$. Therefore, TiSi$_2$ exhibit higher elastic moduli because of the stronger binding forces of the more tight Si-Si bonds [12,13].

The room temperature elastic moduli , such as the compression or bulk modulus 'K', Young's modulus 'E', and shear modulus 'G' of the Ti$_5$Si$_3$ and TiSi$_2$ compounds are presented in table II. The bulk and shear moduli are relatively low in comparison to the Young's moduli. This implies that Poisson's ratio is about $v = 0,24$ or less indicating that the elastic transverse

strain or contraction tends to be decreasing with increasing lattice energy and higher elastic stiffness.

Another important fact is the influence of the atomic volume of the unit cells ($\frac{V_{cell}}{N}$) of the silicides on the bulk moduli. N is the number of atoms per unit cell. For Ti_5Si_3 the unit cell volume is $V_{Ti_5Si_3} = 246{,}95 \text{ Å}^3$ and $N_{Ti_5Si_3} = 16$ atoms. $TiSi_2$ possesses a volume of the unit cell of $V_{TiSi_2} = 339{,}3 \text{ Å}^3$ and $N_{TiSi} = 24$ atoms. It can be easily shown, that the atomic volumes are $V^*_{Ti_5Si_3} = 15{,}433 \text{ Å}^3 \text{ atom}^{-1}$ and $V^*_{TiSi_2} = 14{,}14 \text{ Å}^3 \text{ atom}^{-1}$. These values are comparable or higher than those of close-packed cubic or hexagonal unit cells of the refractory transition metals exhibiting high binding energies.

Table II: Elastic moduli K, E, G of Ti_5Si_3 and $TiSi_2$ at room temperature.

	bulk modulus K (GPa)	Young's modulus E (GPa)	shear modulus G (GPa)
Ti_5Si_3	110 ± 5	156 ± 8	61 ± 3
$TiSi_2$	125 ± 8	256 ± 10	103 ± 5

4.4   Yield stress and plastic strain

The flow stresses of the intermetallic Ti_5Si_3 and $TiSi_2$ compounds were determined in compression tests in air at the strain rate of $\dot{\varepsilon} = 10^{-2} \text{ s}^{-1}$ in the temperature range from 700 to 1500 °C. Figure 8 presents the true yield stress vs. temperature curves.

These show remarkable differences in the yield stresses of the two silicides in the temperature range from 1000 to 1300 °C. Flow stresses of about 1050 MPa for Ti_5Si_3 and 230 MPa for $TiSi_2$ at 1000 °C were recorded. In the temperature range between 700 and 1300 °C the flow stress of $TiSi_2$ decreases from 900 to 17 MPa. The Ti_5Si_3 compound exhibits at 1500 °C still a flow stress of 50 MPa. This fact is quite remarkable in comparison to other high temperature materials, such as the high melting point aluminides NiAl (Re, Mo) of quasi-binary eutectic microstuctures [14]. At 700 °C the total amount of macroscopic plastic deformation of the $TiSi_2$ compression test samples was about $\varepsilon_{pl} = 4.5\%$ without crack formation.

At 1000 °C the plastic deformation of Ti_5Si_3 was of the order of $\varepsilon_{pl} = 1.5\%$. Generally, with increasing deformation temperature a remarkable decrease of the yield stress occurred. This is caused by activated slip systems for dislocation glide on (001) [110] and (001) [$1\overline{1}0$] slip systems in $TiSi_2$ and on pyramidal ($\overline{1}101$) or ($2\overline{3}11$) slip planes in Ti_5Si_3. Another acting mechanism is the enhanced mobility of jogged screw dislocations. The large numbers of atoms per unit cell - Ti_5Si_3 (16 atoms) and $TiSi_2$ (24 atoms) -

cause enlarged Burgers' vectors of higher energy, which tend to be more sessile. The complex lattice structure and their pronounced Peierls' potential will also restrict the dislocation mobility in the materials.

It should be mentioned that solid solution hardening of Ti_5Si_3, alloyed with larger amounts of the transition metals (T^{Me}) Nb or Cr replacing Ti atoms in the lattice, was observed [15]. In earlier investigations solid solution softening was detected by alloying the compound with Al and replacing Si atoms [16]. The crystallographic structure of the $D8_8$-type of the modified $(Ti_{5-x}T_x^{Me} Si_3)$ and $Ti_5 (Si_{3-y}Al_y)$ compounds remains unchanged.
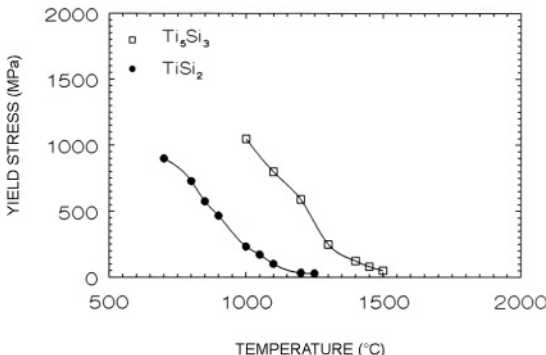
Figure 8. Yield stress vs. test temperature of the monolithic intermetallic Ti_5Si_3 and $TiSi_2$ compounds.

4.5   Fracture toughness

The temperature dependence of the fracture toughness was determined in a four-point bend test in the temperature range from 25 to 1000 °C in air. K_{IC} values are an important design criterion for applications as engine parts of these materials. In general, fracture toughness measurements are limited to high strength materials in which the yield to tensile stress ratio is more than 0.75. However, this is here not the case. The influence of temperature on the K_{IC} values is presented in fig. 9.

The investigated silicides exhibit poor fracture toughness at room and elevated temperatures below the brittle-ductile transition. The Ti_5Si_3 compound reveals fracture toughness at room temperature of about 2.1 MPa $m^{1/2}$ and the disilicide $TiSi_2$ shows a K_{IC} value of 1.9 MPa $m^{1/2}$. Above 1000 °C significant improvement of ductility was detected of Ti_5Si_3. Controversy, $TiSi_2$ reveals a sharp brittle-ductile transition at 805 °C.

Scanning electron microscopy (SEM) examinations of the cracked specimens show transgranular crack propagations at room and somewhat higher temperatures of about 500 °C. Crack initiation takes place by intrinsic stresses, based on structural inhomogeneities or impurities [16]. However, grain boundaries may play an important role in crack propagation, e.g. if precipitations of oxides or segregations of impurities are present. It was clearly observed by Auger spectroscopy that small amounts of segregated impurities on grain boundaries caused in the temperature range from 500 to 700 °C the decrease in the K_{IC} curve. It should be noted that the stress intensity factors of the silicides will be markedly increased by a factor of two due to microstructural refinements by using ultrafine grained alloy powders.
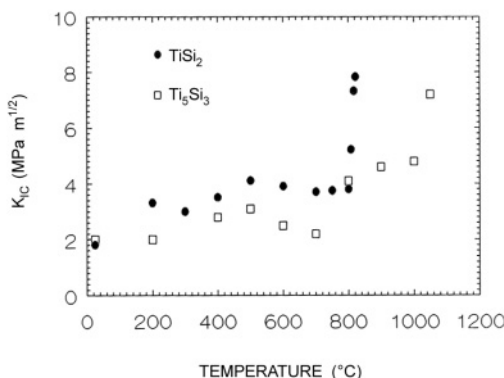
Figure 9. Stress intensity factors of the intermetallic Ti_5Si_3 and $TiSi_2$ compounds as function of test temperature.

4.6   Creep properties

Ti$_5$Si$_3$ and TiSi$_2$ samples were creep tested in compression in the temperature rage from 800 to 1200 °C in air at constant strain rates. The creep properties of the silicides can be quantitatively described by the well known power law equation [17] as follows:

$$\dot{\varepsilon}_s = A \frac{D_L G |\vec{b}|}{kT} \left(\frac{\sigma}{G}\right)^n \qquad (1)$$

where '$\dot{\varepsilon}$' is the creep rate; 'A' is a structure factor; $D_L = D_0 \exp\left(-\dfrac{Q}{RT}\right)$ describes the lattice diffusion; '$\vec{b}$' is the Burgers vector of mobile dislocations; 'σ/G' is the shear modulus compensated creep stress; 'R' represents the universal gas constant; 'k' is the Boltzmann's constant, and 'T' is the absolute temperature.
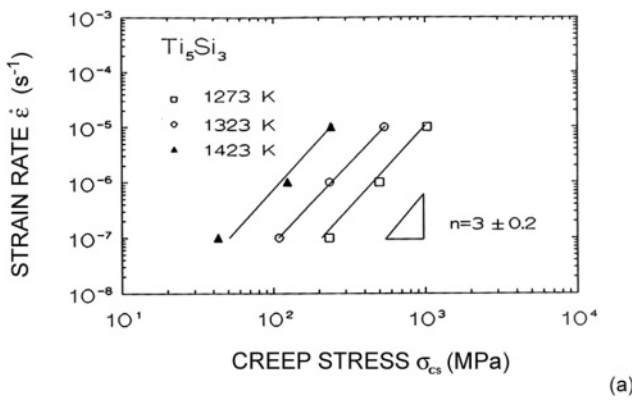
(a)
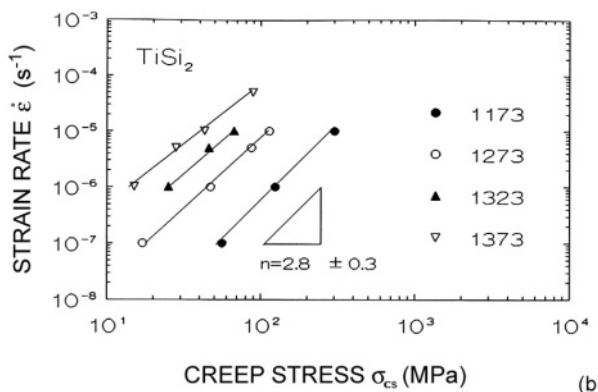

(b)

Figure 10. Stress exponent **n** derived from the slope of the log $\dot{\varepsilon}$ vs. log. σ plot for (a) Ti$_5$Si$_3$ and (b)TiSi$_2$.

According to figs. 10a and 10b, the stress exponents where calculated from the slope of the creep stress vs. strain rate curves. The n value for creep of the Ti$_5$Si$_3$ compound is n=3.0±0.2. This predicts a power law creep behavior based on viscous glide of dislocations sustained by diffusion

mechanisms. For the TiSi$_2$ material, the stress exponent was determined to n=2.8±0.2. However, it should be noted that deviations from the straight $\dot{\varepsilon}$ vs. σ curve occurred at high temperatures and low stresses. The creep stresses in the temperature range from 900 to 1000 °C were determined to 56 and 17 MPa at a strain rate of $\dot{\varepsilon} = 10^{-7}$ s^{-1}. The dominant rate-controlling process is based on thermally activated dislocation glide and jogs of screw dislocation segments. At very high temperatures screw dislocations may climb with the aid of diffusional mass transport [18,19]. Grain boundary sliding may have a small contribution to creep deformation. The activation energies 'Q' have been determined from the Arrhenius plot using the relation:

$$Q = -R\left(\frac{\partial \log \dot{\varepsilon}}{\partial (1/T)}\right)_{\sigma} \tag{2}$$

The intermetallic Ti$_5$Si$_3$ compound exhibits an activation energy of Q = 350 ± 20 kJmol^{-1}, and for the TiSi$_2$ compound Q = 320 ± 20 kJmol^{-1} was determined. The apparent activation energies of the titanium silicides in high temperature creep experiments are independent on the stress level. It is well known that the activation energies for creep of intermetallic compounds are always higher than those of non-ordered alloys and of the activation energy for lattice self diffusion [20,21]. However, there is also a strong influence of the complex lattice structures on the creep resistance in comparison with other high strength intermetallics like γ-TiAl, Ni$_3$Al or NiAl-based alloys with L1$_0$-, L1$_2$- or B2-ordered lattice structures of higher symmetry [22].

4.7   Applications

Titanium silicides are under development as structural materials and coatings for high temperature applications, e.g. turbine airfoils, burning chamber parts and missile nozzles because of their excellent oxidation or hot gas corrosion resistance and high creep strength. A hybrid design concept for silicides as turbine airfoils has been evaluated. Specifically, TiSi$_2$ airfoil shells work as shielding to prevent high temperature or hot gas corrosion attack on the airfoil cores. The airfoils were fabricated by powder metallurgy on laboratory scale and tested in a combustion chamber at 1400 °C for 100 h without any damages, see fig. 11. The evaluation of the potential application of silicides for jet engine parts requires the development of a feasible processing route, which meets the requirements of porous and crack-free structural parts. Machining of silicides is very difficult and very expensive, similar to that of ceramic parts. Injection moulding might be a promising fabrication route for the production of near-net-shape components.
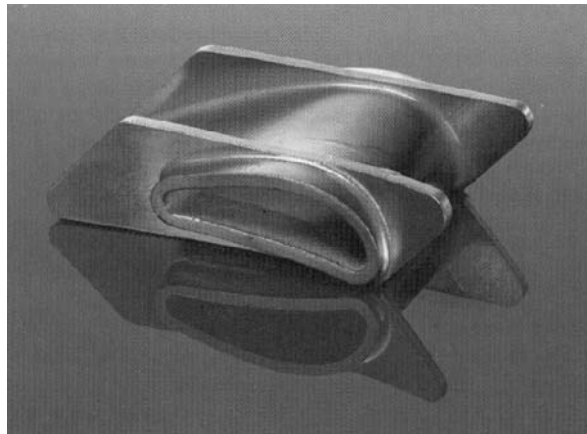
Figure 11. Powder metallurgy processed air foil of TiSi$_2$ tested in a combustion chamber at
1400 °C for 100 h.

5.   ALPHA TITANIUM-Ti$_3$Si$_3$ ALLOYS

5.1   Microstructures

Alpha titanium was particle strengthened and fiber reinforced by Ti$_5$Si$_3$. The material was produced as cast hypoeutectic alloys or directionally solidified eutectic composites. A typical microstructure of a hypereutectic Ti-Si7,5-Al1 alloy is illustrated in fig. 12a. Dendritic α-Ti grains are randomly distributed in the finely dispersed eutectic α-Ti-Ti$_5$Si$_3$ matrix. With increasing silicon content up to about 9 wt. % the microstructures of the as cast samples consist of a fine dispersion of Ti$_5$Si$_3$ silicide particles within the α-Ti(Si) solid solution matrix. This microstructure exhibits microhardness values of 360 to 390 HV$_{0.3}$ and possesses an excellent wear resistance [23]. Directional solidification produces an anisotropic microstructure, which is presented in figures 12b and c. The SEM images of longitudinal (a) and cross (b) sections reveal discontinuous Ti$_5$Si$_3$ fibers of hexagonal shape perpendicular to the fiber axis with an average thickness dimension of about 3 microns. The crystallographic c-axis of the fibers is oriented parallel to the rod axis. Some microcracks are located at the edges of the fibers. Blunted crack tips in the Ti-matrix were detected on both sides of the Ti$_5$-Si$_3$ fibers. These defects were induced by thermal stresses acting at the fiber-matrix interfaces.
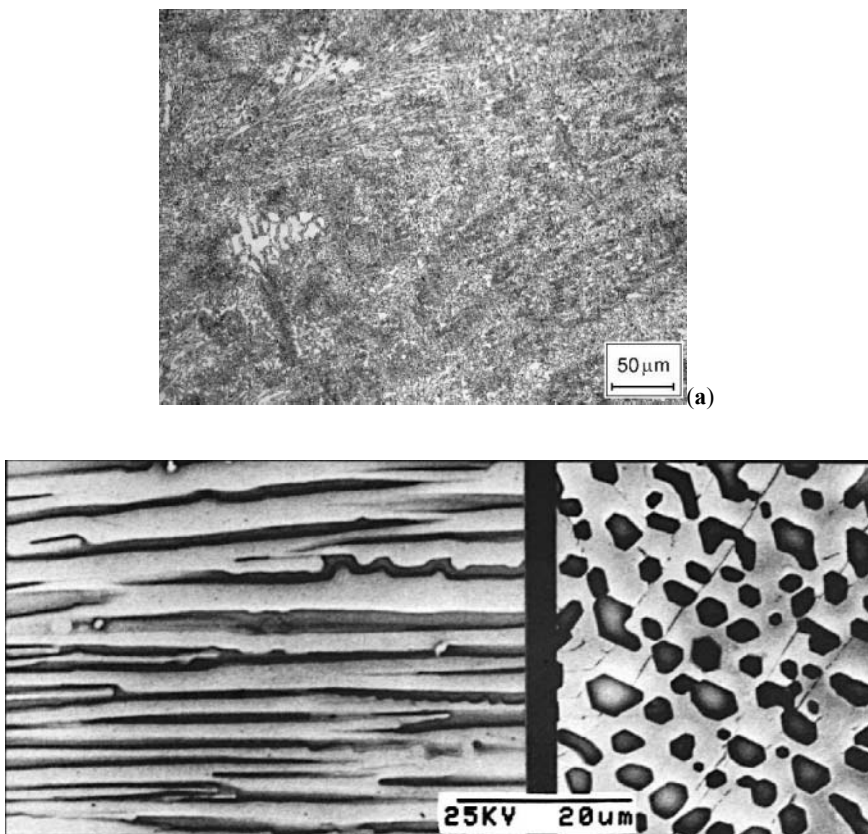
Figure 12. (a) Optical micrograph of the hypoeutectic Ti-7,5Si-Al1 illustrating primary solidified α-Ti solid solution grains (white areas) and fine grained eutectic. (b-c) SEM micrographs showing the fiber structure of a unidirectionally solidified eutectic Ti-Ti$_5$Si$_3$ composite in (b) longitudinal and (c) cross section.

5.2   Thermal expansion

The hypoeutectic alloy and the directionally solidified eutectic composite exhibit similar expansion coefficients, as shown in fig. 13. The α(T) values of the hypoeutectic material Ti-7.5Si-Al1 are slightly higher. In the temperature range between 25 °C and 200 °C the thermal expansion coefficient of the eutectic Ti-Ti$_5$Si$_3$ composite is about 9 to $10.0 \times 10^{-6} \text{K}^{-1}$ and the hypoeutectic alloy exhibits α(T) values of 10 to $11 \times 10^{-6} \text{ K}^{-1}$. For the Ti$_5Si_3$ compound the expansion coefficient was determined to a somewhat lower value of $\alpha = 7.1 \times 10^{-6} \text{K}^{-1}$. At 1000°C the thermal expansion coefficients of the directionally solidified eutectic Ti-Ti$_5$Si$_3$ increases to $\alpha = 13.8 \times 10^{-6} \text{ K}^{-1}$ and the hypoeutectic material reaches about 14.5 to $15 \times 10^{-6} \text{ K}^{-1}$. The polycrystalline Ti$_5Si_3$ compound exhibits an α-value of

about $9.1 \times 10^- 11.8$ x $10^{-6} K^{-1}$ at room temperature depending upon the anisotropy of $\alpha_\perp$ and $\alpha_\parallel$ and the present texture or preferential grain orientations. It should be noted that the Ti$_5$Si$_3$ compound shows also a strong anisotropy of its expansion coefficients. Parallel to the c-axis $\alpha_\parallel^{Ti_5Si_3}$ is about 9 x 10^{-6} K^{-1}. A lower thermal expansion coefficient of $\alpha_\perp^{Ti_5Si_3}$ = 3 x 10^{-6} K^{-1} was determined perpendicular to the c-axis at room temperature.
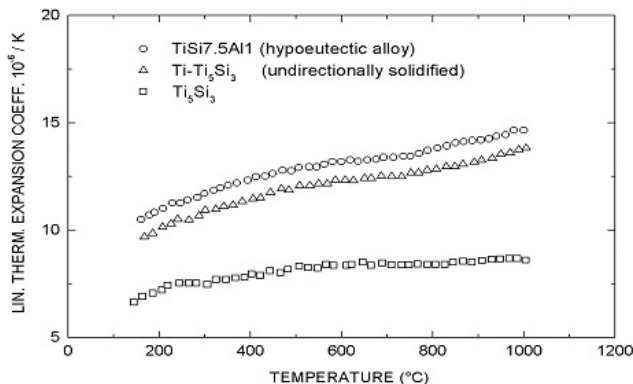
Figure 13. Temperature dependence of thermal expansion coefficients of Ti$_5$Si$_3$, the hypoeutectic Ti-Si7.5-Al1 alloy and the unidirectionally solidified eutectic Ti-Ti$_5$Si$_3$ composite.

5.3   Elastic moduli

The elastic moduli vs. temperature curves of the hypoeutectic Ti-Si7.5-Al1 alloy and of the directionally solidified eutectic α-Ti-Ti$_5$Si$_3$ composite with discontinuous Ti$_5$Si$_3$ fibers -aspect ratio of $l_f/d_f \approx 50$- are depicted in fig. 14. In comparison the temperature-dependent Young's modulus of the polycrystalline Ti$_5$Si$_3$ compound is also shown in the diagram. A detailed description and discussion of the elastic moduli of the pure silicides is given in section 4.3.

The Young's moduli of the α-Ti-Ti$_5$Si$_3$ composite at room- and elevated temperatures up to 600 °C are improved by stiff Ti$_5$Si$_3$ fibers. The difference between the Young's moduli of the polycrystalline compound and the composite is small. Considering the anisotropy of the microstructure and the rule of mixture for reinforced composites with discontinuous fibers a higher elastic modulus of the Ti$_5$Si$_3$ filaments in the direction of the c-axis than that of the quasi-isotropic polycrystalline Ti$_5$Si$_3$ material is expected. The elastic modulus parallel to the c-axis was determined to about $E_\parallel^{Ti5Si3}$ = 265 GPa. This value is slightly higher than $E_\parallel^{Ti5Si3}$ = 240 GPa, published by Crossman

et al. [24]. At temperatures above 700 °C a larger deviation of the moduli curves occurs. The Young's modulus of the two-phase alloy is governed by the softer α-titanium matrix. The hypoeutectic Ti-Si7,5-Al1 alloy shows a similar temperature dependence of the Young's modulus as the unidirectionally solidified eutectic. However, these values are slightly lower than those of the eutectic composite with fibrous microstructure.

It should be noted that the elastic values of the composite are remarkably higher at all investigated temperatures than those of the conventional Ti-Al6V4 or other advanced dispersion strengthened titanium alloys, such as IMI 834, respectively.
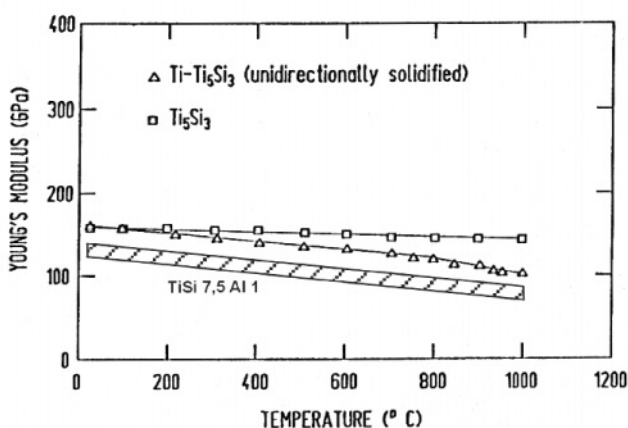
Figure 14. Young's moduli of the monolithic Ti_5Si_3 compound and of the hypoeutectic Ti-Si7.5-Al1 and the unidirectionally solidified eutectic Ti-Ti_5Si_3 alloy as function of the test temperature.

5.4   Yield stress

The temperature dependent yield stresses of the investigated samples were determined in compression tests at a strain rate of $(-\dot{\varepsilon}) = 10^{-4}s^{-1}$. The load axis was parallel to the Ti_5Si_3 fiber direction. Figure 15 illustrates the yield stress vs. temperature curves of the hypoeutectic Ti-Si7,5-Al1 alloy, the fiber reinforced eutectic Ti-Ti_5Si_3 composite, and of the polycrystalline Ti_5Si_3 compound as comparison. The flow stress curves of the investigated materials reveal two regimes. These are: The hypoeutectic and the unidirectionally solidified eutectic alloys show at room temperature flow stresses of the order of 1030 and 1080 MPa, respectively. The amount of plastic deformation in crack-free samples yields to $\varepsilon_{pl} = 10\%$ for the hypoeutectic alloy and about 3.5% for the unidirectionally solidified eutectic composite. With increasing temperature the compressive flow stresses decrease steadily to 200 MPa at 800 ºC - hypoeutectic

alloy – and to 250 MPa at 1000 °C of the unidirectionally solidified eutectic composite . At the maximum operation temperature of 650 °C of titanium-based alloys the hypoeutectic Ti-Si7,5-Al1 shows flow stresses of about 350 to 380 MPa. The reinforcing fiber structure of the eutectic composite leads to higher flow stresses of about 550 MPa. It should be noted that the widely used TiAl6V4 alloy with two phase α+β lamellar microstructure exhibits in the optimal processed state flow stresses of 350 MPa. This value is comparable with the flow stress of the hypoeutectic alloy. However, the unidirectionally solidified eutectic composite shows improved strength properties at higher temperature.

In comparison the refractory intermetallic Ti_5 Si_3 compound is brittle at deformation temperatures below 950 °C and no macroscopic ductility has been observed under compressive load. At the test temperature of 1000 °C a remarkable high flow stress of about 1050 MPa was achieved. Crack initiation revealed after plastic deformation of $\varepsilon_{pl} \approx 1.5\%$.

In the temperature range between 1000 °C and 1500 °C the flow stress of Ti_5Si_3 decreases from 1048 MPa to about 50 MPa. However, at 1300 °C beyond the maximum application temperature of nickel-based superalloys of about 1100 °C the Ti_5Si_3 compound possesses still a considerably high flow stress of 250 MPa.
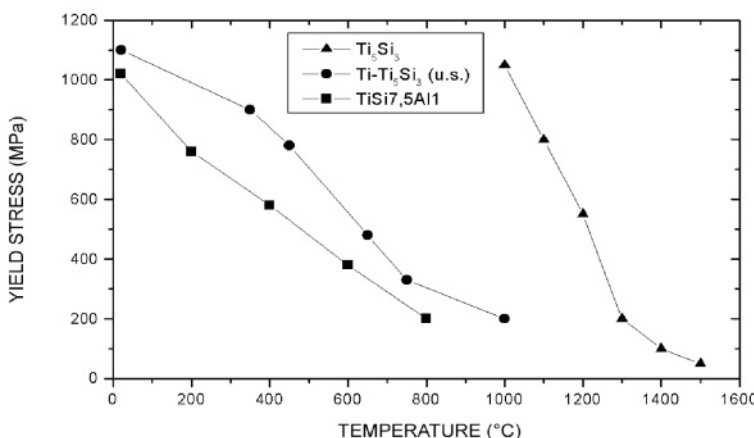
Figure 15. Yield stress as function of temperature of the hypoeutectic Ti-Si7.5-Al1 alloy and the unidirectionally solidified eutectic Ti-Ti₅Si₃ composite. In comparison the yield stress curve of the Ti₅Si₃ compound is plotted in the diagram.

The flow stress of the reinforced composite can be described quantitatively by the rule of mixture:

$$\sigma_0^C = V_f E_f \varepsilon_0^C + V_m E_m \varepsilon_0^C \tag{3}$$

where $E_{f/m}$ are the Young's moduli of the oriented fiber and the matrix; $V_{f/m}$ defines the volume fractions of the components, and $\varepsilon_0^C = 0.2\%$ is the plastic strain at the yield point of the composite.

Despite the fact that the reinforcing Ti_5Si_3 fibers are not continuously aligned within the α-titanium matrix the rule of mixture can be applied because the aspect ratio: $l_F/d_F = 50$ is fairly high and sufficient enough to transfer the load from the solid solution strengthened matrix to the fibers [25]. Assuming that the solid solution α-Ti(Si) matrix has a flow stress of about $\sigma_m = E_m \cdot \varepsilon_0^C = 300$ MPa at room temperature, the effective flow stress of the Ti_5Si_3 fibers was estimated to 2530 MPa. This value is higher than the fiber strength reported in the paper of Crossman et al. [24]. The estimated stress is of the order of the strength of titanium silicide whiskers prepared by chemical vapor deposition. However, it should be noted that it is very difficult to determine the exact flow stress and tensile strength at room and somewhat higher temperatures because of the brittle behaviour of the Ti_5Si_3 fibers.

The decrease of the yield stress of the composite with increasing temperature is strongly influenced by dominant softening mechanisms of the titanium matrix phase. At 1000 °C, where conventional titanium alloys are loosing completely their strength, a considerable flow stress of 150 MPa of the α-Ti-Ti_5Si_3 composite was determined.

5.5   Fracture toughness

The fracture toughness of the hypoeutectic alloy with a fine-grained eutectic matrix possessing primary alpha titanium grains of dendritic morphology is relatively high compared to the Ti_5Si_3 compound. At room temperature K_{IC}-values of about 21 to 23 MPa $\sqrt{m}$ were achieved. At higher temperatures at 600 °C and above the fracture toughness is increasing to 30 MPa $\sqrt{m}$ and higher for the hypoeutectic material. This is caused by the dominating ductile alpha titanium matrix. The relatively low fracture toughness of the monolithic Ti_5Si_3 up to 800 °C corresponds primarily to insufficiently activated slip systems and to SiO_2 precipitations at grain boundaries. Segregated impurities on grain boundaries of selected Ti_5Si_3 test samples have been detected using Auger spectroscopy. The results show that some oxygen is in the bounded state forming silicon oxide. Above 700 °C thermally activated dislocation motion and twinning on pyramidal glide and twin plans occurs. The K_{IC} value of Ti_5Si_3 is about 7 MPa $\sqrt{m}$ and somewhat higher at 1050 °C. A similar brittle-ductile transition in the temperature range from 850 °C to 1000 °C has also been observed for the flow stress of the $Ti_5Si_3(Al)$ material.
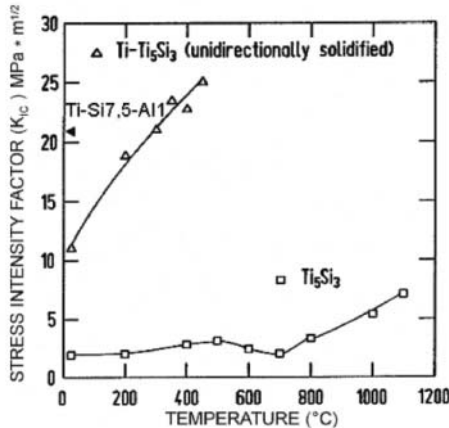
Figure 16. Stress intensity factors as function of temperature of the hypoeutectic Ti-Si7.5-Al1 alloys and of the directionally solidified Ti-Ti$_5$Si$_3$ composite in comparison to the Ti$_5$Si$_3$ compound.

The unidirectionally solidified Ti-Ti$_5$Si eutectic behaves more ductile and the stress intensity factor exhibits a strong increase up to 500 °C and higher. No ductile-to-brittle transition occurs below room temperature. This behavior is caused by the sufficient ductility of the α-titanium matrix.

The superior fracture toughness of the hypoeutectic Ti-Si7.5-Al1 alloy and of the Ti-Ti$_5$Si$_3$ composite at room and higher temperature is positively influenced by the ductile α-titanium matrix which is lowering the stress concentration at the crack tips and at the fiber – matrix interfaces by local slip. Another important mechanism is blunting the sharp crack tips. These governing mechanisms are diminishing the crack nuclei and the stable crack propagation at the circumference of the Ti$_5$Si$_3$ fibers in the reinforced composite.

6.   CONCLUSIONS

The refractory titanium silicides Ti$_5$Si$_3$ and TiSi$_3$ show promising properties, such as low density, high melting temperature, high elastic stiffness, as well as excellent creep and hot gas corrosion resistance. These silicides are under development as structural materials and coatings for high temperature applications, e.g. turbine airfoiles, burning chamber parts, and missile nozzles.

Other applications are wear resistant coatings and thin layers for diverse electronic and surface engineering purposes. The main disadvantage of the silicides is their intrinsic brittleness at room temperature up to the brittle-ductile transition at temperatures of 700 °C to 900 °C. However,

alpha titanium-Ti_5Si_3 composite materials exhibit improved ductility at room temperature and combine the advantages of high flow stresses and improved oxidation resistance at elevated temperatures. Therefore, these materials show considerable potential applications for blades in axial compressors and outlet valves in internal combustion engines.

REFERENCES

1. W.Y. Yang, H. Iwakuro, H. Yagi, T. Kudora, and S. Nakamura, Jpn. J. Appl. Phys. **23** (1984) 1560.
2. N.G. Einspruch and G.B. Karrabee, VLSI Electronics Microstructure Science, **vol. 6**, Academic Press, New York 1983.
3. M. Hansen, H.D. Kessler, and D.J. McPherson, Trans. ASM **44** (1952) 518.
4. V.N. Svechnikov, A.Kocherzhisky, L.M. Yupko, O.G. Kulik, and E.A. Shishkin, Dok. Akad. Nauk SSSR **193** (2) (1970) 393.
5. J.J. Nickl and K.K. Schweitzer, Z. Metallkde. **61** (1970) 54.
6. T.B. Massalski (ed.), Binary Alloy Phase Diagrams, **vol. 2**, American Society of Metals, Metals Park, Ohio, (1986) 2054.
7. J. Quakernaat and J.W. Visser, High Temperature – High Pressures 6 (1974) 515.
8. Strukturberichte **4** (1936) 24.
9. K. Cenzual and E. Parthé, Acta Cryst. **C42** (1986) 1101.
10. W. Jeitschko, Acta Cryst. **B33** (1977) 2347.
11. G. Frommeyer, R. Rosenkranz, R. Rablbauer and W. Smarsly. Materials Science and Eng. **A 152** (1992) 288.
12. H.J. Goldschmit, Interstitial Alloys. Butterworth, London 1967.
13. R. Rosenkranz and G. Frommeyer, Z. Metallkde. **83** (1992) 685.
14. G. Frommeyer and R. Rablbauer in: Defect Properties and Related Phenomena in Intermetallic Alloys, eds. E. P. George, H. Inui, M. J. Mills & G.Eggeler, Mat. Research Society, Boston MA (2002) 193.
15. L. Zhang and J. Wu, Acta mater. **vol. 46**, (1998) 3535.
16. H. Vehoff, S. Reuss, W. Vogt, and P. Specht in: Structural Intermetallics, R. Dariola, J.J. Lewandowski, C.T. Liu, P. L. Martin, D. B. Miracle, and M. V. Nathal eds., TMS, Warrendale, PA. (1993) 567.
17. O.D. Sherby and P.M. Burke, Prog. Mat. Sci. **13** (1967) 325.
18. C.R. Barret and W.D. Nix, Acta Metall. **13** (1965) 1247.
19. J. Weertmann, J. Appl. Phys. **28** (1957) 123.
20. N.S.Stoloff, Intern. Metals Reviews **29** (1984) 123.
21. G. Sauthoff: Intermetallics, Wiley VCH, Weinheim, 1995.
22. Intermetallic Compounds **vol. 1-4**, 2nd edition, J.H. Westbrook, R.L. Fleischer eds., Wiley and Sons, New York, 2000.
23. H. Dong, A. Bloyce. P.H. Morton, and T. Bell, Proceedings of the Eight World Conference on Titanium 1995, Volume III, Cambridge University Press, UK (1996), 1999.
24. F.W. Crossman and A.S. Yue, Metall. Trans. **2** (1971) 1545.
25. G. Frommeyer and S. Knippscheer in: Handbook of Aluminium, **vol.2**, eds. G.E. Totten and D. Scott McKenzie, Marcel Dekker. Inc., New York, Basel 2003.

REFRACTORY METAL / SILICIDE MULTIPHASE SYSTEMS FOR HIGH TEMPERATURE STRUCTURAL APPLICATIONS

M.G. Mendiratta, S.K. Menon, T.A. Parthasarathy
UES Inc., 4401 Dayton-Xenia Rd., Dayton OH 45432-1894.

Abstract: Alloys within the two systems Mo-Si-B and Nb-Ti-Cr-Si-X (X = Hf, Al, Sn) are currently being explored as high temperature structural materials for jet engines. The goal of this research is to develop materials with temperature capability significantly exceeding that of the best current Ni-base superalloys thus leading to higher engine thrust and higher structural efficiency. These multiphase alloys consist mainly of i) a solid solution refractory metal phase which provides some degree of resistance to fracture and ii) silicide and other intermetallic phases responsible for high temperature oxidation and creep resistance. This presentation is an overview of the progress made on these systems through continuing research at AFRL/UES and other organizations. The focus will be on composition selection, processing, microstructural evolution, oxidation behavior and mechanical properties. The processing methods consist of ingot casting, powder metallurgy and hot extrusion. Cyclic oxidation experiments have been carried out from 600-1350°C. Tensile, compressive, fatigue, toughness, and creep properties have been determined from RT-1400°C. These properties and failure mechanisms will be discussed and compared for the two systems. Venues for further research will also be presented.

Key words: Mo-Si-B and Nb-Ti-Cr-Si Alloys, Phase Relations, Processing, Mechanical Properties.

1.   INTRODUCTION

Alloys within the two systems Mo-Si-B and Nb-Ti-Cr-Si-X (X: Hf, Al, Sn) are currently being explored as high temperature structural materials for

jet engines. The goal of this research is to develop materials with temperature capability significantly exceeding that of the best current Ni-base superalloys thus leading to higher engine thrust and higher structural efficiency. This paper presents a brief overview and highlights of phase relations, oxidation behavior, processing, microstructures and mechanical properties including tensile, compressive, fatigue, toughness and creep. These properties and failure mechanisms are discussed for the two systems. The research venues needed to accomplish the development goals are presented. The latest compilation of published papers can be found in two recent reviews of these individual material systems [1,2].

2.   PHASE RELATIONS

2.1   Mo-Si-B Systems

Recent studies on phase relations in the ternary Mo-Si-B have focused on the Mo-rich portion of the phase diagram. Of particular interest is the Mo(ss) + Mo_5SiB_2(T2) + Mo_3Si(A15) 3-phase field with alloy compositions consisting of 60-70% volume fraction of the refractory metal phase and 30-40% volume fraction of simple mixture of line compounds. Thus the system provides thermodynamically stable mixture of phases up to at least 1600°C. The metal phase may provide resistance to low temperature fracture while the intermetallic phases maybe responsible for oxidation and creep resistance. Selected investigations have indicated phase modifications by quaternary and higher order alloying additions using some of the transition metals. Alloying with different transition metals provides a variety of phase equilibria including Mo(ss) + T2 + A15, Mo(ss) + T2 + Mo_5Si_3(Tl), and Mo(ss) + T2 + $D8_8$ ternary phase fields. However, the engineering development has been restricted to the alloys within the Mo_{ss} + T2 + A15 phase field with minor alloying additions.

2.2   Nb-Ti-Cr-Si-X System

A number of alloying studies have been carried out on this multicomponent system to establish phase equilibria. Because of a large number of elements investigated, the phase equilibria and phase stability are complex, and -- depending on alloying elements selected -- different phase-fields are obtained. In the main, however, the equilibrium phase fields, for example, at 1400°C are: (1) β solid solution Nb phase (Nb_{ss}) + Nb_5Si_3 + (Ti, Nb)$_3$Si and (2) Nb_{ss} + Cr_2Nb + Nb_5Si_3 + Ti_5Si_3. Within these phase fields a variety of microstructures can be obtained. The volume fractions can range from 45 - 55% for Nb_{ss}, 35 - 45% for Nb and Ti

silicides and 5 - 10% of Cr_2Nb. Unlike Mo-Si-B system however, the solubility of some elements in the Nb_{ss} phase, e.g. Cr and Si, may vary significantly with temperature above 1000°C, thus creating some phase instability with temperature.

3.   PHYSICAL PROPERTIES

Some of the physical properties are important for design considerations. They include density, elastic modulus, thermal expansion coefficient, and thermal conductivity. Melting temperature should be high for creep consideration at operating temperatures. The density of Mo-Si-B alloys is in the neighborhood of ~ 9.5 Mg/m^3, this is slightly higher or equal to the best Ni-base superalloys. Thus use of Mo-based alloys, as a structural material in jet engines will not result in significant weight penalty. The Nb-base alloys have density in the vicinity of ~ $7Mg/m^3$, this is about 25% less than the Ni-base alloys, and therefore, may result in significant weight saving provided that the high temperature strength and creep resistance are adequate. The thermal expansion ranges from 7 – 11 x 10-6 μm/μm and 8.1 - 8.6 x 10^{-6} μm/μm for Mo and Nb-base systems respectively in the temperature range of room temperature to 1400°C; these values are 3 - 4 x lower than those of Ni-base superalloys. The thermal conductivity for the Mo-base system is 50 - 112 W/m-k, these values are 2 - 4 x greater than those for Ni-base superalloys over the operating temperature range. Thermal conductivity for the Nb-base alloys, ranging from 8.6 - 28 W/m-k is lower than those for the Ni-base alloys. For the Mo system, these properties are favorable for reducing thermal stresses and reducing cooling air, thus providing more design flexibility. The elastic modulus values vary from 327 - 171 GPa for the Mo-system and 158 – 130 GPa for the Nb-system in the operating temperature range; the Mo system is considerably stiffer, and therefore less thermal shock resistant from this consideration alone. Based upon the physical properties given above, for both the Mo and Nb-based alloys new designs will be needed. The melting temperature of Mo-based alloys is the neighborhood of ~2100°C, while for Nb-based alloys, it ranges from 1700-1800°C.

4.   OXIDATION BEHAVIOR

4.1   Mo-Si-B System

Some fundamental and engineering investigations have been carried out on the static and cyclic oxidation response of these alloys in the laboratory air from 600 - 1400°C. The dominant mechanism of oxidation is the competition

between voltalization of Mo_{ss} phase as MoO_3 gas and the formation of protective borosilicate glass ($B-SiO_2$) scale. At 600°C, solid MoO_3 oxide forms with very small weight gains, and from 600 - 750°C the behavior is totally governed by rapid voltalization of the Mo_{ss} phase, without formation of $B-SiO_2$, and, therefore, no oxidation protection. With increasing temperature, there is progressively greater tendency toward formation of a protective continuous external $B-SiO_2$ layer after an initial transient weight loss due to formation and escape of MoO_3 gas. The best oxidation protection happens in the 1000 - 1300°C range, above this temperature the $B-SiO_3$ glass has less viscosity and there is also a more rapid inward diffusion of oxygen. Even though reasonable oxidation resistance is available in part of the operating temperature range, long-term structural use may require oxidation protection coating. Si-rich (e.g., $MoSi_2$) external coating is being explored currently.

4.2   Nb-Ti-Cr-Si-X System

The oxidation behavior in this multi-component system is complex. Initial protection (e.g. ~100 h at 1200°C) is provided by the formation of mixed, multiphase, complex (NbTi) and Si oxides with a high degree of internal oxidation due to rapid transport of oxygen from external oxides into the substrate alloys. After some time interval, the oxide scales begin to spall due to high growth stresses causing rapid weight loss. In addition to this overall behavior, at lower exposure temperatures (700 - 900°C) there is extensive silicide cracking in the substrate due to stresses caused by dissolved oxygen in the Nb_{ss} phase. Overall, these alloys thus exhibit limited oxidation resistance in the operating range. This will necessitate development of oxidation protection coating; this effort is currently in progress.

5.   PROCESSING

Processing of both systems containing refractory metal phases and silicide intermetallics is proving to be quite challenging. For the Mo-Si-B system, the preferred processing route has included a variety of powder metallurgy (P/M) methods involving pre-alloyed powder preparation by plasma-arc rotating electrode process and elemental-powder blending, cold pressing and sintering. Methods for powder consolidation and further thermomechanical processing to obtain desired microstructures are still in the early stages of exploration.

For Nb-based alloys a variety of processing methods are being attempted with varying degree of success in obtaining sound material containing desirable microstructures. These methods include non-consumable arc-melting, plasma arc melting, induction skull melting, investment casting,

directional solidification and powder-metallurgy processing. Hot-extrusions have been successful in hot working the cast ingots although large silicide phase constituents did not break or plastically deform. Investment casting of near-net shape components has recently been explored, however, successful development of this technique will require considerable effort.

6. MECHANICAL PROPERTIES

Only limited studies have been carried out to systematically investigate the mechanical behavior of these materials. Comprehensive data on composition-processing-microstructure property relations are lacking due to difficulty in processing these brittle/ductile multiphase systems. In general, well processed alloys containing controlled microstructures are not available.

6.1 Tensile/Compressive Yield and Fracture Strength

Limited results on not optimally processed Mo-Si-B alloys indicate that the brittle-to-ductile (B/D) transition temperature in tension is at temperatures ≥ 1100°C. Compressive yield strength varies approximately linearly from ~ 1500 MPa at room temperature to ~ 400 MPa at 1370°C. Tensile fracture strengths below the B/D temperature are in the neighborhood of ~ 600 MPa, and exhibit considerable microstructural sensitivity and large scatter.

Alloys within Nb system are also brittle in tension up to 1000°C. They exhibit compressive yield strengths of ~ 1600 MPa at room temperature, ~ 1500 MPa at 800°C and then rapid drop to ~ 600 MPa at 1000°C and ~ 300 MPa at 1100°C. Below the B/D transition temperature, the tensile fracture strengths exhibit considerable scatter with average values of ~ 250 MPa. In both systems fractography reveals that below the B/D transition temperature, the tensile fracture is initiated by large silicides or silicide agglomerates.

6.2 Toughness and Fatigue Crack Growth (FCG)

For the Mo-Si-B, the fracture toughness values range from 4 - 7 MPa√m at room temperature, and from 7 - 12 MPa√m at room 1300°C. In contrast, the Nb-based alloys are much tougher; depending on composition and thermomechanical processing they exhibit toughness values of 10 - 20 MPa√m at room temperature and up to 30 MPa√m at 1200°C. For the Mo-based alloys, the threshold values for the fatigue crack growth are 4 MPa√m at room temperature and 8PMa√m at 1300°C and crack-growth-rate slopes in the Paris-law regime are in the 40 - 60 range from room temperature to 1300°C. For Nb-based alloys the FCG behavior

exhibits threshold values of 7 - 11 MPa√m and Paris-law slope of 7 - 12 at room temperature; data are not available for elevated temperature.

6.3   Creep Behavior

There is hardly any published data on tensile creep on these systems. Compressive creep rates for the Mo-base materials exhibited minimum creep rates of 1 x 10^{-9}/s at 1200°C / 100 MPa and 1 x 10^{-8}/s at 1300°C / 100 MPa.   For Nb-based alloys the minimum creep rates are 5 x 10^{-8}/s at 1200°C / 100 MPa and 10^{-7}/s at 1300°C / 100 MPa. Much work is needed in determining tensile creep mechanisms and damage in both these systems.

7.   SUMMARY

Both the Mo and Nb-base refractory metal/silcide systems exhibit promising microstructural stability and reasonable mechanical properties for further development as jet engine structural materials. Both systems are brittle at low temperatures. Mo system exhibits poor fatigue and impact resistance. Novel design methods will be required for successful implementation of these brittle/ductile materials. Mo system exhibits adequate oxidation resistance from 900 - 1350°C while the Nb system exhibits limited protection up to 1200°C. Both systems will require environmental resistant coatings for long-term service at high temperatures. Processing and scale-up are major developmental issues and there is a lack of comprehensive composition / processing / microstructures /property data for both systems.

ACKNOWLEDGEMENTS

REFERENCES

1. D.M. Dimiduk and J.H. Perepezko "Mo-Si-B Alloys – Developing A Revolutionary Turbine-Engine Material", MRS Bulletin "in press" (September 2003, devoted to "Ultrahigh Temperature Materials for Jet Engines").
2. B.P. Bewleay, M.R. Jackson, J.-C. Zhao, P.R. Subramanian, M.G. Mendiratta and J.J. Lewandowsky, "Very High-Temperature Nb-Silicide Composites," MRS Bulletin "in press" (September 2003, devoted to "Ultrahigh Temperature Materials for Jet Engines).

MICROSTRUCTURAL EFFECTS AND KINETICS OF HIGH TEMPERATURE OXIDATION IN NB-SI BASE ALLOYS

E. Sarath K Menon, Triplicane A. Parthasarathy and Madan G. Mendiratta
UES Inc., 4401 Dayton-Xenia Road, Dayton, OH 45432-1894, USA

Abstract: Multiphase Niobium-Silicon alloys offer great potential as a new generation of refractory material system that could meet the high-temperature capability envisaged to exceed the application temperatures of Ni base superalloys. One of the serious concerns in the application of Nb based alloys is their poor oxidation resistance at elevated temperatures. However, alloying of the Nb solid solution phase can be quite effective in obtaining remarkably improved high-temperature oxidation resistance without compromising other high-temperature mechanical properties. Several researchers have investigated microstructures and properties of Nb-Ti alloys containing Si as one of the main alloying additions, together with other elements such as Cr, Al, Mo and Hf. Alloy systems containing high volume fractions of high-melting intermetallic silicide phase together with the ductile refractory solid-solution phase have been studied in detail in the past. In this paper an overview of the high temperature oxidation resistance of these multiphase alloys will be provided. Calculated phase diagrams were examined with a view to exploring a variety of possible invariant reactions in these systems and the effect of alloying elements on the stability and distribution of silicides, mainly Nb_3Si and Nb_5Si_3 will be illustrated. The effect of microstructural distribution on high temperature oxidation resistance of multiphase alloys will be discussed. In addition, the overall kinetics of the oxidation reaction, the nature of the reaction products and the development of the oxidation products as well as the mechanism of oxidation will be discussed.

O.N. Senkov et al. (eds.), Metallic Materials with High Structural Efficiency, 315–326.
© 2004 *Kluwer Academic Publishers. Printed in the Netherlands.*

1.   INTRODUCTION

Alloying of Nb with Ti and other elements has been found to be an effective method to greatly improve its oxidation resistance at high temperatures where these alloys offer great potential [1-7]. Nb-Si alloys containing a variety of other alloying elements, principally Ti offer a good combination of mechanical properties at elevated temperatures. Detailed reviews of recent studies are available [1-12] and here aspects of high temperature oxidation resistance of multiphase Nb alloys containing Si will be discussed. Extensive investigations aimed at achieving oxidation-resistant Nb alloys have indeed been carried out in the past and serve as useful guidelines in the recent alloy-development studies [13-15]. Many of these efforts were based on the development of Nb-Al alloys, and the formation of marginally protective alumina scales at high-temperatures was reported for some complex alloys [16-18]. The recent alloy-development efforts have focussed on the promising potential of silicide-bearing multicomponent Nb alloys, and this study was initiated to examine the oxidation behavior of this class of Nb alloys. Silica can provide a stable surface oxide to higher temperatures than alumina and the lower activation energy for oxygen diffusion in silica may make it more effective than alumina at higher temperatures [16]. Other major alloying additions in promising Nb alloys include Ti, Al and Hf, all of which form oxides that are even more thermodynamically stable than silica, and since SiO_2 and Nb_2O_5 have virtually no solubility in the solid state, complex oxide scale formation is expected to occur during oxidation of the multicomponent Nb alloys. A crucial drawback is the fact that the binary phase diagrams for these oxides with Nb_2O_5 (melting point ~ 1550° C) indicate eutectic formation [18, 19] and hence the maximum useful or safe temperatures before catastrophic melting of the oxide scales may be further lowered.

Thus, it is important that a fundamental understanding of the influence of chemistry and microstructure on the nature, sequences and mechanisms of oxidation at various temperatures be gathered. We have recently examined the kinetics of oxidation of advanced Nb-Ti-Si based alloys [20] and thus, in this paper only some of the results of current efforts on microstructural effects on oxidation resistance of Nb alloys will be emphasized.

2.   PHASE TRANSFORMATIONS AND MICROSTRUCTURES

The equilibrium diagrams Nb-Si and Ti-Si show eutectic reactions of the form $L \rightarrow \beta + Nb_3Si$ and $L \rightarrow \beta + Ti_5Si_3$ and consequently the ternary diagram

exhibits eutectic groves nearly parallel to the Nb-Ti binary and terminate in a Class II invariant reaction, $L+(Nb,Ti)_3Si \rightarrow \beta+ (Ti,Nb)_5Si_3$. A peretectic ridge from the reaction, $L+(Nb,Ti)_5Si_3 \rightarrow (Nb,Ti)_3Si$ also exists at Si contents slightly higher than the eutectic grove at higher Nb compositions and these reactions control the microstructures resulting from solidification of alloys of interest to the present discussion. The binary Ti_3Si phase forms from the peretectoid reaction, $\beta+Ti_5Si_3 \rightarrow Ti_3Si$ while the binary Nb_3Si phase undergoes the eutectoid reaction, $Nb_3Si \rightarrow \beta+Nb_5Si_3$. This eutectoid reaction was found to be extremely sluggish in binary Nb-Si alloys as can be seen from Figure 1 (a).
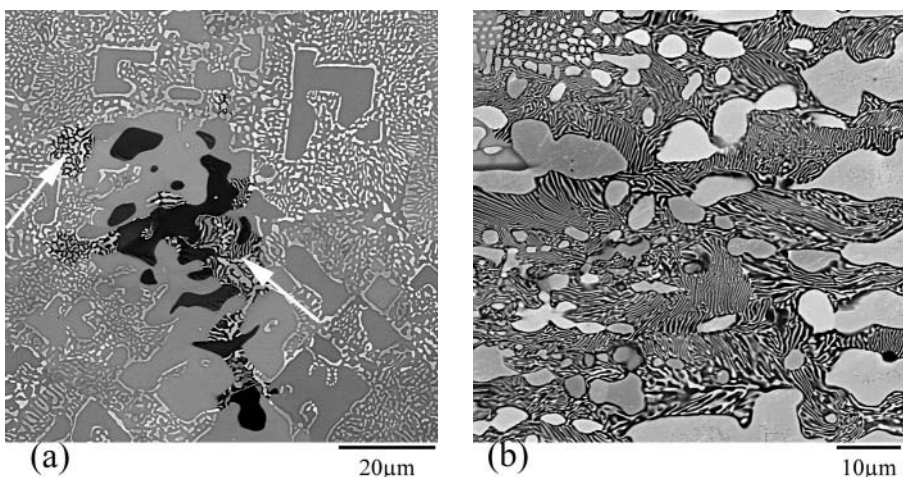
Figure 1. (a) Nb-17.2 Si, arrows indicate areas where eutectoid reaction has occurred. (b) Nb-15Si-12.5Ti. Both alloys were aged at 1200°C for 120 hrs.

Examination of ternary Nb-Ti-Si alloys showed that the eutectoid reaction was considerably accelerated and a lamellar product of β + $(Nb,Ti)_5Si_3$ formed during lower temperature heat treatments as shown in Figure 1. Microstructures resembling that of hypo-eutectoid steels constituting pearlite and proeutectoid ferrite could be produced in ternary alloys as illustrated in Figure 1(b). Increasing Ti contents of ternary alloys to about 20at% resulted in stabilizing the Nb_3Si phase even after prolonged aging as shown in Figure 2(a). Interestingly, addition of quaternary alloying elements such as Al, Cr or C was found to completely suppress the formation of the Nb_3Si phase, instead leading to formation of the Nb_5Si_3 phase from the liquid phase itself. In fact addition of Al to Ti-free Nb-Si alloy lead to eutectic solidification resulting in a fine microstructure composed of β and Nb_5Si_3. Figure 2 illustrates some examples of

microstructures that result from different alloying additions to Nb-Si alloys. From these micrographs it is clear that a wide variety of microstructures can indeed be generated in Nb alloys with careful alloying and suitable heat treatments. The microstructures associated with most alloys studied and characterized in detail is similar to that shown in figure 1(c) and is constituted of a distribution of large areas of Nb_5Si_3 in β matrix and depending upon exact alloy composition and heat treatment, smaller volume fractions of other phases like Ti_5Si_3 and Cr_2Nb may also be present.
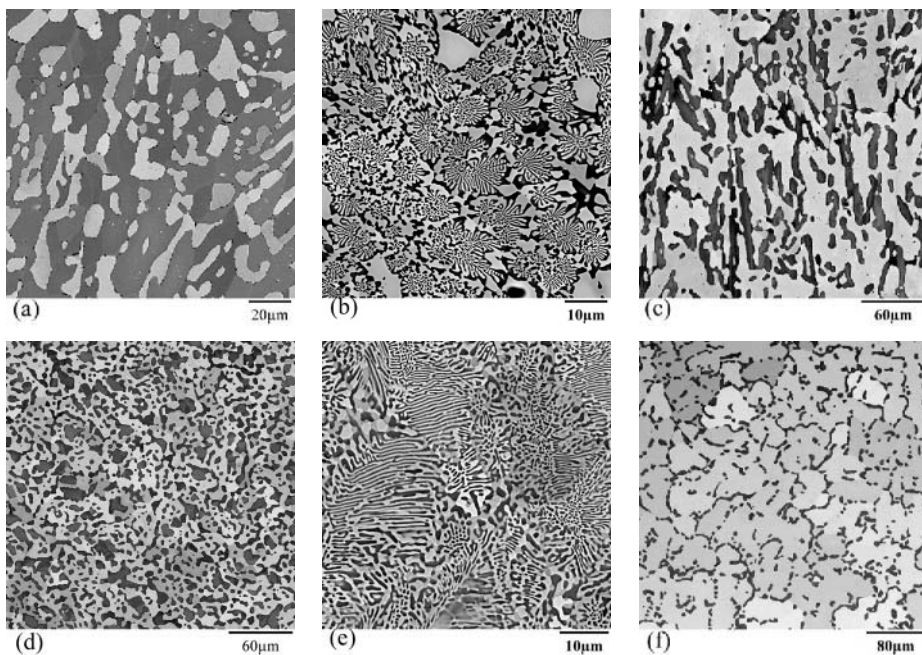
Figure 2. (a) Nb-20.8Ti-15.8Si (b) Nb-12.6Ti-14.0Si-2.3C (c) Nb-12.0Ti-13.6Si-9.81Cr (d) Nb-20.8Ti-15.7Si-4.3Al (e) Nb-16.1Si-4.9Al (f) Nb-20.5Ti-7.6Si-4.54Al.

3.   KINETICS OF OXIDATION

Cyclic oxidation experiments conducted on a large number of alloys can be classified together and figure 3 illustrates some examples. As can be seen in Figure 3(a), oxidation behavior of Nb alloys is very sensitive to alloying contents and the oxidation resistance can be significantly increased over pure Nb by judicious choice of alloying. All alloys show a two-stage oxidation reaction with an initial slow oxidation region followed by a rapid linear oxidation region. The second stage can be described as a breakaway oxidation reaction where rapid oxidation and oxide spallation occurs. Alloys

containing ~10at%Mo were found to be more spallation-resistant in comparison to other alloys. The onset of the breakaway oxidation is strongly temperature dependent and occurs earlier in time as the temperature is raised as illustrated in Figure 3(b). Role of different alloying elements upon oxidation kinetics have been discussed in earlier papers [10,20].
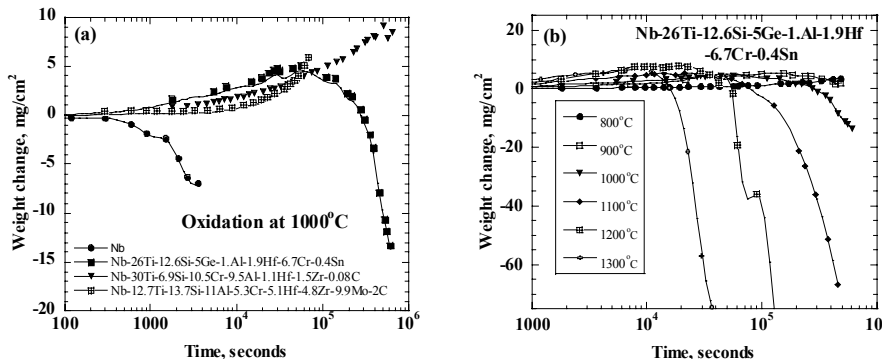
Figure 3. (a) Comparison of cyclic oxidation (in static air) behavior of 4 alloys as indicated. (b) Influence of temperature of oxidation.

Results of weight change data such as those in Figure 3(b) can be analyzed by using the equation, $\Delta w = K t^n$, where Δw is the weight change per unit area, t is the reaction time; K and n are constants. The oxidation reaction kinetics is then characterized as linear, parabolic, cubic, etc. depending upon the value of the exponent n. Wagner showed that the kinetics of oxidation can be treated as a diffusion problem and a simple parabolic law (i.e. n = 0.5 in equation (1)) derived to explain the kinetics of the reaction [21,22]. The oxidation of pure Nb in oxygen (at partial pressures high enough to form Nb_2O_5), as well as static air, follows a parabolic law at short times (i.e. n = 0.5) and becomes linear at longer exposure times. The oxidation kinetics of Si-containing, multicomponent Nb alloys appear to be somewhat different from those of Nb-Ti-Al base where the value of n was found to be usually very close to unity [14,15] indicating much faster oxidation kinetics. This is best seen in Figure 4 where the values of the kinetic law exponent, n, of Nb-Ti-Al alloys are compared with those of Nb-Ti-Si alloys. It must be cautioned that in the cyclic-oxidation experiments performed here, weight changes reported do not account for any weight losses due to spallation and thus the value of the exponent n in the kinetic law deduced from these data may actually be somewhat less than the true parameter.
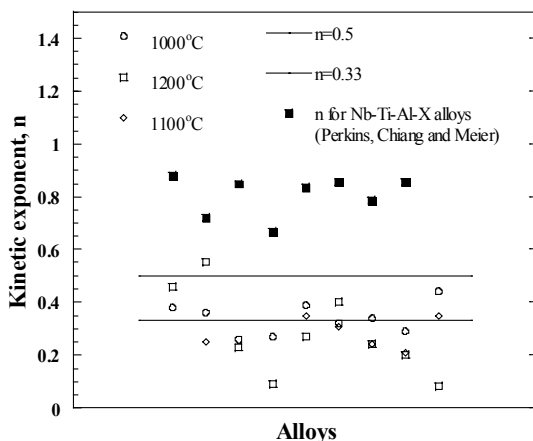
Figure 4. Comparison of experimentally determined values of the kinetic exponent, n, for a number of muticomponent Nb alloys. Data from Perkins, Chiang and Meier [15] is shown with filled square symbols whereas our data is shown using open symbols. Perkins, Chiang and Meier study [15] used several alloys having the composition (25-40) at% Nb- (23-32) at% Ti – (22-44) at% Al with other additions. Data for Si-bearing alloys show n ~ ⅓ while for the Al-rich alloys n~1.

Figure 4 indicates that the time dependence of oxidation (or the rate of oxidation) for high Si-bearing Nb alloys is less than that of Al-rich Nb-base alloys. While analyzing the oxidation kinetics data in the light of Wagner theory for high-temperature oxidation, one must bear in mind that the assumption of thermodynamic equilibrium at the metal / oxide interface is not realized. This is especially true during oxidation of transition elements belonging to groups IVA (Ti, Zr, Hf) and group VA (V, Nb and Ta) since the solubility of oxygen in these metals is high at high-temperatures [23]. Oxygen solubility in Nb is substantial at these temperatures and may be influential in determining the oxidation resistance of multicomponent Nb alloys as well. Thus, in reality, the reaction-rate constant, K, represents the sum of reaction rates associated with the dissolution of oxygen in the alloy and the growth of an oxide on the surface of the alloy. One must also bear in mind that the derivation of the parabolic law for oxide growth is based on volume diffusion of oxygen through the oxide while it is certainly possible that short-circuit diffusion could play a significant role in cases like the one in this study. For these the microstructure of the oxide film offers sufficient heterogeneities and oxide cracking as well as spallation occurs, such that oxygen maybe transported to the metal-oxide interface at much higher rates than that afforded by volume diffusion alone. Further, if oxygen diffusion in the alloy occurs to appreciable levels, internal oxidation is likely to occur since elements like Hf, Al, Cr that have high affinity for oxygen are also

present in the alloy. Microstructural examination of oxidized samples revealed that at high temperatures, adherent oxide layer formed quickly and upon prolonged oxidation, spallation of the oxide occurred. Detailed description of these can be found in ref. 10 and 20. It was always found that the β phase as well as the β/Nb_5Si_3 interface was preferentially oxidized while the silicide phase resisted oxidation till much longer oxygen exposure. Microstructures of internally oxidized samples are shown in Figure 5. Clearly, the finer microstructure (figure 5(b)) is associated with relatively reduced internal oxidation. Several component as well as complex oxide phases formed in these samples as described elsewhere [10].
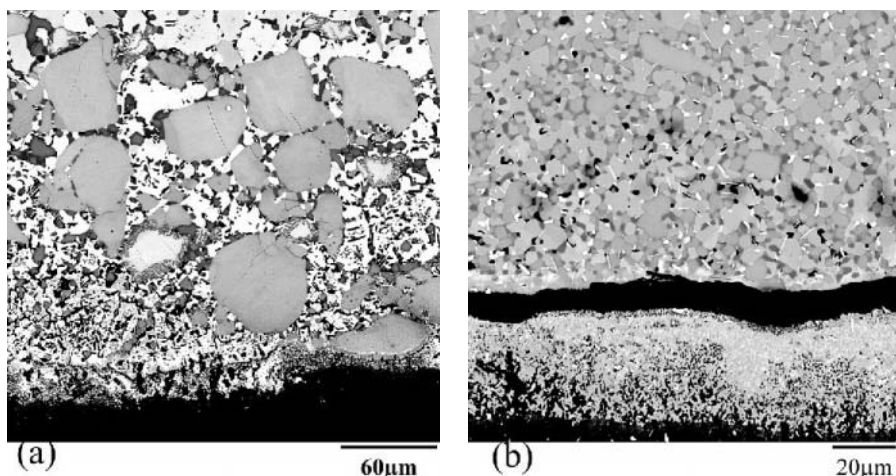

Figure 5. Internal oxidation after oxidation at 1200°C in Nb-20Ti-11Si-5Ge-6Cr-3Fe-2.5Al-2Hf-1.3Sn in (a) cast and heat-treated alloy and (b) in P/M processed alloy. Notice the preferential oxidation of β and the interface in relation to the Nb_5Si_3 phase clear in (a). Oxide layer thickness in (a) was > 100μm and was lost during polishing.

4.   OXIDATION AT LOW TEMPERATURES

Weight-change data for most of the alloys at temperatures below 900°C did not show a breakaway oxidation period at least till about 150 hours. However, a common microstructural observation made in all the alloys that were oxidized at temperatures of 900°C or less was that the surfaces of all the alloys were characterized by cracks parallel to the surfaces just below the oxide layer as illustrated in Figure 6(a). Cracks form just below the surface oxide layer (see figure 6(a)) and these cracks appear mostly in the silicide phase, though one can see them in the β phase as well to a lesser extent. This

observation has been made in a wide variety of Nb alloys in our study. Internal cracking of the silicide phase could be controlled to a remarkable extent by a finely distributed microstructure as can be seen in figure 6(b). However the cracks appear along the β/Nb_5Si_3 interfaces in this sample.
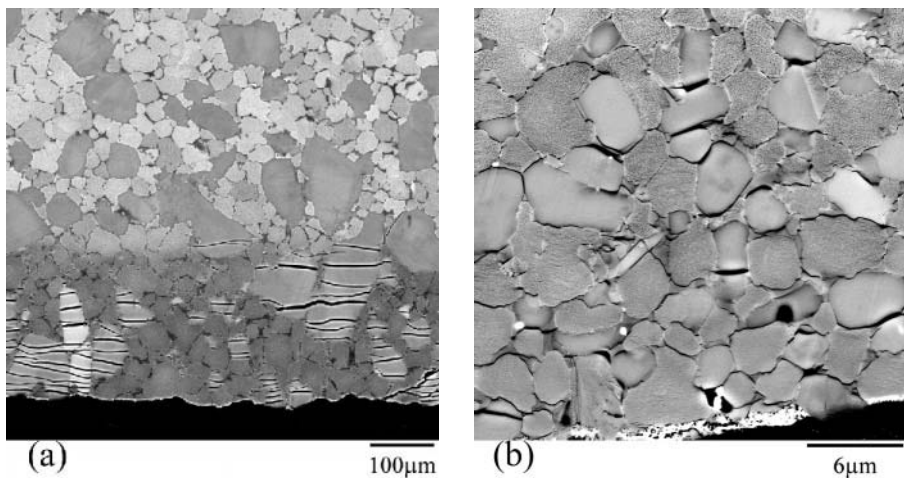
Figure 6. Internal oxidation after oxidation at 800°C in Nb-20Ti-11Si-5Ge-6Cr-3Fe-2.5Al-2Hf-1.3Sn in (a) cast and heat-treated alloy and (b) in P/M processed alloy. Notice the cracks in silicide phase in (a) and mostly at the β/silicide interface in (b)

The surface cracks forming in the alloy appear to follow the sample geometry, or in other words the oxygen concentration profile and were absent in Ar- or vacuum encapsulated samples heat-treated at the same temperature. Cooling rates from the heat treatment temperature also had no influence as far as surface cracking was concerned ensuring that these cracks did not result from thermal stresses. It appears that high residual stresses are being developed in the β phase during oxidation, and the silicide that is presumably brittle even at these temperatures fractures under these stresses. Nb_2O_5 has a negative thermal expansion coefficient and fine-scale precipitation of the oxide such as that shown in figure 7 may lead to generation of residual stresses in the β phase at these temperatures. The monoclinic to orthorhombic allotropic transformation reported in Nb_2O_5 at ~830°C –900°C also may contribute to residual stresses. The micrograph shown in Figure 7(a) shows oxide precipitation in the β phase and the associated cracking of the silicide phase. The oxide grows as needles or rods as can be seen in Figure 7(b) that also demonstrates the extremely rapid and copious growth of the oxides in the β phase and a relatively reduced formation in the silicide phase. This secondary electron image obtained from the surface of a sample that was polished prior to oxidation at 800°C just for 30 minutes illustrates the nature of the oxidation process very well. At

higher temperatures, lower thermal-expansion coefficient, together with the ability of the silicide phase to sustain plastic flow prevents fracture of the silicide phase. To test this hypothesis, residual stresses generated during oxidation of polished samples at 800°C were measured from X-ray diffraction experiments. Figure 8 shows the plot of residual stresses as oxidation progresses, demonstrating that compressive stresses are quickly developed within the β phase during the initial stages of oxidation. Further, it appears that once the stresses reach a critical value, fracture of the brittle phase (silicide) occurs, thus relieving the stresses. SEM examination of the surface of these samples showed that oxide whiskers grew in the β phase very early during oxidation and as oxygen diffuses deeper in to the sample with longer exposure, oxide precipitation occurs and consequently, β regions inside the sample are stressed to a point when fracture of the silicide phase becomes inevitable.
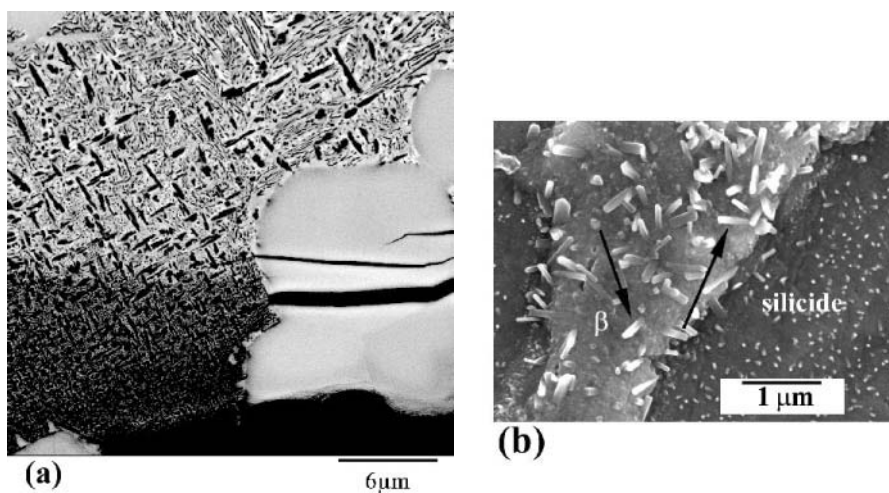
Figure 7. (a) Nb-30Ti-7Si-10.5Cr-9.5Al-1.1Hf-1.5Zr-0.08C, oxidized at 900°C for 16 hours, showing the oxide precipitation in the   phase (left side of micrograph) and cracks in the silicide (right side of micrograph). (b) Nb-25.99Ti-12.61Si-4.94Ge-1.92Al-1.90Hf-6.73Cr-0.43Sn oxidized at 800°C for 30 minutes. SEM secondary electron micrograph obtained from the surface of a sample that was polished and then oxidized. Arrows point to the oxide needles formed in the   phase.

Oxidation of ternary Nb-Ti-Si alloys possessing microstructures like those in Figure 1(b) invariably lead to cracking of the fine Nb_5Si_3 phase, as illustrated in Figure 9(a). In alloys containing Nb_3Si also the silicide phase was found to undergo similar effects of cracking as shown in Figure 9 (b).
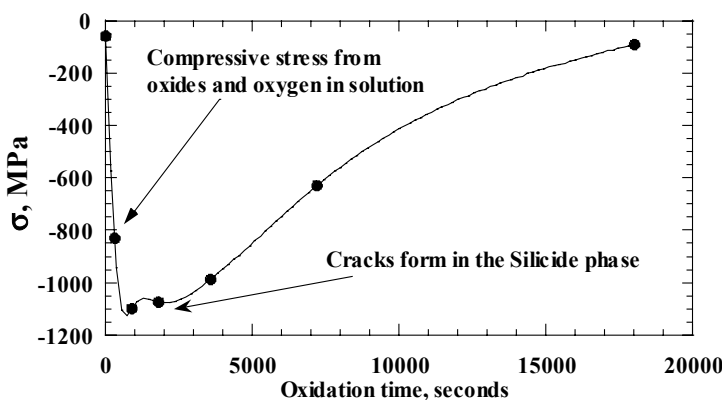
*Figure 8.* Residual stresses as determined by XRD in Nb-25Ti-13Si-5Ge-6Cr-2Al-2Hf alloy oxidized at 800°C.
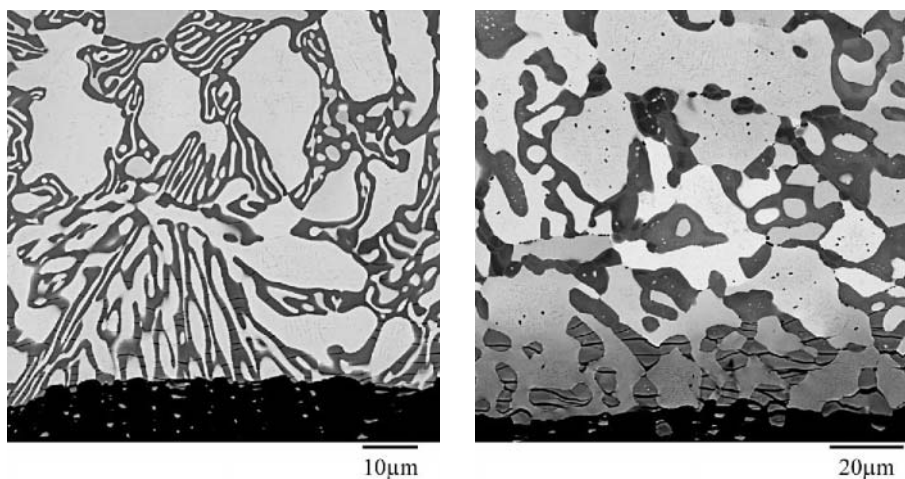
Figure 9. Internal oxidation after oxidation for 4 hours at 800°C in (a) Nb-10.5Ti16.2Si (b) Nb-20.8Ti-15.8Si. The dark phase is Nb3Si and the bright phase is   solid solution.

5.   SUMMARY

A wide variety of microstructures can be obtained by suitable alloying in Nb alloys and the oxidation resistance of Nb alloys can be dramatically improved by alloying. It is important to investigate the microstructural aspects associated with oxidation in order to establish the high temperature behavior of these alloys. Here an overview of the effects of alloying on microstructural development was illustrated and their effects on oxidation

examined. At lower temperatures, oxidation is accompanied by high residual stress build-up and the brittle silicide phase undergoes cracking.

ACKNOWLEDGEMENTS

REFERENCES

1. High-temperature Niobium Alloys: Eds. J. J. Stephens and I. Ahmad, Proceedings of a symposium, TMS, 1991.
2. E. N. Sheftel and O. A. Bannykh, "Niobium base alloys", Proceedings of the 13th International Plansee Seminar, Eds. Bildstein and R. Eck, Metallwerk Plansee, Reutte (1993) 43- 69.
3. P. R. Subramanian, M. G. Mendiratta and D. M. Dimiduk, "The development of Nb-based advanced intermetallic alloys for structural applications," J. of Met., 48 (1) (1996), 33-38.
4. E. N. Sheftel and O. A. Bannykh, "Principles of Alloying and design of structure of high-temperature high-strength niobium alloys," Tungsten and Refractory Metals-1994, eds. A. Bose and R. J. Dowding (Metals Powder Industries Federation, New Jercy, 1995) 629-655.
5. M. R. Jackson, "Alloying concepts for Nb-base refractory metals," Tungsten and Refractory Metals-1994, eds. A. Bose and R. J. Dowding (Metals Powder Industries Federation, New Jercy, 1995) 665-672.
6. P. R. Subramanian, M. G. Mendiratta and D. M. Dimiduk, "Development approaches for advanced intermetallic materials – Historical perspective and selected successes," Structural Intermetallics, Eds. R. Darolia, J. J. Lewandowski, C. T. Liu, P. L. Martin, D. B. Miracle and M. V. Nathal (TMS, 1993) 619-630.
7. P. R. Subramanian, M. G. Mendiratta, D. M. Dimiduk and M. A. Stucke, "Advanced intermetallic alloys – beyond gamma titanium aluminides'" Mat. Sci. Engg., A239-240 (1997) 1-13.
8. M. R. Jackson, "Ductile low-density alloys based on niobium," Tungsten and Refractory Metals-1994, eds. A. Bose and R. J. Dowding (Metals Powder Industries Federation, New Jercy, 1995) 65- 72.
9. P. R. Subramanian, M. G. Mendiratta and D. M. Dimiduk, "Microstructures and mechanical behavior of Nb-Ti base beta + silicide alloys," High-temperature Silicides and Refractory Alloys, eds. C. L. Briant, J. J. Petrovic, B. P. Bewlay, A. K. Vasudevan and H. A. Lipsitt (MRS, Pittsburgh, 1994) 491-502.
10. E.S.K. Menon, M.G. Mendiratta and D.M. Dimiduk, Niobium -Science and Technology, Proceedings of the International Symposium Niobium 2001, Published by Niobium 2001 Ltd., Bridgeville, PA, 121-145.

11. Y. Murayama and S. Hanada, "High temperature strength, fracture toughness and oxidation resistance of Nb-Si-Al-Ti multiphase alloys", Sci. and Tech. of Adv. Matls., 3 (2002) 145-156

12. J. Sha, H. Hirai, T. Tabaru, A. Kitahara, H. Ueno and S. Hanada, "Effect of carbon on microstructure and high-temperature strength of Nb-Mo-Ti-Si in situ composites prepared by arc-melting and directional solidification", Mat. Sci. Engg., A343 (2003) 282-289.

13. T. N. Rhodin, Jr., and Del. Wilmington, "Metal Production", US Patent # 2,838,396, 1958.

14. R. C. Svedberg, R. L. Ammon, "Oxidation resistant niobium alloy − Mechanically alloying niobium intermetallic and niobium alloy", US Patent # 4,836,849, 1989.

15. R. A. Perkins, K. T. Chiang and G. H. Meier, " Effect of alloying, rapid solidification, and surface kinetics on the high-temperature environmental resistance of niobium," (AFOSR report, LMSC-F195926, 1987).

16. R. A. Perkins, K. T. Chiang, G. H. Meier and R. Miller, "Formation of alumina on niobium and titanium alloys," Oxidation of High-temperature Intermetallics, eds. T. Grobstein and J. Doychak (TMS, Warrendale, 1988) 157-169.

17. R. A. Perkins, K. T. Chiang and G. H. Meier, "Formation of alumina on Nb-Al alloys" , Scripta Metall., 22 (1988) 419-424.

18. E. M. Levin, C. R. Robbins and H. F. McMurdie, Phase diagram for ceramics (The American Ceramic Society, 1964) 142-363.

19. D. A. Prokoshkin and E. V. Vasileva, "Alloys of niobium", A. M. Samarin, editor ; translated from Russian by N. Kaner ; translation edited by Molly Gleiser, Jerusalem : Israel Program for Scientific Translations, 1965.

20. E. S. K. Menon, M. G. Mendiratta and D. M. Dimiduk, "High temperature oxidation mechanisms in Nb-silicide bearing multicomponent alloys", Structural Intermetallics 2001, Eds K. J. Hemker, D. M. Dimiduk, H. Clemens, R. Darolia, H. Inui, J. M. Larsen, V. K. Sikka, M. Thomas and J. D. Whittenberger (TMS, 2001) 591-600.

21. O. Kubaschewski and B. E. Hopkins, Oxidation of Metals and Alloys (Academic Press, Belfast, 1962) 82-87.

22. P. Kofstad, High-temperature Oxidation of Metals (John Wiley & Sons, Inc., New York, 1966), 112-146.

23. P. Kofstad, High-temperature Oxidation of Metals (John Wiley & Sons, Inc., New York, 1966), 147-227.

DEVELOPMENT OF DUCTILE CR-RE ALLOYS FOR HIGH TEMPERATURE APPLICATION IN AGGRESSIVE ATMOSPHERE
Overview

Lluís Gimeno-Fabra [1], Nikolaj P. Brodnikovsky [2], Nikolaj O. Krapivka [2], María Corzo [3], Marc Anglada i Gomila [3], Johannes Vlcek [1]
[1] *European Aeronautic Defence and Space Company (EADS),* [2] *Institute for Problems in Material Science (IPMS),* [3] *Technical University of Catalonia (UPC)*

Abstract: Mechanical properties, oxidation and thermal shock resistance of Cr-Re solid solution alloys manufactured by arc melting have been characterized. Samples of pure Cr, Cr-18at%Re and Cr-35at%Re alloys have been tested at temperatures up to 1400°C for compression resistance. Oxidation resistance of the alloys has been tested up to 1600°C in air and thermal shock resistance at heating kinetics of 500°C/s and 500°C/mm has been investigated. Results confirm the potential of near solid solution limit Cr-Re alloys as high temperature materials for operation in aggressive atmosphere. In as cast condition Cr-35at%Re alloys present a room temperature compressive yield stress of 900 MPa and show relatively good ductility (6%) under tension. Yield stress under compression at 1400°C is 168 MPa and 140 MPa under tension at 1200 °C. 4 hours exposure to air at 1600°C produced a metal recession of about 15μm and a diffusion layer of 50μm. Thermal shock of the alloys under the conditions described above produced small cracks on the surface. Further work will include the determination of the alloy resistance to pure nitrogen at high temperature and the measurement of the thermal properties and thermal expansion coefficients of the alloys.

Key words: Refractory alloys, rhenium effect, Cr-Re alloys, mechanical properties, high temperature, oxidation resistance, thermal shock resistance.

1.   INTRODUCTION

1.1   Background

The effect of rhenium on the properties of refractory metals has been a research topic of discontinuous relevance since its discovery in the 1950's [1, 2]. Several works have been devoted to the mechanical property enhancement seen in VIb group transition metals when solid solution alloyed with rhenium [3-12]. In the 1970's the works of
Trefilov, Milman et al [5-8] linked the rhenium-induced ductility increase of IVb refractory metals to changes in their electronic structure when in solid solution alloying with Re. Indeed VIb group metals find themselves at a minimum in the plot of density of states at Fermi level (DOS), presenting very directional bonds [7, 8, 13]. Characteristic of this type of structure is an elevated value of the Peierls stress and the stacking fault energy, which render deformation by slip at room temperature complicated and by twinning impossible. Trefilov and Milman state that near solid solution Re alloying with refractory metals increase sharply the DOS at Fermi level, braking the ideal conditions for directional bonding and rendering deformation by slip and twinning possible effectively decreasing the Ductile to Brittle Transition Temperature (DBTT) of the alloys.

The calculations on the electronic structure and Fermi surface of Cr-Re alloys carried out by Medvedeva et al. [9, 10] concluded that even small percentages of Re alloying sharply increase the DOS and weaken the Cr-Cr bonding, rendering dislocation motion ar room temperature possible. A further ductilizing phenomenon presented by Medvedeva, the formation of impurity scavenging Cr-Re A15 type structures at near solid solution Re percentages is still opened for discussion.

At a more practical level, most of the applied research works carried out to date in this field have been focussed on W-Re and Mo-Re alloys which are mainly used in thermocouples [14]. Recent interest in Cr-Re alloys is focussed on their electromagnetic properties but not on their potential to be used as structural materials for high temperature applications [16].

Besides the fundamental work cited above, IPMS in Kiev did carry out some research work in the field of Cr-Re structural alloys, unfortunately the works were stopped in the mid-80's, with the clear statement that Re alloying strongly decreased the DBTT of Cr-Re alloys, but without providing precise data neither on their mechanical, chemical nor thermal properties. The joint research projects between IPMS, UPC and EADS that this document partly summarizes aims at designing a suitable manufacturing process for these alloys and characterize the relevant properties for EADS related applications.

1.2   The planned application field of the alloys

The interest of the EADS in Cr-Re alloys is to investigate potential candidates to be used as uncoated structural materials in satellite thruster combustion chambers. These devices experience thermal loads between 1200°C to 1600 °C. Satellite thruster combustion chambers are cooled by a liquid film of fuel on the part adjacent to the injector head (figure 1) to protect it and the walls from reverse heat flow from first stage of combustion. This fuel film evaporates at a given point (labeled C in figure 1), leaving the walls of the chamber exposed to the high temperature gasses. This point, presents the highest thermal gradient of the structure (500K/mm) and the associated thermo mechanical constraints are regarded as critical for the structure integrity.
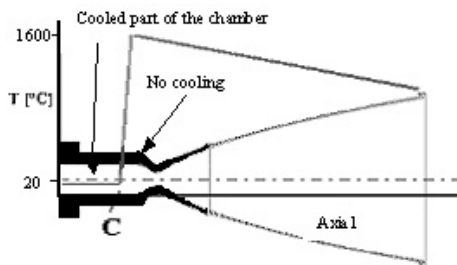
Figure 1. *Temperature profile in the internal wall of a satellite thruster combustion chamber*

Table 1. *Properties of state of the art Pt based alloys and desired properties of potential candidates*

Property	State of the art Pt based alloys	Desired alloy properties
T_m	1800 °C	> 2000 °C
Max. op. T	1600 °C	1800 °C
DBTT	< -60 °C	< -60 °C
$\sigma_{0.2}$ at 1400 °C	40 MPa	> 80 MPa
CTE (x10^{-6})		6 (Room T)
λ		70 W/Km
ρ	20 g/cm³	< 20 g/cm³
Weldability		With Ni
Stable against (1400°C)	C, N, O	H, C, N, O
Price	30 €/g	< 10 €/g

Satellite thruster combustion chambers manufactured by EADS Space Transportation are machined from massive Pt based alloys, which are capable of operating at about 1600°C in continuous mode. Main inconvenient of such chambers is the elevated raw material cost of about 30€/gr. Other qualified materials for the application are silicide coated Nb,

with a service temperature of around 1400°C and Ir coated Re produced by Chemical Vapour Deposition that with a service temperature of around 2000°C provides the highest performance in the segment [17-18], but which has the inconvenient of being dependent on a coating, a point which is often seen as critical by satellite constructors.

Despite the experience of the EADS with Pt-based alloys and their good acceptance, the increasingly competitive satellite market demands structural materials with lower prices that nevertheless must remain chemically stable (no coating). This motivated research in the field of Cr based alloys.

1.3   Manufacturing process of Cr-Re alloys

Cr, Cr-18Re and Cr-35Re alloys were arc molten in water-cooled cooper crucibles under argon at 1200 mBar pressure. As Cr and Re have a very strong tendency to micro-segregation and dendritization, alloys were re-molten up to five times. In figures 2a, 2b and 2c the influence of additions of 5 weight percent of Ce and Sc on the alloy microstructure is shown. These were added to improve alloy purity by the absorption of dissolved nitrogen and oxygen in the melt and the formation of stable oxides and nitrides, which simultaneously increases of nuclei density improving the alloy homogeneity. Formation of a fine dispersion of ScO was evident by SEM, which may be beneficial for the high temperature mechanical properties.
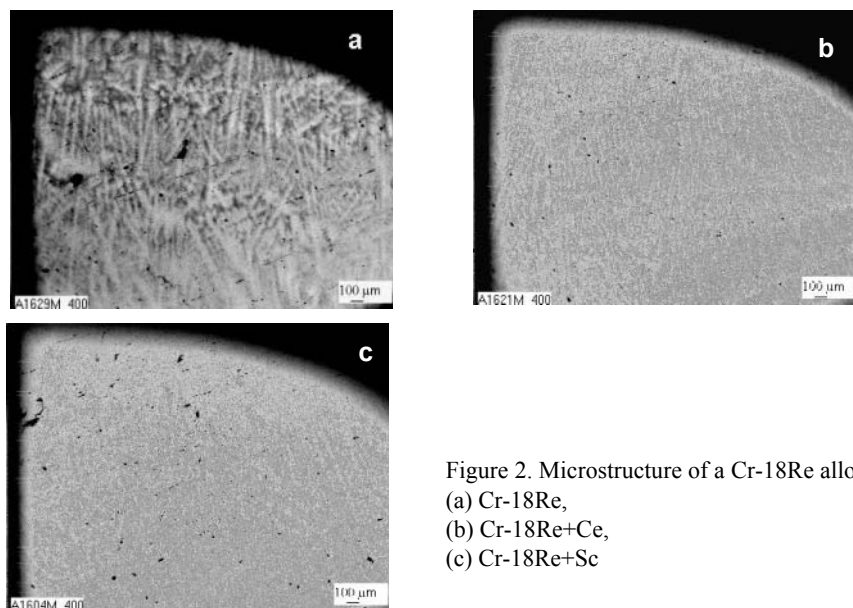
Figure 2. Microstructure of a Cr-18Re alloys
(a) Cr-18Re,
(b) Cr-18Re+Ce,
(c) Cr-18Re+Sc

Average interstitial element concentration in Cr-Re alloys with rare earth doping was below 200ppm oxygen and 50 ppm nitrogen independent of the Re concentration.

2.   ALLOY PROPERTIES

2.1   Mechanical properties of the alloys

Cr, Cr-18Re and Cr-35Re alloys were tested under compression (ASTM E-9 81) at a strain rate of 0,0028 s^{-1}. Samples were cut perpendicularly to the grain growth direction.
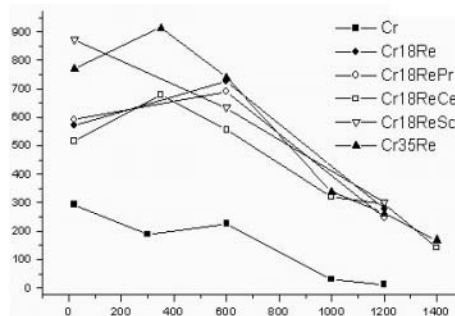
Figure 3. Yield stress dependence [MPa] on temperature [°C] under compression for various Cr-Re alloys.

Dependence of yielding limit of chromium and CrRe alloys in as cast condition on temperature is shown in figure 3. Rhenium alloying considerably increases the strength of Cr in a wide temperature range. Cr35Re alloy presents a remarkably higher strength than Cr18Re up to 600°C. From there on the influence of the extra Re content on the strength of the alloys is barely noticeable.

It is interesting to observe the increase of strength related the rare earth element doping. The effect is specially marked with addition of up to 0,25 wt% of Sc. This is connected to the influence that the active components have on the homogeneity of the alloy and on the elimination of interstitial impurities.

Deformation mechanisms of Cr18Re and Cr35Re alloys differ from those of pure chromium by availability mechanical twinning (figure 4) up to relatively high temperature (600°C for Cr-35Re). Twinning is result of

decrease of the stacking fault energy and the decrease of the formation stress of twinning dislocations [6-8].
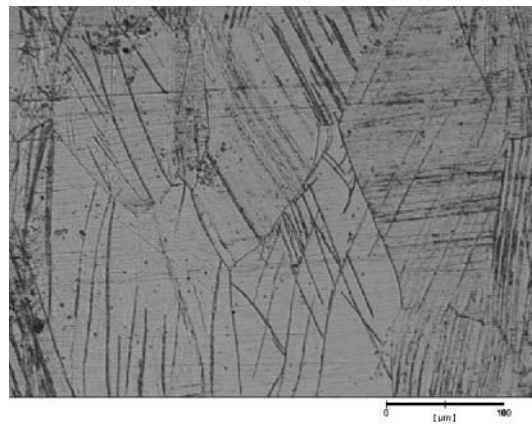
Figure 4. High density of mechanical twins on Cr-35Re deformed 71% at room temperature under compression.
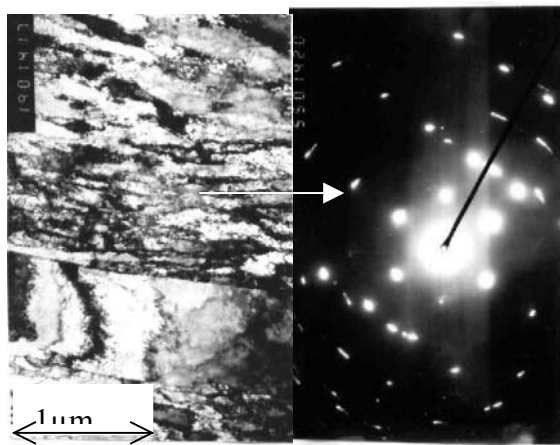
Figure 5. (a) TEM microstructure of Cr-35 at. % Re alloy deformed at 20 ^{o}C, ε = 71%; cell structure has formed. (b) Corresponding selected area diffraction pattern (SADP).

Twinning facilitates relaxation of stress by plastic deformation but interaction of twin bands with grain boundaries may initiate cracks. Plasticity of Cr18Re and Cr35Re alloys is sufficient to impeach the formation of such cracks even after 71% deformation at room temperature.

On both Cr18Re and Cr35Re alloys, the main contribution to deformation is nevertheless by dislocation slip. Even at room temperature dislocation mobility in Cr-35Re alloys is enough form localized cellular

structure after 70% deformation. Formation of intergranular small-angle borders (cells) can be seen as breaking up of diffraction reflexes at figure 5b instead of an elongation of diffraction reflex from planes without characteristic of a smooth variation of disorientation along the grain and a uniform distribution of dislocation density.

With a value of 28%, the necessary deformation to from a cell structure at 600 °C is considerably lower than at room temperature (fig. 6a) and is also confirmed by breaking up of diffraction reflexes (fig. 6b). Dislocation structure of deformed Cr-18Re and Cr-35Re alloys similar.
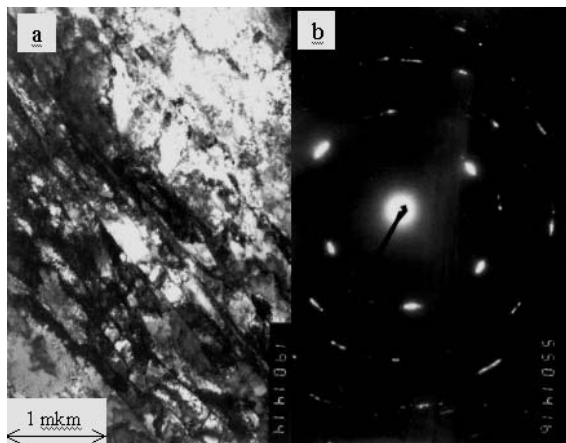
Figure 6. (a) TEM microstructure and (b) SADP of Cr35Re deformed 28% at 600°C under compression.

2.2 Oxidation resistance of Cr-Re alloys

Oxidation behavior of Cr, Cr-18Re and Cr-35Re was investigated on cylindrical samples with a diameter of 4 mm and a height of 8 mm. Tests were conducted in air at 1400°C, 1500°C and 1600°C for 2 and 4 hours. Samples were polished with 1200 grade paper before testing. All results presented here correspond to the tests carried out for 4 hours at 1600°C.

2.2.1 Oxidation behaviour of pure Cr

Oxidation behavior of pure Cr is well known and it is shown here only for comparison purposes with Cr-Re alloys. It is characterized by the formation of a protective Cr_2O_3 layer which is stable up to approximately 900°C. From there on it looses adhesion and at temperatures above 1200 °C it completely delaminates from the substrate. This is translated in the

exposition of the base material to oxygen and nitrogen resulting in its internal oxidation and nitridation, as figure 7 shows. Preferential precipitation of nitrides at grain boundaries and other crystal lattice defects is related to low interstitial solubility of light elements in chromium [11].

Comparison of chromium exposed to atmospheric air at 1600°C with chromium exposed to combustion chamber solicitations (figure 8) permitted to conclude that mechanisms responsible for the material failure were similar for both cases so testing in high temperature air is a representative method to obtain qualitative results on chemical resistance of Cr-based alloys to combustion chamber gasses.

Nitrogen pick up during test is the most important degradation mechanism, both in combustion chamber service and in air, as the chemical analysis in table 2 shows. Besides the chemical reaction with air, further factors render impossible the use of chromium at the specified temperature, in particular recrystallisation and grain growth.
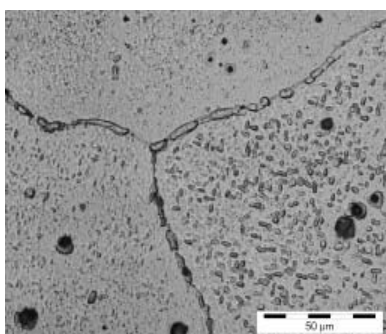
Figure 7. Internal oxidation of pure chromium after 4 hours exposure to air at 1600°C.
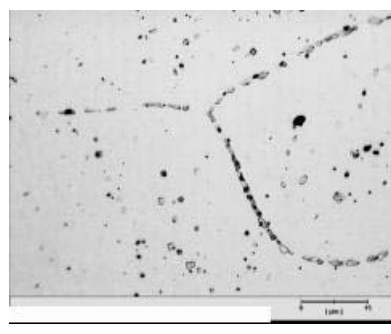
Figure 8. Precipitation of nitrides at grain boundaries and internal oxidation in a pure chromium satellite thruster combustion chamber fired in a hot gas test

Table 2. Impurity concentration in µg/g in the combustion chamber material before and after firing at 1500°C for 2 hours.

	C	H	O	N
Before	7	2	135	218
After	8	2,5	610	710

2.2.2   Oxidation behaviour of Cr-18Re

The surface oxide layer of Cr-18Re presented a better adhesion than that of pure Cr. Despite this debonding of the oxide layer took place in some areas. EDX analysis did not permit to detect the presence of Re in the oxide

layer of Cr-18Re. The most peculiar phenomenon found in Cr18Re alloys consists of the spontaneous grain boundary fracture when exposing the alloy to air at 1600°C (Fig. 9). Diffusion of O and N through the oxide layer and along the grain boundaries and the subsequent localized precipitation of low melting ternary Cr-Re-O or Cr-Re-N compounds could explain this phenomenon. In the back scattering SEM image shown in figure 9 it is evident that grain boundaries in Cr-18Re alloys are Cr-rich, this renders them vulnerable to nitrogen attack. Cr concentration at grain boundaries should nevertheless not fall below 20 at% in order to render them oxygen resistant.

In Figure 10 a preferential orientation of the serrations in the grain boundaries is evident, indicating the existence of preferential diffusion paths for the liquid phase in the grains.
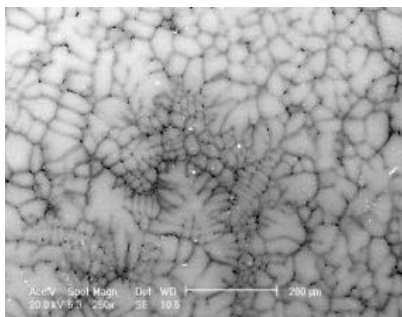
Figure 9. BSSEM image of a Cr-18Re alloy. Dark colored areas correspond to the Cr-rich grain boundaries.
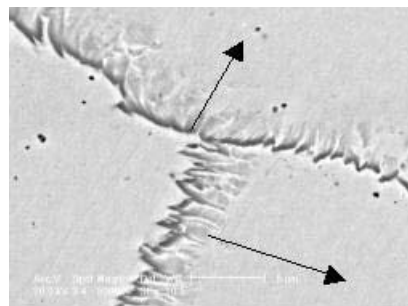
Figure 10. Grain boundary instability in Cr-18Re alloys after 4 h at 1600 °C in air. Arrows indicate the preferred direction of attack.

2.2.3   Oxidation behaviour of Cr-35Re

Oxidation behaviour of Cr-35Re up 1600°C is characterized by the formation of a stable Cr_2O_3 protective layer adherent to the substrate. As seen in figure 11, exposure to air during 4h at 1600°C produced a 20µm thick Cr_2O_3 layer and a Re rich diffusion area of about 50µm at the interface, some Frenel porosity is evident in this area (Fig. 12). EDX analysis did not reveal the presence of any Re in the oxide layer but microprobe analysis would necessary to provide a definitive value. As nitrogen has a very low solubility in Re, this layer isolates the substrate against nitrogen from the atmosphere.
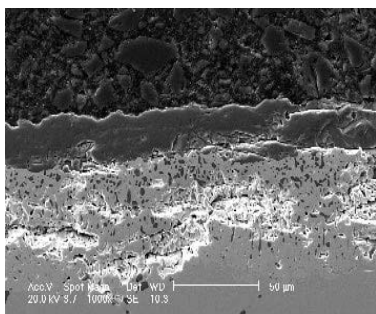
Figure 11. Oxidation profile perpendicular to the surface in a Cr35Re alloy exposed 4 hours to air at 1600°C.
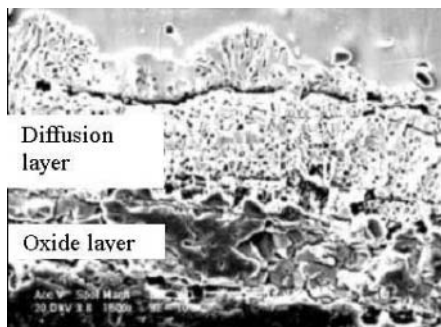
Figure 12. Frenel porosity under the oxide layer in a Cr-35Re alloy exposed 4 hours at 1600°C to air.

2.3   Thermal shock resistance of Cr-Re alloys

Thermal shock resistance of Cr, Cr-18Re and Cr-35Re alloys was investigated under the most severe solicitations found in combustion chambers. This corresponds to the area where the cooling film breaks (point C in figures 1 and 13). Sample geometry was prismatic with dimensions of 5 X 5 X 10mm and heating atmosphere was argon, with a partial oxygen pressure of approximately 0,1 Pa.
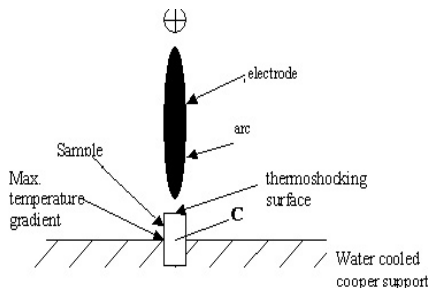
Figure 13. Schema of the experimental device used to test the thermal shock resistance. Conditions in point C correspond to the cooling film braking point in the application.

Samples were clamped on its base on a copper water cooled table (Fig 13), so that in addition to the electric arc-induced thermal shock of about 500°C/s, a gradient of approximately 500°C/mm was present in the clamping area, reproducing the temperature gradient of point C in figures 1 and 13. After peak temperature of 1870°C was reached, samples cooled down

attaining room temperature at the centre of the unclamped area after approximately 2 minutes.

A maximum cooling rate of 200°C/s was obtained during the first 2 to 4 seconds directly after electric arc removal. Samples were cycled 100 times and characterised for microstructure and micro cracking after the test.

2.3.1   Thermal shock resistance results

Thermal stress was sufficient to warp pure Cr but could not permanently deform Cr–Re samples. Despite no apparent warping, both Cr-18Re and Cr-35Re samples presented grain boundary micro cracks on the heating surfaces up a depth of approximately 200µm, as figure 14 shows. Grain boundary strengthening to diminish micro cracking may be achieved through deformation of the alloys. Pure chromium presents no micro cracking at grain boundaries of the thermally shocked surface, but it is very possible that localised melting has occurred.

The shape stability observed in Cr-Re alloys is related to their ability to accommodate deformation by the building of twinning bands under stress, a phenomenon specially intense in Cr-35Re. Figure 15 shows the elevated twin density in the thermally cycled part of the boundary region between heated and cooled areas in a Cr-35Re alloy. In the cold area, were temperature is around 20°C, the plasticity of the alloy is enough to impeach the formation of cracks. No cracks were evident even on the vicinity of twin band / grain boundary interfaces, which is in accordance with the behaviour observed on mechanical testing.
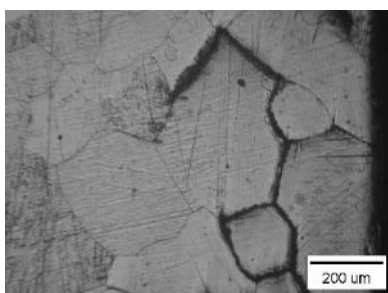

*Figure 14.* Grain boundary fracture through thermal shocking in a Cr-35Re alloy.
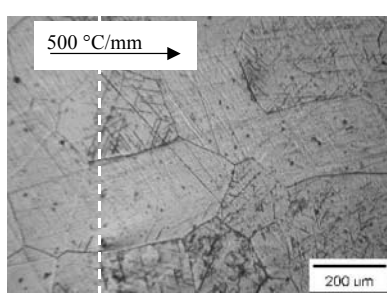
Figure 15. Boundary area between heated and cooled zones in a Cr-35Re sample after 100 thermal shocks between room temperature and 1870°C. Line indicates the limit of the water cooled clamps

Behavior of Cr-18Re alloys was similar to Cr-35Re alloys. Some micro cracking at grain boundaries up to a depth of 200 µm on the thermally

shocked surface was evident. Neither shape change nor internal cracking took place. Twin density was nevertheless much lower; this may also be previewed from the results obtained during mechanical testing.

3.   DISCUSSION

As discussed on previous works [3-12], the effect of rhenium in the mechanical properties of Cr is similar to that seen in Mo and W. The activation of mechanical twinning at room temperature observed in the alloys happened nevertheless at much lower alloying percentages of Re than the near solid solution limit conditions previewed by previous works [8]. It is possible that the higher purity of the raw materials is responsible for this phenomenon and the associated ductility of Cr-18Re alloys. Despite the similarity of the mechanical properties between Cr-18Re and Cr-35Re, the twin density on the first is much lower, indicating a smaller ductility reserve, which could be critical for the lowest operation temperature demanded by the application (approximately 210K). DBTT of both alloys has not yet been assessed.

Rhenium content played a major influence on the oxidation resistance of Cr-Re alloys. Rhenium has been found to stabilize the protective oxide layer on Cr-Re alloys by decreasing its growth stress with the substrate. Increasing Re concentration in the alloy dramatically increases the adherence of the oxide layer. The formation of a Re-rich interface contributes to the improvement of the alloy resistance against nitrogen and other interstitials. Lower than expected chemical resistance of Cr-18Re was due to Re heterogeneous distribution in the alloy: Cr-rich grain boundaries led to selective attack at high temperature, formation of unstable phases (Cr-Re-O, Cr-Re-N) and grain boundary fracture.

Thermal shock resistance of Cr-Re alloys was sufficient to withstand conditions similar to those imposed by the application. The ability to mechanically twin permitted the accommodation of thermal deformation in the boundary area between the hot and cold zones of the combustion chamber, which is acknowledged to be the its most solicited area. Grain boundary micro cracking on the thermally shocked surface might be overcome by strengthening of the grain boundaries through thermo mechanical treatment.

4.   CONCLUSIONS

The characterization of the mechanical properties, oxidation resistance and thermal shock resistance of Cr-Re alloys has demonstrated their potential as high temperature structural materials. The availability of mechanical twinning has a strong influence on the ductility at low temperature and thermal shock resistance of Cr-18Re and Cr-35Re alloys. Main contribution to plastic deformation was nevertheless dislocation slip. Formation of cellular dislocation structure has been observed in both Cr-18Re and Cr-35Re. Necessary strain prior to the beginning of the formation of cellular structure increased with deformation temperature. Investigation of the chemical properties of the alloys revealed that oxidation resistance of Cr-18Re was meagre, characterized by Cr-rich grain boundary selective attack by atmospheric gases. The excellent oxidation resistance of Cr-35Re alloys is related to the increase of the adherence of the protective oxide layer.

ACKNOWLEDGMENTS

REFERENCES

1.   J.E. Hughes and G.A. Geach, in: Proceedings of the 2nd Plansee Seminar, (Plansee AG, 1956).
2.   A. H. Sully, E.A. Brendes, Chromium (Butterwoth, UK, 1967).
3.   J. Wadsworth et al in: Critical Issues in the Development of High Temperature Structural Materials, (The Minerals and Materials Society , 1993) 189-202.
4.   C.S. Wukusick, Refractory Metals and Alloys IV, vol. 41, No. 1, (1961).
5.   V. Trefilov and Yu. V. Milman, in: Proceedings on the 10 th Plansee Seminar. (Hugo M. Ortner, 1981) 15-26.
6.   Yu. V. Milman, Journal de Physique IV, **5** (1995) 67-75.
7.   V. Trefilov., Yu. V. Milman, S. Firstov, Physical Fundamentals of the Strength of Refractory Metals. (Nuakova Dumka, Ukraine, 1975).
8.   Yu.V. Milman, G.G. Kurdyumova, in: B.B. Bryskin (ed.) Rhenium and Rhenium Alloys, (TMS, Warrendale, 1997), pp. 717-728.

9.   N. Medvedeva et al. Acta Materialia, **50** (2002), 2471-2476.
10. N. Medvedeva, et al. Physical Reviews, **B67** (2003) 134204.
11. K. B. Povarova et al. in: B.B. Bryskin (ed.) Rhenium and Rhenium Alloys (TMS, Warrendale, 1997) pp. 647-659.
12. K.B. Povarova et al. in: B.B. Bryskin (ed.) Rhenium and Rhenium Alloys (TMS, Warrendale, 1997), pp. 691-705.
13. I.V. Gridneva, Yu. V. Milman, V. Trefilov, Phys. Stat. Sol. **36** (1969) 59-67
14. R.S. Jaffee, et al., in: Proceedings of the 3rd Plansee Seminar, (Plansee, AG, 1959) 380-411.
15. N.P. Brodnikovskyy et al, in: B.B. Bryskin (ed.) Rhenium and Rhenium Alloys, (TMS, Warrendale, 1997), pp 551-556
16. B. Damashke and W. Felsh, Condensed Matter **63** (1986) 179-784.
17. A.J. Fortini, R.H. Tuffias, R.B. Kaplan, A.J. Duffy, B.E. Williams, J.W. Brockmeyer, Iridium, (TMS, Warrendale, 1997), pp. 217-225
18. R.H. Tuffias, G.J. Melden, J.T. Harding, R.B. Kaplan, Surface Modification Technologies, Vol. 4 (TMS, Warrendale, 1997), pp. 855-864.

STRUCTURE, MECHANICAL BEHAVIOR AND NANOHARDNESS OF CHROMIUM AND MOLYBDENUM PRODUCED BY MAGNETRON SPUTTERING

S.A. Firstov, T.G. Rogul, S.N. Dub*, V.L. Svetchnicov**,
H.W. Zandbergen**
*Institute for Problems of Materials Science of the National Academy of Science of Ukraine,
Kyiv, Ukraine*
**Institute for Superhard Materials of the National Academy of Science of Ukraine*
 Kyiv, Ukraine
***NCHREM, The Netherlands*

Abstract: Comparative analysis of structure, mechanical behavior and nanohardness of
               chromium and molybdenum coatings has been performed. To explain the
               super high values of hardness of polycrystalline chromium with ultra-fine
               grain structure the original mechanism has been proposed.

Key words: chromium, molybdenum, coatings, ultra-fine grain structure, nanohardness.

1.   INTRODUCTION

It has been shown that hardness of fine grain chromium films and coatings produced by physical evaporation, hollow cathode discharge and magnetron sputtering may reach the values of 15000 – 26000 MPa that is more 9-10 times higher in comparison with cast chromium [1-3].

As is well known that mechanical properties of chromium are essentially depend on its purity [4]. At the same time the grains size decrease to nanocrystalline size in polycrystalline materials leads to increase 3-5 times in hardness and yield point [5]. Thus, extremely high values of

microhardness of chromic coatings cannot be explained only by presence of the interstitial elements or only by presence of fine-grained structure.

To clarify the nature of extra-high hardness of fine grain chromium coatings produced by vacuum technology the structure, mechanical behavior and nanohardness of coatings of metals-analogues chromium and molybdenum were studied.

2.   EXPERIMENTAL DETAILS

The 80 nm, 400 nm and 2 μm thickness chromium and molybdenum coatings were produced by magnetron sputtering under the same conditions on the silicon substrates. The initial pressure in a chamber was about $5*10^{-4}$ Pa, after pure argon introduced in the chamber the total pressure was 0,3 Pa.

The detailed structure investigations and the phase analysis were performed by methods of transmission electron microscopy on JEM-100CX device at 100 kV accelerating voltage, and also on device Philips CM30UTFEG at an accelerating voltage 300 kV.

The mechanical behavior of coatings under point loading conditions was studied by nanoindentation using Berkovich indenter on Nano Indenter-II (MTS Systems Corporation, Oak Ridge, TN, USA). The nanohardness of chromium and molybdenum coatings was determined by the Oliver and Pharr analysis.

The image and cross-section of the indentation were investigated by atomic force microscopy (AFM) "Nanoscop-111A" in a mode of periodic contact with silicon probes with nominal radius of an edge with 10 nm.

3.   RESULTS AND DISCUSSION

It is shown, that chromium and molybdenum coatings have ultra-fine grain structure (Fig. 1). So, the grains size in 80 and 400 nm thickness chromium and molybdenum coatings are equal to 40 –50 nm and 20 nm accordingly. The diffraction pattern shows that only lines corresponding to lines body-centered cubic lattices chromium and molybdenum are precisely fixed, additional lines are not revealed.

The high-resolution Philips CM30UTFEG device (about 1 A) has allowed detailed study of the grains and grains boundaries (Fig. 2). It is established, that grains boundaries of chromium and molybdenum films are partly amorphous.

a   b
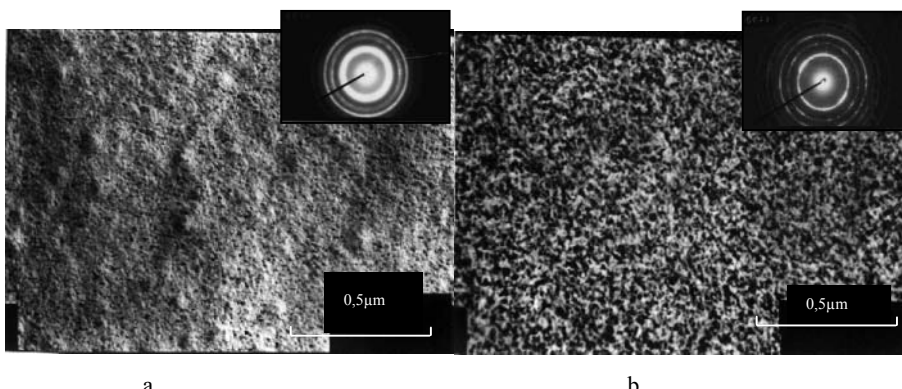
Figure 1. The electron microscope image of the 80 nm thickness molybdenum (a) and
chromium (b) coating.

The nanohardness of 400 nm thickness chromium coatings with ultra-fine grain (nanocrystalline) structure is equal to 21.61 GPa (Table1), which is 8-9 times higher than that of cast chromium. At the same time the nanohardness of molybdenum coatings, which characterized even more fine-grain structure, is equivalent to 9.98 GPa. It is necessary to note, that in a massive state hardness of polycrystalline chromium is lower than hardness of polycrystalline molybdenum (2 GPa and 1.3 GPa for polycrystalline molybdenum and chromium accordingly [7]).
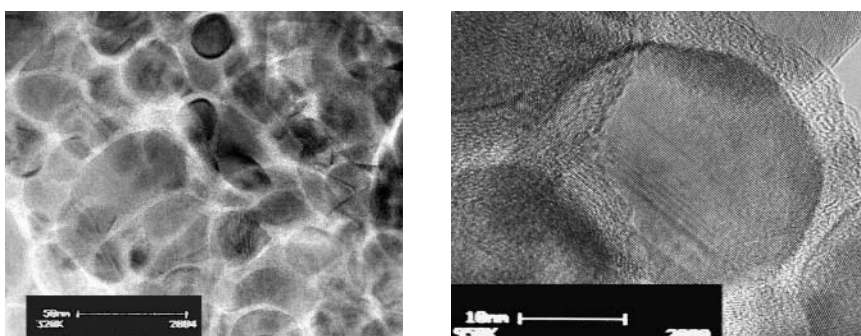
Figure 2. High resolution image of the 400 nm thickness chromium coating.

The increase in thickness of chromium and molybdenum coatings up to 2 μm results in some grain size growth and entail to nanohardness reduction (Table 1). However, its values remain much above tabulated values of nanohardness of these metals in a massive state and nanohardness of chromium coatings still remains above molybdenum.

Table1.

Coatings	Thickness	H (GPa)	H/E	λ
Chromium	400 nm	21.61	0.077	0.552
	2 μm	15.5	0.056	
Molybdenum	400 nm	9.98	0.031	0.801
	2 μm	8.5	0.026	

It can be seen from Fig.3 that chromium films differ from molybdenum films in the mechanical behavior essentially. So, unloading curve for chromium at depth about 330 nm shows displacement discontinuity that, as is known, testifies to phase transition in silicon under loading (a metal phase of high pressure Si II [6]). On unloading curve for molybdenum the phase transition in silicon is not fixed. Besides average contact pressure in molybdenum film is lower, than in a chromium film more than in 2 times and this distinction increases with reduction of depth of contact.
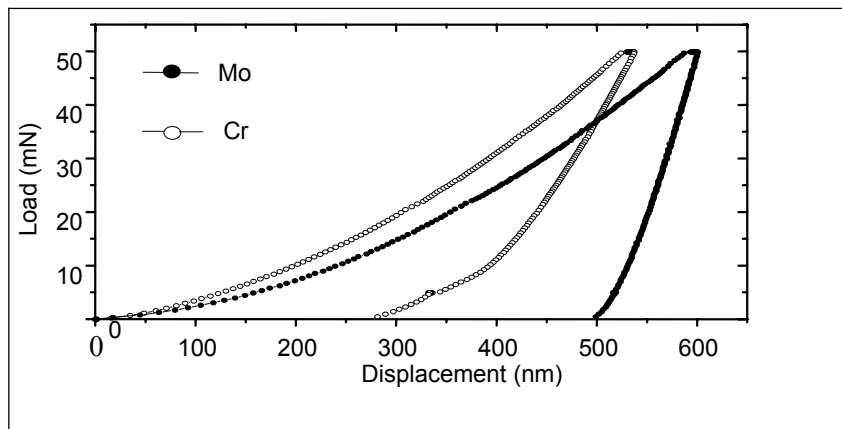

Figure 3. Load versus indenter displacement for 400 nm Cr and Mo films on silicon substrates.

The plasticity characteristic λ was calculated as the ratio of the work spent for plastic deformation of the material to the total work spent for elastic - plastic deformation of a material under indenter. It is shown (Table 1), that λ for 400 nm thickness molybdenum coatings is higher, than its value for chromium coatings of the same thickness.

The image of indentation and cross-section AFM observation in the chromium and molybdenum coatings (Fig.4) are evidence of higher pile-up in the molybdenum coatings as compared with chromium coatings. The indentation edges in the chromium coatings are concave down whereas they are concave up in the molybdenum coatings.

The extra-high hardness of chromium coatings cannot be explained only by presence of the nanocrystalline structures. As has been shown earlier [2] the

coatings produced by magnetron sputtering became saturated with oxygen. So it is more probable to suppose that hardening of chromium coatings is a result of oxygen atoms embedding in nanocrystalls boundaries, i.e. "healing" of defects in weak points on grain boundaries. It is possible due to strong chemical bond in the Cr-O system. The polycrystalline chromium is characterized by stronger Me-O bond in comparison with Me-Me bond, in contrast to polycrystalline molybdenum (Table 2) [8]. It is also true for partially amorphous grain boundaries, which is characterized low consistence.
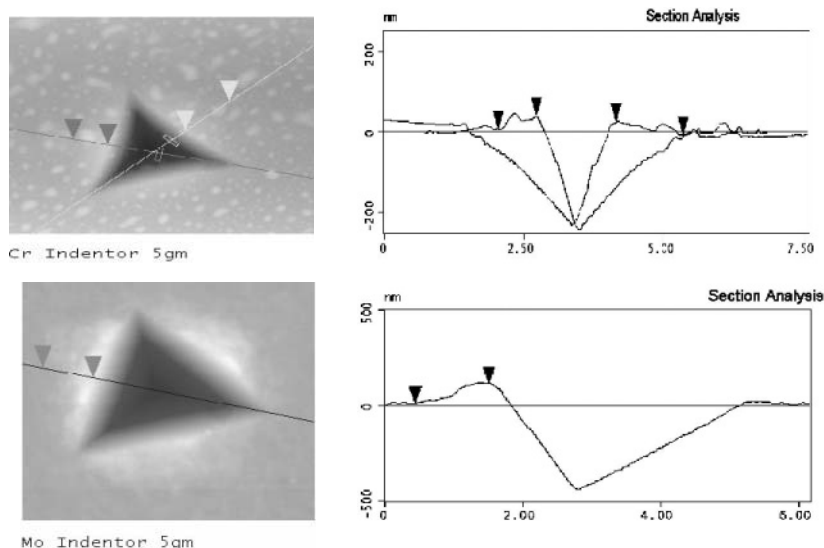
Figure 4. AFM images of indentation obtained in the chromium and molybdenum produced by magnetron sputtering on silicon substrates.

Table 2.

	$-\Delta H_{298}$		
	Kilojoules/mole	Kilocalorie/mole	T melting, K
Cr	397.75	95.0	Cr
Cr_2O_3	1130.4	270.0	Cr_2O_3
Mo	659.42	157.5	Mo
MoO_2	548	131	MoO_2

This mechanism is similar to the mechanism of drastic hardness increasing in nanocrystalline composite materials, which was proposed for multi-component system by S. Veprek [8]. In general it is possible to assume that for multi-component system after achievement of some critical grain sizes and at a correct choice of components transition to nanocrystalline or to an amorphous state should be accompanied not only prevention downturn of the hardness and yield point, but also considerably increase them in contrast to one-component system.

The presence of phase transition in silicon during chromium coatings indentation (metallic phase of high pressure, Si II) is corresponded with calculated plasticity characteristics (Table 1) and with observable in AFM various behavior of a material around of prints in molybdenum and chromium coatings. These results suggest that the chromium coatings have lower plasticity than molybdenum coatings and can be explained by the proposed mechanism of oxygen atoms embedding in nanocrystalls boundaries also. So, oxygen atoms embedding in molybdenum nanocrystalls boundaries leads to weakening cohesion between grain boundaries. That is why the plasticity of molybdenum coatings is higher than chromium ones. The plastic molybdenum film "envelops" the indenter and work as a solid lubricant. At that time the sufficient pressure on coating-Si boundary for metallic phase Si II formation does not reach.

4.   SUMMARY

The extra-high hardness of chromium coatings with ultra-fine grain structure is a result of oxygen atoms embedding in nanocrystalls boundaries and i.e. "healing" of defects in weak points on grain boundaries as Cr-O chemical bond is stronger in comparison with Cr-Cr chemical bond.

Embedding of oxygen atoms in molybdenum nanocrystalls boundaries leads to weakening cohesion between grain boundaries because Mo-O chemical bond is weaker than Mo-Mo chemical bond. That is why the molybdenum coatings plasticity is higher and its hardness is lower than chromium ones.

REFERENCES

1.   V. Guilbaud-Massereau, A. Celerier, Thin Solid Films, 258 (1995) 185-193.

2.   A. Rakitskiy,et al., Poroshkovaya Metallurgiya, (in Russian), No. 2 (1992) 56-63.
3.   Yu. Milman, et al., Poroshkovaya Metallurgiya, (in Russian), No. 8 (1993) 70-75.

4.   N. Krapivka, N. Korzhova, et al., Metally, (in Russian), No. 4 (1992) 178-184.
5.   N. Noskova, A. Korznikov et al., Fiz. Met. Metalloved., 89 (4) (2000) 113-116.
6.   Yu.G. Gogotsi, V. Domnich, et al., J. Mater. Res., 15 (2000) 871-879.
7.   A. Zephirov, Thermodynamic Properties of Materials, (in Russian), (Atomizdat, Moscow, 1965).
8.   S. Veprek, S. Reiprich, Li Shizhi, Appl. Phys. Lett. 66 (20), 15 May 1995.

BORON DISTRIBUTION AND MICROSTRUCTURE IN MOLYBDENUM-BORON ALLOYS

F. Morito[a,#], N.I.Danylenko[a], H.Saito[b] and A.V.Krajnikov[a]

[a] *Institute for Problems of Materials Science, 3, Krzhizhanivsky Street, Kiev 03142, Ukraine,*
[b] *Chiba Institute of Technology, 2-17-1 Tsudanuma, Narashino 275-0016, Japan;*
[#] *Permanent address: National Institute for Materials Science, 1-2-1 Sengen, Tsukuba 305-0047, Japan.   E-mail: morito.fumio@nims.go.jp*

Abstract: Boron distribution and characteristics of boron precipitates in molybdenum-boron alloys were studied not only by particle-tracking autoradiography (PTA) but also by tritium autoradiography (TA). Specimens were prepared by melting methods such as plasma-beam, electron-beam and arc melting. Content of boron was between less than 0.02 ppm and 920 ppm. With an increase of boron, fine boride precipitates were uniformly observed in the matrix. By PTA, we were successful to detect precipitates even in Mo with less than 0.02 ppm B. Above the content of 50 ppm B, needle-like precipitates were often recognized, which grew to the <110> direction in the matrix and along grain boundaries. By TA, it is clearly demonstrated that such boride precipitates behaved as trapping sites for hydrogen diffusion. Furthermore it is also clear that only a small amount of boron addition made a significant improvement to mechanical properties of molybdenum.

Key words: Mo-B alloy, Grain boundary segregation, Precipitates, Particle-tracking autoradiography (PTA), Tritium autoradiography (TA).

1.   INTRODUCTION

Molybdenum has been known as excellent materials with good thermal stability and resistivity for chemical corrosion. Moreover it has shown that intergranular fracture in molybdenum was improved by a small addition of boron. The reason is supposed that boron segregates along grain boundaries,

by which energy of grain boundaries was largely reduced. As a result, the bonding strength of the grain boundary increased by an addition of boron so that the grain boundary cracking was suppressed (1-3). Effect and distribution of boron in iron base alloys was previously studied by PTA reaction (^{10}B (n, α) ^{7}Li) (4-6). As for visualization of boron in molybdenum, we were successful by PTA method in recent papers (7, 8). Specimens doped by boron content from a small amount of less than 2 ppm to several hundred ppm were irradiated by atomic reactor in Rikkyo University and by JRR-4 in JAERI. Segregation characteristics of boron, which concentrated at grain boundaries and in the matrix, were analyzed quantitatively. Visualization of boron in molybdenum was tried in cold rolled specimens followed by annealing at high temperature. In addition, we could also demonstrate that boride precipitates exhibit a role of effective trap site for hydrogen by TA method (3).

2. EXPERIMENTAL

2.1 Materials and procedure

Molybdenum alloys containing a small amount of boron were prepared by plasma-beam, electron beam and arc melting. Chemical composition of B, C and O in typical Mo-B alloys is shown in Table 1.

Table 1. Chemical composition of typical Mo-B alloys. (mass ppm)

Specimen	Processing	B	C	O
1.1 B	As-cast	1.1	80	6
140 B	As-cast	140	70	3
<0.02 B	Sheet	<0.02	-	<1
1.3 B	Sheet	1.3	20	<1
2.5 B	Sheet	2.5	40	<1

Several alloys were rolled to sheet of 1 mm thick. Heat treatment was conducted for 3.6 Ks between 1173 K and 1773 K by the furnace with a vacuum less than 2 x 10 $^{-3}$ Pa. Mechanical properties were examined by bend test. Microstructure was observed by optical microscope and scanning electron microscope (SEM).

2.2   Particle-tracking autoradiography (PTA)

Specimen surface was polished electrochemically by mixed solution of sulfuric acid and ethyl alcohol (1:3). After polishing, the surface of the specimen was adhered by a film of nitric acid cellulose using acetic acid methyl solution. Specimens were then sealed in the polyethylene sheet and irradiated for 43.2 Ks (12 h) by the atomic reactor in Rikkyo University (thermal neutron = 1.1 x 10^{10} n/cm^2 s) or JRR-4 in JAERI (1.5 x 10^9 n/cm^2 s). After cooling down for 0.61 Ms (7days), the film of nitric acid cellulose was striped off from specimen. Boron distribution in the specimen corresponds to particle-tracks produced on the film of nitric acid cellulose by the interaction between thermal neutron and boron: (^{10}B (n,α) ^{7}Li). Using 2.5N-NaOH solution at 303 K, particle-tracks by α-rays produced by thermal neutron with boron were etched for 2.7 ks. Then etched films were washed for 10.8 ks in flowing water. We observed microstructure by optical microscopy and SEM.

2.3   Tritium autoradiography (TA)

After polishing and drying specimens, platinum wire (0.15 mm diameter) as a leading-in point for electric current was spot welded to a corner of specimens. Tritium was then introduced to specimens by cathodic electrolytic charging method (6, 9, 10) at an electric current density of 5 mA/cm^2 for 3.6 Ks in aqueous solution of 1N-sodium hydroxide, where the specific radioactivity of tritium was 5 x 10^{11} Bq/cm^3 (0.1 Ci/cm^3). After tritium charging, specimens were exposed for 0.26 Ms (3 days) at room temperature. In order to detect non-diffusible tritium only, the surface of specimen was then covered with a collodion film about 10 nm by dipping loop method and adhered by a film of photographic nuclear emulsion (Ilford L4). Such specimens were exposed for 8.4 Ms (97 days) at 253K. Afterwards these photographic films were treated by development, fixation and washing in water. After drying, they were examined by SEM and a liquid scintillation counter (9, 10).

3.   RESULTS AND DISCUSSION

3.1   Boron distribution by PTA

Boron distribution in as-cast Mo-1.1 ppm B visualized by PTA method was shown in Fig. 1. Black dots correspond to boron tracks etched in the film of nitric acid cellulose. The density of these dots is proportional to

boron concentration in this area. Black lines and black points exhibited the presence of boron along grain boundaries and in the matrix, respectively. It is clear that boron distributed not only along grain boundaries, but also in the matrix rather uniformly. By such a rather low magnification of optical microscope, boron distribution seemed to distribute uniformly along grain boundaries. But boron distribution along grain boundaries was clearly different and depended on each grain boundary character, when we magnified largely in the part of Fig. 1. It is also demonstrated that boron tracks near the triple point of grain boundaries did not distribute homogeneously.
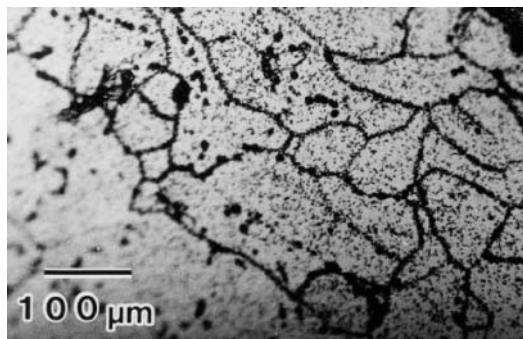
Figure 1. Boron distribution in Mo-1.1 ppm B.

3.2   Quantitative analysis of boron distribution at grain boundaries and in the matrix.

We examined boron distribution along grain boundaries in the vicinity of grain boundary triple point in more detail. Considering that boron distribution strongly depends on each grain boundary character, we analyzed relative density of boron distribution by statistical frequency distribution (ρ_{min}/ρ_{av}) of unit area (per 10 μm square) at the location from the grain boundary triple point away to about 10 μm, whereρ is the number of boron tracks along grain boundary, ρ_{min} is the lowest value of ρ among grain boundaries andρ_{av} is average value of ρ. When one grain boundary shows a small quantity of boron distribution compared to other two grain boundaries, boron distribution approaches to be 0.5. On the other hand, boron distribution becomes to be 1.0, when all the grain boundaries exhibit equal distribution at the grain boundary triple point.
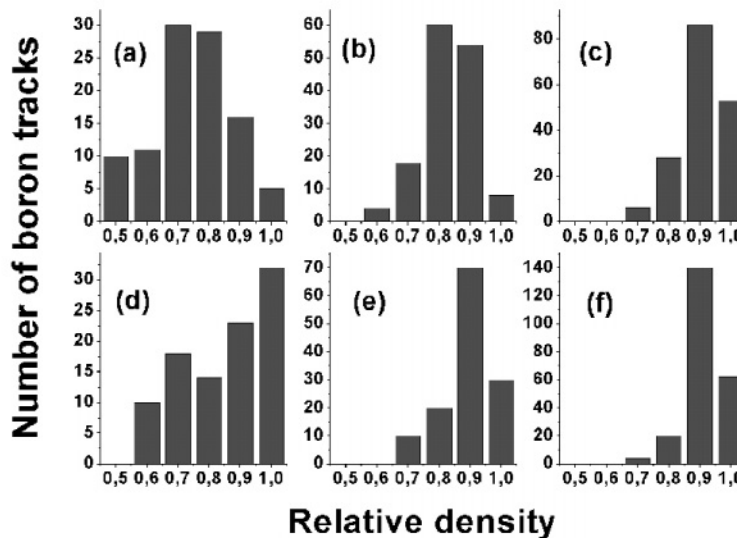
Figure 2. Statistical frequency distribution of boron at grain boundaries and in the matrix of (a), (d) Mo-<0.02 ppm B, (b), (e) Mo-1.3 ppm B and (c), (f) Mo-2.5 ppm B, respectively .

Fig. 2 shows the result of analysis by the statistical frequency distribution of boron tracks at grain boundaries and in the matrix in Mo-<0.02, 1.3 and 2.5 ppm B, respectively. Total number of grain boundaries (N) is 100 - 180 grain boundaries as shown in Fig. 2. Boron distribution of many grain boundaries exhibited to be 0.7 - 0.9 in Fig. 2(b) and (c). This is because each grain boundary has nearly identical boron distribution. In the case of grain boundaries, relative density of boron distribution approaches to 1.0 with rather higher boron content. In lower boron content, it becomes to 0.6 - 0.5, showing that boron distribution at the grain boundary triple point is not identical. In addition, it was clear that relative density in the matrix in Fig. 2(d) to (f) exhibited a tendency of identical distribution with higher boron content. Therefore boron distribution both at grain boundaries and in matrix was evidenced to have a tendency of identical distribution in rather higher boron content than in lower boron content. Above the content of 50 ppm B, needle-like precipitates were often recognized, which grew to the <110> direction in the matrix and along grain boundaries.

3.3   Released characteristics of tritium and boron visualization by TA

After tritium electrolytic charging, tritium behavior in Mo-B alloys was measured by a liquid scintillation counter. Released characteristics of tritium in Mo-<0.02 ppm B and Mo-2.5 ppm B are shown in Fig. 3, analyzing continuously for three days from measurable start. Diffusible tritium was almost released nearly after two days. They became to a constant value after three days and non-diffusible tritium of about 0.09 ppm was remained in specimens.
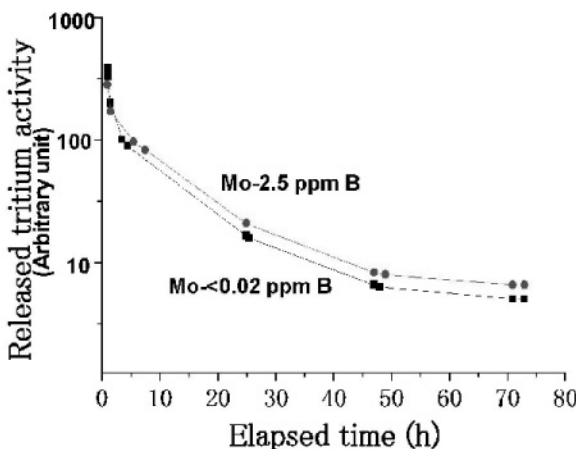
Figure 3. Released characteristics of tritium in Mo-<0.02 ppm B and Mo-2.5 ppm B by a liquid scintillation counter.

Afterwards we started to examine tritium autoradiography. Such tritium autoradiographs exposed for 97 days are shown in Fig. 4, where (a) and (b) correspond to Mo-1.3 ppm B and pure molybdenum, respectively. In this case, TA was observed by reflection method using SEM so that white dots and lines corresponded to tritium containing phases such as precipitates and grain boundaries. It is clear that grain boundaries were covered with grain boundary precipitates containing tritium by TA. In Fig. 4 (b) of pure Mo without boron, white dots and lines are seemed to be dislocations in the matrix trapped by tritium. Therefore hydrogen analysis by TA is very effective to detect such trapping sites as precipitates and dislocations for hydrogen distribution. However it is also clear that resolution of TA is not so good compared to PTA.
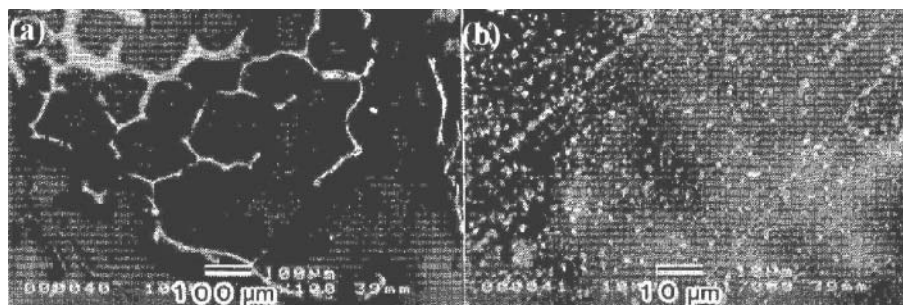
Figure 4. Boron distribution by TA: (a) Mo-1.3 mass ppm B and (b) pure Mo.

In a summary, visualization of boron in Mo-B alloys was demonstrated by PTA method using thermal neutron reaction (^{10}B (n,α) ^{7}Li). Boron was found to segregate at grain boundaries and in the matrix. Distribution of boron adjacent to grain boundary triple point was analyzed quantitatively by statistical frequency method. In a lower content of boron, distribution of boron was shown inhomogeneously segregating along grain boundaries. In a higher content of boron, distribution of boron was evidenced rather homogeneously along grain boundaries. On the other hand, boron distribution was demonstrated almost equally in the matrix regardless the concentration of boron. In addition, we could clearly demonstrate by TA method that such precipitates and dislocations containing boron behaved as trapping sites for hydrogen diffusion. It made clear that TA is very effective method for examining hydrogen behavior in materials.

ACKNOWLEDGEMENTS

REFERENCES

1. F. Morito, Surface and Interface Analysis, 15 (1990), 427.
2. F. Morito, Colloque de Physique, C1-51(1990), 281.
3. F. Morito, T. Noda and A. V. Krajnikov, Proc. Intern. Conf. on SM-2002, (2002), I-102.
4. H. Saito and M. Mori, Metals, Agune Publishing, 12(1997), 1027.

5. K. Shibata, Radioisotopes, 46 (1997), 413.
6. H. Saito, K. Miyazawa and M. Mori: J. Japan Inst. Metals, 62 (1998), 215.
7. F. Morito, A. V. Krajnikov and H. Saito, Proc. Intern. Conf. on SM-2002, (2002), VI-101,
8. H. Saito and F. Morito, Tetsu-to-Hagane, 89(2003), 750.
9. H.Saito, N. Nogawa, T. Asaoka, N. Morikawa and Y. Ishida, Radioisotopes, 39 (1990), 249.
10. M. Aoki, H. Saito, M. Mori, Y. Ishida and M. Nagumo, J. Jpn. Inst. Metals, 58 (1994), 1141.

PART 6

ADVANCED METHODS AND PROCESSES

DYNAMIC RECRYSTALLIZATION OF LOW STACKING FAULT ENERGY METALS

Frank Montheillet and Jean-Philippe Thomas
Ecole des Mines (Center for Materials Science and Structures), Plasticity, Damage and Corrosion of Materials CNRS Laboratory, Saint-Etienne, France

Abstract: Dynamic recrystallization mechanisms in an austenitic stainless steel and a nickel base superalloy are compared. In the latter alloy, recrystallization may occur by "continuous nucleation", but develops slowly due to more efficient dynamic recovery, and reduced grain boundary mobility.

Key words: thermomechanical processing, dynamic recrystallization

1.   INTRODUCTION

Thermomechanical processing (TMP) has first been developed in the second half of the last century for decreasing the ductile to brittle transition temperature of construction steels. It has then progressively been extended to other categories of structural metallic materials, such as titanium alloys or nickel base superalloys for aircraft forged turbine parts. More recently, investigations have been carried out to assess the possibility and advantage of TMP for ferritic and austenitic stainless steels.

The basic underlying idea is to control the microstructural transformations occurring during and after hot deformation for improving the mechanical properties of the workpiece, such as yield stress, fatigue or creep resistance, toughness, etc. Among these transformations, dynamic recrystallization (DRX) plays a major role, since it is associated with the key parameters of the hot worked microstructure, i.e. recrystallized fraction, average grain size, and the nature of grain boundaries. It has been claimed that the control of grain boundary character distributions ("grain boundary engineering") would

357

be a promising way to reach higher resistance levels. For instance, it has been shown that an increase of the twin boundary area fraction improves creep resistance in a nickel base alloy [1]. Similarly, it has been suggested that incomplete DRX leading to partially recrystallized "duplex" microstructures could be beneficial.

Although DRX mechanisms are not yet fully understood and may considerably differ from one alloy to the other, recent results make it possible to propose here a short summary of the present knowledge, while a more comprehensive synthesis may be found in [2]. More precisely, the present paper will focus on the DRX mechanisms occurring in two low stacking fault energy structural materials, viz. an austenitic stainless steel (close to the 304 grade), and a nickel base superalloy (718 grade). It is now well known that low to medium stacking fault energy metals, like carbon steels within the austenitic range or copper, undergo "discontinuous" (or "classical") DRX during hot deformation. Such typical behaviour will be illustrated below by the austenitic steel. By contrast, in the 718 alloy, nucleation of new grains involves an original mechanism, referred to as "continuous nucleation" [3], quite similar to "continuous dynamic recrystallization" (CDRX) commonly observed in high stacking fault energy materials, such as aluminium [4].

2.   CONTINUOUS VS. DISCONTINUOUS DYNAMIC RECRYSTALLIZATION

Various recent experimental data have given new insight into the high temperature deformation mechanisms associated with hot working of metals [5,6]. First, large to very large strain torsion data have been obtained; second, the availability of automated Electron BackScattering Diffraction (EBSD) devices has allowed detailed and statistical analyses of the deformed microstructures to be collected; finally, models have been developed to better understand the basic mechanisms. It is now well established that two types of dynamic recrystallization may operate during hot deformation: continuous dynamic recrystallization (CDRX), also sometimes called "apparent dynamic recrystallization" or "extended dynamic recovery", and discontinuous dynamic recrystallization (DDRX), formerly referred to merely as dynamic recrystallization.

a) In high stacking fault energy materials (e.g., aluminium alloys or ferritic steels), since dynamic recovery is very efficient, the dislocation density differences across grain boundaries, which are the main driving forces for dynamic grain boundary migration, are small; thus migration rate is low. In addition, dislocations organize into subgrain boundaries, the

misorientation angle θ of which, typically less than 15°, may progressively increase during straining (the misorientation is defined as the minimum rotation angle between two adjacent crystals). Part of the dislocation walls transform continuously into large angle grain boundaries (θ > 15°). Such mechanism of CDRX leads at very large strains ($\varepsilon \approx 50$) to steady state microstructures made of "crystallites", delimited partly by subgrain boundaries and partly by grain boundaries. On a crystallite scale (typically a few micrometers), the microstructure is very homogeneous. A flat maximum followed by slow decay systematically characterizes the stress-strain curves pertaining to CDRX. A flow stress and microstructure steady state is reached only after very large deformations. Such von Mises equivalent strains ε, ranging from a few units to several tenths, can only be achieved by torsion tests or special devices such as Equal Channel Angular Extrusion (ECAE) or 3-dimensional "ABC" forging.

b) In materials with medium or low stacking fault energy, the reduced mobility of dislocations lowers the efficiency of recovery. High local gradients of dislocation density induce large grain boundary migration rates (typically 10 to 100 times larger than for CDRX). An important consequence is that the above-mentioned transformation of subgrain into grain boundaries has not enough time to take place. Each material element undergoes successive cycles of strain hardening and recrystallization, such that the microstructure is very inhomogeneous on a grain scale. For low values of the Zener-Hollomon parameter Z (low strain rates and/or high temperatures), recrystallization takes place very quickly, such that the cycles can be synchronized within the testing specimen. This leads to wavy or multiple peak stress-strain curves generally associated with grain growth, which are never observed for CDRX. By contrast, at large Z values (high strain rates and/or low temperatures), synchronization does not occur and the flow curves exhibit one single peak, while grain refinement occurs. In both cases, a steady state is attained at strains not larger than $\varepsilon \approx 0.5$ to 1.0.

A simple criterion for the occurrence of CDRX or DDRX has been recently proposed [7]: let t_1 be the time necessary for generating a new grain boundary, i.e. for creating a subgrain boundary and transform the latter into a grain boundary; t_2 the time needed for a grain boundary to sweep a crystallite volume. CDRX occurs only if t_1 is less than t_2, since otherwise the new subgrain boundaries are wiped out before their transformation into grain boundaries. Grain boundary mobility clearly may decide which type of DRX is likely to occur, which suggests that transitions may be observed for a given material, for instance by changing its purity. This is effectively the case in high purity aluminium [8] and α-iron [9], where DDRX takes place instead of CDRX.

3.   DRX IN AN AUSTENITIC STAINLESS STEEL

Results reported below were obtained on a high purity base austenitic stainless steel, close to the commercial 304 grade, containing 18 %Cr, 12.2 %Ni, in which the level of solutes was reduced to 15 ppm C, 10 ppm S, and 10 ppm N [10]. In such a material, grain boundary mobility is likely to be very high, so that "classical" DDRX is expected.

3.1   Stress-strain curves

Figure 1 shows uniaxial compression flow curves at various temperatures for two different initial grain sizes.
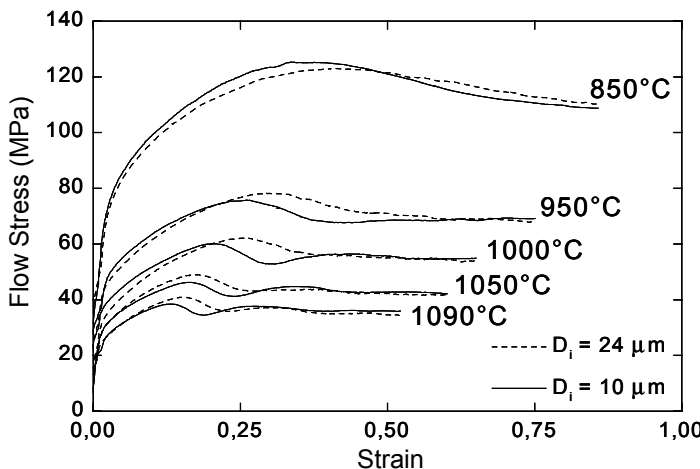
Figure 1. Typical flow curves of an austenitic stainless steel in the hot working range $(\dot{\varepsilon} = 10^{-3} \text{ s}^{-1})$ [11]

Although the oscillations of the curves are not much marked, a transition from multiple to single peak behaviour is observed roughly between 1000 and 950 °C with decreasing temperature. Using the apparent activation energy for hot deformation $Q \approx 400$ kJ/mol [11], the transition occurs within the range of $Z \approx 10^{13}$ to 10^{14} s^{-1}. The flow stress of the steel with the smaller initial grain size (10 μm) is slightly larger in the work hardening range, which is in agreement with the classical Hall-Petch effect. By contrast, the peak values are reached at lower strains and are generally smaller than for the steel with an initial grain size of 24 μm. This can be attributed to the nucleation of new grains, which occurs preferentially on the original grain boundaries, and therefore more rapidly in the fine grained material. At large strains, flow stress reaches a steady state, where it is

independent of the initial grain size. (Note, however, that flow stress may become constant much before the microstructure and texture have reached their respective steady states).

3.2 DRX mechanisms

Figure 2 illustrates the microstructural changes occurring in the above austenitic steel during straining at 850 °C, 10^{-3} s^{-1}, which is associated with grain refinement.


50 μm initial state	$\varepsilon = 0.1$
$\varepsilon = 0.7$	$\varepsilon = 1.5$
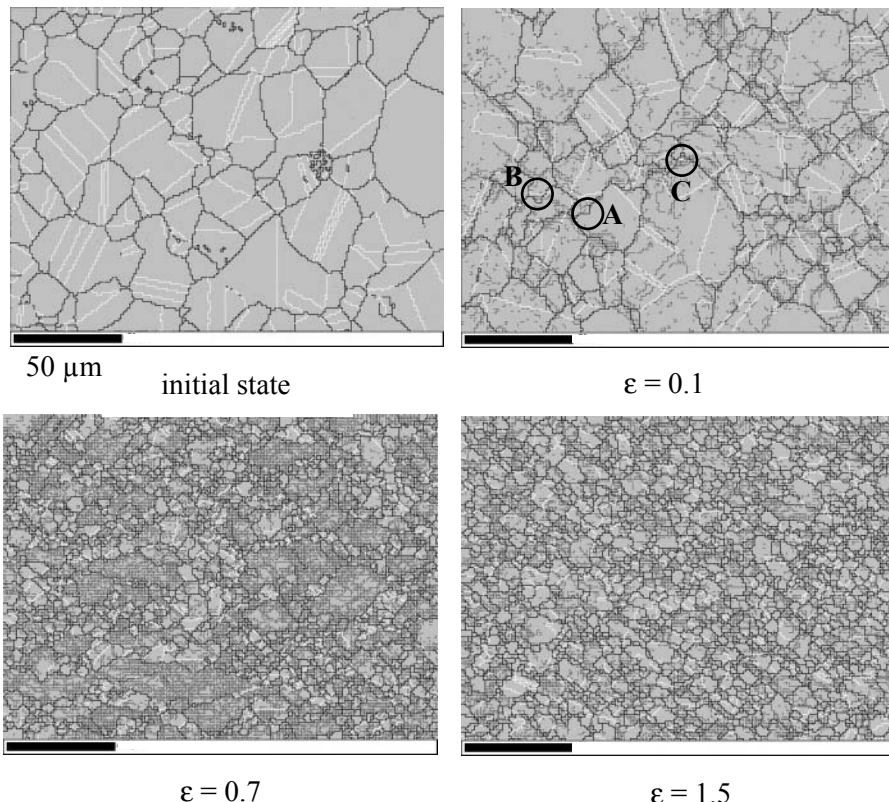
Figure 2. Microstructural evolutions during hot working of the austenitic stainless steel at 850°C, 10^{-3} s^{-1} (the axis of uniaxial compression is vertical) [11]

The above images were obtained by scanning electron microscopy in Electron BackScattering Diffraction (EBSD) mode. Three types of interface are indicated: subgrain boundaries ($1 < \theta < 15°$) −light grey lines, ordinary high angle boundaries ($\theta > 15°$) −black lines, and twin boundaries associated with a rotation of 60° around a common <111> type crystallographic axis −white lines. At low strains ($\varepsilon = 0.1$), subgrain boundaries form

preferentially in the vicinity of the original grain boundaries due to deformation incompatibilities between neighbouring grains. Simultaneously, the initial boundaries become serrated and nucleation occurs by grain boundary bulging (see circles A, B, C). As already pointed out in various investigations, the nucleus is separated from the original grain either by a low angle boundary (e.g., A), or by a twin boundary (e.g., B) [12]. At a strain $\varepsilon = 0.7$, the microstructure consists of two types of grain: the larger ones, which are remnants of the original grains, contain a large amount of subgrain boundaries, while the smaller are freshly recrystallized grains, inside of which twin boundaries are clearly visible.

50 µm
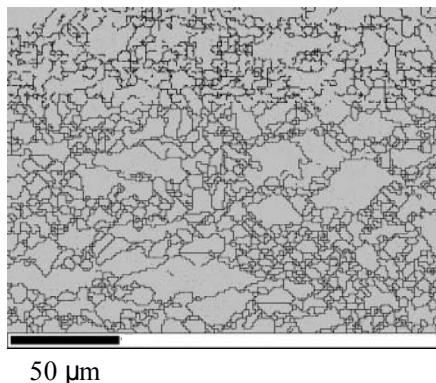
Figure 3. Same area as in Figure 2, $\varepsilon = 0.7$. The subgrain boundaries have been removed.

In figure 3, where the subgrain boundaries have been removed, necklace DRX becomes more apparent. Finally, at a strain of 1.5, which is close to the steady state, the microstructure is very inhomogeneous: "younger" grains contain few subgrain boundaries but a large number of twin boundaries, while it is the inverse for "older" grains. It should be noted that small grains may belong to the second as well as to the first of these two categories. Figure 4 displays the strain dependence of the twin boundary area fractions in both the single peak and multiple peak curve cases. The initial fraction, close to 45 % first decreases, since twin boundaries progressively loose their special character due to strain induced grain rotations. Then it increases again with the occurrence of DDRX, which is particularly visible in the multiple peak case, where each "recrystallization wave" is associated with an increase in twin boundary fraction. This means that (growth) twinning is one of the main mechanisms involved in the generation of new grains.

(a)

(b)
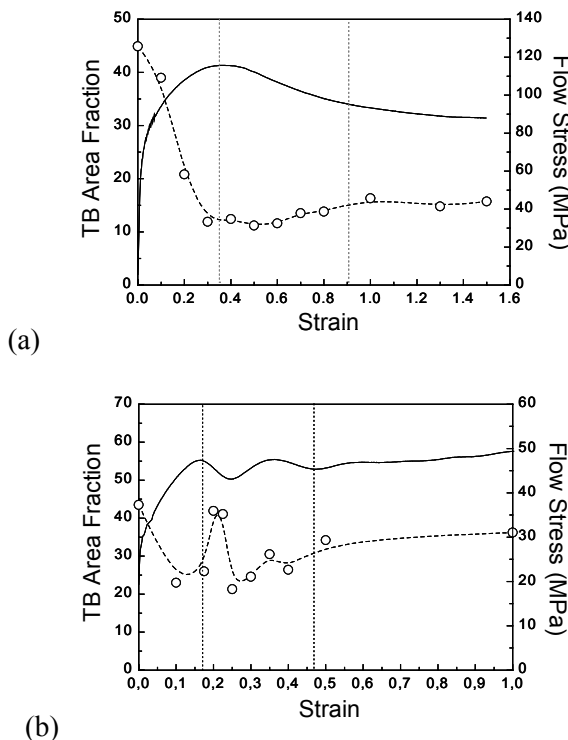
Figure 4. Strain dependence of the twin boundary (TB) area fractions in an austenitic stainless steel: (a) single peak case (850 °C, 10^{-3} s^{-1}); (b) multiple peak case (1050 °C, 10^{-3} s^{-1}) [11]

4. DRX IN A 718 NICKEL BASE SUPERALLOY

The following results were obtained on a 718 grade nickel alloy strained in compression or torsion after solution treatment of the δ (Ni_3Nb) phase, within the temperature and strain rate ranges usually employed for hot forging of turbine disks [3].

4.1 Stress-strain curves

Due to the large initial grain sizes available, flow curves are all of the single peak type, associated with grain refinement (figure 5). Softening appears later and with less efficiency for a coarser initial microstructure, like in the austenitic stainless steel, which confirms that DRX is delayed by large initial grains. Furthermore, the steady state flow stress is not yet reached at a strain $\varepsilon = 1$, which means that DRX kinetics is low in this alloy.

Nevertheless, the measured apparent activation energy, $Q \approx 400$ kJ/mol, is identical to that of 304 stainless steel.
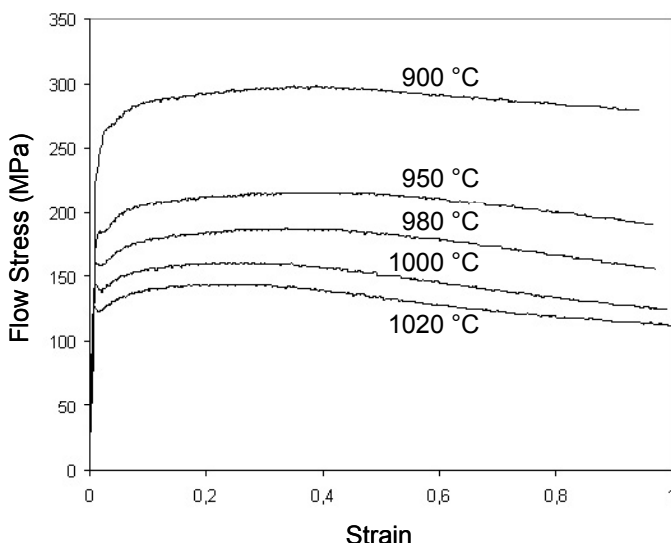

Figure 5. Stress-strain curves of a 718 nickel base superalloy deformed in compression ($\dot{\varepsilon} = 10^{-2}$ s^{-1}) and various temperatures in the hot working range (D$_i$ = 50 µm)

4.2   DRX mechanisms

During the first steps of deformation, strain inhomogeneities appear within the initial grains, as illustrated in figure 6 in which the various grey intensities show the local changes of crystallographic orientation. The latter are accommodated by subgrain boundaries progressively generated by the rearrangement of geometrically necessary dislocations. This leads to the fragmentation of the initial microstructure, before the onset of DRX.

At larger strains (figure 7), nucleation of the first recrystallized grains occurs, leading to a typical necklace microstructure, although nuclei appear not only on the initial grain boundaries, but also on the new boundaries generated by grain fragmentation. Recrystallization then progresses through the deformed microstructure. In the same way as in the stainless steel, migrating grain boundaries leave twin boundaries behind them. Indeed, after an initial decrease due to straining, the twin boundary fraction increases again at a level quite similar to that of alloy 304. Twinning constitutes therefore a first mechanism of nucleation.

500 μm
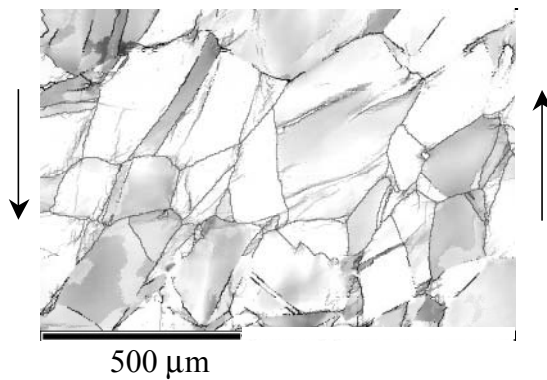
Figure 6. Fragmentation of the initial microstructure of 718 alloy. Torsion at 900 °C, $\dot{\varepsilon} = 10^{-2}$ s^{-1}, $\varepsilon = 0.4$ [3]

200 μm

$\varepsilon = 0.4$

$\varepsilon = 0.7$

$\varepsilon = 1.0$
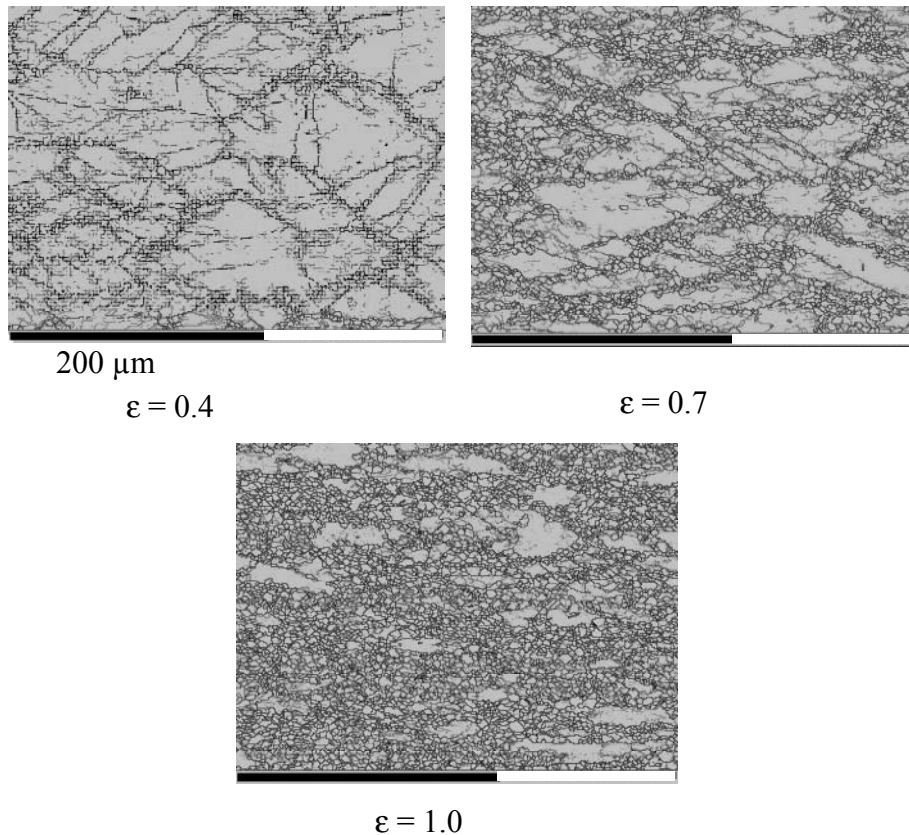
Figure 7. Microstructural evolutions during hot working of alloy 718 at 980 °C, 10^{-2} s^{-1}; the axis of uniaxial compression is vertical (twin boundaries are not specified)

However, since grain boundary migration is slower than in the stainless steel, some subgrain boundaries may reach a misorientation larger than 15° before they are wiped out by moving boundaries. Figure 8 shows the strain dependence of the subgrain boundary misorientation distribution function. The latter can be described by a power law relationship $\varphi(\theta) = k\,\theta^{-q}$, where the exponent q increases with strain. When applied to the steady state $(q = q_s)$, flux conservation within the distribution of subgrain boundaries requires that $\varphi(\theta)\,\dot\theta = k\,\theta^{-q_s}\dot\theta$ be constant, wherefrom $\dot\theta(\theta) = C\,\theta^{q_s}$. This means that the misorientation rate of a given subgrain boundary increases with θ, which may be related to the fact that highly misoriented boundaries are located in the parts of the material which are the most affected by strain inhomogeneities, e.g. in the vicinity of the original grain boundaries. This contrasts with the case of aluminium alloys, where it has been shown that $\dot\theta = $ constant is a good approximation [13]. Numerical simulations have shown that the above power law misorientation rate relationship effectively leads to the observed misorientation distribution functions.
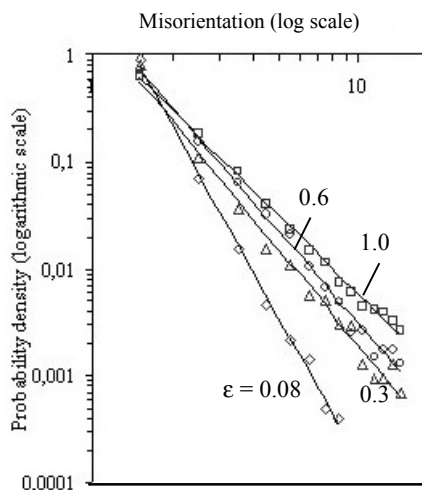

Figure 8. Strain dependence of the subgrain boundary misorientation distributions in alloy 718 at 1030 °C and $10^{-2}\ \mathrm{s}^{-1}$

The generation of high angle boundaries by the progressive misorientation of subgrain boundaries leads to the formation of nuclei for DRX (figure 9). By reference to CDRX, this second mechanism may thus be termed "continuous nucleation". Finally, the mechanism of nucleation by bulging of initial grain boundaries is also observed, but with a contribution to the nucleation rate at least one order of magnitude lower than that due to continuous nucleation.

5. CONCLUSIONS

From the above comparisons, it may be concluded that DDRX in low stacking fault energy metals occurs with variable kinetics, e.g. much more slowly in alloy 718 than in the 304 austenitic steel. Since the generation rates of new grains by (growth) twinning are quite similar in both cases, this can be attributed to different high angle grain boundary migration rates. On the one hand, the driving force seems to be smaller in alloy 718, due to dynamic recovery, which is in agreement with the formation of DRX nuclei by "continuous nucleation"; on the other hand, grain boundary mobility is certainly reduced by the presence of niobium atoms in solid solution.

50 μm
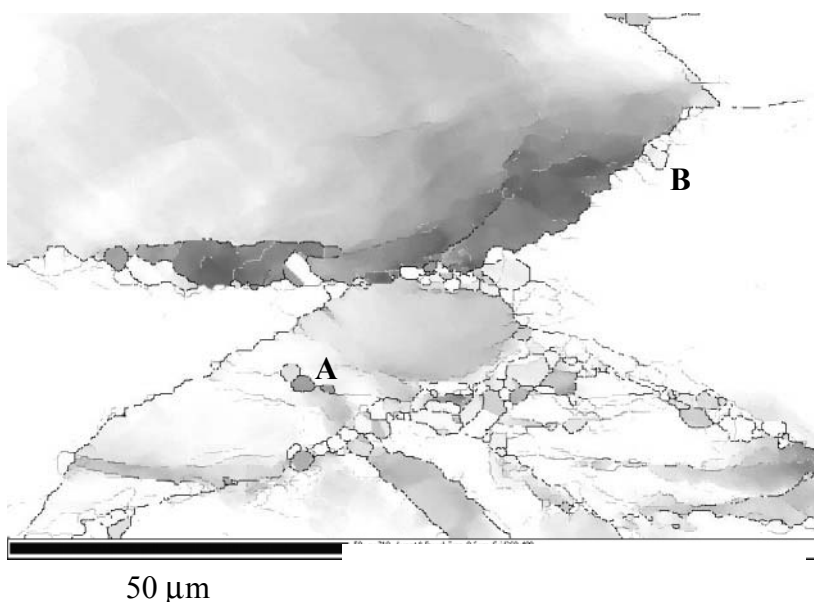
Figure 9. Alloy 718 deformed at 980 °C, 10^{-2} s^{-1} to $\varepsilon = 0.4$ in uniaxial compression, exhibiting continuous nucleation (A), as well as nucleation by grain boundary bulging (B)

Finally, it is suggested that the respective contributions of CDRX and DDRX during the thermomechanical treatment of nickel base superalloys could be controlled by adjusting the volume fraction of niobium or other addition elements. In this way, it would be possible to modify the hot deformation microstructures, e.g., the recrystallized fractions for a given accumulated strain, or the respective surface fractions of low angle, general high angle, and twin boundaries, in order to optimize the service properties.

REFERENCES

1. C.J. Boehlert, S. Civelekoglu, N. Eisinger, G. Smith, J. Crum, in: Int. Conf. on Processing & Manufacturing of Advanced Materials (Eds. T. Chandra, J.M. Torralba, T. Sakai), Trans. Tech. Publ., Mater. Sci. Forum 426-432, Part 1, 2003, p.761.
2. F. Montheillet, in: Moving Interfaces in Crystalline Solids (Eds. F.D. Fischer, M. Berveiller), CISM Course, 2003, Udine, to be published.
3. J.-Ph. Thomas, F. Montheillet, Ch. Dumont, in: Int. Conf. on Processing & Manufacturing of Advanced Materials (Eds. T. Chandra, J.M. Torralba, T. Sakai), Trans. Tech. Publ., Mater. Sci. Forum 426-432, Part 1, 2003, p.791.
4. S. Gourdet, F. Montheillet, Mater. Sci. Eng. A283, 2000, 274.
5. F. Montheillet, J.J. Jonas, Dynamic recrystallization, in: Encyclopedia of Applied Physics, vol.16, VCH Publishers, 1996, p.205.
6. F. Montheillet, Rev. Métall.-CIT/Sci. Génie Matér. 99, 2002, 767.
7. C. Chovet, S. Gourdet, F. Montheillet, Mater. Trans. 41, 2000, 109.
8. H. Yamagata, Scripta Metall. Mater. 27, 1992, 201.
9. G. Glover, C.M. Sellars, Metall. Trans. 4, 1973, 765.
10. L. Gavard, F. Montheillet, J. Le Coze, Scripta Mater. 39, 1998, 1095.
11. L. Gavard, PhD Thesis, Ecole des Mines, Saint-Etienne, France, 2001.
12. T. Sakai, in: Thermomechanical Processing of Steel (Eds. S. Yue, E. Es-sadiqi), The Metallurgical Society, Ottawa, Canada, 2000, p.47.
13. S. Gourdet, F. Montheillet, Acta Mater. 51, 2003, 2685.

ATOMIC-SCALE MODELING OF CROSS SLIP AND ITS CONTRIBUTION TO THE UNDERSTANDING OF TEXTURE AND FATIGUE IN FCC MATERIALS

T. Leffers and O.B. Pedersen
Materials Research Department, Risø National Laboratory, DK-4000 Roskilde, Denmark

Abstract: The procedures for the atomic-scale modeling of cross slip in copper are described, and the resulting activation energies and activation volumes for cross slip of non-jogged and jogged screw dislocations are recapitulated. The application of the results on the fcc rolling-texture transition and on fatigue in copper is demonstrated.

Key words: cross slip, atomic-scale modeling, rolling texture, fatigue

1. INTRODUCTION

Cross slip is the process where a dislocation – a screw dislocation – changes its slip plane. The concept of cross slip was introduced on the basis of slip-line observations on polished surfaces [1] at an early stage of the investigation of the behavior of dislocations

A dislocation is normally dissociated in its slip plane, and therefore cross slip requires some kind of constriction which means that cross slip is, generally speaking, a thermally activated process, e.g. [2]. This does not exclude that the activation energy may be zero for certain conditions.

It is widely accepted that cross slip plays a decisive role in various processes during monotonic and cyclic plastic deformation. Seeger [3] suggested that the transition to stage III in the plastic deformation of fcc single crystals is governed by cross slip. Mott [4] suggested that cross slip is

essential for the fatigue process. Smallman and Green [5] and Dillamore and Roberts [6] suggested that cross slip governs the rolling-texture transition in fcc polycrystals. However, until the late nineteen-nineties the quantification of these ideas was hampered by the lack of quantitative knowledge of the cross-slip process. Cross slip involves atomic rearrangements in the dislocation cores, and therefore the continuum approach to cross slip, which was the only approach available, was of limited value.

Now the situation is different. Recent progress in the theoretical understanding of the interatomic potentials coupled with the increase in computer capacity has made it possible to do atomic-scale modeling of the cross-slip process. In collaboration with the CAMP centre at the Technical University of Denmark the present authors have been involved in atomic-scale modeling of cross slip in copper. Here we recapitulate the results of this atomic-scale modeling – and the limitations we are up against. And we describe the application of the results on the fcc rolling-texture transition and on fatigue.

2.   ATOMIC-SCALE MODELING OF CROSS SLIP

2.1   Modeling procedure

We used an interatomic potential derived from *Effective Medium Theory* as described in [7]. This potential reproduces the elastic properties of copper quite well, but the derived stacking fault energy, $31 mJm^{-2}$, is somewhat lower than the normally quoted value for copper of $\sim 50 mJm^{-2}$ [8].

The ideal procedure for the cross-slip modeling would be *Molecular Dynamics*, e.g. [9]. Unfortunately, the capacity of presently available computers is in the general case insufficient for molecular-dynamics modeling of the complex cross-slip process. Therefore, we have largely used an alternative procedure, the *Nudged Elastic Band* (NEB) [10]. With this procedure we define the initial and the final atomic configuration, and the computer then finds *a low-energy path* in multidimensional configuration space which in practice is *the lowest-energy path*. The principle behind the NEB is sketched in *Figure 1*.
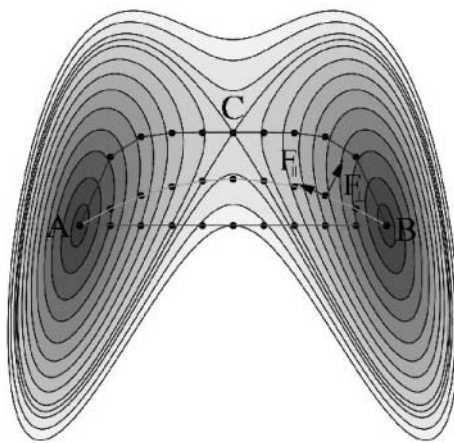
Figure 1. The principle behind NEB as referred to a two-dimensional potential-energy surface. The initial state A and the final state B are energy minima, and NEB finds the minimum-energy path between them: the path where the forces from the potential perpendicular to the path are zero. We start with a path which is a linear interpolation between A and B. In a number of steps NEB then approaches the minimum-energy path through the saddle point C. From [11].

2.2   Cross slip without jogs

As the first significant result of our atomic-scale modeling of cross slip Rasmussen et al. [12] determined the activation energy for cross slip of a single non-jogged screw dislocation to ~3eV. The cross-slip mechanism corresponded to that suggested by Friedel [13] and Escaig [14]. An activation energy of this magnitude is prohibitively high for cross slip at room temperature. Rao et al. [15] suggested a substantially lower activation energy for cross slip of a non-jogged screw dislocation in copper (~1.15eV) based on atomic-scale modeling of cross slip in nickel (with a different procedure), but this "translation" from nickel to copper has been questioned by Rasmussen [16] and Vegge [17].

Cross slip may be assisted by stresses, for instance the attractive stress between the two dislocations in a screw-dislocation dipole. This was investigated by Rasmussen et al. [18]. They found an approximately linear relation between the inverse dipole height and the activation energy for dipole annihilation by cross slip as shown in *Figure 2*. For dipole heights less than five or six {111} interplanar spacings (depending on the configuration) the activation energy is zero, i.e. the two screw dislocations annihilate by spontaneous cross slip. From *Figure 2* Rasmussen et al. derived an activation volume for cross slip of ~15b^3 (b being the Burgers vector) which is substantially smaller than the experimental value for the

activation volume for cross slip in copper ($\sim 250b^3$) derived by Bonneville et al. [19]. We shall return to this discrepancy in section 3.
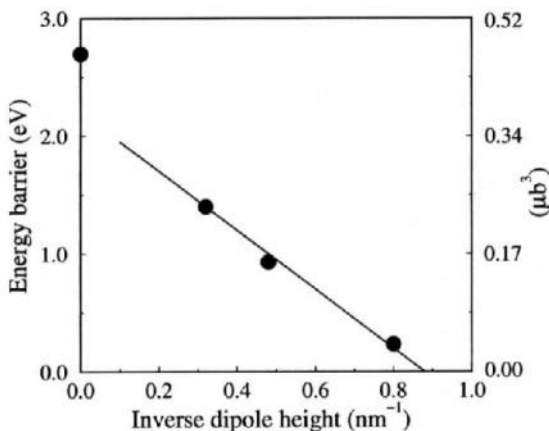

Figure 2. The activation energy for the annihilation of non-jogged screw-dislocation dipoles in copper by cross slip versus inverse dipole height. From [18] (where the alternative ordinate axis is also explained).

For screw-dislocation dipoles with dipole height just above the critical dipole height for annihilation by spontaneous cross slip the activation energy is so low that the annihilation process can be modeled by molecular dynamics (Vegge et al. [20]). This allowed us to determine the preexponential for cross slip P (with dimension $m^{-1}s^{-1}$) in the equation

$$F = P \exp (-E/kT) \tag{1}$$

where F is the cross-slip frequency per metre per second, E is the activation energy, k is Boltzmann's constant and T is the temperature in K. The resulting P value was $2 \cdot 10^{23} m^{-1} s^{-1}$ or $5 \cdot 10^{13} b^{-1} s^{-1}$, b being the Burgers vector. This is the first example of such a determination of the pre-exponential for a complex process like dipole annihilation by cross slip. One notices that P as referred to the Burgers vector is of about the same magnitude as the Debye frequency as one would expect intuitively. One also notices that the activation energy for cross-slip annihilation of a screw-dislocation dipole with inverse dipole height 0.77 nm^{-1} in [20] is 0.29eV which agrees with *Figure 2*. Thus, for the one set of conditions where molecular dynamics and NEB overlap, the resulting activation energies agree.

2.3 Cross slip with jogs

In 2.2 we derived an activation energy of ~3eV for cross slip of a single non-jogged screw dislocation in copper – a magnitude which is prohibitively high for cross slip at room temperature. We also considered the substantial reduction of the activation for cross slip for sufficiently narrow screw-dislocation dipoles.

Jogs on the screw dislocations would provide ready-made constrictions, thus presumably reducing the activation energy for cross slip. Therefore, Vegge et al. [21] modelled cross slip of jogged screw dislocations in copper, finding activation energies of 0.86eV or 0.87eV (depending on the jog configuration). This dramatic reduction (from ~3eV for a non-jogged screw dislocation) means that the theoretical activation energy for cross slip is reduced to a level which allows cross slip at room temperature. And it means that the theoretical activation energy is brought to (approximate) agreement with the experimental activation energy for cross slip in copper determined by Bonneville et al. [19], 1.15eV±0.37eV.

The logical next step is to repeat the work of Rasmussen et al. [18] on the annihilation of non-jogged screw-dislocation dipoles by cross slip for jogged screw-dislocation dipoles as actually done by Vegge et al. [8]. As it turned out, the computer found a thermally activated process for dipole annihilation with a very low activation energy as an alternative to thermally activated cross slip, *concerted jog migration*: concerted (stress assisted) migration of jogs of specific types on the two screw dislocations makes them approach each other until they come so close that they annihilate by spontaneous cross slip – at a distance of eleven {111} interplanar spacings (to be compared with a critical distance for spontaneous cross slip of four or five {111} interplanar spacings for non-jogged screw-dislocation dipoles). The activation energy for jog migration was found to be 15meV or less, decreasing with decreasing dipole height.

In the computer the unlimited supply of jogs of specific types, which is a necessary condition for concerted jog migration, is a result of the periodic-boundary conditions. In connection with cyclic plasticity/fatigue, where the governing process is dipole annihilation, it probably corresponds to the actual physical conditions as discussed in section 5. For monotonic deformation concerted jog migration is not considered to be relevant, e.g. section 3.

3.   CONCLUSION OF THE ATOMIC-SCALE MODELING

The activation energy for cross slip of individual non-jogged screw dislocations in copper (~3eV) is prohibitively high for cross slip at room temperature. However, non-jogged screw-dislocation dipoles with sufficiently low dipole height may annihilate by cross slip at room temperature – a process which is important for fatigue, e.g. section 5. From the annihilation of non-jogged screw-dislocation dipoles we derive an activation volume for cross slip of ~15b^3.

For individual jogged screw dislocations in copper the activation energy for cross slip is ~0.9eV, which would allow cross slip at room temperature (and which agrees with the experimental activation energy for cross slip in copper derived by Bonneville et al. [19]). In accordance with Bonneville et al. we consider the effect of cross slip in monotonic deformation to be to help screw dislocations to bypass obstacles. Therefore, we want to determine a theoretical value for the activation volume for cross slip of individual jogged screw dislocations (for the stress dependence of the activation energy for cross slip of jogged screw dislocations). We cannot directly use the annihilation of dipoles as Rasmussen et al. [18] did for non-jogged screw dislocations, because the computer introduces concerted jog migration as the thermally activated process for the annihilation of jogged screw-dislocation dipoles – a mechanism which we consider to be irrelevant for monotonic deformation.

So far we have not been clever enough to produce a computer program which can directly provide the activation volume for cross slip of single jogged screw dislocations. Therefore, we have to use an indirect method. We postulate that there is a linear relation between the activation energy for *cross-slip* annihilation of jogged screw-dislocation dipoles and the inverse dipole height (corresponding to the approximately linear relation for non-jogged screw-dislocation dipoles in *Figure 2*) as an alternative to annihilation by concerted jog migration, which we in connection with monotonic deformation consider to be an artifact introduced by the periodic-boundary conditions in the computer program. At present we can only base this postulated linear relation on two points: the activation energy of 0.86eV/0.87eV for an isolated jogged screw dislocation (inverse dipole height zero) and activation energy zero for eleven {111} interplanar spacings (inverse dipole height 0.45nm^{-1}). The resulting relation is shown in *Figure 3*. In *Figure 3* we have added an alternative abscissa axis in terms of applied stress as explained in [22] (according to basically the same principle as that used by Rasmussen et al. [18] to derive an activation volume from *Figure 2*). From *Figure 3* we derive an activation volume of ~10b^3.
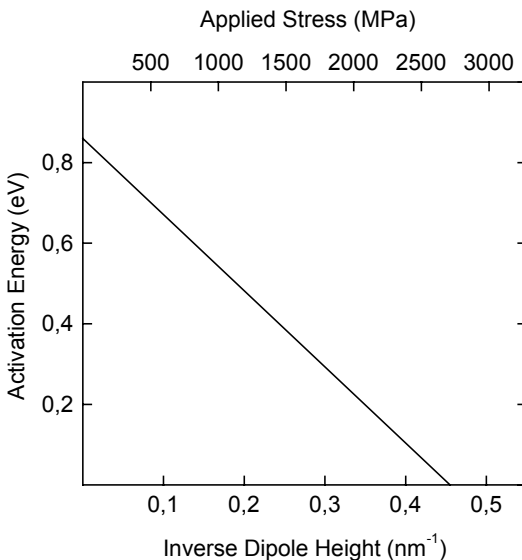
Figure 3. The postulated linear relation between inverse dipole height and the activation energy for cross-slip annihilation of jogged screw-dislocation dipoles in copper - based on two points: the point at 0.45 nm^{-1} where annihilation becomes spontaneous (activation energy zero) and the point corresponding to an islolated screw dislocation (at 0 nm^{-1}). An alternative absciss axis in terms of applied stress is added. From [22].

The activation volumes for cross slip in copper derived from *Figure 2* and *Figure 3*, 15b^3 and 10b^3, are very different from the experimental activation volume of ~250b^3 quoted by Bonneville et al. [19]. From atomic-scale modeling of cross slip in nickel Rao et al. [15] also found a quite low activation volume of 20b^3. In a recent review about cross slip Püschl [23] has discussed this discrepancy. He suggested that in reality Bonneville et al. considered a process more complex than the simple cross-slip process considered in the computer modeling – a point of view which we agree with.

4.   THE FCC TEXTURE TRANSITION

Since the early days of texture research the fact that fcc metals and alloys develop two different types of rolling texture, the copper type and the brass type, has been a mystery to the texture community. One may say that it is *the* classical texture problem. As mentioned in section 1 it was already in the nineteensixties suggested, on the basis of circumstantial evidence, that the texture transition is governed by cross slip. In 1968 one of the present

authors [24] determined the activation energy for the texture transition in Cu-5%Zn on the basis of its dependence on temperature and strain rate from the equation

$$E = R \ln\left(\dot{\varepsilon}_1 / \dot{\varepsilon}_2\right)(1/T_2 - 1/T_1) \tag{2}$$

where R is the gas constant, and $\dot{\varepsilon}_1, T_1$ and $\dot{\varepsilon}_2, T_2$ are two sets of strain rates and temperatures (in K) which result in the same texture ($\dot{\varepsilon}_1 > \dot{\varepsilon}_2$ and $T_1 > T_2$). He stated that the activation energy determined (10kcal/mole) might correspond to the activation energy for cross slip. However, at that time there was a very great uncertainty about the theoretical activation energy for cross slip.

Today the situation is different. We have a reasonable estimate of the activation energy for cross slip (of jogged screw dislocations) versus applied stress as shown in *Figure 3*. A revised experimental estimate of the activation energy for the texture transition in Cu-5%Zn (at stresses in the range 80-400 MPa) is 0.70eV±0.10eV [22,25], which agrees quite well with the theoretical activation energy for cross slip in the relevant stress range, 0.73-0.83eV (see *Figure 3*). As mentioned in 2.1 the interatomic potential used gives a stacking fault energy of 31mJm^{-2} which is somewhat lower than the value of ~50mJm^{-2} normally quoted for copper. However, it is quite close to the stacking fault energy in Cu-5%Zn [22].

Thus, the atomic-scale modeling provides a convincing support for the idea that the texture transition is governed by cross slip as suggested on the basis of circumstantial evidence. As opposed to the original suggestion [5,6] we suggest an *indirect* ("catalytic") effect of cross slip [22,25].

5.   THERMALLY ACTIVATED FATIGUE

When pure annealed fcc metals are cyclically strained at constant low plastic strain amplitudes the stress amplitude increases from half-cycle to half-cycle untill it saturates at a maximum stress amplitude, the 'saturation stress'. This behaviour is associated with initiation of fatigue cracks in 'persistent slip bands' (PSBs), which nucleate in nanostructures of edge-dislocation dipole loops (EDLs) evolving during cyclic hardening and early saturation. A satisfactory theory of fatigue must first explain [26] the three-dimensional (3-D) dislocation dynamics of fatigue hardening by EDL formation and clustering into dense 'walls' acting as obstacles to glide.

Mesoscopic computer simulations [27] of the 3-D dislocation dynamics of fatigue hardening reveal that dipoles forming in one half-cycle 'unzip' during the next, unless stabilized to form EDLs via annihilation. This

observation translates into a required annihilation rate A>2f, where f is the frequency of fatigue cycling. If annihilation occurs by cross-slip, then the hardening theory may be compared quantitatively with experimentally observed EDL heights using equation (1) and the requirement that A=F=2f.

According to a recent *nanotheory* [28], the structural transition from cyclic hardening to saturation is initiated when the stress amplitude reaches a level where EDLs in the most highly stressed walls 'flip' to produce a mobile nanostructure of superjogged screw dislocations. The subsequent PSB nucleation is a thermally activated process, whereby superjogged screw dislocations glide to dipole trapping and annihilation. Pedersen combines a 3-D model of stress-induced EDL flipping with a model of thermally activated PSB nucleation by avalanches of glide to mutual annihilation of non-jogged screw dislocations.

The nanotheory implies that cyclic saturation is a thermally activated process of PSB plasticity by repeated avalanches of slip producing intense surface fatigue damage at the nanoscale. The relevant activation energy E_{sat} for recovery by annihilation of the 'flip-induced' non-jogged screw dislocations to maintain the stress amplitude constant during cyclic saturation is determined from measurements of the rate- and temperature sensitivity of the saturation stress [29]. The nanotheory emphasizes that PSB walls are sufficiently stressed for edge dislocation segments to penetrate their EDL-nanostructure in a steady-state process of vacancy production and absorption.

Brown's statistical theory [30] of annihilation of screw dislocation dipoles by thermally activated jog migration determines the PSB nanostructure and the saturation stress. The statistical theory is compatible with the nanotheory and the required activation energies are available for both cross-slip and jog motion in copper, as described in 2.2 and 2.3. What remains is to combine and quantify the above theories of thermally activated fatigue hardening, PSB nucleation, cyclic saturation and PSB surface damage to test their quantitative predictions against experimental data.

ACKNOWLEDGEMENTS

REFERENCES

1. R. Maddin, C.H. Mathewson and W.R. Hibbard, Metals Trans. 175 (1948) 86.
2. H. Wolf, Z. Naturforsch. 15a (1960) 180.
3. A. Seeger, in: Dislocations and Mechanical Properties of Crystals, Eds. J.C. Fisher et al., (John Wiley and Sons, New York, 1957) p. 243.
4. N.F. Mott, Acta Metall. 6 (1958) 195.
5. R.E. Smallman and D. Green, Acta Metall. 12 (1964) 145.
6. I.L. Dillamore and W.T. Roberts, Acta Metall. 12 (1964) 281.
7. K.W. Jacobsen, J.K. Nørskov and M.J. Puska, Phys. Rev. B 35 (1987) 7423.
8. T. Vegge, O.B. Pedersen, T. Leffers and K.W. Jacobsen, Mat. Res. Soc. Symp. Proc. Vol. 578 (2000) 217.
9. J.B. Gibson, A.N. Goland, M. Milgram and G.H. Vineyard, Phys. Rev. 120 (1960) 1229.
10. H. Jónsson, G. Mills and K.W. Jacobsen, in: Classical and Quantum Dynamics in Condensed Phase Simulations, (World Scientific, Singapore, 1998) p. 385.
11. T. Vegge, T. Leffers, O.B. Pedersen and K.W. Jacobsen, Mater. Sci. Eng. A 319-321, (2001) 119.
12. T. Rasmussen, K.W. Jacobsen, T. Leffers, O.B. Pedersen, S.G. Srinivasan and H. Jónsson, Phys. Rev. Lett. 79 (1997) 3676.
13. J. Friedel, in: Dislocations and Mechanical Properties of Crystal, Eds. J.C. Fisher et al., (John Wiley and Sons, New York, 1957) p. 330.
14. B. Escaig, in: Dislocation Dynamics, Eds. A.R. Rosenfield et al., (McGraw-Hill, New York, 1968) p. 655.
15. S. Rao, T.A. Parthasarathy and C. Woodward, Phil. Mag. A 79 (1999) 1167.
16. T. Rasmussen, Phil. Mag. A 80 (2000) 1291.
17. T. Vegge, Mater. Sci. Eng. A 309-310 (2001) 113.
18. T. Rasmussen, T. Vegge, T. Leffers, O.B. Pedersen and K.W. Jacobsen, Phil. Mag. A 80 (2000) 1273.
19. J. Bonneville, B. Escaig and J.L. Martin, Acta Metall. 36 (1988) 1989.
20. T. Vegge, T. Rasmussen, T. Leffers, O.B. Pedersen and K.W. Jacobsen, Phys. Rev. Lett. 85 (2000) 3866.
21. T. Vegge, T. Rasmussen, T. Leffers, O.B. Pedersen and K.W. Jacobsen, Phil. Mag. Lett. 81 (2001) 137.
22. T. Leffers and O.B. Pedersen, Risø-R-1308 (EN), 2002. Available electronically via http://www.risoe.dk/rispubl/AFM/ris-r-1308.htm
23. W. Püschl, Prog. Mater. Sci. 47 (2002) 415.
24. T. Leffers, Scripta Metall. 2 (1968) 447.
25. T. Leffers and O.B. Pedersen, Scripta Mater. 46 (2002) 741.
26. J.C. Grosskreutz and H. Mughrabi, in: Constitutive Equations in Plasticity, Ed. A.S. Argon, (MIT Press, Massachusetts, 1975) p.251.
27. L.P. Kubin and B. Devincre, in: Proc. 20th Risø Internat. Symp. on Materials Science, Eds. J.B. Bilde-Sørensen et al., (Risø National Laboratory, Roskilde, 1999) p.61.
28. O.B. Pedersen, Z. Metallkde. 93 (2002) 790.
29. Z.S. Basinski and S.J. Basinski, Prog. Mater. Sci. 36 (1992) 89.
30. L.M. Brown, Phil. Mag. A 82 (2002) 1691.

STRUCTURAL METALLIC MATERIALS BY INFILTRATION

Jean-François Despois, Randoald Müller, Ali Miserez, Ludger Weber, Andreas Rossoll and Andreas Mortensen
Laboratory for Mechanical Metallurgy, Institute of Materials, Swiss Federal Institute of Technology in Lausanne (EPFL), CH-1015 Switzerland.

Abstract: An overview is presented of current research at EPFL on structural metallic materials produced by infiltration processing. The paper comprises a brief introduction to the infiltration process, then presents results on particle reinforced metals and open-celled aluminium foams.

Key words: infiltration, particle reinforced metals, metal matrix composites, metal foams, microcellular aluminium

1.   INTRODUCTION

Many high-performance structural metallic materials contain two or more phases. Most often these are created starting with a homogeneous melt or material, and phase transformations create the various phases that make the final material microstructure. Not all two-phase materials can, however, be produced in this way. Thermodynamics and kinetics place restrictions on the nature, shape and mechanical properties of phases that can be combined within a single material. Alternative processes have therefore been devised for the production of multiphase materials. The result is then generally a composite material, because its different phases originate, not from a common melt, but from initially distinct starting materials [1].

One such process is infiltration. Materials produced by this process can be designed with wide latitude in the nature, size, shape, or distribution of phases present, and can also be produced to high microstructural quality, meaning free of defects such as pores or unwanted additional phases. We begin by providing a succinct presentation of the process, and then present

an overview of our current work on two classes of materials that can be produced by infiltration, namely ceramic particle reinforced aluminium composites and microcellular metal foams.

2.   INFILTRATION PROCESSING

Infiltration combines a melt with a porous free-standing solid (the "preform"). In the main and defining step of the process, the melt flows into open pores of the preform; after solidification a new material results. Composites of all classes (polymer, ceramic and metal) are produced by this process, as are compounds such as "reaction bonded" silicon carbide. The process can also be adapted to make open-pored foams of carbon, ceramic, polymer or metal.

Detailed coverage of the fundamentals of metal infiltration processing can be found in Refs. [2-4]. Basic characteristics of the process derive from the fact that metallic melts generally have high surface tensions (on the order of a Joule per square metre) combined with low viscosities (similar to water) [4]. If the contact angle between the liquid and the reinforcing phase is very small (significantly less than 90 degrees), given the high capillary forces and low viscous flow resistance, the metal penetrates spontaneously and rapidly into the preform. Although there are a few well-known examples of spontaneous infiltration (*e.g.,* Cu-W), this is generally not observed. Two approaches can then be used. The first is chemical tailoring of the system to induce strong wetting of the solid by the liquid. This approach has often been used; however, the price generally paid is a sharp loss of freedom in microstructural design. Composite properties are then nearly always suboptimal. The other pathway is to drive the metal into the preform mechanically using a piston or pressurized gas, or alternatively using more exotic methods such as electromagnetic, centrifugal or ultrasonic force. This requires somewhat heavier equipment; however, considerable latitude is then available to tailor the composite composition and microstructure for optimisation of its properties. This feature also makes pressure-infiltrated materials interesting for research, since "clean" model materials can be produced.

As the porous preform must be free-standing prior to infiltration, this process is restricted to a limited range of variation in phase volume fraction, which depends on the morphology of the reinforcing phase. It cannot, for example, produce low-volume fraction particle reinforced metals unless specific additional processing steps are used.
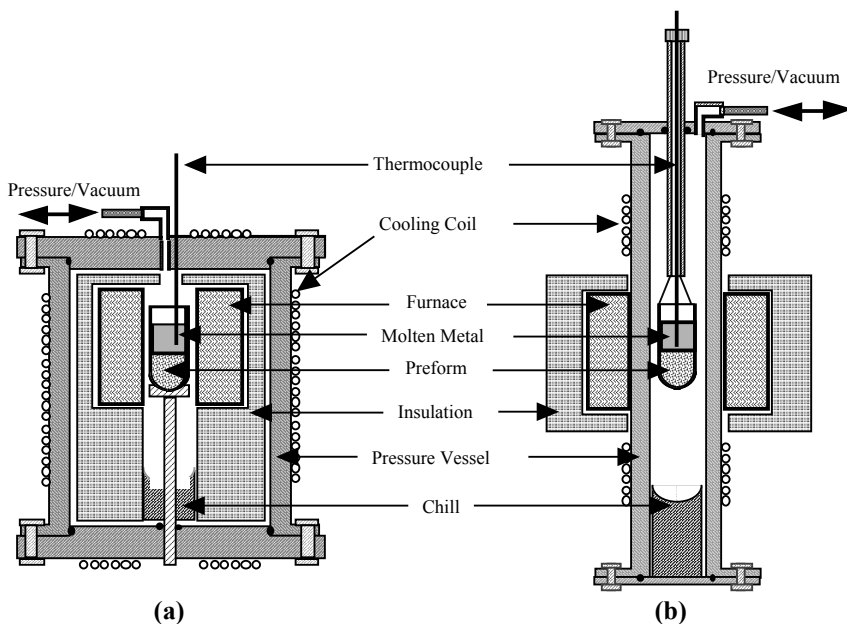
Figure 1. Schematic of pressure-infiltration apparatuses at EPFL: (a) cold-wall and (b) hot-wall designs. In both cases infiltration is conducted within an alumina crucible into a previously evacuated preform.

Gas-pressure infiltration is the process used in our laboratory. As the name implies, it uses contact of the metal surface with pressurised gas to drive the molten metal into the preform against adverse capillary forces. Several apparatus designs exist for gas-pressure infiltration; all by definition comprise a reasonably strong pressure vessel. Indeed, with a surface tension of $1 \text{ J} \cdot \text{m}^{-2}$, a pressure of about 1 MPa (ten atmospheres) is required to drive a meniscus of molten metal bent to a curvature of $1 \text{ } \mu\text{m}^{-1}$. Various designs of the process exist; the two that are used in our laboratory are sketched in Fig. 1. Other significant variations in apparatus design lie in the type of heating mechanism (resistance, induction, …), the nature of the mold containing the preform, the preform evacuation method or the general flow path of the metal (upwards or downwards, with or without a gate, etc.).

Principal advantages of gas-pressure infiltration over other mechanically driven pressure infiltration processes are that infiltration parameters are controlled with precision and that weak molds can be used, which can be used to minimise impurities in the composite. It is thus an attractive method for academic research; however, it is also used industrially, to produce electronic substrates for example. After infiltration, the metal is solidified. We use directional solidification, induced by lowering the mold onto a chill (Fig. 1), to avoid shrinkage cavity formation in the composite. The applied

pressure is generally maintained during solidification, so as to assist the feeding of shrinkage within the composite.

3.   INFILTRATED CERAMIC PARTICLE REINFORCED ALUMINIUM

By infiltrating a packed bed of unbonded randomly oriented close-packed ceramic particles with metal, a composite is produced that, despite being around 50% ceramic, is capable of global plastic deformation. Indeed, even though each ceramic particle contacts its neighbours, it is still free to move or rotate. The ceramic phase can thus accompany overall deformation of the elastoplastic metallic matrix, such that the composite is itself elastoplastic. The resulting two-phase material is, in this respect, fundamentally different from the other two isotropic metal/ceramic composite classes, namely interpenetrating phase composites (co-continuous ceramic and metal phases) and metal toughened ceramics (continuous ceramic, discontinuous metal): these cannot accommodate bulk composite plastic flow.
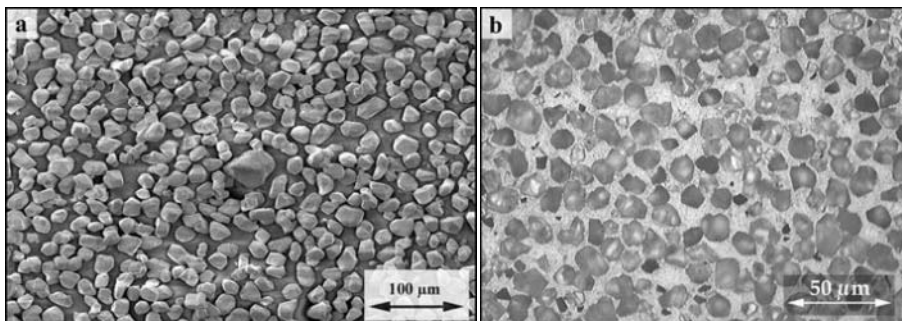
Figure 2. Equiaxed polygonal "Sumicorundum™" alumina particles (left) are packed in a preform, and infiltrated with aluminium or its alloys to produce composites such as that on the right.

We have developed the infiltration process for the laboratory-scale production of aluminium matrix composites reinforced with monosized B_4C or Al_2O_3 particles of diameter varying from 5 to 100 μm. The composites contain between 40 and 60 vol. pct. ceramic, the volume fraction depending mainly on the particle shape. Three ceramic particles have been explored: (i) conventional angular Bayer alumina, (ii) angular boron carbide and (iii) high purity (99.99%) Al_2O_3 "Sumicorundum™" particles of polygonal shape. These last particles are shown in Fig. 2(a) before infiltration, and in Fig. 2(b)

combined with a pure aluminium matrix. Three matrices have been explored: (i) 99.99% pure aluminium, (ii) Al-2 wt. pct. Cu and (iii) Al-4.5 wt. pct. Cu.
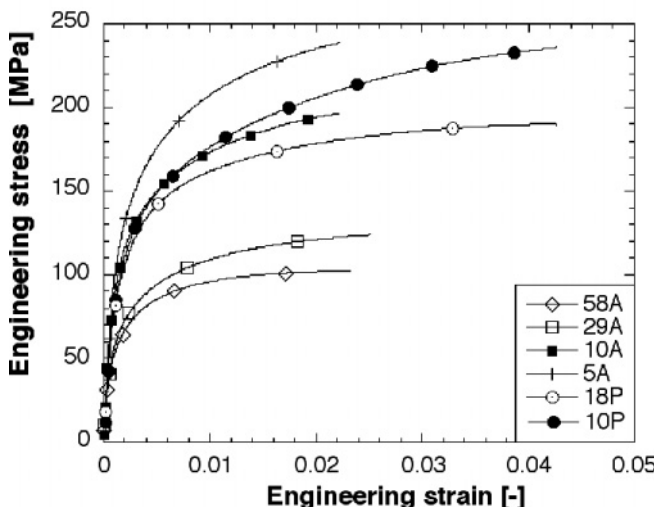

Figure 3. Tensile flow curves of pure aluminium matrix composites, reinforced with angular (A) and polygonal (P) alumina particles (see Fig. 2), of diameter given in µm by the legend of the curves. The 10 and 5 µm angular particle reinforced composites fail before tensile instability is reached.

In tension, the composites display a capacity for plastic deformation [5,6]. Figure 3 gives examples of the tensile behaviour of pure aluminium reinforced with particles of the two types of alumina. Plastic yielding begins very early upon tensile loading, and tensile failure is generally initiated by the onset of tensile instability (except with the finer and weaker particle composites, which fail in brittle manner). Total elongations to failure often exceed one percent, Fig. 3. Also visible in Fig. 3 is the size effect that is displayed by these composites. This is caused by geometrically necessary dislocations, generated first to relieve thermal mismatch strains between the particles and the metal, and after plastic deformation to accommodate matrix/reinforcement plastic strain incompatibility [7-10].

Internal damage takes two forms in these composites: particle fracture and matrix voiding, the nature and rate of accumulation of damage being a strong function of the reinforcement nature. The elongation to failure can also be linked in a simple expression to the rate of accumulation of internal damage [5, 6, 9,11].

There are significant differences in composite mechanical performance as the ceramic particle quality is varied: this is visible in Fig. 3. Far higher

tensile elongations are obtained when the more regularly shaped and defect-free (and also significantly more expensive) Sumicorundum™ polygonal alumina particles are used. With alloyed matrices the point is exacerbated: the composites are then significantly stronger and less ductile, and it is only with the stronger polygonal alumina particle that the composite can deform in tension past one percent strain, Fig. 4.
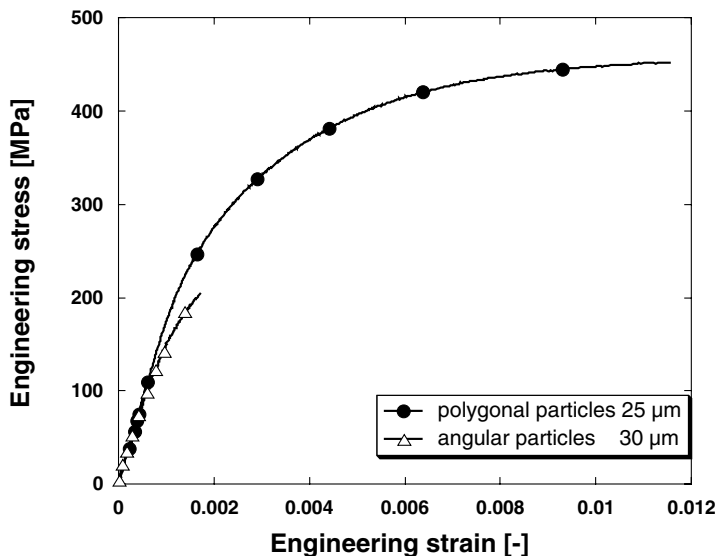

Figure 4. Tensile flow curves of two Al-4.5 wt.% Cu reinforced with aluminium matrix composites, reinforced with angular and polygonal alumina particles of roughly the same size. The data show the significant improvements brought by matrix alloying (see Fig. 3) as well as the strong influence of the ceramic particle type on the composite mechanical performance. With the stronger ceramic, the material features high strength and acceptable tensile ductility despite the fact that it is more than 50% ceramic.

The importance of the ceramic phase is also reflected in the fracture toughness of these materials [12, 13]. Toughness was measured using two methods: with a pure Al matrix, the composites were too soft and tough to be characterized in small-scale yielding: *J*-integral testing following ASTM E-1737 was therefore used. Stable crack propagation coupled with significant *R*-curve behaviour is observed. To quantify the composite fracture toughness, the values of *J* at the onset of macroscopic crack advance by ductile tearing were converted into the equivalent stress intensity factor using the standard plane-strain formula. With Al-Cu matrices, fracture toughness could be measured in small-scale yielding using chevron-notched fracture samples according to ASTM E-1304. Typical properties for selected

composites are reported in Table I. It is seen that, despite their high ceramic loadings, these materials are not only relatively ductile in tension but also surprisingly tough. Pure Al matrix composites display toughness values up to 40 MPa√m, while with Al-Cu matrices K_{Ic} reaches 33 MPa√m. For comparison, strength and toughness take values of 25 to 31 MPa√m and 490 MPa for high-strength aluminium alloy 2124-T8, 20 to 33 MPa√m and 500 MPa for alloy 7075-T73, respectively [14]. Basic underlying reasons for the toughness and ductility of these infiltrated composites are (i) that these materials are capable of bulk plastic deformation, just like a metal, and (ii) that the ceramic particles strongly constrain plastic deformation in the matrix. This causes the build-up of high triaxial stresses in the matrix when it fails, which in turn raises the composite toughness.

Table 1. Mechanical properties of selected pressure-infiltrated ceramic particle reinforced aluminium composites: Young's modulus (E), yield and ultimate tensile strengths ($\sigma_{0.2}$, σ_{UTS}), tensile elongation (ε_f), and fracture toughness parameters. Toughness K_{Ic} was measured from *J-R* curves on pure Al matrix composites and by chevron-notch fracture testing on Al-Cu matrix composites. $V_{f\,Al_2O_3}$ is the volume fraction of ceramic particles in the composite.

Matrix	Al$_2$0$_3$ particle type and diameter	$V_{f\,Al_2O_3}$ [%]	E [GPa]	$\sigma_{0.2}$ [MPa]	σ_{UTS} [MPa]	ε_f [%]	K_{Ic} [MPa√m]
Pure Al	Angular 30 μm	45	141	80	125	3.2	25.8
	Polygonal 25 μm	59	175	120	190	4.5	40
Al-Cu2%	Angular 30 μm	45	144	170	170	0.35	23.3
	Polygonal 25 μm	59	183	255	340	1.4	32.5
Al-Cu4.5%	Angular 30 μm	50	148	210	210	0.1	24.6
	Polygonal 25 μm	60	187	370	443	1.1	33.3

4.   OPEN-PORE MICROCELLULAR ALUMINIUM FOAMS

Open-pore microcellular aluminium foams can be produced by a process known as "replication". This consists in infiltration of NaCl powder preforms by a melt, which is then solidified to form a composite. The NaCl is subsequently leached out with water, to leave a network of open pores, of volume fraction roughly varying between 65 and 90% [15]. The foams can be produced to feature good microstructural homogeneity over a comparatively wide range of metal alloy compositions, pore size and component shape. They furthermore serve as attractive model materials for the investigation of microstructure/property relations in metal foams because of their macroscopically uniform and fine-scale microstructure, and because the metal making the foam can be varied with relatively wide latitude and produced free of internal defects.
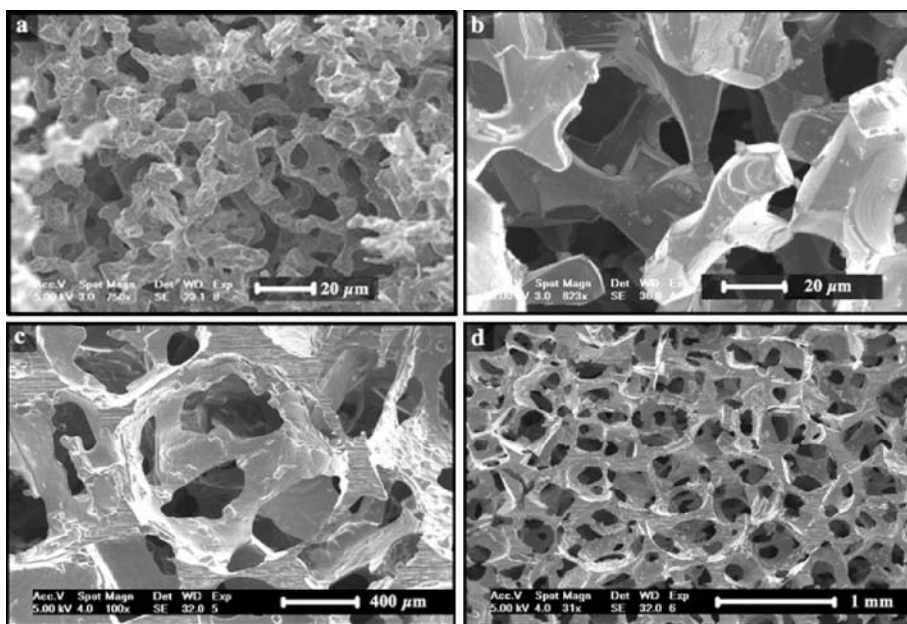
Figure 5. SEM pictures of pure Al foams made by gas pressure infiltration of a sodium chloride open pore pattern: (a) 26 µm NaCl, $V_{f\,Al}$ = 18 %, (b) 75 µm NaCl sintered 24h at 750°C, $V_{f\,Al}$ = 18 %, (c) and (d) 400 µm NaCl, $V_{f\,Al}$ = 16 %.

The pore size is controlled by sieving the salt, while the volume fraction metal is controlled during preform preparation. We have used commercially available NaCl powder sieved into several classes of grain size, each class being identified with its mean grain size: (i) 20-32 µm (26 µm), (ii) 63-90 µm (75 µm), (iii) >250 µm (400 µm). The salt preform volume fraction is controlled using a combination of cold isostatic pressing (CIP) and sintering. Foams in Fig. 5 (a), (c) and (d) were made with CIPed preforms while the foam on Fig. 5 (b) results from a preform that was CIPed and then sintered for 24 h at 750°C. The internal architecture of the foam can be controlled by tailoring the internal microstructure of the NaCl preform. For instance, variations in internal geometry can be obtained by varying the densification mechanism. It is known that the sintering of NaCl leads to densification if the particles are small, the dominant sintering mechanism being volume diffusion. For larger particles, the evaporation-condensation mechanism dominates and no densification is noticed. The critical particle size between these two mechanisms is around $100 - 150$ µm. Figure 6 shows the structure of two Al foams produced with the same 75 µm NaCl powder, illustrating differences in microstructure that can be generated in this way. We are also exploring other means for microstructural control of these foams: control of

the initial salt particle shape, which we vary using a process known as antisolvent precipitation, and control of the infiltration pressure.
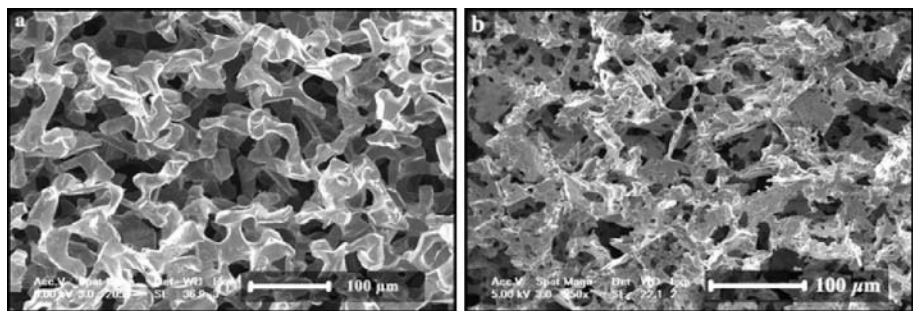

Figure 6. SEM pictures of pure Al foams made by gas pressure infiltration of a sodium chloride open pore pattern. In both cases a) and b) the average volume fraction of metal in the foam is 18 % and the salt used had a mean grain size of 75 μm. In case a) the salt preform was first CIPed and then sintered 24h at 750°C, while in case b) the preform was only CIPed.
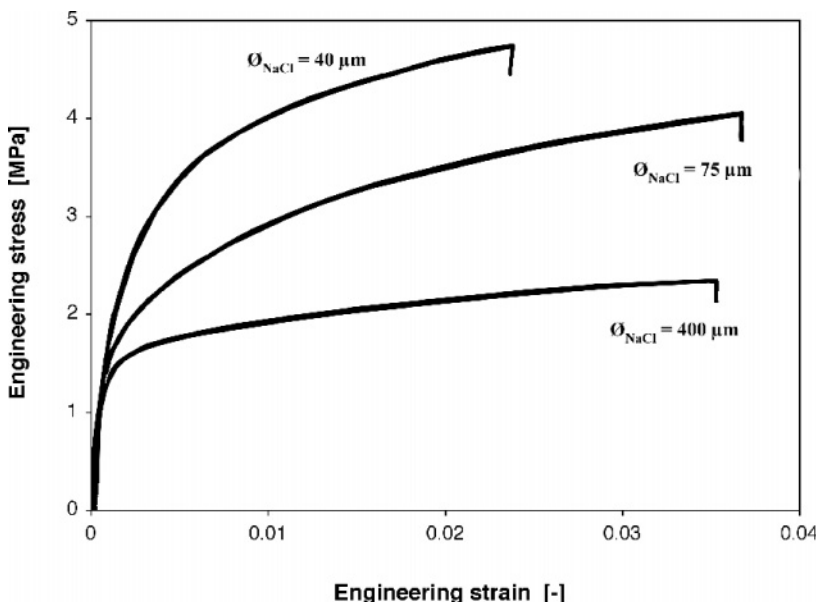
Figure 7. Tensile test curves recorded for 99.99% pure Al foams with pores 40, 75 and 400 μm in diameter. The volume fraction of metal in the foams is near 30% for all specimens.

Mechanical properties of the foams are characterised by compressive and tensile testing. In compression, the foams deform extensively, producing smooth ascending compression curves, free of irregularities observed with

current commercial closed-cell foams. Their initial behaviour roughly follows the classical power-law characteristic of the metal they are made from [16, 17]. Typical tensile curves for pure aluminium foams are shown in Fig. 7. One can see that, as with the composites, there is a size-effect: the finer the pores the higher the flow stress. In foams, the size effect can be attributed to two mechanisms: (i) geometrically necessary dislocations (produced during cooldown of the NaCl/Al composite) and (ii) the presence of oxide on the pore surface, the volume fraction of which obviously increases as the pore diameter decreases. The behaviour of these fine-scale metal foams resembles that of infiltrated particle reinforced metals in other respects; in particular, internal damage build-up is also important. Here, damage takes the form of localised fracture of individual struts, an example of which can be seen in Fig. 8. Keeping in mind that the grain size in these foams far exceeds the pore size, each strut is a single crystal: it therefore deforms and damages as a small single-crystalline tensile bar. Such internal damage, in turn, strongly influences tensile deformation of the foam, as for composites.
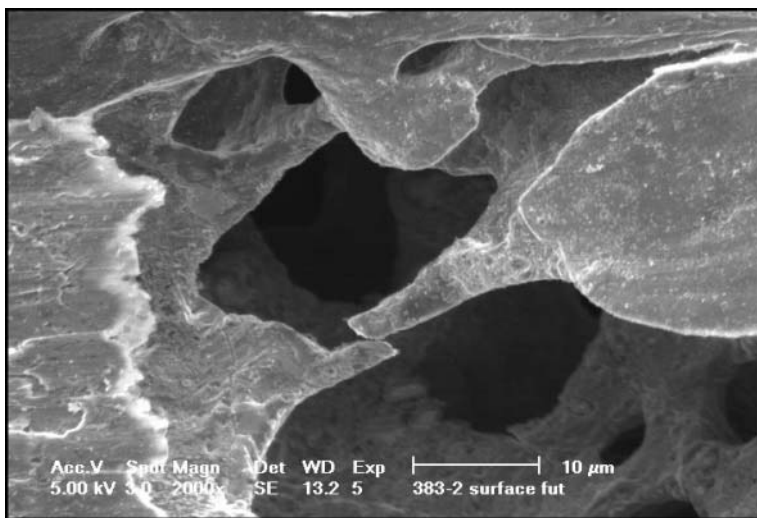
Figure 8. Internal damage in the form of failure of a single strut in pure Al foam deformed in tension.

5.   CONCLUSION

Infiltration processing provides a flexible process for the production of two-phase or porous materials that cannot be obtained using conventional alloying and heat-treating. These materials can be made free of defects and

their microstructure can be varied systematically, making them attractive model materials for research.

This feature of the process is used in current research on composites and metal foams, both based on aluminium, to explore the relation between basic microstructural parameters and the mechanical performance of general two-phase isotropic materials. It is shown that materials with attractive properties can be produced, and that systematic relations can be established between microstructure and properties, for example between their microstructural scale and their tensile behaviour.

ACKNOWLEDGEMENTS

REFERENCES

1. A. Kelly and A. Mortensen, in: Encyclopaedia of Materials: Science and Technology (Eds. K.H.J. Buschow, R.W. Cahn, M.C. Flemings, B. Ilschner, E.J. Kramer, and S. Mahajan), Elsevier Science Ltd., Oxford, 2001, pp. 1361-1371.
2. A. Mortensen and I. Jin, Intern. Mater. Rev., vol. 37, 1992, pp. 101-128.
3. A. Mortensen, in: Comprehensive Composite Materials, Vol. 3: Metal Matrix Composites (Ed. T.W. Clyne)., Pergamon, Oxford UK, 2000, pp. 521-554.
4. V. Michaud and A. Mortensen, Composites Part A, vol. 32, 2001, pp. 981-996.
5. M. Kouzeli, L. Weber, C.San Marchi, and A. Mortensen, Acta Mater., vol. 49, 2001, pp. 3699-3709.
6. M. Kouzeli, C.San Marchi, and A. Mortensen, Mater. Sci. Eng., vol. A337, 2002, pp. 264-273.
7. T.W. Clyne and P.J. Withers, in: An Introduction to Metal Matrix Composites, Cambridge University Press, Cambridge, U.K., 1993, 509 pp.
8. R.B. Calhoun and D.C. Dunand, in: Comprehensive Composite Materials, Vol. 3: Metal Matrix Composites (Ed. T.W. Clyne), Pergamon, Oxford UK, 2000, pp. 27-59.
9. M. Kouzeli and A. Mortensen, Acta Mater., vol. 50, 2002, pp. 39-51.
10. M. Kouzeli, L. Weber, C. San Marchi, and A. Mortensen: "Corrigendum on the Tensile Behaviour of Infiltrated Alumina Particle Reinforced Aluminium Composites", Acta Mater., in print.
11. L. Weber, M. Kouzeli, C.San Marchi, and A. Mortensen, Scripta. Mater., vol. 41, 1999, pp. 549-551.
12. A. Miserez: *Fracture and Toughening of High Volume Fraction Ceramic Particle Reinforced Metals,* PhD thesis No. *2703*, Ecole Polytechnique Fédérale de Lausanne (2002) -*available on-line at:< http://library.epfl.ch/theses/?display=detail&nr=2703>.*
13. A. Miserez, S. Stücklin, A. Rossoll, C.San Marchi, and A. Mortensen, Mater. Sci. Technol., vol. 18, 2002, pp. 1461-1470.
14. I.J. Polmear, in: Light Alloys - Metallurgy of the Light Metals, Third Edition, Arnold, London, UK, 1995, 362 pp.

15. C. San Marchi and A. Mortensen, "Chapter 2.6: Infiltration and the Replication Process for Producing Metal Sponges", in: Handbook of Cellular Materials - Production, Processing, Applications (Ed. H.P. Degischer), Wiley-VCH, Weinheim, 2002, pp. 44-56.
16. C. San Marchi, J.F. Despois and A. Mortensen, in: Metal Matrix Composites and Metallic Foams, Euromat 99 Conf. Proc., Vol. 5 (Eds. T.W. Clyne and F. Simancik), Munich, DGM/Wiley-VCH, Weinheim, Germany, October 1999, pp. 34-39.
17. C. San Marchi and A. Mortensen, Acta Mater. vol. 49, 2002, pp. 3959-3969.

MICROSTRUCTURE AND MECHANICAL BEHAVIOR OF FRICTION STIR WELDED TITANIUM ALLOYS

K.V. Jata and A. P. Reynolds[+]

Air Force Research Laboratory, Materials and Manufacturing Directorate, AFRL/MLL, 2230 Tenth Street, WPAFB, Ohio 45433, USA, [+]Department of Mechanical Engineering, University of South Carolina,Columbia, South Carolina 29208, USA

Abstract: Friction stir welding (FSW) has evolved extremely rapidly into a viable and affordable technology to join metallic alloys to manufacture structures for use in transportation systems. Automotive, aircraft, space and ship building industries have been actively pursuing this technology for the last eight to ten years to join aluminum alloys, steels and recently titanium alloys. Research work is progressing at a vigorous pace on all fronts, including novel tool design, optimization of process parameters to produce mechanical properties equal to or better than fastened structures, and process models to understand and guide the FSW process Friction stir welding of aluminum alloys is nearing maturation and a number of applications have been identified for complex aerospace components in defense and commercial industry. However, a number of issues still remain to be investigated to provide a confident solution for *long term usage* of friction stir welded aluminum structures. This paper primarily presents a general overview of the friction stir welding of Ti alloys.

Key words: Friction stir welding , tensile properties, titanium alloys, fatigue crack growth

1.   INTRODUCTION

Welding of advanced Ti alloys is in general difficult, therefore complex aircraft engine components are made from large castings and forgings that limit design flexibility and decrease effective materials utilization. Solid-state joining processes appear attractive and processes such as friction welding and

inertia welding are routinely used in the aircraft engine industry. Enormous success in joining aluminum alloys using friction stir welding (FSW) has inspired many of the FSW researchers to investigate viability of FSW to join Ti alloys. However joining of Ti alloys using friction stir welding is challenging because of the temperatures needed to "plasticize" the Ti alloy is quite high and require strong wear-resistant high temperature tool materials. The industry has predominantly used W and Mo for FSW of Titanium. Due to the reactive nature of Titanium alloys inert atmosphere is usually employed while performing FSW on Ti. Although it is quite common to have threads and a variety of machined-in tool pin-shapes for FSW of aluminum alloys, tool-pins required for Ti alloys cannot be complex.

The feasibility of FSW of titanium was first demonstrated prior to 1997 at which time a TWI group sponsored project (GSP 5689) was instituted to further the development of FSW in titanium alloys [1]. Proof- of-concept and initial development was performed mainly on Ti-6Al-4V. While some reports of FSW of titanium are available in conference proceedings or have been presented at conferences [2-6] no papers in the archival literature have been published on the subject. Conceptually, FSW of titanium is attractive because it may mitigate some problems associated with fusion welding of titanium alloys. For example, because peak temperatures in FSW are necessarily lower than those encountered in fusion welds, problems such as grain growth in the HAZ and embrittlement due to contamination by interstitial elements (O, N, C) uptake may be reduced.

The thermophysical properties of titanium alloys may also contribute to difficulty encountered during friction stir welding. Some numerical simulations of the FSW process indicate that low thermal diffusivity can contribute to the formation of advancing side wormhole or tunnel defects in friction stir welds: the thermal diffusivities of titanium alloys are among the lowest of all metals.

2.   GENERAL CHARACTERISTICS OF THE FRICTION STIR WELDS OF TI ALLOYS

Alloys from all three classes, α, β, and α–β, have been successfully friction stir welded at the University of South Carolina. 2 mm thick sheets of α-Ti, Ti-15V-3Sn-3Cr-3Al and Ti-6Al-4V have been FS welded at a welding speed of 100mm/min at a tool rate of 200 rpm. The CP-Ti and the Ti 15-3-3-3 were welded using z-axis load control. Load control welding on Ti-6-4 was not stable, so that alloy was welded using position control. The β-transus temperatures for the three alloys are CP-Ti= 915°C, Ti-6-4= 995°C, and Ti-15-3-3-3= 770°C.

The Ti 15-3-3-3 alloy was the most easily friction stir weldable of the three alloys examined and the surface finish was quite good (see figure 1a). Sheet thinning in the weld zone was minimal and defect free welds were produced. Based on the lack of weld discoloration, it can be concluded that the argon shielding used was effective in prevention of oxidation.
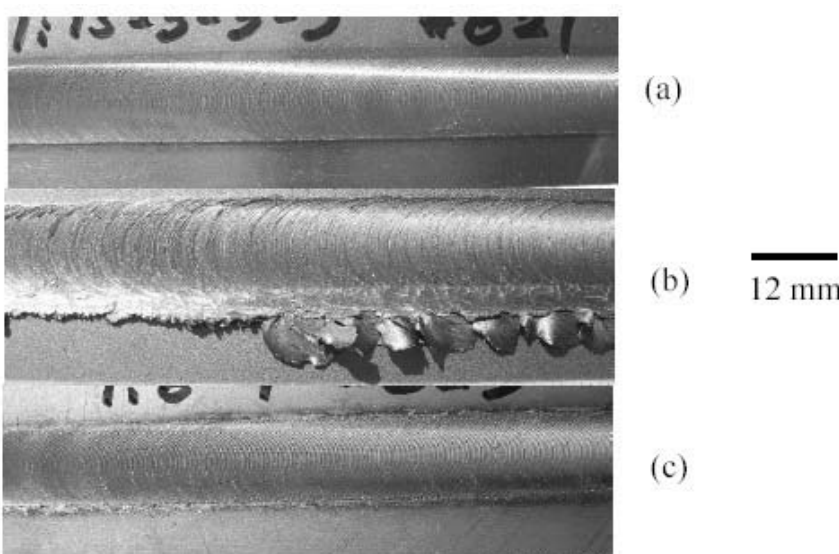

Figure 1. Crown surface view of the three Ti alloys (a) Ti-15-3-3-3, (b) α -Ti (c) Ti-6-4. Welding direction is from left to right.

Weldability of the CP-Ti was not as good as that of the Ti 15-3-3-3. Sound welds were produced, but flash was excessive and the volume of material expelled from the weld zone resulted in substantial sheet thinning; the sheet thinning was particularly significant because of the gage of the base metal sheet (2 mm). Figure 1b shows a top surface view of the weld in which the heavy flash is visible. The production of flash appears to be related to sticking of weld material to the FSW tool. Weld parameter optimization should result in improved weld quality.

Like the other two alloys examined, the Ti-6-4 friction stir weld exhibits a highly refined weld zone microstructure and substantial overmatching in the weld zone. A crown side view of the weld is shown in figure 1(c).

3.   MICROSTRUCTURE OF TITANIUM FS WELDS

3.1   Ti-15-3-3-3

Light optical microscopy of the Ti-15-3-3-3 base metal and the weld nugget material showed that both were comprised solely of β grains; however, the grain size in the base metal ranged between 25-75 μm, while the weld nugget grain size was on average 15 μm (see figure 2a and 2b). Grains in both the base metal and stir zone were equiaxed. No evidence of grain coarsening in the HAZ was observed. Microstructural refinement in the nugget region (stir zone) of friction stir welds is a nearly universal observation and is presumed to be due to the severe plastic deformation coupled with the high temperature transient experienced by the material. Microhardness traverses on transverse cross sections indicate weld overmatching most likely due to the observed microstructural refinement. Subsequent welding trials on Ti 15-3-3-3 and Timetal 21S indicate that β-titanium alloy sheets can be successfully welded at speeds approaching 1 meter/minute.

3.2   α-Ti

Optical microscopy (figure 2c) of a transverse cross section revealed an equiaxed α grain structure in the base metal (average grain size 25 μm) and a highly refined, equiaxed α grain structure in the weld zone (figure 2d) presumably resulting from deformation above the beta transus and subsequent β–α transformation on cooling. As for the Ti 15-3-3-3, the microstructural refinement in the CP-Ti weld zone results in some overmatching evidenced by increased nugget hardness relative to the base metal. Subsequent trials have demonstrated the capability of producing double pass welds in 6.4 mm thick plate of CP-Ti. Process forces are low indicating that thicker plate should be readily weldable also.   Figure 3 shows side bend specimens from the thicker CP plate.

3.3   Ti-6Al-4V

In the base metal, the structure consists of primarily α with some grain boundary β phase (figure 2e). The average base metal α grain size is approximately 20 μm. The nugget or stir zone grain size is less than 5 μm and the phase distribution in the nugget was not observable with optical microscopy (figure 2f). As stated previously, z-axis load control welding of this alloy was not stable and the best welds were made using position control.
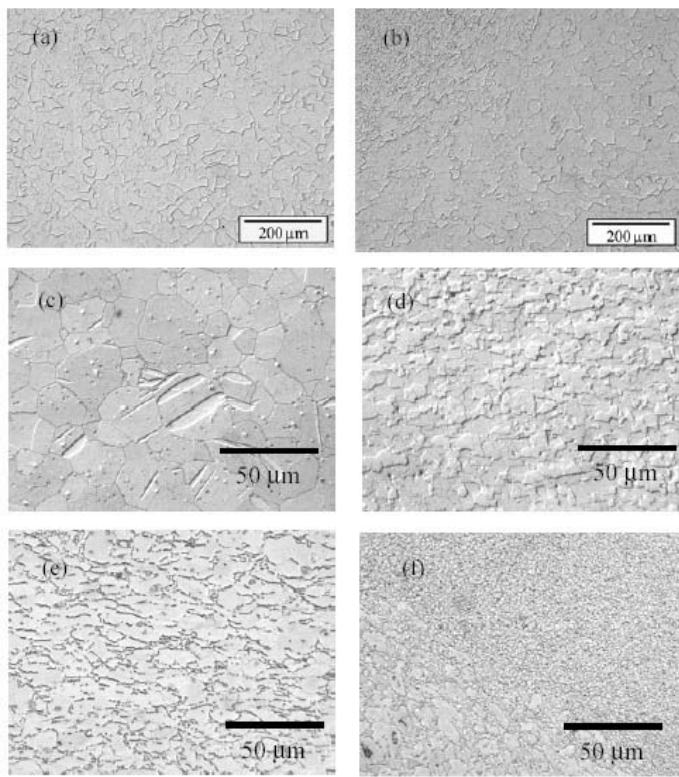
Figure 2. Optical microscopy (a) Ti-15-3-3-3 base metal and (b) transition from weld nugget (upper left hand corner) to HAZ; (c) α-Ti base metal and (d) α-Ti nugget; (e) Ti-6-4 base metal and (f) Ti-6-4 transition from nugget (upper right hand corner) to HAZ.

4. MECHANICAL PROPERTIES OF Ti FS WELDS TESTED ALONG TRANSVERSE DIRECTION

Transverse tensile properties of the friction stir welded samples are shown in Table 1.

The friction stir welded Ti-15-3-3-3 alloy exhibited greater strength than the parent material but the elongation to fracture is substantially reduced. This is due to the weld overmatching and the low elongation of the hard weld nugget. The % elongation was calculated based on the specimen nominal gage length. Note that the relatively hard (strong) weld nugget is centered in the specimen gage length and the effective gage length of the specimen is reduced by more than half.

Table 1. Tensile properties of Ti alloy friction stir welds

Alloy & condition	UTS (MPa)	% elongation	Failure location
Ti-15-3-3-3- Parent	769	28	-
Ti-15-3-3-3- FSW	821	6.4	Parent material
α-Ti- Parent	453	22	-
α-Ti- FSW	393	2.6	Weld nugget
Ti-6-4-Parent	1059	18	-
Ti-6-4-FSW	1028	4.5	LOP defect in nugget[+]
Ti-6-4-FSW (REF. 2)	1012 (REF. 2)	12.7 (REF. 2)	Parent metal (REF. 2)

+ LOP defect: Lack of penetration defect most likely caused from using displacement control method

Sheet thinning (reduced thickness in the weld) was observed in the friction sir welds of the α-Ti alloy. The weld ultimate strength was calculated based on the original sheet thickness and not the reduced section in the weld region. The α-Ti tensile specimens failed in the weld region and the elongation to fracture was low due to strain localization in the weld accompanied by sheet thinning.

The welds of Ti-6-4 were made in displacement control rather than z-axis load control. Typically, this resulted in the formation of a small lack of penetration (LOP) defect in the weld nugget. The lack of penetration defect caused tensile failure to occur through the weld nugget. The low elongation can also be attributed to the LOP defect. Tensile properties of a second friction stir welded Ti-6-4 specimen which did not contain a LOP defect is also shown in the Table. As can be seen from this table the % elongation is much higher in this case.

Bend tests were performed on friction stir welded samples and examples of the bend specimens for α-Ti and Ti-6-4 samples are shown in Figure 3. As seen here these samples could be bent without fracture. The Ti-6-4 specimen was friction stir welded at the Edison Welding Institute [2] whereas the α-Ti specimen was friction stir welded the University of South Carolina. The photograph showing the bend specimen for α-Ti is a double-pass weld in a 6.4 mm thick specimen.
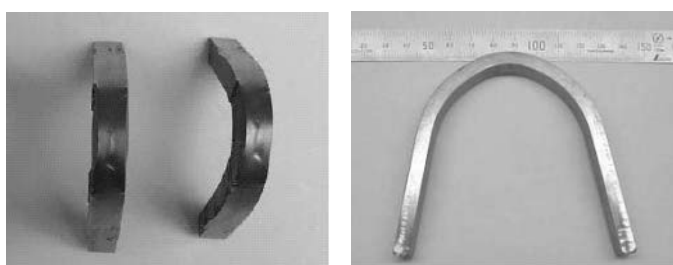
Figure 3. Room temperature bend tests on double pass friction stir welded α-Ti alloy (left photo) and Ti-6-4 (right photo).

5.   FATIGUE CRACK GROWTH (FCG)

FCG rates were obtained on the 6.35 mm thick friction stir welded Ti-6-4 plate plat welded at a translation speed of 100 mm/min to understand the microstructure transformations and residual stresses effects. Initially ASTM standard compact tension (CT) geometry specimens were employed to obtain the FCG rates. The notches were machined along the weld nugget and along the HAZ. However, crack growth rates could not be obtained from the C(T) specimen geometry because of severe out -of-plane cracking. Similar observations were also made on FSW Al alloys when CT geometries were tested. Such out of plane cracking suggests that residual stresses have a large impact on the inherent bending effects present in the C(T) specimen geometry. Tests were discontinued on this C(T)s and instead center cracked tension specimens, M(T), were machined in conformance with ASTM standards. This specimen geometry provides pure tensile mode. Crack growth rates were obtained on these specimens. Fatigue crack growth rates in the weld nugget, are shown in Figure 4 for growth rates above 10^{-9} mm/cycle for three stress ratios.

As shown in Figure 4 fatigue crack growth rates in the weld nugget were four times faster than in the parent material. Crack growth rates were also obtained below 10^{-9} mm/cycle rates in the weld nugget; fatigue thresholds were also reduced in the weld nugget compared to that of the parent material, but are not shown here due to space limitation.

In a detailed study of fatigue crack growth rates in friction stir welded aluminum alloys [7] it was shown that residual stresses and microstructure play a role in controlling crack growth rates in friction stir welded alloys. Here also there is a combined effect of microstructure and residual stress. It is well documented in the literature that equiaxed grain structure morphology will be the least resistant and large Widmansttaten /acicular /basketweave microstructure colony structures will be the most resistant to FCG [8]. Tensile residual stresses perpendicular to the crack growth direction will increase the FCG rates.

The residual stresses perpendicular to the crack growth direction, shown in Figure 5, suggest that the residual stresses in the middle of the crack plane are tensile and at the edges of the crack front the stresses are compressive. Therefore the mid-section portion of the crack will be subjected to a tensile stress whereas the crack edges will be pinned to the surfaces due to compressive residual stresses giving the appearance of a tunneled crack. Overall the effect of the residual stresses measured here will be to accelerate the FCG rates. Crack morphology will be a tunneled crack as was observed in the scanning electron microscope. The weld nugget microstructure as

discussed before consists of 2-3 µm thick grain boundary alpha allotriomorphs with lamellar colony microstructure.   Although the weld microstructure is conducive to high FCG resistance, as discussed above, the tensile residual stresses were dominant and increased the FCG rates. Again it needs to be noted that the increase in the FCG rates is only a factor four.
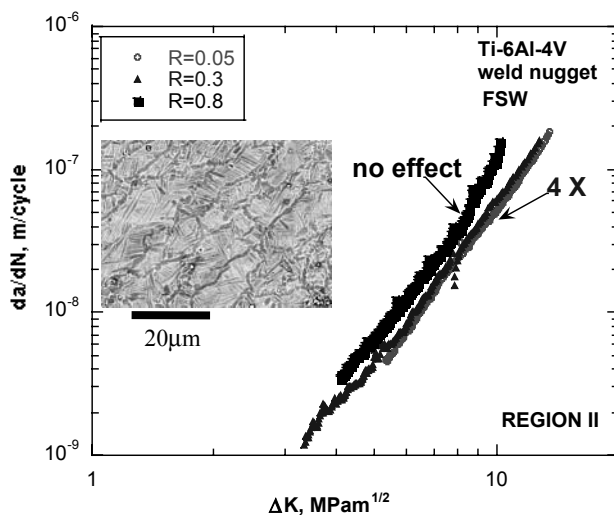

Figure 4. Fatigue crack growth rates in Ti-6-4 center crack geometry specimens, M(T) in the weld nugget. At stress ratio of 0.05 crack growth rates in the weld nugget are 4 times faster than the parent material, mill annealed Ti-6-4. Crack growth rates at R=0.8 were unaffected. Micrograph shows the weld nugget microstructure.
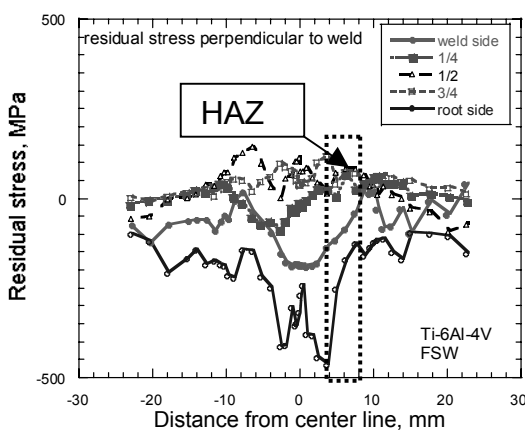
Figure 5. Residual stresses perpendicular to the weld direction also crack growth direction; stresses measured on the M(T) specimen used for obtaining the crack growth rates.

Fatigue crack growth rates were also obtained in the heat-affected zone, Figure 6, using the center crack specimen geometry at three stress ratios, R=0.05, 0.3 and 0.8. Fatigue crack growth threshold at R=0.05 dropped from 4.2 MPa-m $^{1/2}$ in the parent material (mill annealed Ti-6-4) to 2 MPa-m$^{1/2}$ in the heat affected zone of the FSW sample. A small decrease, 2.2 to 1.8 MPam $^{1/2}$ in the threshold is also observed at the R=0.8. Crack growth rates are faster (factor of 2 to 10X) in the heat-affected zone compared to the parent material. The heat affected zone microstructure is a bimodal microstructure. In a future paper the details of the microstructure and residual stresses effects on fatigue thresholds and growth rates will be discussed.
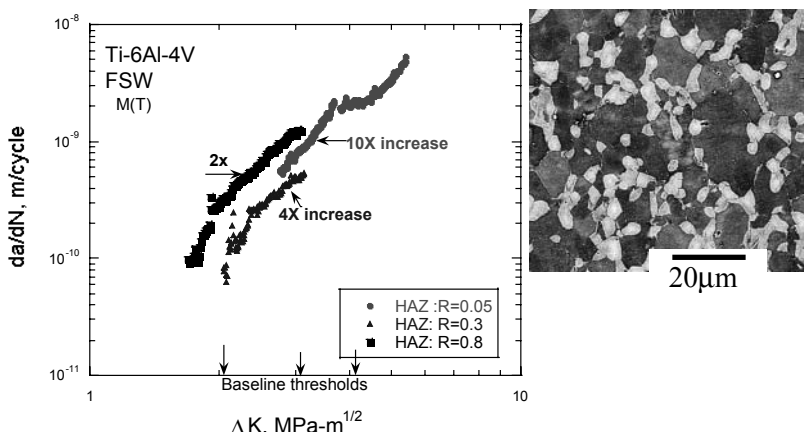
Figure 6. Fatigue crack growth rates in Ti-6-4 center crack geometry specimens, M(T) in the heat-affected zone. Fatigue crack growth thresholds in the heat-affected zone decrease for all stress ratios. Arrows represent FCG thresholds for the parent material mill annealed Ti-6-4. The right-most arrow represents FCG threshold for the base material at R=0.05 and the left most arrow for R=0.8. Between stress ratios of 0.05 and 0.3 crack growth rates are 4 to 10 times faster than in the parent material. Crack growth rates at R=0.8 are twice as fast as that in the parent Ti-6-4.

6. CONCLUSIONS

It is shown here that alpha, beta and alpha-beta titanium alloys can be friction stir welded. The phase transformations that occur in the nugget region and the heat affected zone are discussed. Residual stresses were found to be quite high in the present work. Tensile properties in transverse direction were

excellent for alpha-beta titanium alloy, Ti-6Al-4V. The decrease in the fatigue crack growth resistance was more in the heat-affected zone than in the weld nugget. Crack growth rates in the heat-affected zone were increased by a factor of 10 compared to the base line at a stress ratio of 0.05.

Study of tool wear and optimum tool material for FSW need to be investigated.

ACKNOWLEDGEMENT

REFERENCES

1. http://www.twi.co.uk/j32k/unprotected/band_1/research_gsp5689_intro.html
2. T. J. Lienert, K. V. Jata, and R. Wheeler, "Friction Stir Welding of Ti-6Al-4V Alloys" Proceedings of the International Conference on Joining of Advanced and Specialty Metals III, eds, M. Singh, J. E. Indacochea, , J. N. Dupont, and T. J. Lienert, 2000.
3. R. L. Goetz and K. V. Jata, "Modeling Friction Stir Welding of Titanium and Aluminum Alloys", in Friction Stir Welding and Processing, eds. K. V. Jata, M. W. Mahoney, R. S. Mishra, S. L. Semiatin, and D. P. Field, TMS, November 2001.
4. A. J. Ramirez and M. C. Juhas, "Microstructural Evolution in Ti-6Al-4V Friction Stir Welds", Materials Science Forum vols. 426-432 (2003) pp. 2999-3004, Trans Tech Publications, Switzerland.
5. T.J. Lienert, W. Tang and A.P. Reynolds "Microstructures, Mechanical Properties and Weldability of Friction Stir Welds on Ti Sheet Alloys", presented at Aeromat 2002, June 2002, Orlando, Florida, USA.
6. P.R. Subramanian, T. Trapp and E. Helder, "Friction Stir Welding of Titanium Alloys for Aircraft Engine Components," Friction Stir Welding and Processing-II, eds. K. V. Jata, M. W. Mahoney, R. S. Mishra, and S. L. Semiatin, TMS, March 2003
7. R. John, K.V. Jata and K. Sadananda, Residual Stress Effects on Near Threshold Fatigue Crack Growth Rates in Aerospace Alloys, In Press, International Journal of Fatigue, 2003.
8. Materials Properties Handbook: Titanium Alloys, Eds. Boyerer, Collings, Welsch Published by ASM International.

FORMATION OF SUBMICROCRYSTALLINE STRUCTURE IN LARGE SIZE BILLETS AND SHEETS OUT OF TITANIUM ALLOYS

G.A. Salishchev, R.M. Galeyev, S.V. Zherebtsov, S.YU. Mironov,
O.R. Valiakhmetov, S.P. Malysheva
Institute for Metals Superplasticity Problems, Ufa, Russia

Abstract: The structure evolution and mechanical behavior of titanium and Ti-64 alloy during successive compression of sample along three orthogonal directions or "abc" deformation were studied. It is shown formation of submicrocrystalline structure in the both materials under warm "abc" deformation. In titanium the structure evolution occurs via formation of deformation induced high angle boundaries and interaction between them that leads to formation of submicrongrained structure and strengthening. In two-phase lamellar alloy plates of phases divide into fragments, which afterwards are spheroidizied due to formation of high angle grain boundaries and transformation of semicoherent interphase boundaries to noncoherent ones. In this case superplastic flow and softening is observed. Large-scale billets and sheets with homogeneous submicrocrystalline structure were produced by "abc" deformation. Advantages of their mechanical properties were showed.

Key words: titanium, titanium alloy, severe plastic deformation, "abc" deformation, submicrocrystalline structure formation, large-scale submicrocrystalline billet, submicrocrystalline sheet

1.   INTRODUCTION

Materials with a submicrocrystalline (SMC) structure have an average grain size less than 1 μm and show increased strength and fatigue resistance [1]. They also exhibit superplastic behavior at temperatures much below the temperature range typical for materials with micron-sized grains [1,2]. Severe plastic

deformation (SPD) of metals and alloys is a method for producing submicrocrystalline structure in large-scale billets. The technique for production of bulk SMC samples, attracted rapt attention of researchers, is equal channel angular pressing (ECAP) [1]. Meantime, "abc" forging, including a set of successive upset/drawing operations, can be used for SMC structure formation [3]. Both ECAP and "abc" forging techniques permit to form SMC structure with close grain size. So, in commercial pure titanium grain size of 0.28 [4] and 0.4 μm [5] were obtained by "abc" forging and ECAP, respectively. To avoid failure of billet because of low ductility of titanium and its alloys deformation is realized at elevated temperatures [5]. Strict supervision deformation regime and choice of optimal deformation scheme is required for formation of uniform SMC structure within the billet.

The common feature of the both techniques is remaining an initial shape of billet almost unchanged for attaining large strains. To increase the uniformity of plastic flow the most useful operation is rotation of a billet for change deformation direction. In this case slip and twinning systems idle earlier are involved in operation. On the other hand the high stresses and density of defects resulted from large strains change the interaction between defects. The mobility of dislocations increases essentially and deformation induced boundaries (DIB) are developed that leads to formation of a lamellar structure being finer than the initial microstructure [6]. Interaction between "new" and "old" DIB at their intersection because of change in the strain path leads to considerable changes in the microstructure formed at previous stage of deformation [6]. Microstructure evolution at ECAP essentially depends on the loading schemes and various deformation directions [1,7]. However, there are no practically investigations revealed features of microstructure evolution and mechanical behavior during "abc" deformation.

The stated considerations are correct for titanium. In titanium alloys evolution of lamellar microstructure (typical for titanium alloys) takes place due to development of globularization [8]. The process develops by means of substructure formation in the lamellas of phases, division of lamellas and transformation of lamellas parts into globular particles. Keep the process its main features in the case of SMC structure formation? There are no such investigations in the scientific literature. The relative simplicity of the method and its commercial application bring up a question to investigate the features of microstructure evolution and mechanical behavior of titanium and its alloys during successive deformation/rotation of samples as well as scale up process capability for production of SMC structure in large-scale billets and sheets.

2. MATERIALS AND PROCEDURES

The commercial pure titanium (impurities content, wt %: 0.25Al, 0.15Fe, 0.07Si, 0.05C, 0.12O, 0.02N, 0.005H) with a mean grain size of 35 μm and the alpha/beta titanium alloy Ti-64 (wt %: 6.3Al, 4.1V, 0.18Fe, 0.03Si, 0.02Zr, 0.01C, 0.18O, 0.01N, 0.002H) beta-annealed and water-quenched with a mean β-grain size of 250 μm were used. The Ti-64 alloy had a beta-transus temperature of 995°C.

Isothermal compression tests of prismatic samples along three orthogonal directions (or so-called "abc" deformation) were realized at temperatures of 400°C for Ti and 550°C for Ti-64 [5,8]. The initial size of samples were 16mm×18mm×20 mm. Prior to each rotation, a prismatic shape was restored to the sample by machining the curved faces. The initial strain rate and strain per deformation step were $10^{-3}s^{-1}$ and ~0.4, respectively. The cumulative strain was calculated as $\Sigma e = e_1 + e_2 + \ldots + e_n$, where e_n is a strain for the each step.

The ability to scale up the "abc" deformation approach to form SMC structure in a large-scale Ti-64 billets was demonstrated via prototype production. The billets (150 mm in diameter and 200 mm in length) solution treated at 1010°C for 0.5 hr followed water cooling were subjected to near-isothermal multi-step forging comprising of specific combination of multiple upset/drawing operations [3] at the thermo-mechanical conditions provided formation of submicron-sized microstructure.

The preforms for rolling cut from submicron-grained billets were warm rolled in sheets at temperatures of 650–550ºC preserving SMC structure. The sheet rolling was carried out by means of cross and pack rolling techniques using a duo rolling mill. The commercial size sheets with dimensions of 500 mm × 1500 mm × 2 mm were produced.

3. RESULTS AND DISCUSSION

3.1 Microstructure Evolution and Mechanical Behavior of Titanium During "ABC" Deformation

Stress versus cumulative strain curve (S-Σe) for Ti was plotted under "abc" deformation (Fig. 1a) at temperature of 400°C and strain rate of $10^{-3}s^{-1}$ (Fig. 1b). One can see that beginning from the second compression step the initial portion of the strain curves is more flat than at first compression. One should also note a non-monotonic dependence of yield strength on a number of compressions. During the first three steps one could observe a sharp increasing of its value, but then yield strength almost did not depend on cumulative strain.
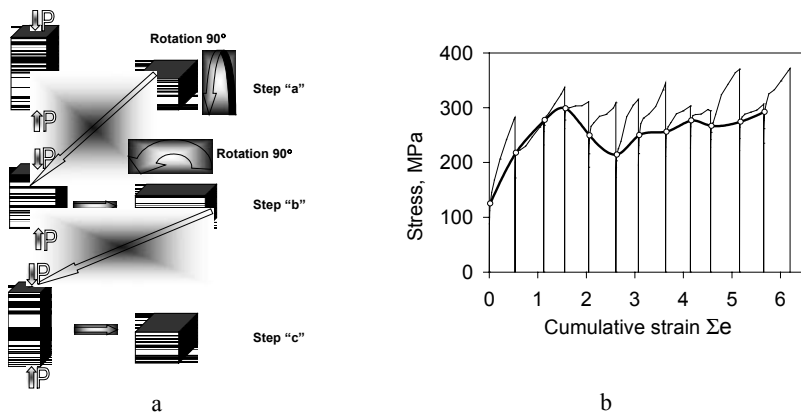
Figure 1. Scheme of "abc" deformation (a) and cumulative S-Σe curve (b) for "abc" deformation of Ti at temperature of 400°C and strain rate of $10^{-3}s^{-1}$.

Investigation of the deformation relief occurring on the surface of samples additionally subjected to by 15% strain after different number of compression steps have shown that "plateau" on the initial portion of strain curves is result of strain localization (Fig. 2a) in macro shear bands (MSB). Its appearance is result of "scattering" some dislocation boundaries onto individual dislocations (Baushinger effect) and formation of "avalanche" of mobile dislocations (Fig. 2b). So, in this case yield of titanium is controlled by substructure that, probably, leads to weak dependence of yield stress on strain. Macrobands formed at the beginning of the cycle of loading remain until the end of loading. So, plastic flow of titanium is localized.
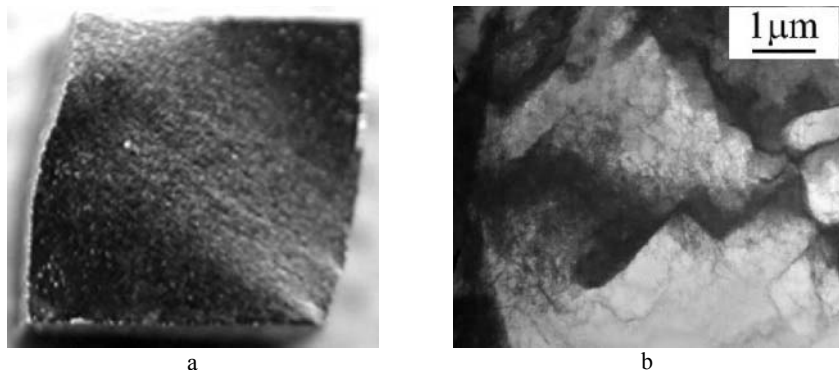
Figure 2. Shear localization in Ti four times compressed and additionally strained by 15% at 400°C: deformation relief (a) and TEM image of dislocation boundary "scattering" (b).

Investigation of texture has shown that every time after changing the axis of loading there occurs formation of qualitatively similar axial texture, in which the prevailing orientation of crystallites was stable. This means that

after changing the loading axis the structure rearranges and adapts to new conditions of deformation.

The results of TEM and EBSD analysis have shown that at all stages the deformation occurs by slip and twining. The main feature of structure inside the MSB is intense formation of deformation-induced boundaries (DIB). The evolution of these boundaries transforms the structure, at first, to the lamellar-type one (Fig. 3a) and, finally, to the equiaxed-type structure (Fig. 3b). Simultaneously, DIB development refines the structure very strong, so, after 12 compression steps a mean grain size is about 0.3 μm.

a   b
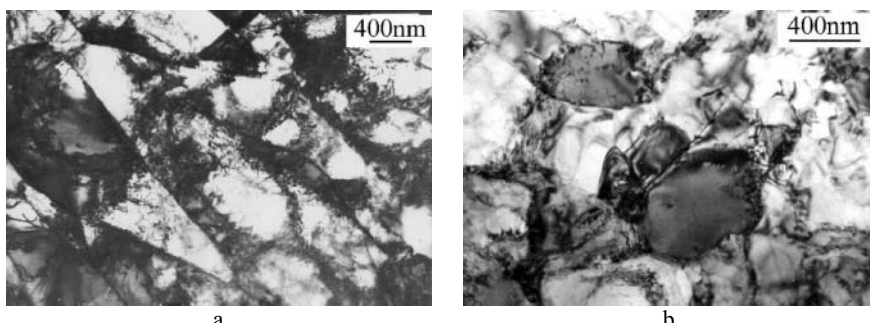
Figure 3. Microstructure evolution of Ti during different steps of "abc" deformation at 400°C and of 10^{-3} s^{-1}: a –3 steps ($\Sigma e \approx 1.5$); b –12 steps ($\Sigma e \approx 6$).

The formation of MSB causes significant macroscopic heterogeneity of the structure, which becomes negligible with increasing the number of compression steps and spreading of new bands.

One of the prominent features of structure evolution was gradual curving of a shape of twins and gradual change of misorientation on its boundaries. This means that misorientation of high-angle boundaries was changed during deformation.
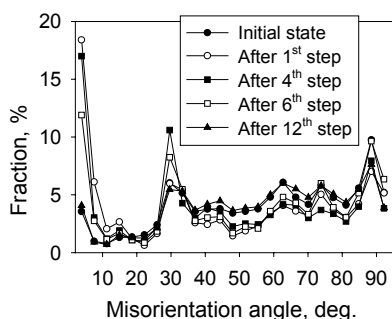
Figure 4. Effect of cumulative strain on the distribution of boundaries by misorientation angles in Ti.

Investigation of evolution of the misorientation distribution function has shown that the almost single consequence of the cumulative strain increasing

is gradual reduction of the low-angle boundaries fraction (Fig. 4). Other characteristics of the misorientation distribution function, namely the distribution of boundaries by misorientation angles and axis, as well as the content of most typical coincident side lattice boundaries and their general content did not almost change.

The fact that misorientation at individual grain boundary constantly changed during deformation, this means that most typical misorientations are repeated again and again. Taking into account the reproduction of textures one can conclude that these two processes are connected. In other words, formation of new DIB is caused by crystals reorientations. Since the shape and size of crystallites inside of macrobands is result of DIB spreading we can conclude, that all this processes are connected.

So, at macroscopic scale deformation developed by formation and spreading of MSB. At the change of the loading axis occurrence new and new MSB took place. It promoted uniformity of macroscopic scale of deformation. Inside MSB the crystals rotated to stable orientations at given loading axis. As a result deformation developed at the mesoscopic scale - new DIB formation and microstructure refinement appeared. DIB formation was result of self-organization of dislocation and twinning. Spreading of new DIB and its intersection each other provided formation of new submicrocrystalline equiaxed grains.

3.2 Microstructure Evolution and Mechanical Behavior of Ti-64 Alloy During "ABC" Deformation.

The plastic-flow behavior of Ti-64 in terms of stress versus cumulative strain (S-Σe) at 550°C and 10^{-3} s^{-1} using strain increments of ~0.4 (Fig. 5a) exhibited a peak stress and flow softening during the initial increments of deformation and steady-state flow at large strains. Specifically, during the first two increments, a peak stress and then flow softening were observed. During later steps, the value of the peak stress decreased, and steady flow behavior appeared; the extent of this stage increased from one step to another. The stress peaks and the subsequent flow softening in the S-Σe curves is explained by strain hardening during the initial stages of deformation due to dislocation multiplication and then softening associated with the bending of non-favorably oriented lamellae and reorientation of favorably oriented ones in regions of localized deformation [9].

At a finer scale, transverse sub-boundaries are formed within in α- and β-phases. As deformation increases further, the misorientation of these sub-boundaries increases as dislocations are absorbed into the sub-boundary walls, thereby leading to high-angle boundaries. Concurrently, the semi-coherent interphase α/β boundaries are transformed to non-coherent ones.

Due to the transformation of the interphase and development of intra-lamellar boundaries, mass transfer becomes more rapid, and grooves are formed on the surface of the α-plates, leading to the segmentation of the alpha plates (Fig. 5b). The fragmented β-interlayers and α-plates are thus spheroidized.
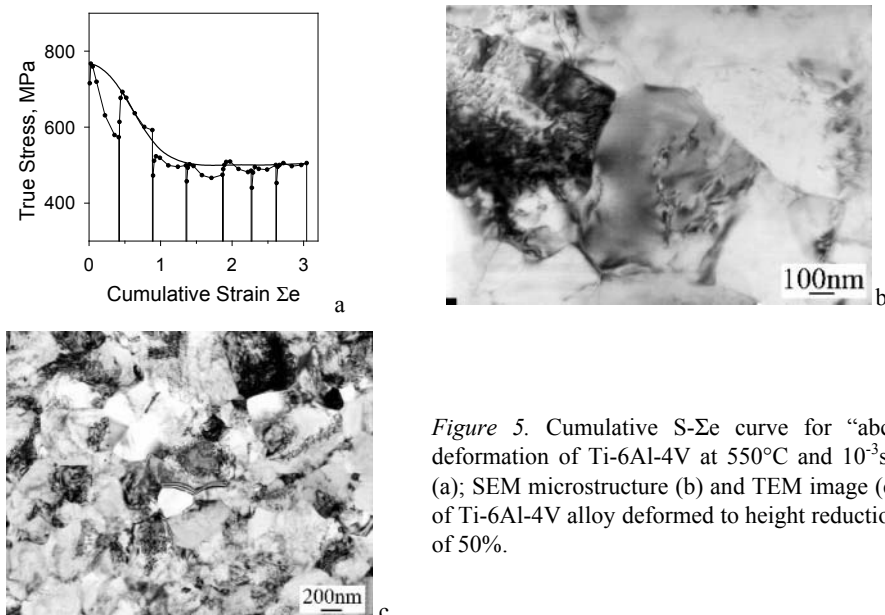

Figure 5. Cumulative S-Σe curve for "abc" deformation of Ti-6Al-4V at 550°C and $10^{-3}s^{-1}$ (a); SEM microstructure (b) and TEM image (c) of Ti-6Al-4V alloy deformed to height reduction of 50%.

At macroscopic scale initial deformation and microstructure transformation occurs in the macro shear band. However, formation of the shear bands is retarded at subsequent deformation since development of globularization in the central area of a sample leads to superplastic flow realization. This accompanied with steady flow stage appearance on the S-Σe curve and increasing of value of the strain-rate-sensitivity m from 0.17 for e = 0.4 to 0.35 for Σe = 0.9. Consequently successive rotations lead to accumulation of strain primarily in the center of the workpiece, and to the formation of a homogeneous microstructure with globular grains of the α- and β-phases with a mean size of ~0.4 μm is formed (Fig. 5c).

At the macroscopic scale, shear localization flow in the alloy develops during initial increments of deformation. Softening and globularization of structure in the macro shear band lead to realization of deformation at mesoscopic scale. In this case the mesoscopic scale deformation is determined by cooperative grain boundary sliding leading to superplastic flow. Superplastic flow results in deformation accumulation in the central area of the sample and impedes in structure transformation in periphery regions.

3.3   Validation / Scale-up of Submicron-Grained Large-Scale Billets out of Ti-64 Alloy

Because of the non-uniform origin of plastic flow the structure refinement occurs first of all in the areas undergoing the most intensive deformation. A higher uniformity of structure within the sample interior can be attained by changing the scheme of deformation (including application of special tooling) for shear-localization bands to be formed in the areas with non-transformed structure. Modeling of plastic flow using software DEFORM-3D shows the change in distribution of efficient strain for the billet turned through 45° to the axis of compression. In case of such a position of the billet the strain is not concentrated in "old" shear bands. New bands are formed and they lead to structure refinement in non- transformed areas.

a   b
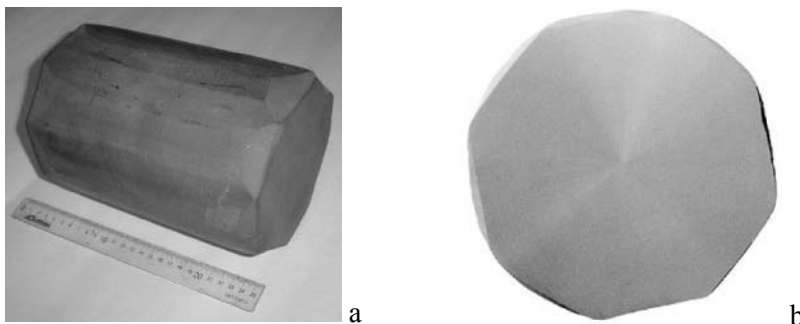
Figure 6. SMC Ti-6Al-4V billet, measuring 150 mm diameter and 200 mm length: a – as-processed billet, b – macrostructure, c – microstructure and d – TEM micrograph.

The laboratory-scale "abc" deformation demonstrated that the formation of SMC microstructure in Ti and Ti-64 should be performed via warm working at temperatures equal to 400 and 550°C respectively (for a strain rate of 10^{-3} s^{-1}). To avoid a macroheterogeneity of structure because of shear localization flow a modified scheme of "abc" deformation was used for production of a large-scale billet. The modified scheme allowed us to produce a homogeneous SMC structure in a large Ti-64 billet measuring 150 mm diameter and 200 mm length via multi-step isothermal forging (Fig. 6a). Metallographic analysis of the billet indicated that its macrostructure is homogeneous across the entire section (Fig. 6b), and its microstructure comprises a uniform distribution of globular of α- and β-phase particles whose size did not exceed 0.5 μm (like showed on the Fig. 5c).

The mechanical properties of the SMC billet are also excellent. After multi-step isothermal forging, the ultimate tensile strength is very high (1360 MPa), and the total elongation is 7% (Table 1). The property uniformity

along the radial and tangential directions is also very uniform. These values can be compared to those in conventionally-processed (microcrystalline) Ti-64. After solution treatment and aging, conventional Ti-64 typically has an ultimate tensile strength no higher than 1100 MPa and an elongation of approximately 8%.

Table 1. Mechanical properties of samples cut out from the Ti-64 SMC billet

Direction of sampling	YS [MPa]	UTS [MPa]	EL [%]	RA [%]
Radial	1350	1360	7	62
Tangential	1335	1355	7	61

3.4 Validation / Scale-up of Submicron-Grained Large-Scale Sheets out of Ti-64 Alloy

While developing a trial thermo-mechanical route of rolling of a preform with SMC structure the following important facts should be taken into account. Firstly, the temperature interval of heating of a preform for rolling should not lead to coarsening of the starting SMC structure. Secondly, the material should possess the required ductility for rolling on commercial mills where deformation of material is performed at high strain rates. Thirdly, due to the fact that rolling is not performed under isothermal conditions it is necessary to prevent subcooling of a preform and, as a result, a decrease in the ductility of the material.

The study of heating temperature effect on grain size and ductility of the SMC Ti-64 alloy was shown that at temperatures above 675–700°C there occurs an intense grain growth, but at temperatures below 600°C a ductility of SMC material decrease essentially. Consequently, rolling of a blank with SMC structure should be carried out in the temperature range of 600–700°C. However, such a narrow temperature interval creates some difficulties during rolling, which are caused by significant subcooling of sheets. One of the methods preventing subcooling is pack rolling of sheets in a can.

Along with parameters of mechanical properties the important characteristic of sheets suitable for SPF, is isotropy of their mechanical properties. It is known that the strong basal texture should promote isotropic properties of the sheet in the rolling plane [10]. The textures of the submicron-grained preform for rolling and sheet samples rolled up to 75, 84 and 90 % reduction at temperatures 600, 650 and 700°C were studied. The results obtained indicated that prior to rolling the submicron-grained material had almost random texture. In contrast a strong basal texture is formed in the sheet during the rolling. The intensity of a basal texture component was increased with decreasing temperature of sheet rolling and

increasing rolling reduction of sheet.

The commercial size sheets that are 500mm×1500mm×2mm thick with SMC structure were produced by the developed thermo-mechanical route of rolling (Fig. 7). During warm rolling the submicron grains of phases in sheet material retained an equiaxed shape; a grain size was equal to 0.4-0.5 μm.
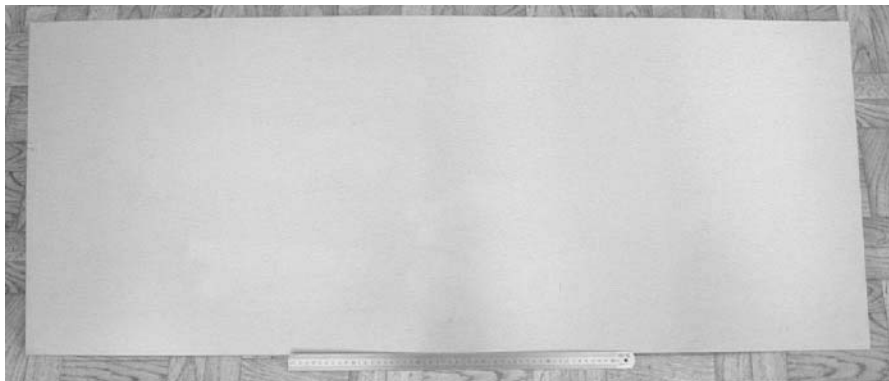

Figure 7. Warm rolled submicron-grained Ti-64 sheet, 500mm×1500mm×2mm thick.

Submicron-grained sheets showed higher ultimate tensile strength (1150-1230 MPa) as compared to conventional superplastic sheet (950-1050 MPa). The properties of SMC sheet slightly depended on the tensile direction demonstrating high mechanical isotropy of the sheet in the rolling plane. Evaluation of superplastic performance of SMC sheet is listed in Table 2.

Table 2. Elevated temperature mechanical properties of SMC Ti-64 sheet

T [°C]	Strain rate [1/s]	Flow stress at 50% strain [MPa]			Elongation [%]			m index
		Direction of sampling, degree						
		0	45	90	0	45	90	
650	3×10^{-4}	48						
	7×10^{-4}	70	71	71	780	830	810	0.44
	7×10^{-3}	179	180	184	720	660	680	0.34
700	3×10^{-4}	30						
	7×10^{-4}	44	48	46	900	910	900	0.37
	7×10^{-3}	110	111	118	890	900	900	0.47
	3×10^{-2}	165	165	165	550	570	600	0.40
750	3×10^{-4}	15						
	7×10^{-4}	27	26	29	1000	970	960	0.62
	7×10^{-3}	95	85	81	1200	1000	1100	0.50
	3×10^{-2}	151	146	147	500	520	500	0.41

The sheet produced demonstrates enhanced superplasticity and isotropy at reduced temperatures of 650−750°C (Table 2). Elongation of 900−1000% was observed at 700−750ºC and strain rate of $7 \times 10^{-4} - 7 \times 10^{-3}$/s. The value of flow stress achieved at 700−750°C and lower strain rates is typical to the

alloy Ti-64 with a microcrystalline structure at higher deformation temperatures of 900–920ºC. Excellent superplastic properties, which are defined as an initial flow stress of 20-40 MPa in the strain rate range of 10^{-4} to 10^{-3}/s at temperatures of 700–750°C should provide sufficient forming capacity of SMC sheet to production of a complex part by SPF at reduced temperatures.

At present, the superplastic performance of commercial size submicrongrained Ti-64 sheet is under study and results will be published later.

4.   CONCLUSIONS

1.   The "abc" deformation of Ti at 400°C and 10^{-3} s^{-1} to a cumulative strain of $\Sigma e = 6$ leads to the formation of a submicrocrystalline structure with a grain size of ~0.4 µm. A hardening during increments of cumulative deformation was observed as the yield stress decreased continuously at every next cycle. The effect is the result of structure change under variation of compress direction. The submicrocrystalline grains under "abc" deformation are formed as a result of formation and crossing of deformation induced high angles boundaries. The final structure is rather heterogeneous; there are subgrains and large (up to 3µm) grains in the structure.

2.   The process of "abc" deformation of alpha/beta Ti-64 titanium alloys at 550°C and 10^{-3} s^{-1} to a cumulative strain of $\Sigma e = 3$ leads to the formation of a homogenous submicrocrystalline structure with a grain size of ~0.3 µm. A peak flow stress in the alloy followed by flow softening and then steady-state flow caused by superplasticity are observed on the cumulative stress-strain curve. Globularization controlled by the formation of high-angle boundaries across the lamellas and transformation of semicoherent interface boundaries into incoherent ones take place. Superplastic flow during the final stages of deformation contributes to an improvement in the homogeneity of the SMC structure.

3.   Using the modified method of "abc" deformation, a large-scale billet (150 mm in diameter and 200 mm in length) out of Ti-64 alloy with a homogeneous microstructure and a grain size less than 0.5 µm was produced. The refined grain size provided a substantial increase in strength without a loss in ductility. Its strength and ductility were almost identical in the tangential and radial test directions.

4.   Warm rolling of preform with a submicrocrystalline structure can be produced at much lower temperatures than generally used. Submicrongrained sheets demonstrate mechanical isotropy and high superplastic properties at reduced temperature range of 650-750°C. The Ti-64 sheets with SMC structure can be successfully used for SPF and SPF/DB applications with significantly decrease in operations temperature (by ~200°C).

5. ACKNOWLEDGEMENTS

6. REFERENCES

1. R.Z. Valiev, R.K. Islamgaliev, I.V. Alexandrov: Progr. Mater. Science **45** (2000), 102.
2. O.A. Kaibyshev: *Superplasticity of Alloys, Intermetallics, and Ceramics* (Springer Verlag, Berlin, 1992).
3. Patent PCT/US97/18642, WO 9817836 A1, (1998).
4. A.V. Sergueeva, V.V. Stolyarov, R.Z. Valiev and A.K. Mukherjee: Scripta Mater. **43** (2000), 819.
5. G.A. Salishchev, S.V. Zherebtsov, R.M. Galeyev: *Ultrafine Grained Materials II* (TMS, Warrendale, PA, 2002), p. 123.
6. V.V. Rybin, *Large Plastic Strains and Fracture of Metals* (Moscow, Metallurgy, 1986)
7. A. Gholinia, P.B. Prangnell, M.V. Markushev, *Acta Mater.* **48** (2000), 1115.
8. S.V. Zherebtsov, G.A. Salishchev, R.M. Galeyev, O.R. Valiakhmetov, S.L. Semiatin: Adv. of Mater. Eng., (2003), in press.
9. R.M. Miller, T.R. Bieler, S.L. Semiatin: *Scripta Mater.* **40** (1999), 1387.
10. M. Peters, G. Luetjering: *4th World Conference on Titanium* (TMS/AIME, Warrendale PA, 1980), p. 925.

MAGNETICALLY-CONTROLLED ELECTROSLAG MELTING (MEM) OF MULTICOMPONENT TITANIUM ALLOYS

Y.Y. Kompan, I.V. Protokovilov
The E. O. Paton Electric Welding Institute of NAS of Ukraine

Abstract: Technology of the magnetically-controlled electroslag melting of titanium alloys has been developed. This technology is peculiar by the use of external magnetic fields during melting. Thus, the directed electrovortical flows (EVF) or vibration of the melt are created in a metal pool.

EVF level the pool temperature field, intensify heat and mass transfer in the metal pool, thus providing the formation of metal with a high chemical and physical homogeneity. Vibration of the melt allows metal structure refining.

It is shown that superposition of external magnetic field on the melting zone makes it possible to control the depth and shape of the metal pool.

Mechanical properties of a new class of titanium alloys with an intermetallic strengthening, produced by MEM method, are given.

Key words: electroslag melting, magnetic field, metal pool, titanium alloys, ingot.

1.   INTRODUCTION

One of the tendencies in the development of advanced titanium alloys is the increase in the degree of their alloying [1,2]. The important factor defining the success of development of these alloys is the technology of their production. However, to produce these alloys using the traditional methods of melting is very difficult.

Thus, at the present time it is not so important only to develop new alloys, but also special methods of melting which guarantee reproducibility of their properties. Here, the degree of chemical and structural homogeneity of metal is so much important characteristic that its improvement should be

considered as one of priory trends in the development of the melting technology.

Unlike the traditional methods of titanium melting, VAR and EBR, the electroslag process is characterized by comparatively low-temperature, non-concentrated heat source, which is a slag pool and, respectively, a low temperature gradient in a metallurgical pool. This influences favorably the homogeneity of multicomponent titanium alloys.

However, the conditions of metal crystallization in ESR, contributing to the formation of coarse-grain structures, limit the possibilities of this method application for melting the multicomponent titanium alloys.

2. ELECTROMAGNETIC CONTROL OF ELECTROSLAG PROCESS

The radically new possibilities of influence the process of melting, transfer and crystallization of metal are provided by the use of external magnetic fields in ESR.

Principle of magnetic control consists in interaction of external magnetic field with electrical current of melting [3]. As a result of this interaction, the volume electromagnetic forces are formed in a current-carrying metallurgical melt, which in their turn cause the melt movement. In this case, the direction and intensity of melt movement are determined by parameters of external magnetic field, i.e. it is possible to control the melt movement.

The main task of the technology of the magnetically-controlled electroslag melting (MEM) is the control of processes of melting, transfer and crystallizaton of metal by creating various trajectories of movement of the metallurgical melt.

From analysis of effect of external magnetic fields on hydrodynamics of metallurgical melt in ESR two main mechanisms of electromagnetic control in ESR have been developed:
− creation of directed electrovortical flows (EVF) in the metallurgical pool;
− creation of vibration of melt.

The directed electrovortical flows (EVF) are created in the slag pool under the action of external longitudinal and longitudinal-radial magnetic fields. These flows equalize the temperature field of the pool, intensify heat- and mass exchange in the metallurgical pool, and as a result they contribute to the formation of metal with a high chemical and physical homogeneity.

The vibration of melt is generated by superposition of steady transverse magnetic field on the melting zone. Vibration of molten metal contributes to the metal crystallization with a fine-grain, homogeneous structure of cast grains.

3.   SCHEME OF MEM PROCESS

MEM of titanium alloys is realized in a pressurized electroslag chamber-type furnace (Figure 1). The melting space is preliminary evacuated, and then filled with an inert gas. This scheme of melting contributes to degassing of the consumable electrode and provides a reliable protection of titanium from harmful impurities.

As consumable electrodes in MEM of titanium, the electrodes pressed from spongy titanium and alloying elements, similar to electrodes, used in VAR, are used.

Figure 1. Scheme of MEM process: *1* – consumable electrode, *2* – slag pool, *3* – metal pool, *4* – ingot, *5* – electromagnetic system, *6* – vacuum chamber, *7* – mould.
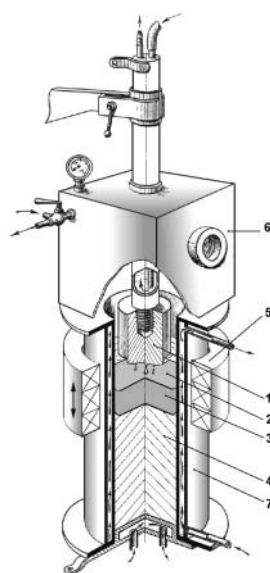
As fluxes for MEM of titanium, the reactive compositions on the base of halogenides of alkali and alkali-earth metals are used. Halogenide fluxes allow the electroslag process to be easily set and provide its stability within the wide range of melting conditions. Rate of dissolution of harmful inclusions of nitrides of titanium in these fluxes much exceeds their rate of dissolution in molten titanium [4]. Thus, the premises for dissolution and grinding of *hard α-phase* type inclusions are created.

Control of hydrodynamic situation in the metallurgical pool is realized by superposition of external magnetic fields on the melting zone. Depending on composition, size and purpose of ingot, different MEM schemes are used [5].

4.   EFFECT OF MAGNETIC FIELDS ON PARAMETERS OF METAL POOL

Volume and shape of metal pool in ESR is one of the most important characteristics, which define the quality of metal of ingot being melted. With increase in volume and depth of metal pool the length of zone of two-phase state is increased which is the source of all defects of a liquation origin. Therefore, to produce quality ingots, it is necessary to approach shallow shape of the metal pool.

In traditional scheme of ESR the flows of melt are formed in the slag pool, which are directed from a consumable electrode, along its axis downward to the metal pool [3]. These flows of overheated slag promote the

formation of a deep, V-shaped metal pool. The V-shaped of crystallization front with radial direction of growth of crystallites deteriorates the conditions of ingot crystallization, promotes the formation of crystalline defects and intensification of liquation processes.

Superposition of external longitudinal magnetic field on the zone of melting changes radically the pattern of flows in slag and metal pools. Under the action of the magnetic field, the slag pool is set into rotation both in horizontal (around symmetry axis) and also in vertical planes. Moreover, the direction of melt rotation in vertical planes is characterized by downward flows at the mould wall and upward flows in the pool central part. Thus, the longitudinal field changes the direction of melt rotation for opposite.

This restructuring of melt circulation changes greatly the distribution of hydrodynamic pressure to the metal pool surface.

Investigations on cold models showed that during melting in longitudinal field the pressure to the metal pool surface in its axis is gradually decreased with increase in induction Bz (Figure 2). This is due to the decrease in rate of a central jet of slag directed from the electrode edge to the metal pool surface.
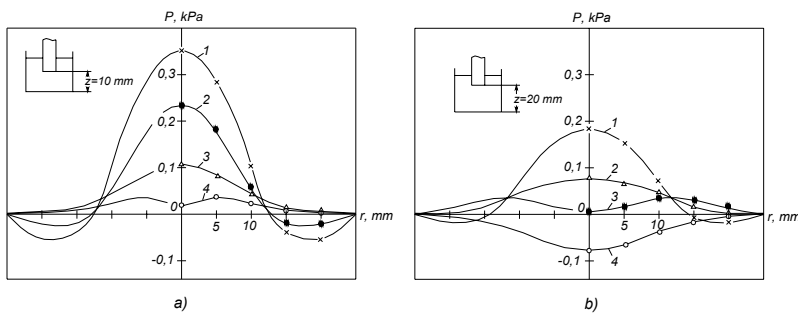
Figure 2. Distribution of pressure to metal pool surface at z =10 mm (*a*) and z=20 mm (*b*) for different values of induction of longitudinal magnetic field B_z:
1 – 0 mT; *2* – 7 mT; *3* – 13 mT; *4* – 20 mT

Redistribution of hydrodynamic pressure to the metal pool surface influences its depth and shape (Figure 3). External longitudinal magnetic field, with increase in its induction, leads first to the equalizing of front of metal crystallization and decrease in pool depth (Figure 3, b). This pool shape is most favorable from the point of view of conditions of metal crystallization. With further increase in induction of the external magnetic field the EVF, directed downward along the mould wall and upward, along the electrode axis, promote the formation of the metal pool with its periphery deepening (Figure 3c).
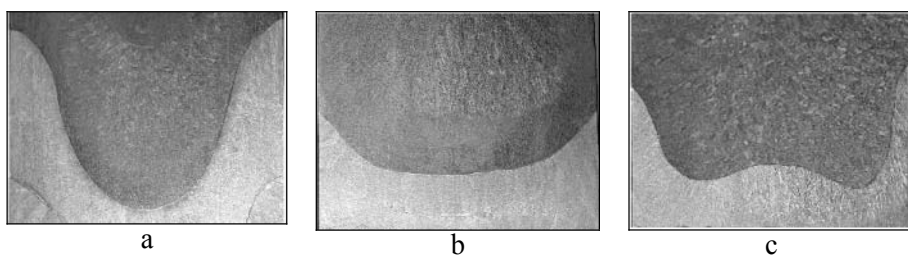
Figure 3. Shape of metal pool during melting in longitudinal field:
a – B=0 T; *b* – B=0,06 T; *c* – B=0,1 T.

5. PROPERTIES OF MULTICOMPONENT ALLOYS

Using MEM technology, the experimental high-strength and heat-resistant titanium alloys, which represent a plastic matrix, strengthened with intermetallics of different volume and shape, were produced.

The analysis carried out showed that the chemical composition of ingots strictly corresponds to the preset composition of the alloy. Alloying elements in section of ingots are distributed uniformly, without signs of liquation.

Table 1 gives mechanical properties of alloys representing a matrix from titanium alloy VT22 (Ti-5%Al-5%Mo-5%V-1%Fe-1%Cr) with additional intermetallic strengthening. In these alloys the intermetallic strengthening is attained by the formation of dispersed compounds of titanium with low-soluble elements, such as carbon, boron, in heat treatment.

Table 1.

Alloy	UTS, MPa	El, %	Red. of Area, %	Impact strength (U-notch), J/cm^2
VT22 + 0,2%C	1288-1366	16,6-14,8	40-37	22-20
VT22 + 0,3%C	1327-1370	13,5-12,1	38,7-37,9	20-20
VT22 + 0,2%B	1330-1340	11,5-8,0	36-27	24-22
VT22 + 0,25%C + 0,2%B	1320-1370	8,6-7,0	28,6-20,5	18-15

Table 2.

Chemical composition, wt.%	UTS, MPa	El, %	Red. of Area, %	Long term strength (100 H, 700^{0}C), MPa
Ti + 4,5 Al + 25 Nb + 5,0 Mo + 0,15 B + 0,15 C + 0,15 Si	1230	4,5	6,5	320
Ti + 4,5 Al + 25 Nb + 5,0 Mo + 0,1 B + 0,1 C + 0,1 Si + 4,0 Fe	1380	3,5	5,5	350

Table 2 presents mechanical properties of alloys with a matrix on the base of solid solution of niobium and molybdenum, dispersion-strengthened with chemical compounds, and also alloy with an additional frame strengthening owing to eutectoid TiFe.

It can be concluded from the data presented that with use of the intermetallic strengthening of titanium alloys it is possible to increase greatly their strength and heat resistance and also to preserve the necessary ductility. Moreover, the developed MEM technology makes it possible to realize the advantages of titanium alloys with an intermetallic type of strengthening that is impossible by using traditional methods of melting.

CONCLUSIONS

1. Development of new advanced titanium alloys is necessary to realize in combination with the development of new methods of melting.
2. The technology of MEM of multicomponent titanium alloys has been developed which can produce ingots with a high chemical and structural homogeneity and precise preset chemical composition.
3. In MEM the directed flows of metallurgical melt are generated which equalize the temperature field of the pool and intensify the heat- and mass exchange in the metallurgical pool.
4. MEM in longitudinal magnetic field makes it possible to decrease in depth (volume) of the metal pool and to equalize the front of metal crystallization.
5. In MEM in transverse magnetic field a vibration of melt, refining the crystalline structure of the ingot, is created.
6. Titanium alloys of MEM technology with intermetallic strengthening possess high strength and heat resistance and preserve the necessary ductility.

REFERENCES

1. E.N.Kablov, Main trends in the development of materials for aerospace engineering of XXI century, Advanced Materials (in Russian), No.3, (2000) 27-36.
2. N.V.Sysoeva , V.N.Moiseev. Titanium Alloys with Intermetallic Type of Strengthening, Coll. Aviation Materials and Technologies, (VIAM, Moscow, 2002).
3. Y.Y.Kompan, E.V.Shcherbinin: Electroslag Welding and Melting with Controllable MHD-Processes. (Mashinostoyeniye, Moscow, 1989).
4. M.G. Benz, A.D. Riabtsev, et al. "Active Slag" ESR Refining of Titanium Alloys for Dissolution of Nitrogen Rich Inclusions, (GE R&D Center, 2000CRD040, April 2000).
5. Y.Y.Kompan, I.V.Protokovilov, Producing High-Alloy Titanium by MEM Method, Teoriya i Praktika Metallurgii (in Russian), No.5 (2001) 25.

LIGHTWEIGHT CELLULAR METALS WITH HIGH STRUCTURAL EFFICIENCY

Wynn S. Sanders

Air Force Research Laboratory, Materials and Manufacturing Directorate, Wright-Patterson Air Force Base, Ohio 45433, USA

Abstract: This paper will provide an overview of the available types of lightweight cellular metals, their production methods, and their performance for various structural applications.   Lightweight cellular metals are low-density materials with multifunctional attributes that make them appealing for numerous uses, including thermal and acoustic insulation, energy absorption (crash protection), lightweight structural sandwich panels (as the core material), and vibration damping devices. Cellular metals are especially efficient for structural applications as they provide a high stiffness-to-weight ratio when loaded in bending. Additionally, their damping capacity is up to a factor of ten larger than that of solid metals. Cellular metals are made by a range of novel processing techniques and are available as stochastic foams (closed- and open-cell), hollow-sphere foams, periodic and optimized truss structures, and honeycombs.

Key words: cellular metals, metallic foam, open- and closed-cell foam, hollow-sphere foam, optimized truss structures, honeycomb.

1.   INTRODUCTION

Cellular solids are a class of materials with low densities and novel physical, mechanical, thermal, electrical, and acoustic properties. Low-density cellular metals can feature a wide variety of topologies to include open-cell foam, closed-cell foam, hollow-sphere foam, periodic/optimized truss structures, and honeycomb. Metallic foams consist of air dispersed in a solid matrix, similar to polymer foams such as polystyrene or food foams such as whipped cream. Closed-cell foams feature solid faces such that each cell is independently sealed from its neighboring cells, whereas open-cell foams (also known as porous metals, metal sponges and truss-type materials) do not contain cell walls; they only have cell edges. Hollow-sphere foams consist of an assembly of individual hollow spheres.

There is an extensive body of literature that discusses the mechanical properties of metallic foams and cellular materials. The book, *Cellular Solids* [1], provides a fundamental understanding of the structure and properties of all types of cellular solids and the ways in which they can be used in engineering design. A more thorough overview dealing specifically with the mechanical behavior of metallic foams can be found in [2]. The book, *Metal Foams: A Design Guide* [3], summarizes many of the concepts introduced in *Cellular Solids* and expands this knowledge in a discussion of the current understanding of the production, properties, and uses of metallic foams in various applications from a properties, design, and economics approach. Low-density metallic structures (or cellular metals) exhibit high stiffness, low weight, and tailorable properties that prove valuable in solving a host of design needs that exist today and exhibit excellent structural efficiency. The multifunctional performance of metal foams make them appealing for numerous uses, including thermal insulation, heat sinks, acoustic insulation, energy absorption devices (crash protection), lightweight structural sandwich panels (as the core material) and vibration damping devices. A detailed discussion of potential applications for metal foams is found in [3]. Critical to the integration of metallic foams into many of these applications is a full understanding of their behavior.

2. MANUFACTURE OF CELLULAR METALS

Foaming a material is an intricate process involving the appropriate interplay between the relevant physical properties. Surface tension, viscosity, film stability, and density are all factors that contribute to the stability of a foam in its liquid state and determine whether or not the foam can be formed [4,5,6]. Unfortunately, metals do not perform well with respect to these properties. Molten metals generally have a high surface tension, which makes it difficult to form air pockets; poor film stability, which allows cell walls to collapse easily; low liquid viscosity, which increases the liquid drainage rate; and a high density, which increases the mass of material that must be supported in the liquid state. This combination of properties inhibits the production of metallic foam from the liquid state. Recently, however, several cost-effective processes for making metallic foams have been developed, increasing their potential use in a number of applications, including: sandwich panels for lightweight structural components, energy absorption systems for protection from impacts, heat sinks for electronic devices, and acoustic insulation.

Open-cell metal foams (Duocel, ERG Materials & Aerospace Corporation; Oakland, CA) can be created using reticulated polymer foam as a consumable "pattern." The polymer foam is infiltrated with a heat-resistant material, the polymer is pyrolyzed, molten metal is cast into the mold, and then the mold

material is removed. This method gives a metal foam that is an exact replica of the original polymer foam, thus overcoming traditional obstacles in manufacturing metallic foam. Open-cell metal foams typically achieve maximum theoretical properties because they contain so few processing defects.

Closed-cell foams are made by both powder- and liquid-based routes. Cymat foam (Cymat; Mississauga, Ontario, Canada) is manufactured by injecting air into an aluminum melt containing 5-15% SiC particles (1-20μm) [7]. The injected air causes bubbles to rise to the surface of the melt; the molten foam is then conveyed off the surface. The ceramic particles stabilize the molten foam to prevent it from collapsing before it cools. Alporas foam (Shinko Wire Co., Amagasaki, Japan) is also made via a liquid-based route using titanium hydride (TiH_2) as a foaming agent. Approximately 1-3% TiH_2 is mixed into molten aluminum containing up to 8% calcium to increase viscosity and stabilize the foam. On heating in the molten aluminum, the TiH_2 decomposes, evolving hydrogen gas forming bubbles in the foam. Fraunhofer (IFAM, Bremen, Germany) and Alulight (Mepura, Ranshofen, Austria) aluminum foams use a powder metallurgical process in which aluminum and TiH_2 powders are mixed together, compacted, placed in a mold, and heated. No stabilizing agents are used. The material is never heated above the melting temperature of aluminum; therefore, foaming occurs in a semi-solid state. [7]

Individual hollow spheres can be bonded together to form a hollow-sphere foam in a number of ways. The interstitial spaces in a three-dimensional array of hollow spheres can be infiltrated with a bonding material such as epoxy or a low melting temperature metal; such materials are commonly referred to as syntactic foams. Examples of such materials include hollow metal spheres bonded with epoxy [8] and hollow alumina spheres in an aluminum [9,10] or magnesium [11-12] matrix. The interstitial volume between the spheres accounts for a substantial fraction of the total volume (26% for a close-packed arrangement of spheres) so that this technique cannot be used to produce low relative density materials. In addition, the use of a polymer or low melting temperature metal to fill the voids detracts from some of the potential benefits of a metal foam, such as high specific strength or high temperature properties. Hollow-sphere foams can also be made by applying heat and pressure to an assembly of metal or ceramic precursor hollow spheres. The combined heat and pressure flattens the contacts between the spheres, which then become diffusion bonded. Metallic foams of this type have been produced using hollow spheres created from gas atomized metallic powders [13] and metal powder slurries [14]. A third method for manufacturing hollow-sphere foams is to bond hollow spheres using a liquid phase that forms a bonded neck region between spheres. Hollow-sphere foams have been manufactured via this third method to form bronze, nickel, steel and titanium foams [8,14].

Optimized truss structures are produced in a similar fashion to open-cell foams. Virtually any castable alloy can be used to form a truss structure (Federal

Technology Group, Boseman, MT; formerly JAMCORP, Boston, MA). Truss structures can also be produced by bonding sheets of woven metal textiles [15].

3.   MECHANICAL BEHAVIOR OF CELLULAR METALS

The relative modulus and relative strength of open- and closed-cell foams can be found in [1] and a refinement for closed-cell foams is discussed in [16]. Open-cell foams exhibit a bending-dominated behavior as the cell struts deform by bending during loading. The theoretical behavior of a closed-cell foam exceeds that of an open-cell foam because there is additional material in the cell faces. Because of this, closed-cell foams exhibit stretching-dominated behavior during deformation. Unfortunately, in commercially available metallic foams, processing defects can dramatically reduce the performance by an order of magnitude at low relative densities [7,17].

A detailed analysis of the behavior of hollow-sphere foams is available in [18,19]. The theoretical performance of hollow-sphere foams is on par with that of closed-cell foams. Since hollow-sphere foams can be produced with fewer defects, they have the potential to perform up to three times better than existing closed-cell foams at a relative density of 10% and ten times better below a relative density of 5% [17]. The behavior of simple cubic packed (SC) and face-centered cubic packed (FCC) hollow-sphere foams is shown in Figure 1. The FCC hollow-sphere foam generally represents the best performance of optimally bonded hollow spheres that was measured in this work and SC hollow-sphere foam generally represents the performance of non-optimally bonded, random packed hollow spheres [17]

A variety of lattice-type materials have been studied in the recent literature including lattice block material [20,21], the octet-truss lattice [22], and most recently, the Kagomé-truss lattice [23]. The octet-truss lattice was studied in depth by [24] and is shown in Figure 1 because it is nearly an isotropic material. The equations for the behavior of the octet-truss lattice were obtained from [24]. The Hashin-Shtrikman upper bound for an isotropic porous material [24,25] is also plotted for comparison.

The performance of honeycomb (both in-plane and out-of-plane) is also shown for comparison in Figure 1 since it is a commonly used engineering material. The out-of-plane properties are directly proportional to the relative density. These represent an absolute upper bound for the performance of any material. An exception to this upper bound occurs in the case of out-of-plane relative strength in uniaxial compression because the honeycomb can undergo plastic buckling (calculated using Wierzbicki's method in [1]). Honeycomb is an extremely anisotropic material and the properties degrade

rapidly when the load is not aligned with the out-of-plane axis. A full description of the behavior of honeycomb is given in [1].
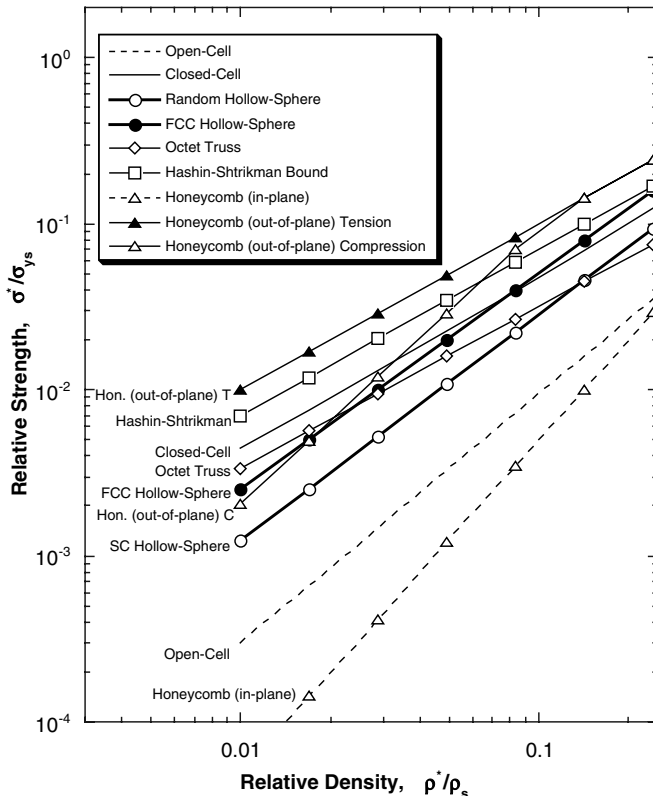
Figure 1. Relative strength versus relative density for different low-density structures. [17]

The relative strength of hollow-sphere foams lies between the theoretical performance of open- and closed-cell foams. The performance of optimized truss structures is similar to that of closed-cell foams and, for the Kagomé truss, approaches the behavior of a Hashin-Shtrikman porous material. Honeycombs are the most efficient structures when loaded purely out-of-plane. However, plastic buckling can decrease its performance at low relative densities. Further, since honeycomb is highly anisotropic, any in-plane loading results in severely reduced performance. Although the theoretical performance of closed-cell foams far exceeds that of open-cell foams, processing defects result in commercially available material that behaves similar to an open-cell material at low relative densities. Commercially available samples of other types of low-density metallic structures behave nearly as predicted. [17]

4.   SUMMARY

An overview was presented of various types of low-density metallic structures. There are numerous methods to manufacture these materials and they exhibit a wide range of mechanical properties. The use of any of these low-density materials will be dictated by the trade-off between cost and performance for a given application. Low-density metallic materials offer an exciting alternative for designers and engineers to achieve high structural efficiency in a variety of applications.

REFERENCES

1. L.J. Gibson, M.F. Ashby. Cellular Solids: Structure and Properties, 2nd Ed., Cambridge, Cambridge University Press, 1997.
2. L.J. Gibson, Annual Review of Materials Science 30, 2000, 191-227.
3. M.F. Ashby,et. al. in: Metal Foams: A Design Guide, Boston, Butterworth Heinemann, 2000.
4. C.J. Benning, in: Plastic Foams: the Physics and Chemistry of Product Performance and Process Technology. New York, Wiley-Interscience, 1969.
5. JJ. Bikerman, Foams, New York, Springer-Verlag, 1973.
6. A.J. Wilson, Foams: Physics, Chemistry and Structure, London, Springer-Verlag, 1989.
7. E. Andrews, W. Sanders, L.J. Gibson, Mat. Sci. Eng. A270,1999, 113-124.
8. J.P. Bonino et. al., Materiaux et Techniques (Paris) 78, 1990, 25-28.
9. S.P. Rawal, B.R. Lanning, M.S. Misra in: ICCM/9. Metal Matrix Composites, Vol. I, University of Zaragoza, Madrid, Spain,1993, 203-210.
10. S.A. Rickles, J.K. Cochran, T.H. Sanders, Jr, Cer. Eng. Sci. Proc. 10,1989, 1472-1484.
11. M. Hartmann, K. Reindel, R.F. Singer in: Porous and Cellular Materials for Structural Applications (Eds. D.S. Schwartz et. al.), Materials Research Society, Warrendale, Pennsylvania, 1998, 211-216.
12. M. Hartmann, Aluminium 75, 1999, 154-156.
13. D.J. Sypeck, P.A. Parrish, H.N.G. Wadley in: Porous and Cellular Materials for Structural Applications (Eds. D.S. Schwartz et. al.), Materials Research Society, Warrendale, Pennsylvania, 1998, 205-210.
14. K.M. Hurysz et. al. in: Porous and Cellular Materials for Structural Applications (Eds. D.S. Schwartz et. al.), Materials Research Society, Warrendale, Pennsylvania, 1998, 191-203.
15. D.J. Sypeck, H.N.G. Wadley, Journal of Materials Research 16, 2001, 890-897.
16. A.E. Simone, L.J. Gibson, Acta Mat. 46, 1998, 2139-2150.
17. W.S. Sanders in: Mechanical Behavior of Closed-Cell and Hollow-Sphere Metallic Foams, Massachusetts Institute of Technology ScD Thesis,USA, 2002.
18. W.S. Sanders, L.J. Gibson, Mat. Sci. Eng. A, 347, 2003, 70-85
19. W.S. Sanders, L.J. Gibson, Mat. Sci. Eng. A, 352, 2003, 150-161
20. J.C. Wallach, L.J. Gibson, Scripta Mat. 45, 2001, 639-644.
21. V.S. Deshpande, M.F. Ashby, N.A. Fleck, Acta Mat. 49, 2001, 1035-1040.
22. R.B. Fuller, U.S. Patent Serial no. 563,931.
23. S. Hyun, S. Torquato, Journal of Materials Research 17, 2002, 137-144.
24. V.S. Deshpande, N.A. Fleck, M.F. Ashby, J. Mech. Phys. Solids 49, 2001, 1747-1769.
25. Z. Hashin, S. Shtrikman., J. Mech. Phys. Solids 11, 1963, 127-140.

NEUTRON AND SYNCHROTRON NON-DESTRUCTIVE METHODS FOR RESIDUAL STRESS DETERMINATION IN MATERIALS FOR INDUSTRIAL APPLICATIONS

Fabrizio Fiori [1,3], Emmanuelle Girardin [2,3], Alessandra Giuliani [2,3], Adrian Manescu [1,3] and Franco Rustichelli[1,3]

1) Univ.Politecnica delle Marche, Dipartimento di Scienze Applicate ai Sistemi Complessi (Sez. Scienze Fisiche) , Via P.Ranieri 65, 60131 Ancona, Italy

2) Univ.Politecnica delle Marche, Dipartimento di Fisica e Ingegneria dei Materiali e del Territorio, Via Brecce Bianche, 60131 Ancona,Italy

3) INFM – Istituto Nazionale per la Fisica della Materia, U.d.R. Ancona, Italy

Abstract: Neutron and synchrotron radiation techniques are very powerful non-destructive methods for the characterisation of a wide variety of materials. In particular, neutron and synchrotron radiation diffraction is nowadays widely used for the evaluation of residual stresses induced by thermal and mechanical treatments in materials and components for industrial applications. A review is presented of the techniques mentioned above, and some applications to materials for technological applications will be presented.

Key words: Neutron diffraction, synchrotron radiation, residual stresses

1.   INTRODUCTION

Among the various non-destructive methods for the analysis of microstructural features of materials for technological applications, neutron and X-ray techniques have become more and more important in the the last decades. The development of Large Scale Facilities around Europe and in the rest of the world have contributed to the approach of more and more scientists to these techniques, for both fundamental and industrial research in the field of materials science. In particular, diffraction techniques have become one of the most used techniques for the analysis of residual stress states in materials and industrial components, induced by different

manufacturing method, thermal and mechanical treatments, as well as operating condition. The experimental determination of residual stresses is very important for what concerns the lifetime prediction of components. In fact their presence can influence, either positively or negatively, the mechanical performance of the material (such as the resistance under external static or fatigue loading). Moreover, the experimentally determined stresses can be used to validate numerical models describing and forecasting the mechanical performances of components. To this end, the standard X-ray diffraction, permitting the analysis of residual stresses only at the level of the surface layers of the material, is complemented by diffraction techniques making use of neutron beams and/or high-energy X-rays (synchrotron radiation), which allow the study of stresses in the bulk material.

Some examples of the application of neutron and high-energy X-ray diffraction for stress determination are reported and discussed in this work.

2.   DESCRIPTION OF THE TECHNIQUE

Exhaustive discussion of the principle of strain/stress measurement by diffraction techniques can be found in [1,2]. Very briefly, the method is based on the well-known Bragg's law

$$\lambda = 2d_{hkl} \sin\theta \tag{1}$$

In the case of neutron diffraction at steady sources (such as nuclear reactors), where the beam is usually monochromatic (fixed λ), the strain is detected in a chosen lattice plane family as the displacement of the Bragg peak angular position 2θ with respect to the unstrained material.

In the case of neutron spallation sources and high-energy X-rays (synchrotron radiation) sources, the beam is polychromatic, allowing the contemporary investigation of several lattice planes. In these cases the scattering angle 2θ is fixed, and the strain is evaluated as the shift in the wavelength corresponding to the Bragg peaks. Through the De Broglie relation, λ is usually linked to the neutron time-of-flight at spallation sources, and to the X-ray energy at synchrotron radiation sources. Finally, from the strain obtained by the measurements described above, stresses are obtained through the well-known elasticity theory equations (Hooke's law).

3.   EXPERIMENTAL RESULTS

3.1   Aluminium Alloy Shrink-Fit Disc-Ring System

The residual stresses induced by a new thermoelastoplastic coupling method for AA6082 aluminium alloy disc-ring systems used in automotive technology were determined by neutron diffraction, and compared to the ones measured in systems coupled through a standard thermoelastic method [3]. The geometry of the studied shrink-fit samples is shown in fig.1. In order to obtain the thermoelastic behaviour the ring was kept at 493 K for 30 minutes, and then it was coupled to the disc, kept at room temperature. Finally, the system was freely cooled in air. For the thermoelastoplastic coupling the ring was kept at 713 K for 30 minutes, and then coupled to the disc, kept at 493 K. Then the whole system was heated back to 713 K and kept there for 15 minutes. Finally, it was freely cooled in air. Neutron diffraction experiments were carried out on both the thermoelastic and the thermoelastoplastic samples.
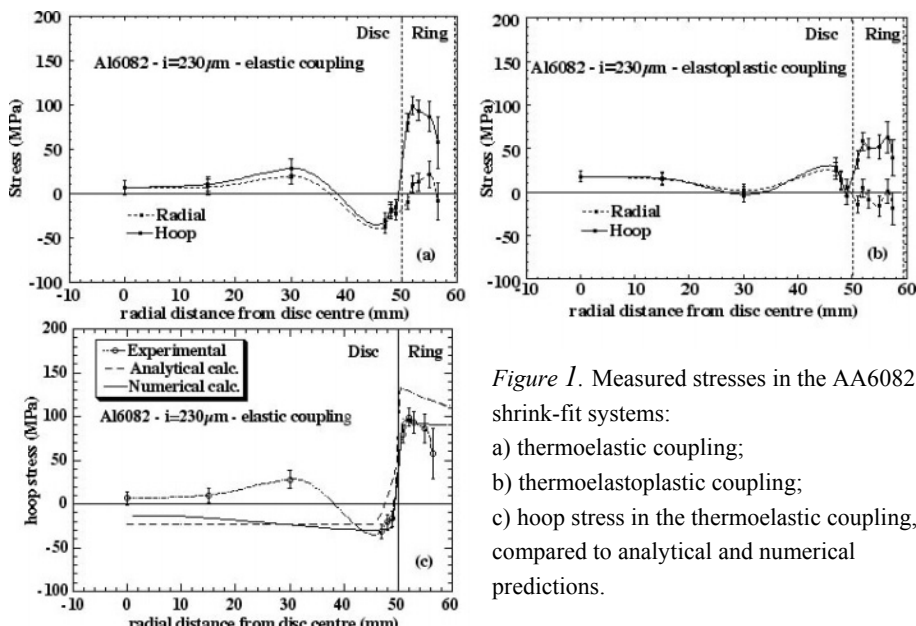
Figure 1. Measured stresses in the AA6082 shrink-fit systems:
a) thermoelastic coupling;
b) thermoelastoplastic coupling;
c) hoop stress in the thermoelastic coupling, compared to analytical and numerical predictions.

Measured stresses (figs.1a, 1b) showed the effectiveness of the thermoelastoplastic coupling, inducing lower tensile residual stresses with respect to the thermoelastic case. The comparison with analytic and

numerical models (fig.1c) showed the presence of already existing stresses (prior to coupling) in the disc, which were actually detected by neutron diffraction in an uncoupled disc [4].

3.2   Welds in Al Alloys for Aerospace Technology

Residual stresses induced by variable polarity plasma arc (VPPA) welding in an Al alloy 2219-T851 plate (6.5 mm thickness – Z direction, 62 mm in the direction parallel to the weld axis – Y direction, 48 mm in the direction perpendicular to it – X direction) were investigated by neutron diffraction [5]. Measurements were performed by neutron diffraction, using the time of flight (TOF) technique, with a 2x10x2 mm^3 sampling volume.
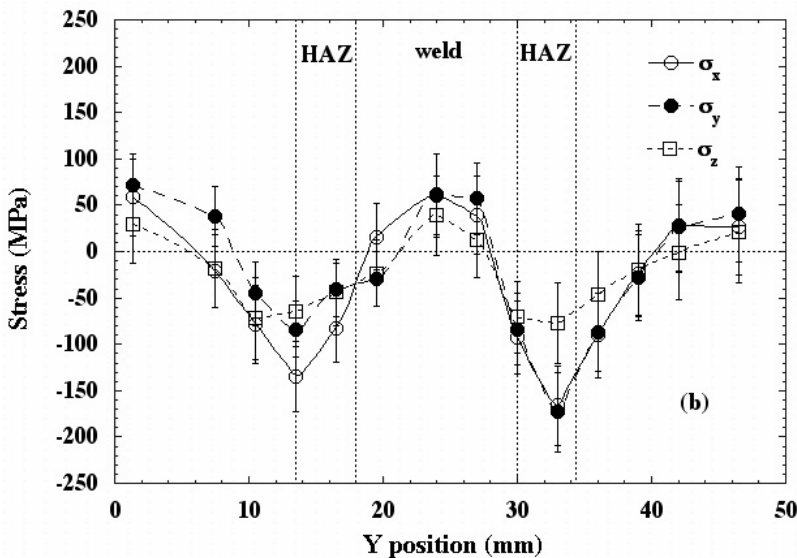
Figure 2. Residual stresses in theAl 2219 welded plate

Results (fig.2) show that the parent material is almost stress free. In the weld pool tensile bulk (around 60 MPa) stresses were found, whereas the opposite occurs in the heat-affected zones (HAZ). Curve shapes are consistent with theoretical and experimental behaviours reported in literature [6,7], and suggest the presence of "structure change stresses", according to Macherauch's definition [7]. This means that a superposition of the shrinkage stress due to different cooling rates inside and at the borders of the weld, and structural change stresses due to the presence of different phases can be outlined.

3.3   **Automotive Steel Crown Gears**

A systematic study of automotive steel crown gears was performed, with the aim of determining the influence of physical and process parameters on their mechanical performances under operation.

Residual stresses were determined by neutron diffraction in a gear manufactured using the net-shape forming technique and submitted to nitrocarburation surface treatment [8], and in gears machined in the standard way, and then submitted to different surface treatments such as multi-frequency induction tempering [9], quenching and nitriding [10] and case-hardening [11]. The results are shown in fig.3. The different surface thermal treatments give rise to comparable residual stresses in the machined gears, while they are sensibly lower in the net-shaped specimen, due to the higher porosity level left by the sintering process.
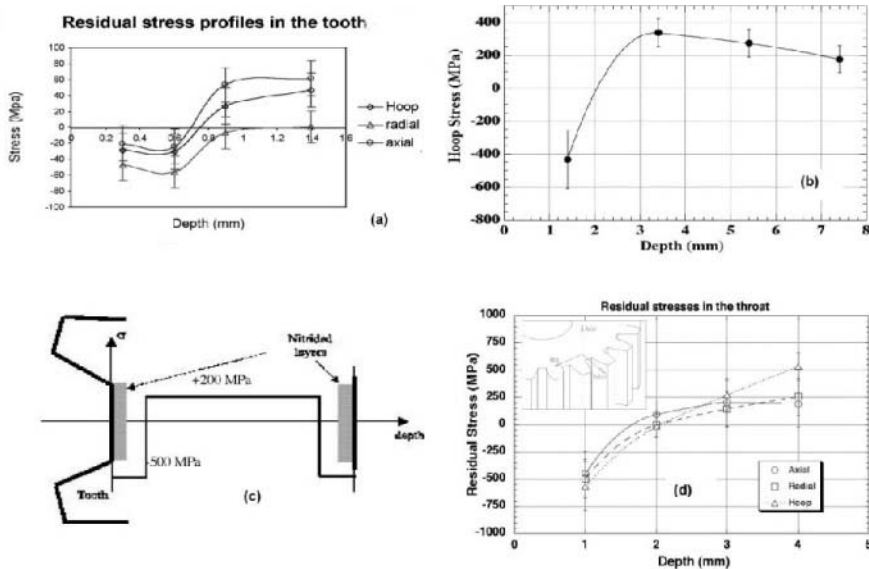
Figure 3. Residual stresses in automotive steel crown gears: (a) net-shaped and submitted to nitrocarburation surface treatment; machined by standard technology and submitted to (b) multi-frequency induction tempering, (c) quenching and nitriding, (d) case-hardening.

3.4   Hydroxyapatite Plasma Sprayed Coatings on Ti Substrate for Biomedical Applications

Energy dispersive synchrotron radiation measurements were performed in order to evaluate the stresses both in the coatings and in the substrates of Ti + HA compositional gradient coated specimens (A1-A4) [12]. The coatings were obtained by plasma spraying on Ti6Al4V substrates. Each of them consists of three different layers: a first layer of Ti (30 μm), a second one of 40% Ti + 60% HA (30 μm) and the last one of HA (120 μm). Also, a reference sample of pure HA coating (A5) on Ti6Al4V substrate was made. Different intensities of the plasma arc current and spraying distances were used for the different layers and coatings. The gauge volume size investigated in the synchrotron radiation experiments was 30x40x500 μm^3. The influence of the plasma spraying parameters on the residual stresses in our coatings is presented in fig.4.
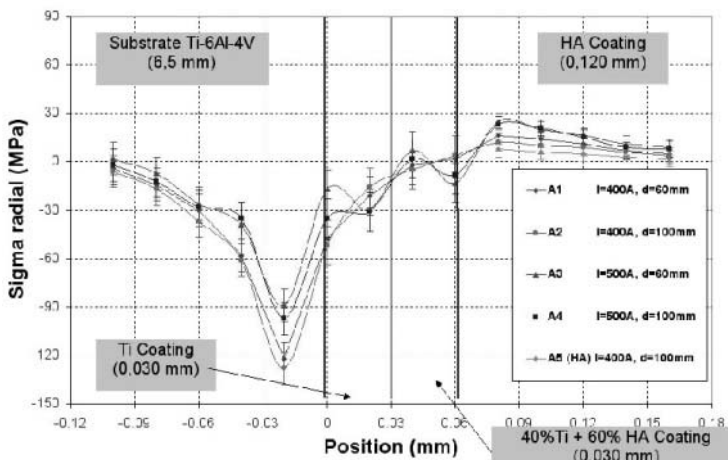
Figure 4. Radial stresses in samples with compositional gradient coatings having different spraying parameters, and in pure HA coating

The stresses in the substrate close to the interface with the Ti layer are higher in absolute value for a lower current intensity of the plasma arc, due to the fact that a higher intensity of the plasma arc implies a higher amount of heat transferred to the substrate, inducing a relaxation of the residual stresses. In the Ti layer, the stresses are slightly compressive. In fact they correspond to values averaged over highly compressive and tensile stresses predicted by the FEM analysis inside the experimental gauge volume. In the Ti + HA layer, negligible averaged macrostresses are obtained, independently from the plasma spraying parameters. In the HA layer, a

slight trend towards higher stress values is observed for a higher current intensity of the plasma arc. The measured tensile stresses are lower than 30 MPa. The stresses in the HA layer of the single coating sample are also tensile, but lower than those obtained for the compositional gradient coating samples, due to a higher level of porosity and microcracks [13]. In the samples with the same current intensity and different plasma spraying distance, no difference in the residual stress values was observed within the experimental error.

4.   CONCLUSIONS

Some examples of applications of neutron and synchrotron radiation diffraction applied to the determination of residual stresses in various industrial and technological components have been presented. The reliability of the technique has been shown, being able to determine residual stresses induced by various thermomechanical treatments, such as shrink-fit joints, welds and surface treatments in automotive and aerospace materials. It has been shown how, by this method, it is possible to determine stresses both in the coating and in the substrate of plasma-spray deposed hydroxyapatite layers on Ti alloy for biomedical applications.

REFERENCES

1. I.C.Noyan, J.B.Cohen, Residual Stresses - Measurement by Diffraction and Interpretation, Springer-Verlag, New York, 1987.
2. V.Hauk, Structural and Residual Stress Analysis by Nondestructive Testing: Evaluation, Application, Assessment, Elsevier Publ., 1997.
3. G.Albertini, M.Ceretti, G.Caglioti, F.Fiori, R.Monzani, L.Viviani, J. Neutron Res. Vol.9, No.2-4 (2001) 459.
4. G.Albertini, G.Caglioti, M.Ceretti, F.Fiori, F.Oggioni, F.Rustichelli, L.Viviani, Rad. Phys. Chem. Vol.51, N.4-6 (1998) 525.
5. G.Albertini, G.Bruno, B.D.Dunn, F.Fiori, W.Reimers, J.S.Wright, Mat. Sci. Engng. A224 (1997) 157.
6. J.Schröder, J.H.Root, T.M.Holden, M.Koçak, GKSS Report 93/E/82.
7. E.Macherauch, H.Wohlfahrt, Materialprüf. 19 (1977) 272.
8. G.Albertini, G.Annibali, F.Fiori, M.Marcantoni, E.Quadrini, F.Turquier, J. Neutron Res. Vol.9, No. 2-4 (2001) 129.
9. G.Albertini, G.Bruno, F.Fiori, E.Girardin, A.Giuliani, E.Quadrini, F.Romani, Physica B 276-278 (2000) 925.
10. G.Annibali, G.Bruno, A.Giuliani, A.Manescu, M.Marcantoni, F.Fiori, F.Turquier, Appl. Phys. A 74 (2002) S1698-S1700.

11. G.Albertini, G.Bruno, F.Fiori, M.Marcantoni, E.Quadrini, F.Turquier, Mat. Sci. Forum Vol. 404-407 (2002) 191.

12. A. Manescu , G. Albertini, P. Fogarassy, A. Lodini, N. Markocsan, presented at MECASENS 2003 (Manchester, UK, September 2003); submitted to J. Neutron Res.

13. A. Manescu, PhD Thesis, University of Ancona, December 2002.

WORKSHOP PARTICIPANTS

Lyudmyla Artyukh
Institute for Problems of
Materials Science, National
Academy of Science
3 Krzhyzhanivskoho Street
Kyiv-142, 03680 Ukraine
dep6@ipms.kiev.ua

Oleg Bankovsky
Institute for Problems of
Materials Science, National
Academy of Science
3 Krzhyzhanivskoho Street
Kyiv-142, 03680 Ukraine
Rapid@materials.kiev.ua

Mykola Bega
Institute for Problems of
Materials Science, National
Academy of Science
3 Krzhyzhanivskoho Street
Kyiv-142, 03680 Ukraine
fsa@materials.kiev.ua

Olga Bilous
Institute for Problems of
Materials Science, National
Academy of Science
3 Krzhyzhanivskoho Street
Kyiv-142, 03680 Ukraine
fsa@materials.kiev.ua

Anatoliy Bondar
Institute for Problems of
Materials Science, National
Academy of Science
3 Krzhyzhanivskoho Street
Kyiv-142, 03680 Ukraine
bondar@materials.kiev.ua

Kelly Brown
UES, Inc.
4401 Dayton-Xenia Rd.
Dayton, Ohio 45432-1894 USA
Kelly.Brown@wpafb.af.mil

Oleksandr Bykov
Institute for Problems of
Materials Science, National
Academy of Science
3 Krzhyzhanivskoho Street
Kyiv-142, 03680 Ukraine
abykov@materials.kiev.ua

Maryna Bulanova
Institute for Problems of
Materials Science, National
Academy of Science
3 Krzhyzhanivskoho Street
Kyiv-142, 03680 Ukraine
bulanova@materials.kiev.ua

Pasquale Cavaliere
Dept. of Ingegneria dell-
Innovazione, University of Lecce,
Via per Arnesano I-73100, Lecce,
Italy
pasquale.cavaliere@unile.it

Anatoliy Demchyshin
Institute for Problems of
Materials Science, National
Academy of Science
3 Krzhyzhanivskoho Street
Kyiv-142, 03680 Ukraine
Rapid@materials.kiev.ua

Sergey Firstov
Institute for Problems of
Materials Science, National
Academy of Science
3 Krzhyzhanivskoho Street
Kyiv-142, 03680 Ukraine
fsa@ipms.kiev.ua

George Frommeyer
Max-Planck-Institute
Max-Planck-Strasse 1
40237 Duesseldorf Germany
frommeyer@mpie.de

Lluis Gimeno-Fabra
European Aeronautic Defense &
Space Co., Metals Corporate
Research Center. 81663 Munich,
Germany
Lluis.Gimeno-Fabra@eads.net

Iryna Gornaya
Institute for Problems of
Materials Science, National
Academy of Science
3 Krzhyzhanivskoho Street
Kyiv-142, 03680 Ukraine
Rapid@materials.kiev.ua

Konstantin Grinkevych
Institute for Problems of
Materials Science, National
Academy of Science
3 Krzhyzhanivskoho Street
Kyiv-142, 03680 Ukraine
Rapid@materials.kiev.ua

Craig Hartley
Air Force Office of Scientific
Research, AFOSR/NA
4015 Wilson Blvd., Room 713
Arlington, VA 22203-1954 USA
Craig.Hartley@afosr.af.mil

Ted Hartwig
Texas A&M University,
Department of Mechanical
Engineering,
College Station, TX 77843-3123
USA
thartwig@mengr.tamu.edu

Ramiz Hasanov
Azerbaijan State Oil Academy
20 Azadlig Ave., Baku 370010,
Azerbaijan
ramizhasanov@box.az

Orest Ivasishin
Kurdyumov Institute for Metal
Physics, National Acad. Science
36 Vernadsky Blvd.
03142 Kyiv, Ukraine
ivas@imp.kiev.ua

Myroslav Karpets
Institute for Problems of
Materials Science, National
Academy of Science
3 Krzhyzhanivskoho Street
Kyiv-142, 03680 Ukraine
Rapid@materials.kiev.ua

Leonid Kulak
Institute for Problems of
Materials Science, National
Academy of Science
3 Krzhyzhanivskoho Street
Kyiv-142, 03680 Ukraine
Rapid@materials.kiev.ua

Kumar Jata
Air Force Research Laboratory
AFRL/MLL, 2230 Tenth Street
Wright-Patterson AFB, OH 45433
USA
Kumar.Jata@wpafb.af.mil

Yaroslav Kompan
Paton Welding Institute
11 Bozhenko Str.,
Kyiv-150, 03680 Ukraine
magnit@ion.kiev.ua

Tatiana Konstantinova
Donetsk Physical and Technical
Institute, 72 Luxemburg Str.,
Donetsk, 83114 Ukraine
tatiana@konstant.fti.ac.donetsk.ua

Oleksandr Koval
Institute for Problems of
Materials Science, National
Academy of Science
3 Krzhyzhanivskoho Street
Kyiv-142, 03680 Ukraine
vasilev@ipms.kiev.ua

Natalya Korzhova
Institute for Problems of
Materials Science, National
Academy of Science
3 Krzhyzhanivskoho Street
Kyiv-142, 03680 Ukraine
milman@ipms.kiev.ua

Mykola Kuzmenko
Institute for Problems of
Materials Science, National
Academy of Science
3 Krzhyzhanivskoho Street
Kyiv-142, 03680 Ukraine
Rapid@materials.kiev.ua

Torben Leffers
Materials Research Department
Riso National Laboratory
DK-4000 Roskilde Denmark
jytte.pihl.nielsen@risoe.dk

Mykola Levitsky
Physico-Technological Institute
of Metals and Alloys
34/1 Vernadsky Ave.,
Kiev-142, 03680 Ukraine
Rapid@materials.kiev.ua

Dina Lotsko
Institute for Problems of
Materials Science, National
Academy of Science
3 Krzhyzhanivskoho Street
Kyiv-142, 03680 Ukraine
lotsko@materials.kiev.ua

Madan Mendiratta
UES, Inc.
4401 Dayton-Xenia Rd.
Dayton, Ohio 45432, USA
Madan.Mendiratta@wpafb.af.mil

Sarath Menon
UES, Inc.
4401 Dayton-Xenia Rd.
Dayton, Ohio 45432, USA
Sarath.Menon@wpafb.af.mil

Yuliy Milman
Institute for Problems of
Materials Science, National
Academy of Science
3 Krzhyzhanivskoho Street
Kyiv-142, 03680 Ukraine
milman@materials.kiev.ua

Daniel Miracle
Air Force Research Laboratory
AFRL/MLLMD, Bldg. 655
2230 Tenth Street
Wright-Patterson AFB
Ohio 45433-7817, USA
Daniel.Miracle@wpafb.af.mil

Oleksandr Molyar
Antonov complex,
1 Tupoleva Street,
Kyiv, 03062 Ukraine
molyar@antonov.com

Frank Montheillet
Ecole Nationale Supérieure des
Mines de Saint-Etienne
Centre Science des Matériaux et
des Structures
42023 Saint-Etienne Cedex 2
France
montheil@sms.emse.fr

Fumio Morito
Chiba Institute of Technology,
Narashino, Chiba Japan
morito.fumio@nims.go.jp

Andreas Mortensen
MX D 121 Laboratory of
Mechanical Metallurgy
Swiss Federal Institute of
Technology EPFL, CH-1015,
Lausanne Switzerland
Andreas.Mortensen@epfl.ch

Oleg Neikov
Institute for Problems of
Materials Science, National
Academy of Science
3 Krzhyzhanivskoho Street
Kyiv-142, 03680 Ukraine
neiko@mail.ru

Orest Ostash
Karpenko Physico-Mechanical
Institute, 5 Naukova Street
Lviv, Ukraine
ostash@ah.ipm.lviv.ua

Ľudovit Parilak
Institute of Materials Research
SAS, Watsonova 47, 04353,
Košice, Slovak Republic
parilak@imrnov.saske.sk

Engels Pechkovskyi
Institute for Problems of
Materials Science, National
Academy of Science
3 Krzhyzhanivskoho Street
Kyiv-142, 03680 Ukraine
epp@materials.kiev.ua

Yuriy Podrezov
Institute for Problems of
Materials Science, National
Academy of Science
3 Krzhyzhanivskoho Street
Kyiv-142, 03680 Ukraine
podrezov@materials.kiev.ua

George Radnoczi
Research Institute for Technical
Physics and Materials Science
Physical Materials Science Dept.,
Konkoly-Thege u. 29-33
1121 Budapest XII, Hungary
radnoczi@mfa.kfki.hu

Tamara Rogul
Institute for Problems of
Materials Science
3 Krzhyzhanivskoho Street
Kyiv-142, 03680 Ukraine
fsa@ipms.kiev.ua

Franco Rustichelli
Istituto di Scienze Fisiche
Universita' degli Studi di Ancona
Via P. Ranieri, 65
60131 Ancona, Italy
isf@alisf1.unian.it

Gennadiy Salishchev
Institute for Metals
Superplasticity Problems,
39 Khalturina Street
Ufa 450001, Russian Federation
gensal@ipsm.rb.ru

Wynn Sanders
Air Force Research Laboratory
Bldg 655, 2230 Tenth Street
Wright-Patterson AFB, OH
45433, USA
Wynn.Sanders@wpafb.af.mil

Oleg Senkov
UES, Inc.
4401 Dayton-Xenia Rd.
Dayton, Ohio 45432, USA
Oleg.Senkov@wpafb.af.mil

Marat Shagiev
Institute for Metals
Superplasticity Problems,
39 Khalturina Street
Ufa 450001, Russian Federation
shagiev@mx.ibaraki.ac.jp

Vaclav Sklenicka
Institute of Physics of Materials
Zizkova, 22,
CZ-616 62, Brno
Czech Republic
sklen@ipm.cz

Oleksandr Sirko
Institute for Problems of
Materials Science, National
Academy of Science
3 Krzhyzhanivskoho Street
Kyiv-142, 03680 Ukraine
milman@ipms.kiev.ua

Oleksandr Slipenyuk
Institute for Problems of
Materials Science, National
Academy of Science
3 Krzhyzhanivskoho Street
Kyiv-142, 03680 Ukraine
milman@ipms.kiev.ua

Hein-Peter Stüwe
Erich Schmid Institute of Material
Science, Austrian Academy of
Sciences in Leoben,
Jahnstrasse 12
A-8700 Leoben, Austria
stuewe@unileoben.ac.at

P.R. Subramanian
GE-Global Research Center
PO Box 8, K1-MB265
Schenectady, NY 12301 USA
subrampr@crd.ge.com

Ruslan Valiev
Institute of Physics of Advanced
Materials, Ufa State Aviation
Technical University
12 K. Marx Street,
Ufa 450000, Russian Federation
RZValiev@mail.rb.ru

Robert Varin
Dept. of Mechanical Engineering
University of Waterloo
Waterloo, Ontario N2L 3G1
Canada
rvarin@uow.edu.au

Victor Varyukhin
Donetsk Physical and Technical
Institute
72 Luxemburg Street,
Donetsk, 83114 Ukraine
var@hpress.dipt.donetsk.ua

438

Oleksandr Vasylyev
Institute for Problems of
Materials Science, National
Academy of Science
3 Krzhyzhanivskoho Street
Kyiv-142, 03680 Ukraine
vasilev@ipms.kiev.ua

Tamara Velikanova
Institute for Problems of
Materials Science, National
Academy of Science
3 Krzhyzhanivskoho Street
Kyiv-142, 03680 Ukraine
dep6@ipms.kiev.ua

Mykokla Yefimov
Institute for Problems of
Materials Science, National
Academy of Science
3 Krzhyzhanivskoho Street
Kyiv-142, 03680 Ukraine
milman@ipms.kiev.ua

Vadym Zamkov
Paton Welding Institute
11 Bozhenko Street,
Kyiv-150, 03680 Ukraine
zamkov@uct.kiev.ua

Subject Index